

# NEW PREDICTION OF CRACKS PROPAGATION IN REPAIRED STEEL PLATE WITH BONDED COMPOSITE PATCH AT CYCLIC LOADING

Sofiane MAACHOU<sup>\*✉</sup>, Belaïd MECHAB<sup>\*\*✉</sup>, Bel Abbès BACHIR BOUIADJRA<sup>\*\*✉</sup>, Mokadem SALEM<sup>\*\*✉</sup>

<sup>\*</sup>University Centre of Maghnia, Algeria. Laboratory of Mechanics and Physics of materials (LMPM),  
University Djillali Liabes of Sidi bel abbes, Algeria

<sup>\*\*</sup>Laboratory of Mechanics and Physics of materials (LMPM),  
University Djillali Liabes of Sidi bel abbes, Algeria

[sofianemaachou@gmail.com](mailto:sofianemaachou@gmail.com), [bmechab@yahoo.fr](mailto:bmechab@yahoo.fr), [bachirbou@yahoo.fr](mailto:bachirbou@yahoo.fr), [moka\\_salem@yahoo.fr](mailto:moka_salem@yahoo.fr)

received 18 October 2023, revised 27 February 2024, accepted 4 March 2024

**Abstract:** This study presents a numerical prediction of the fatigue life of steel panels repaired by a composite patch. The effect of length cracks, the stress ratio  $R$  and properties of the patch is presented. The obtained results show that the bonded composite repair significantly reduces the stress intensity factors at the tip of repaired cracks. The results are in a good agreement with those in the literature. The Monte Carlo method is used to predict the distribution function governing crack propagation in fatigue analysis. In computing the failure probability of the structure, we consider the statistical uncertainty associated with key variables, along with the previously discussed model uncertainty. The results obtained highlight the considerable impact of variations in crack length and stress ratio on the distribution function. Notably, uncertainty in these parameters significantly amplifies the probability of structural failure in plates, thereby diminishing overall structural durability.

**Keywords:** Repair composite plate, fracture mechanics, fatigue, Monte Carlo method, stress ratio

## 1. INTRODUCTION

Fatigue is a phenomenon where, due to the influence of cyclic, repetitive, or fluctuating stresses or strains, there is a transformation in the material's local characteristics, potentially resulting in the development of cracks and, eventually, structural failure. Accurately predicting fractures and ensuring the reliability of structures across diverse real-world applications are of utmost importance, considering their significant implications for both economic considerations and safety [1].

The repairing damaged structures by composite patch are applied in marine structures, in oil and gas industries for the repair of corroded pipes and pressure vessels as well as in civil engineering. Lifetime prediction is necessary for the design of structures subjected to fatigue loads, [2, 3].

A.A. Baker [4] is credited as the initial trailblazer in these explorations, which took place at the aeronautical and maritime research laboratory of the Royal Australian Air Force. The challenge of implementing composite patches arises from a complex interplay of numerous factors. These factors encompass the mechanical characteristics of diverse materials (such as aluminum panels, composites, and adhesives), the geometric attributes of the composite patch, and the specific loading conditions.

Several authors have computed the stress intensity factor at the crack tip of repairing cracks among them [5 – 14]. These researches have shown that, after repair, the stress intensity factor exhibits an asymptotic behaviour as the crack length increases. The durability and reliability of structures repaired with composite patches depend mainly on the mechanical and thermal behavior of the adhesive layer. These are the most essential points for studying the causes of failure and the degradation of the entire repair [15 – 23].

The primary objectives of this investigation are to estimate the fatigue life of steel panels that have undergone repair using a composite patch and to examine the influence of crack length, the stress ratio  $R$ , and patch properties. The study employs the Monte Carlo method to forecast the distribution function governing crack propagation in fatigue. Additionally, the calculation of the structural failure probability takes into consideration both the statistical uncertainty associated with fundamental variables and the model uncertainty, as previously outlined.

## 2. PRESENTATION OF THE MODEL

### 2.1. Geometrical of the model

The basic geometry of the cracked structure considered in this study is shown in Fig. 1. Consider a plate with the following dimensions: width  $W_p=100\text{mm}$  and thickness  $T_p=2\text{mm}$ . The plate is subjected to uniaxial tensile following a stress value equal to 100 MPa for elastic analysis. A central crack of length  $2a=6\text{mm}$  perpendicular to the loading axis was supposed to exist in the plate.

This crack is repaired with boron/epoxy and graphite/epoxy composites patches. The laminate consists of 11 symmetrical plies with a thickness of 0.132mm per ply ( $T_r=1.452\text{mm}$ ), and the stacking sequence is as follows  $[-45^\circ, 0^\circ, 0^\circ, +90^\circ, 0^\circ, 0^\circ, 0^\circ, 0^\circ, 0^\circ, +45^\circ]$ s. With width  $W_r=99\text{mm}$ .

The adhesive is used to bond the patch on cracked plate: FM73 (tab. 2), Epoxy adhesive. The adhesive thickness  $T_a$  is taken equal to 0.132mm.

The boundary conditions are:  $U_x = U_z = U_{Rx} = U_{Ry} = U_{Rz} = 0$  and  $U_y \neq 0$ .

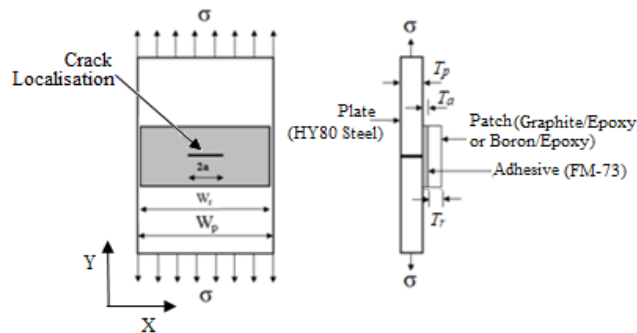


Fig. 1. Geometrical model

## 2.2. Elastic properties of the model

The elastic properties of the HY80 steel plate used for the manufacture of gas pipelines and the composite patch are given in Table 1, and the adhesive is given in Table 2.

Tab. 1. Mechanical properties of model studied [24]

	HY80 steel	Boron/epoxy	Graphite/epoxy
$E_L$ [MPa]	$20.6843 \times 10^4$	$20.6843 \times 10^4$	$17.2369 \times 10^4$
$E_T$ [MPa]	-	$19.3053 \times 10^3$	$10.3421 \times 10^3$
$G_{LT}$ [MPa]	-	$5.17107 \times 10^3$	$4.82633 \times 10^3$
$\nu_{LT}$	0.33	0.3	0.31
$\nu_{TL}$	-	0.14	0.13
$\alpha_L$ [K <sup>-1</sup> ]	-	$4.3 \times 10^{-6}$	$-7 \times 10^{-7}$
$\alpha_T$ [K <sup>-1</sup> ]	-	$1.87 \times 10^{-5}$	$3.6 \times 10^{-5}$

Tab. 2. Mechanical properties of Adhesive FM-73 [24]

$G_{LT}$ [MPa]	413.368
$\nu_{LT}$	0.33

## 2.3. Theoretical model

We used a calculation code for studying fatigue crack propagation to predict the fatigue life of metal structures called AF-GROW.

The NASGRO model was developed and modified by Maierhofer et al. [25] is applied to predict crack propagation. The crack propagation equation used by NASGRO is:

$$\frac{da}{dN} = C \left[ \left( \frac{1-f}{1-R} \right) \Delta K \right]^n \frac{\left( 1 - \frac{\Delta K_{th}}{\Delta K} \right)^p}{\left( 1 - \frac{K_{max}}{K_{cr}} \right)^q} \quad (1)$$

where:

$$\Delta K = K_{max} - K_{op} \quad (2)$$

$K_{max}$  : maximum stress intensity factor;

$$K_{max} = Y \sigma_{max} \sqrt{\pi a} \quad (3)$$

$K_{op}$  : crack opening stress intensity factor corresponds to the minimum value;

$$K_{op} = Y \sigma_{min} \sqrt{\pi a} \quad (4)$$

$K_{cr}$  : critical stress intensity factor

$$K_{cr} = Y \sigma_{cr} \sqrt{\pi a_{cr}} \quad (5)$$

The function  $f$  is:

$$f = \frac{K_{op}}{K_{max}} \quad (6)$$

Tab. 3. NASGRO equation parameters for HY80 steel [24]

C	n	p	q
$3.0101 \times 10^{-11}$	2.5	0.25	0.25

## 3. RESULTS AND DISCUSSION

### 3.1. Comparison of FEM and analytical results

Fig. 2 shows a comparative analysis of the stress intensity factor SIF variation obtained from the FEM results, developed in this work, and that resulting from an analytical solution (7). The stress intensity factor SIF is the only significant parameter, the relation between the far applied stress on the plate  $\sigma$  and the stress intensity factor  $K_I$  is as follows:

$$K_I = Y \sigma \sqrt{\pi a} \quad (7)$$

with:  $Y = 1.12$

It can be seen, according to Fig. 2 that the presence of the patch has a considerable effect on the stress intensity factor SIF variation at the crack tip. It shows that the patch repair highly decreases the stress intensity factor, the maximum reduction of stress intensity factor  $K_I$  is about 70% of the crack length  $a=40$ mm.

The analytical solution gives a good agreement of the stress intensity factor compared with the finite element method.

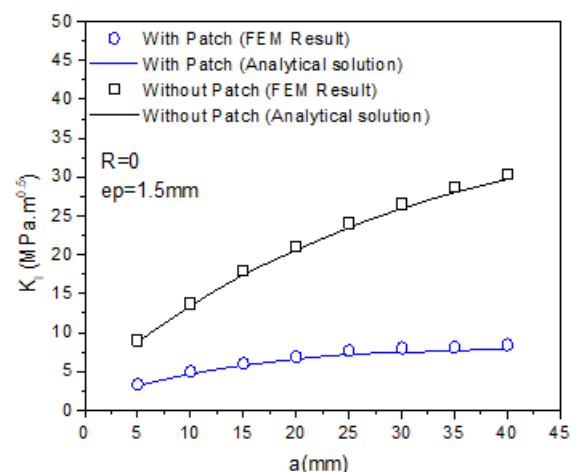


Fig. 2. Variation of the SIF according to the crack length for the cases with and without patch for analytical and FEM solution

### 3.2. Effect of the stress ratio R

In cyclic loading, the stress ratio plays an important role in the development of fatigue cracking in healthy and repaired structures.

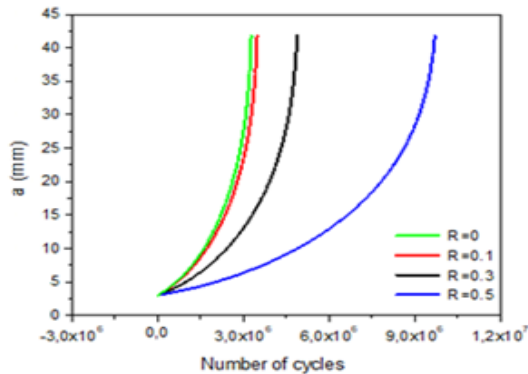


Fig. 3. Illustrates the effect of the variation in crack length as a function of the number of cycles for different value of R

The study showed that the fatigue life increases for the repaired plate compared with the unrepaired one, the cycle of failure

is double for all stress ratios studied. When the stress ratio R increases from 0 to 0.5 the cycle of failure increases because of higher stress values (See Fig. 3).

### 3.3. Effect of patch properties

To evaluate the influence of the patch material on crack propagation (initial crack  $a=3\text{mm}$ ) and to highlight the repair process of a central crack, we chose two patches, boron/epoxy and graphite/epoxy, with identical geometric shapes and different mechanical properties, to repair a cracked HY80 steel plate.

Fig. 4 illustrates the effect of the mechanical properties of the patch on the variation in crack length as a function of the number of cycles without repair and with repair (boron/epoxy and graphite/epoxy).

For the variation in crack propagation life, for the unrepaired and repaired plate with boron/epoxy and graphite/epoxy, for the different stress ratios is very distinct, seeing the better properties of the composite patches for repair and absorption of the stresses that stress the crack head, since these patches improve and increase the life of this plate.

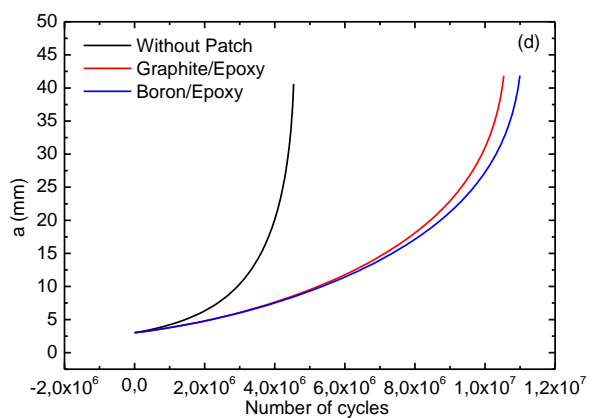
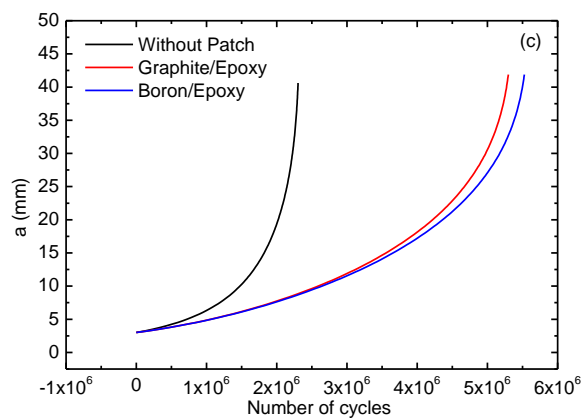
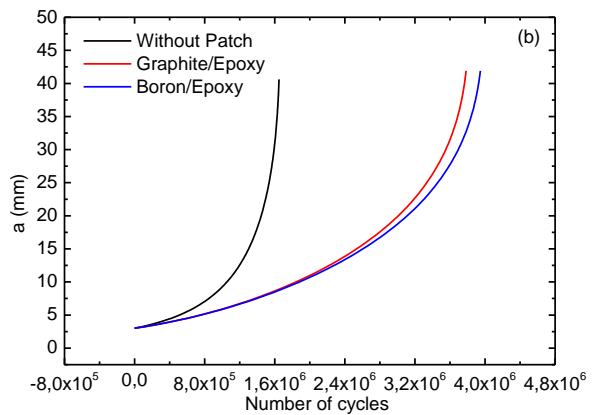
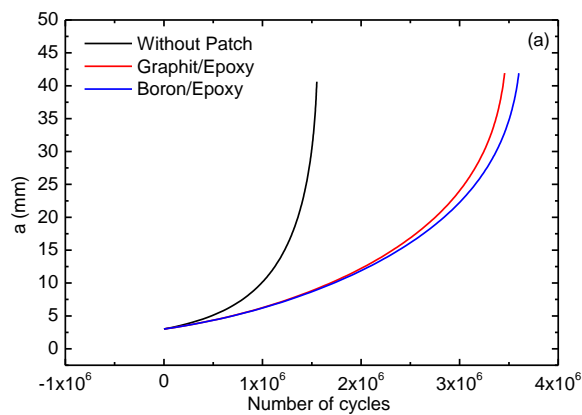


Fig. 4. Illustrates the effect of the specimen structure on the variation in crack length as a function of the number of cycles without repair and with repair process (boron/epoxy and graphite/epoxy). a)  $R=0$ , b)  $R=0.1$ , c)  $R=0.3$ , d)  $R=0.5$

## 4. PROBABILISTIC ANALYSIS

### 4.1. Random parameters and fracture response

The density function is evaluated by using Monte Carlo method. The basic idea is to draw random samples for the input parameters, then to compute the mechanical response for each sample. we have realised this work by the FORTRAN program, response by using Monte Carlo method. To achieve a high accuracy of the results, we have carried out 105 simulations.

Consider a cracked structure with uncertain mechanical and geometric characteristics that is subject to random loads. Denote by  $X$  an  $N$ -dimensional random vector with components characterizing all uncertainties in the system and loading parameters. For example, the possible random components are: geometric parameters,  $H$ ,  $W$ , and  $L$ , mechanical parameters,  $E$ ,  $\nu$ , ratio  $R$  varies from 0 to 0.5 and length of cracks  $a$  varies from 5 to 30mm: All or some of these variables can be modeled as random variables. Hence, any relevant fracture response, such as the  $K_I$  and  $(a)$ , may be evaluated by the probability.

The Monte Carlo method is used to predict the distribution function of the mechanical response, the sensitivities of the mechanical response are evaluated regarding the uncertainties in the design variables. The fundamental concept involves generating random samples for the input parameters and subsequently calculating the mechanical response for each one. As a substantial number of Monte Carlo samples are collected, it enables us to perform statistical analysis on the response datasets, ultimately yielding the probability density function.

The basic idea is to draw random samples for the input parameters, then to compute the mechanical response. In order to capture the role of the random variables, the sensitivity of the  $R(x)$  regarding the uncertainties of the input parameters was analysed, Table 4.

Tab. 4. Random variables and corresponding parameters

Variable	Mean	Coefficient of variation (COV)
$E(\text{MPa})$	20.6843.104	1%
$\nu$	0.3	1%
$HP(\text{mm})$	100mm	2%
$WP(\text{mm})$	100mm	2%
$TP(\text{mm})$	100mm	2%
$a(\text{mm})$	20mm	3%

Tab. 5. Mean  $R(x)$  and fitting error for probabilistic distributions

Fitting probability density functions	Average $R(x)$	Least square fitting error
Gaussian	2,72474.106	0%

Tab. 6. Random variables and corresponding parameters of stress intensity factor

Length of crack (a)	Mean	Standard deviation
20	6,88762	3,44381

### 4.2. Probabilistic results

Fig. 5 plots the histograms of the  $R$  obtained by Monte Carlo simulations. The probability density function PDF is obtained by fitting the histogram with theoretical models three distribution laws are investigated: Gaussian it can be clearly observed that the three distributions give more or less good approximation of the  $R$  probability density function, with good estimation of the average.

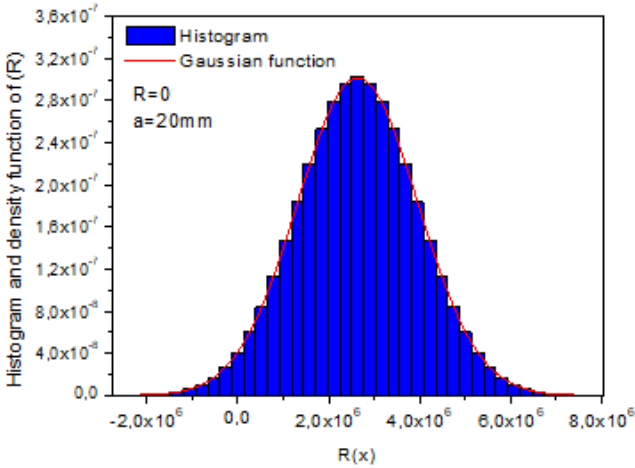


Fig. 5. Histogram and probability density function of  $R$

Figs. 6 - 7 show the probability density of the ratio  $R$  and the crack length  $a$ . We have noted that when the value of the ratio  $R$  and the crack length  $a$  is large, the value of the probability density is low and the failure rate is high.

It can be seen that the margin increases significantly with the uncertainties associated with the ratio  $R$  is the crack length  $a$ , leading to a higher probability of failure.

Finally, we note that the ratio  $R$  and the crack length  $a$ , are the important factor influencing on the durability of structure.

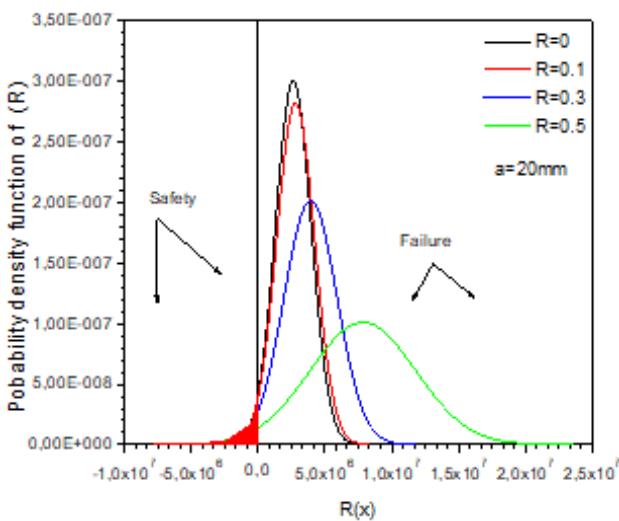


Fig. 6. Probability density function of  $R$



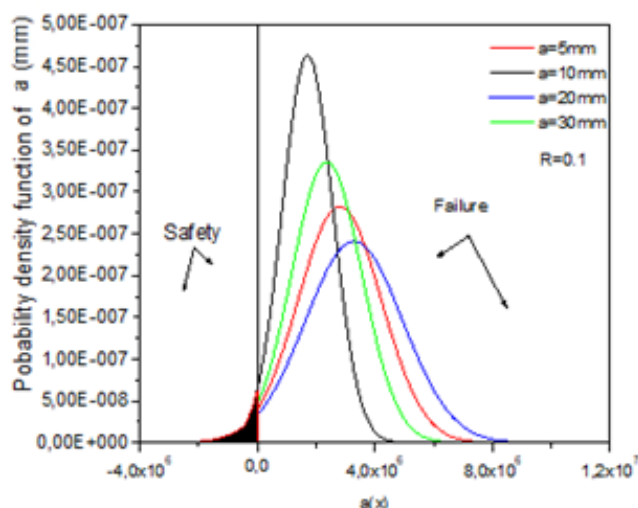


Fig. 7. Probability density function of a

## 5. CONCLUSIONS

The work we have carried out has enabled us to examine the influence of patch material properties on the fracture parameter values calculated for a plate subjected to tensile stress containing a central crack. The qualities of the patch material, the crack length and the stress ratio have a direct influence on the fatigue life of the structures.

Fatigue results have shown that increasing the stress ratio increases crack propagation velocity, leading to an increase in the values of cycles to fracture. For composite patch-repaired plates, an increase in stress ratio leads to a reduction in repair efficiency, resulting in an increase in numbers of cycles to fracture.

The presence of a patch considerably reduces crack propagation, which can delay the speed of cracking and subsequently increase the fatigue life of the structure. The results are in a good agreement with those in the literature [26]. The Monte Carlo method is used to predict the distribution function of propagation of crack in the fatigue.

The failure probability of the structure was calculated by taking into account both the statistical uncertainty on the basic variables and the model uncertainty as previously discussed.

According to the obtained results, we note that the crack length variations and the stress ratio are important factors influencing the distribution function.

Finally, we note that the ratio  $R$  and the crack length  $a$ , are the important factor influencing on the durability of structure.

## List of Symbols


$W_P$	Width of plate [mm]
$T_P$	Thickness of plate [mm]
$\sigma$	Stress [MPa]
$a$	Length of crack [mm]
$T_r$	Thickness of patch [mm]
$W_r$	Width of patch [mm]
$T_a$	Thickness of adhesive [mm]
$E_L$	Longitudinal Young's modulus [N/mm <sup>2</sup> ]
$E_T$	Transverse Young's modulus [N/mm <sup>2</sup> ]
$G_{LT}$	Shear modulus in XY- plane direction [N/mm <sup>2</sup> ]
$\nu_{LT}$	Poisson's ratio modulus in XY- plane direction

$\nu_{TL}$	Poisson's ratio modulus in YX- plane direction
$\alpha_L$	Longitudinal coefficients of thermal expansion [K <sup>-1</sup> ]
$\alpha_T$	Transverse coefficients of thermal expansion [K <sup>-1</sup> ]
$C, n, p$ and $q$	Material parameters (see Tab. 3);
$R$	Stress ratio;
$K_{max}$	Maximum stress intensity factor [MPa.m <sup>1/2</sup> ]
$K_{op}$	Crack opening stress intensity factor [MPa.m <sup>1/2</sup> ]
$K_{cr}$	Critical stress intensity factor [MPa.m <sup>1/2</sup> ]
$K_I$	Stress intensity factor [MPa.m <sup>1/2</sup> ]

## REFERENCES


- Mechab B, Medjahdi M, Salem M, Serier B. Probabilistic elastic-plastic fracture mechanics analysis of propagation of cracks in pipes under internal pressure. *Frattura Ed Integrità Strutturale*. 2020;14(54):202-210. Available from: <https://doi.org/10.3221/IGF-ESIS.54.15>
- Mechab B, Serier B, Kaddouri K, Bachir Bouiadja B. Probabilistic elastic-plastic analysis of cracked pipes subjected to internal pressure load. *Nuclear Engineering and Design*. 2014;275:281-286. Available from: <https://doi.org/10.1016/j.nucengdes.2014.05.008>
- Mechab Belaïd, Chioukh N, Mechab Boubaker, Serier B. Probabilistic Fracture Mechanics for Analysis of Longitudinal Cracks in Pipes Under Internal Pressure. *J of Fail Anal and Pre*. 2018;18(6):1643-1651. Available from: <https://doi.org/10.1007/s11668-018-0564-8>
- Baker AA. Repair efficiency in fatigue-cracked aluminium components reinforced with boron/epoxy patches. *Fatig Fract Eng Mater Struct*. 1993;16(7):753-765. Available from: <https://doi.org/10.1111/j.1460-2695.1993.tb00117.x>
- Salem M, Mhamdia R, Mechab B, Bachir Bouiadja B. Effect of the stiffness ratio on the growth of repaired fatigue cracks with composite patch. *Mech Based Des of Struct and Mach*. 2023;52(5):2679-2697. Available from: <https://doi.org/10.1080/15397734.2023.2189941>
- Salem M, Berrahou M, Mechab B, Bachir Bouiadja B. Analysis of the Adhesive Damage for Different Patch Shapes in Bonded Composite Repair of Corroded Aluminum Plate Under Thermo-Mechanical Loading. *J Fail Anal and Preven*. 2021;21(2):1274-1282. Available from: <https://doi.org/10.1007/s11668-021-01167-x>
- Ibrahim N.C.M, Serier B, Mechab B. Analysis of the crack-crack interaction effect initiated in aeronautical structures and repaired by composite patch. *Fratt ed Integrità Strut*. 2018;12(46):140-149. Available from: <https://doi.org/10.3221/IGF-ESIS.46.14>
- Salem M, Berrahou M, Mechab B, Bachir Bouiadja B. Effect of the angles of the cracks of corroded plate in bonded composite repair. *Fratt ed Integrità Strut*. 2018;12(46):113-123. Available from: <https://doi.org/10.3221/IGF-ESIS.46.12>
- Berrahou M, Salem M, Mechab B, Bachir Bouiadja B. Effect of the corrosion of plate with double cracks in bonded composite repair. *Struct Eng and Mech*. 2017;64(2):323-328. Available from: <https://doi.org/10.12989/sem.2017.64.3.323>
- Mechab B, Chama M, Kaddouri K, Slimani D. Probabilistic elastic-plastic analysis of repaired cracks with bonded composite patch. *Steel and Comp Struct*. 2016;20(6):1173-1182. Available from: <https://doi.org/10.12989/scs.2016.20.6.1173>
- Salem M, Bachir Bouiadja B, Mechab B, Kaddouri K. Elastic-plastic analysis of the J integral for repaired cracks in plates. *Advance in mat Res*. 2015;4(2):87-96. Available from: <https://doi.org/10.12989/amr.2015.4.2.087>
- Serier N, Mechab B, Mhamdia R, Serier B. A new formulation of the J integral of bonded composite repair in aircraft structures. *Struct Eng and Mech*. 2016;58(5):745-755. Available from: <https://doi.org/10.12989/sem.2016.58.5.745>
- Salem M, Mechab B, Berrahou M, Bachir Bouiadja B, Serier B. Failure Analyses of Propagation of Cracks Repaired Pipe Under Internal Pressure. *J of Fail Anal and Pre*. 2019;19(2):212-218. Available from: <https://doi.org/10.1007/s11668-021-01167-x>

14. Pan X, Jiang Y, Li M, Su Z. Theoretical and numerical investigation of mode-I delamination of composite double-cantilever beam with partially reinforced arms. *Fatigue Fract Eng Mater Struct*. 2021;44(12):3448–3462. Available from: <https://doi.org/10.1111/ffe.13577>
15. Fotouhi M, Damghani M, Leong MC, Fotouhi S, Jalalvand M, Wisnom MR. A comparative study on glass and carbon fibre reinforced laminated composites in scaled quasi-static indentation tests. *Compos Struct*. 2020;245:112–327. Available from: <https://doi.org/10.1016/j.compstruct.2020.112327>
16. Yu Z, Zhang J, Shen J, Chen HN. Simulation of crack propagation behavior of nuclear graphite by using XFEM, VCCT and CZM methods. *Nucl Mater Energy*. 2021;29(1):101–063. Available from: <https://doi.org/10.1016/j.nme.2021.101063>
17. Ravikumar P, Santosh B, Praveen B, Kumar BN. Mode I delamination analysis and its comparative study of carbon/epoxy, graphite/epoxy and Kevlar/epoxy composite structures using VCCT in Ansys. *Int J Mech Prod Eng Res Dev*. 2017;7(5):269–278. Available from: <https://doi.org/10.24247/ijmpredoct201728>
18. ADİN H, YILDIZ B, ADİN MŞ. Numerical Investigation of Fatigue Behaviours of Non-Patched and Patched Aluminium Pipes. *Eur J Tech*. 2021;11(1):60–65. Available from: <https://doi.org/10.36222/ejt.893327>
19. Hakima B, Kouider K, Slimane M, Laid R. Effect of behavior patch and aging adhesive exposed with temperature in modeling of a damaged and repaired plate in aluminum (2024-T3). *Int J Eng Res Africa*. 2020;50:48–63. Available from: <https://doi.org/10.4028/www.scietific.net/JERA.50.48>
20. Talbi S, Salem M, Mechab B, Ghomari T, Allam A, Salem MK, Bachir Bouiadjra B. Numerical and analytical prediction of the propagation of delamination of bonded composite repair plates under mechanical loading. *Journal of the Serbian Society for Computational Mechanics*. 2023;17(2):103–124. Available from: <https://doi.org/10.24874/jsscm.2023.17.02.08>
21. Allem A, Salem M, Talbi S, Sahli A. Numerical study of mechanical behavior of repaired inclined cracked under complex shear-shear load: performance and durability of aluminum 2024-t3 plate. *Journal of the Serbian Society for Computational Mechanics*. 2023;17(2):38–54. Available from: <https://doi.org/10.24874/jsscm.2023.17.02.04>
22. Talbi S, Salem M, Mechab B, Ghomari T, Allam A, Bachir Bouiadjra B, Benelmaarouf M. New investigation of delamination using the VCCT method to predict the damage in bonded composite repair plates subjected to tensile load. *International Journal of Structural Integrity*. 2024;15(1):1757–9864. Available from: <https://doi.org/10.1108/IJSI-11-2023-0113>
23. Moulgada A, Zagane MES, Sahli A, Ait Kaci D, Zahi R. Comparative study of the repair of cracked plates with two different composite patches. *Fat ed Integrita Strutt*. 2020;14(53):187–201. Available from: <https://doi.org/10.3221/IGF-ESIS.53.16>
24. AFGROW users guide and technical manual: AFGROW for Windows 2K/XP. 2006;Version 4.0011.14. Air Force Research Laboratory.
25. Maierhofer b, Pippanb R, Ganser HP. Modified NASGRO equation for physically short cracks, *International Journal of Fatigue*. 2014;59(6):200–207. Available from: <https://doi.org/10.1016/j.ijfatigue.2013.08.019>
26. Griffith AA. The phenomena of ruptures and flow in solids, *transactions. Royal soc London. serie A*. 1920;221:163–198. Available from: <https://doi.org/10.1098/rsta.1921.0006>

Sofiane Maachou:  <https://orcid.org/0009-0000-6202-3708>

Belaid Mechab:  <https://orcid.org/0009-0000-7483-5527>

Bel Abbes Bachir Bouiadjra:  <https://orcid.org/0000-0002-1925-7194>

Mokadem Salem:  <https://orcid.org/0000-0001-7558-714X>



This work is licensed under the Creative Commons BY-NC-ND 4.0 license.

## RESEARCH OF DYNAMIC PROCESSES IN A LAYER DURING COLLISION WITH AN IMPACTOR

Yuriy PYR'YEV\*, Marek PAWLIKOWSKI\*\*, Rafał DROBNICKI\*\*, Andrzej PENKUL\*\*\*

\* Faculty of Mechanical and Industrial Engineering, Institute of Mechanics and Printing, Department of Printing Technologies, Warsaw University of Technology, Konwiktorska 2, 00-217 Warsaw, Poland

\*\* Faculty of Mechanical and Industrial Engineering, Institute of Mechanics and Printing, Department of Construction Engineering and Biomedical Engineering, Warsaw University of Technology, Narbutta 85, 02-524 Warsaw, Poland

\*\*\* Faculty of Mechanical and Industrial Engineering, Institute of Mechanics and Printing, Department of Mechanics and Weaponry Technology, Warsaw University of Technology, Narbutta 85, 02-524 Warsaw, Poland

[yuriy.pyryev@pw.edu.pl](mailto:yuriy.pyryev@pw.edu.pl), [marek.pawlikowski@pw.edu.pl](mailto:marek.pawlikowski@pw.edu.pl), [rafal.drobnicki@pw.edu.pl](mailto:rafal.drobnicki@pw.edu.pl), [andrzej.penkul@pw.edu.pl](mailto:andrzej.penkul@pw.edu.pl)

received 20 May 2024, revised 20 June 2024, accepted 27 June 2024

**Abstract:** The article concerns the modeling of the transverse impact of an impactor (test sample) on the surface of an infinite elastic layer. The Laplace transform with respect to time and the Hankel transform with respect to the radius for the axisymmetric case were applied. The propagation of elastic waves in the layer and local deformations in the contact zone are taken into account. Impact force, impact time and the coefficient of restitution were examined. The results are compared with the elastic half-space. The calculations carried out showed that for layer thicknesses of more than five impactor diameters, the layer can be considered as a half-space.

**Key words:** collision, impactor, anvil, elastic layer, plate, Hertz's theory, elastic waves, impact speed, integral transforms

### 1. INTRODUCTION

The purpose of the paper is to analyse the wave phenomena occurring during the impact of an impactor (rod, test sample) against an anvil (elastic layer) and to develop a method for calculating the parameters of selected physical quantities occurring in the anvil and impactor in the initial post-impact period. The paper continues the analysis of modelling of the anvil considered in [1] as an elastic half-space.

Many examples of impact-type transient processes with different strain rates can be found in the fields of seismology, earthquake engineering, dynamic soil-substrate interactions and terrain characterization, aviation, machinery, transportation, civil engineering, agriculture, military applications, mathematical modeling of erosion processes, spraying [2-11].

A study of the transient waves generated in the layer by the application of a normal linear and point load with rapid changes in time was carried out in papers [7, 10, 12-14]. The Laplace transform with respect to time and the exponential Fourier transform with respect to the longitudinal variable for the linear load and the Hankel transform due to the radius for the axisymmetric case were applied.

The infinite plate model was formulated in papers [15, 16] as a closed form approximation for the initial elastic impact response of an isotropic plate. In paper [17] an analytical solution of the Zener equation was proposed to predict elastic impact of a sphere on the large plate. Energy loss caused by bending wave and motions of the sphere and the plate were studied utilising contact force history.

It was later extended to orthotropic plates [18, 19], which was used to study the elastic impact of orthotropic composite laminates. In the paper [20], plastic deformation and bending vibra-

tions were taken into account for such a model, a non-linear elastic-plastic model was presented to evaluate the coefficient of restitution  $R_t$ .

In paper [21] the authors replaced the nonlinear contact law with the linear one to solve Zener model for elastic sphere impacts on large, thin plates. They concluded that the solution well agree for  $\lambda^* < 0.85$  and  $R_t^* > 0.2$  (defined in section 3.2). Such a linearisation method was utilised to investigate the contact time [22] and the energy dissipation [23]. The effect of elastic waves on elastoplastic strain was studied in [24].

The problem of collision of elastic bodies in terms of their deformation has a rich history. Elementary collision theory uses the coefficient of restitution  $R_t$  as the key parameter to characterise the deformation properties of colliding bodies and does not reflect the various characteristics of the internal state of bodies [5, 25].

In practice, the Hertzian impact theory is used to determine the stresses occurring during the interaction of two bodies [6].

Sears [26] considered the influence of the spherical shape of the rod ends on the obtained results. In these studies, he took into account both local deformations and wave propagation. This approach led to a good agreement of theoretical and experimental results and is used in many subsequent works [27, 28].

The theory of crossbeam impact comes from Timoshenko [29].

Paper [7] presents an overview of the approaches developed by the author and his colleagues to study the effect of a blunted elastic body on the surface of an elastic medium. Mathematically, the problem is generally formulated as a non-stationary mixed boundary problem of continuum mechanics, in which the unknown contact limit varies in time and space. The process of collision between a blunt body and an elastic medium always involves a supersonic phase, during which the boundary value problem can

be formulated as a non-mixed boundary and thus solved by simpler methods [7, 8, 30].

The impact of the supersseismic phase on the collision process immediately after the first contact is investigated within the framework of Hertz's theory of impacts in [30]. For small values of the  $\alpha_A$  parameter (defined in point 4), the influence of the supersseismic state on the course of the impact can be neglected.

Paper [31] presents a numerical analysis of the plastic target plate behaviour evoked by the high-velocity impact of a blunt-nosed cylindrical rigid projectile. The impact strength of elastic bars of variable cross-section was analysed in [32] to investigate the relation between the restitution coefficient and the impacting body shape.

We will consider the collision of an impactor with an elastic layer. The study will be carried out under the basic geometrical assumptions of Hertzian theory [33]

We limit ourselves to considering the direct interaction of the central bodies, i.e. we assume that they are the resultant of the dynamic contact pressures applied to the colliding bodies, directed along a straight line connecting their centers of inertia and coinciding with the normal to the compression surface at the point of initial contact of the non-deformed the surface of these bodies.

This simplifying assumption will allow us to consider only one component of the displacement of bodies at a point coinciding with their point of initial contact.

## 2. IMPACT PROBLEM STATEMENT

Assuming that a heavy body strikes an elastic layer and, at the moment of contact, a layer of thickness  $h$  has a velocity of  $V_0$ . Under impact, local deformations will occur in the elastic layer and in an impact cylinder of radius  $r_0$ , and, in addition, vibrations of the layer are produced. We assume that the friction between the contacting surfaces is negligible and that the elastic layer material with Young's modulus  $E$  and Poisson's ratio  $\nu$  does not undergo plastic deformation or cracking.

The assumption of elastic behaviour of the metal layer (anvil) can be extended to the case of real processes where there is only local plastic deformation in the material, limited by the proximity of the initial point of contact; moreover, the energy required to produce a residual indentation is only a small fraction of the initial kinetic energy [34].

Continuing with the contact between the impactor and the layer, the displacements of the impactor will consist of a part dependent on the local compression and a part determined by the dynamic deflections of the layer. As is known, the dynamic deflections of the layer satisfy the differential equations [10].

### 2.1. Mathematical model of the elastic layer

A point source gives rise to volumetric longitudinal (P) and shear (S) waves, Rayleigh-Lamb waves and Rayleigh (R) waves. In [35], Lamb considered the problems of wave propagation in an isotropic elastic layer.

Let us consider in a cylindrical coordinate system  $(r, \theta, z)$  a layer ( $0 \leq z < h$ ), where  $r$  – radial and  $z$  – axial coordinates;  $\theta$  – angular coordinate (Fig. 1). The medium is assumed to be homogeneous and isotropic. Axially symmetric non-stationary loads depending on position and time act on the surface  $p(r, t)$  with relative spatial distribution  $Z(r)$  and the resultant  $P(t)$ ; i.e.

$p(r, t) = Z(r)P(t)$  in time  $t > 0$ . As a result of this action, there is a vector field of displacement in the structure  $U \equiv (u, 0, w)$ , where  $u, w$  are the components of the displacement vector on the axis,  $r, z$  respectively.

An elastic layer is characterized by the velocities of longitudinal (P)  $c_1$  and shear (S)  $c_2$  waves or the Lamé constants  $\lambda, \mu$ , and density  $\rho$ , which are related by  $c_1 = ((\lambda + 2\mu)/\rho)^{1/2}$ ,  $c_2 = (\mu/\rho)^{1/2}$ .

On the free surface of the medium, stresses  $\sigma_{zz}, \sigma_{z\theta}, \sigma_{zz}$  are either converted to zero or take values corresponding to a given limit load.

We assume that the medium is at rest and at the initial moment  $t = 0$  the axisymmetric disturbance source starts to act  $p(r, t) = Z(r)P(t)$ .

As a rule, the forces arising during an impact  $P(t)$  (impact force) are not known in advance, they must be determined in the problem-solving process, and only in some cases can they be considered predetermined.

The discussed issue boils down to solving Lamé displacement equations in a cylindrical coordinate system [10, 12]:

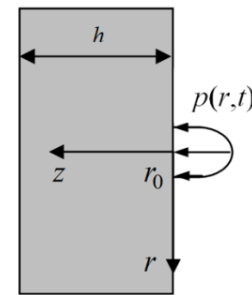


Fig. 1. Physical model of an anvil (elastic layer) with a surface area load with  $r_0$  radius

$$\begin{aligned} (\lambda + 2\mu) \left( \frac{\partial^2 u}{\partial r^2} + \frac{1}{r} \frac{\partial u}{\partial r} - \frac{u}{r^2} \right) + \mu \frac{\partial^2 u}{\partial z^2} + (\lambda + \mu) \frac{\partial^2 w}{\partial r \partial z} &= \rho \frac{\partial^2 u}{\partial t^2}, \\ (\lambda + \mu) \left( \frac{\partial^2 u}{\partial r \partial z} + \frac{1}{r} \frac{\partial u}{\partial r} \right) + \mu \left( \frac{\partial^2 w}{\partial r^2} + \frac{1}{r} \frac{\partial w}{\partial r} \right) + (\lambda + 2\mu) \frac{\partial^2 w}{\partial z^2} &= \rho \frac{\partial^2 w}{\partial t^2}, \\ 0 \leq r < \infty, 0 \leq z \leq h, t \geq 0 \end{aligned} \quad (1)$$

at boundary conditions:

$$\sigma_{zz}(r, 0, t) = -p(r, t) = -Z(r)P(t), 0 \leq r < \infty, t \geq 0 \quad (2)$$

$$\sigma_{rz}(r, 0, t) = 0, 0 \leq r < \infty, t \geq 0 \quad (3)$$

$$\sigma_{zz}(r, h, t) = 0, \sigma_{rz}(r, h, t) = 0, 0 \leq r < \infty, t \geq 0 \quad (4)$$

and the initial conditions  $t = 0$  [10]:

$$u = 0, \frac{\partial u}{\partial t} = 0, w = 0, \frac{\partial w}{\partial t} = 0, 0 \leq r < \infty, 0 \leq z \leq h \quad (5)$$

$p(r, t)$  is the contact pressure distributed over the contact area  $\omega(t)$ . Due to the axis of symmetry,  $\omega(t)$  is a circle with a radius  $a(t)$ . We assume that the contact area does not change with time and from the beginning the radius is equal to  $r_0$ .

We will consider the sources  $Z(r)$  on the surface for which the following condition is met

$$2\pi \int_0^\infty Z(r)P(t)rdr = P(t), \quad (6)$$

where [6]

$$Z(r) = \frac{1}{\pi r_0^2} \sqrt{\left(1 - \frac{r^2}{r_0^2}\right) H\left(1 - \frac{r^2}{r_0^2}\right)}. \quad (7)$$

where  $H(t)$  Heaviside function:  $H(t) = 0$  for  $t < 0$ ,  $H(t) = 1$  for  $t \geq 0$ .

For comparison, we will model the anvil as an elastic plate. In this analysis of the response of large plates to localised impulse forces, we will use the usual approximate theory of thin plates. This theory assumes that the radius of curvature of the plate is everywhere large compared to its thickness, and that the angle between the plate and the original plane is everywhere small. From this approximate theory it follows that the displacement  $w^*(0, t)$  of the point of application is proportional to the impulse  $P(t)$  [15]

$$w^* = \alpha^* \int_0^t P(t') dt' \quad (8)$$

with

$$\alpha^* = \sqrt{\frac{3\rho(1-\nu^2)}{E}} \frac{1}{16\rho(h^*)^2},$$

where  $h^*$  is the half-thickness of the plate. The displacement  $w^*$  refers strictly to the displacement of the centre plane of the plate.

## 2.2. Mathematical model of the impactor hitting the layer

In the study of the response of the layer to impact, the system of equations describing the behaviour of waves in the layer integrates simultaneously with the equation of motion of the impactor and the condition of compliance of displacements. The last one takes into account a contact approximation of a sample with mass  $m_1$  and layer. One of the ends of the cylindrical rod is hemispherical. We will consider that for the considered impact of the impactor, the contact approximation can be determined based on the solution to the dynamic problem of Hertz for pressing a ball into an elastic half-space [6].

Let us denote, after S.P. Timoshenko [29], the total displacement of the hitting body (impactor) from the start of the impact as  $W(t)$ , and local compression as  $\alpha_H$ . Then, of course [19, 29]

$$W = \alpha_H + w \quad (9)$$

where  $w = w(0, 0, t)$  deflection of the elastic layer surface under the impactor. The displacement  $W(t)$  satisfies the differential equation of motion

$$m_1 \frac{d^2 W(t)}{dt^2} = -P(t) \quad (10)$$

under initial conditions:

$$W(0) = 0, \frac{dW}{dt} = V_0, \quad t = 0 \quad (11)$$

here  $P(t)$  is the resultant of the contact pressure.

In the following part, we assume that

$$\frac{m_1}{P} \frac{\partial^2 w_e}{\partial t^2} \ll 1 \quad (12)$$

where  $w_e(r, z, t)$  characterizes the relative displacement of the sample elements due to its deformation.

## 3. SOLUTION METHOD

### 3.1. Key dependencies for the flexible layer

In this article, the approach [10] was used to find the stress-strain state of an elastic layer with a thickness  $h$ . Applying the Laplace and Hankel transformations to equations (1) and taking

into account uniform initial conditions (5), we obtain linear differential equations with respect to the variable  $z$ . Since the solution to these equations depends on four unknowns, they can be found using the four boundary conditions (2)-(4). Using the inverse Laplace and Hankel transformations, we obtain the desired relationships. The displacements  $u$ ,  $w$  and stresses can be expressed by the Duhamel integral

$$\{u(r, z, t), w(r, z, t)\} = \int_0^t \{u_\delta(r, z, t - t'), w_\delta(r, z, t - t')\} \cdot P(t') dt' = \{u_\delta(r, z, t), w_\delta(r, z, t)\} * P(t) \quad (13)$$

$$\{\sigma_{zz}, \sigma_{rr}, \sigma_{\theta\theta}, \sigma_{rz}\} = \{\sigma_{zz,\delta}, \sigma_{rr,\delta}, \sigma_{\theta\theta,\delta}, \sigma_{rz,\delta}\} * P(t) \quad (14)$$

where  $u_\delta(r, z, t)$ ,  $w_\delta(r, z, t)$  are solutions to problem (1)-(6) for the impulse function  $P(t) = \delta(t)$ :  $\delta(t) = \infty$  for  $t = 0$ ,  $\delta(t) = 0$  for  $t \neq 0$  and

$$\int_{-\infty}^{+\infty} \delta(t) dt = 1. \quad (15)$$

Applying the Laplace and Hankel integral transformations to the considered problem (1) - (6) [10] e.g. for displacement  $w_\delta(r, z, t)$

$$w_\delta^L(r, z, s) = \int_0^\infty w_\delta(r, z, t) e^{-st} dt \quad (16)$$

$$w_\delta^{LH}(k, z, s) = \int_0^\infty w_\delta^L(r, z, s) r J_0(kr) dr \quad (17)$$

we get a solution to the problem of the following form [36]:

$$\{u_\delta, w_\delta\} = \frac{1}{2\pi i} \int_{c_0 - i\infty}^{c_0 + i\infty} \{u_\delta^L, w_\delta^L\} e^{st} ds \quad (18)$$

$$\{\sigma_{zz,\delta}, \sigma_{rr,\delta}, \sigma_{rz,\delta}\} = \frac{1}{2\pi i} \int_{c_0 - i\infty}^{c_0 + i\infty} \{\sigma_{zz,\delta}^L, \sigma_{rr,\delta}^L, \sigma_{rz,\delta}^L\} e^{st} ds \quad (19)$$

where:

$$\{w_\delta^L, \sigma_{zz,\delta}^L\} = \int_0^\infty \{w_\delta^{LH}, \sigma_{zz,\delta}^{LH}\} Z^H(k) k J_0(kr) dk \quad (20)$$

$$\{u_\delta^L, \sigma_{rz,\delta}^L\} = \int_0^\infty \{u_\delta^{LH}, \sigma_{rz,\delta}^{LH}\} Z^H(k) k J_1(kr) dk \quad (21)$$

$$\sigma_{rr,\delta}^L = \int_0^\infty \sigma_{rr,\delta}^{LH0} Z^H(k) k J_0(kr) dk + \frac{1}{r} \int_0^\infty \sigma_{rr,\delta}^{LH1} Z^H(k) k J_1(kr) dk \quad (22)$$

$J_n(kr)$  is a Bessel function of the first kind of order  $n$  ( $n = 0, 1, \dots$ ),  $k$  is positive parameter,  $c_0$  is a real number so that the contour path of integration is in the region of convergence of  $u_\delta^{LH}(k, z, s)$ ,  $w_\delta^{LH}(k, z, s)$ .

Integral expressions in (18)-(22) marked with "LH" have the following form

$$u_\delta^{LH}(k, z, s) = -(D_1 k \operatorname{ch}(\alpha_1 z) + D_2 k \frac{\operatorname{sh}(\alpha_1 z)}{\alpha_1} + D_3 \alpha_2^2 \frac{\operatorname{sh}(\alpha_2 z)}{\alpha_2} + D_4 \operatorname{ch}(\alpha_2 z)) \quad (23)$$

$$w_\delta^{LH}(k, z, s) = (D_1 \alpha_1^2 \frac{\operatorname{sh}(\alpha_1 z)}{\alpha_1} + D_2 \operatorname{ch}(\alpha_1 z) + D_3 k \operatorname{ch}(\alpha_2 z) + D_4 k \frac{\operatorname{sh}(\alpha_2 z)}{\alpha_2}) \quad (24)$$

$$\sigma_{zz,\delta}^{LH}(k, z, s) = \mu(D_1 \gamma \operatorname{ch}(\alpha_1 z) + D_2 \gamma \frac{\operatorname{sh}(\alpha_1 z)}{\alpha_1} + D_3 2k \alpha_2^2 \frac{\operatorname{sh}(\alpha_2 z)}{\alpha_2} + D_4 2k \operatorname{ch}(\alpha_2 z)), \quad (25)$$

$$\sigma_{rz,\delta}^{LH}(k, z, s) = -\mu(D_1 2k \alpha_1^2 \frac{\operatorname{sh}(\alpha_1 z)}{\alpha_1} + D_2 2k \operatorname{ch}(\alpha_1 z) + D_3 \gamma \operatorname{ch}(\alpha_2 z) + D_4 \gamma \frac{\operatorname{sh}(\alpha_2 z)}{\alpha_2}), \quad (26)$$

$$\sigma_{rr,\delta}^{LH0}(k, z, s) = -(D_1 (k^2 (\lambda + 2\mu) - \alpha_1^2 \lambda) \operatorname{ch}(\alpha_1 z) + D_2 (k^2 (\lambda + 2\mu) - \alpha_1^2 \lambda) \frac{\operatorname{sh}(\alpha_1 z)}{\alpha_1} + 2D_3 k \alpha_2^2 \mu \frac{\operatorname{sh}(\alpha_2 z)}{\alpha_2} + D_4 2k \mu \operatorname{ch}(\alpha_2 z)) \quad (27)$$

$$\sigma_{rr,\delta}^{LH1}(k, z, s) = 2\mu(D_1 k \operatorname{ch}(\alpha_1 z) + D_2 k \frac{\operatorname{sh}(\alpha_1 z)}{\alpha_1} + D_3 \alpha_2^2 \frac{\operatorname{sh}(\alpha_2 z)}{\alpha_2} + D_4 \operatorname{ch}(\alpha_2 z)), \quad (28)$$



$$\sigma_{\theta\theta,\delta}^{LH0}(k, z, s) = \lambda \alpha^2 s^2 (D_1 \text{ch}(\alpha_1 z) + D_2 \frac{\text{sh}(\alpha_1 z)}{\alpha_1}) \quad (29)$$

$$\begin{aligned} \sigma_{\theta\theta,\delta}^{LH1}(k, z, s) &= -2\mu(D_1 k \text{ch}(\alpha_1 z) + D_2 k \frac{\text{sh}(\alpha_1 z)}{\alpha_1} + \\ &D_3 \alpha_2^2 \frac{\text{sh}(\alpha_2 z)}{\alpha_2} + D_4 \text{ch}(\alpha_2 z)), \\ D_1 &= -Z^H \gamma (8k^2 (1 - C_1 C_2) + 2\gamma^2 S_1 S_2) / D, \\ D_2 &= -Z^H 2\gamma (4k^2 \alpha_1^2 S_1 C_2 - \gamma^2 C_1 S_2) / D, \\ D_3 &= Z^H 4k (4k^2 \alpha_1^2 S_1 C_2 - \gamma^2 C_1 S_2) / D, \\ D_4 &= -Z^H 4k (\gamma^2 (1 - C_1 C_2) + 4k^2 \alpha_1^2 \alpha_2^2 S_1 S_2) / D, \\ D(k, s) &= 2\mu \{ 8k^2 \gamma^2 (1 - C_1 C_2) + (\gamma^4 + (4k^2 \alpha_1 \alpha_2)^2) S_1 S_2 \}, \\ \gamma &= 2k^2 + c_2^{-2} s^2, \end{aligned} \quad (30)$$

$$C_j = \text{ch}(h\alpha_j), S_j = \frac{\text{sh}(h\alpha_j)}{\alpha_j}, \alpha_j = \sqrt{k^2 + c_j^{-2} s^2}, j = 1, 2 \quad (31)$$

Hankel transform  $Z^H(k)$  of the  $Z(r)$  source on the surface (7)

$$Z^H(k) = \frac{3(\sin(r_0 k) - r_0 k \cos(r_0 k))}{2\pi r_0^3 k^3} \quad (32)$$

Analysis of the elements of the characteristic equation  $D(k, s)=0$  was carried out for example in [37].

In order to receive the function  $w_\delta(0,0,t)$  for the initial moment  $t \rightarrow 0$  we find the properties of the Laplace transform for  $s \rightarrow \infty$

$$w_\delta^{LH}(k, z, s) = \frac{c_2^2 e^{-\frac{zs}{c_1}}}{\mu c_1} \left( \frac{1}{s} - \frac{c_1 z k^2}{2s^2} + \dots \right) - \frac{2c_2^4 k^2 e^{-\frac{zs}{c_2}}}{\mu c_1 s^3}. \quad (33)$$

In the initial moment we get

$$w_\delta(0,0,t) = \frac{c_2^2}{\mu c_1} H(t) Z(0), t \rightarrow 0 \quad (34)$$

$$\sigma_{zz,\delta}(0,z,t) = -\delta(t - z/c_1) Z(0), t - z/c_1 \rightarrow 0 \quad (35)$$

Asymptotics (35) shows that for the calculation of stresses it is better to use

$$\sigma_{zz}(r, z, t) = \int_0^t \sigma_{zz,H}(r, z, t - t') \frac{d}{dt'} P(t') dt' \quad (36)$$

where  $\sigma_{zz,H}(k, z, s) = \sigma_{zz,\delta}(k, z, s) / s$ .

The calculations of the inverse integral Laplace and Hankel transformations were performed in the same way as in the papers [36,38].

### 3.2. Solution method for the impactor

Integrating the equation (10) using the Laplace transform and the initial conditions (11), we obtain

$$W(t) = V_0 t - \frac{1}{m_1} \int_0^t (t - t') P(t') dt' \quad (37)$$

On the other hand, according to the theory of Hertz [6], we can assume

$$\alpha_H = (P/K)^{2/3} = k_0 P^{2/3} \text{ or } P = K \alpha_H^{3/2} \quad (38)$$

where  $K$  is determined from the equation [6]

$$K = \frac{4E^* \sqrt{r_0}}{3}, k_0 = K^{-2/3}, \frac{1}{E^*} = \frac{1 - \nu_1^2}{E_1} + \frac{1 - \nu^2}{E} \quad (39)$$

Taking (9), (37), (38) into account, we obtain the equation

$$V_0 t - \frac{1}{m_1} \int_0^t (t - t') P(t') dt' = k_0 P(t)^{2/3} + w(0,0,t) \quad (40)$$

At the moment of time  $t = t_n = n\Delta t$ ,  $n = 0, 1, 2, \dots$ ,  $\Delta t$  integration time is assumed to take place

$$V_0 t_n - \frac{1}{m_1} \int_0^{t_n} (t_n - t') P(t') dt' = k_0 P(t_n)^{2/3} + w_n \quad (41)$$

where  $w_n = w(0,0,t_{n-1})$ .

In the initial moment  $t = 0$  ( $n = 0$ ), sample displacement  $W = 0$ , displacement of half-space  $w = 0$ , sample speed  $v = V_0$ .

In moment  $t = t_1$  ( $n = 1$ ), sample displacement  $W(t_1) = W_1 = V_0 t_1$ , deflection of half-space  $w(0,0,t_0) = w_1 = 0$ , impact force (pressure)  $P(t_1) = P_1 = K(W_1 - w_1)^{3/2}$ , acceleration of the sample  $a_1 = -P_1/m_1$ , sample speed  $v(t_1) = v_1 = V_0$ .

In the time moment  $t = t_2$  ( $n = 2$ ), sample displacement  $W(t_2) = W_2 = W_1 + v_1 \Delta t + a_1 (\Delta t)^2/2$ , deflection of layer  $w(0,0,t_1) = w_2$ , impact force (pressure)  $P(t_2) = P_2 = K(W_2 - w_2)^{3/2}$ , acceleration of the sample  $a_2 = -P_2/m_1$ , sample speed  $v(t_2) = v_2 = v_1 + a_1 \Delta t$ .

The further course of the calculations is obvious. Let us write directly the formulas related to the  $n$ th stage:

$$W(t_n) = W_n = W_{n-1} + v_{n-1} \Delta t + a_{n-1} (\Delta t)^2/2 \quad (42)$$

$$w_n = \Delta t \sum_{m=1}^{n-2} w_\delta(0,0,t_{n-1}-t_m) P_m + \frac{\Delta t}{2} w_\delta(0,0,0) P_{n-1} \quad (43)$$

$$P(t_n) = P_n = K(W_n - w_n)^{3/2} \quad (44)$$

$$a_n = -P_n/m_1 \quad (45)$$

$$v(t_n) = v_n = v_{n-1} + a_{n-1} \Delta t \quad (46)$$

For the impactor impact issue with a  $2h^*$  thick plate, the contact condition will be [19, 29]

$$W = \alpha_H + w^* \quad (47)$$

We can therefore obtain a single equation for only one dependent variable  $\alpha_H$  by differentiating equation (8) twice with respect to time and then subtracting this equation from equation (10). Taking into account condition (47), the following equation is obtained [15]:

$$\frac{d^2 \alpha_H}{dt^2} + \frac{1}{m_1} P(\alpha_H) + \alpha^* \frac{d}{dt} P(\alpha_H) = 0 \quad (48)$$

The non-linear differential equation proposed by Zener [15] is transformed to provide a solution by simplifying the Hertzian force  $P$  as a function of local compression  $\alpha_H$ . Thus, equation (48) is rewritten as

$$\frac{d^2 \alpha_H}{dt^2} + \frac{1}{m_1} K \alpha_H^{3/2} + \frac{3}{2} \alpha^* K \alpha_H^{1/2} \frac{d \alpha_H}{dt} = 0 \quad (49)$$

under initial conditions:

$$\alpha_H(0) = 0, \frac{d \alpha_H}{dt} = V_0, t = 0 \quad (50)$$

A problem formulated in this way can be transformed into a dimensionless form

$$\frac{d^2 \alpha}{d\tau^2} + \alpha^{3/2} + \frac{3}{2} \lambda^* \alpha^{1/2} \frac{d \alpha}{d\tau} = 0 \quad (51)$$

under initial conditions:

$$\alpha(0) = 0, \frac{d \alpha}{d\tau} = 1, \tau = 0 \quad (52)$$

where  $\alpha = \alpha_H / (TV_0)$ ,  $\tau = t / T$ ,  $T = (m_1)^{2/5} V_0^{-1/5} K^{-2/5}$ .

$$\lambda^* = \alpha^* K V_0^{1/2} T^{3/2}. \quad (53)$$

By solving the problem (51), (52) the semi-imperial formula for the coefficient of restitution was derived  $R_f^*$  [15] as a function of inelasticity parameter  $\lambda^*$

$$R_f^* = \exp(-1.7191\lambda^*). \quad (54)$$

#### 4. NUMERICAL RESULTS

A numerical analysis of the collision of a copper test sample with a steel anvil was carried out [1]. The parameters are given in Tab. 1. The mass of the tested sample  $m_1 = 0.0122$  kg, sample radius  $r_0 = 0.004$  m, collision speed  $V_0 = 10$  m s<sup>-1</sup> i  $V_0 = 100$  m s<sup>-1</sup>.

For the problem under consideration [39], the  $\alpha_A = (\pi \rho r_0^3 / m_1)^{1/2} (V_0 / c_1)^{3/2} = 0.785 \cdot 10^{-3}$  parameter was calculated. Due to the low value of  $\alpha_A$ , the influence of the super-seismic state on the course of the impact can be neglected as a whole.

Tab. 1. Mechanical properties of steel and copper

Properties	copper	steel
Longitudinal wave speed $c_1$ [m s <sup>-1</sup> ]	4597	5994
Shear wave speed $c_2$ [m s <sup>-1</sup> ]	2263	3204
Density $\rho$ [kg m <sup>-3</sup> ]	8960	7830
Coefficient $\lambda$ [GPa]	97.53	120.6
Shear modulus of elasticity $G, \mu$ [GPa]	45.9	80.4
Poisson number $\nu$ [-]	0.34	0.3
Young's module $E$ [GPa]	123	209
Yield point $R_y$ [MPa]	57	1000
Tensile strength $R_m$ [MPa]	227	1200

Figures 2-5 show the time courses of the impactor characteristics during impact. It can be seen that, initially, the force acting on the impactor  $P(t)$  during impact increases and reaches a maximum of  $P_{max}$  at  $t_{max}$ ,  $P_{max} = P(t_{max})$ .

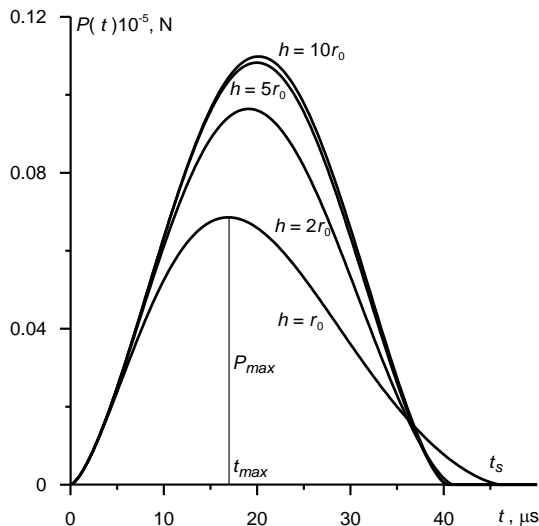


Fig. 2. Variation in impact force  $P$  over time for impact velocity  $V_0 = 10$  m s<sup>-1</sup>

A graph of the  $P(t)$  relationship is shown in Figure 2 for different layer thicknesses. Impact velocity  $V_0 = 10$  m s<sup>-1</sup>. As the layer thickness increases, the values of  $P_{max}$  and  $t_{max}$  and for thickness  $h$  above  $10 r_0$  the layer can be regarded as a half-space. Time of

the event  $t_s$  decreases with increasing layer thickness,  $P(t_s) = 0$ . In case of impactor collision with an elastic body  $t_{max}$  is less than half the impact time  $t_s$ . The sudden decrease of the impact force value observed in the figures is attributed to plasticity of the impact [40] and contact adhesion [41,42].

Figure 3 shows the change in impact force on the impactor  $P$  over time during a Hertz impact for an impact velocity of  $V_0 = 100$  m s<sup>-1</sup>. An increase in impact velocity leads to an increase in the maximum value of the interaction force  $P_{max}$  and reducing the impact time  $t_s$  and  $t_{max}$ . Qualitatively, the  $P$  runs have the same appearance. The quantitative values of the impact parameters are given in Tables 1 and 2 respectively for the impact velocity  $V_0 = 10$  m s<sup>-1</sup> and  $V_0 = 100$  m s<sup>-1</sup>.

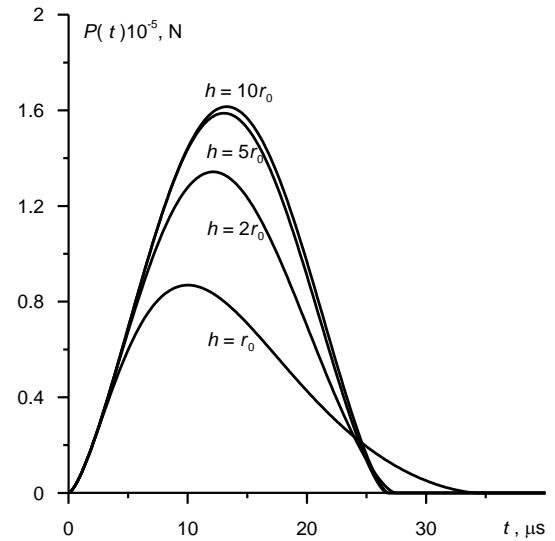


Fig. 3. Time variation of force on impactor  $P$  during Hertz impact for velocity  $V_0 = 100$  m s<sup>-1</sup>.

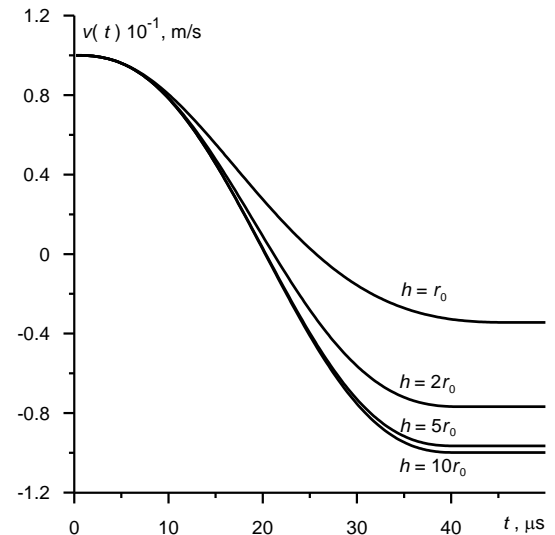


Fig. 4. Variation of the impactor velocity  $v$  in time during a Hertzian impact for the velocity  $V_0 = 10$  m s<sup>-1</sup>

Figures 4 and 5 show the velocity of the impactor  $v(t)$  under impact with a layer of different thicknesses at different initial velocities. The velocity of the bumper decreases due to the force  $P(t)$  to zero at a time greater than  $t_{max}$ , so it changes sign and reaches  $V_s = v(t_s)$  at time  $t_s$ . The rebound velocity of the impactor will be used to calculate the coefficient of restitution  $R_f = V_s / V_0$ .

The numerical values of  $R_f$  are shown in Tables 2 and 3. This coefficient is the ratio of the velocity of the body after impact  $v(t_s)$  to the velocity just before impact  $V_0$ . As the thickness of the layer increases, the rebound velocity  $V_s$  increases and for thickness  $h$  above  $10 r_0$  the rebound velocity equals the rebound velocity from the elastic half-space.

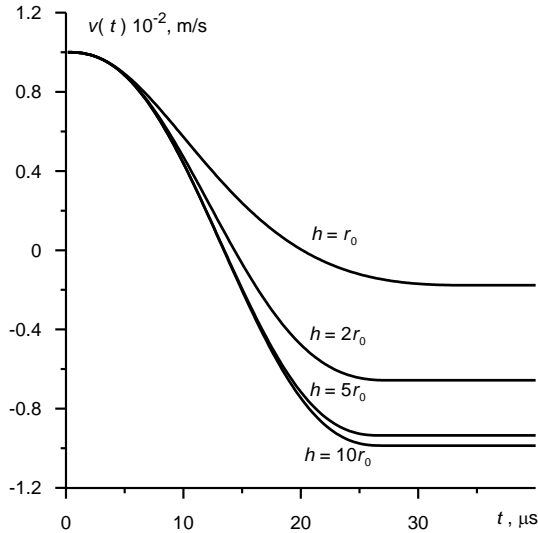


Fig. 5. Change of the impactor speed  $v$  in time during a Hertzian impact for the collision velocity  $V_0=100 \text{ m s}^{-1}$

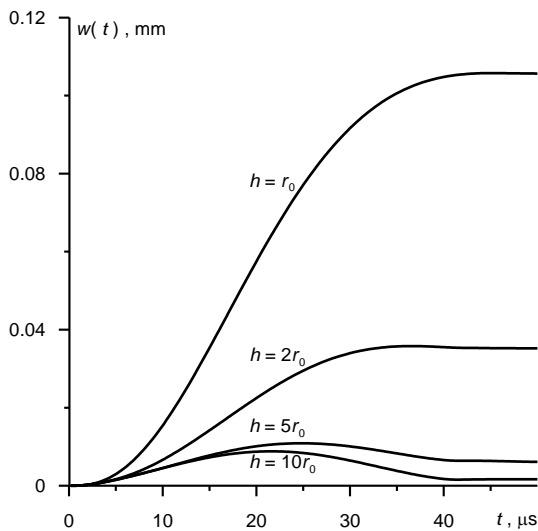


Fig. 6. Change of half-space deflection  $w$  in time during a Hertzian impact for the collision velocity  $V_0=10 \text{ m s}^{-1}$

In Figures 6 and 7 the displacement of the surface of the layer  $w(t)=w(0,0,t)$  of different thickness during collision with the impactor at different initial speeds  $V_0 = 10 \text{ m s}^{-1}$  and  $100 \text{ m s}^{-1}$  is shown. The displacement  $w(t)$  for a small layer thickness ( $h = r_0$ ) increases with time and reaches the greatest significance for  $t = t_s$ . Increasing the layer thickness causes the appearance of a maximum in the  $w(t)$  relationship. An increase in the initial velocity causes an increase in the deflection of the layer at the collision point. Qualitatively, the deflections have the same appearance.

Numerical parameter values presented in Tables 2 and 3. Collision time  $t_s$  decreases with increasing layer thickness from  $46 \text{ } \mu\text{s}$  for thickness  $h = r_0 = 4 \text{ mm}$  to  $40.20 \text{ } \mu\text{s}$  for thickness  $h = 10 r_0$  (see the first row of Tab. 2). A tenfold increase in the collision

speed leads to the collision time  $t_s$  decreasing with increasing layer thickness from  $34.30 \text{ } \mu\text{s}$  to  $26.72 \text{ } \mu\text{s}$  (see the first row of Tab. 3). For such a speed, the duration of the collision  $t_s$  is too long to see the moments of arrival of the longitudinal  $P$  wave, transverse  $S$  wave and Rayleigh  $R$  wave. For a thickness  $h = 5 r_0$ , the time of collision with the layer does not differ from the time of collision with the elastic half-space.

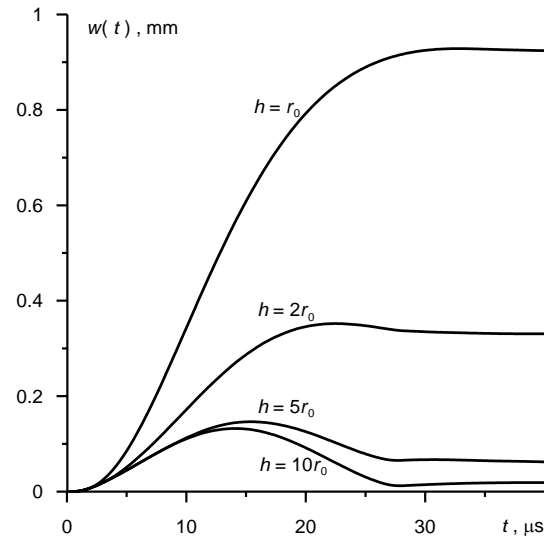


Fig. 7. Change of half-space deflection  $w$  in time during a Hertzian impact for collision velocity  $V_0=100 \text{ m s}^{-1}$

Tab. 2. Parameters of collision of the sample with a plate of thickness  $h$  for  $V_0 = 10 \text{ m s}^{-1}$

	$h = 1 r_0$	$h = 2 r_0$	$h = 5 r_0$	$h = 10 r_0$	$h = \infty$
$t_s [\mu\text{s}]$	46.00	41.00	40.20	40.20	40.4
$t_s^* [\mu\text{s}]$	46.5	40.8	39.8	39.6	40.8
$t_{max} [\mu\text{s}]$	17.00	19.00	20.00	20.02	20.02
$t_{max}^* [\mu\text{s}]$	16.7	19.00	19.65	19.5	19.65
$P_{max} [\text{kN}]$	6.856	9.639	10.83	10.98	11.00
$P_{max}^* [\text{kN}]$	6.812	9.7345	10.048	11.26	11.32
$V_s=v(t_s) [\text{m s}^{-1}]$	3.44	7.68	9.65	9.98	10.0
$R_f = V_s/V_0 [-]$	0.344	0.768	0.965	0.998	1.00
$\lambda^* [-] (53)$	0.6330	0.1582	0.025	0.0063	0.0016
$R_f^* [-] (54)$	0.3368	0.7618	0.9574	0.9892	0.9973
$E_a [\text{mJ}]$	538	250	42.0	2.44	0.00

Tab. 3. Parameters of collision of the sample with a plate of thickness  $h$  for  $V_0 = 100 \text{ m s}^{-1}$

	$h = 1 r_0$	$h = 2 r_0$	$h = 5 r_0$	$h = 10 r_0$	$h = \infty$
$t_s [\mu\text{s}]$	34.3	27.40	26.72	26.72	27.0
$t_s^* [\mu\text{s}]$	34.05	26.3	25.1	24.5	24.98
$t_{max} [\mu\text{s}]$	10.08	12.16	13.12	13.28	13.28
$t_{max}^* [\mu\text{s}]$	10.00	11.75	12.4	12.5	12.5
$P_{max} [\text{kN}]$	86.9	134.3	158.8	161.5	161.5
$P_{max}^* [\text{kN}]$	87.28	142.45	172.3	177.8	179.
$V_s=v(t_s) [\text{ms}^{-1}]$	17.67	65.67	93.52	98.65	99.13
$R_f = V_s/V_0 [-]$	0.177	0.657	0.935	0.986	0.991
$\lambda^* [-] (53)$	1.0032	0.2508	0.0401	0.0100	0.0025
$R_f^* [-] (54)$	0.1782	0.6498	0.9333	0.9829	0.9957
$E_a [\text{J}]$	59.1	34.7	7.65	1.64	1.06

Analysis of the numerical values of  $P_{max}$  indicates that there is an increase from 6.856 kN to 10.98 kN with increasing layer thickness for an impact velocity of 10 m s<sup>-1</sup> and from 86.9 to 161.5 for  $V_0 = 100$  m s<sup>-1</sup>. We can also conclude that for layer thicknesses above  $h = 5 r_0$ , the maximum value of the impactor force  $P_{max}$  to the third significant digit does not differ from this value for the half-space.

The rebound velocity  $V_s = v(t_s)$  increases from 3.44 m s<sup>-1</sup> for layer thickness  $h = r_0$  to 9.98 m s<sup>-1</sup> for  $h = 10 r_0$ , initial velocity  $V_0 = 10$  m s<sup>-1</sup>. For the initial velocity  $V_0 = 100$  m s<sup>-1</sup>, the rebound velocity increases from  $V_s = 17.67$  m s<sup>-1</sup> for the layer  $h = r_0$  to the value of 98.65 m s<sup>-1</sup> for the layer with a thickness  $h = 10 r_0$ . Fig. 8 shows the values of the restitution coefficient  $R_f = V_s/V_0$  as a function of the ratio of the layer thickness to the impactor diameter ( $h/r_0$ ) for the impact speed  $V_0 = 10$  m s<sup>-1</sup> and  $V_0 = 100$  m s<sup>-1</sup>. As you can see from this figure, the coefficient of restitution increases and strive for the value of the coefficient of restitution for the elastic half-space.

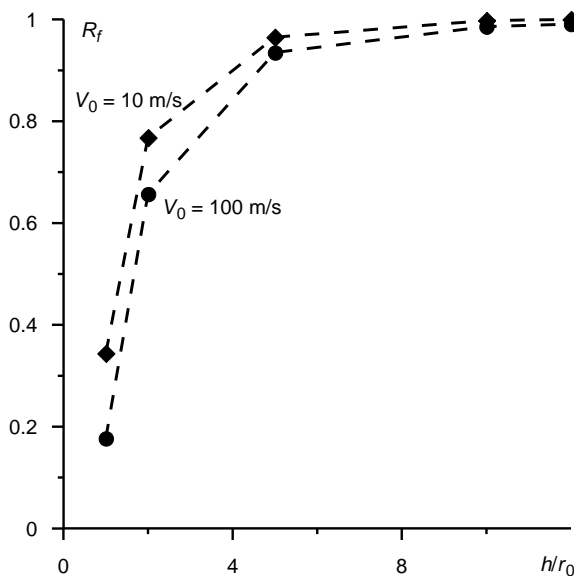


Fig. 8. Dependence of the coefficient of restitution  $R_f$  on the dimensionless parameter  $h/r_0$  for collision velocities  $V_0=10$  m s<sup>-1</sup> and  $V_0=100$  m s<sup>-1</sup>

The last rows in Tables 2-3 present the absorption energy  $E_a$ . The conversion of kinetic energy is transformed into strain energy resulting from deformation

$$E_a = \frac{m_1 V_0^2}{2} - \frac{m_1 V_s^2}{2} \quad (55)$$

Research has shown that thin layers have the best ability to absorb energy. The deformation energy at impact decreases as the collision speed increases.

Tables 2 and 3 show the corresponding kinematic and dynamic values (marked with an asterisk) calculated according to solving problem (49), (50) (Zener model [15]) taking into account (8), (47). Comparing the values without asterisks with the values with asterisks, we see that they come very close to a thin slab with thickness  $h = 2 h^*$ . This allows us to carry out the calculation of the impact parameters in a much simpler way.

Fig. 9, based on Tables 2 and 3, shows the results of the dependence of the coefficient of restitution  $R_f$  on the dimensionless parameter  $\lambda^*$  which is referred to in the literature as the inelasticity parameter [15]. Inelasticity is the dissipation of energy during a

collision due to the formation of elastic waves which lift the energy away from the collision point.

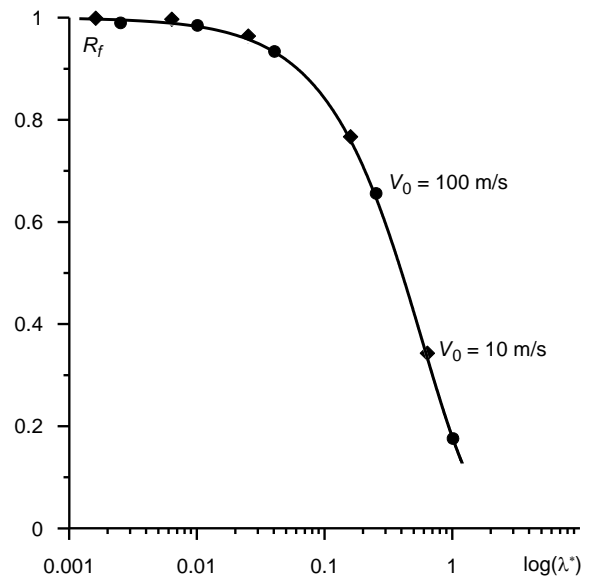


Fig. 9. Dependence of the coefficient of restitution  $R_f$  on inelasticity parameter  $\lambda^*$  for collision velocities  $V_0=10$  m s<sup>-1</sup> and  $V_0=100$  m s<sup>-1</sup>. Results from Tab. 2 presented in diamonds, results from Tab. 3 presented in circles, the solid line corresponds to formula (54) for  $R_f^*$

For velocity  $V_0 = 10$  m s<sup>-1</sup>, the results are presented in diamonds and for  $V_0 = 100$  m s<sup>-1</sup> they are presented in circles. The solid line corresponds to the semi-empirical relationship (54) of the coefficient of restitution  $R_f^*$  with  $\lambda^*$ . The calculated results from the tables correlate well with this curve.

## 5. SUMMARY

A mathematical model of the dynamics of the contact system between a bumper and a layer of finite thickness during their collision has been developed. The proposed calculation method using classical Laplace and Hankel transforms allows to solve the problem of the spatial model of the body.

The proposed analysis makes it possible to calculate the stresses and displacements in the elastic layer, as well as the kinematics of the impactor.

Original elements of the paper include the proposed general approach to solving the contact dynamics problem. The approach presented is to determine the impact force on the sample  $P(t)$  during impact as a joint solution of the problem for the impactor and the problem for the elastic layer under the assumptions of Hertzian theory. The resulting force  $P(t)$  allows the determination of displacements and stresses.

The calculations carried out showed that for layer thicknesses of more than five impactor diameters, the layer can be considered as a half-space. The model of the anvil will be a half-space.

Let us point out that the Zener model [15] of the coefficient of restitution (54) for the elastic plate under the conditions considered agrees well with the results for the elastic layer including and for the half-space (Fig.9).

The proposed method can be useful for the dynamic analysis of issues such as the collision of a sample with a layered body [43].

## REFERENCES

1. Pyr'yev Y, Penkul A, Cybula L. Research of dynamic processes in an shield during a collision with a sample. *Acta Mechanica et Automatica*. 2023;6(3):77-87.
2. Taylor G. The use of flat-ended projectiles for determining dynamic yield stress. I. Theoretical considerations. *Proc. R. Soc. London Ser. A*. 1948;194:289-299.
3. Włodarczyk E, Michałowski M. Penetration of metallic half-space by a rigid bullet. *Issues of Armament Technology*. 2002;31(82):93-102.
4. Świerczewski M, Kłasztorny M, Dziwulski P, Gotowicki P. Numerical modelling, simulation and validation of the SPS and PS systems under 6 kg TNT blast shock wave. *Acta Mechanica et Automatica*. 2012;6(3):77-87.
5. Kil'chevskii NA. Dynamic Contact Compression of Two Bodies. Impact [in Russian]. Kiev: Naukova Dumka; 1976.
6. Johnson KL. Contact mechanics. Cambridge: Cambridge University Press; 1985.
7. Kubenko VD. Impact of blunted bodies on a liquid or elastic medium. *International Applied Mechanics*. 2004;40(11):1185-1225.
8. Kubenko VD. Nonstationary deformation of an elastic layer with mixed boundary conditions. *International Applied Mechanics*. 2016; 52(6):563-580.
9. Ruta P, Szydio A. Drop-weight test based identification of elastic half-space model parameters. *Journal of Sound and Vibration*. 2005;282:411-427.
10. Achenbach JD. Wave propagation in elastic solids. North-Holland: Elsevier. 1973.
11. Senderowski C. Iron-aluminium inter metallic coatings synthesized by supersonic stream metallization. Warsaw: Bel Studio; 2015.
12. Miklowitz J. Transient Compressional Waves in an Infinite Elastic Plate or Elastic Layer Overlying a Rigid Half-Space. *Journal of Applied Mechanics*. 1962;29(1):53-60.
13. Valeš F, Šebková H. The state of stress in non-stationary loaded thin belt. *Acta Technica ČSAV*. 1976;4:439-458.
14. Kubenko VD, Salenko SD. Wave Formation in an Elastic Layer Under Moving Nonstationary Load. *International Applied Mechanics*. 2019;55(2):175-186.
15. Zener C. The intrinsic inelasticity of large plates. *Physical Review*. 1945;59(8):669-673.
16. Raman CV. On Some Applications of Hertz's Theory of Impact. *Phys. Rev.* 1920;15(4):277-284.
17. Peng Q, Liu X, Wei Y. Elastic impact of sphere on large plate. *Journal of the Mechanics and Physics of Solids*. 2021;156:104604.
18. Olsson R. Impact Response of Orthotropic Composite Laminates Predicted by a One-Parameter Differential Equation. *AIAA Journal*. 1992;30(6):1587-1596.
19. Smetankina NV, Shupikov AN, Sotrikhin SYu, Yareshchenko VG. A Noncanonically Shape Laminated Plate Subjected to Impact Loading: Theory and Experiment. *J. Appl. Mech.* 2008;75(5):051004.
20. Patil D, Higgs CF. A coefficient of restitution model for sphere-plate elastoplastic impact with flexural vibrations. *Nonlinear Dynamics*. 2017;88(3):1817-1832.
21. Mueller P, Boettcher R, Russell A, Truee M, Tomas J. A novel approach to evaluate the elastic impact of spheres on thin plates. *Chem. Eng. Sci.* 2015;138:689-697.
22. Muller P, Bottcher R, Russell A, True M, Aman S, Tomas J. Contact time at impact of spheres on large thin plates. *Adv. Powder Technol.* 2016;27:1233-1243.
23. Boettcher R, Russell A, Mueller P. Energy dissipation during impacts of spheres on plates: Investigation of developing elastic flexural waves. *Int. J. Solids Struct.* 2017;106:229-239.
24. Green I. The prediction of the coefficient of restitution between impacting spheres and finite thickness plates undergoing elastoplastic deformations and wave propagation. *Nonlinear Dynamics*. 2022; 109(4), 2443-2458.
25. Awrejcewicz J, Pyryev Yu. Nonsmooth Dynamics of Contacting Thermoelastic Bodies. New York: Springer Verlag; 2009.
26. Sears JE. On the longitudinal impact of metal rods with rounded ends. *Proc. Cambridge Phil. Soc.* 1908;14:257-286.
27. Hunter SC. Energy absorbed by elastic waves during impact. *J. Mech. Phys. Solids*. 1957;5:162-171.
28. Andersson M., Nilsson F. A perturbation method used for static contact and low velocity impact. *Int. J. Impact Eng.* 1995;16:759-775.
29. Timoshenko SP, Young DH, Weaver WJr. *Vibration Problems in Engineering*. New York: Wiley. 1974.
30. Argatov II. Asymptotic modeling of the impact of a spherical indenter on an elastic half-space. *International Journal of Solids and Structures*. 2008;45:5035-5048.
31. Rathore KK, Jasra Y, Saxena RK. Numerical simulation of fracture behavior under high-velocity impact for Aluminium alloy 6060 target plate. *Materials Today Proceedings*. 2020; 28(3):1809-1815.
32. Patra S, DasGupta A. Dependence of the coefficient of restitution on the shape of an impacting body. *International Journal of Solids and Structures*. 2023;281:112437.
33. Hertz H. Über die Berührung fester elastischer Körper [in German]. *Journal für die reine und angewandte Mathematik*. 1881;92:156-171.
34. Popov SN. Impact of a rigid ball onto the surface of an elastic half-space. *Soviet Applied Mechanics*. 1990;26(3):250-256.
35. Lamb H. On Waves in an Elastic Plate. *Proceedings of the Royal Society*. 1917; A, 93:114-128.
36. Awrejcewicz J, Pyryev Yu. The Saint-Venant principle and an impact load acting on an elastic half-space. *Journal of Sound and Vibration*. 2003;264(1):245-251.
37. Grinchenko VT, Meleshko VV. Harmonic vibrations and waves in elastic bodies [In Russian]. Kiev: Naukova Dumka; 1981.
38. Piessens R, Doncker-Kapenga ED, Überhuber CW, Kahaner DK. Quadpack. A Subroutine Package for Automatic Integration. Berlin Heidelberg: Springer-Verlag. 2011.
39. Argatov II, Fadin YA. Excitation of the Elastic Half-Space Surface by Normal Rebounding Impact of an Indenter. *Journal of Friction and Wear*. 2009;30(1):1-6.
40. Peng Q, Jin Y, Liu X, Wei YG. Effect of plasticity on the coefficient of restitution of an elastoplastic sphere impacting an elastic plate. *Int. J. Solids Struct.* 2021;222-223. 111036:1-11.
41. Ciavarella M, Joe J, Papangelo A, Barber JR. The role of adhesion in contact mechanics. *J. R. Soc. Interface*. 2019;16(151):20180738.
42. Peng B, Feng XQ, Li QY. Decohesion of a rigid flat punch from an elastic layer of finite thickness. *J. Mech. Phys. Solids*. 2020;139:103937.
43. Kulczycki-Żyhajło R, Kołodziejczyk W, Rogowski G. Selected issues of theory of elasticity for layered bodies. *Acta Mechanica et Automatica*. 2009;3(3):32-38.

Yuriy Pyr'yev:  <https://orcid.org/0000-0002-9824-2846>

Marek Pawlikowski:  <https://orcid.org/0000-0002-3950-691X>

Rafał Drobnicki:  <https://orcid.org/0000-0003-0582-5346>

Andrzej Penkul:  <https://orcid.org/0000-0001-9855-6610>



This work is licensed under the Creative Commons BY-NC-ND 4.0 license.



# DETERMINATION OF STATIC FLOW CHARACTERISTICS OF A PROTOTYPICAL DIFFERENTIAL VALVE USING COMPUTATIONAL FLUID DYNAMICS

Marcin KISIEL<sup>\*</sup>, Dariusz SZPICA<sup>\*</sup>

<sup>\*</sup>Faculty of Mechanical Engineering, Bialystok University of Technology, Wiejska 45C, 15-351 Bialystok, Poland

[marcin.kisiel@sd.pb.edu.pl](mailto:marcin.kisiel@sd.pb.edu.pl), [d.szpica@pb.edu.pl](mailto:d.szpica@pb.edu.pl)

received 21 November 2023, revised 18 May 2024, accepted 20 May 2024

**Abstract:** The paper describes the numerical calculations of a conceptual air brake valve of a trailer equipped with a differential section, which is intended to shorten response time and braking distance. The static flow characteristics have been determined using computational fluid dynamics (CFD). Mixed (global and local) computational meshes were used in the paper to determine the static flow characteristics of the valve sections. The use of the local mesh was relevant for valve openings smaller than 0.5mm. Using CFD, it was possible to determine the static flow characteristics of the main, auxiliary feed and the differential sections, which were linear, degressive and progressive depending on the section. The analyzes, which have not yet been described in the literature, showed a significant difference in the MFR of the additional and main feed tracts, which reached 52.29%. The results are applicable to the configuration of the braking system. Further research will include performing dynamic simulations using dedicated software and building a test rig to validate the CFD calculation results.

**Key words:** Mechanical engineering, differential braking valve, pneumatic braking valve, CFD, static flow characteristics

## 1. INTRODUCTION

Technological developments in agriculture [1][2], particularly organic farming [3]-[5], have encouraged the increasing use of air and hydraulic braking systems widely used in crop trailers. What works in favour of pneumatic systems is the lack of possibility of environmental and groundwater contamination [6] in the event of damage. Maintaining the agricultural tractor, machinery and trailers in good working order contributes to reducing the possibility of environmental pollution. Replacement of pneumatic solutions for trailer braking systems used in agriculture with hydraulic solutions has made it possible to improve the performance of the system with a concomitant increase in the risk of environmental pollution from hydraulic oil [7]. Environmental pollution can occur during coupling, uncoupling of the trailer or in the event of a system failure, while the use of a pneumatic braking system neutralizes this risk, limiting it to the emission of only the products of wear of the friction material of the brake linings [8][9] used in transport trailers.

Pneumatic braking systems are widely used in the transportation industry, both on truck tractors and agricultural tractors, as well as semi-trailers and trailers. Due to the increasing normative requirements [10] imposed by regulations, classical systems controlled by pneumatic signals are gradually being replaced by hydraulic systems and electropneumatic solutions [11]. This is due to the much faster response time of the above systems compared to fully pneumatic systems [12]. The authors noted the possibility of introducing design changes, in one of the most widely used classic valves for activating the brakes of a trailer Visteon 44100110, also called HZS-02 valve, introducing a differential (accelerating) section. On the basis of preliminary analyses [13], it was noted that the response time of the system was significantly

reduced compared to the original solution, and the performance of hydraulic and electro-pneumatic systems was brought closer [14].

Computational fluid dynamics (CFD) is finding increasing application in various industries due to its capabilities and reliable results. The results of CFD numerical calculations are obtained by solving a system of differential equations describing the flow of a gas or liquid in a simulated system [15]. Numerical modeling using CFD provides an alternative approach to determining flow parameters such as velocity, pressure, flow type and temperature at any point in a concentrated volume with respect to complex and elaborate analytical models. CFD methods use the Reynolds-Averaged Navier-Stokes (RANS) equations [16][17] to search for a solution and allow evaluation of the effect of changing the model boundary conditions on the static characteristics of the valve without the need for verification on a laboratory bench. Determining the pressure in the concentrated volume and the MFR (Mass Flow Rate) or VFR (Volumetric Flow Rate) gives the possibility to determine the static characteristics of the valve depending on its degree of opening and varying boundary conditions. The solution of the stream flow equations by local resistances, which are structural elements of the geometry under consideration, allow determining the velocity and pressure in any section of the simulation model. Numerical methods are used to determine flow parameters [18][19] and static characteristics [20] necessary for the correct selection of pneumatic and hydraulic components, including valves [21]-[24].

The high level of accuracy and quality of the simulation results obtained is largely dependent on the degree of discretization of the model resulting from the computational mesh used [25][26]. Over-densification of the global mesh in the clustered volume does not significantly improve the obtained results, but increases the simulation time [27][28]. In order to densify the model in sensitive areas (narrow gaps), SolidWorks uses additional tools like

channels and equidistant refinement, that create a local mesh in the declared area bounded by the model planes. Other CFD tools, including Ansys Fluent, allow changing the shapes of computational mesh elements and creating hybrid meshes that form a combination of two or more default mesh types.

Attempts at numerical modeling of pneumatic brake valves [29]-[31] have been noted among numerous research papers. The authors recognized a research gap related to the lack of studies containing attempts to simulate models of pneumatic brake valves as whole actuating components, using computational fluid mechanics (CFD) tools.

Pneumatic systems, although increasingly displaced by hydraulic systems, do not pose an environmental hazard in the event of a system leak. Despite the longer response time of the pneumatic system compared to the hydraulic system in agricultural transport, the most common are combination systems that allow connection with the air or hydraulic braking system of the tractor.

The following sections of the article present the structure of the research object, the proposal of design changes introducing the differentiation term proposed by the authors, the theoretical basis for the numerical solution of flow problems and the boundary conditions of the performed numerical analyses. Mesh convergence assessment enabled the selection of appropriate settings for a given geometry while maintaining optimal simulation time. Based on the selected mesh settings, CFD simulations were performed for three sections of the considered valve, taking into account different degrees of opening or diameter of the flow channel, taking into account the simplifications required for the correct implementation of the model in the CFD environment. The determined MFR values made it possible to determine the static flow characteristics of the trailer's pneumatic brake valve in its various power supply sections, which constitutes a research gap and is an introduction to the analysis of the results obtained using numerical and experimental methods, which are the authors' research area. The proposed modification of the structure of the trailer brake valve will shorten the response of the braking system in emergency braking situations and will probably lead to its implementation in industry, after additional numerical and experimental tests.

## 2. OBJECT OF RESEARCH

### 2.1. Trailer air brake valve Visteon 44100110

For the implementation of the prototype differential valve, the Visteon 44100110 trailer brake valve was used (Fig. 1).



Fig. 1. Visteon 44100110 trailer brake valve

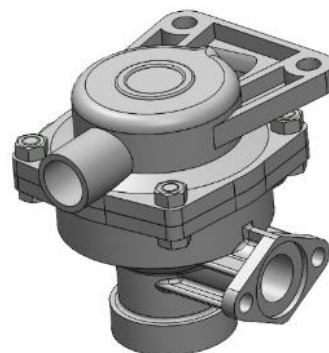


Fig. 2. CAD model of Visteon 44100110 brake valve

Fig. 1 shows a view of the original valve, while Fig. 2 shows a CAD model of the valve created in SolidWorks software. The selected valve can work with both single- and dual-line systems, and a description of the valve's connection to both types of tractor air brake systems is shown in Tab. 1.

Tab.1. Description of valve connections

Symbol	M	Zm	V	Z
Single line system	Connected with brake supply and control section	Not connected and sealed	Connected with compressed air reservoir of a trailer	Connected directly into brake actuator or brake force regulator
Dual line system	Connected with brake supply section	Connected with brake control section		

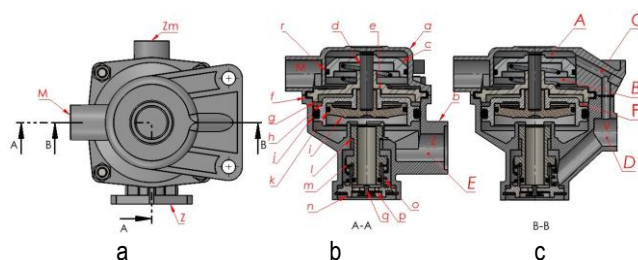


Fig. 3. View of the valve: a - top view; b - A-A cross-sectional view of main supply line; c - B-B cross-sectional view of additional supply line

Based on the valve construction diagram Fig. 3, it should be noted that during single-line operation, the pneumatic control and supply signal from the *M* connection feeds the compressed air tank chamber of the trailer *D* by flowing between the surface of the piston *c* with lip seal *r* and the valve body *a* and further through channel *C*. During driving, the valve performs the function of supplying the reservoir, and the chamber *E* is vented through the vent *p* due to the passage between the seat in the piston *i* and the bushing *l*. Applying the brakes causes a pressure drop in the *M* connection and chamber *A*, which translates into a pressure difference between the reservoir connection *V* and the supply and control connection *M*. The pressure difference causes the chamber over the piston *c* to seal, overcoming the tension force of the spring *e* and displacing the piston *c* together with the guide *d* and piston *i* to the bushing *l* closing the connection with the atmosphere and opening the passage between the bushing *l* and the

body  $b$  from the tank chamber  $D$  to the chamber  $E$  connected with brake actuator. The increasing pressure in the chamber under the piston  $i$  and the force of the tension of the spring  $o$  causes the gradual movement of the piston assembly and bushing  $l$  until the connection between the output connection  $Z$  and the chamber of the tank  $D$  is closed. Depending on the ratio of pressures above and below the piston  $i$ , the braking force is reduced, causing the trailer to be decelerated and the air cylinders to be vented through the vent  $p$ .

Connection of the valve in a two-line system requires the use of a control port  $Zm$  connected to the control chamber  $F$  under the element  $g$ . When the brakes are applied, the increasing pressure in the  $Zm$  connection causes the displacement of pistons  $h$  and  $i$  down into bushing  $l$  and the closing of the connection of chamber  $E$  with atmospheric pressure through vent  $p$ . The downward displacement of bushing  $l$ , after overcoming the force in spring  $o$ , causes the connection of chambers  $D$  and  $E$  and the application of the trailer brakes. The pressure drop in the  $Zm$  connection caused by the deceleration of the vehicle combination causes the displacement of pistons  $h$  and  $i$  and the opening of the passage between piston  $i$  and bushing  $l$ , while closing the connection of chambers  $D$  and  $E$ . When the valve is switched to the reservoir supply function, the chambers of the pneumatic cylinders are vented through the vent  $p$ , and the trailer brakes are released.

## 2.2. Conceptual differential braking valve

The conceptual differential valve was obtained by appropriate modifications to the base valve shown in Fig. 3. The modified valve is shown in Fig. 4. The main change was the replacement of the main supply connection with a tee  $p$ , which also supplies through the s-connector and  $t$ -wire a chamber  $A$  above piston  $c$ .

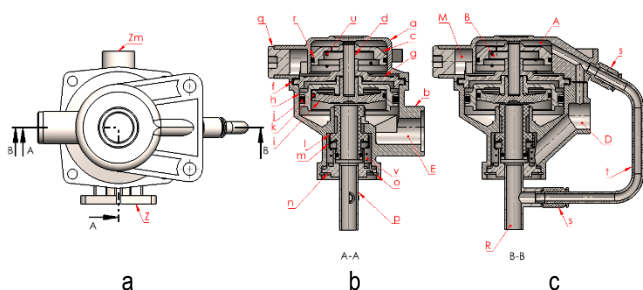


Fig. 4. View of differential valve; a - top view; b - A-A cross-sectional view of main supply tract; b - B-B cross-sectional view of differential tract

The existing supply connection  $M$  has been plugged with a plug  $q$ . At the same time, the valve is supplied by bushing  $l$  and the gap under piston  $i$  is adjusted by the position of piston  $i$  and bushing  $l$  regulates the supply of chamber  $E$  connected directly to the brake actuator. In the case of slow braking (Fig. 5), the tee  $p$  connection is supplied with compressed air and further supplies the output connection. The differential section in this case remains inactive, due to the small pressure difference between chambers  $A$  and  $B$ .

In the case of panic braking (Fig. 6), there is a rapid pressure increase in the chamber  $A$ . The nozzle used with the appropriate cross-section restricts the flow between chambers. The increasing pressure in chamber  $A$  causes the valve's differential section to operate and move the piston  $c$  together with the pin  $d$  and the pistons  $h$ ,  $i$  toward bushing  $l$  and close the supply from the tee  $p$ .

The movement of the pistons and resting on the wall of bushing  $l$  causes it to move downward and open the supply to chamber  $E$  from an additional compressed air reservoir (chamber  $D$ ) located near the valve.

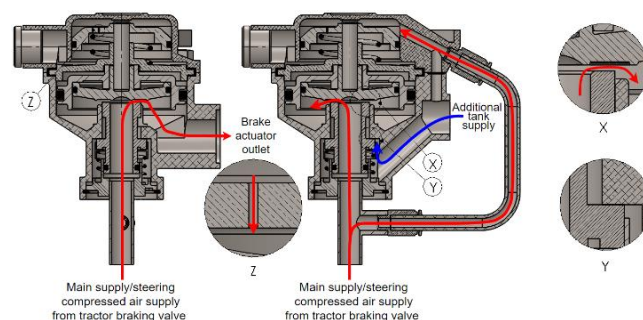


Fig. 5. Slow braking

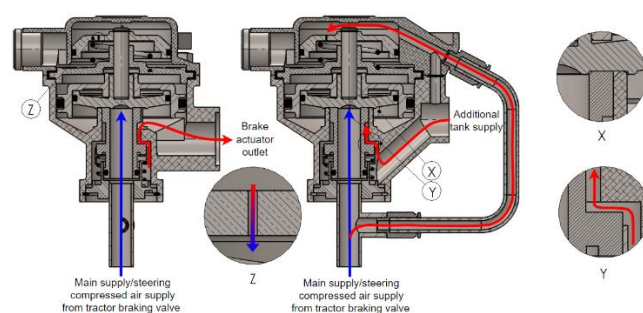


Fig. 6. Emergency, rapid braking

In the situation of equalization of pressures in chambers  $A$  and  $B$  (Fig. 7) there is an upward displacement of pistons  $c$ ,  $h$ ,  $i$  with the pin  $d$  caused by the force in the spring  $u$ . This action causes deactivation of differential section and closure of the valve supply from the additional air reservoir and transition to the tracking action resulting from the valve supply from the tee  $p$ .

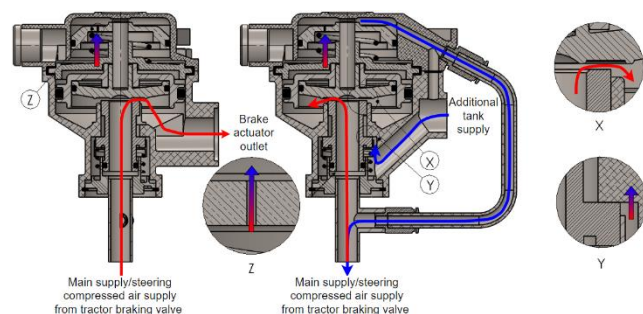


Fig. 7. Switching the braking valve to tracking function

## 3. CALCULATION METHODOLOGY

### 3.1. Theoretical basis

The preponderance of flow calculation software uses the Finite Volume Method (FVM) [32][33]. This method is based on the division of extended geometries into smaller volumes, in which it is possible to determine the distributions of characteristic quantities, mainly flow velocity, pressure, density, temperature and others, without having to search for a general solution for the entire model. The division of concentrated volumes into individual



cells makes it possible to determine the values of its flow parameters on the basis of the balance of a given cell and neighboring cells.

The SolidWorks Flow Simulation used in this study uses an orthogonal mesh of concentrated volumes based on orthogonal cells with walls parallel to the planes of the model's main coordinate system. The computational mesh, depending on the declared settings, can be the same size throughout the model cross-section (global mesh) or thicken in sensitive areas with a limited flow field (local mesh). By default, the mesh tools available in SolidWorks Flow Simulation allow the definition of seven degrees of global mesh density. The quality of the clustered volume mesh has a key impact on accuracy and calculation time, so local global mesh densities are used to minimize model discretization errors. However, the final mesh selection should be preceded by an assessment of mesh convergence for a given geometry. Local mesh options include additional tools such as equidistant refinement and channels. Equidistant refinement allows a 9-degree thickening of the liquid or working gas area within a normal distance from the selected model element. Channels allows the mesh to be compacted into narrow channels bounded by the model walls to obtain the best flow velocity distribution profile.

The finite volume method, which is the basis of CFD numerical calculations, including SolidWorks Flow Simulation, is based on dividing a continuous flow area into a set of discrete cells of a certain volume depending on the grid size, and determining by numerical methods the flow parameters of a liquid or gas stream by obtaining the solution of a system of differential equations. The search for a solution is limited to the principle of conservation of momentum for a moving gas according to the conservation of mass (1) [34] and the Navier-Stokes equations (2) [35]. The solution of these equations makes it possible to determine the velocity and pressure in any section of the model for any geometry.

$$\frac{\partial p}{\partial t} + \nabla(pv) = 0 \quad (1)$$

$$p \frac{\partial v}{\partial t} = -\nabla p + \rho g + \mu \nabla^2 v \quad (2)$$

SolidWorks Flow Simulation allows simulation of laminar as well as turbulent flows, with the Navier-Stokes equations with Favre mass averaging [36][37] being used for turbulent flows of compressible gases. This type of calculation provides an opportunity to take into account the effect of turbulence on flow parameters using the  $k$ - $\varepsilon$  turbulence model, the solution of which is to find the value of  $\mu_t$  shown in equations (3) and (4) based on the kinetic energy of the vortices  $k$  and the rate of dispersion  $\varepsilon$ .

$$\mu_t = \rho v_t = \rho C_\mu \frac{k^2}{\varepsilon} \quad (3)$$

$$C_\mu = \left(\frac{3C_k}{2}\right)^{-3} \cong 0.1 \quad (4)$$

where:  $\varepsilon$  – rate of dispersion,  $k$  – kinetic energy of vortices for RANS model,  $\rho$  – gas density,  $C_\mu$  – constant  $\sim 0.1$ ,  $C_k$  – Kolomogorow constant,  $C_k=1.4$ -1.5,  $v_t$  – turbulent viscosity coefficient.

The components of equation (3) for the kinetic energy of turbulence are shown in equation (5), and for the energy of dispersion in (6):

$$\frac{\partial \rho k}{\partial t} + \frac{\partial \rho k v_i}{\partial x_i} = \frac{\partial}{\partial x_i} \left( \left( \mu + \frac{\mu_t}{\sigma_k} \right) \frac{\partial k}{\partial x_i} \right) + \tau_{ij}^R \frac{\partial v_i}{\partial x_j} - \rho \varepsilon + \mu_t P_B \quad (5)$$

$$\frac{\partial p k}{\partial t} + \frac{\partial \rho \varepsilon v_i}{\partial x_i} = \frac{\partial}{\partial x_i} \left( \left( \mu + \frac{\mu_t}{\sigma_k} \right) \frac{\partial k}{\partial x_i} \right) + C_{\varepsilon 1} \frac{\varepsilon}{k} \left( f_1 \tau_{ij}^R \frac{\partial v_i}{\partial x_j} + C_B \mu_t P_B \right) - f_2 C_{\varepsilon 2} \frac{\rho \varepsilon^2}{k} \quad (6)$$

where:  $\sigma_{k,\varepsilon}$  – turbulent Prandtl number.

### 3.2. Calculation plan

The CFD numerical calculations included an assessment of the convergence of the global mesh for the geometry under consideration. Using all available mesh sizes in SolidWorks Flow Simulation, a simulation was carried out using constant boundary conditions in all variants to determine the effect of the mesh used on the values of the average relative and absolute error.

The second step involved determining the static characteristics of the main supply section of the prototype differential valve over the entire operating range (0...2.0) mm with a step of 0.1 mm. The defined boundary conditions made it possible to evaluate the effect of the degree of valve opening on the Mass Flow Rate (MFR) at the pneumatic actuator port Z (Fig. 4).

The third step involved the determination of the static characteristics of the additional accelerating tract in the situation of activating the differential section according to Section 2.2. The static characteristics were determined over the full operating range (0...1.7) mm with a step of 0.1 mm.

The last step of the calculation was to determine the static flow characteristics for the differential system with a nozzle of (0.75...3) mm in diameter in 0.25 mm increments placed in the piston c (for simplicity, the nozzle model was replaced by a hole) between chambers A and B of the simulation model.

Before determining the static characteristics of the conceptual valve, it was predicted that in the case of a slow build-up of pressure in the control connection, the pressure difference in the differential section (chambers A and B) will be negligibly small. In the case of sudden (panic) braking, a large difference in pressure between chambers A and B will cause activation of the differential section, closure of the control signal supply to the control-power connection and opening of the supply to the connection with an additional pressure reservoir located in a short distance from the valve, which will switch the valve to the acceleration function. Once the pressures in chambers A and B are equalized, the supply from the additional reservoir will be closed with a slight pressure surge due to the higher pressure value in the executive connection with respect to the supply and control connection.

## 4. RESULTS AND DISCUSSION

### 4.1. Assessment of the sensitivity of the computational mesh

As specified in the calculation plan, the sensitivity of the calculation grid was first evaluated. Based on the basic mesh sizes and fixed boundary conditions defined in SolidWorks Flow Simulation, the effect of the global mesh size on the MFR was investigated with the main valve feed section opening at the center of the operating range - 1.0 mm.

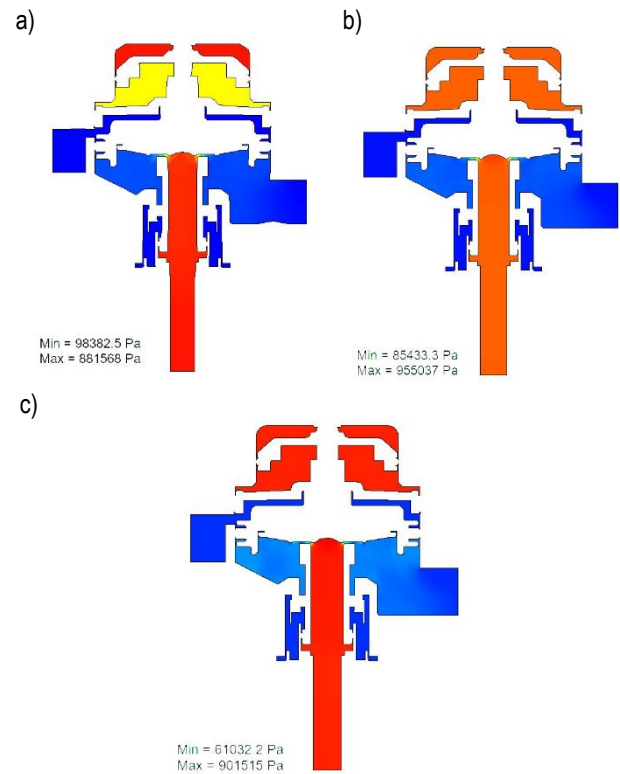


Fig. 8. Pressure distribution for different global mesh densities in SW Flow Simulation: a – first level; b – fourth level; c – seventh level

Tab. 2. Results of mesh convergence assessment

Mesh size	1	2	3	4	5
MFR [kg/s]	0.090821	0.089119	0.092036	0.093707	0.093245
Fluid cells	7209	4228	19449	45606	128290
Cells	6817	4076	14610	29170	65336
Iterations	46	45	104	132	150
Time [s]	15	11	45	105	251
MAE	0.001671	0.003374	0.000457	0.001215	0.000752
MAPE[%]	1.8%	3.6%	0.5%	1.3%	0.8%
Mesh size	6	7			
MFR [kg/s]	0.094412	0.094110			
Fluid cells	13295523	3512115			
Cells	44101	889461			
Iterations	259	365			
Time [s]	3678	13056			
MAE	0.001919	0.001617			
MAPE[%]	2.1%	1.7%			

Based on the results obtained, as shown in Tab. 2, it was concluded that a global mesh size of 3 or 5 should be adopted for further study, as they have the lowest MAPE (Mean Absolute Percentage Error) in the case under consideration. Careful observation of the distribution of the global mesh in both cases and solver errors reporting the occurrence of turbulence affecting the final results decided to exclude these two grid sizes from further study.

In order to reduce simulation time, authors decided to use the global mesh in 6th size with an additional local mesh with the channels and equidistant refinement tools in critical areas. Using a finer mesh would have significantly increased computation time.

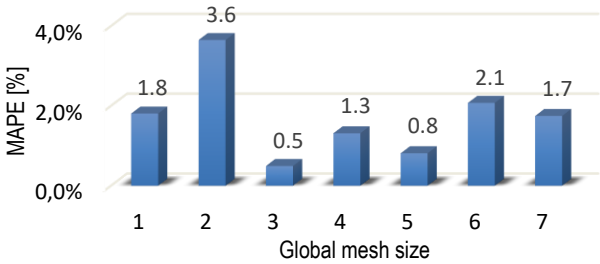


Fig. 9. MAPE value for different global mesh sizes

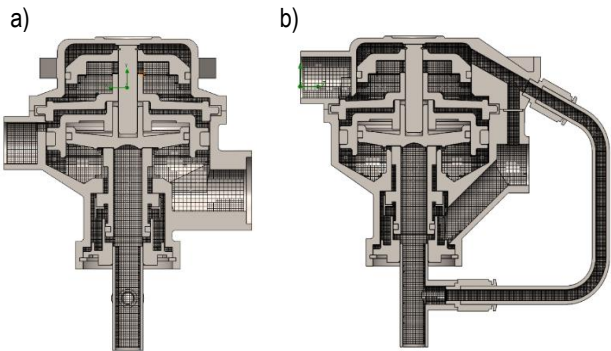


Fig. 10. Cross-sectional view of model with global mesh in 6th size: a - front plane view; b - right plane view

#### 4.2. Determining the static flow characteristics

Before the appropriate calculations in SolidWorks Flow Simulation, the model has been simplified to enable correct implementation in the numerical environment:

- the pressure value in the main supply port was replaced by a fixed value of 901325 Pa, in the other connections of the valve the value was set to 101325 Pa. In the case of the implementation of the simulation of the acceleration section, the value of 901325 Pa was declared in the connection of the additional compressed air tank, and the pressure in the main supply connection was replaced by the value of atmospheric pressure 101325 Pa,
- the springs  $u$ ,  $v$  were removed (Fig. 4),
- all o-ring seals were replaced with square seals,
- The circlips were removed and replaced with ring elements (the circlips caused leaks in the model).

According to the calculation plan presented in Section 3.2, three static characteristics of a conceptual brake valve with a differential section were determined. Tab. 3 shows the basic simulation parameters used throughout the study, while Tab. 4 presents the parameters of the local grids used in all configurations - the variables for each of the three cases were the limiting planes of the critical areas.

The use of SolidWorks Flow Simulation software makes it possible to determine the static characteristics of the prototype differential valve solution, with other CFD tools to be used in the course of further work due to the high complexity of the valve's operation and the dynamic processes taking place. The built-in automation tools, including Parametric study and What If Analysis, enabled the valve elements' distance relationships to be changed



smoothly by creating separate simulation configurations. Consideration of each configuration enabled analysis and observation of the MFR and pressure distribution in valve's each chamber.

Tab. 3. Settings of simulation

Parameter	Value
Unit system	SI
Analysis type	Internal
Fluid	Air
Flow type	Laminar and turbulent
Default wall thermal condition	Adiabatic wall
Pressure	$p_0 = 101325$ Pa
Temperature	$T_0 = 293.2$ K
Turbulence intensity	2%
Turbulence length k	0.0010745 m

Tab. 4. Settings of local mesh

Parameter	Value
Level of refining fluid cells 0-9	3
Level of refining cells at fluid/solid boundary 0-9	3
Number of shells 0-3	2
Maximum equidistant level 0-9	3
Offset distance #1	0.025 mm
Offset distance #2	0.05 mm
Characteristic number of cells across channel	5
Maximum channel refinement level 0-9	3

#### 4.2.1. Static flow characteristics of main supply tract

Following the assumptions of the research plan and the defined boundary conditions of the model, numerical calculations of the main supply tract were carried out over the entire range of operation, and the obtained results are shown in Tab. 5.

Tab. 5. MFR of main supply tract

$h$ , mm	0	0.1	0.2	0.3	0.4	0.5
MFR, kg/s	0	0.008656	0.018604	0.028012	0.038925	0.050228
$h$ , mm	0.6	0.7	0.8	0.9	1	1.1
MFR, kg/s	0.059643	0.068209	0.076077	0.086252	0.096242	0.105225
$h$ , mm	1.2	1.3	1.4	1.5	1.6	1.7
MFR, kg/s	0.112869	0.119811	0.128374	0.137250	0.146309	0.153989
$h$ , mm	1.8	1.9	2.0			
MFR, kg/s	0.160861	0.168466	0.175830			

The pressure distribution for three different degrees of opening of the main supply tract is shown with a view of the model's computational mesh and in the sensitive area (Fig. 11 – Fig. 13).

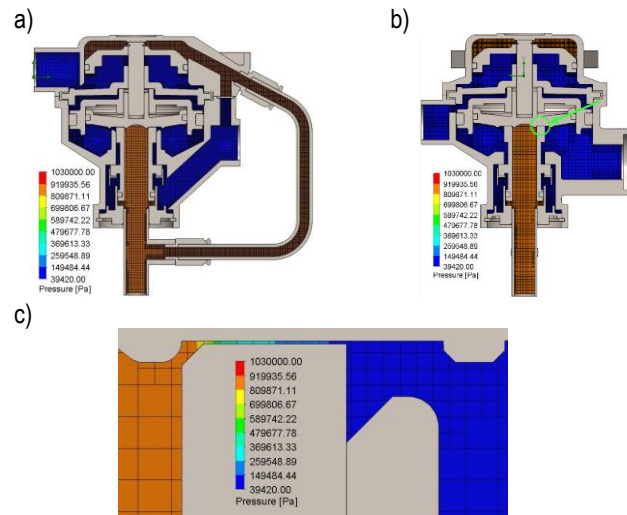


Fig. 11. Pressure distribution for 0.1 mm opening of main supply tract: a – right plane cross-sectional view; b – front plane cross-sectional view; c – detailed view

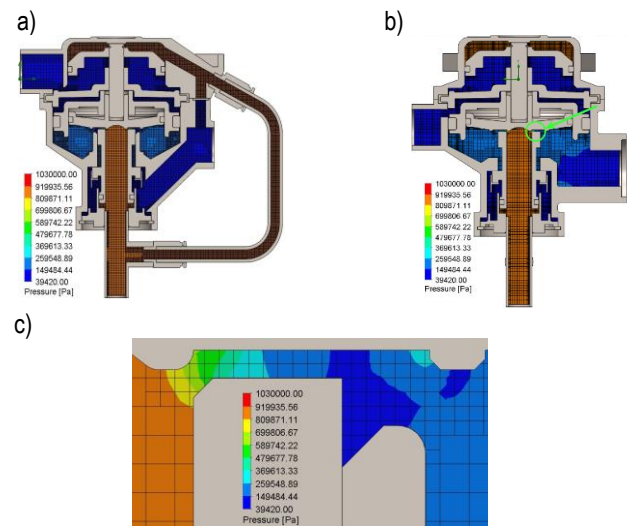


Fig. 12. Pressure distribution for 1.0 mm opening of main supply tract: a – right plane cross-sectional view; b – front plane cross-sectional view; c – detailed view

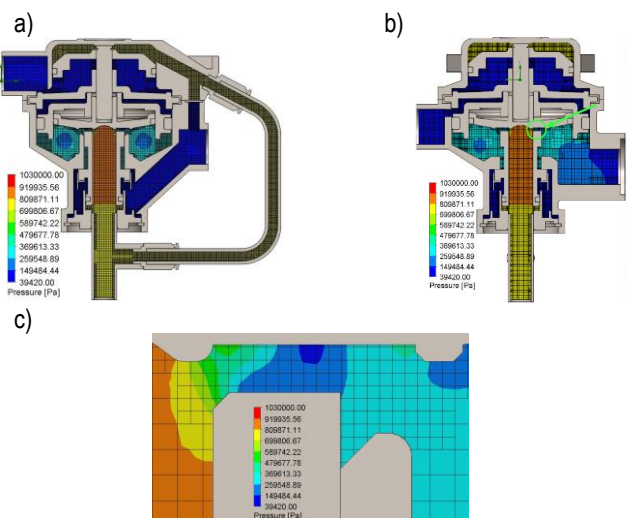


Fig. 13. Pressure distribution for 2.0 mm opening of main supply tract: a – right plane cross-sectional view; b – front cross-sectional view; c – detailed view

Based on the results obtained, the static characteristic of the main supply tract were plotted, which takes on an approximately linear character. In addition, the equation of the regression line shown in Fig. 14 was determined.

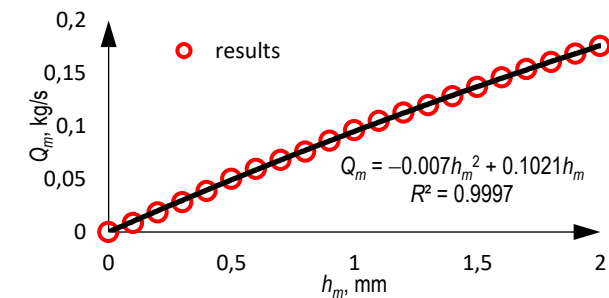


Fig. 14. Static flow characteristic of main supply tract

#### 4.2.2. Static flow characteristics of additional supply tract

Changing the boundary conditions and the direction of the compressed air flow in the model according to the assumptions presented in Section 2.2 will make it possible to determine the static characteristics of the additional supply tract. The results of the numerical calculations carried out for such a configuration are shown in Tab. 6.

Tab. 6. MFR of additional supply tract

$h$ , mm	0	0.1	0.2	0.3	0.4	0.5
MFR, kg/s	0	0.012464	0.029531	0.049478	0.062523	0.076488
$h$ , mm	0.6	0.7	0.8	0.9	1	1.1
MFR, kg/s	0.091224	0.107007	0.122079	0.131205	0.138388	0.144086
$h$ , mm	1.2	1.3	1.4	1.5	1.6	1.7
MFR, kg/s	0.149517	0.153732	0.155939	0.156892	0.157722	0.158217

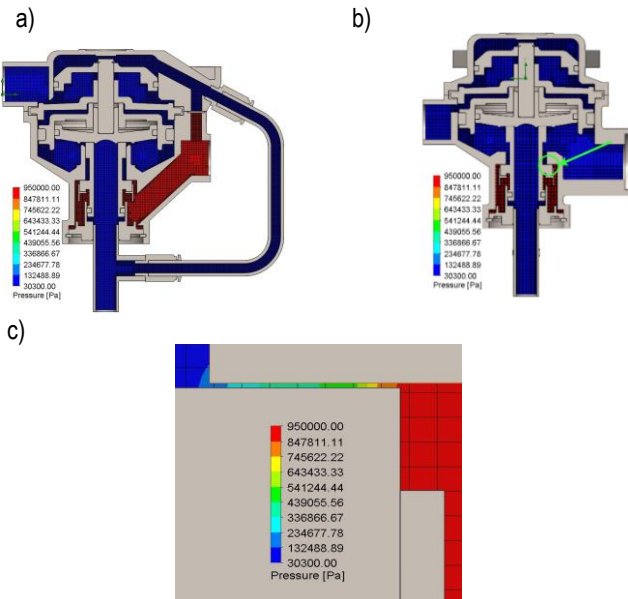


Fig. 15. Pressure distribution for 0.1 mm opening of additional supply tract: a – right plane cross-sectional view; b – front plane cross-sectional view; c – detailed view

The distribution of compressed air pressures for three different degrees of opening of the additional supply tract is shown with a view of the calculation grid in Fig. 15 – Fig. 17.

Based on the obtained MFR values for all degrees of opening of the additional supply tract, the static characteristics was plotted in Fig. 18.

The additional accelerating section of the differential section adopts a degressive character in the range of 1.4-1.7 mm valve opening. It is consistent with authors' previous results obtained in research on the unmodified Visteon valve, so the modifications did not affect the loss of the valve's original performance.

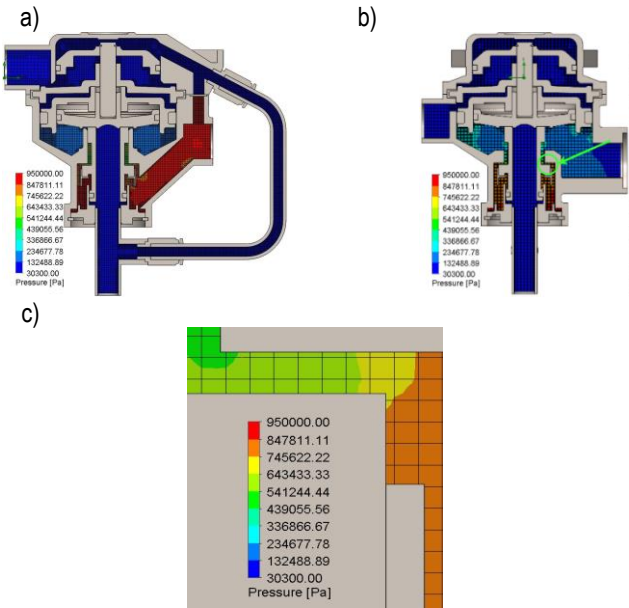


Fig. 16. Pressure distribution for 1.0 mm opening of additional supply tract: a – right plane cross-sectional view; b – front plane cross-sectional view; c – detailed view

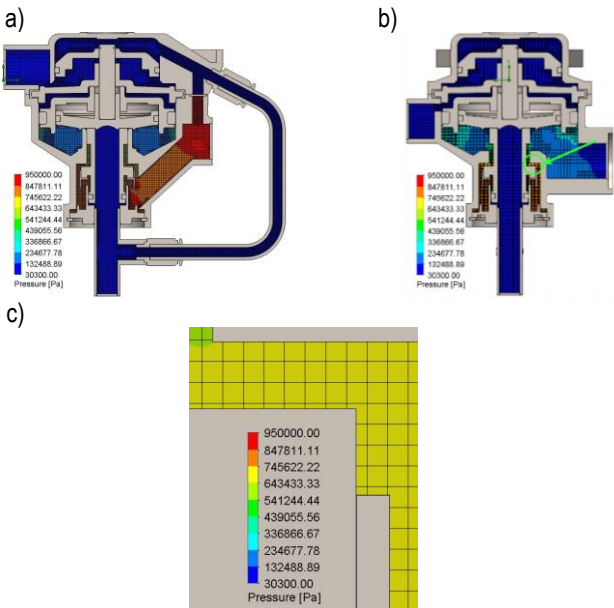


Fig. 17. Pressure distribution for 1.7 mm opening of additional supply tract: a – right plane cross-sectional view; b – front plane cross-sectional view; c – detailed view

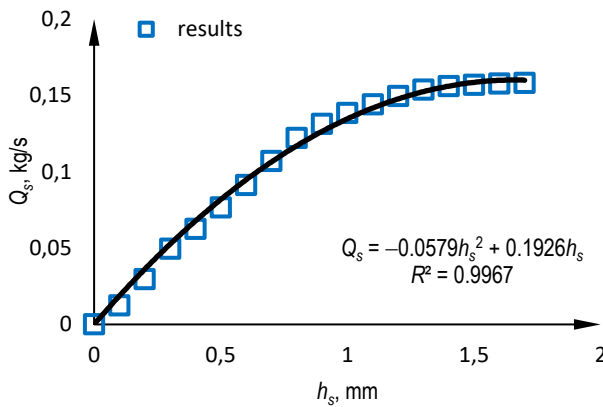


Fig. 18. Static flow characteristics of additional supply tract

#### 4.2.3. Static flow characteristics of differential section

In order to determine the static flow characteristics of the nozzle of the differential section, the model was further simplified by considering only its upper part to reduce calculation time. The nozzle was replaced by a hole in the piston c (Fig. 4) with the diameter assumed in the simulation plan presented in Section 3.2. The results of the numerical calculations carried out for this configuration are shown in Tab. 7.

Tab. 7. MFR of differential tract

$h$ , mm	0.75	1.00	1.25	1.50	1.75
MFR, kg/s	0.000629	0.001243	0.002006	0.002979	0.004078
$h$ , mm	2.00	2.25	2.50	2.75	3.0
MFR, kg/s	0.005387	0.006841	0.008508	0.010271	0.012234

The distribution of compressed air pressures in the differential section for the four nozzle diameters is shown along with views of the calculation grids in Fig. 19.

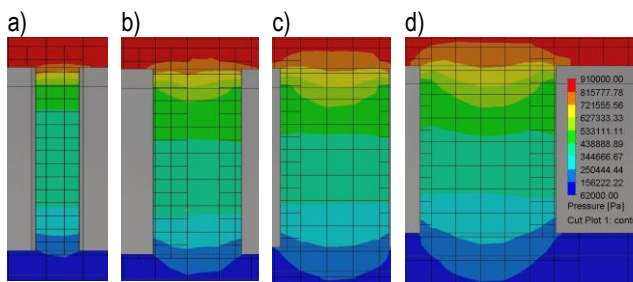


Fig. 19. Pressure distribution for different nozzle diameter: a - 0.75mm; b - 1.50mm; c - 2.25mm; d - 3.0mm

Experimental selection of the diameter of the nozzle connecting the chambers of the differential section, taking into account the geometry of the valve, made it possible to determine the static characteristics of a progressive nature (Fig. 20), with the correct range of nozzle diameters used in the real model to be selected during experimental testing.

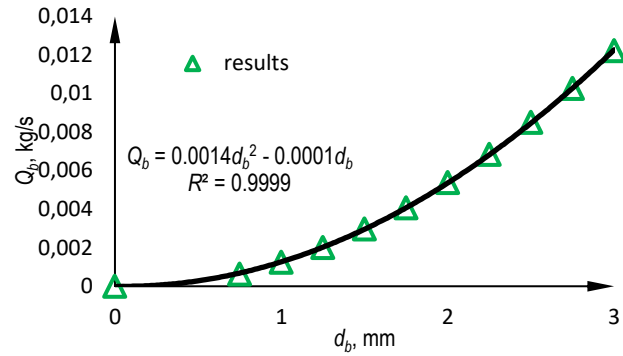


Fig. 20. Bore of the differential section

#### 4.3. Results discussion

Comparing the results of the calculations on a single graph (Fig. 21), there are visible differences in the shapes of the characteristics of the two valve supply tracts. For the purpose of comparisons, the two series of results were matched using the same regression equation based on the least squares method of deviations.

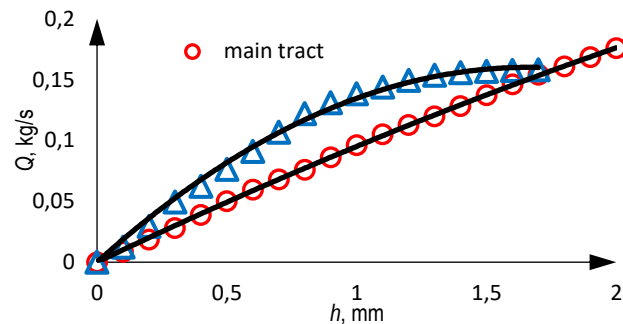


Fig. 21. Main and secondary tract comparison chart

In the main tract, the characteristics are very close to linear, and with a maximum opening of 2 mm the mass flow rate is 0.1758 kg/s. The secondary tract has characteristics with larger increments in the initial opening, while at a maximum opening of 1.7 mm it allows a mass flow rate of 0.1582 kg/s. The final opening range is characterized by a small gradient of increments. Transferring the determined characteristics to the operation of the differential valve, in the case of trailing action, the main-tract characteristics close to linear give the possibility of obtaining proportional action. The intentions of the brake pedal operator are translated into the responses of the braking system. With differential action (emergency braking), the secondary tract guarantees a large increase in mass flow rate even at small openings (at 0.5 mm, the MFR value of the secondary tract is 52.29% higher than the main tract), which promotes acceleration of the braking system. Further down the line, the secondary tract's characteristics stabilize, and at 1.7 mm it approaches the main tract. The differential action of the valve is to accelerate the system in the first phase, which is presented by the secondary line, and in the later stage return to the main tract supply. The important thing here is also the issue of the length of the air supply lines to the main and secondary lines, which are different and have different pressure drop along their length.

An indispensable element affecting the performance of the differential valve is the bore of the differential valve. As can be seen from Fig. 20, changing the diameter of the bore of the piston results in large changes in mass flow rate. Therefore, this diameter and the resulting flow cross-sectional area should be carefully selected for the specific trailer model and even the degree of loading. A large diameter guarantees a rapid return from accelerating to tracking action, while a small diameter delays the process. An inadequate diameter selection can cause trailer jerking in the initial phase of braking under sudden forcing, as well as in the transition from acceleration to tracking. Continuous control of the diameter of the valve that implements the differential action would be required, which is the basis for further work by the authors of the study. As a result, a mechatronic system will be proposed for the permanent correction of the differential action. The characteristics determined in the study are static characteristics applicable to the initial configuration of the pneumatic braking system. Ultimately, it is planned to carry out dynamic calculations in dedicated software for this purpose where it will be possible to evaluate the influence of individual components on the course of the response of the braking system under different types of operator action.

The application of the procedure path presented in the study can find its main application in the configuration of air brake systems, already at the stage of creating new solutions. It can also be useful when retrofitting a design to achieve certain characteristics. Knowledge of the static flow characteristics of flow element determines its performance and functional properties and allows to assess the applicability to a specific usage.

## 5. CONCLUSIONS

In the study, a series of CFD analyses were carried out to determine the static flow characteristics of the brake valve. The use of global and local computational meshes in the critical flow channels, bounded by the planes of the 3D model geometry of the valve, made it possible to determine the static characteristics of the valve for different tracts of compressed air flow. The limitation of the use of CFD to determine flow parameters is the need to take into account simplifications in the construction of the 3D model and the declaration of constant flow parameters, which may be variable values in the actual operation of the valve, such as temperature. The limitation of the use of SolidWorks Simulation is strictly defined settings of mesh parameters, which cannot be additionally edited and the impact of mesh selection cannot be assessed through indicators such as orthogonal quality and aspect ratio. In further work, the obtained results will be compared with the results obtained in Ansys Fluent and on the constructed test rig. Based on the calculations and analyses, the following conclusions were drawn:

- The static flow characteristics of the main supply tract assume a near linear character. The determined regression equation in the form  $Q_m = -0.007 h_m^2 + 0.1021 h_m$  with a coefficient of determination equals  $R^2 = 0.9997$  makes it possible to estimate with a high degree of probability the value of the MFR for any degree of opening of the main supply tract. The maximum value of the absolute error was 5.61% with a flow channel height of 0.1 mm.
- The static flow characteristics of the additional supply tract adopted a degressive character, and the determined equation of the regression line  $Q_s = -0.0579 h_s^2 + 0.1926 h_s$  and the value of the coefficient of determination equals  $R^2 = 0.9967$  testify to a high degree of fit. The estimation of the value of the

mass flow rate of the additional supply tract is correct. In the above model configuration, the maximum absolute error value was 8.85% with a flow channel height of 0.2 mm.

- In the last stage of the study, the static characteristics of the differential section were determined at constant volumes of chambers A and B, the variable was the diameter of the hole in the range (0.75..3.0) mm. The characteristics of the differential section took on a progressive character, and the equation of the regression line  $Q_b = 0.0014 d_b^2 - 0.0001 d_b$  and the value of the coefficient of determination equals  $R^2 = 0.9999$  testify to a very good fit. The maximum value of the absolute error in the case under consideration was 3.90% for a nozzle with a diameter of 1.25 mm.
- Despite the use of local mesh densification, it was noted that the maximum absolute error values occur for channels with heights less than 0.5 mm, while additional local mesh densification would result in significantly longer calculations with little improvement in the obtained result. In addition, in several of the considered model configurations, the SolidWorks Flow Simulation solver reported the occurrence of turbulence, which could disturb the quality of the obtained results, which should be verified using another CFD environment and experimental studies.

Further research work will include the use of dynamic simulations using Ansys Fluent, as well as the construction of a test rig. In the course of further research work, additional parameters affecting the nature of the valve's operation will be taken into account, including the stiffness of the springs used and the diameter of the nozzle using model in Matlab Simulink.

## REFERENCES

1. Polichshuk Y, Laptev N, Komarov A, Murzabekov T, Grebenyuk K. Development of agrotechnological requirements for manufacturers of technical tools and agricultural products used in precision farming. *Siberian Herald of Agricultural Science*. 2023;53:98–106.
2. Polischuk Y, Laptev N, Komarov A. The use of automatic and parallel driving systems in agricultural production of the Republic of Kazakhstan and the efficiency of their use. *Agrarian Bulletin of the*. 2020;196:11–9.
3. Ume C. The role of improved market access for small-scale organic farming transition: Implications for food security. *J Clean Prod* [Internet]. 2023;387:135889. Available from: <https://www.sciencedirect.com/science/article/pii/S0959652623000471>
4. Squalli J, Adamkiewicz G. The spatial distribution of agricultural emissions in the United States: The role of organic farming in mitigating climate change. *J Clean Prod* [Internet]. 2023;414:137678. Available from: <https://www.sciencedirect.com/science/article/pii/S095965262301836X>
5. Sivaranjani S, Rakshit A. Organic Farming in Protecting Water Quality. In: *Organic Farming*. 2019; 1–9.
6. Parizad S, Bera S. The effect of organic farming on water reusability, sustainable ecosystem, and food toxicity. *Environmental Science and Pollution Research*. 2021 Sep;30:1–12.
7. Vdovin S, Bogatyrev M, Nikonov K, Korotkov P. Reducing the fluid loss in case of depressurization of tractors' hydraulic drive. *Tractors and Agricultural Machinery*. 2023;90:5–12.
8. von Uexküll O, Skerfving S, Doyle R, Braungart M. Antimony in brake pads-a carcinogenic component? *J Clean Prod* [Internet]. 2005;13(1):19–31. Available from: <https://www.sciencedirect.com/science/article/pii/S0959652603001835>
9. Liu Y, Wu S, Chen H, Federici M, Perricone G, Li Y, et al. Brake wear induced PM10 emissions during the world harmonised light-duty vehicle test procedure-brake cycle. *J Clean Prod* [Internet].



- 2022;361:132278. Available from: <https://www.sciencedirect.com/science/article/pii/S0959652622018820>
10. Commission Regulation (EU) No 1230/2012 of 12 December 2012 implementing Regulation (EC) No 661/2009 of the European Parliament and of the Council with regard to type-approval requirements for masses and dimensions of motor vehicles and their trailers and amending Directive 2007/46/EC of the European Parliament and of the Council.
11. Koonthalakadu Baby D, Sridhar N, Patil H, Subramanian S. Delay compensated pneumatic brake controller for heavy road vehicle active safety systems. *Proc Inst Mech Eng C J Mech Eng Sci.* 2020;235.
12. Kazama T. Comparison of power density of transmission elements in hydraulic, pneumatic, and electric drive systems. *Mechanical Engineering Letters.* 2019;5.
13. Kisiel M, Szpica D, Czaban J. Determination of the flow characteristics of the trailer brake valve using computational fluid mechanics. In: *Proceedings of the 27th International Scientific Conference Mechanika.* 2023.
14. Subramanian S. Electro-Pneumatic Brakes for Commercial Vehicles – Model Based Analysis for Control and Diagnosis. In: *Schritte in die künftige Mobilität.* 2013; 133–45.
15. Kisiel M, Szpica D, Czaban J. Effect of differential valve chamber volume on trailer brake system response time. In: *Mechanika 2022 Proceedings of the 26th International Scientific Conference.* Kaunas: Kaunas University of Technology. 2022;32–3.
16. Basara B, Krajnović S, Pavlovic Z, Ringqvist P. Performance analysis of Partially-Averaged Navier-Stokes method for complex turbulent flows. 2011.
17. Huang X, Pang B, Chai X, Yin Y. Proposal of a turbulent Prandtl number model for Reynolds-averaged Navier–Stokes approach on the modeling of turbulent heat transfer of low-Prandtl number liquid metal. *Front Energy Res.* 2022;10:928693.
18. Sang Y, Wang X, Sun W. Analysis of fluid flow through a bidirectional cone throttle valve using computational fluid dynamics. *Australian Journal of Mechanical Engineering.* 2019;19:1–10.
19. Lee JH, Song X, Park YC, Kang SM. Computational fluid dynamic analysis of flow coefficient for pan check valve. In: *Proceedings of the 9th WSEAS International Conference on Applied Computer and Applied Computational Science.* ACACOS '10. 2010; 157–60.
20. Zhou XM, Wang ZK, Zhang YF. A simple method for high-precision evaluation of valve flow coefficient by computational fluid dynamics simulation. *Advances in Mechanical Engineering.* 2017;9.
21. Gabel T, Mitra H, Williams D, Koeck F, Ostilla-Mónico R, Alba K. Incompressible flow through choke valve: An experimental and computational investigation. *J Fluids Struct.* 2022;113:103669.
22. Garcia S, Iglesias-Rey P, Mora-Meliá D, Martínez-Solano F, Fuentes-Miquel V. Computational Determination of Air Valves Capacity Using CFD Techniques. *Water (Basel).* 2018;10:1433.
23. Mitra H, Gabel T, Williams D, Koeck F, Ostilla-Mónico R, Alba K. Computational study of compressible flow through choke valve. *J Fluids Struct.* 2022;113.
24. Hazzi F, Cardona CS, Pairetti C, Venier C. CFD analysis on flow control using a ball valve. *Anales AFA.* 2022;33:21–5.
25. Gukop N, Kamtu P, Lengs B, Babawuya A, Adegoke A. Effect of Mesh Density on Finite Element Analysis Simulation of a Support Bracket. *FUOYE Journal of Engineering and Technology.* 2021;6.
26. Lubimyi N, Mihail G, Andrey P, Arseniy S. Methodology for the Selection of Optimal Parameters of the Finite Element Mesh in Composite Materials Calculation. In 2023. p. 66–72.
27. Pisarciuc C, Dan I, Cioară R. The Influence of Mesh Density on the Results Obtained by Finite Element Analysis of Complex Bodies. *Materials.* 2023;16:2555.
28. Jurkowski S, Janisz K. Analiza wpływu parametrów siatki obliczeniowej na wynik symulacji przepływomierza. *Autobusy.* 2020;12:129–34.
29. Kamiński Z, Kulikowski K. Measurement and evaluation of the quality of static characteristics of brake valves for agricultural trailers. *Measurement.* 2017;106:173–8.
30. Kamiński Z, Kulikowski K. Determination of the functional and service characteristics of the pneumatic system of an agricultural tractor with mechanical brakes using simulation methods. *Eksploatacja i Niezawodność.* 2015;17(3):355–64.
31. Kamiński Z. Mathematical modelling of the trailer brake control valve for simulation of the air brake system of farm tractors equipped with hydraulically actuated brakes. *Maintenance and Reliability.* 2014;16(4):637–43.
32. Wu CC, Völker D, Weisbrich S, Neitzel F. The finite volume method in the context of the finite element method. *Mater Today Proc.* 2022;62.
33. Yang P, Wang X, Li Y. Construction and analysis of the quadratic finite volume methods on tetrahedral meshes. *Sci China Math.* 2023;66:855–86.
34. Jonuskaite A. Flow simulation with SolidWorks. [Helsinki]: Arcada University of Applied Sciences. 2017.
35. Sobachkin A, Dumnov G. Numerical Basis of CAD-Embedded CFD. *NAFEMS World Congress.* 2013.
36. Wang F, di Mare L. Favre-Averaged Nonlinear Harmonic Method for Compressible Periodic Flows. *AIAA Journal.* 2019;57:1–10.
37. Pavlenko A, Nadrygailo T. On one simulation method of turbulent flows. *Journal of New Technologies in Environmental Science.* 2019;3(4):169–78.

This research was financed through subsidy of the Ministry of Science and Higher Education of Poland for the discipline of mechanical engineering at the Faculty of Mechanical Engineering Białystok University of Technology WZ/WM-IIM/5/2023.

Marcin Kisiel  <https://orcid.org/0000-0002-4576-0447>

Dariusz Szpica  <https://orcid.org/0000-0002-7813-8291>



This work is licensed under the Creative Commons BY-NC-ND 4.0 license.



# THE CONSTRUCTION OF ANALYTICAL EXACT SOLITON WAVES OF KURALAY EQUATION

Waqas Ali FARIDI<sup>✉</sup>, Muhammad ABU BAKAR<sup>✉\*</sup>, Zhaidary MYRZAKULOVA<sup>✉\*\*</sup>, Ratbay MYRZAKULOV<sup>✉\*\*</sup>,  
Mawahib ELAMIN<sup>✉\*\*\*</sup>, Lakhdar RAGOUR<sup>✉\*\*\*\*</sup>, Lanre AKINYEMI<sup>✉\*\*\*\*\*</sup>

\*Department of Mathematics, University of Management and Technology, Lahore, Pakistan

\*\*Ratbay Myrzakulov Eurasian International Centre for Theoretical Physics, Astana, Kazakhstan

\*\*\*Department of Mathematics, College of Science, Qassim University, Buraydah, 51452, Saudi Arabia

\*\*\*\*Mathematics Department, University of Prince Mughrin, P.O. Box 41040, Al Madinah 42241, Saudi Arabia

\*\*\*\*\*Department of Mathematics, Hampton University, Hampton, Virginia, USA

[Wa966142@gmail.com](mailto:Wa966142@gmail.com), [m.abubakar055@gmail.com](mailto:m.abubakar055@gmail.com), [zmyrzakulova@gmail.com](mailto:zmyrzakulova@gmail.com), [myrzakulov.r@enu.kz](mailto:myrzakulov.r@enu.kz),  
[ma.elhag@qu.edu.sa](mailto:ma.elhag@qu.edu.sa), [l.ragoub@upm.edu.sa](mailto:l.ragoub@upm.edu.sa), [lanre.akinyemi@hamptonu.edu](mailto:lanre.akinyemi@hamptonu.edu)

received 30 August 2023, revised 12 October 2023, accepted 18 October 2023

**Abstract:** The primary objective of this work is to examine the Kuralay equation, which is a complex integrable coupled system, in order to investigate the integrable motion of induced curves. The soliton solutions derived from the Kuralay equation are thought to be the supremacy study of numerous significant phenomena and extensive applications across a wide range of domains, including optical fibres, nonlinear optics and ferromagnetic materials. The inverse scattering transform is unable to resolve the Cauchy problem for this equation, so the analytical method is used to produce exact travelling wave solutions. The modified auxiliary equation and Sardar sub-equation approaches are used to find solitary wave solutions. As a result, singular, mixed singular, periodic, mixed trigonometric, complex combo, trigonometric, mixed hyperbolic, plane and combined bright–dark soliton solution can be obtained. The derived solutions are graphically displayed in 2-D and 3-D glances to demonstrate how the fitting values of the system parameters can be used to predict the behavioural responses to pulse propagation. This study also provides a rich platform for further investigation.

**Key words:** The Kuralay equation; modified auxiliary equation method; analytical solitary wave solutions

## 1. INTRODUCTION

As technology advances, partial differential equations (PDEs) have proven to be an essential tool for scientists and researchers for understanding physical phenomena. By employing various methodologies and technologies, they have achieved a higher level of precision in examining the structures of various physical phenomena. The use of nonlinear partial differential equations (NLPDEs) is particularly valuable in modelling nonlinear phenomena in various applied as well as in natural sciences, such as acoustics physics, plasma and solid-state physics. These equations provide an in-depth and clear understanding of the observed physical phenomena, allowing for precise predictions of their future propagation. Furthermore, use of NLPDEs in travelling wave profile's analysis has an impact as an invaluable tool in a variety of fields, ranging from quantum mechanics and fluid mechanics to different fields in engineering. Consequently, a multitude of researchers have delved into diverse nonlinear partial differential models, aiming to attain a more profound understanding of the dynamics exhibited by the examined physical phenomena. Recent examinations have encompassed investigations of Date–Jimbo–Kashiwara–Miwa equation [1–3], Riemann wave equation [4,5], Schrödinger equation [6–11], Navier–Stokes equations [12–15], Lakshmanan–Porseizian–Daniel equation [16,17], Chen–Lee–Liu dynamical equation [18–21] and many others [22–30].

Many researchers have paid attention to the field of analytical solutions. Kumar and Niwas have discussed the dynamical as-

pects and constructed the soliton solutions of the distinct governing models [31–33]. El-Ganaini et al. [34] utilised the Lie symmetry approach and analytical method to develop the invariant solutions. Kumar et al. [35] investigated the Kudryashov–Sinelshchikov equation by using the generalised exponential rational function (GERF) method. Abdou et al. [36] applied the he generalised Kudryashov (GK) approach and the sine–Gordon expansion approach to the deoxyribonucleic acid model for constructing new specific analytical solutions. Kumar and Kumar [37] executed the GERF method to construct numerous and large numbers of exact analytical solitary wave solutions of the nonlinear extended Zakharov–Kuznetsov equation. Mathanaranjan [38,39] has developed the soliton solutions by using analytical techniques. Zhao et al. [40] applied a new GERF method on the nonlinear wave model and constructed the analytical solutions. Mathanaranjan et al. [41] utilised the extended sine–Gordon equation expansion method and developed the soliton solutions. Mathanaranjan and Vijayakumar [42] discussed the fractional soliton solutions by executing the analytical solutions. Mathanaranjan et al. [43] generated the chirped optical solitons and examined the stability analysis of the nonlinear Schrödinger equation.

Furthermore, an area witnessing a notable surge in the application of NLPDEs is the exploration of soliton waves (distinct wave formations that uphold their form and speed throughout propagation). Diverse nonlinear physical models are being employed by researchers on solitons waves to comprehend and prognosticate their propagation. Consequently, these waves have gained escalating significance across various domains like optical

fibres, nonlinear optics and ferromagnetic materials. Recent accomplishments in the exploration of soliton waves are documented in Refs [44–49]. By cultivating a deeper comprehension of soliton waves, scholars can propel advancements in these realms and uncover novel applications.

The integrable complex coupled Kuralay governing system (K-IIIE) as referenced in [50] is as follows:

$$\begin{aligned} iK_t - K_{xt} - VK &= 0 \\ iR_t + R_{xt} + VK &= 0, \\ V_x + 2d^2(RK)_t &= 0. \end{aligned} \quad (1)$$

In this context,  $K(x, t)$  signifies a complex function, accompanied by its corresponding complex conjugate denoted as  $K^*(x, t)$ . In contrast,  $V$  stands for a real potential function conditional upon the autonomous spatial 'x' and temporal variables 't'. Furthermore, the (K-IIIE) equation incorporates two supplementary variations, specifically (K-IIAE) and (K-IIBE) [51–53].

Assuming  $d = 1$  and  $R = \epsilon K^*$ , where  $\epsilon = \pm 1$ , the aforementioned equation system transforms into:

$$\begin{aligned} iK_t - K_{xt} - VK &= 0, \\ V_x - 2\epsilon(|K|^2)_t &= 0. \end{aligned} \quad (2)$$

Recently (2023), Mathanaranjan [54] applied F-expansion and new extended auxiliary equation methods and constructed the solitary waves and elliptic function solutions of Kuralay equation. Many novel solutions have been generated, other dynamical aspects analysed and the conserved quantities of the Kuralay equation developed. However, many solutions and families were missing such as periodic patterns featuring elevated crests and troughs, as well as anti-peaked crests and troughs, periodic kinks, anti-kinks and compactons in both bright and dark forms. Thus, in order to fill this gap, this study is carried out utilising the modified auxiliary equation and Sardar sub-equation method.

Apart from the benefits associated with employing NLPDEs, the quest for precise analytical solutions to these equations presents challenges. To tackle this, a variety of techniques have been formulated. These approaches encompass the inverse scattering method [55], variational iteration method [56,57], integral scheme [58], soliton perturbation theory [59], positive quadratic function method [60], (G'/G<sup>2</sup>)-expansion method [61] and Lie symmetry approach [62], among others. This article investigates soliton solutions for the (K-IIIE) equation by employing two distinctive methodologies: the modified auxiliary equation method [63] and the Sardar sub-equation approach [64]. Employing these methodologies results in a broad spectrum of solutions, spanning rational, trigonometric and hyperbolic manifestations.

The techniques described in Section (2) are explained in this article. The solutions derived from the model are then examined in Section (3), where various parameter values acquired using the used approaches are used. The presentation of graphical representations is also included in this section. Section (4) involves a visual evaluation of the solutions and the article concludes in Section (5), with a summary of the results.

## 2. DESCRIPTION OF ANALYTICAL METHODS

Consider an NLPDE of the following form:

$$Y(U, U_t, U_x, U_{tt}, U_{xx}, \dots) = 0. \quad (3)$$

Its NODE will be:

$$\mathbb{Q}(\mathbb{R}, \mathbb{R}', \mathbb{R}'', \dots) = 0. \quad (4)$$

Consider:

$$\mathbb{U}(x, t) = \mathbb{U}(\Omega) \quad (5)$$

where  $\Omega = mx + ct$ . The prime notations within Eq. (4) signify the differentiation order concerning distinct variables within the equation.

### 2.1. Modified auxiliary equation method

Utilising the MAE approach [63], we can regard the subsequent equation as the general solution for Eq. (4):

$$\mathbb{U}(\Omega) = \alpha_0 + \sum_{i=1}^N [\alpha_i z^{h(\Omega)} + \beta_i z^{-h(\Omega)}] \quad (6)$$

$\alpha_i, \beta_i$  are constants of the equation and  $\Omega = k_1(x + y) + k_2t$ . The function  $h(\Omega)$  can be described by the auxiliary equation that follows:

$$h'(\Omega) = \frac{\beta + \alpha z^{-h(\Omega)} + \gamma z^{h(\Omega)}}{\ln(z)}. \quad (7)$$

Here,  $\gamma, z, \alpha$  and  $\beta$  are real arbitrary constants, where  $z > 0$  and  $z \neq 1$ . Furthermore,  $\alpha_i$ s and  $\beta_i$ s cannot be zero at the same time.

Eq. (7) has the following solutions:

If  $\gamma \neq 0$  and  $\Xi < 0$ ,

$$z^{h(\Omega)} = - \left[ \frac{\beta + \sqrt{-\Xi} \tan\left(\frac{\sqrt{-\Xi}\Omega}{2}\right)}{2\gamma} \right] \text{ or } z^{h(\Omega)} = - \left[ \frac{\beta + \sqrt{-\Xi} \cot\left(\frac{\sqrt{-\Xi}\Omega}{2}\right)}{2\gamma} \right]. \quad (8)$$

If  $\gamma \neq 0$  and  $\Xi > 0$ ,

$$z^{h(\Omega)} = - \left[ \frac{\beta + \sqrt{\Xi} \tanh\left(\frac{\sqrt{\Xi}\Omega}{2}\right)}{2\gamma} \right] \text{ or } z^{h(\Omega)} = - \left[ \frac{\beta + \sqrt{\Xi} \coth\left(\frac{\sqrt{\Xi}\Omega}{2}\right)}{2\gamma} \right]. \quad (9)$$

If  $\gamma \neq 0$  and  $\Xi = 0$ ,

$$z^{h(\Omega)} = - \left[ \frac{2 + \beta\Omega}{2\gamma\Omega} \right], \quad (10)$$

where  $\Xi = \beta^2 - 4\alpha\gamma$ .

### 2.2. Sardar sub-equation method

By employing the Sardar sub-equation approach [64], we can view the ensuing equation as the general solution for Eq. (4):

$$U(\Omega) = \sum_{i=0}^N (a_i M^i(\Omega)), \quad 0 \leq i \leq N, \quad (11)$$

where  $a_i$  in Eq. (11) are real constants and  $M(\Omega)$  satisfy the

$$M'(\Omega) = \sqrt{\zeta + \nu M(\Omega)^2 + M(\Omega)^4}, \quad (12)$$

with real constants  $\zeta$  and  $\nu$ .

Eq. (12) has the following solutions:

Case 1: if  $u > 0$  and  $\zeta = 0$ ;

ODE of the following form:

$$M_1^\pm(\Omega) = \pm\sqrt{-pqv} \operatorname{sech}_{pq}(\sqrt{v}\Omega) \quad (13)$$

$$M_2^\pm(\Omega) = \pm\sqrt{pqv} \operatorname{csch}_{pq}(\sqrt{v}\Omega) \quad (14)$$

where

$$\operatorname{sech}_{pq}(\Omega) = \frac{2}{pe^\Omega + qe^{-\Omega}}, \quad \operatorname{csch}_{pq}(\Omega) = \frac{2}{pe^\Omega - qe^{-\Omega}}.$$

Case 2: if  $u < 0$  and  $\zeta = 0$ :

$$M_3^\pm(\Omega) = \pm\sqrt{-pqv} \operatorname{sec}_{pq}(\sqrt{-v}\Omega), \quad (15)$$

$$M_4^\pm(\Omega) = \pm\sqrt{-pqv} \operatorname{csc}_{pq}(\sqrt{-v}\Omega) \quad (16)$$

where

$$\operatorname{sec}_{pq}(\Omega) = \frac{2}{pe^{i\Omega} + qe^{-i\Omega}}, \quad \operatorname{csc}_{pq}(\Omega) = \frac{2i}{pe^{i\Omega} - qe^{-i\Omega}}.$$

Case 3: if  $u < 0$  and  $\zeta = \frac{v^2}{4}$ :

$$M_5^\pm(\Omega) = \pm\sqrt{-\frac{v}{2}} \tanh_{pq}\left(\sqrt{-\frac{v}{2}}\Omega\right), \quad (17)$$

$$M_6^\pm(\Omega) = \pm\sqrt{-\frac{v}{2}} \coth_{pq}\left(\sqrt{-\frac{v}{2}}\Omega\right), \quad (18)$$

$$M_7^\pm(\Omega) = \pm\sqrt{-\frac{v}{2}} (\tanh_{pq}(\sqrt{-2v}\Omega) \pm \sqrt{pq} \operatorname{sech}_{pq}(\sqrt{-2v}\Omega)), \quad (19)$$

$$M_8^\pm(\Omega) = \pm\sqrt{-\frac{v}{2}} (\coth_{pq}(\sqrt{-2v}\Omega) \pm \sqrt{pq} \operatorname{csch}_{pq}(\sqrt{-2v}\Omega)), \quad (20)$$

$$M_9^\pm(\Omega) = \pm\sqrt{-\frac{v}{8}} (\tanh_{pq}\left(\sqrt{-\frac{v}{8}}\Omega\right) + \coth_{pq}\left(\sqrt{-\frac{v}{8}}\Omega\right)), \quad (21)$$

where

$$\tanh_{pq}(\Omega) = \frac{pe^\Omega - qe^{-\Omega}}{pe^\Omega + qe^{-\Omega}},$$

$$\coth_{pq}(\Omega) = \frac{pe^{i\Omega} + qe^{-i\Omega}}{pe^{i\Omega} - qe^{-i\Omega}}.$$

Case 4: if  $u > 0$  and  $\zeta = \frac{v^2}{4}$ :

$$M_{10}^\pm(\Omega) = \pm\sqrt{\frac{v}{2}} \tan_{pq}\left(\sqrt{\frac{v}{2}}\Omega\right), \quad (22)$$

$$M_{11}^\pm(\Omega) = \pm\sqrt{\frac{v}{2}} \cot_{pq}\left(\sqrt{\frac{v}{2}}\Omega\right), \quad (23)$$

$$M_{12}^\pm(\Omega) = \pm\sqrt{\frac{v}{2}} (\tan_{pq}(\sqrt{2v}\Omega) \pm \sqrt{pq} \operatorname{sec}_{pq}(\sqrt{2v}\Omega)), \quad (24)$$

$$M_{13}^\pm(\Omega) = \pm\sqrt{\frac{v}{2}} (\cot_{pq}(\sqrt{2v}\Omega) \pm \sqrt{pq} \operatorname{csc}_{pq}(\sqrt{2v}\Omega)), \quad (25)$$

$$M_{14}^\pm(\Omega) = \pm\sqrt{\frac{v}{8}} (\tan_{pq}\left(\sqrt{\frac{v}{8}}\Omega\right) + \cot_{pq}\left(\sqrt{\frac{v}{8}}\Omega\right)), \quad (26)$$

where

$$\tanh_{pq}(\Omega) = -i \frac{pe^\Omega - qe^{-i\Omega}}{pe^{i\Omega} + qe^{-i\Omega}},$$

$$\coth_{pq}(\Omega) = i \frac{pe^{i\Omega} + qe^{-i\Omega}}{pe^{i\Omega} - qe^{-i\Omega}}.$$

The functions mentioned are trigonometric and hyperbolic functions that have parameters represented by  $p$  and  $q$ . When  $p$  and  $q$  are both equal to 1, these functions become the known trigonometric and hyperbolic functions.

### 3. THE FORMULATION OF SOLITON SOLUTION OF KURALAY EQUATION

This section includes the presentation of the soliton solution, along with graphical representations that illustrate these solutions for the model being studied.

Now, in order to find the soliton solutions, the travelling wave transformation will be used, which is given as follows:

$$\mathbb{K}(x, t) = \mathbb{U}(\Omega) e^{i(kx + wt + \eta)},$$

$$\mathbb{V}(x, t) = \mathbb{V}(\Omega) e^{i(kx + wt + \eta)},$$

$$\Omega = mx + ct. \quad (27)$$

Thus,

$$\mathbb{K}_t = (c\mathbb{U}' + i\omega\mathbb{U}) e^{i(kx + wt + \eta)},$$

$$\mathbb{K}_x = (m\mathbb{U}' + ik\mathbb{U}) e^{i(kx + wt + \eta)}, \quad (28)$$

$$\mathbb{K}_{xt} = (cm\mathbb{U}'' + i\omega m\mathbb{U}' + i\omega k\mathbb{U}' + ikw\mathbb{U}) e^{i(kx + wt + \eta)}.$$

Eqs (27) and (28) are substituted into Eq. (2) and the following is obtained:

$$i(c\mathbb{U}' + i\omega\mathbb{U}) - (cm\mathbb{U}'' + i\omega m\mathbb{U}' + i\omega k\mathbb{U}' - kw\mathbb{U}) - \mathbb{V}\mathbb{U} = 0,$$

$$m\mathbb{V}' - 4vc\mathbb{U}\mathbb{U}' = 0. \quad (29)$$

On integrating the second part of Eq. (29)

$$\mathbb{V} = \frac{2vc\mathbb{U}^2}{m} - \frac{c_1}{m}. \quad (30)$$

Eq. (30) is plugged into Eq. (29) and we obtain as follows:

$$i(c\mathbb{U}' + i\omega\mathbb{U}) - (cm\mathbb{U}'' + i\omega m\mathbb{U}' + i\omega k\mathbb{U}' - w\mathbb{U}) - \left(\frac{2vc\mathbb{U}^2}{m} - \frac{c_1}{m}\right)\mathbb{U} = 0, \quad (31)$$

where  $n = \frac{c}{m}$ . The real and imaginary parts of Eq. (31) are given, respectively, as

$$\mathbb{U}'' + \frac{(w(1-k)-n)}{cm}\mathbb{U} + \frac{2v\mathbb{U}^3}{m^2} = 0, \quad (32)$$

$$(c - wm - ck)\mathbb{U}' = 0. \quad (33)$$

From the imaginary part (Eq. (33)) is implied the following value of  $m$ :

$$m = \frac{c(k-1)}{w}. \quad (34)$$

By plugging Eq. (34) into Eq. (32), we obtain as follows:

$$\mathbb{U}'' + \frac{w(w(1-k)-n)}{c^2(k-1)}\mathbb{U} + \frac{2w^2v\mathbb{U}^3}{c^2(k-1)^2} = 0. \quad (35)$$

### 3.1. Solution by applying MAE method

The solution using the MAE method for Eq. (35) can be expressed as follows, after determining the homogeneous balancing constant  $N = 1$ :

$$U(\Omega) = \alpha_0 + \alpha_1 z^{h(\Omega)} + \beta_1 z^{-h(\Omega)}. \quad (36)$$

To obtain the system of equations, the solution from Eq. (36) was substituted into Eq. (35), and the varying power coefficients of  $zh(\Omega)$  were calculated. The algebraic equation system that was obtained was then solved using the Mathematica software, which resulted in four distinct families of values for  $\alpha_0$ ,  $\alpha_1$  and  $\beta_1$ . By using each family of values separately, the following solutions are obtained:

#### 3.1.1. Family 1

$$\alpha_0 = \pm \frac{\beta \sqrt{(k-1)(kw+n-w)}}{\sqrt{2w\epsilon\Xi}}, \alpha_1 = \pm \frac{2\gamma \sqrt{(k-1)(kw+n-w)}}{\sqrt{2w\epsilon\Xi}}, \beta_1 = 0, c = \pm \frac{\sqrt{2} \sqrt{w((k-1)w+n)}}{\sqrt{(1-k)\Xi}}, \quad (37)$$

General solution for family 1,

$$U(\Omega) = \pm \frac{\sqrt{(k-1)(kw+n-w)}}{\sqrt{2w\epsilon\Xi}} (\beta \pm 2\gamma z^{h(\Omega)}). \quad (38)$$

Observing that numerous solutions can be obtained by substituting Eqs (8)–(10) into Eq. (38), the resulting solutions are as follows:

Case1: If  $\Xi < 0$ ,  $\gamma \neq 0$ ;

$$\mathbb{K}_{1,1}(x, t) = \pm \left( \frac{\sqrt{((n+(k-1)w)(1-k))} \tan\left(\frac{1}{2}\Omega\sqrt{-\Xi}\right)}{\sqrt{2w\epsilon}} \right) e^{i(kx+et+\eta)} \quad (39)$$

$$\mathbb{V}_{1,1}(x, t) = \frac{2cv}{m} \left( \frac{\sqrt{((n+(k-1)w)(1-k))} \tan\left(\frac{1}{2}\Omega\sqrt{-\Xi}\right)}{\sqrt{2w\epsilon}} \right) - \frac{c_1}{m}, \quad (40)$$

or

$$\mathbb{K}_{1,2}(x, t) = \pm \left( \frac{\sqrt{((n+(k-1)w)(1-k))} \cot\left(\frac{1}{2}\Omega\sqrt{-\Xi}\right)}{\sqrt{2w\epsilon}} \right) e^{i(kx+wt+\eta)}, \quad (41)$$

$$\mathbb{V}_{1,2}(x, t) = \frac{2cv}{m} \left( \frac{\sqrt{((n+(k-1)w)(1-k))} \cot\left(\frac{1}{2}\Omega\sqrt{-\Xi}\right)}{\sqrt{2w\epsilon}} \right) - \frac{c_1}{m}, \quad (42)$$

Case2: If  $\Xi > 0$ ,  $\gamma \neq 0$ ;

$$\mathbb{K}_{1,3}(x, t) = \pm \left( \frac{\sqrt{((n+(k-1)w)(1-k))} \tanh\left(\frac{1}{2}\Omega\sqrt{\Xi}\right)}{\sqrt{2w\epsilon}} \right) e^{i(kx+et+\eta)}, \quad (43)$$

$$\mathbb{V}_{1,3}(x, t) = \frac{2cv}{m} \left( \frac{\sqrt{((n+(k-1)w)(1-k))} \tanh\left(\frac{1}{2}\Omega\sqrt{\Xi}\right)}{\sqrt{2w\epsilon}} \right) - \frac{c_1}{m}, \quad (44)$$

or

$$\mathbb{K}_{1,4}(x, t) = \pm \left( \frac{\sqrt{((n+(k-1)w)(1-k))} \coth\left(\frac{1}{2}\Omega\sqrt{\Xi}\right)}{\sqrt{2w\epsilon}} \right) e^{i(kx+wt+\eta)}, \quad (45)$$

$$\mathbb{V}_{1,4}(x, t) = \frac{2cv}{m} \left( \frac{\sqrt{((n+(k-1)w)(1-k))} \coth\left(\frac{1}{2}\Omega\sqrt{\Xi}\right)}{\sqrt{2w\epsilon}} \right) - \frac{c_1}{m}. \quad (46)$$

#### 3.1.2. Family 2

$$\alpha_0 = \pm \frac{\beta \sqrt{((n+(k-1)w)(1-k))}}{\sqrt{2w\epsilon\Xi}}, \alpha_1 = 0, \beta_1 = \pm \frac{2\alpha \sqrt{((n+(k-1)w)(1-k))}}{\sqrt{2w\epsilon\Xi}}, c = \pm \frac{\sqrt{2} \sqrt{w((k-1)w+n)}}{\sqrt{((1-k)(\Xi))}}. \quad (47)$$

General solution for family 2,

$$U(\Omega) = \frac{\beta \sqrt{((n+(k-1)w)(1-k))}}{\sqrt{2w\epsilon\Xi}} \pm \frac{2\alpha z^{-h(\Omega)} \sqrt{(k-1)(kw+n-w)}}{\sqrt{2w\epsilon\Xi}} \quad (48)$$

It is observed that numerous solutions can be obtained by substituting equations Eq. (8)–(10) into Eq. (48). The resulting solutions are as follows:

Case1 : If  $\gamma \neq 0$ ,  $\Xi < 0$ ;

$$\mathbb{K}_{2,1}(x, t) = \pm \left( \frac{\sqrt{((n+(k-1)w)(1-k))} (\beta (\sqrt{-\Xi} \tan\left(\frac{1}{2}\Omega\sqrt{-\Xi}\right) + \beta) - 4\alpha\gamma)}{(\sqrt{-\Xi} \tan\left(\frac{1}{2}\Omega\sqrt{-\Xi}\right) + \beta) \sqrt{2w\epsilon(\Xi)}} \right) e^{i(kx+et+\eta)}, \quad (49)$$

$$\mathbb{V}_{2,1}(x, t) = \frac{2cv}{m} \left( \frac{\sqrt{((n+(k-1)w)(1-k))} (\beta (\sqrt{-\Xi} \tan\left(\frac{1}{2}\Omega\sqrt{-\Xi}\right) + \beta) - 4\alpha\gamma)}{(\sqrt{-\Xi} \tan\left(\frac{1}{2}\Omega\sqrt{-\Xi}\right) + \beta) \sqrt{2w\epsilon(\Xi)}} \right) - \frac{c_1}{m}, \quad (50)$$

$$\mathbb{K}_{2,2}(x, t) = \pm \left( \frac{\sqrt{((n+(k-1)w)(1-k))} (\beta (\sqrt{-\Xi} \cot\left(\frac{1}{2}\Omega\sqrt{-\Xi}\right) + \beta) - 4\alpha\gamma)}{(\sqrt{-\Xi} \cot\left(\frac{1}{2}\Omega\sqrt{-\Xi}\right) + \beta) \sqrt{2w\epsilon(\Xi)}} \right) e^{i(kx+et+\eta)}, \quad (51)$$

$$\mathbb{V}_{2,2}(x, t) = \frac{2cv}{m} \left( \frac{\sqrt{((n+(k-1)w)(1-k))} (\beta (\sqrt{-\Xi} \cot\left(\frac{1}{2}\Omega\sqrt{-\Xi}\right) + \beta) - 4\alpha\gamma)}{(\sqrt{-\Xi} \cot\left(\frac{1}{2}\Omega\sqrt{-\Xi}\right) + \beta) \sqrt{2w\epsilon(\Xi)}} \right) - \frac{c_1}{m}, \quad (52)$$

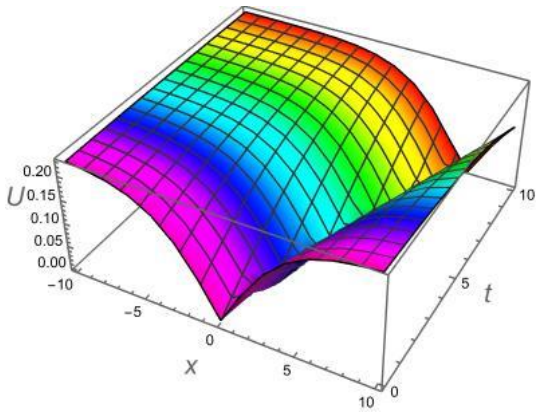
$$\mathbb{K}_{2,3}(x, t) = \pm \left( \frac{\sqrt{((n+(k-1)w)(1-k))} (\beta (\sqrt{\Xi} \tanh\left(\frac{1}{2}\Omega\sqrt{\Xi}\right) + \beta) - 4\alpha\gamma)}{(\sqrt{\Xi} \tanh\left(\frac{1}{2}\Omega\sqrt{\Xi}\right) + \beta) \sqrt{2w\epsilon(\Xi)}} \right) e^{i(kx+et+\eta)}, \quad (53)$$

$$\mathbb{V}_{2,3}(x, t) = \frac{2cv}{m} \left( \frac{\sqrt{((n+(k-1)w)(1-k))} (\beta (\sqrt{\Xi} \tanh\left(\frac{1}{2}\Omega\sqrt{\Xi}\right) + \beta) - 4\alpha\gamma)}{(\sqrt{\Xi} \tanh\left(\frac{1}{2}\Omega\sqrt{\Xi}\right) + \beta) \sqrt{2w\epsilon(\Xi)}} \right) - \frac{c_1}{m}, \quad (54)$$

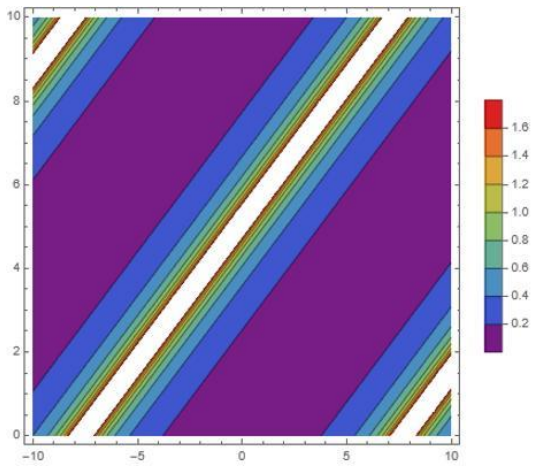
$$\mathbb{K}_{2,4}(x, t) = \pm \left( \frac{\sqrt{((n+(k-1)w)(1-k))} (\beta (\sqrt{\Xi} \coth\left(\frac{1}{2}\Omega\sqrt{\Xi}\right) + \beta) - 4\alpha\gamma)}{(\sqrt{\Xi} \coth\left(\frac{1}{2}\Omega\sqrt{\Xi}\right) + \beta) \sqrt{2w\epsilon(\Xi)}} \right) e^{i(kx+et+\eta)}, \quad (55)$$

or

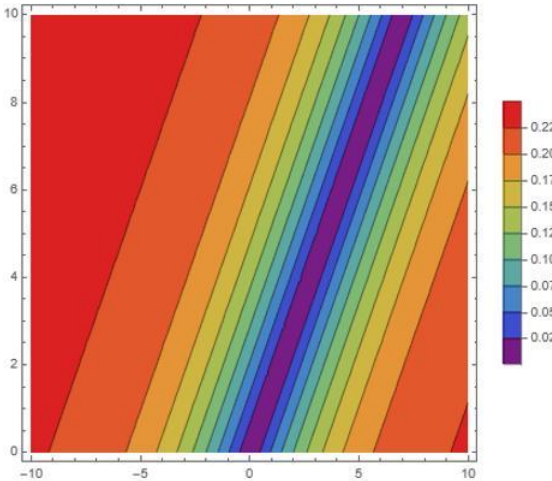
$$\mathbb{V}_{2,4}(x, t) = \frac{2cv}{m} \left( \frac{\sqrt{((n+(k-1)w)(1-k))} (\beta (\sqrt{\Xi} \coth\left(\frac{1}{2}\Omega\sqrt{\Xi}\right) + \beta) - 4\alpha\gamma)}{(\sqrt{\Xi} \coth\left(\frac{1}{2}\Omega\sqrt{\Xi}\right) + \beta) \sqrt{2w\epsilon(\Xi)}} \right) e^{i(kx+wt+\eta)} - \frac{c_1}{m}. \quad (56)$$



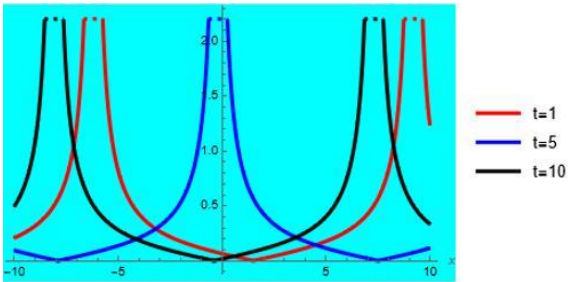
(a)



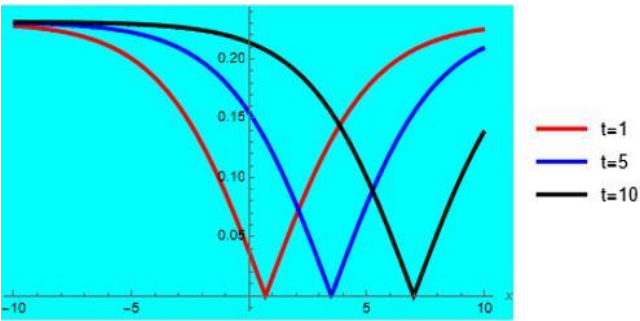
(e)



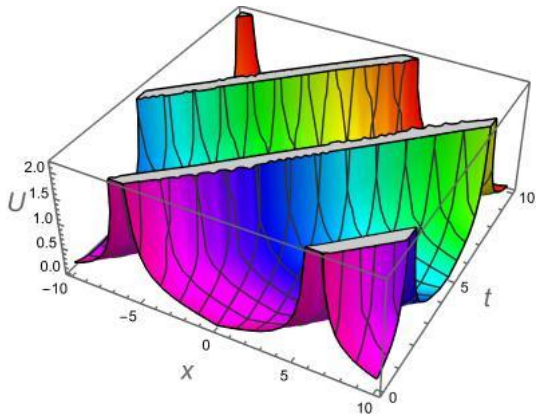
(b)



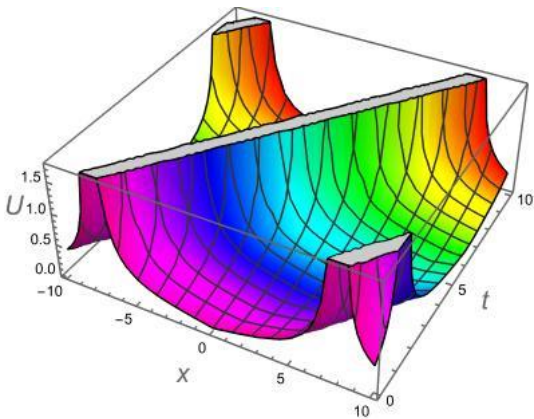
(f)



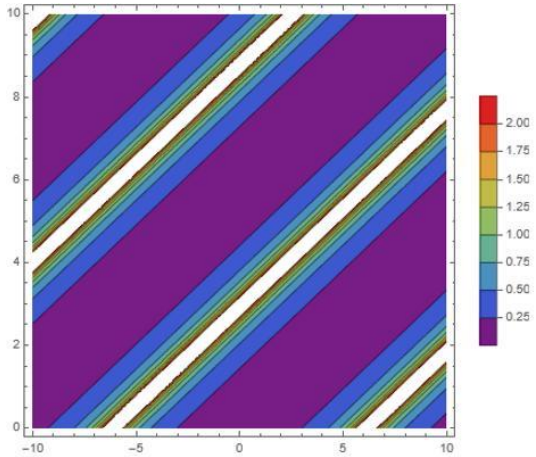
(c)



(g)

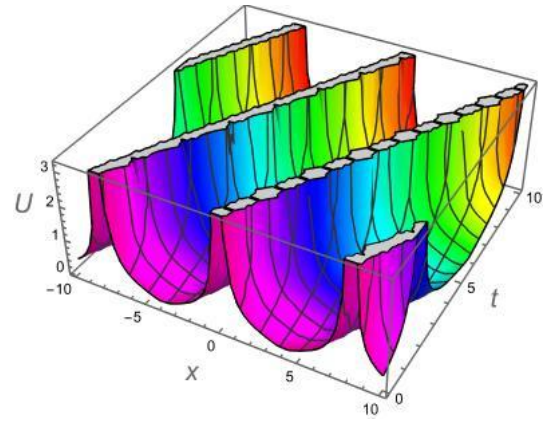
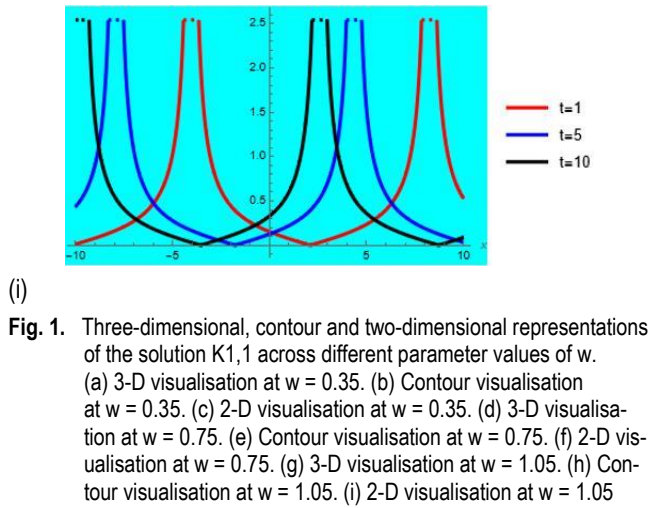


(d)

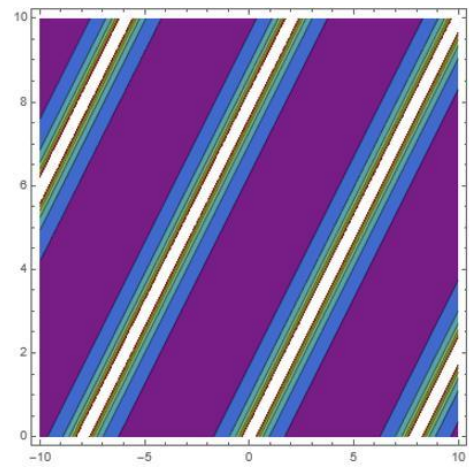


(h)

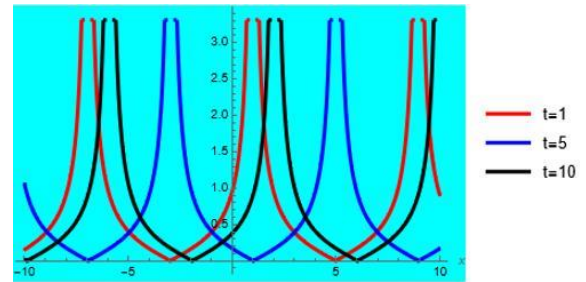
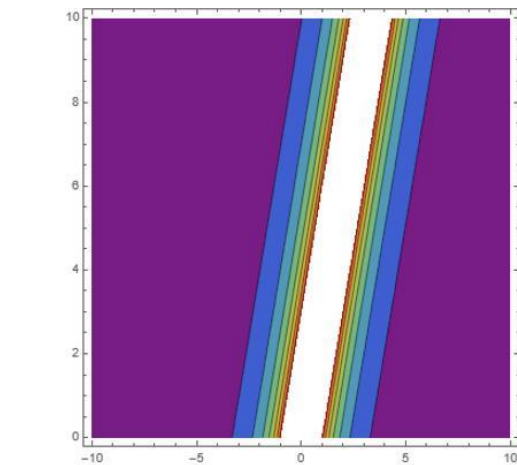
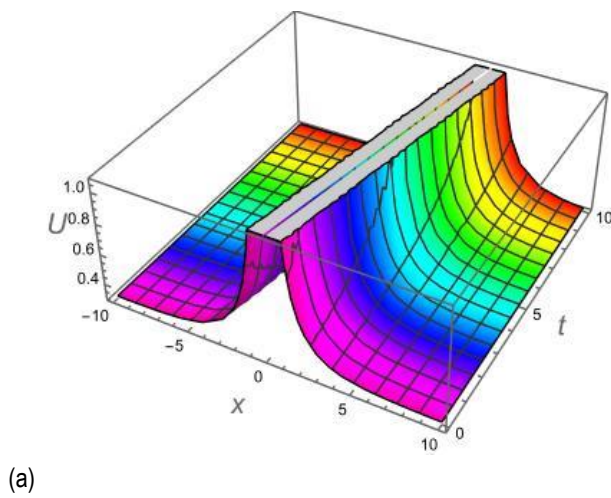




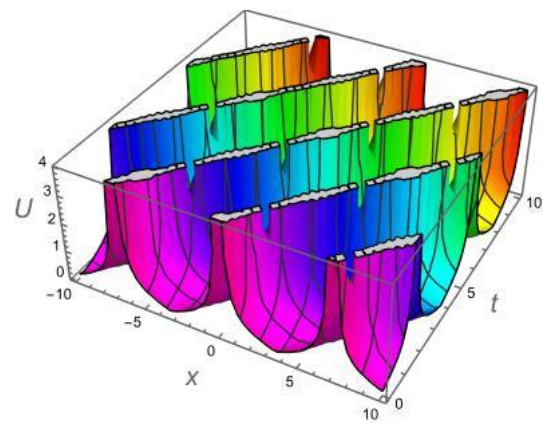
(d)



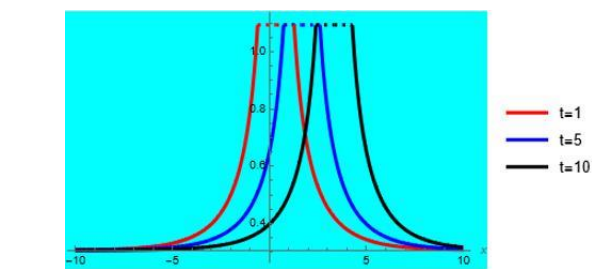
(e)



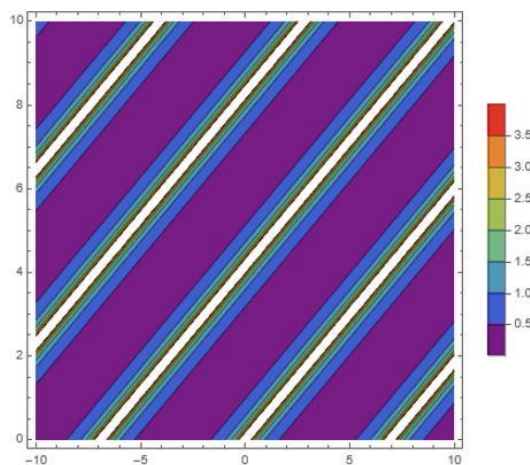
(f)



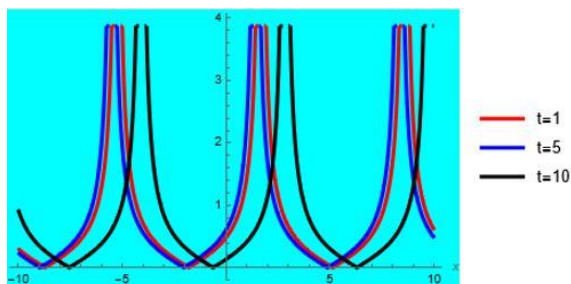
(g)



(c)



(h)



(i)

**Fig. 2.** Three-dimensional, contour and two-dimensional representations of the solution  $K_{1,4}$  across different values of  $w$ . (a) 3-D visualisation at  $w = 0.25$ . (b) Contour visualisation at  $w = 0.25$ . (c) 2-D visualisation at  $w = 0.25$ . (d) 3-D visualisation at  $w = 0.75$ . (e) Contour visualisation at  $w = 0.75$ . (f) 2-D visualisation at  $w = 0.75$ . (g) 3-D visualisation at  $w = 1.25$ . (h) Contour visualisation at  $w = 1.25$ . (i) 2-D visualisation at  $w = 1.25$

### 3.2. Solution by applying Sardar sub-equation method

The solution using the Sardar sub-equation method for Eq. (35) can be expressed as follows, after determining the homogeneous balancing constant  $N = 1$ :

$$U(\Omega) = a_0 + a_1 M(\Omega) \quad (57)$$

To obtain the system of equations, the solution from Eq. (57) was substituted into Eq. (35), and the varying power coefficients of  $M(\Omega)$  were calculated. The algebraic equation system that was obtained was then solved using the Mathematica software, which resulted in a family of values for  $a_0$ ,  $a_1$  and  $c$ . By Using this family, we got solutions as follows:

#### 3.2.1. Family

$$a_0 = 0, a_1 = \pm \frac{\sqrt{(k-1)w+n}}{\sqrt{vw\epsilon}}, c = \pm \frac{\sqrt{w(-(k-1)w-n)}}{\sqrt{v-kv}}. \quad (58)$$

General solution for family,

$$U(\Omega) = \frac{\sqrt{(n+(k-1)w)(1-k)}}{\sqrt{vw\epsilon}} M(\phi), \quad (59)$$

After using the general solution of Eq. (59) in Eqs (27) and (30), we get the following solutions: Case 1: if  $u > 0$  and  $\zeta = 0$ ;

$$\mathbb{K}_1(x, t) = \pm \sqrt{\frac{((n+(k-1)w)(1-k)pq)}{w\epsilon}} (\operatorname{sech}_{pq}(\sqrt{v}\Omega)) e^{i(kx + et + \eta)} \quad (60)$$

$$\mathbb{V}_1(x, t) = \frac{2vc}{m} \left( \sqrt{\frac{((n+(k-1)w)(1-k)pq)}{w\epsilon}} (\operatorname{sech}_{pq}(\sqrt{v}\Omega)) \right)^2 e^{i(kx + wt + et + \eta)} - \frac{c_1}{m}, \quad (61)$$

$$\mathbb{K}_2(x, t) = \pm \left( \sqrt{\frac{((n+(k-1)w)(1-k)pq)}{w\epsilon}} (\operatorname{csch}_{pq}(\sqrt{v}\Omega)) \right) e^{i(kx + et + \eta)}, \quad (62)$$

$$\mathbb{V}_2(x, t) = \frac{2vc}{m} \left( \sqrt{\frac{((n+(k-1)w)(1-k)pq)}{w\epsilon}} (\operatorname{csch}_{pq}(\sqrt{v}\Omega)) \right)^2 e^{i(kx + wt + et + \eta)} - \frac{c_1}{m}. \quad (63)$$

Case 2: if  $u < 0$  and  $\zeta = 0$ ;

$$\mathbb{K}_3(x, t) = \pm \left( \sqrt{\frac{((n+(k-1)w)(1-k)pq)}{w\epsilon}} (\operatorname{sec}_{pq}(\sqrt{-v}\Omega)) \right) e^{i(kx + et + \eta)}, \quad (64)$$

$$\mathbb{V}_3(x, t) = \frac{2vc}{m} \left( \sqrt{\frac{((n+(k-1)w)(1-k)pq)}{w\epsilon}} (\operatorname{sec}_{pq}(\sqrt{-v}\Omega)) \right)^2 e^{i(kx + wt + et + \eta)} - \frac{c_1}{m}, \quad (65)$$

$$\mathbb{K}_4(x, t) = \pm \left( \sqrt{\frac{((n+(k-1)w)(1-k)pq)}{w\epsilon}} (\operatorname{csc}_{pq}(\sqrt{-v}\Omega)) \right) e^{i(kx + et + \eta)}, \quad (66)$$

$$\mathbb{V}_4(x, t) = \frac{2vc}{m} \left( \sqrt{\frac{((n+(k-1)w)(1-k)pq)}{w\epsilon}} (\operatorname{csc}_{pq}(\sqrt{-v}\Omega)) \right)^2 e^{i(kx + wt + et + \eta)} - \frac{c_1}{m}. \quad (67)$$

Case 3: if  $u < 0$  and  $\zeta = \frac{v^2}{4}$ ;

$$\mathbb{K}_5(x, t) = \pm \left( \sqrt{\frac{((n+(k-1)w)(k-1))}{2w\epsilon}} (\tan_{pq}(\sqrt{-\frac{v}{2}}\Omega)) \right) e^{i(kx + et + \eta)}, \quad (68)$$

$$\mathbb{V}_5(x, t) = \frac{2cv}{m} \left( \sqrt{\frac{((n+(k-1)w)(k-1))}{2w\epsilon}} (\tan_{pq}(\sqrt{-\frac{v}{2}}\Omega)) \right)^2 e^{i(kx + et + \eta)} - \frac{c_1}{m}, \quad (69)$$

$$\mathbb{K}_6(x, t) = \pm \left( \sqrt{\frac{((n+(k-1)w)(k-1))}{2w\epsilon}} (\coth_{pq}(\sqrt{-\frac{v}{2}}\Omega)) \right) e^{i(kx + et + \eta)}, \quad (70)$$

$$\mathbb{V}_6(x, t) = \frac{2vc}{m} \left( \sqrt{\frac{((k-1)((k-1)w+n))}{2w\epsilon}} (\coth_{pq}(\sqrt{-\frac{v}{2}}\Omega)) \right)^2 e^{i(kx + wt + et + \eta)} - \frac{c_1}{m}, \quad (71)$$

(59)

$$\mathbb{K}_7(x, t) = \pm \left( \sqrt{\frac{((n+(k-1)w)(k-1))}{2w\epsilon}} (\tanh_{pq}(\sqrt{-2v}\Omega)) \pm i\sqrt{-pq} \operatorname{sech}_{pq}(\sqrt{-2v}\Omega) \right) e^{i(kx+et+\eta)}, \quad (72)$$

$$\mathbb{V}_7(x, t) = \frac{2vc}{m} \left( \sqrt{\frac{(k-1)((k-1)w+n)}{2w\epsilon}} (\tanh_{pq}(\sqrt{-2v}\Omega) \pm i\sqrt{pq} \operatorname{sech}_{pq}(\sqrt{-2v}\Omega)) \right)^2 e^{i(kx+wt+\eta)} - \frac{c_1}{m}, \quad (73)$$

$$\mathbb{K}_8(x, t) = \pm \left( \sqrt{\frac{((n+(k-1)w)(k-1))}{2w\epsilon}} (\coth_{pq}(\sqrt{-2v}\Omega)) \pm i\sqrt{-pq} \operatorname{csch}_{pq}(\sqrt{-2v}\Omega) \right) e^{i(kx+et+\eta)}, \quad (74)$$

$$\mathbb{V}_8(x, t) = \frac{2vc}{m} \left( \sqrt{\frac{(k-1)((k-1)w+n)}{2w\epsilon}} (\coth_{pq}(\sqrt{-2v}\Omega) \pm \sqrt{pq} \operatorname{csch}_{pq}(\sqrt{-2v}\Omega)) \right)^2 e^{i(kx+wt+\eta)} - \frac{c_1}{m}, \quad (75)$$

$$\mathbb{K}_9(x, t) = \pm \left( \frac{1}{2} \sqrt{\frac{((n+(k-1)w)(k-1))}{2w\epsilon}} (\tanh_{pq}(\frac{1}{2} \sqrt{-\frac{v}{2}} \Omega)) \pm \coth(\frac{1}{2} \sqrt{-\frac{v}{2}} \Omega) \right) e^{i(kx+et+\eta)}, \quad (76)$$

$$\mathbb{V}_9(x, t) = \frac{2vc}{m} \left( \frac{1}{2} \sqrt{\frac{(k-1)((k-1)w+n)}{2w\epsilon}} (\tanh_{pq}(\frac{1}{2} \sqrt{-\frac{v}{2}} \Omega) \pm \coth_{pq}(\frac{1}{2} \sqrt{-\frac{v}{2}} \Omega)) \right)^2 e^{i(kx+wt+\eta)} - \frac{c_1}{m}. \quad (77)$$

Case 4: if  $u > 0$  and  $\zeta = \frac{v^2}{4}$ ;

$$\mathbb{K}_{10}(x, t) = \pm \left( \sqrt{\frac{((n+(k-1)w)(1-k))}{2w\epsilon}} (\tanh_{pq}(\sqrt{\frac{v}{2}} \Omega)) \right) e^{i(kx+et+\eta)}, \quad (78)$$

$$\mathbb{V}_{10}(x, t) = \frac{2cv}{m} \left( \sqrt{\frac{((n+(k-1)w)(1-k))}{2w\epsilon}} (\tanh_{pq}(\sqrt{\frac{v}{2}} \Omega)) \right)^2 e^{i(kx+et+\eta)} - \frac{c_1}{m}, \quad (79)$$

$$\mathbb{K}_{11}(x, t) = \pm \left( \sqrt{\frac{((n+(k-1)w)(1-k))}{2w\epsilon}} (\cot_{pq}(\sqrt{\frac{v}{2}} \Omega)) \right) e^{i(kx+et+\eta)}, \quad (80)$$

$$\mathbb{V}_{11}(x, t) = \frac{2vc}{m} \left( \sqrt{\frac{(n+w(k-1))(1-k))}{2w\epsilon}} (\cot_{pq}(\sqrt{\frac{v}{2}} \Omega)) \right)^2 e^{i(kx+wt+\eta)} - \frac{c_1}{m}, \quad (81)$$

$$\mathbb{K}_{12}(x, t) = \pm \left( \sqrt{\frac{((n+(k-1)w)(1-k))}{2w\epsilon}} (\tan_{pq}(\sqrt{2v}\Omega)) \pm \sqrt{pq} \operatorname{sec}_{pq}(\sqrt{2v}\Omega) \right) e^{i(kx+et+\eta)}, \quad (82)$$

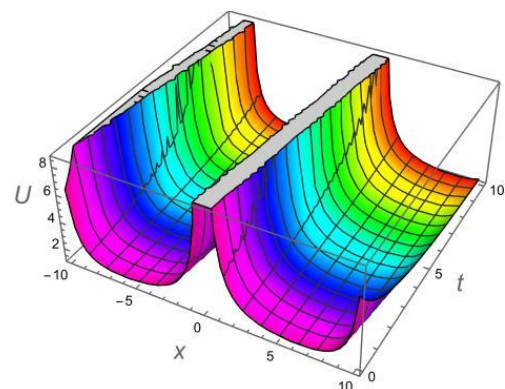
$$\mathbb{V}_{12}(x, t) = \frac{2vc}{m} \left( \sqrt{\frac{(n+w(k-1))(1-k))}{2w\epsilon}} (\tan_{pq}(\sqrt{2v}\Omega) \pm \sqrt{pq} \operatorname{sec}_{pq}(\sqrt{2v}\Omega)) \right)^2 e^{i(kx+wt+\eta)} - \frac{c_1}{m}, \quad (83)$$

$$\mathbb{K}_{13}(x, t) = \pm \left( \sqrt{\frac{((n+(k-1)w)(1-k))}{2w\epsilon}} (\cot_{pq}(\sqrt{2v}\Omega)) \pm \sqrt{pq} \operatorname{csc}_{pq}(\sqrt{2v}\Omega) \right) e^{i(kx+et+\eta)}, \quad (84)$$

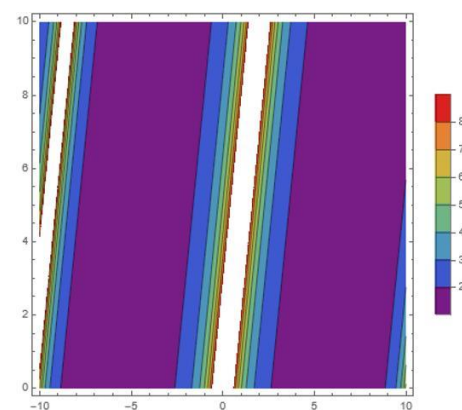
$$\mathbb{V}_{13}(x, t) = \frac{2vc}{m} \left( \sqrt{\frac{(n+w(k-1))(1-k))}{2w\epsilon}} (\cot_{pq}(\sqrt{2v}\Omega) \pm \sqrt{pq} \operatorname{csc}_{pq}(\sqrt{2v}\Omega)) \right)^2 e^{i(kx+wt+\eta)} - \frac{c_1}{m}, \quad (85)$$

$$\mathbb{K}_{14}(x, t) = \pm \left( \frac{1}{2} \sqrt{\frac{((n+(k-1)w)(1-k))}{2w\epsilon}} (\tan_{pq}(\sqrt{\frac{v}{8}} \Omega)) \pm \cot(\sqrt{\frac{v}{8}} \Omega) \right) e^{i(kx+et+\eta)}, \quad (86)$$

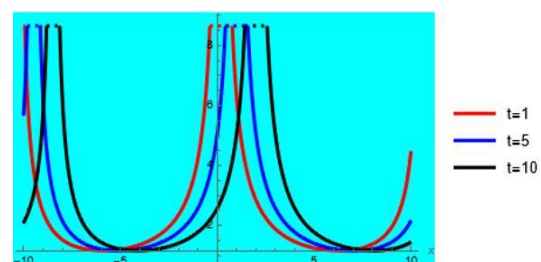
$$\mathbb{V}_{14}(x, t) = \frac{2vc}{m} \left( \frac{1}{2} \sqrt{\frac{(n+w(k-1))(1-k))}{w\epsilon}} (\tan_{pq}(\sqrt{\frac{v}{8}} \Omega) + \cot_{pq}(\sqrt{\frac{v}{8}} \Omega)) \right)^2 e^{i(kx+wt+\eta)} - \frac{c_1}{m}. \quad (87)$$



(a)

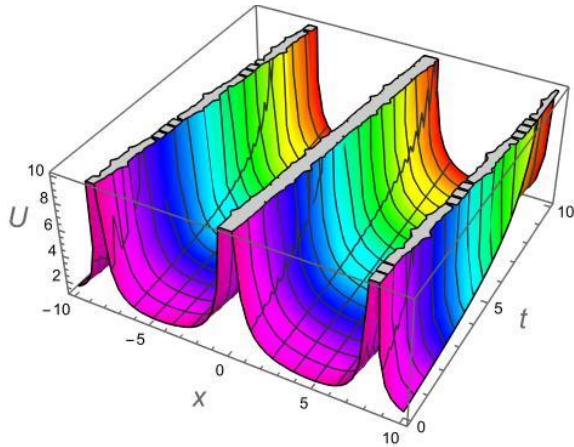


(b)

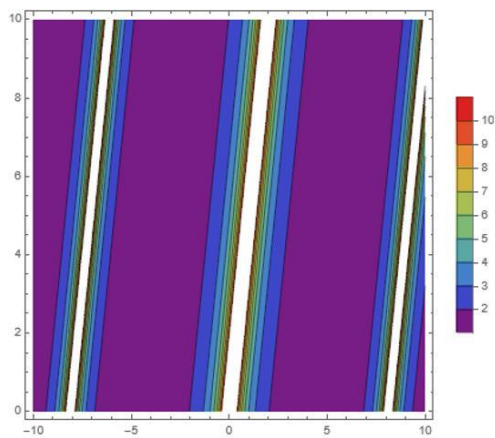




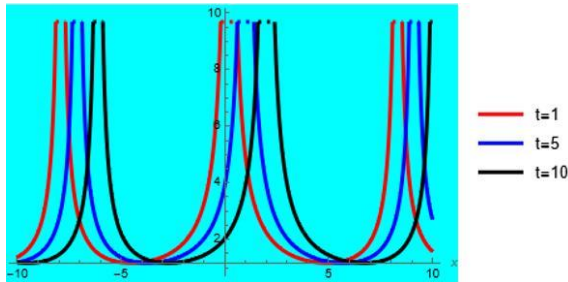
(c)



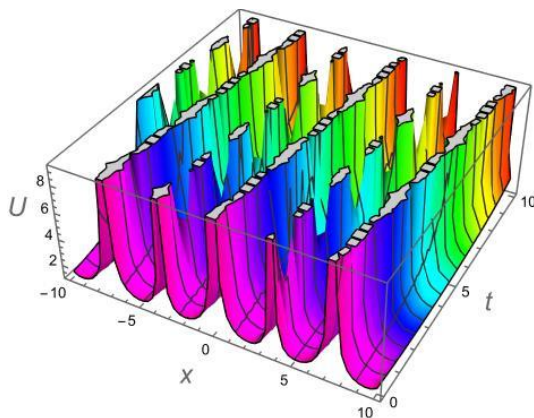
(d)



(e)

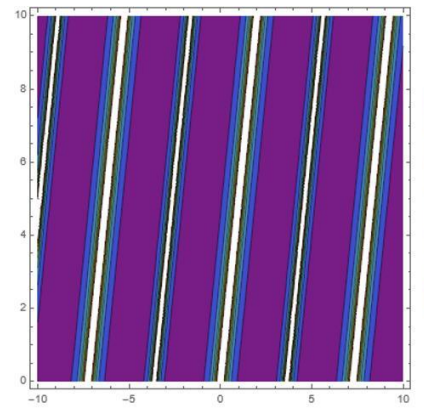


(f)

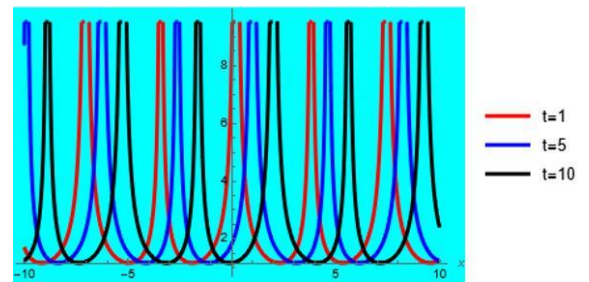


(g)

(h)

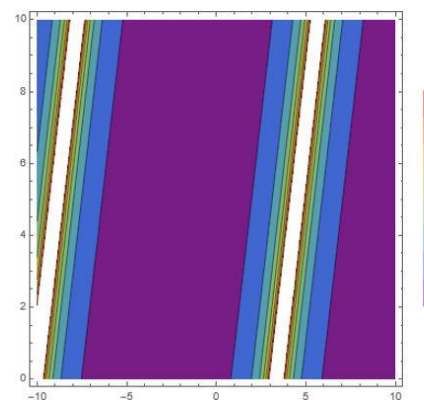
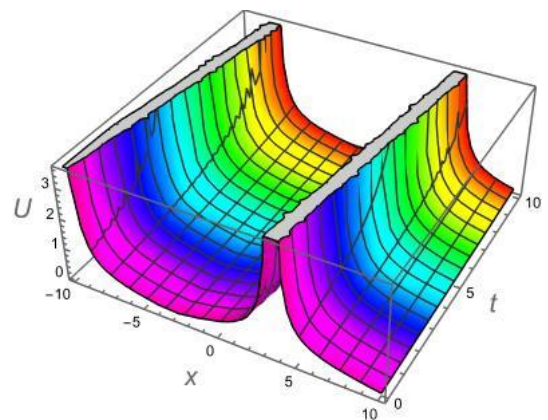


(i)



**Fig. 3.** Three-dimensional, contour and two-dimensional representations of the solution K8 across different parameter values of  $u$ . (a) 3-D visualisation at  $u = -1.25$ . (b) Contour visualisation at  $u = -1.25$ . (c) 2-D visualisation at  $u = -1.25$ . (d) 3-D visualisation at  $u = -0.75$ . (e) Contour visualisation  $u = -0.75$ . (f) 2-D visualisation  $u = -0.75$ . (g) 3-D visualisation  $u = -0.15$ . (h) Contour visualisation  $u = -0.15$ . (i) 2-D visualisation  $u = -0.15$

(a)



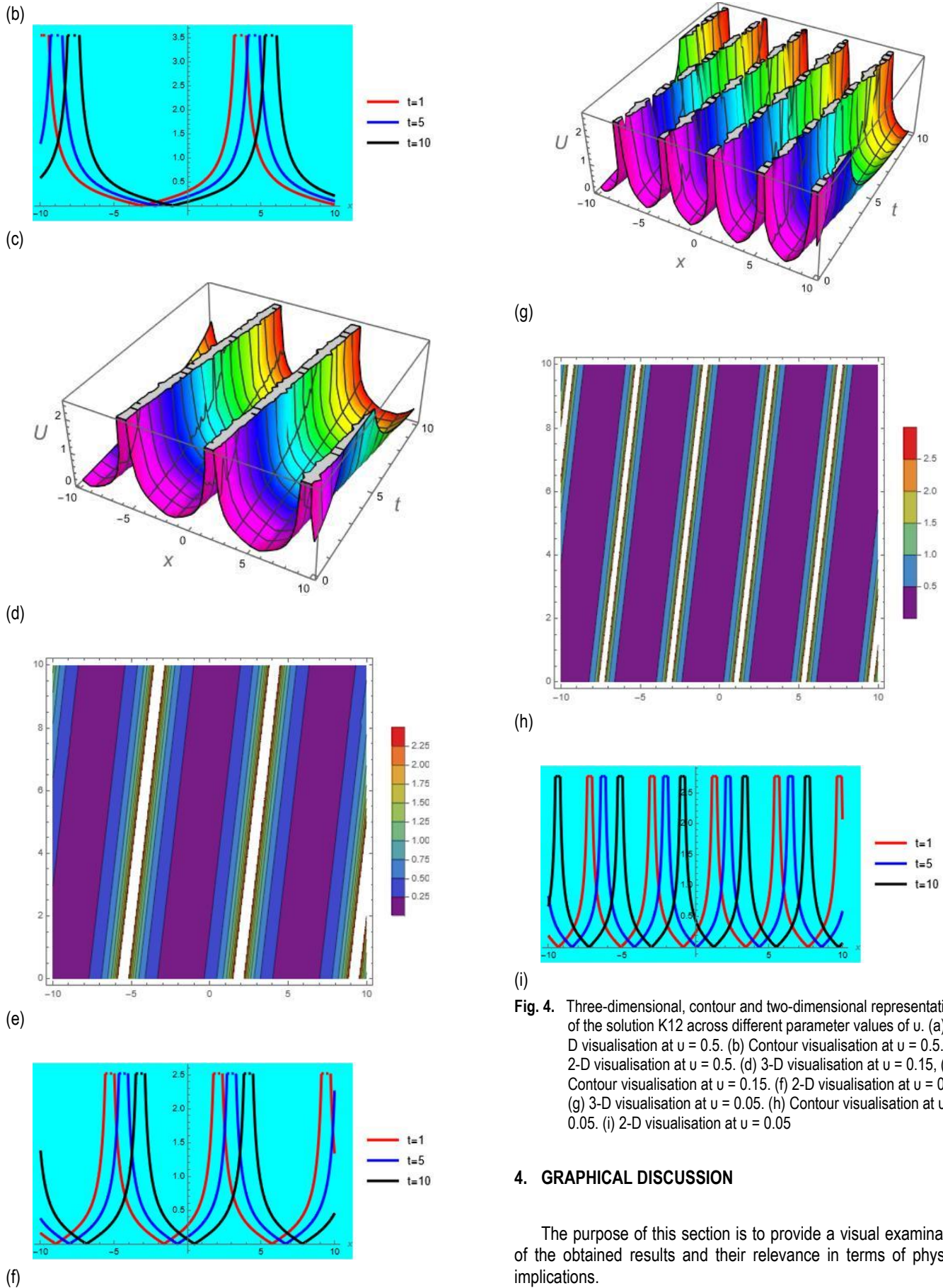


**Fig. 4.** Three-dimensional, contour and two-dimensional representations of the solution K12 across different parameter values of  $u$ . (a) 3-D visualisation at  $u = 0.5$ . (b) Contour visualisation at  $u = 0.5$ . (c) 2-D visualisation at  $u = 0.5$ . (d) 3-D visualisation at  $u = 0.15$ . (e) Contour visualisation at  $u = 0.15$ . (f) 2-D visualisation at  $u = 0.15$ . (g) 3-D visualisation at  $u = 0.05$ . (h) Contour visualisation at  $u = 0.05$ . (i) 2-D visualisation at  $u = 0.05$

#### 4. GRAPHICAL DISCUSSION

The purpose of this section is to provide a visual examination of the obtained results and their relevance in terms of physical implications.

Fig. 1 illustrates the transmission behaviour of the solution K1,1 at designated parameter values,  $\alpha = 0.25$ ,  $\gamma = 0.5$ ,  $k = 0.5$ ,



$\beta = 0.1$  and  $n = 0.25$ . This solution anticipates an anti-kink periodic pattern exhibited by a travelling soliton, where the frequency rises as the parameter  $w$  increases. Fig. 2 illustrates the transmission behaviour of the solution K1,4 at designated parameter values,  $\alpha = 0.25$ ,  $\gamma = 0.5$ ,  $k = 0.5$ ,  $\beta = 0.1$  and  $n = 0.25$ . This solution anticipates an anti-kink periodic pattern exhibited by a travelling soliton, where the frequency rises as the parameter  $w$  increases.

Fig. 3 shows the propagating behaviour of the solution K8 at designated parameter values,  $w = 15$ ,  $k = 0.5$ ,  $n = 0.25$ ,  $p = 0.26$  and  $q = 0.25$ . The proposed solution can forecast the behaviour of a travelling soliton that displays periodic patterns characterised by anti-peaked crests and anti-troughs. Furthermore, the frequency of this pattern is observed to increase as the value of the parameter  $u$  increases.

Fig. 4 shows the propagating behaviour of the solution K12 at designated parameter values,  $w = 0.15$ ,  $k = 0.35$ ,  $n = 0.15$ ,  $p = 0.52$  and  $q = 0.5$ . The proposed solution can forecast the behaviour of a travelling soliton that displays periodic patterns characterised by anti-peaked crests and anti-troughs. Furthermore, the frequency of this pattern is observed to increase as the value of the parameter  $u$  increases.

## 5. CONCLUSION

In this study, numerous novel solitons to the Kuralay equation are constructed through use of the modified auxiliary equation approach and the Sardar sub-equation method. Thus, numerous types of solitons such as a plane solution, periodic-stumpions, compacton, smooth soliton, multi-smooth kink, mixed-hyperbolic, periodic and mixed-periodic, compacton with singular peaks, mixed-trigonometric, trigonometric solution, peakon soliton, anti-peaked with decay, mixed-shock singular, mixed-singular, and singular and shock wave solutions are developed which are more generalised than the existing results. The propagation of solitons is graphically displayed in 3-D, contour and 2-D visualisation. The observed wave propagation displayed diverse behaviours, encompassing periodic patterns featuring elevated crests and troughs, as well as anti-peaked crests and troughs, periodic kinks, anti-kinks and compactons in both bright and dark forms. It is observed that the wave number is responsible to control the propagation of a solitary wave. Some appropriate values are selected for the involved free parameters in order to enlighten the graphical behaviour of the optical pulses using the developed analytical solutions. In interpreting the physical perspective of the nonlinear model, the proposed solutions may be considered to be authoritative. The modified auxiliary equation approach and the Sardar sub-equation method is a reliable and effective mathematical technique that can be applied to propose the analytical solutions to a number of other difficult physical phenomena. Additionally, there is potential to broaden the scope of this study to encompass lump interactions, multiple solitons and rogue wave breathers, thus expanding its practical utility.

## REFERENCES

1. Iqbal MA, Wang Y, Miah MM, Osman MS. Study on date–Jimbo–Kashiwara–Miwa equation with conformable derivative dependent on time parameter to find the exact dynamic wave solutions. *Fractal and Fractional*. 2021;6(1):4.
2. Eidinejad Z, Saadati R, Li C, Inc M, Vahidi J. The multiple exp-function method to obtain soliton solutions of the conformable Date–Jimbo–Kashiwara–Miwa equations. *International Journal of Modern Physics B*. 2023;2450043.
3. Singh S, Ray SS. Integrability and new periodic, kink-antikink and complex optical soliton solutions of  $(3+1)$ -dimensional variable coefficient DJKM equation for the propagation of nonlinear dispersive waves in inhomogeneous media. *Chaos, Solitons & Fractals*. 2023;168:113184.
4. Majid SZ, Faridi WA, Asjad MI, Abd El-Rahman M, Eldin SM. Explicit soliton structure formation for the Riemann wave equation and a sensitive demonstration. *Fractal and Fractional*. 2023;7(2):102.
5. Muhamad KA, Tanriverdi T, Mahmud AA, Baskonus HM. Interaction characteristics of the Riemann wave propagation in the  $(2+1)$ -dimensional generalized breaking soliton system. *International Journal of Computer Mathematics*. 2023;100(6):1340-55.
6. Skipp J, Laurie J, Nazarenko S. Hamiltonian derivation of the point vortex model from the two-dimensional nonlinear Schrödinger equation. *Physical Review E*. 2023;107(2):025107.
7. Wang KJ, Liu JH. Diverse optical solitons to the nonlinear Schrödinger equation via two novel techniques. *The European Physical Journal Plus*. 2023 Jan;138(1):1-9.
8. Rizvi ST, Seadawy AR, Ahmed S, Bashir A. Optical soliton solutions and various breathers lump interaction solutions with periodic wave for nonlinear Schrödinger equation with quadratic nonlinear susceptibility. *Optical and Quantum Electronics*. 2023;55(3):286.
9. Asjad MI, Inc M, Faridi WA, Bakar MA, Muhammad T, Rezazadeh H. Optical solitonic structures with singular and non-singular kernel for nonlinear fractional model in quantum mechanics. *Optical and Quantum Electronics*. 2023;55(3):219.
10. Abu Bakar M, Owyed S, Faridi WA, Abd El-Rahman M, Sallah M. The First Integral of the Dissipative Nonlinear Schrödinger Equation with Nucci's Direct Method and Explicit Wave Profile Formation. *Fractal and Fractional*. 2022;7(1):38.
11. Akinyemi L, Şenol M, Osman MS. Analytical and approximate solutions of nonlinear Schrödinger equation with higher dimension in the anomalous dispersion regime. *Journal of Ocean Engineering and Science*. 2022;7(2):143-54.
12. Brûé E, De Lellis C. Anomalous dissipation for the forced 3D Navier–Stokes equations. *Communications in Mathematical Physics*. 2023;400(3):1507-33.
13. Hess MW, Quaini A, Rozza G. A data-driven surrogate modeling approach for time-dependent incompressible Navier–Stokes equations with dynamic mode decomposition and manifold interpolation. *Advances in Computational Mathematics*. 2023;49(2):22.
14. Lange T. Regularization by noise of an averaged version of the Navier–Stokes equations. *Journal of Dynamics and Differential Equations*. 2023;1-26.
15. Brûé E, De Lellis C. Anomalous dissipation for the forced 3D Navier–Stokes equations. *Communications in Mathematical Physics*. 2023;400(3):1507-33.
16. Wu XH, Gao YT, Yu X, Ding CC, Li LQ. Modified generalized Darboux transformation and solitons for a Lakshmanan–Porsezian–Daniel equation. *Chaos, Solitons & Fractals*. 2022;162:112399.
17. AA AQ, AM B, ASHF M, AA A, HO B. Dark and singular cubic-quartic optical solitons with Lakshmanan–Porsezian–Daniel equation by the improved Adomian decomposition scheme. *Ukrainian Journal of Physical Optics*. 2023;24(1).
18. Faridi WA, Asjad MI, Jarad F. Non-linear soliton solutions of perturbed Chen–Lee–Liu model by  $\Phi$  6-model expansion approach. *Optical and Quantum Electronics*. 2022;54(10):664.
19. Khater MM, Zhang X, Attia RA. Accurate computational simulations of perturbed Chen–Lee–Liu equation. *Results in Physics*. 2023;45:106227.
20. Khatun MM, Akbar MA. New optical soliton solutions to the space-time fractional perturbed Chen–Lee–Liu equation. *Results in Physics*. 2023;46:106306.
21. Kumar S, Niwas M. New optical soliton solutions and a variety of dynamical wave profiles to the perturbed Chen–Lee–Liu equation in optical fibers. *Optical and Quantum Electronics*. 2023;55(5):418.

22. Qureshi ZA, Bilal S, Khan U, Akgül A, Sultana M, Botmart T, Zahran HY, Yahia IS. Mathematical analysis about influence of Lorentz force and interfacial nano layers on nanofluids flow through orthogonal porous surfaces with injection of SWCNTs. *Alexandria Engineering Journal*. 2022;61(12):12925-41.
23. Shah IA, Bilal S, Akgül A, Tekin MT, Botmart T, Zahran HY, Yahia IS. On analysis of magnetized viscous fluid flow in permeable channel with single wall carbon nano tubes dispersion by executing nano-layer approach. *Alexandria Engineering Journal*. 2022;61(12):11737-51.
24. Faridi WA, Asjad MI, Jarad F. The fractional wave propagation, dynamical investigation, and sensitive visualization of the continuum isotropic bi-quadratic Heisenberg spin chain process. *Results in Physics*. 2022;43:106039.
25. Asjad MI, Faridi WA, Jhangeer A, Ahmad H, Abdel-Khalek S, Alshehri N. Propagation of some new traveling wave patterns of the double dispersive equation. *Open Physics*. 2022;20(1):130-41.
26. Almusawa H, Jhangeer A. A study of the soliton solutions with an intrinsic fractional discrete nonlinear electrical transmission line. *Fractal and Fractional*. 2022;6(6):334.
27. Asjad MI, Faridi WA, Jhangeer A, Aleem M, Yusuf A, Alshomrani AS, Baleanu D. Nonlinear wave train in an inhomogeneous medium with the fractional theory in a plane self-focusing.
28. Fahim MR, Kundu PR, Islam ME, Akbar MA, Osman MS. Wave profile analysis of a couple of (3+ 1)-dimensional nonlinear evolution equations by sine-Gordon expansion approach. *Journal of Ocean Engineering and Science*. 2022;7(3):272-9.
29. Liu JG, Osman MS. Nonlinear dynamics for different nonautonomous wave structures solutions of a 3D variable-coefficient generalized shallow water wave equation. *Chinese Journal of Physics*. 2022;77:1618-24.
30. Baber MZ, Seadway AR, Iqbal MS, Ahmed N, Yasin MW, Ahmed MO. Comparative analysis of numerical and newly constructed soliton solutions of stochastic Fisher-type equations in a sufficiently long habitat. *International Journal of Modern Physics B*. 2023; 37(16): 2350155.
31. Kumar S, Niwas M. Optical soliton solutions and dynamical behaviors of Kudryashov's equation employing efficient integrating approach. *Pramana*. 2023;97(3):98.
32. Kumar S, Niwas M. Abundant soliton solutions and different dynamical behaviors of various waveforms to a new (3+ 1)-dimensional Schrödinger equation in optical fibers. *Optical and Quantum Electronics*. 2023;55(6):531.
33. Niwas M, Kumar S. New plenteous soliton solutions and other form solutions for a generalized dispersive long-wave system employing two methodological approaches. *Optical and Quantum Electronics*. 2023;55(7):630.
34. El-Ganaini S, Kumar S, Niwas M. Construction of multiple new analytical soliton solutions and various dynamical behaviors to the nonlinear convection-diffusion-reaction equation with power-law nonlinearity and density-dependent diffusion via Lie symmetry approach together with a couple of integration approaches. *Journal of Ocean Engineering and Science*. 2023;8(3):226-37.
35. Kumar S, Niwas M, Dhiman SK. Abundant analytical soliton solutions and different wave profiles to the Kudryashov-Sinelshchikov equation in mathematical physics. *Journal of Ocean Engineering and Science*. 2022;7(6):565-77.
36. Abdou MA, Ouahid L, Kumar S. Plenteous specific analytical solutions for new extended deoxyribonucleic acid (DNA) model arising in mathematical biology. *Modern Physics Letters B*. 2023;37(34): 2350173.
37. Kumar S, Kumar A. A study of nonlinear extended Zakharov-Kuznetsov dynamical equation in (3+ 1)-dimensions: Abundant closed-form solutions and various dynamical shapes of solitons. *Modern Physics Letters B*. 2022;36(25):2250140.
38. Mathanaranjan T. New Jacobi elliptic solutions and other solutions in optical metamaterials having higher-order dispersion and its stability analysis. *International Journal of Applied and Computational Mathematics*. 2023;9(5):66.
39. Mathanaranjan T. Optical solitons and stability analysis for the new (3+ 1)-dimensional nonlinear Schrödinger equation. *Journal of Nonlinear Optical Physics & Materials*. 2023;32(02):2350016.
40. Zhao YH, Mathanaranjan T, Rezazadeh H, Akinyemi L, Inc M. New solitary wave solutions and stability analysis for the generalized (3+ 1)-dimensional nonlinear wave equation in liquid with gas bubbles. *Results in Physics*. 2022;43:106083.
41. Mathanaranjan T, Kumar D, Rezazadeh H, Akinyemi L. Optical solitons in metamaterials with third and fourth order dispersions. *Optical and Quantum Electronics*. 2022;54(5):271.
42. Mathanaranjan T, Vijayakumar D. New soliton solutions in nanofibers with space-time fractional derivatives. *Fractals*. 2022;30(07): 2250141.
43. Mathanaranjan T, Hashemi MS, Rezazadeh H, Akinyemi L, Bekir A. Chirped optical solitons and stability analysis of the nonlinear Schrödinger equation with nonlinear chromatic dispersion. *Communications in Theoretical Physics*. 2023;75(8):085005.
44. Hosseini K, Hincal E, Salahshour S, Mirzazadeh M, Dehgingia K, Nath BJ. On the dynamics of soliton waves in a generalized nonlinear Schrödinger equation. *Optik*. 2023;272:170215.
45. Aksoy A, Yenikaya S. Soliton wave parameter estimation with the help of artificial neural network by using the experimental data carried out on the nonlinear transmission line. *Chaos, Solitons & Fractals*. 2023;169:113226.
46. Khater MM. Computational and numerical wave solutions of the Caudrey-Dodd-Gibbon equation. *Heliyon*. 2023;9(2).
47. Al Alwan B, Abu Bakar M, Faridi WA, Turcu AC, Akgül A, Sallah M. The Propagating Exact Solitary Waves Formation of Generalized Calogero-Bogoyavlenskii-Schiff Equation with Robust Computational Approaches. *Fractal and Fractional*. 2023;7(2):191.
48. Khater MM. A hybrid analytical and numerical analysis of ultra-short pulse phase shifts. *Chaos, Solitons & Fractals*. 2023;169:113232.
49. Ozdemir N, Secer A, Bayram M. Extraction of soliton waves from the longitudinal wave equation with local M-truncated derivatives. *Optical and Quantum Electronics*. 2023;55(4):313.
50. Zahran EH, Bekir A, Ibrahim RA, Sagidullayeva Z, Myrzakulov R. New diverse types of the soliton arising from the integrable Kuralay equations against its numerical solutions.
51. Zahran EH, Bekir A. Unexpected configurations for the optical solitons propagation in lossy fiber system with dispersion terms effect. *Mathematical Methods in the Applied Sciences*. 2023;46(4):4055-69.
52. Zahran EH, Bekir A. New unexpected behavior to the soliton arising from the geophysical Korteweg-de Vries equation. *Modern Physics Letters B*. 2022;36(08):2150623.
53. Raheel M, Zafar A, Ali MR, Myrzakulova Z, Bekir A, Myrzakulov R. New analytical wave solutions to the M-fractional Kuralay-II equations based on three distinct schemes.
54. Mathanaranjan T. Optical soliton, linear stability analysis and conservation laws via multipliers to the integrable Kuralay equation. *Optik*. 2023;290:171266.
55. Bettelheim E, Smith NR, Meerson B. Inverse scattering method solves the problem of full statistics of nonstationary heat transfer in the Kipnis-Marchioro-Presutti model. *Physical Review Letters*. 2022;128(13):130602.
56. Gonzalez-Gaxiola O, Biswas A, Ekici M, Khan S. Highly dispersive optical solitons with quadratic-cubic law of refractive index by the variational iteration method. *Journal of Optics*. 2022;1-8.
57. Al-Tai MH, Al-Fayadh A. Solving two dimensional coupled Burger's equations using transform variational iteration method. In *AIP Conference Proceedings* 2023; 2414(1):040030. AIP Publishing LLC.
58. Zhang Y, Dang S, Li W, Chai Y. Performance of the radial point interpolation method (RPIM) with implicit time integration scheme for transient wave propagation dynamics. *Computers & Mathematics with Applications*. 2022;114:95-111.
59. Zagorac JL, Sands I, Padmanabhan N, Easter R. Schrödinger-Poisson solitons: Perturbation theory. *Physical Review D*. 2022;105(10):103506.

60. He XJ, Lü X. M-lump solution, soliton solution and rational solution to a  $(3+1)$ -dimensional nonlinear model. *Mathematics and Computers in Simulation*. 2022;197:327-40.
61. Aniq A, Ahmad J. Soliton solution of fractional Sharma-Tasso-Olevers equation via an efficient  $(G'/G)$ -expansion method. *Ain Shams Engineering Journal*. 2022;13(1):101528.
62. Kumar S, Malik S, Rezazadeh H, Akinyemi L. The integrable Boussinesq equation and its breather, lump and soliton solutions. *Nonlinear Dynamics*. 2022;1-4.
63. Akram G, Sadaf M, Zainab I. Bright, dark, periodic and kink solitary wave solutions of evolutionary Zoomeron equation. *Authorea Preprints*. 2022.
64. Asjad MI, Munawar N, Muhammad T, Hamoud AA, Emadifar H, Hamasalh FK, Azizi H, Khademi M. Traveling wave solutions to the Boussinesq equation via Sardar sub-equation technique. *AIMS Mathematics*. 2022;7(6):11134-49.

This work was supported by the Ministry of Science and Higher Education of the Republic of Kazakhstan, Grant AP14870191.

Waqas Ali Faridi:  <https://orcid.org/0000-0003-0713-5365>

Muhammad Abu Bakar:  <https://orcid.org/0000-0003-3903-098X>

Zhaidary Myrzakulova:  <https://orcid.org/0000-0002-4047-4484>

Ratbay Myrzakulov:  <https://orcid.org/0000-0002-5274-0815>

Mawahib Elamin:  <https://orcid.org/0000-0002-7907-4672>

Lakhdar Ragoub:  <https://orcid.org/0000-0001-8747-1814>

Lanre Akinyemi:  <https://orcid.org/0000-0002-5920-250X>



This work is licensed under the Creative Commons BY-NC-ND 4.0 license.

## ANALYTICAL ANALYSIS FOR SPACE FRACTIONAL HELMHOLTZ EQUATIONS BY USING THE HYBRID EFFICIENT APPROACH

Adnan KHAN<sup>\*/\*\*</sup>, Muhammad Imran LIAQAT<sup>\*/\*\*</sup>, Asma MUSHTAQ<sup>\*\*</sup>

<sup>\*</sup>National College of Business Administration & Economics, Lahore, Pakistan

<sup>\*\*</sup>Abdus Salam School of Mathematical Sciences, Government College University, 68-B,  
 New MuslimTown, Lahore 54600, Pakistan

[adnankhantariq@ncbae.edu.pk](mailto:adnankhantariq@ncbae.edu.pk), [imran\\_liaqat\\_22@sms.edu.pk](mailto:imran_liaqat_22@sms.edu.pk), [Asmafaizan624@gmail.com](mailto:Asmafaizan624@gmail.com)

received 11 Septemeber 2023, revised 6 March 2024, accepted 20 March 2024

**Abstract:** The Helmholtz equation is an important differential equation. It has a wide range of uses in physics, including acoustics, electrostatics, optics, and quantum mechanics. In this article, a hybrid approach called the Shehu transform decomposition method (STDM) is implemented to solve space-fractional-order Helmholtz equations with initial boundary conditions. The fractional-order derivative is regarded in the Caputo sense. The solutions are provided as series, and then we use the Mittag-Leffler function to identify the exact solutions to the Helmholtz equations. The accuracy of the considered problem is examined graphically and numerically by the absolute, relative, and recurrence errors of the three problems. For different values of fractional-order derivatives, graphs are also developed. The results show that our approach can be a suitable alternative to the approximate methods that exist in the literature to solve fractional differential equations.

**Key words:** Helmholtz equations, Shehu transform, Adomian decomposition method, Mittag-Leffler function, Caputo derivatives

### 1. INTRODUCTION

The fractional calculus (FC) results from several straightforward questions regarding the concept of derivatives: why does a function's half-order derivative reveal information that the first-order derivative does not? By providing answers to these issues, researchers create a new window of opportunity between the mathematical and physical worlds, leading to several exciting new questions and findings. For instance, unlike the conventional derivative, the fractional-order derivative (FOD) of a constant function is not always zero [1].

The memory idea is the most beneficial interpretation of FC. In general, systems are considered to be memoryless when their output at each time  $t$  depends only on the input at time  $t$ . However, when the system has to remember past values of the input to compute the present value of the output, these systems are referred to as memory systems or non-memoryless systems. The memory property of FOD refers to their ability to capture and incorporate information from past states. Instead of traditional integer-order derivatives, which rely solely on the current state of a system, FOD retain memory of past states over a certain time horizon. This memory property is particularly useful in modeling and analyzing systems with long-term dependencies or non-local effects, where past events continue to influence the system's dynamics alongside the current state. By incorporating information from past states, FOD provide a more accurate representation of the system's behavior and enable better predictions of its future evolution. In practical terms, the memory property of FOD allows for a more nuanced understanding of complex phenomena in various fields, including physics, engineering, biology, finance, and more. It facilitates the development of more accurate models and control strategies for systems exhibiting non-local or long-term memory effects.

Different from integer-order derivatives, there are several kinds of definitions for FOD [2-5]. These definitions are generally not equivalent to each other. In the following, we introduce several definitions.

The natural derivative is fundamentally extended into a fractional derivative by the Grünwald-Letnikov derivative. Both Anton Karl Grünwald and Aleksey Vasilievich Letnikov introduced it in 1867 and 1868, respectively [6]. It is therefore written as:

$$\mathfrak{I}^{\varsigma} \mathcal{E}(\tau) = \lim_{h \rightarrow 0} \frac{1}{h} \sum_{\kappa=0}^{\infty} (-1)^{\kappa} \binom{\varsigma}{\kappa} \mathcal{E}(\tau - \kappa h),$$

where  $\kappa \in \mathbb{N}$ , and the gamma function is used to determine the binomial coefficient,

$$\left[ \begin{matrix} \varsigma \\ \kappa \end{matrix} \right] = \frac{\varsigma(\varsigma-1)(\varsigma-2)(\varsigma-3) \cdots (\varsigma-\kappa+1)}{\kappa!}.$$

In 1847, Riemann defined the new fractional order derivative that is called Riemann-Liouville fractional derivatives (RLFD) [7]. It is defined as follows:

$$\mathfrak{I}_{0,\tau}^{\varsigma} \mathcal{E}(\tau) = \frac{d^{\kappa}}{d\tau^{\kappa}} D_{0,\tau}^{-(\kappa-\varsigma)} \mathcal{E}(\tau) = \frac{1}{\Gamma(\kappa-\varsigma)} \frac{d^{\kappa}}{d\tau^{\kappa}} \int_0^{\tau} (\tau - \Upsilon)^{\kappa-\varsigma-1} \mathcal{E}(\Upsilon) d\Upsilon,$$

where  $\kappa - 1 \leq \varsigma < \kappa \in \mathbb{Z}^+$

The Caputo fractional derivative (CFD) was established in 1967 [8] because it was ineffective in the description and modeling of some complicated events.

$$\mathfrak{I}_{0,\tau}^{\varsigma} \mathcal{E}(\tau) = D_{0,\tau}^{-(\kappa-\varsigma)} \frac{d^{\kappa}}{d\tau^{\kappa}} \mathcal{E}(\tau) = \frac{1}{\Gamma(\kappa-\varsigma)} \int_0^{\tau} (\tau - \Upsilon)^{\kappa-\varsigma-1} \frac{d^{\kappa}}{d\tau^{\kappa}} \mathcal{E}(\Upsilon) d\Upsilon,$$

where  $\kappa - 1 \leq \varsigma < \kappa \in \mathbb{Z}^+$

The RLFD of a constant  $W$  is given by  $\frac{W\tau^{-\kappa}}{\Gamma(1-\kappa)}$ . As a result, the CFD's ability to provide the derivative of a constant zero, as in an ordinary derivative, is one of its strengths.

It is important to keep in mind that while all FOD behave the same when the order is an integer, they may behave differently when the order is not an integer. For instance, in a non-integer order, the CFD of a constant behaves differently than the RLFD because it is zero. There are more fractional derivatives; the interested reader is referred to [9-12] for further details.

Fractional-order differential equations (FODEs) are mathematical representations of natural and physical phenomena that occur in the fields of science and engineering. As a result, we detect the mechanism of these FODEs through the study of the approximate and exact solution, and their genuine physical intention can be understood from the graphical representation of the solution.

Due to their arbitrary features, FODEs are thought to be more difficult to compute than integer-order differential equations. In the literature, several methods are developed over the past few decades, namely the invariant subspace method [13], the Lie symmetry approach [14], the (G/G)-Expansion Method [15], the Haar wavelet method [16], the operational matrix method [17], and the sub-equation method [18] to solve the fractional differential and integral equations.

However, in some circumstances, especially when dealing with large and complex problems, the approximate solution technique for handling FODEs proves to be more effective and practical. As a result, different approximate techniques are created by researchers to solve various types of FODEs. For instance, the operational matrix approach [19], the Elzaki residual power series approach [20], the homotopy analysis method [21], and the decomposition method [22], for more approximate techniques, see [23-25]. Absolute, relative, and recurrence errors are commonly used to assess the accuracy of approximate methods in solving mathematical problems. By analyzing these error measures, researchers can gain a comprehensive understanding of the performance of approximate methods. Indeed, most researchers commonly utilize absolute, relative, and recurrence errors as primary metrics for assessing the accuracy and convergence of approximate methods in solving mathematical problems [26-29].

The wave equation can be used to derive the Helmholtz equation (HH-E), an elliptic partial differential equation. The HH-E is used to explain a variety of phenomena, including electromagnetic waves in fluids, vibrating lines, plates, and walls, as well as acoustics, magnetic fields, nuclear power plants, and geoscience. Take into account a 2D non-homogeneous isotropic material whose Euclidean space velocity is  $V$ . The wave result,  $\Xi(v, \omega)$ , which has the harmonic origin  $\Theta(v, \omega)$  as its point of vibration and vibrates at the fixed frequency  $\omega > 0$ , satisfies the HH-E for the defined area  $R$ .

$$\frac{\partial^2}{\partial v^2} \Xi(v, \omega) + \frac{\partial^2}{\partial \omega^2} \Xi(v, \omega) + \Omega \Xi(v, \omega) = -\Theta(v, \omega),$$

where  $\Xi(v, \omega)$  is an appropriately differentiable function at the boundary of  $R$ , and  $\Theta(v, \omega)$  is a specified function,  $\Omega > 0$  is a constant value, and  $\sqrt{\Omega} = \frac{\omega}{V}$  is a wave number with a wavelength of  $\frac{2\pi}{\sqrt{\Omega}}$ .

In this research, STDM is applied to the HH-E in the sense of CFD of  $x$ -space in the following form:

$$\Im_{\omega}^{\varsigma} \Xi(v, \omega) + \frac{\partial^2}{\partial \omega^2} \Xi(v, \omega) + \Omega \Xi(v, \omega) = -\Theta(v, \omega), 1 < \varsigma \leq 2,$$

subject to the initial conditions (I-Cs)

$$\Xi(v, 0) = \Psi(\omega), \Xi_v(v, 0) = T(\omega).$$

Furthermore, we similarly apply STDM to the HH-E in terms of the CFD of  $y$ -space:

$$\Im_{\omega}^{\varsigma} \Xi(v, \omega) + \frac{\partial^2}{\partial v^2} \Xi(v, \omega) + \Omega \Xi(v, \omega) = -\Theta(v, \omega), 1 < \varsigma \leq 2.$$

with the following I-Cs:

$$\Xi(v, 0) = \Phi(v), \Xi_{\omega}(v, 0) = P(v).$$

In general, boundary conditions for the HH-E specify the behavior of the solution at the boundaries of the domain in which the equation is being solved. These boundary conditions can be of various types, including Dirichlet boundary conditions, Neumann boundary conditions, or mixed boundary conditions.

**Dirichlet boundary conditions:** These specify the value of the solution at the boundary of the domain. Mathematically, it can be expressed as  $\Xi(v, \omega) = g(v, \omega)$ , where  $g(v, \omega)$  is a given function describing the boundary values.

**Neumann boundary conditions:** These specify the normal derivative of the solution at the boundary of the domain. Mathematically, it can be expressed as

$$\frac{\partial}{\partial n} \Xi(v, \omega) = f(v, \omega),$$

where  $f(v, \omega)$  is a given function describing the normal derivative on the boundary.

**Mixed boundary conditions:** These are a combination of Dirichlet and Neumann boundary conditions, specifying both the value of the solution and its normal derivative at different parts of the boundary.

The choice of boundary conditions depends on the physical problem and the geometry of the domain. For example, in acoustic problems, Dirichlet boundary conditions might be used to specify the pressure at the boundaries of a room, while in electromagnetic problems, Neumann boundary conditions might be used to specify the normal component of the electric field at a conducting boundary.

The solution of the HH-E holds significant importance across various fields of science and engineering due to its wide range of applications. Here are some reasons highlighting its importance:

**Acoustics:** In acoustics, the HH-E describes the behavior of sound waves in different media. Solutions to this equation help in understanding phenomena such as sound propagation, resonance, and wave interference. Applications include designing concert halls, noise control, and ultrasound imaging.

**Electromagnetics:** In electromagnetics, the HH-E describes the behavior of electromagnetic fields, such as those produced by antennas, waveguides, and resonant cavities. Solutions to this equation are crucial for designing communication systems, radar systems, and microwave devices.

**Optics:** In optics, the HH-E governs the propagation of light waves through various optical media. Solutions to this equation are essential for designing optical components, such as lenses, mirrors, and optical fibers, as well as for understanding phenomena like diffraction and interference.

**Quantum mechanics:** In quantum mechanics, the HH-E appears in the context of the Schrödinger equation, which describes the behavior of quantum particles in potential fields. Solutions to this equation provide insights into the energy levels and wave functions of quantum systems, with applications in atomic physics, solid-state physics, and quantum chemistry.



**Engineering:** In general engineering applications, the HH-E arises in problems involving wave propagation, vibration analysis, and structural dynamics. Solutions to this equation are essential for designing structures, predicting their response to external forces, and optimizing their performance.

Overall, the solution of the HH-E plays a crucial role in understanding and modeling various physical phenomena, enabling the development of innovative technologies and solutions across different fields.

One of the most helpful mathematical methods is the use of integral transforms to solve differential equations (DEs) and integral equations. DEs can be expressed in terms of a straightforward algebraic equation by selecting the appropriate integral transform (IT). Many mathematicians are interested in a novel IT known as the "Shehu transforms (Sh-T)". The suggested IT is effectively applied to both ordinary and partial DEs, and it is derived from the classical Fourier IT.

In this paper, the HH-E problem is solved in the context of CFD using the Shehu transform (Sh-T) and the Adomian decomposition method (ADM). The primary advantage of this method is that it does not call for the solution of any parameters in the equation. Consequently, it circumvents certain limitations associated with traditional perturbation techniques. The accuracy and effectiveness of the STDm are confirmed by comparing the approximate solution (App-S) and the exact solution (Ex-S). Additionally, 2D graphs are generated for various values of FOD, illustrating the convergence of the approximation solution to the Ex-S as FOD increases. Therefore, results show that the fifth-step App-S perfectly agrees with the exact solution. The numerical analysis in the sense of absolute errors (Abs-Er), relative errors (Rel-Er), and recurrence errors (Rec-Er) evaluations establish the correctness and convergence, proving the effectiveness of the suggested method. Therefore, our suggested approach is effective and simple to apply to many different kinds of related scientific and technical problems.

The major contributions of this paper include at least the following aspects: The system we study is more generalized because it includes the FOD. For the first time in literature, we use the Shehu transform to solve fractional Helmholtz equations. We obtain both approximate and exact solutions. The suggested approach is a useful tool for both exact and approximate FODE solutions. The strength of the scheme lies in the modest size of computation required for the proposed approach, which yields accuracy with fewer computations. The efficiency and reliability of the recommended approach are demonstrated by the error analysis.

The following is how this study is structured: First, in Section 2, we use key definitions and findings from FC theory. The algorithm STDm for solving space-fractional Helmholtz equations is then covered in Section 3. Some problems in Section 4 are solved with the use of STDm. In Section 5, we also present a graphic and numerical comparison of approximate and exact solutions in terms of Abs-Er, Rel-Er, and Rec-Er, demonstrating the validity of the suggested approach. Lastly, we provide a summary of our findings in the conclusion.

## 2. PRELIMINARY CONCEPTS

We provide some helpful definitions related to FC in this section. The Mittag-Leffler function (ML-F), which is important in FC,

is defined first. Next, we go through some fundamental Sh-T terms, definitions, and theorems that are relevant to this study.

**Definition 1.** [30] A direct generalization of the exponential function,  $e^v$ , is the ML-F. The power series formula for the two-parameter ML-F is as follows:

$$E_{\alpha,\beta}(v) = \sum_{\kappa=0}^{\infty} \frac{v^{\kappa}}{\Gamma(\alpha\kappa+\beta)}, \alpha > 0, \beta > 0.$$

The definition of the one-parameter ML-F is:

$$E_{\alpha}(v) = \sum_{\kappa=0}^{\infty} \frac{v^{\kappa}}{\Gamma(\alpha\kappa+1)}, \alpha > 0.$$

We get well-known classical functions when the parameters  $\alpha$ ,  $\beta$  are chosen in specific ways.

$$E_{1,1}(v) = e^v, E_{1,2}(v) = \frac{e^v - 1}{v}, E_{2,1}(v^2) = \cosh v, E_{2,2}(v^2) = \frac{\sinh v}{v}.$$

**Definition 2.** [31] The Sh-T is defined as follows:

$$S[\Xi(v, \varpi)] = P(\mu, \eta) = \int_0^{\infty} \Xi(v, \varpi) e^{\frac{-\mu v}{\eta}} dv, v > 0,$$

The inverse Sh-T is given by

$$S^{-1}\{P(\mu, \eta)\} = \Xi(v, \varpi) = \frac{1}{2\pi i} \int_{w-i\infty}^{w+i\infty} \frac{1}{v} P(\mu, \eta) e^{\frac{-\mu v}{\eta}} d\mu,$$

where  $\mu$  and  $\eta$  are the Sh-T variables, and  $w$  is a real constant, and the integral is taken along  $\mu = w$  in the complex plane  $s = v + \varpi i$ .

Some important properties of Sh-T are as follows [32]

$$S[A_1 \Xi_1(v) + A_2 \Xi_2(v)] = A_1 S[\Xi_1(v)] + A_2 S[\Xi_2(v)].$$

$$S[1] = \frac{\mu}{\eta}.$$

$$S\left[\frac{v^n}{n!}\right] = \left(\frac{\mu}{\eta}\right)^{n+1} \text{ for } n = 0, 1, 2, 3, \dots$$

$$S[v^{\zeta}] = \left(\frac{\mu}{\eta}\right)^{\zeta+1} \Gamma(\zeta + 1).$$

**Definition 3.** [32] The Sh-T for  $n$ th derivatives is defined as

$$S[\Im^{(n)} \Xi(v)] = \frac{\mu^n}{\eta^n} S[\Xi(v)] - \sum_{\kappa=0}^{n-1} \left(\frac{\mu}{\eta}\right)^{n-\kappa-1} \Xi^{(\kappa)}(0), n \geq 1.$$

**Definition 4.** [33] The Sh-T of CFD of  $\Xi(v, \varpi)$  with order  $\zeta$  is defined as

$$S[\Im^{(\zeta)} \Xi(v)] = \frac{\mu^{\zeta}}{\eta^{\zeta}} S[\Xi(v)] - \sum_{\kappa=0}^{\zeta-1} \left(\frac{\mu}{\eta}\right)^{\zeta-\kappa-1} \Xi^{(\kappa)}(0), \kappa-1 < \zeta < \kappa.$$

## 3. ALGORITHM OF THE SHEHU TRANSFORM DECOMPOSITION METHOD

The primary goal of this section is to provide a series-form solution for the HH-E using STDm. The main algorithms of STDm are as follows: To do so, first apply the Sh-T to both sides of the given problem to convert the given model into algebraic expressions, and then use the inverse Sh-T to convert the obtained algebraic expression into the model's real domain. In the next step, we provide the series solutions of the model by using the ADM on the algebraic expressions that are attained with the help of Sh-T and inverse Sh-T.

As the fundamental idea of the suggested technique, we take into consideration a general form of HH-E:

$$\frac{\partial^2}{\partial v^2} \Xi(v, w) + \frac{\partial^2}{\partial w^2} \Xi(v, w) + \Omega \Xi(v, w) = -\theta(v, w), \quad (1)$$

with the I-Cs

$$\Xi(0, w) = \Phi(w), \Xi_v(0, w) = P(w). \quad (2)$$

Applying the Sh-T to Eq. (1), we use the differentiation property of the Sh-T, and after some calculation, as a result, we get as follows:

$$S[\Xi(v, w)] = \frac{\eta}{\mu} \Phi(w) - \left(\frac{\eta}{\mu}\right)^\varsigma S\left[\frac{\partial^2}{\partial w^2} \Xi(v, w)\right] - \left(\frac{\eta}{\mu}\right)^\varsigma \Omega S\left[\frac{\partial^2}{\partial \lambda^2} \Xi(v, w)\right] - \left(\frac{\eta}{\mu}\right)^\varsigma S[\theta(v, w)], \quad (3)$$

Taking the inverse Sh-T on Eq. (2), we have

$$\Xi(v, w) = S^{-1}\left[\frac{\eta}{\mu} \Phi(w)\right] - S^{-1}\left[\left(\frac{\eta}{\mu}\right)^\varsigma S\left[\frac{\partial^2}{\partial w^2} \Xi(v, w)\right]\right] - S^{-1}\left[\left(\frac{\eta}{\mu}\right)^\varsigma \Omega S\left[\frac{\partial^2}{\partial \lambda^2} \Xi(v, w)\right]\right] - S^{-1}\left[\left(\frac{\eta}{\mu}\right)^\varsigma S[\theta(v, w)]\right], \quad (4)$$

Implementing ADM in Eq. (4), therefore, supposes that the solution of Eq. (1) can be expressed as follows:

$$\Xi(v, w) = \sum_{\kappa=0}^{\infty} \Xi_{\kappa}(v, w). \quad (5)$$

Using Eq. (5) in Eq. (4).

$$\begin{aligned} \Xi(v, w) &= S^{-1}\left[\frac{\eta}{\mu} \Phi(w)\right] - \\ &S^{-1}\left[\left(\frac{\eta}{\mu}\right)^\varsigma S\left[\frac{\partial^2}{\partial w^2} \sum_{\kappa=0}^{\infty} \Xi_{\kappa}(v, w)\right]\right] - \\ &S^{-1}\left[\left(\frac{\eta}{\mu}\right)^\varsigma \Omega S\left[\frac{\partial^2}{\partial \lambda^2} \sum_{\kappa=0}^{\infty} \Xi_{\kappa}(v, w)\right]\right] - S^{-1}\left[\left(\frac{\eta}{\mu}\right)^\varsigma S[\theta(v, w)]\right]. \end{aligned} \quad (6)$$

By comparing the two sides of Eq. (6), we arrive at the following terms for the series solution:

$$\Xi_0(v, w) = S^{-1}\left[\frac{\eta}{\mu} \Phi(w)\right] - S^{-1}\left[\left(\frac{\eta}{\mu}\right)^\varsigma S[\theta(v, w)]\right].$$

$$\begin{aligned} \Xi_1(v, w) &= -S^{-1}\left[\left(\frac{\eta}{\mu}\right)^\varsigma S\left[\frac{\partial^2}{\partial w^2} \Xi_0(v, w)\right]\right] - \\ &S^{-1}\left[\left(\frac{\eta}{\mu}\right)^\varsigma \Omega S\left[\frac{\partial^2}{\partial \lambda^2} \Xi_0(v, w)\right]\right]. \end{aligned}$$

$$\begin{aligned} \Xi_2(v, w) &= -S^{-1}\left[\left(\frac{\eta}{\mu}\right)^\varsigma S\left[\frac{\partial^2}{\partial w^2} \Xi_1(v, w)\right]\right] - \\ &S^{-1}\left[\left(\frac{\eta}{\mu}\right)^\varsigma \Omega S\left[\frac{\partial^2}{\partial \lambda^2} \Xi_1(v, w)\right]\right]. \end{aligned}$$

$$\begin{aligned} \Xi_{\kappa+1}(v, w) &= -S^{-1}\left[\left(\frac{\eta}{\mu}\right)^\varsigma S\left[\frac{\partial^2}{\partial w^2} \Xi_{\kappa}(v, w)\right]\right] - \\ &S^{-1}\left[\left(\frac{\eta}{\mu}\right)^\varsigma \Omega S\left[\frac{\partial^2}{\partial \lambda^2} \Xi_{\kappa}(v, w)\right]\right]. \end{aligned}$$

We can quickly reach the convergent series because it is simple to determine the  $\Xi(v, w)$  component. We can acquire as  $\kappa \rightarrow \infty$ .

$$\Xi(v, w) = \lim_{\kappa \rightarrow \infty} \Xi_{\kappa}(v, w).$$

#### 4. NUMERICAL EXAMPLES

To comprehend the steps of the suggested approach, we apply the STDM to three problems in this section of the paper.

Example 3.1 Consider the  $v$ -space fractional-order HH-E.

$$\Im_v^\varsigma \Xi(v, w) + \frac{\partial^2}{\partial w^2} \Xi(v, w) - \Xi(v, w) = 0, 1 < \varsigma \leq 2, \quad (7)$$

with the I-Cs

$$\Xi(0, w) = w, \Xi_v(0, w) = 0. \quad (8)$$

Applying the Sh-T of Eq. (8), and making some calculations as a result, we get the following:

$$S[\Xi(v, w)] = \frac{\eta}{\mu} w - \left(\frac{\eta}{\mu}\right)^\varsigma S\left[\frac{\partial^2}{\partial w^2} \Xi(v, w)\right] + \left(\frac{\eta}{\mu}\right)^\varsigma S[\Xi(v, w)], \quad (9)$$

Taking the inverse Sh-T on Eq. (9), we have

$$\begin{aligned} \Xi(v, w) &= S^{-1}\left[\frac{\eta}{\mu} w\right] - S^{-1}\left[\left(\frac{\eta}{\mu}\right)^\varsigma S\left[\frac{\partial^2}{\partial w^2} \Xi(v, w)\right]\right] + \\ &S^{-1}\left[\left(\frac{\eta}{\mu}\right)^\varsigma S[\Xi(v, w)]\right]. \end{aligned} \quad (10)$$

Implementing ADM in Eq. (10), therefore, supposes that the solution of Eq. (7) can be expressed as follows:

$$\Xi(v, w) = \sum_{\kappa=0}^{\infty} \Xi_{\kappa}(v, w). \quad (11)$$

Using Eq. (11) in Eq. (10).

$$\begin{aligned} \sum_{\kappa=0}^{\infty} \Xi_{\kappa}(v, w) &= S^{-1}\left[\frac{\eta}{\mu} w\right] - \\ &S^{-1}\left[\left(\frac{\eta}{\mu}\right)^\varsigma S\left[\frac{\partial^2}{\partial w^2} \sum_{\kappa=0}^{\infty} \Xi_{\kappa}(v, w)\right]\right] + \\ &S^{-1}\left[\left(\frac{\eta}{\mu}\right)^\varsigma S\left[\sum_{\kappa=0}^{\infty} \Xi_{\kappa}(v, w)\right]\right]. \end{aligned}$$

We obtain the following terms for the series solution by using the method described in the preceding section:

$$\Xi_0(v, w) = S^{-1}\left[\frac{\eta}{\mu} w\right],$$

$$\Xi_0(v, w) = w.$$

$$\Xi_1(v, w) = w \frac{v^\varsigma}{\Gamma(\varsigma+1)}.$$

$$\Xi_2(v, w) = w \frac{v^{2\varsigma}}{\Gamma(2\varsigma+1)}.$$

$$\Xi_3(v, w) = w \frac{v^{3\varsigma}}{\Gamma(3\varsigma+1)}.$$

$$\Xi_4(v, w) = w \frac{v^{4\varsigma}}{\Gamma(4\varsigma+1)}.$$

$$\Xi_5(v, w) = w \frac{v^{5\varsigma}}{\Gamma(5\varsigma+1)}.$$

The series forms a solution to the given problem, and we have

$$\begin{aligned} \Xi(v, w) &= w + w \frac{v^\varsigma}{\Gamma(\varsigma+1)} + w \frac{v^{2\varsigma}}{\Gamma(2\varsigma+1)} + w \frac{v^{3\varsigma}}{\Gamma(3\varsigma+1)} + \\ &w \frac{v^{4\varsigma}}{\Gamma(4\varsigma+1)} + w \frac{v^{5\varsigma}}{\Gamma(5\varsigma+1)} + \dots. \end{aligned}$$

$$\begin{aligned} \Xi(v, w) &= w \left(1 + \frac{v^\varsigma}{\Gamma(\varsigma+1)} + \frac{v^{2\varsigma}}{\Gamma(2\varsigma+1)} + \frac{v^{3\varsigma}}{\Gamma(3\varsigma+1)} + \frac{v^{4\varsigma}}{\Gamma(4\varsigma+1)} + \right. \\ &\left. \frac{v^{5\varsigma}}{\Gamma(5\varsigma+1)} + \dots \right). \end{aligned}$$

$$\Xi(v, w) = w \sum_{\kappa=0}^{\infty} \frac{v^{\kappa\varsigma}}{\Gamma(\kappa\varsigma+1)}.$$

Using the M-L function, we may establish the Ex-S to Eq. (7) with respect to I-Cs.

$$\Xi(v, w) = w E_\varsigma(v^\varsigma),$$

such that, where  $E_\varsigma(v^\varsigma)$  is the M-L function. If  $\varsigma = 2$ , then

$$E_2(v^2) = \sum_{k=0}^{\infty} \frac{v^{2k}}{\Gamma(2k+1)} = \sum_{k=0}^{\infty} \frac{v^{2k}}{(2k)!} = \cosh v.$$

The Ex-S to Example 1 when  $\varsigma = 2$  is  $\Xi(v, w) = w \cosh v$ . Similarly, STDM can be used to derive the  $w$ -space solution as

$$\mathfrak{I}_{\omega}^{\varsigma} \mathcal{E}(\nu, \omega) + \frac{\partial^2}{\partial \nu^2} \mathcal{E}(\nu, \omega) - \mathcal{E}(\nu, \omega) = 0, 1 < \varsigma \leq 2, \quad (12)$$

with the I-Cs:

$$\mathcal{E}(\nu, 0) = \nu, \mathcal{E}_{\omega}(\nu, 0) = 0. \quad (13)$$

Thus, the series-form solution of Eq. (12) is obtained.

$$\mathcal{E}(\nu, \omega) = \nu \left( 1 + \frac{\omega^{\varsigma}}{\Gamma(\varsigma+1)} + \frac{\omega^{2\varsigma}}{\Gamma(2\varsigma+1)} + \frac{\omega^{3\varsigma}}{\Gamma(3\varsigma+1)} + \frac{\omega^{4\varsigma}}{\Gamma(4\varsigma+1)} + \frac{\omega^{5\varsigma}}{\Gamma(5\varsigma+1)} + \dots \right).$$

In the case when  $\varsigma = 2$ , then the solution through STDm is  $\mathfrak{E}(\nu, \omega) = \nu \cosh \omega$ .

Example 2. Consider the  $\nu$ -space fractional-order HH-E.

$$\mathfrak{I}_{\nu}^{\varsigma} \mathcal{E}(\nu, \omega) + \frac{\partial^2}{\partial \omega^2} \mathcal{E}(\nu, \omega) + 5\mathcal{E}(\nu, \omega, \lambda) = 0, \quad (14)$$

with the I-Cs

$$\mathcal{E}(0, \omega) = \omega, \mathcal{E}_{\nu}(0, \omega) = 0. \quad (15)$$

Applying the Sh-T of Eq. (14), and making some calculations as a result, we get the following:

$$S[\mathcal{E}(\nu, \omega)] = \frac{\eta}{\mu} \omega - \left( \frac{\eta}{\mu} \right)^{\varsigma} S \left[ \frac{\partial^2}{\partial \omega^2} \mathcal{E}(\nu, \omega) \right] - 5 \left( \frac{\eta}{\mu} \right)^{\varsigma} S[\mathcal{E}(\nu, \omega)], \quad (16)$$

Taking the inverse Sh-T on Eq. (16), we have

$$\mathcal{E}(\nu, \omega) = S^{-1} \left[ \frac{\eta}{\mu} \omega \right] - S^{-1} \left[ \left( \frac{\eta}{\mu} \right)^{\varsigma} S \left[ \frac{\partial^2}{\partial \omega^2} \mathcal{E}(\nu, \omega) \right] \right] - 5 S^{-1} \left[ \left( \frac{\eta}{\mu} \right)^{\varsigma} S[\mathcal{E}(\nu, \omega)] \right]. \quad (17)$$

Implementing ADM in Eq. (17), therefore, supposes that the solution of Eq. (14) can be represented in the following form:

$$\mathcal{E}(\nu, \omega) = \sum_{\kappa=0}^{\infty} \mathcal{E}_{\kappa}(\nu, \omega). \quad (18)$$

$$\begin{aligned} \sum_{\kappa=0}^{\infty} \mathcal{E}_{\kappa}(\nu, \omega) &= S^{-1} \left[ \frac{\eta}{\mu} \omega \right] - \\ S^{-1} \left[ \left( \frac{\eta}{\mu} \right)^{\varsigma} S \left[ \frac{\partial^2}{\partial \omega^2} \sum_{\kappa=0}^{\infty} \mathcal{E}_{\kappa}(\nu, \omega) \right] \right] - \\ 5 S^{-1} \left[ \left( \frac{\eta}{\mu} \right)^{\varsigma} S \left[ \sum_{\kappa=0}^{\infty} \mathcal{E}_{\kappa}(\nu, \omega) \right] \right]. \end{aligned}$$

By using the procedure as explained in the previous section, we get the following terms for the series solution:

$$\mathcal{E}_0(\nu, \omega) = S^{-1} \left[ \frac{\eta}{\mu} \omega \right],$$

$$\mathcal{E}_0(\nu, \omega) = \omega.$$

$$\mathcal{E}_1(\nu, \omega) = (-5) \omega \frac{\omega^{\varsigma}}{\Gamma(\varsigma+1)}.$$

$$\mathcal{E}_2(\nu, \omega) = (-5)^2 \omega \frac{\omega^{2\varsigma}}{\Gamma(2\varsigma+1)}.$$

$$\mathcal{E}_3(\nu, \omega) = (-5)^3 \omega \frac{\omega^{3\varsigma}}{\Gamma(3\varsigma+1)}.$$

$$\mathcal{E}_4(\nu, \omega) = (-5)^4 \omega \frac{\omega^{4\varsigma}}{\Gamma(4\varsigma+1)}.$$

$$\mathcal{E}_5(\nu, \omega) = (-5)^5 (\omega + \lambda) \frac{\omega^{5\varsigma}}{\Gamma(5\varsigma+1)}.$$

The series forms a solution to the given problem, and we have

$$\begin{aligned} \mathcal{E}(\nu, \omega) &= \omega + (-5) \omega \frac{\omega^{\varsigma}}{\Gamma(\varsigma+1)} + (-5)^2 \omega \frac{\omega^{2\varsigma}}{\Gamma(2\varsigma+1)} + \\ &(-5)^3 \omega \frac{\omega^{3\varsigma}}{\Gamma(3\varsigma+1)} + (-5)^4 \omega \frac{\omega^{4\varsigma}}{\Gamma(4\varsigma+1)} + (-5)^5 \omega \frac{\omega^{5\varsigma}}{\Gamma(5\varsigma+1)} + \dots \\ \mathcal{E}(\nu, \omega) &= \omega \left( 1 + \frac{(-5\omega^{\varsigma})}{\Gamma(\varsigma+1)} + \frac{(-5\omega^{\varsigma})^2}{\Gamma(2\varsigma+1)} + \frac{(-5\omega^{\varsigma})^3}{\Gamma(3\varsigma+1)} + \frac{(-5\omega^{\varsigma})^4}{\Gamma(4\varsigma+1)} + \right. \\ &\left. \frac{(-5\omega^{\varsigma})^5}{\Gamma(5\varsigma+1)} + \dots \right). \end{aligned}$$

We can determine the Ex-S to Eq. (14) with respect to I-Cs by using the ML-F

$$\mathcal{E}(\nu, \omega) = \omega E_{\varsigma}(-5\omega^{\varsigma}).$$

If  $\varsigma = 2$ , then

$$\begin{aligned} E_2(-5\omega^2) &= \sum_{k=0}^{\infty} \frac{(-5\omega^2)^k}{\Gamma(2k+1)} = \sum_{k=0}^{\infty} \frac{(-1)^k (\sqrt{5}\omega)^{2k}}{\Gamma(2k+1)} = \\ \sum_{k=0}^{\infty} \frac{(-1)^k (\sqrt{5}\omega)^{2k}}{(2k)!} &= \cosh \sqrt{5} \omega. \end{aligned}$$

The Ex-S to Example 2 when  $\varsigma = 2$  is  $\mathfrak{E}(\nu, \omega) = \omega \cosh \sqrt{5} \omega$ . Similarly, STDm can be used to derive the  $\omega$ -space solution as

$$\mathfrak{I}_{\omega}^{\varsigma} \mathcal{E}(\nu, \omega) + \frac{\partial^2}{\partial \nu^2} \mathcal{E}(\nu, \omega) + 5\mathcal{E}(\nu, \omega, \lambda) = 0, \quad (19)$$

with the I-Cs

$$\mathcal{E}(\nu, 0) = \nu, \mathcal{E}_{\omega}(\nu, 0) = 0. \quad (20)$$

Thus, the series-form solution of Eq. (19) is obtained.

$$\mathcal{E}(\nu, \omega) = \nu \left( 1 + \frac{(-5\omega^{\varsigma})}{\Gamma(\varsigma+1)} + \frac{(-5\omega^{\varsigma})^2}{\Gamma(2\varsigma+1)} + \frac{(-5\omega^{\varsigma})^3}{\Gamma(3\varsigma+1)} + \frac{(-5\omega^{\varsigma})^4}{\Gamma(4\varsigma+1)} + \frac{(-5\omega^{\varsigma})^5}{\Gamma(5\varsigma+1)} + \dots \right).$$

In the case when  $\varsigma = 2$ , then the solution through STDm is  $\mathfrak{E}(\nu, \omega) = \nu \cosh \sqrt{5} \omega$ .

Example 3. Consider the  $\nu$ -space fractional-order HH-E.

$$\mathfrak{I}_{\nu}^{\varsigma} \mathcal{E}(\nu, \omega) + \frac{\partial^2}{\partial \omega^2} \mathcal{E}(\nu, \omega) - 2\mathcal{E}(\nu, \omega, \lambda) = (12\nu^2 - 3\nu^4) \sin \omega, 1 < \varsigma \leq 2, 0 < \omega \leq 2\pi, \quad (21)$$

with the I-Cs

$$\mathcal{E}(0, \omega) = 0, \mathcal{E}_{\nu}(0, \omega) = 0. \quad (22)$$

Applying the Sh-T to Eq. (21), we use the differentiation property of the Sh-T, and after some calculation, as a result, we get as follows:

$$\begin{aligned} S[\mathcal{E}(\nu, \omega)] &= - \left( \frac{\eta}{\mu} \right)^{\varsigma} S \left[ \frac{\partial^2}{\partial \omega^2} \mathcal{E}(\nu, \omega) \right] + 2 \left( \frac{\eta}{\mu} \right)^{\varsigma} S[\mathcal{E}(\nu, \omega)] + \\ \left( \frac{\eta}{\mu} \right)^{\varsigma} \left( 12 \times 2! \left( \frac{\mu}{\eta} \right)^3 - 3 \times 4! \left( \frac{\mu}{\eta} \right)^4 \right) \sin \omega. \end{aligned} \quad (23)$$

Taking the inverse Sh-T on Eq. (23), we have

$$\begin{aligned} \mathcal{E}(\nu, \omega) &= S^{-1} \left[ - \left( \frac{\eta}{\mu} \right)^{\varsigma} S \left[ \frac{\partial^2}{\partial \omega^2} \mathcal{E}(\nu, \omega) \right] \right. \\ &\quad \left. + S^{-1} \left[ 2 \left( \frac{\eta}{\mu} \right)^{\varsigma} S[\mathcal{E}(\nu, \omega)] \right] \right. \\ &\quad \left. + S^{-1} \left[ \left( \frac{\eta}{\mu} \right)^{\varsigma} \left( 12 \times 2! \left( \frac{\mu}{\eta} \right)^3 - 3 \times 4! \left( \frac{\mu}{\eta} \right)^4 \right) \sin \omega \right] \right]. \end{aligned} \quad (24)$$

Implementing ADM in Eq. (24), therefore, supposes that the solution of Eq. (21) can be represented in the following form:

$$\mathcal{E}(\nu, \omega) = \sum_{\kappa=0}^{\infty} \mathcal{E}_{\kappa}(\nu, \omega). \quad (25)$$

$$\begin{aligned} \sum_{\kappa=0}^{\infty} \mathcal{E}_{\kappa}(\nu, \omega) &= S^{-1} \left[ - \left( \frac{\eta}{\mu} \right)^{\varsigma} S \left[ \frac{\partial^2}{\partial \omega^2} \sum_{\kappa=0}^{\infty} \mathcal{E}_{\kappa}(\nu, \omega) \right] \right] \\ &+ S^{-1} \left[ 2 \left( \frac{\eta}{\mu} \right)^{\varsigma} S \left[ \sum_{\kappa=0}^{\infty} \mathcal{E}_{\kappa}(\nu, \omega) \right] \right] + \\ &S^{-1} \left[ \left( \frac{\eta}{\mu} \right)^{\varsigma} (12 \times 2! \left( \frac{\mu}{\eta} \right)^3 - 3 \times 4! \left( \frac{\mu}{\eta} \right)^4) \sin \omega \right]. \end{aligned} \quad (26)$$

By using the procedure as explained in the previous section, we get the following terms for the series solution:

$$\mathcal{E}_0(\nu, \omega) = S^{-1} \left[ \left( \frac{\eta}{\mu} \right)^{\varsigma} (12 \times 2! \left( \frac{\mu}{\eta} \right)^3 - 3 \times 4! \left( \frac{\mu}{\eta} \right)^4) \sin \omega \right],$$

$$\mathcal{E}_0(\nu, \omega) = (12\nu^2 - 3\nu^4) \sin \omega.$$

$$\mathcal{E}_1(\nu, \omega) = S^{-1} \left[ - \left( \frac{\eta}{\mu} \right)^{\varsigma} S \left[ \frac{\partial^2}{\partial \omega^2} \mathcal{E}_0(\nu, \omega) \right] \right] +$$

$$S^{-1} \left[ 2 \left( \frac{\eta}{\mu} \right)^{\varsigma} S \left[ \mathcal{E}_0(\nu, \omega) \right] \right],$$

$$\mathcal{E}_1(\nu, \omega) = \left( 72 \frac{\nu^{\varsigma+2}}{\Gamma(\varsigma+2)} - \frac{216\nu^{\varsigma+4}}{\Gamma(\varsigma+4)} \right) \sin \omega.$$

$$\mathcal{E}_2(\nu, \omega) = S^{-1} \left[ - \left( \frac{\eta}{\mu} \right)^{\varsigma} S \left[ \frac{\partial^2}{\partial \omega^2} \mathcal{E}_1(\nu, \omega) \right] \right] +$$

$$S^{-1} \left[ 2 \left( \frac{\eta}{\mu} \right)^{\varsigma} S \left[ \mathcal{E}_1(\nu, \omega) \right] \right].$$

$$\mathcal{E}_2(\nu, \omega) = \left( \frac{216\nu^{2\varsigma+2}}{\Gamma(2\varsigma+2)} - \frac{648\nu^{2\varsigma+4}}{\Gamma(2\varsigma+4)} \right) \sin \omega.$$

$$\mathcal{E}_3(\nu, \omega) = \left( \frac{648\nu^{3\varsigma+2}}{\Gamma(3\varsigma+2)} - \frac{1944\nu^{3\varsigma+4}}{\Gamma(3\varsigma+4)} \right) \sin \omega.$$

$$\mathcal{E}_4(\nu, \omega) = \left( \frac{1944\nu^{4\varsigma+2}}{\Gamma(4\varsigma+2)} - \frac{5842\nu^{4\varsigma+4}}{\Gamma(4\varsigma+4)} \right) \sin \omega.$$

$$\mathcal{E}_5(\nu, \omega) = \left( \frac{5832\nu^{5\varsigma+2}}{\Gamma(4\varsigma+2)} - \frac{17496\nu^{5\varsigma+4}}{\Gamma(4\varsigma+4)} \right) \sin \omega.$$

The series forms a solution to the given problem, and we have

$$\begin{aligned} \mathcal{E}(\nu, \omega) &= (12\nu^2 - 3\nu^4) \sin \omega + \left( \frac{216\nu^{2\varsigma+2}}{\Gamma(2\varsigma+2)} - \frac{648\nu^{2\varsigma+4}}{\Gamma(2\varsigma+4)} \right) \sin \omega + \\ &\left( \frac{648\nu^{3\varsigma+2}}{\Gamma(3\varsigma+2)} - \frac{1944\nu^{3\varsigma+4}}{\Gamma(3\varsigma+4)} \right) \sin \omega + \\ &\left( \frac{1944\nu^{4\varsigma+2}}{\Gamma(4\varsigma+2)} - \frac{5842\nu^{4\varsigma+4}}{\Gamma(4\varsigma+4)} \right) \sin \omega + \left( \frac{5832\nu^{5\varsigma+2}}{\Gamma(4\varsigma+2)} - \frac{17496\nu^{5\varsigma+4}}{\Gamma(4\varsigma+4)} \right) \sin \omega \dots \end{aligned}$$

The Ex-S to Example 3 when  $\varsigma = 2$  is  $\Xi(\nu, \omega) = 9\nu^4 \sin \omega + 12\nu^2 \sin \omega$ . Similarly, STDm can be used to derive the  $\omega$ -space solution as

$$\begin{aligned} \mathfrak{S}_{\omega}^{\varsigma} \mathcal{E}(\nu, \omega) + \frac{\partial^2}{\partial \nu^2} \mathcal{E}(\nu, \omega) - 2\mathcal{E}(\nu, \omega, \lambda) \\ = (12\omega^2 - 3\omega^4) \sin \nu, 1 < \varsigma \leq 2, 0 < \nu \leq 2\pi, \end{aligned}$$

with the I-Cs

$$\mathcal{E}(\nu, 0) = 0, \mathcal{E}_{\omega}(\nu, 0) = 0.$$

Thus, the series-form solution of  $\omega$ -space problem is obtained.

$$\begin{aligned} \mathcal{E}(\nu, \omega) &= (12\omega^2 - 3\omega^4) \sin \nu + \left( \frac{216\omega^{2\varsigma+2}}{\Gamma(2\varsigma+2)} - \frac{648\omega^{2\varsigma+4}}{\Gamma(2\varsigma+4)} \right) \sin \nu + \\ &\left( \frac{648\omega^{3\varsigma+2}}{\Gamma(3\varsigma+2)} - \frac{1944\omega^{3\varsigma+4}}{\Gamma(3\varsigma+4)} \right) \sin \nu + \\ &\left( \frac{1944\omega^{4\varsigma+2}}{\Gamma(4\varsigma+2)} - \frac{5842\omega^{4\varsigma+4}}{\Gamma(4\varsigma+4)} \right) \sin \nu + \left( \frac{5832\omega^{5\varsigma+2}}{\Gamma(4\varsigma+2)} - \frac{17496\omega^{5\varsigma+4}}{\Gamma(4\varsigma+4)} \right) \sin \nu \dots \end{aligned}$$

In the case when  $\varsigma = 2$ , then the solution through STDm is  $(\nu, \omega) = 9\omega^4 \sin \nu + 12\omega^2 \sin \nu$ .

## 5. GRAPHICAL AND NUMERICAL RESULTS WITH DISCUSSION

In this section, we assess the numerical and graphic outcomes of the App-S and Ex-S to the models discussed in Examples 1, 2, and 3. The precision and efficiency of the approximate approach can be assessed using error functions. An approximate analytical solution is provided by STDm in terms of an infinite fractional power series, and the approximate solution's errors must be specified. Rec-Er, Abs-Er, and Rel-Er functions are the functions that we use to illustrate the precision and efficiency of STDm.

The Abs-Er, Rel-Er, and Rec-Er are defined as follows:

$$\mathcal{E}(\nu, \omega) \approx \Xi^{\kappa}(\nu, \omega), \kappa = 1, 2, 3, \dots$$

where,  $\Xi^{\kappa}(\nu, \omega)$  and  $\Xi(\nu, \omega)$  are the  $\kappa$ th-step App-S and Ex-S respectively.

The Abs-Er for the  $\kappa$ th-step App-S is calculated as

$$\text{Abs. Er}^{\kappa} = |\mathcal{E}(\nu, \omega) - \Xi^{\kappa}(\nu, \omega)|.$$

The Rel-Er for the  $\kappa$ th-step App-S is calculated as

$$\text{Rel. Er}^{\kappa} = \frac{|\mathcal{E}(\nu, \omega) - \Xi^{\kappa}(\nu, \omega)|}{|\mathcal{E}(\nu, \omega)|}.$$

The Rec-Er for the  $\kappa$ th-step App-S is calculated as

$$\text{Rec. Error}^{\kappa} = |\Xi^{\kappa+1}(\nu, \omega) - \Xi^{\kappa}(\nu, \omega)|.$$

The two-dimensional graphs of the App-S acquired from five iterations and the Ex-S derived by STDm for  $\varsigma = 1.6, 1.7, 1.8, 1.9$  and  $2$  are shown in Figures 1 of Examples 1–3. These graphs show how, when  $\zeta \rightarrow 2$  occurs, the App-S converges to the Ex-S. The App-S interaction with the Ex-S when  $\zeta = 2$  occurs demonstrates the accuracy of the proposed approach.

The Abs-E and Rel-E in the interval  $\nu \in [0, 1]$  between the Ex-S and fifth-order App-S derived by STDm in Problems 1–3 at  $\varsigma = 2$  are shown in graphs 2 and 3 respectively. The graphs demonstrate that the App-S and Ex-S are almost in agreement, which attests to the STDm's efficiency.

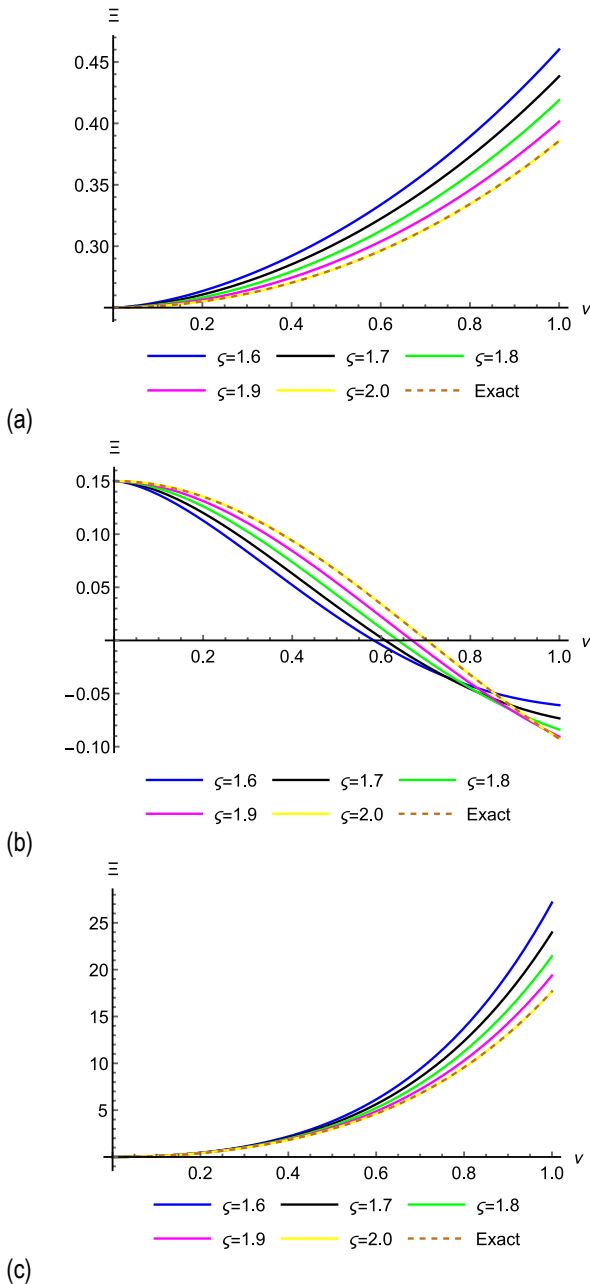
Tables 1–3 display Abs-Er at reasonable nominated grid points in the interval  $\nu \in [0, 1]$  amongst the 5th-step App-S and Ex-S attained using STDm of Examples 1, 2, and 3 at  $\varsigma = 1.6, 1.7, 1.8, 1.9$  and  $2$ . From Tables 1–3, we observe that the Abs-Er for test examples for all FOD is very small. If we increase the order of the FOD of the 5th-step App-S, the Abs-Er further decreases.

The convergence of the App-S to the Ex-S for Examples 1, 2, and 3 is shown numerically with the help of Rec-Er at reasonable nominated grid points in the interval  $\nu \in [0, 1]$ , as shown in Tables 4–9. We see from Tables 4–9 that, on increasing the order of the FOD, the 5th-step App-S obtained by the proposed approach

converges rapidly to the Ex-S. We can see from Tables 4–6 that there is a very minor Abs-Er for all of the test problems for 4th-step App-S. We see from Tables 7–9 that, considering the 5th-step App-S results in an even smaller Rec-Er, since our suggested approach is accurate, as seen by this process of Rec-Er, the App-S is rapidly approaching the Ex-S. Thus, we deduce that the suggested approach is a useful and efficient approach for solving FODE with a reduced number of computations and iteration steps.

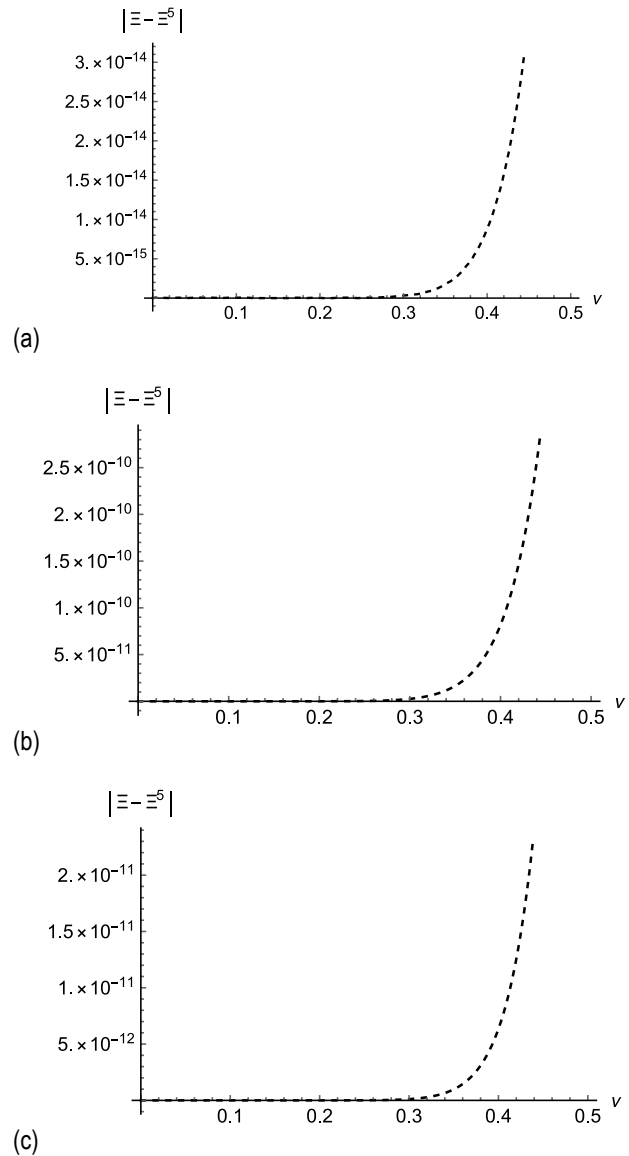
The graphs and tables show that the App-S and Ex-S agree, confirming the effectiveness of the recommended approach. Therefore, based on Figures 1-3 and Tables 1–9, we deduce that STDM provides us with a solution in a fractional power series that has a small error.

The following are the 2D graphs showing the  $\Xi(v, \varpi)$  and  $\Xi^5(v, \varpi)$  at  $\varsigma = 1.6, 1.7, 1.8, 1.9$  and 2 in the interval  $v \in [0, 1]$  for Examples 1, 2, and 3.



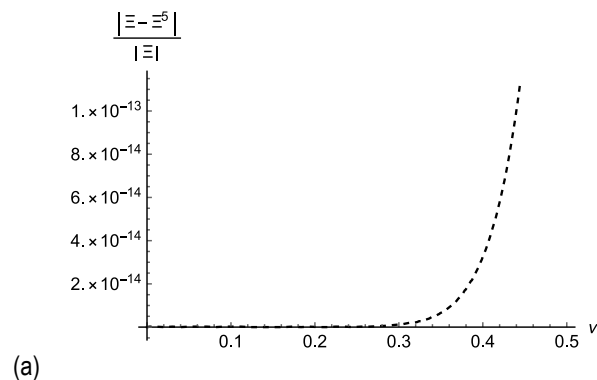
**Fig. 1.** The 5th-step App-S and Ex-S at  $\varsigma = 1.6, 1.7, 1.8, 1.9$ , and 2 for Example 1, 2 and 3. (a): Example 1 when  $\varpi = 0.25$ , (b): Example 2 when  $\varpi = 0.15$ , (c): Example 3  $\varpi = 1$ .

The following are the 2D graphs showing the Abs-Er of  $\Xi(v, \varpi)$  and  $\Xi^5(v, \varpi)$  at  $\varsigma = 2$  in the interval  $v \in [0, 1]$  for Examples 1, 2, and 3.



**Fig. 2:** The Abs-Er of Examples 1, 2, and 3. (a): Example 1 when  $\varpi = 0.25$ , (b): Example 2 when  $\varpi = 0.15$ , (c): Example 3  $\varpi = 1$ .

The following are the 2D graphs showing the Rel-Er of  $\Xi(v, \varpi)$  and  $\Xi^5(v, \varpi)$  at  $\varsigma = 2$  in the interval  $v \in [0, 1]$  for Examples 1, 2, and 3.





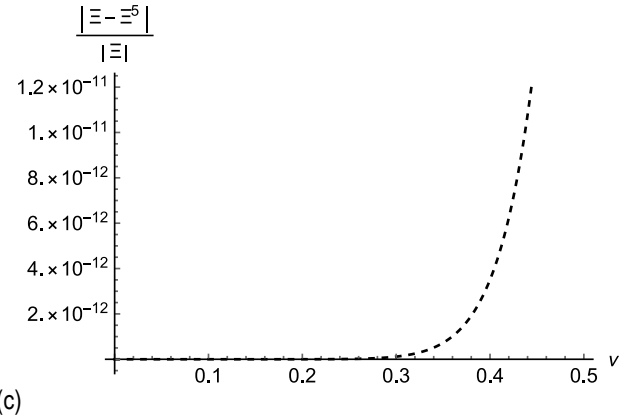
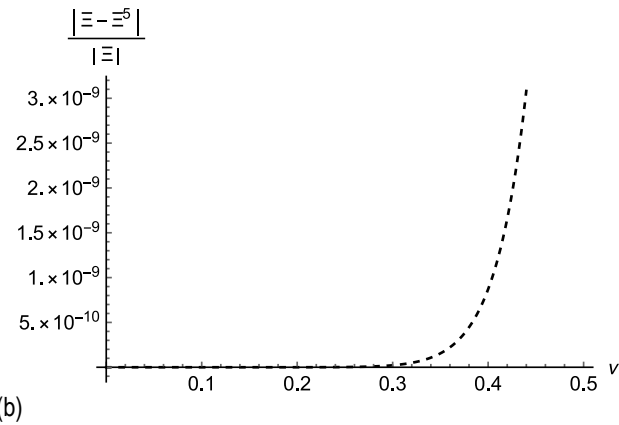


Fig. 3. The Rel-Er of Examples 1, 2, and 3. (a): Example 1 when  $\omega = 0.25$ , (b): Example 2 when  $\omega = 0.15$ , (c): Example 3  $\omega = 1$

Tab. 1. The Abs-Er for  $\Xi^5(\nu, \omega)$  when  $\omega = 0.25$  in Example 1 for  $\zeta = 1.7, 1.8, 1.9$  and  $2.0$

$\nu$	$\zeta = 1.7$	$\zeta = 1.8$	$\zeta = 1.9$	$\zeta = 2.0$
0.1	0.00198	0.00111	0.00047	0
0.2	0.00557	0.00327	0.00144	0
0.3	0.00998	0.00598	0.00269	$2.775 \times 10^{-16}$
0.4	0.01493	0.00908	0.00415	$8.715 \times 10^{-15}$
0.5	0.02029	0.01248	0.00576	$1.275 \times 10^{-13}$
0.6	0.02602	0.01612	0.00751	$1.138 \times 10^{-12}$
0.7	0.03209	0.020007	0.00937	$7.243 \times 10^{-12}$
0.8	0.03852	0.02411	0.01135	$3.599 \times 10^{-11}$
0.9	0.04533	0.02847	0.01344	$1.480 \times 10^{-10}$
1.0	0.05257	0.03310	0.01567	$5.247 \times 10^{-10}$

Tab. 2. The Abs-Er for  $\Xi^5(\nu, \omega)$  when  $\omega = 0.15$  in Example 2 for  $\zeta = 1.7, 1.8, 1.9$  and  $2.0$

$\nu$	$\zeta = 1.7$	$\zeta = 1.8$	$\zeta = 1.9$	$\zeta = 2.0$
0.1	0.00580	0.00328	0.00139	0
0.2	0.01520	0.00909	0.00407	$2.00117700 \times 10^{-14}$
0.3	0.02431	0.01516	0.00704	$2.59392507 \times 10^{-12}$
0.4	0.03092	0.02005	0.00964	$8.17310941 \times 10^{-11}$
0.5	0.03361	0.02273	0.01134	$1.1864156 \times 10^{-9}$
0.6	0.03158	0.02252	0.01175	$1.0546420 \times 10^{-8}$
0.7	0.02466	0.01909	0.01062	$6.6822825 \times 10^{-8}$
0.8	0.01324	0.01244	0.00788	$3.30409738 \times 10^{-7}$
0.9	0.00182	0.00295	0.00357	0.000001351
1.0	0.01922	0.00872	0.002042	0.0000047612

Tab. 3. The Abs-Er for  $\Xi^5(\nu, \omega)$  when  $\omega = 1$  in Example 3 for  $\zeta = 1.7, 1.8, 1.9$  and  $2.0$

$\nu$	$\zeta = 1.7$	$\zeta = 1.8$	$\zeta = 1.9$	$\zeta = 2.0$
0.1	$4.4 \times 10^{-3}$	$4.3 \times 10^{-3}$	$4.1 \times 10^{-4}$	0
0.2	$4.5 \times 10^{-3}$	$4.4 \times 10^{-3}$	$4.0 \times 10^{-4}$	0
0.3	$4.6 \times 10^{-3}$	$4.5 \times 10^{-3}$	$7.0 \times 10^{-4}$	$1.5 \times 10^{-17}$
0.4	$4.7 \times 10^{-3}$	$4.6 \times 10^{-3}$	$9.6 \times 10^{-4}$	$1.71 \times 10^{-16}$
0.5	$4.8 \times 10^{-3}$	$4.7 \times 10^{-3}$	$1.1 \times 10^{-4}$	$1.98 \times 10^{-15}$
0.6	$4.9 \times 10^{-3}$	$4.8 \times 10^{-3}$	$1.1 \times 10^{-4}$	$2.05 \times 10^{-14}$
0.7	$5.0 \times 10^{-3}$	$4.9 \times 10^{-3}$	$1.0 \times 10^{-4}$	$2.08 \times 10^{-13}$
0.8	$5.1 \times 10^{-3}$	$5.0 \times 10^{-3}$	$7.8 \times 10^{-4}$	$2.09 \times 10^{-11}$
0.9	$5.2 \times 10^{-3}$	$5.1 \times 10^{-3}$	$3.5 \times 10^{-4}$	$2.31 \times 10^{-11}$
1.0	$5.3 \times 10^{-3}$	$5.2 \times 10^{-3}$	$2.0 \times 10^{-4}$	$2.39 \times 10^{-11}$

Tab. 4. The Rec-Er for  $\Xi^4(\nu, \omega)$  when  $\omega = 0.25$  for  $\zeta = 1.7, 1.8, 1.9$  and  $2.0$  for Example 1

$\nu$	$\zeta = 1.7$	$\zeta = 1.8$	$\zeta = 1.9$	$\zeta = 2.0$
0.1	$1.17 \times 10^{-11}$	$2.0 \times 10^{-12}$	$3.6 \times 10^{-13}$	$6.2 \times 10^{-14}$
0.2	$1.3 \times 10^{-9}$	$3.0 \times 10^{-10}$	$7.0 \times 10^{-11}$	$1.5 \times 10^{-11}$
0.3	$2.0 \times 10^{-8}$	$5.6 \times 10^{-9}$	$1.5 \times 10^{-9}$	$4.0 \times 10^{-10}$
0.4	$1.4 \times 10^{-7}$	$4.5 \times 10^{-8}$	$1.3 \times 10^{-8}$	$4.0 \times 10^{-9}$
0.5	$3.0 \times 10^{-8}$	$2.2 \times 10^{-7}$	$7.4 \times 10^{-8}$	$2.4 \times 10^{-8}$
0.6	$6.4 \times 10^{-9}$	$8.3 \times 10^{-7}$	$2.9 \times 10^{-7}$	$1.0 \times 10^{-7}$
0.7	$6.5 \times 10^{-6}$	$2.5 \times 10^{-6}$	$9.6 \times 10^{-7}$	$3.5 \times 10^{-7}$
0.8	$1.6 \times 10^{-5}$	$6.6 \times 10^{-6}$	$2.6 \times 10^{-6}$	$1.0 \times 10^{-6}$
0.9	$3.6 \times 10^{-5}$	$1.5 \times 10^{-5}$	$6.4 \times 10^{-6}$	$2.6 \times 10^{-6}$
10	$7.4 \times 10^{-5}$	$3.3 \times 10^{-5}$	$1.4 \times 10^{-5}$	$6.2 \times 10^{-6}$

Tab. 5. The Rec-Er for  $\Xi^4(\nu, \omega)$  when  $\omega = 0.15$  for  $\zeta = 1.7, 1.8, 1.9$  and  $2.0$  for Example 2

$\nu$	$\zeta = 1.7$	$\zeta = 1.8$	$\zeta = 1.9$	$\zeta = 2.0$
0.1	$4.3 \times 10^{-9}$	$7.8 \times 10^{-10}$	$1.3 \times 10^{-10}$	$2.3 \times 10^{-11}$
0.2	$4.9 \times 10^{-7}$	$1.1 \times 10^{-7}$	$2.6 \times 10^{-8}$	$5.9 \times 10^{-9}$
0.3	$7.7 \times 10^{-6}$	$2.1 \times 10^{-6}$	$5.7 \times 10^{-7}$	$1.5 \times 10^{-7}$
0.4	$5.4 \times 10^{-5}$	$1.6 \times 10^{-5}$	$5.1 \times 10^{-6}$	$1.5 \times 10^{-6}$
0.5	$2.4 \times 10^{-4}$	$8.4 \times 10^{-5}$	$2.7 \times 10^{-6}$	$9.0 \times 10^{-6}$
0.6	$8.6 \times 10^{-4}$	$3.1 \times 10^{-4}$	$1.1 \times 10^{-4}$	$3.9 \times 10^{-5}$
0.7	$2.4 \times 10^{-3}$	$9.5 \times 10^{-4}$	$3.6 \times 10^{-4}$	$1.3 \times 10^{-4}$
0.8	$6.0 \times 10^{-3}$	$2.4 \times 10^{-3}$	$9.9 \times 10^{-4}$	$3.9 \times 10^{-4}$
0.9	$1.3 \times 10^{-2}$	$5.8 \times 10^{-3}$	$2.4 \times 10^{-3}$	$1.0 \times 10^{-3}$
10	$2.7 \times 10^{-2}$	$1.2 \times 10^{-2}$	$5.4 \times 10^{-3}$	$2.3 \times 10^{-3}$

Tab. 6. The Rec-Er for  $\Xi^4(\nu, \omega)$  when  $\omega = 1$  for  $\zeta = 1.7, 1.8, 1.9$  and  $2.0$  for Example 3

$\nu$	$\zeta = 1.7$	$\zeta = 1.8$	$\zeta = 1.9$	$\zeta = 2.0$
0.1	$9.8 \times 10^{-11}$	$1.6 \times 10^{-11}$	$2.7 \times 10^{-12}$	$4.5 \times 10^{-13}$
0.2	$4.3 \times 10^{-8}$	$9.7 \times 10^{-9}$	$2.1 \times 10^{-9}$	$4.6 \times 10^{-10}$
0.3	$1.5 \times 10^{-6}$	$4.0 \times 10^{-7}$	$1.0 \times 10^{-7}$	$2.6 \times 10^{-8}$
0.4	$1.9 \times 10^{-5}$	$5.7 \times 10^{-6}$	$1.6 \times 10^{-6}$	$4.7 \times 10^{-7}$
0.5	$1.3 \times 10^{-4}$	$4.4 \times 10^{-5}$	$1.4 \times 10^{-5}$	$4.3 \times 10^{-6}$
0.6	$6.8 \times 10^{-4}$	$2.3 \times 10^{-4}$	$8.0 \times 10^{-5}$	$2.6 \times 10^{-5}$
0.7	$2.6 \times 10^{-3}$	$9.7 \times 10^{-4}$	$3.5 \times 10^{-4}$	$1.2 \times 10^{-4}$
0.8	$8.5 \times 10^{-3}$	$3.3 \times 10^{-3}$	$1.2 \times 10^{-3}$	$4.7 \times 10^{-4}$
0.9	$2.3 \times 10^{-2}$	$9.7 \times 10^{-3}$	$3.9 \times 10^{-3}$	$1.5 \times 10^{-3}$
10	$5.9 \times 10^{-2}$	$2.5 \times 10^{-2}$	$1.0 \times 10^{-2}$	$9.0 \times 10^{-2}$

**Tab. 7.** The Rec-Er for  $\Xi^5(v, \omega)$  when  $\omega = 0.25$  for  $\varsigma = 1.7, 1.8, 1.9$  and  $2.0$  for Example 1

$\nu$	$\varsigma = 1.7$	$\varsigma = 1.8$	$\varsigma = 1.9$	$\varsigma = 2.0$
0.1	$6.6 \times 10^{-15}$	$6.8 \times 10^{-16}$	$6.9 \times 10^{-17}$	$6.8 \times 10^{-18}$
0.2	$2.3 \times 10^{-12}$	$3.5 \times 10^{-13}$	$5.0 \times 10^{-14}$	$7.0 \times 10^{-15}$
0.3	$7.5 \times 10^{-11}$	$1.3 \times 10^{-11}$	$2.3 \times 10^{-12}$	$4.0 \times 10^{-13}$
0.4	$8.6 \times 10^{-10}$	$1.8 \times 10^{-10}$	$3.6 \times 10^{-11}$	$7.2 \times 10^{-12}$
0.5	$5.7 \times 10^{-9}$	$1.3 \times 10^{-9}$	$3.0 \times 10^{-10}$	$6.7 \times 10^{-11}$
0.6	$2.7 \times 10^{-8}$	$6.9 \times 10^{-9}$	$1.7 \times 10^{-9}$	$4.1 \times 10^{-10}$
0.7	$1.0 \times 10^{-7}$	$2.7 \times 10^{-8}$	$7.4 \times 10^{-9}$	$1.9 \times 10^{-9}$
0.8	$3.1 \times 10^{-7}$	$9.2 \times 10^{-8}$	$2.6 \times 10^{-8}$	$7.3 \times 10^{-9}$
0.9	$8.5 \times 10^{-7}$	$2.6 \times 10^{-7}$	$8.1 \times 10^{-8}$	$2.4 \times 10^{-8}$
10	$2.0 \times 10^{-6}$	$6.8 \times 10^{-7}$	$2.2 \times 10^{-7}$	$6.8 \times 10^{-8}$

**Tab. 8.** The Rec-Er for  $\Xi^5(v, \omega)$  when  $\omega = 0.15$  for  $\varsigma = 1.7, 1.8, 1.9$  and  $2.0$  for Example 2

$\nu$	$\varsigma = 1.7$	$\varsigma = 1.8$	$\varsigma = 1.9$	$\varsigma = 2.0$
0.1	$1.2 \times 10^{-11}$	$1.2 \times 10^{-12}$	$1.3 \times 10^{-13}$	$1.2 \times 10^{-14}$
0.2	$4.4 \times 10^{-9}$	$6.6 \times 10^{-10}$	$9.4 \times 10^{-11}$	$1.3 \times 10^{-11}$
0.3	$1.4 \times 10^{-7}$	$2.5 \times 10^{-8}$	$4.4 \times 10^{-9}$	$7.6 \times 10^{-10}$
0.4	$1.6 \times 10^{-6}$	$3.3 \times 10^{-7}$	$6.8 \times 10^{-8}$	$1.3 \times 10^{-8}$
0.5	$1.0 \times 10^{-5}$	$2.5 \times 10^{-6}$	$5.7 \times 10^{-7}$	$1.2 \times 10^{-7}$
0.6	$5.1 \times 10^{-5}$	$1.3 \times 10^{-5}$	$3.2 \times 10^{-7}$	$7.8 \times 10^{-7}$
0.7	$1.8 \times 10^{-4}$	$5.2 \times 10^{-5}$	$1.3 \times 10^{-5}$	$3.6 \times 10^{-6}$
0.8	$5.8 \times 10^{-4}$	$1.7 \times 10^{-4}$	$4.9 \times 10^{-5}$	$1.3 \times 10^{-5}$
0.9	$1.6 \times 10^{-3}$	$5.0 \times 10^{-4}$	$1.5 \times 10^{-4}$	$4.5 \times 10^{-5}$
10	$3.9 \times 10^{-3}$	$1.2 \times 10^{-3}$	$4.1 \times 10^{-4}$	$1.2 \times 10^{-4}$

**Tab. 9.** The Rec-Er for  $\Xi^5(v, \omega)$  when  $\omega = 1$  for  $\varsigma = 1.7, 1.8, 1.9$  and  $2.0$  for Example 3

$\nu$	$\varsigma = 1.7$	$\varsigma = 1.8$	$\varsigma = 1.9$	$\varsigma = 2.0$
0.1	$1.3 \times 10^{-13}$	$1.3 \times 10^{-14}$	$1.3 \times 10^{-15}$	$1.2 \times 10^{-16}$
0.2	$1.9 \times 10^{-10}$	$2.7 \times 10^{-11}$	$3.7 \times 10^{-12}$	$5.0 \times 10^{-13}$
0.3	$1.3 \times 10^{-8}$	$2.3 \times 10^{-9}$	$3.9 \times 10^{-10}$	$6.5 \times 10^{-11}$
0.4	$2.8 \times 10^{-7}$	$5. \times 10^{-8}$	$1.0 \times 10^{-8}$	$2.0 \times 10^{-9}$
0.5	$2.9 \times 10^{-6}$	$6.5 \times 10^{-7}$	$1.4 \times 10^{-7}$	$2.9 \times 10^{-8}$
0.6	$2.0 \times 10^{-5}$	$4.8 \times 10^{-6}$	$1.1 \times 10^{-6}$	$2. \times 10^{-7}$
0.7	$1.0 \times 10^{-4}$	$2.6 \times 10^{-5}$	$6.7 \times 10^{-6}$	$1.6 \times 10^{-6}$
0.8	$4.0 \times 10^{-4}$	$1.1 \times 10^{-4}$	$3.1 \times 10^{-5}$	$8.3 \times 10^{-6}$
0.9	$1.4 \times 10^{-3}$	$4.1 \times 10^{-4}$	$1.2 \times 10^{-4}$	$3.4 \times 10^{-5}$
10	$4.2 \times 10^{-3}$	$1.3 \times 10^{-3}$	$4.0 \times 10^{-4}$	$2.5 \times 10^{-5}$

## 6. CONCLUSION

In order to obtain both approximate and exact solutions for the Helmholtz problems in the sense of space CFD, a coupling approach has been employed in this study. An analysis in the form of absolute, relative, and recurrence errors by graphical and numerically means has been done to illustrate the correctness of our approach. For different values of fractional order derivatives, 2D graphs are also established that show the convergence of the approximate solution to the exact solution. These graphs show how, when  $\varsigma \rightarrow 2$  occurs, the approximate solution converges to the exact solution. The approximate interaction with the exact solution when  $\varsigma = 2$  occurs demonstrates the accuracy and efficacy of the proposed approach.

The STDM distinguishes itself from other approximate analytical methods with the following features: The advantage of this

method is that it does not call for any presumptions regarding significant or minor physical factors. Because of this, it circumvents some of the drawbacks of conventional perturbation techniques. In contrast to earlier analytic approximation methods, the STDM may generate expansion solutions for FODEs without the need for perturbation, linearization, or discretization. In light of the outcomes, we concluded that STDM is straightforward to use, precise, and effective. We intend to use the STDM in the future to solve diverse nonlinear fractional models that arise in engineering and biological systems.

## REFERENCES

- Djaouti AM, Khan ZA, Liaqat MI, Al-Quran A. A novel technique for solving the nonlinear fractional-order smoking model. *Fractal and Fractional*. 2024; 8(5):286. <https://doi.org/10.3390/fractalfract8050286>
- Liaqat MI, Etemad S, Rezapour S, Park C. A novel analytical Aboodh residual power series method for solving linear and nonlinear time-fractional partial differential equations with variable coefficients. *AIMS Mathematics*. 2022; 7(9):16917-16948. <https://doi.org/10.3934/math.2022929>
- Djaouti AM, Khan ZA, Liaqat MI, Al-Quran A. Existence uniqueness and averaging principle of fractional neutral stochastic differential equations in the  $L_p$  Space with the framework of the  $\Psi$ -Caputo derivative. *Mathematics*. 2024;12(7): 1-21. <https://doi.org/10.3390/math12071037>
- Owolabi KM, Hammouch Z. Spatiotemporal patterns in the Belousov-Zhabotinskii reaction systems with Atangana-Baleanu fractional order derivative. *Physica A: Statistical Mechanics and its Applications*. 2019; 523: 1072-1090. <https://doi.org/10.1016/j.physa.2019.04.017>
- Djaouti AM, Khan ZA, Liaqat MI, Al-Quran A. A Study of Some Generalized Results of Neutral Stochastic Differential Equations in the Framework of Caputo-Katugampola Fractional Derivatives. *Mathematics*. 2024;12(11): 1654. <https://doi.org/10.3390/math12111654>
- Tenreiro Machado JA. The bouncing ball and the Grünwald-Letnikov definition of fractional derivative. *Fractional Calculus and Applied Analysis*. 2021; 24(4): 1003-1014. <https://doi.org/10.1515/fca-2021-0043>
- Ahmad B, Ntouyas SK, Alsaedi A. Fractional order differential systems involving right Caputo and left Riemann-Liouville fractional derivatives with nonlocal coupled conditions. *Boundary value problems*. 2019(1): 1-12. <https://doi.org/10.1186/s13661-019-1222-0>
- Sene N. Analysis of a fractional-order chaotic system in the context of the Caputo fractional derivative via bifurcation and Lyapunov exponents. *Journal of King Saud University-Science*. 2021; 33(1): 101275. <https://doi.org/10.1016/j.jksus.2020.101275>
- Shah K, Alqudah MA, Jarad F, Abdeljawad T. Semi-analytical study of Pine Wilt Disease model with convex rate under Caputo-Febrizio fractional order derivative. *Chaos, Solitons&Fractals*. 2020;135: 109754. <https://doi.org/10.1016/j.chaos.2020.109754>
- Ghanbari B, Djilali S. Mathematical and numerical analysis of a three-species predator-prey model with herd behavior and time fractional-order derivative. *Mathematical Methods in the Applied sciences*. 2020; 43(4):1736-1752. <https://doi.org/10.1002/mma.5999>
- Liaqat MI, Akgül A, Prosviryakov EY. An efficient method for the analytical study of linear and nonlinear time-fractional partial differential equations with variable coefficients. *Journal of Samara State Technical University. Ser. Physical and Mathematical Sciences*. 2023; 27(2): 214-240. <https://doi.org/10.14498/vsgtu2009>
- Liaqat MI, Akgül A, De la Sen M, Bayram, M. Approximate and exact solutions in the sense of conformable derivatives of quantum mechanics models using a novel algorithm. *Symmetry*. 2023; 15(3): 744. <https://doi.org/10.3390/sym15030744>

13. Cheng X, Hou J, Wang L. Lie symmetry analysis, invariant subspace method and q-homotopy analysis method for solving fractional system of single-walled carbon nanotube. *Computational and Applied Mathematics*. 2021; 40:1-17.  
<https://doi.org/10.1007/s40314-021-01486-7>
14. Paliathanasis A, Bogadi RS, Govender M. Lie symmetry approach to the time-dependent Karmarkar condition. *The European Physical Journal C*. 2022; 82(11): 987. <https://doi.org/10.1140/epjc/s10052-022-10929-2>
15. Sahoo S, Ray SS, Abdou M.A. New exact solutions for time-fractional Kaup-Kupershmidt equation using improved (G'/G)-expansion and extended (G'/G)-expansion methods. *Alexandria Engineering Journal*. 2020; 59(5): 3105-3110.  
<https://doi.org/10.1016/j.cjph.2016.10.019>
16. Jena SK, Chakraverty S. Dynamic behavior of an electromagnetic nanobeam using the Haar wavelet method and the higher-order Haar wavelet method. *The European Physical Journal Plus*. 2019;134(10): 538.  
<https://doi.org/10.1140/epjp/i2019-12874-8>
17. Yi M, Huang J. Wavelet operational matrix method for solving fractional differential equations with variable coefficients. *Applied Mathematics and Computation*. 2014; 230: 383-394.  
<https://doi.org/10.1016/j.amc.2013.06.102>
18. Cinar M, Secer A, Ozisik M, Bayram M. Derivation of optical solitons of dimensionless Fokas-Lenells equation with perturbation term using Sardar sub-equation method. *Optical and Quantum Electronics*. 2022; 54(7): 402. <https://doi.org/10.1007/s11082-022-03819-0>
19. Atabakzadeh MH, Akrami MH, Erjaee GH. Chebyshev operational matrix method for solving multi-order fractional ordinary differential equations. *Applied Mathematical Modelling*. 2013; 37(20-21): 8903-8911. <https://doi.org/10.1016/j.apm.2013.04.019>
20. Liaqat MI, Akgül A, Bayram M. Series and closed form solution of Caputo time-fractional wave and heat problems with the variable coefficients by a novel approach. *Optical and Quantum Electronics*. 2024;56(2):203.  
<https://doi.org/10.1007/s11082-023-05751-3>
21. Naik PA, Zu J, Ghoreishi M. Estimating the approximate analytical solution of HIV viral dynamic model by using homotopy analysis method. *Chaos, Solitons & Fractals*. 2020;131:109500.  
<https://doi.org/10.1016/j.chaos.2019.109500> Get rights and content
22. Zeidan D, Chau CK, Lu TT, Zheng WQ. Mathematical studies of the solution of Burgers' equations by Adomian decomposition method. *Mathematical Methods in the Applied Sciences*. 2020; 43(5): 2171-2188. <https://doi.org/10.1002/mma.5982>
23. Samaniego E, Anitescu C, Goswami S, Nguyen-Thanh VM, Guo H, Hamdia K, Rabczuk T. An energy approach to the solution of partial differential equations in computational mechanics via machine learning: Concepts, implementation and applications. *Computer Methods in Applied Mechanics and Engineering*. 2020; 362:112790.  
<https://doi.org/10.1016/j.cma.2019.112790>
24. Majeed A, Kamran M, Iqbal MK, Baleanu D. Solving time fractional Burgers' and Fisher's equations using cubic B-spline approximation method. *Advances in Difference Equations*. 2020;(1):1-15.  
<https://doi.org/10.1186/s13662-020-02619-8>
25. Ganji RM, Jafari H, Baleanu D. A new approach for solving multi variable orders differential equations with Mittag-Leffler kernel. *Chaos, Solitons & Fractals*. 2020; 130:109405.  
<https://doi.org/10.1016/j.chaos.2019.109405>
26. Eriqat T, El-Ajou A, Moa'ath NO, Al-Zhour Z, Momani S. A new attractive analytic approach for solutions of linear and nonlinear neutral fractional pantograph equations. *Chaos, Solitons & Fractals*. 2020; 138: 109957. <https://doi.org/10.1016/j.chaos.2020.109957>
27. Yüzbaşı Ş. Numerical solutions of fractional Riccati type differential equations by means of the Bernstein polynomials. *Applied Mathematics and Computation*. 2013;219(11): 6328-6343.  
<https://doi.org/10.1016/j.amc.2012.12.006>
28. Liaqat MI, Akgül A, Abu-Zinadah H. Analytical investigation of some time-fractional Black-Scholes models by the Aboodh residual power series method. *Mathematics*. 2023;11(2): 276.  
<https://doi.org/10.3390/math11020276>
29. Jafarian A, Mokhtarpour M, Baleanu D. Artificial neural network approach for a class of fractional ordinary differential equation. *Neural Computing and Applications*. 2017; 28: 765-773.
30. Li HL, Jiang YL, Wang Z, Zhang L, Teng Z. Global Mittag-Leffler stability of coupled system of fractional-order differential equations on network. *Applied Mathematics and Computation*. 2015;270: 269-277.  
<https://doi.org/10.1016/j.amc.2015.08.043>
31. Qureshi S, Kumar P. Using Shehu integral transform to solve fractional order Caputo type initial value problems. *Journal of Applied Mathematics and Computational Mechanics*. 2019; 18(2):75-83.  
<https://doi.org/10.17512/jamcm.2019.2.07>
32. Jena SR, Sahu I. A novel approach for numerical treatment of traveling wave solution of ion acoustic waves as a fractional nonlinear evolution equation on Shehu transform environment. *Physica Scripta*. 2023; 98(8): 085231.  
<https://doi.org/10.1088/1402-4896/ace6de>
33. Shah R, Saad Alshehry A, Weera W. A semi-analytical method to investigate fractional-order gas dynamics equations by Shehu transform. *Symmetry*. 2022; 14(7): 1458.  
<https://doi.org/10.3390/sym14071458>

Authors are most thankful to the handling editor and reviewers for their constructive suggestions and queries which has greatly helped in improving the quality of the manuscript.

Adnan Khan:  <https://orcid.org/0000-0002-1490-8576>

Muhammad Imran Liaqat:  <https://orcid.org/0000-0002-5732-9689>

Asma Mushtaq:  <https://orcid.org/0009-0007-3822-114X>



This work is licensed under the Creative Commons BY-NC-ND 4.0 license.

## ENHANCED BROADBAND TRI-STABLE ENERGY HARVESTING SYSTEM BY ADAPTING POTENTIAL ENERGY – EXPERIMENTAL STUDY

Andrzej KOSZEWNIK\*, Bartłomiej AMBROŹKIEWICZ\*\*

\*Faculty of Mechanical Engineering, Białystok University of Technology,  
 Wiejska 45C Street, 15-351 Białystok, Poland

\*\*Faculty of Mathematics and Information Technology, Lublin University of Technology,  
 Nadbystrzycka 38 Street, 20-618 Lublin, Poland

[a.koszewnik@pb.edu.pl](mailto:a.koszewnik@pb.edu.pl), [b.ambrozkiwicz@pollub.pl](mailto:b.ambrozkiwicz@pollub.pl)

*received 3 November 2023, revised 11 March 2024, accepted 7 April 2024*

**Abstract:** This paper presents the process optimization of some key parameters, such as the size of the air gap and distance between fixed neodymium magnets to enhance the vibration-based energy harvesting effect in the tri-stable energy harvesting systems and the improved tri-stable energy harvesting system being the proposed solution under weak excitation. In order to do it, firstly the distributed parameters model of the magnetic coupling energy harvesting system, including macro fiber composites of the 8514 P2 with a homogenous material in the piezoelectric fiber layer and nonlinear magnetic force, was determined. The performed numerical analysis of the conventional and the improved tri-stable energy harvesting system indicated that introducing an additional magnet to the tri-stable system leads to the shallowing of the depth of a potential well by decreasing the air gap between magnets and consequently generating higher power output and improving the effectiveness of the proposed improved tri-stable energy harvesting system. Experiments carried out on the laboratory stand allowed us to verify the numerical results as well as determine the optimal parameters of the magnetic coupling system. Due to it, the effectiveness of the proposed system versus the conventional tri-stable energy harvesting system is most enhanced.

**Keywords:** macro-fiber composite, homogenized material, conventional TPEH, improved TPEH system, tailoring potential energy

### 1. INTRODUCTION

Low-power sensor systems and wireless networks typically rely on external energy sources, but batteries present challenges like short lifespan and bulkiness. To address this, researchers are increasingly focused on harvesting energy from the ambient environment, particularly from mechanical vibrations, to provide continuous power for low-power devices [1-4]. Piezoelectric cantilever harvesters offer advantages like simplicity, high energy density, and no startup power. However, they are sub-optimal under variable frequencies and wideband vibrations, generating maximum energy only at the resonance frequency [3-5]. In order to obtain a wide spectrum response and adapt the harvester to the vibration source, a nonlinear piezoelectric cantilever energy harvester with an external magnetic field has been investigated [6-8]. Exemplary research, where a bi-stable generator was conducted and described, is presented in the paper written by Cottone [9]. In this paper, the authors demonstrated that the bi-stable piezoelectric energy harvesting (BPEH) system can overcome the limitations of linear harvesters and provide much more energy. In other papers written by Stanton [10] and Ferrari [11], the authors proved that BPEH systems can generate high output voltage due to the broadband effect. In order to broaden the bandwidth of BPEHs, other authors proposed a magnetic coupled piezoelectric energy harvester by introducing a magnetic oscillator to enhance the output power at relatively low excitation [12]. Although these methods somewhat enhance the performance of the BPEH sys-

tem, the governing energy functions are intrinsically bi-stable, which limits further improvement of output performances. Currently, tri-stable energy harvesters have attracted researchers' interest [13]. The prototype of these considerations is discussed in a paper written by Zhou and his group, who proposed a tri-stable piezoelectric energy harvester (TPEH) with two rotatable external magnets [14]. Simulations and experiments were conducted at different harmonic excitation levels, which proved wider-range frequencies of energy output. Then, they used Genetic Algorithms to identify the parameters of the EH system and verified the TPEH system can achieve higher values of the output energy [15]. In another paper, Cao et al [16] analyzed the influence of the energy potential well depth on the energy harvesting performance and they indicated that a shallower potential well depth will enhance the effective frequency width under low-frequency excitations. Another paper by Kim et al. [17,18] explored a cantilever-based magnetically coupled TPEH system. The results obtained allowed us to claim the advantages of the TPEH in broadband vibration energy harvesting under low-level excitations. Similar results were presented in a paper [19] where the authors explored the influence of the fractional-order viscoelastic material on the energy harvesting performances of the TPEH system. Yet another examples are papers [20,21], where TPEH is used to harvest energy from random excitations [22], while in [23] nonlinear magnetic force model for the magnetic coupled EH system was theoretically presented and experiment-tally verified to enhance the harvesting effect.

The review suggests that TPEH systems hold an advantage over BPEH systems, particularly in achieving higher efficiency through excitation with large amplitude vibrations. To address the efficiency maintenance, an improved tri-stable energy harvesting system is proposed in this paper. Considering an additionally fixed magnet with a low magnetic moment in the proposed EH system with a micro-fiber composite (MFC) element, consisting of homogenized material in the active layer, in contrast to [24,25], allows adapting the potential energy shaper, especially under weak random excitations. This effect can be achieved by improving the electromechanical properties of this composite, which is a result of considering the multiphase construction of the MFC element (thin piezoelectric fibers mixed with a softer passive epoxy material) [3, 26, 27, 28, 29]. As a result, such considered structure and the proposed EH system connected with an innovative storing unit containing a reed switch or a synchronized switch, harvesting on inductor units allow faster and better powering of small electrical devices with a lower power demand [30]. Taking into account this fact and to show the novelty of this paper, related to using the MFC element with homogenized material in the active layer, the manuscript is organized as follows. The electromechanical model of the magnetic coupled energy harvesting system as well as a model of nonlinear magnetic force in the TPEH and improved tri-stable piezoelectric energy harvester (ITPEH) systems derived by using the magnetization current method are described in Section 2. In Section 3, the numerical simulations are derived to compare the performances of TPEH and ITPEH systems in the form of potential energy diagrams are presented. Next, in Section 4, experimental investigations of both systems carried out in the lab stand on various initial parameters are presented and the results obtained are discussed. In addition, the Poincare maps analysis of both systems in this section are performed. Section 5 concludes the main findings of this work.

## 2. THE TRI-STABLE AND IMPROVED TRI-STABLE PIEZOELECTRIC ENERGY HARVESTING SYSTEM MODELING

In Fig.1a, a conventional tri-stable piezoelectric energy harvesting system, composed of a piezoelectric cantilever beam is presented. Magnet A was located on the free end of this beam, and two fixed external magnets, B and C, located on the frame. Under ambient vibrations or random excitation, the beam oscillations lead to deformation of the piezo-composite and convert the mechanical energy into electrical energy via the piezoelectric effect.

The difference between the tri-stable (TPEH) and bi-stable (BPEH) piezoelectric energy harvesting systems is related to the number of fixed external magnets. Similarly, in the case of the improved TPEH system, where the additional magnet located on the base between external magnets, is also considered (see Fig.1b). In this configuration, the ITPEH system has three magnets separated by a distance of  $x_3$  (being one half of distance  $x_1$  related to a conventional TPEH system), which are repelled by magnet A at the free end of the beam located in a distance  $x_2$ . As a result, such modified configurations of the TPEH system lead to the increase of the potential energy in the middle well potential and, consequently, to improve the output performances of this system, which will be presented in the next Sections of this paper.

Taking into account the review of papers [17,18], as well as considering the case of the TPEH and ITPEH systems [24-33], the

governing equation of the electromechanical model of vibration energy harvesters is shown in Fig.2, and it can be written in the following form:

$$\begin{aligned} M_{eq}\ddot{x}(t) + C_{eq}\dot{x}(t) + K_{eq}x(t) + F_m(x) - \theta_0 v(t) &= F \cdot \cos(\omega t) \\ C_p \dot{v}(t) + \frac{v(t)}{R_L} + \theta_0 \dot{x}(t) &= 0 \end{aligned} \quad (1)$$

where:  $M_{eq}$  – the equivalent mass,  $C_{eq}$  – the equivalent damping,  $K_{eq}$  – the equivalent stiffness,  $C_p$  – the equivalent capacitance,  $R_L$  – the load resistance,  $\theta_0$  – the electromechanical coupling factor,  $v(t)$  – the voltage output across by the resistive load,  $F \cos(\omega t)$  – the equivalent external excitation force ( $F = \mu M_{eq} F_0$ ,  $\mu$  – the amplitude-wise correction factor while  $F_0$  – the amplitude of base acceleration excitation),  $F_m(x)$  – the nonlinear equivalent magnetic force,  $x(t)$  – transverse deflection of a cantilever beam.

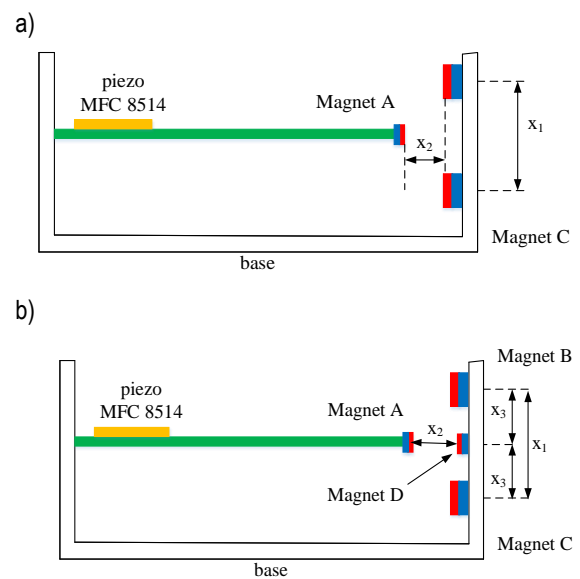


Fig.1 The scheme of a) conventional tri-stable piezoelectric energy harvesting (TPEH) system, b) improved tri-stable piezoelectric energy harvesting (ITPEH) system

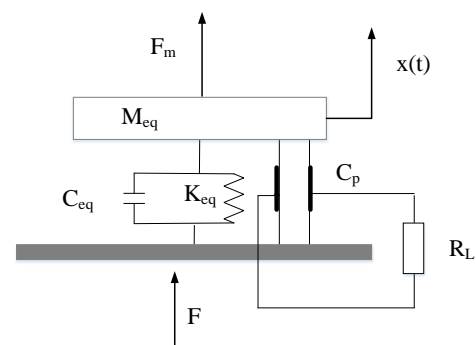


Fig. 2. The equivalent model of the coupled magnetic piezoelectric energy harvesting system

Then, considering also the approximated form of a magnetic force  $F_m(x)$  expressed in the form:

$$F_m(x) = \omega_0^2 x(t) + a_1 x(t)^3 + a_2 x(t)^5 + a_3 x(t)^7 \quad (2)$$

where  $\omega_0^2$ ,  $a_{10}$ ,  $a_{20}$ , and  $a_{30}$  are coefficients, which determines the electromechanical equation of both TPEH and IPTEH systems



rewritten in the following form:

$$\ddot{x}(t) + \frac{c}{M_{eq}} \dot{x}(t) + \frac{\omega_0^2}{M_{eq}} x(t) + \frac{a_{10}}{M_{eq}} x(t)^3 + \frac{a_{20}}{M_{eq}} x(t)^5 + \frac{a_{30}}{M_{eq}} x(t)^7 - \frac{\theta_0}{M_{eq}} v(t) = \mu F_0 \cdot \cos(\omega t)$$

$$\dot{v}(t) + \frac{v(t)}{C_p R_L} + \frac{\theta_0}{C_p} \dot{x}(t) = 0 \quad (3)$$

Moreover, introducing non-dimensional parameters listed below

$$c = \frac{c_{eq}}{M_{eq}}, \theta = \frac{\theta_0}{M_{eq}}, \omega^2 = \frac{\omega_0^2}{M_{eq}}, f = \frac{\mu F_0}{M_{eq}}, \lambda = \frac{1}{R_L C_p},$$

$$g = \frac{\theta_0}{C_p} a_1 = \frac{a_{10}}{M_{eq}}, a_2 = \frac{a_{20}}{M_{eq}}, a_3 = \frac{a_{30}}{M_{eq}}$$

The following non-dimensional governing electromechanical model can be expressed as:

$$\ddot{x}(t) + c\dot{x}(t) + \omega^2 x(t) + a_1 x(t)^3 + \dots + a_2 x(t)^5 + a_3 x(t)^7 - \theta v(t) = f \cdot \cos(\omega t)$$

$$\dot{v}(t) + \lambda v(t) + g\dot{x}(t) = 0 \quad (4)$$

### 3. POTENTIAL ENERGY AND MAGNETIC FORCE

The conducted analysis of the TPEH system and the performed simulations of the tri-stable energy harvesting system described in [1,8] indicated that one of the bigger difficulties is calculating the magnetic force  $F_m$  which is closely related to the system design and performances of the magnetic coupling energy harvesting systems. Considering the findings [8], it is known that

$$H_{yb}(x, y, z) = \frac{M_B}{4\pi} \left( \tan^{-1} \left( \frac{x_{B,O1} z_{B,O1}}{y \sqrt{x_{B,O1}^2 + z_{B,O1}^2 + y^2}} \right) + \tan^{-1} \left( \frac{x_{B,O2} z_{B,O2}}{y \sqrt{x_{B,O2}^2 + z_{B,O2}^2 + y^2}} \right) \right. \\ \left. - \tan^{-1} \left( \frac{x_{B,O2} z_{B,O1}}{y \sqrt{x_{B,O2}^2 + z_{B,O1}^2 + y^2}} \right) + \tan^{-1} \left( \frac{x_{B,O1} z_{B,O2}}{y \sqrt{x_{B,O1}^2 + z_{B,O2}^2 + y^2}} \right) \right)$$

In addition, setting the center of magnets located on the frame as well as considering proper space coordinates of points O1 and O2 for particular magnets B, C and D are:

$$\left( x + \frac{h_A}{2} \cdot \cos \varphi - \frac{x_1}{2}, x_2 - \frac{h_A}{2} \cdot \sin \varphi, 0 \right),$$

$$\left( x - \frac{h_A}{2} \cdot \cos \varphi - \frac{x_1}{2}, x_2 - \frac{h_A}{2} \cdot \sin \varphi, 0 \right): \text{magnet B,}$$

$$\left( x + \frac{h_A}{2} \cdot \cos \varphi + \frac{x_1}{2}, x_2 - \frac{h_A}{2} \cdot \sin \varphi, 0 \right),$$

$$\left( x - \frac{h_A}{2} \cdot \cos \varphi + \frac{x_1}{2}, x_2 - \frac{h_A}{2} \cdot \sin \varphi, 0 \right): \text{magnet C,}$$

$$\left( x + \frac{h_A}{2}, x_2 - \frac{h_A}{2}, 0 \right), \left( x - \frac{h_A}{2}, x_2 - \frac{h_A}{2}, 0 \right): \text{magnet D}$$

can express the magnetic force given by Eq.(5a) for TPEH system and Eq.(5b) for ITPEH system in rewritten transformed form as:

$$F_m = \mu_0 M_A S \left\{ \begin{array}{l} H_{yb2} \left( x - \frac{h_A}{2} \cdot \cos \varphi - \frac{x_1}{2}, x_2 - \frac{h_A}{2} \cdot \sin \varphi, 0 \right) \\ - H_{yb1} \left( x + \frac{h_A}{2} \cdot \cos \varphi - \frac{x_1}{2}, x_2 - \frac{h_A}{2} \cdot \sin \varphi, 0 \right) \\ + H_{yc2} \left( x - \frac{h_A}{2} \cdot \cos \varphi + \frac{x_1}{2}, x_2 - \frac{h_A}{2} \cdot \sin \varphi, 0 \right) \\ - H_{yc1} \left( x + \frac{h_A}{2} \cdot \cos \varphi + \frac{x_1}{2}, x_2 - \frac{h_A}{2} \cdot \sin \varphi, 0 \right) \end{array} \right\} \quad (6a)$$

choosing appropriate magnets and their interval is of great importance to give the cantilever a higher transition probability. The mentioned problem for the conventional tri-stable piezoelectric EH system, as well as for the improved tri-stable piezoelectric EH system, is solved by using the magnetizing current method [23]. As a result, taking this method into account, the magnetic force acting in the TPEH and ITPEH systems shown in Fig.3 being the simultaneous reaction of magnet A to a magnetic field produced by magnets located on the frame can be expressed in the following forms, respectively:

$$F_m = F b_x + F c_x = \mu_0 M_A S [(H_{yb2} - H_{yb1}) + (H_{yc2} - H_{yc1})] \quad (5a)$$

$$F_m = F b_x + F c_x + F_{Dx} = \mu_0 M_A S [(H_{yb2} - H_{yb1}) + (H_{yc2} - H_{yc1}) + (H_{yD2} - H_{yD1})] \quad (5b)$$

where:  $\mu_0$  – the permeability of vacuum,  $M_A$  – the magnitude of magnet's A magnetization,  $S$  – the area of magnet's A the top or bottom surface,  $H_{yb2}$ ,  $H_{yb1}$  – the magnitudes of the magnetic field strength generated by the magnet B at the centers of magnet A's top or bottom surfaces in y direction,  $H_{yc2}$ ,  $H_{yc1}$  – the magnitudes of the magnetic field strength generated by the magnet C at the centers of magnet A's top or bottom surfaces in y direction,  $H_{yD2}$ ,  $H_{yD1}$  – the magnitudes of the magnetic field strength generated by the magnet D at the centers of magnet A's top or bottom surfaces in y direction.

While the field of the magnetic field strength according to [22] is expressed as:

$$F_m = \mu_0 M_A S \left\{ \begin{array}{l} H_{yb2} \left( x - \frac{h_A}{2} \cdot \cos \varphi - \frac{x_1}{2}, x_2 - \frac{h_A}{2} \cdot \sin \varphi, 0 \right) \\ - H_{yb1} \left( x + \frac{h_A}{2} \cdot \cos \varphi - \frac{x_1}{2}, x_2 - \frac{h_A}{2} \cdot \sin \varphi, 0 \right) \\ + H_{yc2} \left( x - \frac{h_A}{2} \cdot \cos \varphi + \frac{x_1}{2}, x_2 - \frac{h_A}{2} \cdot \sin \varphi, 0 \right) \\ - H_{yc1} \left( x + \frac{h_A}{2} \cdot \cos \varphi + \frac{x_1}{2}, x_2 - \frac{h_A}{2} \cdot \sin \varphi, 0 \right) \\ + H_{yD2} \left( x + \frac{h_A}{2}, x_2 + \frac{h_A}{2}, 0 \right) \\ - H_{yD1} \left( x - \frac{h_A}{2}, x_2 - \frac{h_A}{2}, 0 \right) \end{array} \right\} \quad (6b)$$

The magnetic forces given by Eq.(6a) and Eq.(6b) lead to calculation the potential energies of TPEH and TPEH systems, including elastic potential energy and magnetic potential energy that can be written in the following forms:

$$U(x) = \frac{K_{ef}^2}{2} x^2 + \int F_m dx \quad (7)$$

where:  $K_{ef}$  – the stiffness of the cantilever beam.

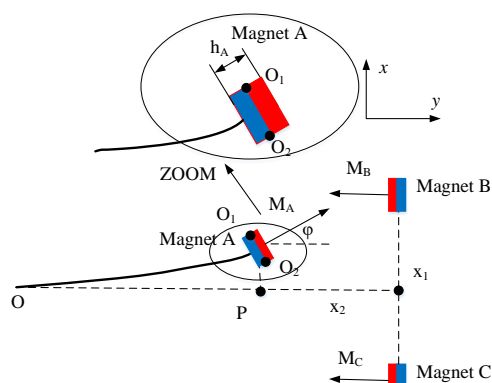


Fig. 3. Schematic of acting magnetic force in the TPEH system

#### 4. NUMERICAL SIMULATIONS

In this section, the abilities of both tri-stable and improved tri-stable piezoelectric energy harvesting systems (TPEH and ITPEH) under weak excitation were compared. To show the difference between them, simulations were conducted in Matlab and Ansys software by assuming that the magnetic moment of both external magnets ( $m_B=m_C=0.844 \text{ Am}^2$ ) is twice higher than the magnetic moments of the tip magnet and the additional magnet ( $m_A=m_D=0.422 \text{ Am}^2$ ). Moreover, to show how the additional magnet  $D$  influences the behavior of the magnetic coupling system and the potential well depth, numerical calculations were performed for varying distance  $x_1$  between fixed magnets located on the frame, as well as varying air gaps  $x_2$  changing within the range of 11-13mm with a step of 1mm. The results of the potential energy calculated according to Eq.(7) are shown in Fig.4.

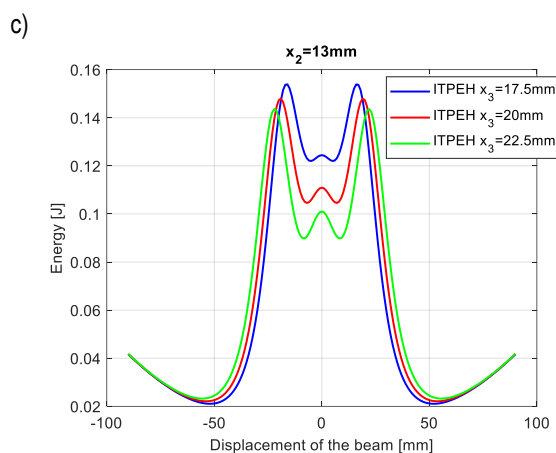


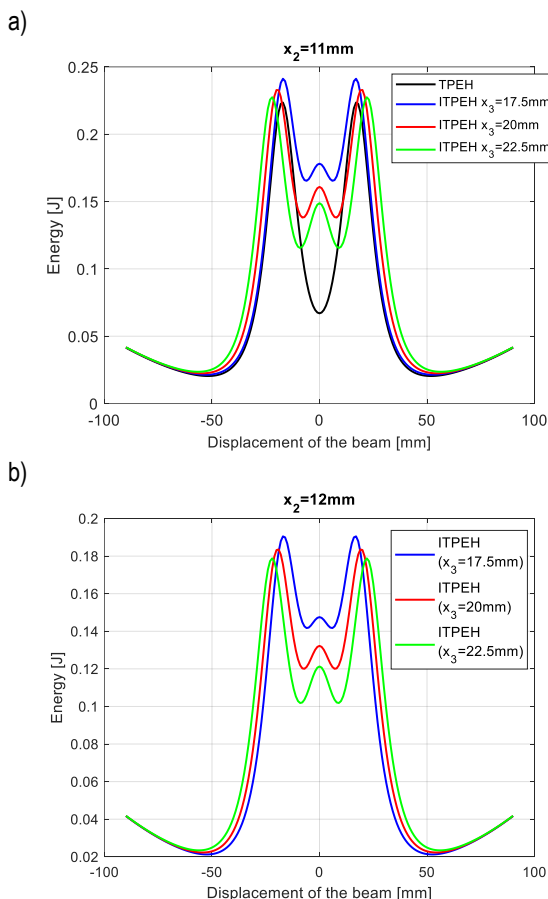
Fig. 4. The comparison of the potential energy generated by the TPEH and ITPEH systems by various air gaps for distance between magnets a)  $x_3=17.5\text{mm}$ , b)  $x_3=20\text{mm}$ , c)  $x_3=22.5\text{mm}$

The analysis of the potential energy in both EH systems indicated a significant influence of additional magnets on the behavior of the improved tri-stable systems. Compared to the TPEH, in the ITPEH system, the depth of the middle potential wells decreases by reducing the air gaps between the tip magnet and the additional magnet. Further analysis allows us to also observe that extending the distance between fixed magnets leads to a higher effect of additional magnets on the vibrating structure, especially in the neutral position of the vibrating beam, as well as to deepening potential barriers. As a result, such behavior of the proposed system leads to the conclusion that the most enhanced broadband energy harvesting effect for all considered air gaps is achieved for the ITPEH system with an air gap of 11mm, as well as by the highest distance between magnets of  $x_3=22.5\text{mm}$ , while the lowest broadband effect [25-27] for the same EH system but with a distance of  $x_3=17.5\text{mm}$ .

In the next step, the behavior of the tri-stable and improved tri-stable energy harvesting systems was analyzed in the time domain by using Matlab software. In order to do this, firstly coefficients of the magnetic force given by Eq.(2) were determined by using the curve fitting method, and next Eq.(3) whereby using Runge-Kutta algorithm values of displacement and voltage generated by the piezo-elements in the time domain are calculated. Simulations were performed for both considered EH systems with three various air gaps between the tip magnet and the fixed magnet ( $x_2=11, 12, 13\text{mm}$ ), as well as three different distances between magnets  $x_3$  which equalled 35mm, 40mm, and 45mm, respectively. In addition, these simulations were also performed for three different base accelerations 0.91g, 1.34g, and 1.73g, respectively. Chosen results are presented in Fig.5, while their deeper analysis versus experimental results is described in the next Section.

The analysis of the voltage signals generated by the piezo-elements in the tri-stable energy harvesting system indicated a significant increase in their values, especially within the range marked by a rectangle with dash line where the influence of the magnetic force on the vibrating structure is higher. As a result, the effectiveness of the improved tri-stable EH system for all considered cases is improved and enhanced.

The last step of numerical simulations was related to comparing the power output generated by the conventional tri-stable energy harvesting system, the improved tri-stable energy harvesting system and bi-stable energy harvesting system where the



same type of the beam, piezo-harvester and magnets were used. In order to do this, the clearance between the tip magnet located on the beam and the fixed magnet  $x_2$  was set at 11mm, while distance  $x_1$  for the TPEH system was set at 45mm, as well as distance  $x_3$  for the ITPEH system was set at 22.5mm. In addition, considering the above parameters, simulations were performed for an impedance load close to the quasi-optimal value ( $R_{opt}=1.5M\Omega$ ), changing within the range of  $1.1M\Omega - 2.1M\Omega$ . The calculated values of the power outputs generated from mathematical models of particular EH systems are presented in Fig.6.

The analysis of the power output generated by each EH system shows that the highest power output (over 80mW) is obtained for the improved tri-stable energy harvesting system connected with the quasi-optimal impedance load, while the lowest output – for the bi-stable energy harvesting system. Such behavior of these systems is due to the considered additional magnet in the system that leads to a stronger impact of the nonlinear magnetic force to the vibrating structure, and to improving the effectiveness of the system.

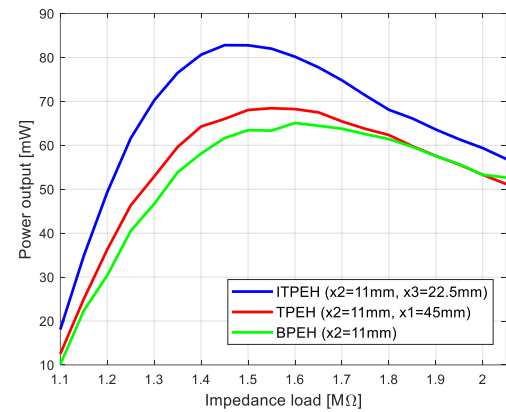


Fig. 6. The comparison of the power output generated by the improved tri-stable EH system, conventional tri-stable EH system and bi-stable EH system by various impedance load connected to the piezo-sensor

## 5. EXPERIMENTAL INVESTIGATIONS

In this section, the process of assessment parameters of both TPEH and ITPEH systems is carried out on the lab stand shown in Fig.7. In order to do this, the fiberglass beam, which represents a host structure, is equipped in a piezo patch composite of type 8514 P2, and it is located 10mm from the fixed end of the beam and the neodymium magnet N35 of type MP 14/4 x 3 placed close to the free end of the same beam, respectively. The parameters of the beam, piezo harvester, and neodymium magnets are collected in Tab.1. Apart from the aforementioned elements, the lab stand is also equipped with a frame where the appropriate amount of neodymium magnets is placed. To perform experimental tests of the tri-stable EH system, two neodymium magnets with the same magnetic moments were located symmetrically versus the beam on the frame. In contrast, in the case of the improved tri-stable energy harvesting system – the lab stand was filled with additional neodymium with the twice lower magnetic moment that was located on the frame in the middle of the external magnets. Additionally, the laboratory stand was retrofitted into two other devices: the signal generator Agilent and the vibration shaker TV51110M with a BAA 120 amplifier, that were used to generate signal excitation and apply it to the vibrating structure. Whereas, from the measurement point of view, the lab stand was equipped with a data acquisition system (DAQ) with a measurement card of type USB-6341, the displacement sensor LG10A65PUQ and the 3-axis accelerometer that is used to measure the voltage generated by the piezo, deflection of the tip mass of the beam, and base acceleration, respectively.

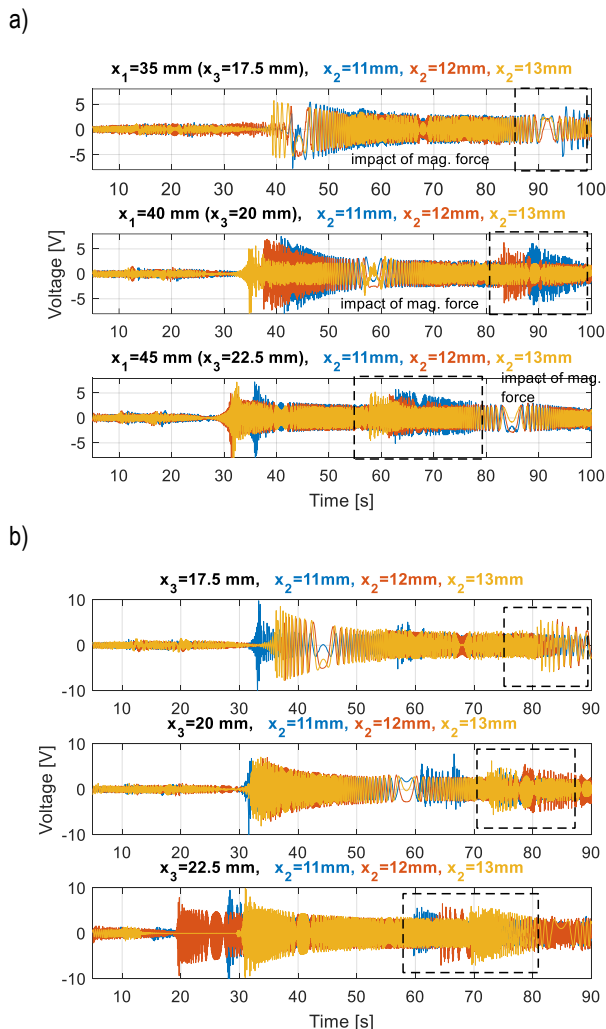


Fig. 5. The comparison of voltage generated by the piezo-element located on the beam excited to vibration with base acceleration increasing up to 1.73g from a) the conventional tri-stable EH system b) the improved tri-stable energy harvesting system

a)



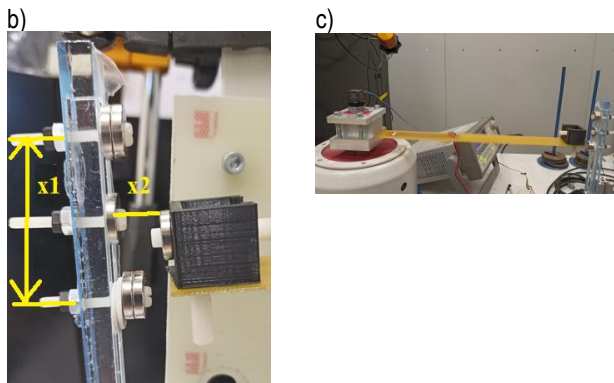


Fig. 7. The photo of the lab stand a) the whole lab stand, b) the view of the frame with three neodymium magnets for testing the ITPEH system, c) the view of the piezoelectric cantilever beam during the test

Tab.1. Parameters of the cantilever beam, piezo patch composites MFC8514 and neodymium magnets

Mechanical Parameters										
Fiber Glass										
Length [mm]		Width [mm]		Length [mm]						
L <sub>F</sub>	270	w <sub>F</sub>	38	t <sub>F</sub>	1.5					
Young's Modulus (GPa)		Poisson's Ratio (-)		Density [kg/m3]						
E <sub>F</sub>	80	ν <sub>F</sub>	0.22	ρ <sub>F</sub> 2600						
Piezo composite MFC										
Young's Modulus (GPa)		Poisson's Ratio (-)				Piezo. Charge Coeff. (pC/N)	Relative Permittivity (-)			
E <sub>x</sub> 31.6	v <sub>xy</sub>	0.4				d <sub>31</sub> -173	ε <sub>r</sub> <sup>T</sup>	2253		
E <sub>y</sub> 17.1	v <sub>yz</sub>	0.2				d <sub>32</sub> -150				
E <sub>z</sub> 9.5	v <sub>xz</sub>	0.4				d <sub>33</sub> 325				
Geometrical parameters										
Overall Length [mm]		Overall Width [mm]		Active Length [mm]		Active Width [mm]		Thick. of PZT fiber layer [μm]	Thick. of electrode layer [μm]	Thick. of Cap-tion layer [μm]
L <sub>p</sub>	103	w <sub>p</sub>	17	85		14		180	25	30
Neodymium magnet N35 – tip magnet A and internal D										
Outer/Inner diameter [mm]			Thickness [mm]			Strength [kg]		Remanence [T]		
14/4			3			2.5		1.2		
Neodymium magnet N35 – external magnet B and C										
14/4			5			5.0		1.21		

In the first step, the experimental tests were focused on assessing the value of the base acceleration by various values of the chirp signal amplitude. To do this, an excitation signal with

three different amplitudes in the range of 3-5V with a step of 1V by linearly increasing frequency from 1Hz to 40Hz in the period of 120s was firstly generated by the signal generator and next applied to the vibration shaker. Then, the 3-axis accelerometer placed directly on the vibration shaker-base with a sensitivity of 104.5mV/g in the vertical axis allowed the assessment of maximum values of the base acceleration 0.91g, 1.34g, and 1.73g, corresponding to the amplitude of the excitation signal 3V, 4V, 5V, by the frequency of 40Hz, respectively.

Next, the behavior of both tri-stable and improved tri-stable energy harvesting systems were compared on the lab stand in the time domain. To do this, all tests were conducted for three different air gaps  $x_2$  changing in the range of 11-13 mm. Moreover, in the case of the tri-stable piezoelectric energy harvesting system, the experimental tests were carried out for three different distances  $x_1$  between the fixed magnets  $B$  and  $C$  in the range of 35-45mm with a step of 5mm. While in the case of the improved tri-stable system - by three different distances  $x_3$  between chosen external fixed magnet  $B$  and additional magnet  $D$  in the range of 17.5-22.5mm with a step of 2.5mm. As a result, it led to the conduct of nine different tests for two separate EH systems by various base accelerations where the AC voltage output from the piezo was measured and recorded for each try. Finally, the results obtained from testing the TPEH system are shown in Fig.8, while from testing the ITPEH system - in Fig.9.

The conducted analysis of the recorded signals shown in Fig.8 for the TPEH system with the narrowest distance between the magnet, as well as the smallest air gap of 11mm indicated a light increase of the voltage output from the piezo only to 3.47V, that is due to a weak impact of the nonlinear magnetic force on the vibrating beam. Other results can be observed for the EH system with magnets spaced 40mm apart and excited to vibration with a lightly higher base acceleration (0.91g) – see Fig.8b. Then, increasing the base acceleration to 1.34g and expanding distance  $x_1$  between magnets leads to increasing the impact of the magnetic force on the structure for all considered air gaps and generating higher voltages than previously. In addition, it can be observed that the widening of the air gap leads to a decreasing amplitude of the magnetic force and consequently to its faster appearance in the magnetic coupling EH system. Yet another behavior can be shown in Fig.8c for the fixed magnets spaced 45 mm apart. Then, the base acceleration equals 1.73g by a frequency of 40Hz leading to an enhanced impact of the magnetic force to the system and appearing additional vibrations with an amplitude of over 5V in a transient period of 55-80s.

Next, the analysis was performed for the ITPEH system. Taking into account the diagrams presented in Fig.9, it can be seen that the considered additional magnet, in the TPEH system, allows for improvement of the behavior of the coupling magnetic EH system. It is especially shown by the configuration of the ITPEH system with the narrowest distance between magnets, as well as the smallest air gap, where the testing system generates higher voltage output (by 0.8V) than the TPEH system at the same base acceleration. Similar results can be observed in Fig.9b and Fig.9c, where the ITPEH system leads to obtaining the voltage output higher by 1.2V at the same initial conditions (distance between magnets equals 17.5mm and air-gap equals 11mm) . As a result, it allows us to conclude that adapting the potential energy of the EH system by considering additional magnets in the coupling magnetic EH system leads to generating higher voltages and, finally, to improve the effectiveness of the proposed ITPEH system.



To confirm the above results, as well as show how nonlinear magnetic force affects the beam structure, a deeper analysis of the recorded voltage output signals was performed in chosen periods of time marked in Fig.8 and Fig.9, where increasing voltage amplitudes can be observed. The obtained results are presented in Fig.10-Fig.12 separately for three different distances between magnets  $x_3$  where voltage output generated by both TPEH and IPTEH systems were compared.

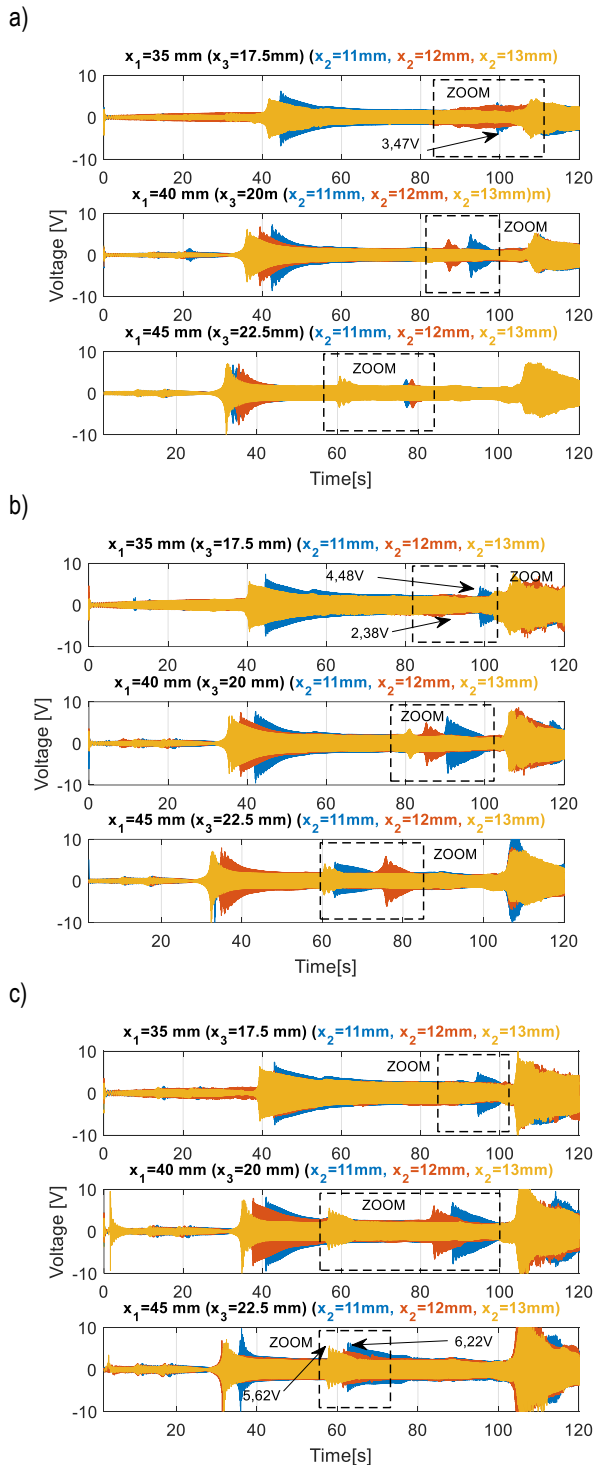


**Fig. 8.** The comparison of the voltage output from the piezo for the TPEH system by various air gaps in the range of 11-13mm and the distance between fixed magnets for a) increasing of the base acceleration to 0.91g, b) increasing the base acceleration to 1.34g, c) increasing the base acceleration to 1.73g

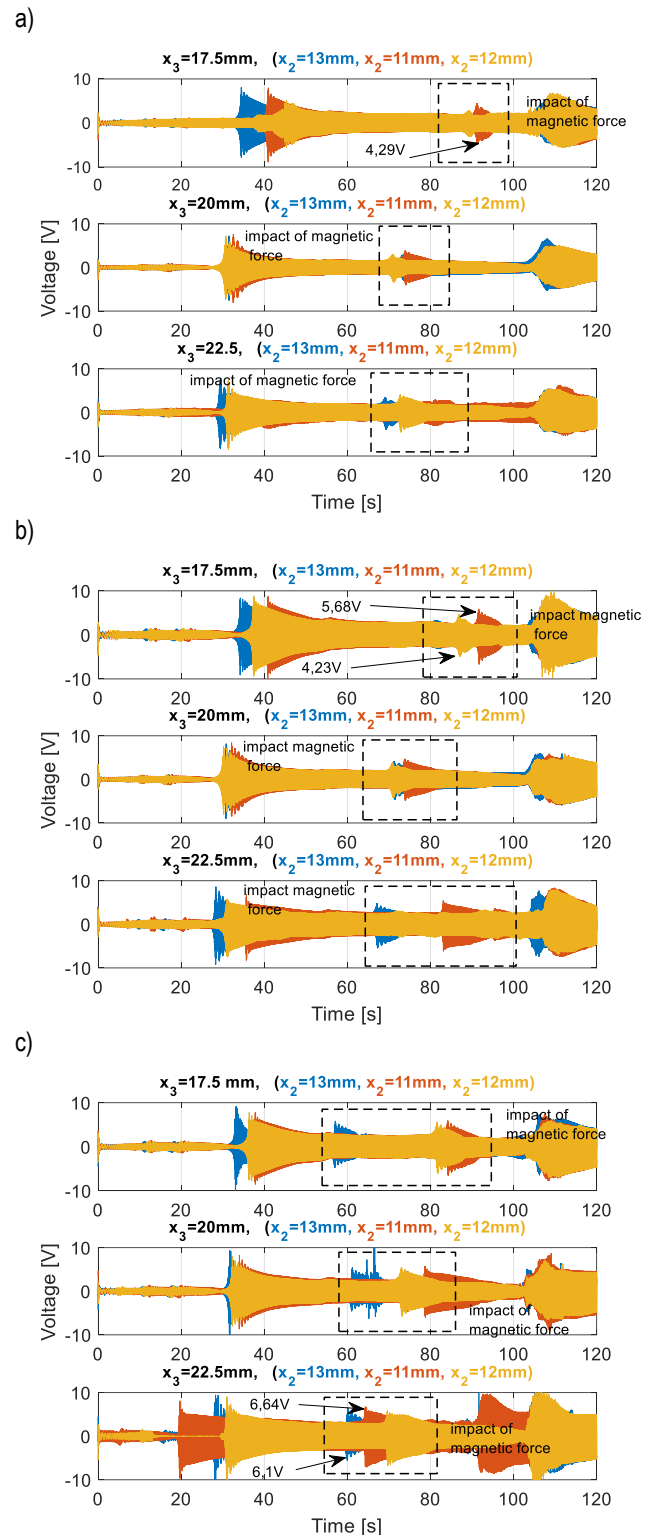


**Fig. 9.** The comparison of the voltage output from the piezo for the IPTEH system by various air gaps in the range of 11-13mm and the distance between fixed magnets for a) increasing the base acceleration to 0.91g, b) increasing the base acceleration to 1.34g, c) increasing the base acceleration to 1.73g

The analysis of these voltage outputs generated by both systems indicated the advantage of the IPTEH system over the TPEH system for each configuration of the magnetic coupled EH system. It is especially visible in Fig.9 where the adapting the potential energy by setting the narrowest distance between the magnets,



air gaps equal 12mm or 13mm, and the amplitude of the base acceleration over 0.91g leads to the appearance of the magnetic force with low amplitude only for the ITPEH system. Another behavior can be observed for both tri-stable systems working with an air gap of 13mm where a weak base excitation leads to the disappearing impact of the magnetic force on the structure. This behavior is caused by a deep middle potential well. Further analysis of diagrams presented in Fig.10 also shows that the ITPEH system works with the narrowest air gap, which equals 11 mm, as well as with the narrowest distance between magnets allowing to better strengthen the impact of the magnetic force on the vibrating structure.

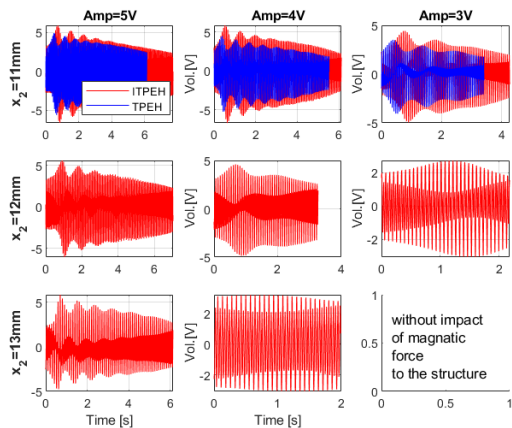


Fig. 10. The comparison of the recorded voltage output signals generated by the TPEH and ITPEH systems in the indicated time period of impacting the magnetic force on the structure by the distance between fixed magnets  $x_3=17.5$  mm

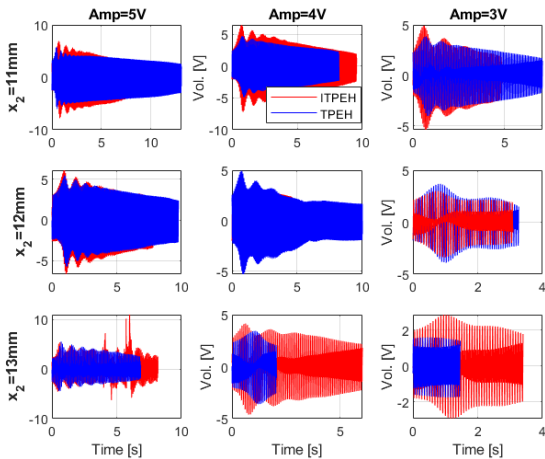


Fig. 11. The comparison of the recorded voltage output signals generated by the TPEH and ITPEH systems in the indicated time period of impacting the magnetic force on the structure by the distance between fixed magnets  $x_3=20$  mm

As a result, the piezo sensor attached to the beam generates a higher amplitude of voltage in a longer time. Similar results can be observed in diagrams presented in Fig.11 and Fig.12 for both EH systems working with two different distances between magnets ( $x_3=20$ mm and  $x_3=22.5$ mm), where considering an additional magnet in the TPEH system allowed to strengthen the impact of the nonlinear magnetic force on the structure and, consequently, to generate voltages with higher amplitudes by the piezo element. Additionally, the RMS values calculated for the total length of

voltage signals presented in Figs.10-12 (see Tab.2) are a confirmation of the obtained results. The analysis of these values indicated the advantage of the ITPEH system over the TPEH system each time. As a result, again the highest value was obtained for the system which operates with the distance between magnets of 22.5mm, the narrowest air gap of 11mm, while the lowest - for the system with the smallest distance  $x_3=17.5$ mm. Thus, taking the obtained results into account, it can be concluded that adapting the potential energy in the tri-stable energy harvesting system under weak excitation leads to increase.

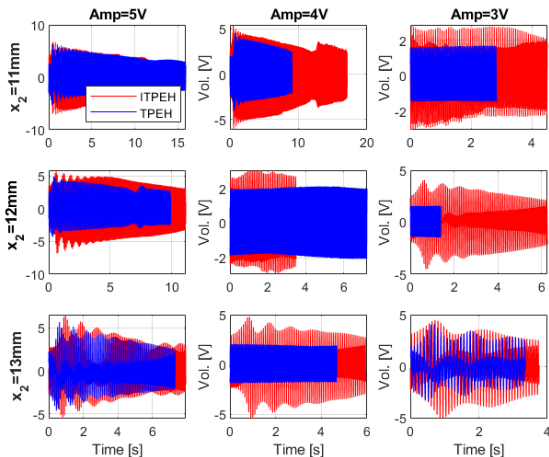
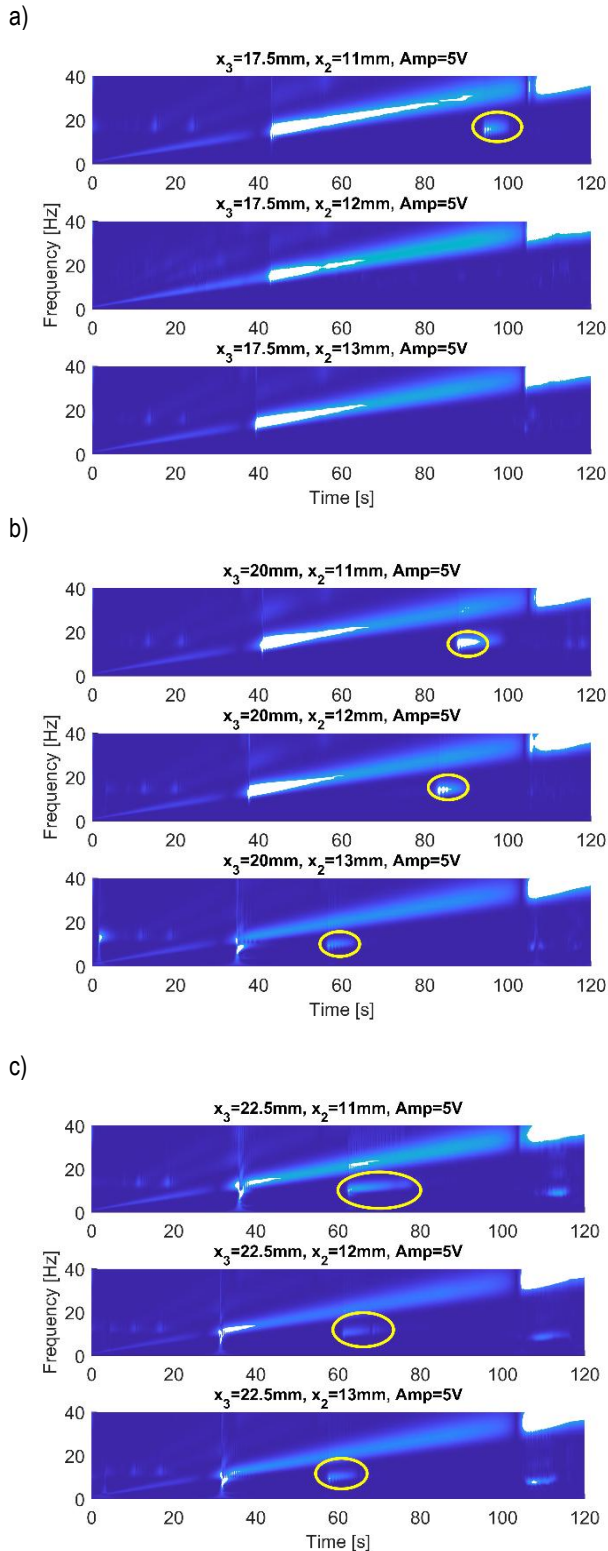


Fig. 12. The comparison of the recorded voltage output signals generated by the TPEH and ITPEH systems in the indicated time period of impacting the magnetic force on the structure by the distance between fixed magnets  $x_3=22.5$  mm

Tab. 2. The calculated RMS values of the recorded voltage signals for TPEH and ITPEH systems (maximal RMS values in each configuration are marked with red font)

The base acceleration from 0 to 0.91g (40Hz)			
air gap $x_2$ [mm]	Distance between fixed magnets $x_3$ [mm]		
	17.5mm	20mm	22.5mm
	TPEH / ITPEH		
11mm	1.5820 / 1.8829	1.5187 / 1.8304	1.0563 / 1.4286
12mm	- / 1.4406	1.3542 / 1.5293	0.9896 / 1.6852
13mm	- / -	0.9394 / 1.2979	1.5469 / 1.5274
The base acceleration from 0 to 1.34g (40Hz)			
air gap $x_2$ [mm]	Distance between fixed magnets $x_3$ [mm]		
	17.5mm	20mm	22.5mm
	TPEH / ITPEH		
11mm	1.9211 / 2.3739	1.8531 / 2.3609	1.7419 / 2.0847
12mm	- / 2.0586	1.6343 / 1.6395	1.3076 / 1.6832
13mm	- / 1.7698	1.5996 / 1.7405	1.3097 / 2.0513
The base acceleration from 0 to 1.73g (40Hz)			
air gap $x_2$ [mm]	Distance between fixed magnets $x_3$ [mm]		
	17.5mm	20mm	22.5mm
	TPEH / ITPEH		
11mm	2.1309 / 2.3189	2.2014 / 2.3609	2.1714 / 2.7127
12mm	- / 2.1607	1.6343 / 2.1017	1.9120 / 2.4722
13mm	- / 2.0208	1.5996 / 2.1633	1.8998 / 2.1865

The obtained results and RMS values were verified additionally by performing the time-frequency analysis of TPEH and ITPEH systems. In order to do this, the continuous wavelet transform method based on analytical Morse wavelet [35,36] was used for the voltage output signals generated by the piezo and systems excited to vibration with the highest considered base acceleration.



**Fig. 13.** The comparison of time-frequency plots of the TPEH system excited to vibration with base acceleration of 1.73g by various air gaps and distance between fixed magnets

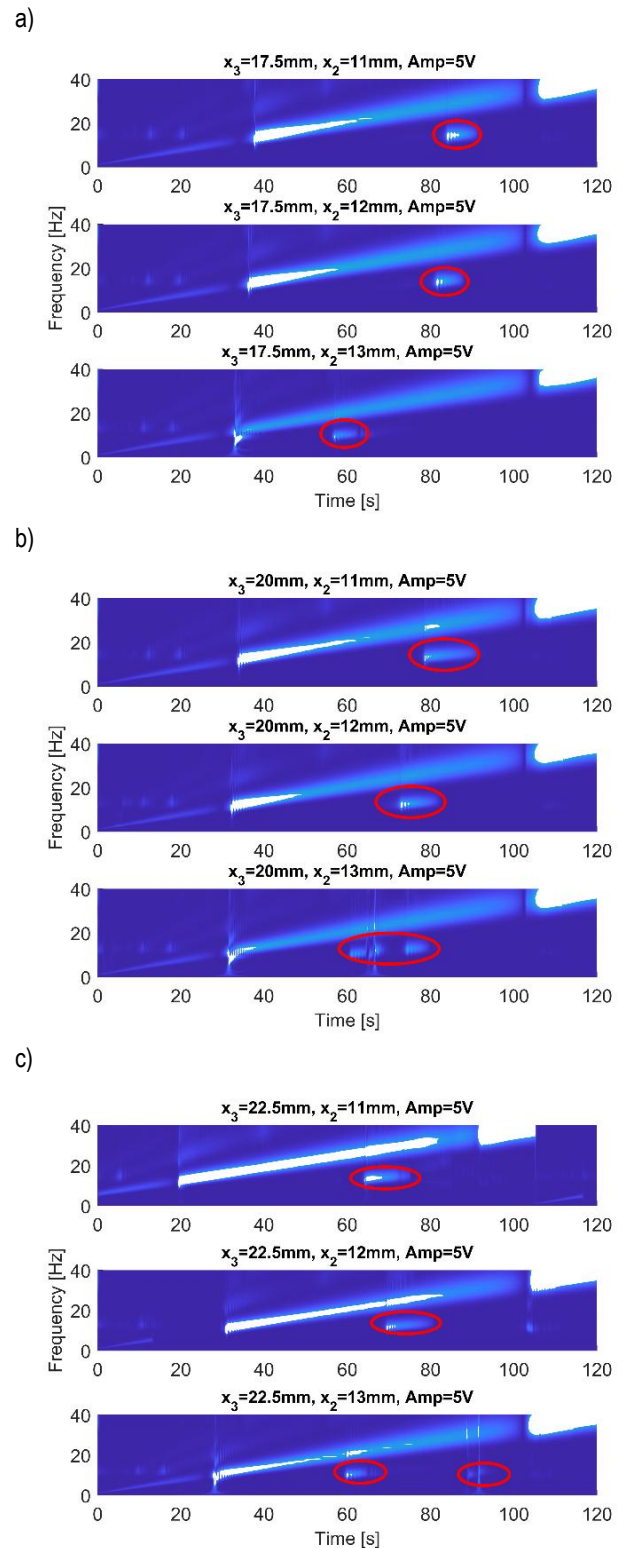


**Fig. 14.** The comparison of time-frequency plots of the ITPEH system excited to vibration with base acceleration of 1.73g by various air gaps and distance between fixed magnets

The analysis of diagrams shown in Fig.13 and Fig.14 indicated once more that the width of the air gap by assuming other parameters of conventional and the improved tri-stable systems, like distance between magnets  $x_3$  and base acceleration, as constant, significantly influence appearing the magnetic force in these systems and, consequently, their behavior. Taking this into

account, nonlinear magnetic force appeared only in the TPEH system working with the narrowest air gap, and excited to vibration with a frequency in the range of 25-29Hz. Further analysis of diagrams presented in Fig.13b shows that the gradual increase of the air gap by widening the distance between the fixed magnets to 40mm leads to the appearance of the magnetic force in a lower range of frequency excitation than it was previously. Similar results were achieved by further expanding the distance between the magnets to 45mm. Then, a gradual increase of clearance between the tip magnet and the fixed magnets leads to a shortened transient period affecting the magnetic force to the structure. As a result, the strongest vibration-based energy harvesting effect is achieved during the analysis of the TPEH system with an air gap of 11mm and the widest distance between fixed magnets (6.22V), while the lowest (5.62V) by the air gap of 13mm.

Further analysis of the time-frequency diagrams determined for the ITPEH system proved again that considering of an additional fixed neodymium magnet, located on the frame, allowed for an improved energy harvesting effect. It is especially observable in diagrams in Fig.14c for the system with an air gap of 11mm, where the transient period of impacting of the magnetic force to the structure is longer and their amplitude is higher in comparison to the TPEH system (see Fig.13c). Similar result was achieved for other ITPEH system activities with the air gap of over 11mm, where impacting of the magnetic force was also higher than in the case of the TPEH system working in the same conditional parameters.

The last step of this subsection is verification of the simulated results. In order to do this, all experimental and simulation results obtained by three various base accelerations, as well as considered different distances of  $x_1$ ,  $x_2$  and  $x_3$ , are collected in Tabs.3-5.

**Tab. 3.** The comparison of the voltage generated by the piezo (simulation and experimental results) by the base acceleration increasing up to 0.91g

Base acceleration 0.91g (TPEH)									
$x_1$ [mm]	Simulation			Experiment			Error		
	air gap $x_2$ [mm]			air gap $x_2$ [mm]			air gap $x_2$ [mm]		
	11	12	13	11	12	13	11	12	13
35mm	4,73	-	-	4,6	-	-	0,1	-	-
							7		
40mm	6,75		-	6,0	5,6		0,7	0,3	-
				4	6		1	4	
45m	6,06	4,7	4,4	5,5	4,2	4,1	0,5	0,1	0,2
		6	0		5	5	6	5	5
Base acceleration 0.91g (ITPEH)									
$x_3$ [mm]	Simulation			Experiment			Error		
	air gap $x_2$ [mm]			air gap $x_2$ [mm]			air gap $x_2$ [mm]		
	11	12	13	11	12	13	11	12	13
17.5m m	-	4,4	2,7	-	3,8	2,4	-	0,5	0,2
		3	0		7	3		6	9
20mm	4,20	3,0	2,7	3,8	2,8	2,5	0,3	0,1	0,1
	V	5	0	2	6	3	8	9	7
22.5m m	3,41	4,2	3,6	3,1	4	3,4	0,3	0,2	0,1
	V		4			5	1		9

**Tab. 4.** The comparison of the voltage generated by the piezo (simulation and experimental results) by the base acceleration increasing up to 1.34g

Base acceleration 1.34g (TPEH)									
$x_1$ [mm]	Simulation			Experiment			Error		
	air gap $x_2$ [mm]			air gap $x_2$ [mm]			air gap $x_2$ [mm]		
	11	12	13	11	12	13	11	12	13
35mm	4,0	-	-	3,7	-	-	0,2	-	-
	5			9			6		
40mm	6,5	4,8	3,1	6,3	4,5	3,3	0,2	0,3	0,2
	5	5		1	4	0	4	1	
45mm	3,9	5,7	2,8	3,7	5,6	3,2	0,2	0,1	0,3
		1	6			5		1	9
Base acceleration 1.34g (ITPEH)									
$x_3$ [mm]	Simulation			Experiment			Error		
	air gap $x_2$ [mm]			air gap $x_2$ [mm]			air gap $x_2$ [mm]		
	11	12	13	11	12	13	11	12	13
17.5m m	6,2	4,4	3,6	5,6	4,2	3,2	0,5	0,1	0,4
	4	4	9	8	3	1	6	9	8
20mm	4,3	3,8	4,3	4,1	3,6	3,8	0,2	0,1	0,5
	6	1	7	6	3		0	8	7
22.5m	5,1	4,9	4,8	4,9	4,7	4,4	0,2	0,2	0,4
	4	3	5			2	4	3	3

**Tab. 5.** The comparison of the voltage generated by the piezo (simulation and experimental results) by the base acceleration increasing up to 1.73g

Base acceleration 1.73g (TPEH)									
$x_1$ [mm]	Simulation			Experiment			Error		
	air gap $x_2$ [mm]			air gap $x_2$ [mm]			air gap $x_2$ [mm]		
	11	12	13	11	12	13	11	12	13
35mm	3,5	-	-	3,2	-	-	0,3	-	-
	5			2			3		
40mm	5,1	3,9	-	4,8	3,6	-	0,3		-
	5	7			8		5		
45mm	3,7	3,4	3,4	3,5	3,2	3,0	0,2	0,2	0,4
	2	2	7			4	2	2	3
Base acceleration 1.73g (ITPEH)									
$x_3$ [mm]	Simulation			Experiment			Error		
	air gap $x_2$ [mm]			air gap $x_2$ [mm]			air gap $x_2$ [mm]		
	11	12	13	11	12	13	11	12	13
17.5m m	5,5	5,2	5,3	5,2	5,4	5,4	0,2	0,2	0,1
				2	2		3	2	
20mm	5,8	5,4	5,7	5,6	5,3	5,4	0,1	0,0	0,3
			2	9	4	2	1	6	
22.5m	6,7	5,5	5,8	6,5	5,4	6,1	0,2	0,1	0,2
	4	3	7	4	1		0	2	3

Taking into account the values of voltage collected in the Tab.3-Tab.5, it can be noticed that the experimental results



properly verified the amplitudes calculated in the numerical way in all considered cases. Their further analysis indicates that the amplitude of voltage generated by the real piezo-composite is lightly lower than those calculated on the basis of the mathematical model. This behavior is due to a lower amplitude of the magnetic force which affects the structure to vibrating, as well as heterogeneity of the adhesive layer between the MFC element and the host structure.

## 6. THE ANALYSIS OF PHASE PORTRAITS OF TPEH AND ITPEH SYSTEMS

The last step of the experimental test was related to determining the portrait phases of both TPEH and ITPEH systems by considering the repulsion effect of the magnetic force. To do this, tests were carried out for chirp signal with frequency increasing from 1Hz to 40Hz, and by three different amplitudes where displacement of the tip mass was measured by using the laser displacement sensor placed 75mm from the vibrating structure for each time. Similarly, as it was previously, tests were carried out for three different distances between magnets  $x_3$  as well as three various air gaps  $x_2$  in the range of 11-13mm. As a result, nine different tests were conducted for each system, where the most interesting ones are presented in Figs.15-17.

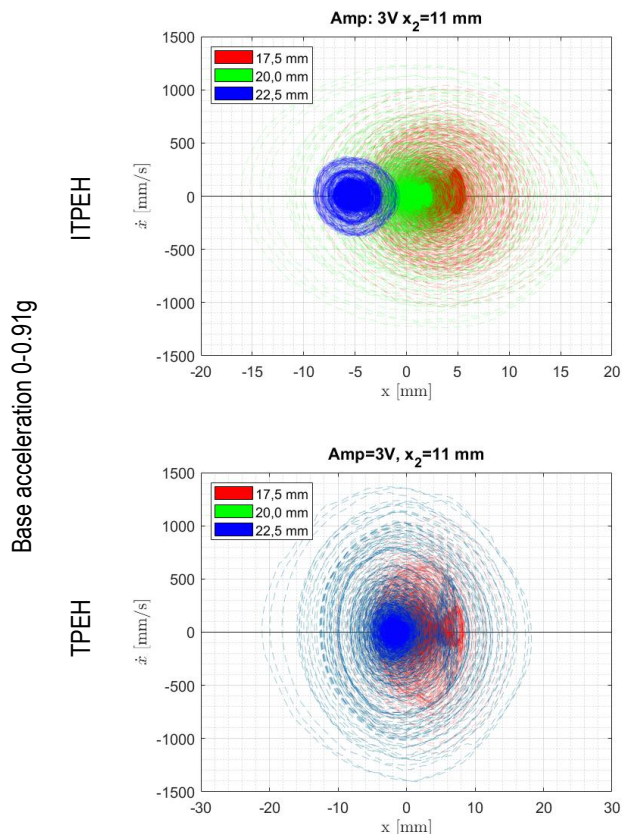


Fig. 15. The comparison phase portrait of both TPEH and ITPEH systems by various air gaps in the range of 11-13mm and increasing base acceleration from 0 to 0.91g

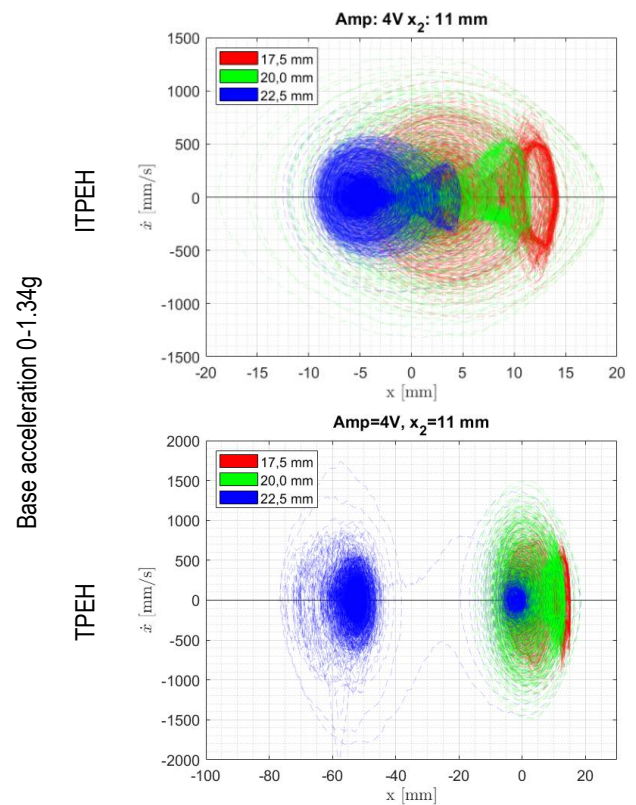


Fig. 16. The comparison phase portrait of both TPEH and ITPEH systems by various air gaps in the range of 11-13mm and increasing base acceleration from 0 to 1.34g

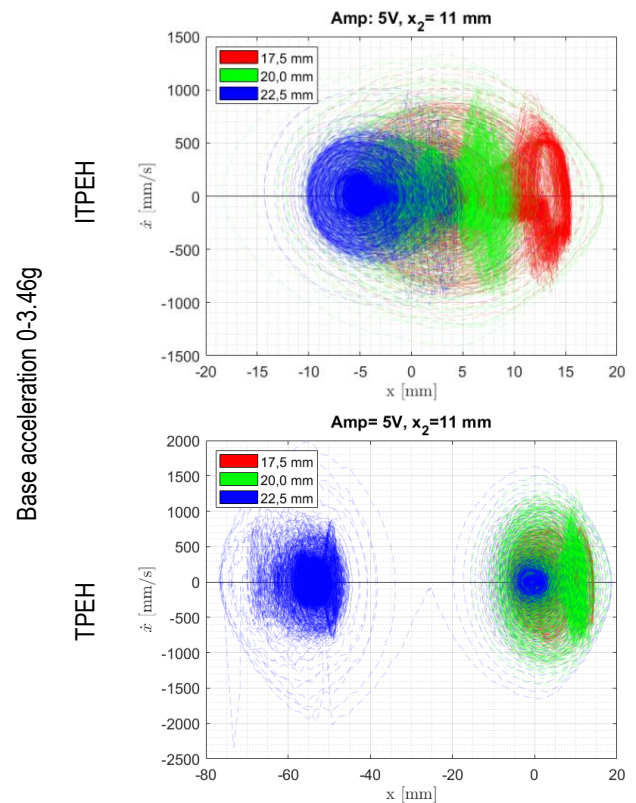


Fig. 17. The comparison phase portrait of both TPEH and ITPEH systems by various air gaps in the range of 11-13mm and increasing base acceleration from 0 to 1.73g

Observing diagrams presented in Fig.15b indicated that low amplitude base acceleration leads to generating three different trajectories of phase portrait of TPEH systems concentrated around the singular equilibrium point. This behavior is due to a weak impact of the magnetic force on the structure, which is also a result of the existent deep middle potential well and high potential barriers. Slightly different behavior can be observed during the analysis of particular portrait phases generated by the improved tri-stable energy harvesting system. Then, the low value of base acceleration and reduced distance between the additional magnet and the external magnets again leads to appearing weak magnetic force and generating small elliptical trajectories in the diagram.

Next, the analysis of portrait phases in Fig.16b shows that a slightly increase of base acceleration and the choice of an appropriate distance between the fixed magnets can significantly affect the behavior of the TPEH system. It is especially shown that the TPEH system works with the highest distance between magnets  $x_3$  of 45mm, where increasing the frequency excitation leads to appearing a higher amplitude of the beam vibration and consequently jumping of EH system to the bottom potential wall. A completely other behavior can be shown during the analysis of the ITPEH system (see Fig.15a) where tailoring potential energy caused by considering additional fixed magnets leads to increasing the magnetic field in the coupling system and generates a conical nature of particular portrait phases. As a result, the highest elliptical trajectories are generated for the system with the narrowest spacing between magnets ( $x_3=17.5\text{mm}$ ), while the lowest one - for the system with the widest spacing ( $x_3=22.5\text{mm}$ ). Slightly different results can be observed during the analysis of both TPEH and ITPEH systems excited to vibration with the highest amplitude of acceleration. Then, strong nonlinearity in the improved tri-stable EH systems leads to increased velocity of vibrations and jumping the vibrating beam between potential wells in all considered configurations.

## 7. SUMMARY AND CONCLUSIONS

The broadband effect of the tri-stable and improved tri-stable energy harvesting systems by various air gaps as well as distances between fixed magnets under weak excitation was analyzed in this paper. To do this, firstly the model of magnetic coupling energy harvesting systems was determined, where nonlinear magnetic force existing in the model was calculated by using the magnetization current method. Next, numerical simulations of the conventional tri-stable and the improved EH systems were performed by using Matlab software. The obtained diagrams of potential energies of both systems by various air gaps changing in the range of 11-13mm and different distances between fixed magnets indicated shallowing of the depth of the middle potential well with a decrease of the air gap and consequently improved behavior of the proposed tri-stable energy harvesting system. In addition, it can be observed that extending the distance  $x_3$  between the fixed magnets leads to a higher effect of an additional magnet in the ITPEH system to vibrating beam as well as deepening of potential barriers. Finally, taking these results into account, the energy harvesting effect was most enhanced for the ITPEH system activities by the narrowest air gap ( $x_2=11\text{mm}$ ) and the distance between the magnets ( $x_3=22.5$ ), while the lowest - for the system activities in configuration  $x_2=11\text{mm}$  and  $x_3=17.5\text{mm}$ .

The experimental tests of the TPEH and ITPEH systems car-

ried out on the lab stand for both real structures properly verified the numerical calculations. Comparing the results of the voltage output from the piezo-sensor again proved that the most impact of nonlinear magnetic force on the vibrating structure is achieved for the improved tri-stable energy harvesting system working with the narrowest air gap and the largest distance between the fixed magnets. The diagrams presented in Figs. 8-10 confirm these results. Their analysis indicated that introducing a singular additional fixed magnet to the conventional TPEH behavior of a magnetic coupling EH system can be increased. Especially, it can be seen in Fig.8 where a low value of base acceleration allows the magnetic force to appear in both systems only by air gap which equal 11mm. In the case of other air gaps, nonlinear magnetic force increasing the effectiveness of the EH system appears only in the ITPEH system.

Further analysis of diagrams in Figs.9-10 shows a significant advantage of the ITPEH system over the TPEH system, where a strong impact of the magnetic force due to considering additional magnet leads to generating a higher voltage output by piezo located on a vibrating beam. The RMS values of the voltage output collected in Tab.2 confirm these results. Taking these values into account, it can be concluded that tailoring potential energy in the tri-stable energy harvesting system leads to increasing the effectiveness of magnetic coupling EH systems.

In conclusion, both the numerical simulations and the experimental findings suggest that incorporating an additional fixed magnet into the conventional tri-stable energy harvesting (TPEH) system induces a nonlinear magnetic force with an increased amplitude, thereby boosts the voltage generated by the energy harvesting (EH) system. Consequently, the improved tri-stable energy harvesting (ITPEH) system, when coupled with a storage unit comprising of an optimal impedance load and a supercapacitor proves to be more efficient in powering small electrical devices with lower power demands compared to conventional TPEH systems.

Looking ahead, future studies could explore alternative methodologies for analyzing nonlinear time-series data, such as recurrence analysis [37] or the 0-1 test [38]. These approaches could provide further insights into the behavior and performance of ITPEH systems, potentially enhancing their applicability and effectiveness in various practical settings.

## REFERENCES

1. Bradai S, Naifar S, Viehweger C, Kanoun O, Litak G. Nonlinear analysis of electrodynamics broadband energy harvester. *European Physical Journal. Special Topics*. 2015; 224: 2919-2927.
2. Chen Y, Yan Z. Nonlinear analysis of axially loaded piezoelectric energy harvesters with flexoelectricity, *International Journal of Mechanical Science*. 2020;173:105473.
3. Koszewnik A, Lesniewski K, Pakrashi V. Numerical Analysis and Experimental Verification of Damage Identification Metrics for Smart Beam with MFC elements to support structural health monitoring. *Sensors*. 2021; 21(20): 6796.
4. Ambroziak L, Oldziej D, Koszewnik A. Multirotor Motor Failure Detection with Piezo Sensor. *Sensors*. 2023; 23(2):1048.
5. Yang F, Gao M, Wang P, Zuo J, Dai J, Cong J. Efficient piezoelectric harvester for random broadband vibration of rail. *Energy* 2021; 218: 119559
6. Koszewnik A. Analytical Modeling and Experimental Validation of an Energy Harvesting System for the Smart Plate with an Integrated Piezo-Harvester. *Sensors*. 2019; 19(4): 812



7. Cahill P, Hazra B, Karoumi R, Mathewson A, Pakrashi V. Vibration energy harvesting based monitoring of an operational bridge undergoing forced vibration and train passage. *Mechanical Systems and Signal Processing* 2018; 106: 265–283.
8. Koszewnik A, Oldziej D, Amaro M., Parameter of a Magnetic Coupled Piezoelectric Energy Harvester with the homogenized Material – numerical approach and experimental study. *Sensors*. 2022; 22: 4073.
9. Cottone F, Vocca H, Gammaitoni L. Nonlinear. Energy harvesting. *Physical Review Letters*. 2009; 102.8:080601.
10. Stanton SC, McGehee CC, Mann BP. Reversible hysteresis for broadband magnetopiezoelectric energy harvesting. *Applied Physical Letters*. 2009;95:174103.
11. Ferrari M, Ferrari V, Guizzetti M, Trigona C. Improved energy harvesting from wideband vibrations by nonlinear piezoelectric converters. *Sensors and Actuators A Physics*. 2010; 162: 425–431.
12. Tang L, Yang Y. A nonlinear piezoelectric energy harvester with magnetic oscillator, *Applied Physical Letters*. 2012; 101: 94102.
13. Margielewicz J, Gaska D, Caban J, Litak G, Dudziak A, Ma X, Zhou S. Double-versus triple-potential well energy harvesters: dynamics and power output. *Sensors* 2023; 23(4): 2185.
14. Zhou S, Cao J, Inman J, Lin D. Harmonic balance analysis of nonlinear tri-stable energy harvesters for performance enhancement. *Journal sound and Vibrations*. 2016; 373: 223-235.
15. Zhou J, Cao D, Inman J, Lin J, Liu S, Wang Z. Broadband tristable energy harvester: modeling and experimental verification. *Applied Energies*. 2014; 133: 33-39.
16. Cao J, Zhou S, Wang W, Lin J. Influence of potential well depth on nonlinear tristable energy harvesting. *Applied Physical Letters*. 2015; 106: 173903.
17. Kim P, Seok J. Dynamic and energetic characteristics of a tri-stable magnetopiezoelectric energy harvester, *Mechanical Machinery Theory*. 2015; 94: 41-63.
18. Kim P, Son D, Seok J. Triple-well potential with a uniform depth: advantageous aspects in designing a multi-stable energy harvester. *Applied Physical Letters*. 2016;108(24):243902
19. Kwiimy C, Wofo P, Tekam G. Analysis of tri-stable energy harvesting system having fractional order viscoelastic material. *Chaos*. 2015;25(1):013112.
20. Li H, Qin W, Lan C, Deng W, Zhou Z. Dynamics and coherence resonance of tri-stable energy harvesting system. *Smart Material Structures*. 2016;25(1):015001.
21. Cao Y, Yang J, Yang D. Coupling nonlinearities investigation and dynamic modeling of a tristable combined beam rotational energy harvesting system. *Mechanical Systems and Signal Processing*. 2023; 200: 110503.
22. Leng Y, Tan D, Liu J, Zhang Y, Fan S. Magnetic force analysis and performance of a tri-stable piezoelectric energy harvester under random excitations. *Journal Sound and Vibrations*. 2017;406:146-60.
23. Tan D, Leng YG, Gao YJ. Magnetic force of piezoelectric cantilever energy harvesters with an external magnetic field, *European Physical Journal Special Topics*. 2015; 224: 2839-2853.
24. Deraemaeker A, Benelechi S, Benjeddou A, Preumont A. Analytical and numerical computation of homogenized properties of MFCs: Application to a composite boom with MFC actuators and sensors. *Proceedings of the III ECCOMAS thematic conference on Smart Structures and Materials*. Gdansk Poland. 9–11 July 2007.
25. Deraemaeker A, Nasser H, Benjeddou A, Preumont A. Mixing Rules for the Piezoelectric Properties of Macro Fiber Composites. *J. Intell. Mater. Syst. Struct.* 2009; 20: 1475–1482.
26. Ksica F, Behal J, Rubes O, Hadas Z. Homogenized Model of Piezoelectric Composite Structures for Sensing Purposes. *Proceedings of International Conference Mechatronics 2019: Recent Advances Towards Industry 4.0*. 2019; 358-365.
27. Hu K, Li H. Large deformation mechanical modeling with bilinear stiffness for Macro-Fiber Composite bimorph based on extending mixing rules. *Journal of Intelligent Material Systems and Structures*. 2020; 1-13.
28. Biscani F, Nasser H, Belouettar S, Carrera E. Equivalent electro-elastic properties of Macro Fiber Composite (MFC) transducers using asymptotic expansion approach, *Composites. Part B*. 2011; 444-455.
29. Koszewnik A. Frequency domain identification of the active 3D mechanical structure for the vibration control system, *Journal of Vibroengineering*. 2012; 14(2): 451-457.
30. Kletsel M, Barukin A, Amirbek D. Reed Switch and Magneto Resistor-Based Differential Protection Featuring Test Diagnostics for Converters. *2020 International Multi-Conference on Industrial Engineering and Modern Technologies*. Russia. 2020; 1-6.
31. Fan K, Tan Q, Liu H, Zhang Y, Cal M. Improved energy harvesting from low-frequency small vibrations through a monostable piezoelectric energy harvester. *Mechanical Systems and Signal Processing*. 2019; 117: 594-608.
32. Lallart M, Anton SR, Inman DJ. Frequency self-tuning scheme for broadband vibration energy harvesting, *Journal of Intelligent Material Systems and Structures*. 2010; 21(9): 897-906.
33. Caban J, Litak G, Ambrozkiewicz B, Gardyński L, Stączek P, Wolszczak P. Impact-based piezoelectric energy harvesting system excited from diesel engine suspension. *Applied Computer Science* 2020; 16(3): 16-29.
34. Erturk A, Hoffmann J, Inman DJ, A piezomagnetoelastic structure for broadband vibration energy harvesting. *Applied Physics Letters*. 2009; 94(25): 254102.
35. Łepicka M, Górski G, Grądzka-Dahlke M, Litak G, Ambrozkiewicz B, Analysis of tribological behaviour of titanium nitride-coated stainless steel with the use of wavelet-based methods. *Archive of Applied Mechanics*. 2021; 91(11): 4475-4483.
36. Wang C, Zhang J, Zhu HP. A combined method for time-varying parameter identification based on variational mode decomposition and generalized morse wavelet. *International Journal of Structural Stability and Dynamics* 2020; 20(7): 2050077.
37. Syta A, Czarnigowski J, Jakliński P. Detection of cylinder misfire in an aircraft engine using linear and non-linear signal analysis. *Measurement: Journal of the International Measurement Confederation*. 2021; 174: 108982.
38. Litak G, Syta A, Budhreja M, Saha LM. Detection of the chaotic behaviour of a bouncing ball by the 0-1 test. *Chaos. Solutions and Fractals* 2009; 42(3): 1511-1517.

This work is supported by the University Work no WZ/WM-IIM/4/2023 of the Faculty of Mechanical Engineering, Białystok University of Technology.

Andrzej Koszewnik:  <https://orcid.org/0000-0001-6430-6007>

Bartłomiej Ambrozkiewicz:  <https://orcid.org/0000-0002-8288-5230>



This work is licensed under the Creative Commons BY-NC-ND 4.0 license.

# EVALUATION OF FLOW RESISTANCE INCREASE DUE TO FOULING IN COOLING CHANNELS: A CASE STUDY FOR RAPID INJECTION MOLDING

Tomasz PRZYBYLIŃSKI<sup>\*✉</sup>, Adam TOMASZEWSKI<sup>\*✉</sup>, Zbigniew KRZEMIANOWSKI<sup>\*/\*\*✉</sup>  
Roman KWIDZIŃSKI<sup>\*✉</sup>, Paulina ROLKA<sup>\*✉</sup>, Grzegorz SAPETA<sup>\*\*✉</sup>, Robert P. SOCHA<sup>\*\*✉</sup>

<sup>\*</sup>Institute of Fluid-Flow Machinery of the Polish Academy of Sciences,  
Józefa Fiszer 14, 80-231, Gdańsk, Poland

<sup>\*\*</sup>CBRTP SA – Research and Development Center of Technology for Industry,  
Ludwika Waryńskiego 3A, 00-645, Warsaw, Poland

[przybylinski@imp.gda.pl](mailto:przybylinski@imp.gda.pl), [atomaszewski@imp.gda.pl](mailto:atomaszewski@imp.gda.pl), [krzemian@imp.gda.pl](mailto:krzemian@imp.gda.pl)  
[rk@imp.gda.pl](mailto:rk@imp.gda.pl), [prolka@imp.gda.pl](mailto:prolka@imp.gda.pl), [grzegorz.sapeta@cbrtp.pl](mailto:grzegorz.sapeta@cbrtp.pl), [robert.socha@cbrtp.pl](mailto:robert.socha@cbrtp.pl)

received 27 November 2023, revised 3 April 2024, accepted 16 April 2024

**Abstract:** After certain time of operation, the cross-section of cooling channels in injection molds may decrease due to fouling, i.e. the formation and growth of a layer of sediment on the walls of the channels. This phenomenon can decrease heat transfer or ultimately completely block the flow of coolant in the channel. The build-up of the sediment layer increases the temperature of the mold, which may consequently reduce the quality of the plastic products. In the paper, the pressure drop in a typical cooling channel of an injection mold is investigated, as well as the effect of the sediment layer on the coolant flow in an example channel with a diameter of 10 mm. A novelty is the developed analytical model that allows determining the pressure drop in the case when two perpendicular channels do not intersect centrally due to manufacturing inaccuracies that often happen when drilling long channels in hard materials. The proposed hydraulic model allows for calculation of the coolant pressure drop in real injection molds and can be an alternative to time-consuming CFD simulations. The presented results of measurements and the hydraulic model calculations show that the thickness of the sediment layer in the tested channel of the actual injection mold can be up to 1.7 mm. The hydraulic model proposed in this work allows for the estimation of the thickness of the sediment layer and the identification of places of local increase in the coolant velocity, where self-cleaning of the channels in injection molds may take place.

**Keywords:** high-pressure injection molding, fouling of injection molds, cooling of mold channels, modeling of pressure losses, CFD

## 1. INTRODUCTION

Injection molding is currently one of the most intensively developing industries. This is due to the huge increase in global demand for thermoplastic products, which include household, electrical, electronic, medical articles, toys and others [1]. Basically, objects made of thermoplastic materials have been in use for a long time (the history of their manufacture dates back to the mid-19th century [2]) and it is no longer possible to imagine the everyday life without them. They are produced in huge quantities around the world and for this reason the use of injection molds is already widespread. However, this also causes certain problems in the operation of injection machines, which include proper cooling of the molds so that they work effectively, i.e. with optimal productivity.

The key problem that occurs during the operation of the injection mold installation is the formation of a layer of sediment in the mold cooling channels. The build-up of the deposits leads to a reduction in the heat transfer between the thermoplastics and cooling fluid. As a result, there is a decrease in mold efficiency, which results in fewer products being formed over time. There are also problems with the product surface quality due to insufficient cooling during mold clamping. One of the reasons for the accumulation of sediment is the presence of chemicals such as calcium and magnesium carbonate in the water flowing through the cool-

ing channel. The second important factor causing the sediments growth is the high temperature of the channel wall, which promotes the formation of structures of living microorganisms that accumulate on the walls and narrow the cooling channel of the injection mold. Sediment restricts coolant flow and reduces heat transfer, increasing energy consumption [3]. A way to slow down fouling is to use self-cleaning surfaces [4] but in the long term a decrease in the heat transfer rate should be expected. Diagnostics of fouled channels is very difficult, but not impossible [5-7], which is why numerical techniques such as CFD are widely used here. CFD simulations allow for the identification of flow-critical zones, which can ultimately lead to the loss of coolant flow and/or local overheating of the thermoplastic material.

Manufacture of parts from thermoplastic material by injection molding consists of a very quick injection of the molten material into a mold shaped like the element being produced. As the temperature of the molding surface is much lower than that of the injected material, the material cools down quickly and solidifies within seconds. Further and deepest cooling occurs after opening of the injection mold, but before that the material should have solidified sufficiently to prevent it from pouring and deforming the final surface. This is one of the key phases of the injection process, having a large impact on the quality of the manufactured elements, especially the thin-walled ones. The temperature distribution in the mold should be as uniform as possible, because

improper cooling of the thermoplastic material causes destruction of the manufactured element if it does not reach solidification temperature in the right time [8]. Therefore, the proper choice of the cooling method is extremely important and gives great technological benefits [9-10]. It should be remembered that the injection is a process with high load dynamics of the injection machine in terms of temperature changes. The procedure of closing the two halves of the injection mold, injection of the raw material and opening of the mold takes place in a short time, counted in several dozen seconds. It is also half of the production time for a single product [11]. This duration is directly related to the efficiency of the cooling channels that must continuously remove heat from the injection mold to ensure proper production quality. Channel surface roughness is a key parameter for coolant flow [12-13].

The gradual narrowing of the cooling channels reduces the cooling intensity and, consequently, leads to the formation of insufficiently cooled areas, around which the molded product is most vulnerable to damage due to shape deformation after opening the mold, as well as to improper shrinkage of the material and the formation of incorrect roundness [14-16]. It is also important to properly distribute the cooling channels in the mold, leading to the so-called conformal layout, ensuring relatively equal distances among them and therefore rational (initial) optimization of the heat transfer and reduction of the cycle time [17-18]. This is the reason for the recent intensive development of methods for designing and optimizing the shape of cooling channels for various thermoplastic objects [19-22]. Thanks to the remarkable development of the injection molding technology in the modern world and striving for high efficiency of the process, many already published papers describe the methods of effective injection through the appropriate distribution of conformal cooling channels (CCC). Silva et al. [23] and Kanbur et al. [24] published reviews, in which they focused on the current state of the design, simulation and optimization of the CCC in injection molds. In turn, Feng et al. [25] presented an overview of the design and manufacturing of the CCC. Generally, in order to achieve uniform and fast cooling, some of the key design parameters of the CCC, related to the shape, position and size of the channel must be carefully calculated and selected, taking into account the cooling capacity, mechanical strength and pressure drop of the coolant. Yao et al. [26] provided an overview of state-of-the-art in rapid heating and cooling in molding technology, aiming to explain the working mechanisms and giving information on the advantages and disadvantages of existing techniques and processes. Muvunzi et al. [27] described a method for design conformal cooling channels in stamping tools. The method uses evaluation of a part to make decision whether it is suitable for additive manufacturing applications, and then determining conformal cooling parameters and analyzing alternative systems.

Kanbur et al. [28] published a paper on metal additive manufacturing (MAM) of inserts for plastic injection molds with various types of CCC, i.e. circular, serpentine and tapered channels. Compared to traditional channels, CCC provide up to 62.9% better cooling efficiency with better thermal uniformity on the mold surfaces. According to Kuo et al. [29-30], MAM techniques are often used in the fabrication of injection molds with CCC to reduce cooling time in the injection molding process. Reducing the cooling time in the cooling stage is essential to reduce energy consumption in mass production. The cooling time of the injection molding process accounts for approximately 60 to 80% of the entire molding cycle. However, the disadvantages include higher production costs and longer processing time when manufacturing an injection mold with CCC.

Kuo et al. [31] also proved that CCC in silicone rubber mold (SRM) after injection molding has a poor cooling performance due to low thermal conductivity. To improve this, the thermal conductivity was intensified by adding fillers (e.g. metal powder) to SRM. As a result, the cooling time of the injection molding could be shortened by up to 69.1% compared to conventional SRM.

Wei et al. [32] pointed out the importance of cooling in injection molds and discussed the development of cooling systems. Park et al. [33] presented a method of a plastic injection molding with increased cooling efficiency. The method leads to an increase in the molding process efficiency due to the use of a properly defined computer-aided engineering technique resulting in the optimal layout of the cooling channels. Papadakis et al. [34] presented a holistic approach to the design and use of additively manufactured mold inserts with conformal cooling channels using selective laser melting (SLM) to shorten process cycles. Jahan et al. [35-36] investigated the influence of critical design parameters of conformal channels and their cross-sectional geometry, and proposed a methodology to generate optimized channel configurations.

This paper concerns the numerical modeling of flow resistance in the cooling channels of the injection mold. In particular, the effect of a sediments accumulating on the cooling channel wall is analyzed for the coolant flow in the selected injection mold channel. For this purpose, calculations were carried out using numerical fluid mechanics simulations and analytical calculations with the equations of own-developed hydraulic model. The hydraulic model equations include new formula for evaluation of the pressure loss in an elbow with contraction found in the investigated cooling channels.

The manuscript presents a new hydraulic model, that can be used to assess the pressure drop in a channel with strongly narrowing flow cross-sections due to fouling of the channel walls. The proposed analytical hydraulic model allows for the first time to determine the pressure drop in the case where two perpendicular channels do not intersect centrally. This imperfection often occurs in real injection mold channels due to the difficulty of maintaining the correct direction when drilling long channels in hard materials. The proposed hydraulic model is relatively simple to implement and can replace time-consuming CFD calculations requiring high computing capacity. The paper draws attention to the strongly non-linear problem of pressure drop in fouled channels caused by the narrowing of their cross-sections. When a certain fouling thickness is exceeded, the circulation pump discharge pressure must be significantly increased to ensure proper operation of the channel at the design flow rate. In practice, this means that after some time the circulation pump is unable to maintain the design flow parameters and the mold in the vicinity of the fouled channel is insufficiently subcooled. This may then cause local distortions of the injected product and defects on its surface, as well as extending the molding cycle, which adversely affects economic efficiency and eliminates the mold from production until it is renovated.

## 2. DESCRIPTION OF THE INVESTIGATED INJECTION MOLD

The object produced in the mold is a basket-like box of the shape shown in Fig. 1 and dimensions 280×190×140 mm (length × width × height). The box is made by injecting plastic material into the injection mold, half of which is shown in Fig. 2. The shape



of the water channel that was selected for the present study is also highlighted there.

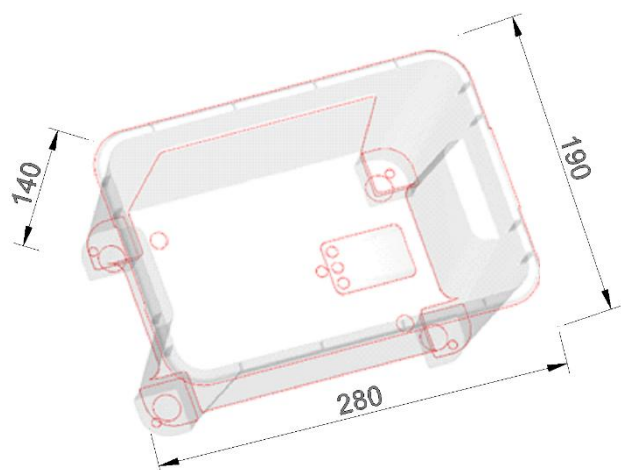


Fig. 1. Shape of the product outer surface in the injection mold

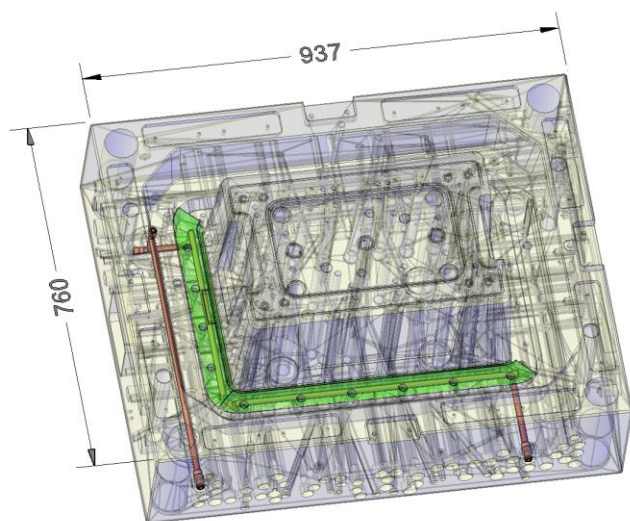


Fig. 2. Water cooling channels in the mold with the selected channel highlighted

The selected channel is shown in detail in Fig. 3 with a portion of the mold encompassing the surface around the top edge of the molded box. Approximately, this part of the product surface is directly cooled by the channel of interest by the coolant (water) that flows in the direction also indicated in the Fig. 3. The heat is transferred to the mold through the surface shown. Then, the heat from this part of the mold is removed by the coolant flow. However, in the further part of the paper, the heat transfer is not considered and only the pressure drop resulting from changes in the channel cross section is investigated. The diameter of the straight sections of the selected channel without sediment is 10 mm.

The main operational problem of the investigated mold is fouling of the cooling channels because the circulating cooling water cannot be properly treated and filtered. An example of a fouled channel in a mold withdrawn from use is presented in Fig. 4. A dead end section of the channel (other than that in Fig. 3) is shown there in two cross-sections – radial and axial. It can be seen in the photographs that an irregular layer of sediment covers the entire inner surface of the channel. The sediment itself has the

appearance of limescale with a very rough surface. The thickness of the sediment varies along the channel and can change significantly even over a short distance. Despite this, in the following studies an average, constant sediment thickness is assumed, although locally it may differ significantly from this average. This simplification results from the difficulty in clearly determining thickness changes using a non-invasive method.

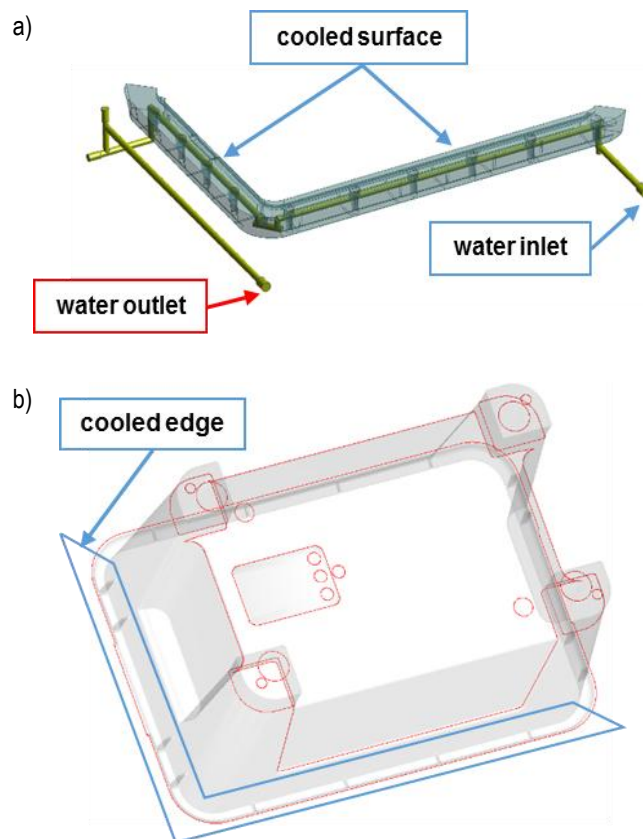
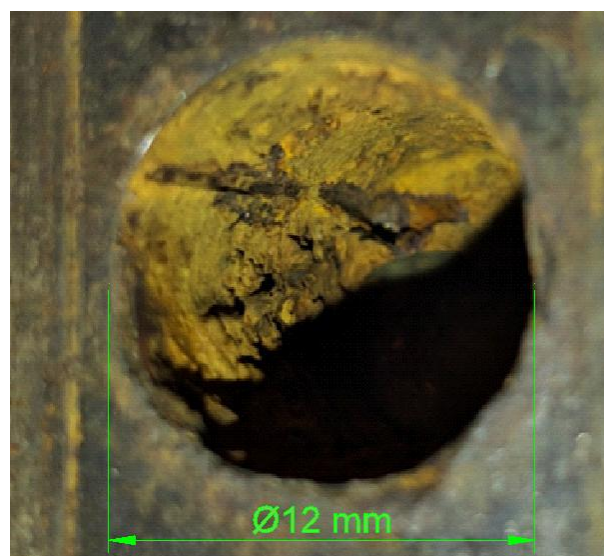
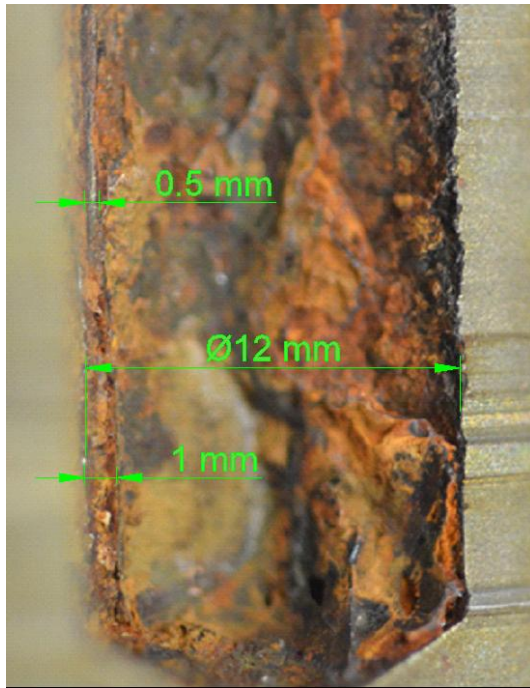


Fig. 3. a) View of the cooling channel that was selected for evaluation of the flow resistance in injection mold; b) location of the edge of the molded box cooled by the selected channel





**Fig. 4.** Sediments in a fouled cooling channel visible in a section cut from a worn-out injection mold; a variable sediment thickness is visible, which is difficult to quantify due to its roughness

### 3. EXPERIMENTAL SET-UP

The experimental set-up was mounted on the injection mold that during the tests was normally operating in production. To register flow data from active water channels, a bypass was made equipped with a pump (1) to circulate water in a single channel under test, see Fig 5. The coolant flow rate was measured by ultrasonic meter Flexim Fluxus 608, (5), and the differential pressure by ZAP IPA-01 transducer, (4). Absolute pressure was also measured by pressure transducers Wika S-20, (3), mounted at the inlet and outlet from each water channel. Temperature difference (2) was measured using two calibrated thermocouples of type K (Czaki TP-234). The accuracy of the measuring instruments was as follows: 1.6% of full scale (FS) for flow rate, 1% FS for differential pressure, 0.25% FS for absolute pressure and 0.1 K for temperature. Measurements were done in 10 channels but only one of them was selected for detailed analysis of the total pressure drop presented in the next sections. Namely, the measured flow rates and pressure differences were used to compare with the results of the developed mathematical model and with CFD simulations for the coolant flow in one of measured channels, depicted in Fig. 3.

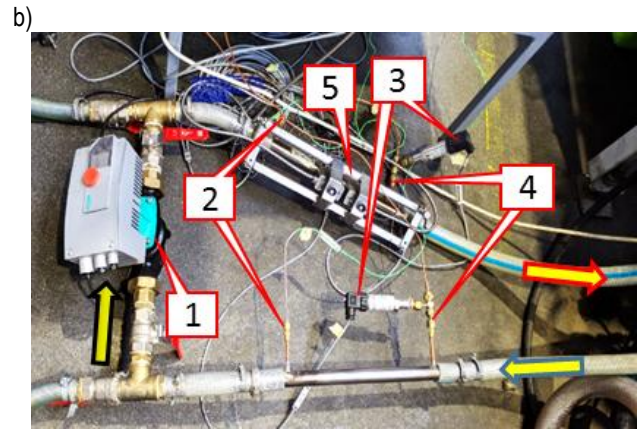
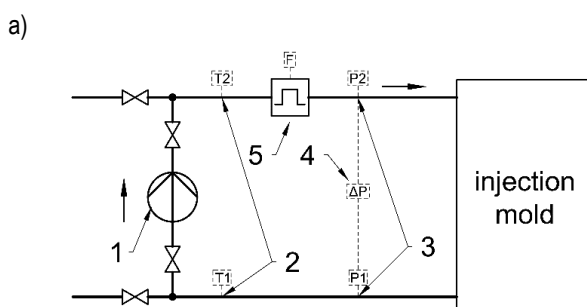


**Fig. 5.** Schematic of the measurement loop (a) and its view during measurement campaign (b): 1 – circulating pump, 2 – two thermocouples, 3 – two absolute pressure transducers, 4 – differential pressure transducer (only its pressure lines are visible in the photograph), 5 – ultrasonic flow meter

### 4. HYDRAULIC MODEL OF PRESSURE LOSSES

To estimate the thickness of sediment layer in the real cooling channel, based on total pressure drop measurement at its ends, and with its 3D geometry available, a theoretical model of the pressure drop was developed. The dependency between pressure drop calculated with this model and the sediment thickness was compared and calibrated with numerical results of the CFD simulations. Then, based on experimental results it was possible to evaluate approximate thickness of the sediment layer for a given pressure drop and mass flow rate of the cooling medium in the real mold.

Analytical calculations were made basing on a mathematical model of hydraulic resistance that allows determining the pressure losses arising in straight sections of the cooling channel as well as the resistance appearing locally in the channel contractions and elbows. The results evaluated from the proposed hydraulic model can then be compared with the pressure profiles from CFD simulations. In the examined cooling channel, there are several sections generating local pressure drop. All of them are identified in Fig. 6. The hydraulic model assumptions and calculation methodology are presented below.

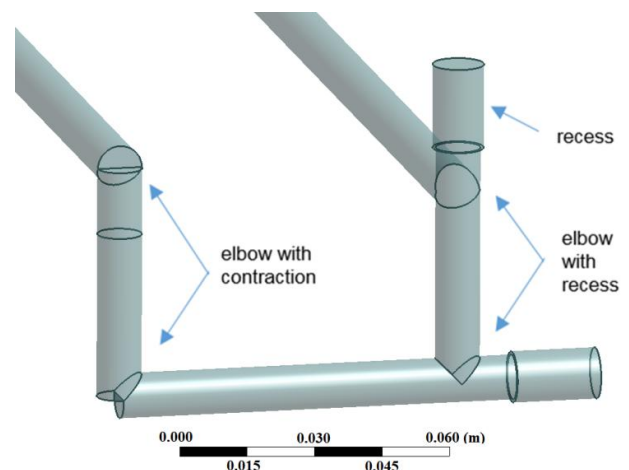


**Fig. 6.** Types of obstructions with significant local pressure drop in the investigated channel



The assumptions made in the formulation of the mathematical model of hydraulic resistance are as follows:

- total hydraulic pressure loss in the channel is superposition of frictional and local losses,
- the pressure loss is proportional to dynamic pressure and a proper resistance coefficient,
- total hydraulic resistance of an elbow with contraction is a sum of three components arising from a locally reduced cross-section, then again a locally increasing cross-section and from a change of the flow direction by  $90^\circ$ ,
- the channel and elbows cross-section areas depend on the thickness of the sediment layer,
- the minimum flow area in the elbow with contraction is a segment of ellipse with semi-axes  $a_0$  and  $b_0$ ,
- the sediment layer is homogenous and of uniform thickness along the whole channel.

The calculations of hydraulic resistance are based on the handbook by Idelchik [38].

#### 4.1. Evaluation of pressure drop on elbows with contraction

Before the hydraulic resistance of the elbow with contraction can be evaluated, first the contraction minimum area as a function of sediment layer thickness needs to be determined.

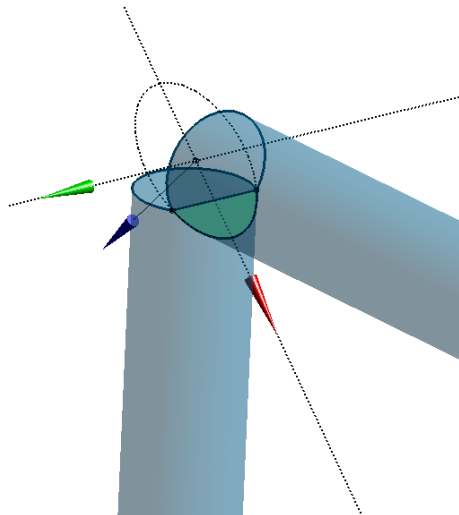
The considered narrowest cross-section surface in the elbow with contraction is an elliptical section shown in Fig. 7. Its area  $A_1$  was evaluated based on analytical geometry, assuming that the ellipse center is located at the origin of the coordinate system. Therefore, the channel cross-sectional area at the narrowest point, expressed as a function of sediment thickness  $\delta$ , is found from the formula:

$$A_1(\delta) = a_0(\delta)b_0(\delta) \arccos\left(\frac{\sqrt{2}\delta}{b_0(\delta)}\right) - \sqrt{2}\delta \sqrt{a_0^2(\delta) - 2\left(\delta \frac{a_0(\delta)}{b_0(\delta)}\right)^2}, \quad (1)$$

$$a_0(\delta) = r_c - \delta \quad (2)$$

$$b_0(\delta) = \sqrt{2}(r_c - \delta) \quad (3)$$

a)



b)

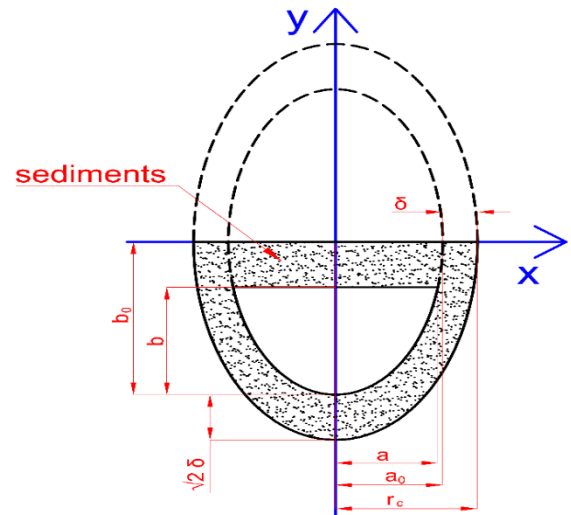


Fig. 7. The minimum cross-section of the channel open for flow in the elbow with contraction (a) is an elliptical segment (b) with dimensions  $a$  and  $b$  that depend on the sediment thickness  $\delta$

Cross section area ratio in the contraction is defined as

$$\beta_1(\delta) = \frac{A_1(\delta)}{A_0(\delta)}, \quad (4)$$

where  $A_0$  is the cross section surface of a straight channel immediately upstream of the elbow, as follows:

$$A_0(\delta) = \pi(r_c - \delta)^2. \quad (5)$$

As already stated, the pressure loss in the elbow is proportional to the dynamic pressure  $p_d$ , which is denoted as  $p_{d0}$  and  $p_{d1}$  in the initial cross-section and on the contraction, respectively, and amounts to:

$$p_{d0}(\delta) = \rho \frac{v_0^2(\delta)}{2}. \quad (6)$$

$$p_{d1}(\delta) = \rho \frac{v_1^2(\delta)}{2}, \quad (7)$$

where the flow velocities are given by equations:

$$v_0(\delta) = \frac{\dot{m}}{\rho A_0(\delta)}. \quad (8)$$

$$v_1(\delta) = \frac{\dot{m}}{\rho A_1(\delta)}. \quad (9)$$

Pressure loss due to local cross-section decrease (the elliptical segment) was calculated from formula:

$$\Delta p_1(\delta) = \xi_1(\delta) p_{d1}(\delta), \quad (10)$$

where  $\xi_1(\delta)$  is the loss coefficient due to a sudden reduction of cross section [38], which is given as follows:

$$\xi_1(\delta) = \frac{0.0765}{\mu_p(\delta)^2} + \left(\frac{1 - \mu_p(\delta)^2}{\mu_p(\delta)}\right), \quad (11)$$

$$\mu_p(\delta) = 0.2487\beta_1^2(\delta) + 0.0496\beta_1(\delta) + 0.6381, \quad (12)$$

that depends both on the sediment thickness  $\delta$  and the area ratio  $\beta_1$ .

The pressure loss due to local cross-section increase at the elbow outlet was calculated from:

$$\Delta p_{12}(\delta) = \xi_{12}(\delta) p_{d1}(\delta), \quad (13)$$

where  $\xi_{12}(\delta)$  is the loss coefficient due to a sudden expansion of cross section [38], which is given as follows:

$$\xi_{12}(\delta) = 1 - \beta_1^2(\delta). \quad (14)$$

In addition, the pressure loss due to a sudden flow direction change by  $90^\circ$  is calculated from:

$$\Delta p_{90}(\delta) = \xi_{90}(\delta) \cdot p_{d0}(\delta), \quad (15)$$

where  $\xi_{90}(\delta) = 2.0$  is the pressure loss coefficient due to the change of flow direction by  $90^\circ$ . The optimal value of this coefficient was determined after comparison with the CFD simulations in order to achieve good agreement of the hydraulic model with the numerical results. However, the Idelchik's handbook [38] recommends lower value of 0.98 for a circular channel and  $90^\circ$  elbow. For the geometry investigated here, the elbow shape is different and using the formulas from Idelchik directly leads to underestimated value of pressure drop in the channel.

Finally, the total pressure drop on the elbow with contraction (Fig. 7) is the sum of three components:

$$\Delta p_{cont}(\delta) = \Delta p_1(\delta) + \Delta p_{12}(\delta) + \Delta p_{90}(\delta), \quad (16)$$

that are evaluated from Eqs. (10, 13, 15).

#### 4.2. Evaluation of pressure drop on $90^\circ$ elbows with recess

To evaluate the pressure loss on the elbows with recess, the previously calculated dynamic pressure in the initial cross-section  $p_{d0}$ , Eq. (6), was used with appropriate coefficient of hydraulic resistance:

$$\Delta p_{elbow}(\delta) = \xi_{elbow}(\delta) p_{d0}(\delta). \quad (17)$$

The coefficient  $\xi_{elbow}$  for the elbow with recess (a dead end) was calculated according to [38]:

$$\xi_{elbow}(\delta) = 1.2 k_{\Delta} k_{Re} C_1 A \xi_1, \quad (18)$$

where:

$$k_{Re} = \frac{45}{(1.8 \log(Re_0) - 1.64)^2}, \quad (19)$$

$$Re_0(\delta) = 2\rho v_0(\delta) \frac{a_0(\delta)}{\mu}, \quad (20)$$

and  $C_1 = 1$ ,  $\xi_1 = 0.99$ ,  $A = 1.2$ ,  $k_{\Delta} = 1$ , are coefficients with values valid to the elbow angle of  $90^\circ$ .

#### 4.3. Evaluation of pressure drop in straight ducts

Pressure losses along straight sections of the cooling channel are proportional to the channel length  $L$  and the friction factor  $\lambda$ . They were evaluated using the Darcy-Weisbach equation:

$$\Delta p_L(\delta) = \lambda(\delta) \frac{L \cdot p_{d0}(\delta)}{2a_0(\delta)}, \quad (21)$$

where:

$$\lambda(\delta) = \frac{0.3164}{Re_0(\delta)^{0.25}}. \quad (22)$$

The above formulas are valid for a turbulent flow in circular channels.

#### 4.4. Total pressure drop in the cooling channel

The total pressure drop in the examined cooling channel is evaluated as the sum of the local losses on three elbows with contractions, seven elbows with recess and frictional loss along the entire channel length:

$$\Delta p(\delta) = 3\Delta p_{cont}(\delta) + 7\Delta p_{elbow}(\delta) + \Delta p_L(\delta). \quad (23)$$

The components in the above sum are evaluated from Eqs. (16, 17, 21).

#### 4.5. The results of the hydraulic model application

Calculations with the equations of the proposed hydraulic model were made for the thickness of sediment layer in a range from 0 mm (clear channel) to 2.0 mm. The results for the channel without sediment are summarized in Table 1. The results for sediments growing from 0 to 2.0 mm are presented in the form of graphs in Fig. 8 and 9.

**Tab. 1.** The results of hydraulic model in the case without sediments

Parameter [unit]	Value
$A_1$ [mm <sup>2</sup> ]	55.5
$A_0$ [mm <sup>2</sup> ]	78.5
$v_0$ [m/s]	1.13
$v_1$ [m/s]	1.6
$p_{d0}$ [kPa]	0.64
$p_{d1}$ [kPa]	1.28
$\Delta p_{cont}$ [kPa]	1.63
$\Delta p_{elbow}$ [kPa]	1.03
$\Delta p_L$ [kPa]	3.65
$\Delta p$ [kPa]	15.74

According to the hydraulic model, the cross-section open to the flow in the elbows with contraction decreases rapidly with the growth of the sediment layer. After reaching some critical value of layer thickness (more than 2 mm), the flow in the channel can be fully blocked. Below, in Fig. 8, the dependency between the flow cross-section area and sediment layer thickness is presented both for the straight channel segments and for the elbow with contraction.

Reduction of the channel cross-section that is open to the coolant flow affects significantly the pressure drop, which is presented in Fig. 9, where all contributions to the total pressure loss are shown. It can be seen that with the growth of the sediment thickness, the pressure loss in the elbows with contractions dominates the other losses, while pressure losses on the elbows with recess and in the straight segments make only a minor contribution to the total pressure loss.

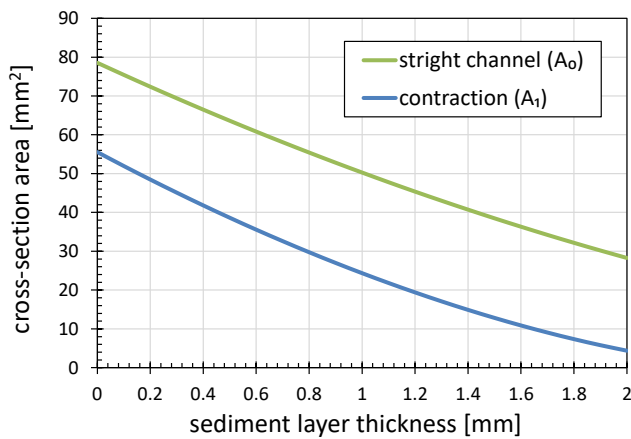


Fig. 8. Cross-section area of the straight channel segments  $A_0$  and of the elbow with contraction  $A_1$  as a function of the sediment layer thickness  $\delta$

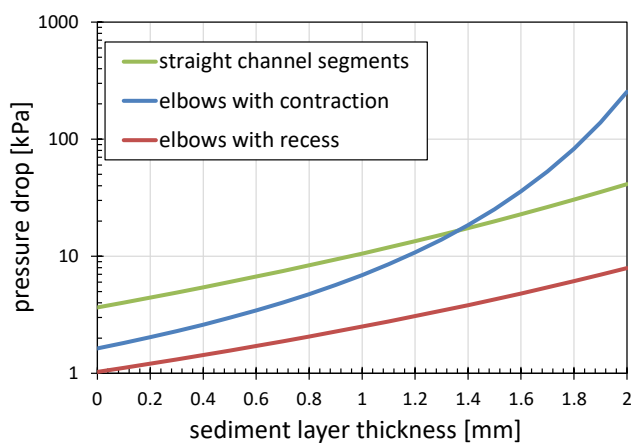


Fig. 9. Pressure drop in three elbows with contraction ( $\Delta p_{\text{cont}}$ ), seven elbows with recess ( $\Delta p_{\text{elbow}}$ ) and along the straight channel segments ( $\Delta p_L$ ) as a function of sediment layer thickness  $\delta$

## 5. NUMERICAL SIMULATION

Numerical simulation was prepared to investigate in detail the fluid flow and pressure drop in the selected cooling channel – Fig. 10. The 3D geometry of the entire injection mold was delivered by manufacturing company involved in the project. Thence, the geometry of single cooling channel was isolated and imported to commercial software where computational domain was prepared. Since the sediment layer was also to be included in the analysis, four different geometries were created for the sediments thickness equal to 0 mm (clean wall), 1.3 mm, 1.7 mm and 2 mm.



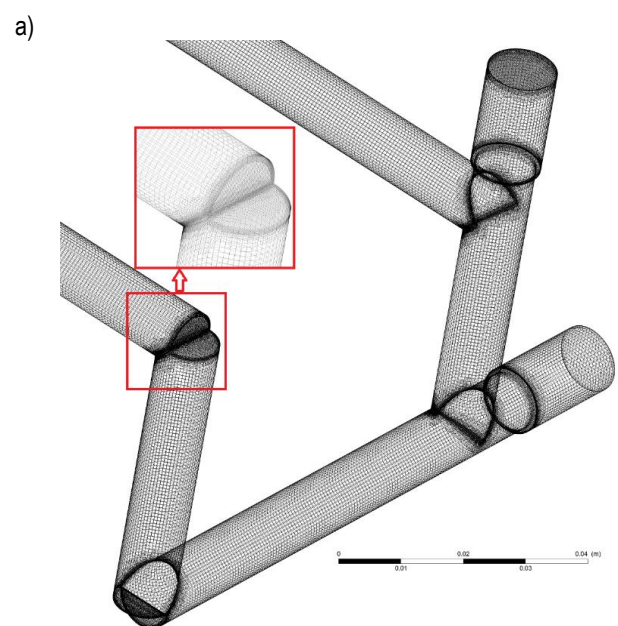
Fig. 10. The computational domain for CFD simulation

Significant heat transfer and flow resistance problems due to the increase in sediment thickness appear in certain places in the channel, predominantly around the elbows. There are two types of elbows in the examined channel, see Fig. 6. The elbows with contraction can become very narrow as the sediments grow and huge pressure losses are expected in these locations. Therefore, alternative (modified) geometry with repaired contractions was also analyzed.

The domain for the case without sediments is depicted in Fig. 10, in which the channel inlet and outlet are also indicated. The next step of the numerical analysis was domain discretization. The domain was imported to meshing software where it was divided into 2 million quadrilateral elements – Fig.11a. The mesh was refined near each elbow and cross-section change. The boundary layer consisting 10 sublayers was also created and the first layer thickness fulfilled the condition of  $Y^+ = 3$ , which was a reasonable value for further calculations.

The computational mesh was imported to CFD solver. Steady state analysis with the use of the “Pressure-Based” solver was performed. Gravity acceleration and realizable  $k-\varepsilon$  model with enabled “Scalable wall function” option were set in the model. Water liquid was flowing through the channel and the water properties such as density and dynamic viscosity were set for the temperature 10°C. The boundary conditions were set as mass flow inlet with the mass flow rate  $\dot{m} = 0.089$  kg/s (6 l/min) and pressure outlet with reference pressure  $p_{\text{out}} = 101.3$  kPa. No slip wall condition was also set in the model on the channel wall.

Numerical results are presented below for three of the investigated cases. The first one represents the original channel without sediment layer, the second one applies to the original channel with sediment layer of 1.7 mm thickness. In the third case the channel geometry was modified and 1.7 mm sediment layer was present. In the modified channel, the contractions in the elbows were removed to avoid excessive pressure losses. For clarity, the calculated distributions of pressure and velocity contours are shown below only for a part of the entire channel, which comprises the two types of elbows and is located close to the channel outlet. This can be seen in Fig.11b.



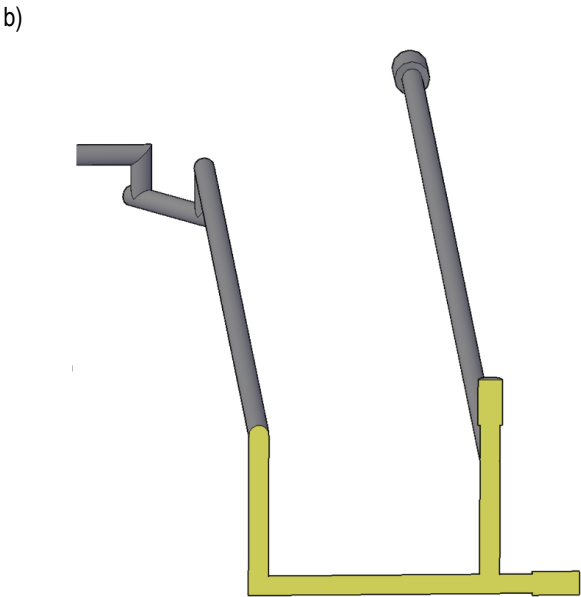


**Fig. 11.** a) Mesh in the computational domain, b) cross-section of the channel (yellow) in which pressure and velocity distributions are presented

Simulation results for the case without sediments (clean wall) and original geometry with contractions are presented in Fig. 12 and 13. Static pressure is shown in Fig. 12 for a segment of the channel that contains both types of elbows. As can be seen in Fig. 6, fluid flows through 4 types of obstacles in this segment that cause significant pressure drop. First, there are two elbows with contraction and then there are two elbows with recess (without contraction). In the figures, cooling water flow direction is from the upper left corner to the upper right corner of the image. The total pressure drop is around 5 kPa (Fig. 12). In the Fig. 13, the contours of velocity are depicted and the highest velocity values are observed inside the contractions due to decreased cross section. The maximum value of water velocity is 2.32 m/s, while the average velocity in straight ducts is around 1 m/s. Even with no sediment layer, the velocity increases by more than 200% in the narrowest cross-section. As can be seen in the figure, there is almost no flow in the recess of the channel (which is at the lower right part of the image).

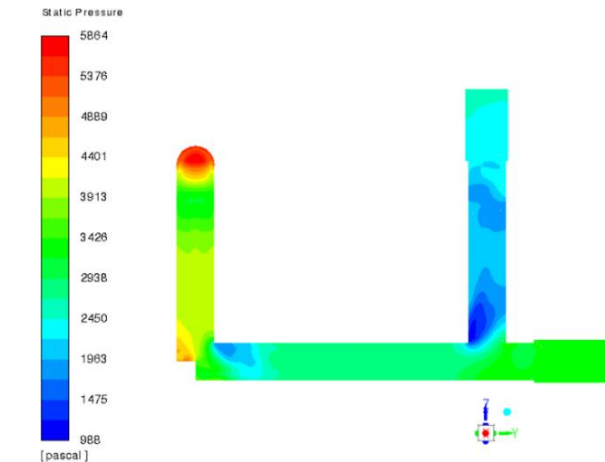


**Fig. 12.** The contours of static pressure distribution in the selected channel section without sediments

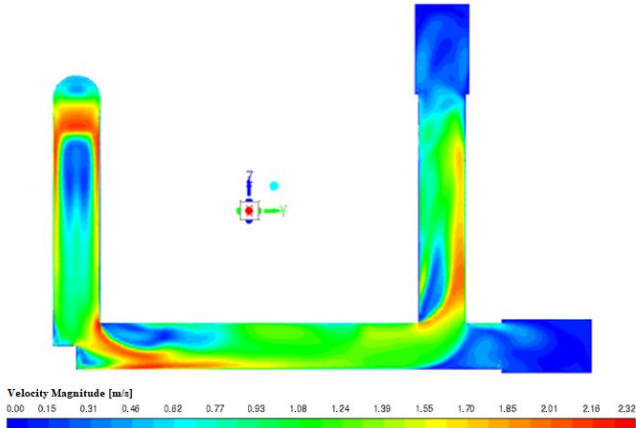


**Fig. 13.** The contours of velocity in the selected channel section without sediments

The case with 1.7 mm thick sediment layer was chosen as a representative due to similar total pressure drop in the whole channel measured in the real mold, which will be shown in the further part of the paper. The contours of static pressure for this case are presented in Fig. 14. The total pressure drop along the section is much higher than for the previous case without sediment layer. The most significant pressure losses are observed on elbows with contraction. They amount to about 50 kPa and are around 10 times higher than for the elbow with recess, where approximately 5 kPa was calculated. In the calculations, the constant mass flow rate in the single channel was forced. However, in reality there are many cooling channels connected in parallel. In such case, the channel with greatest contraction will have a significantly reduced coolant flow and eventually the flow may be completely blocked. In Fig. 15, there are presented contours of velocity, which maximum value is 12.25 m/s and is much higher than recommended design standard. The maximum value should be around 3 m/s. The velocity in the contraction is over 6 times higher than the value in the same location without sediment. For the elbow without contraction, high values of velocity around 5 m/s are also observed. Based on Fig. 13 and Fig. 14, it can be concluded that the calculated values of pressure and velocity in the channel with 1.7 mm of sediment are very far from the appropriate and recommended standards adopted in the design process of heat exchangers. In such case, the channels should be immediately regenerated to ensure adequate cooling.

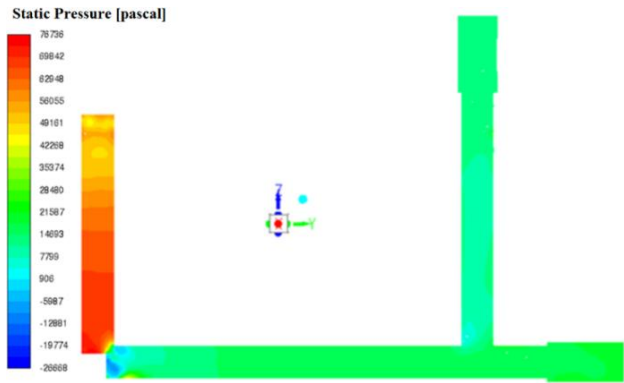


**Fig. 14.** The contours of static pressure distribution in the selected channel section with 1.7 mm thick sediment layer

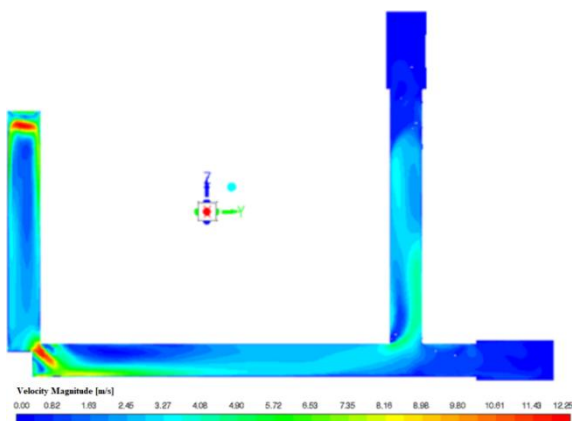


Fig. 15. The contours of velocity in the selected channel section with 1.7 mm thick sediment layer

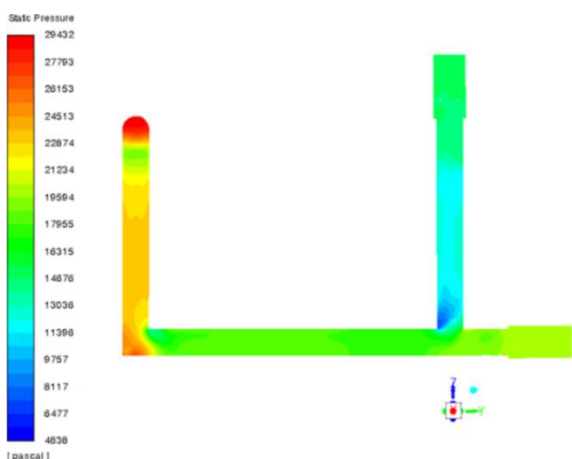


Fig. 16. The contours of static pressure distribution in the selected channel section with modified elbows geometry (contractions eliminated) and 1.7 mm thick sediment layer

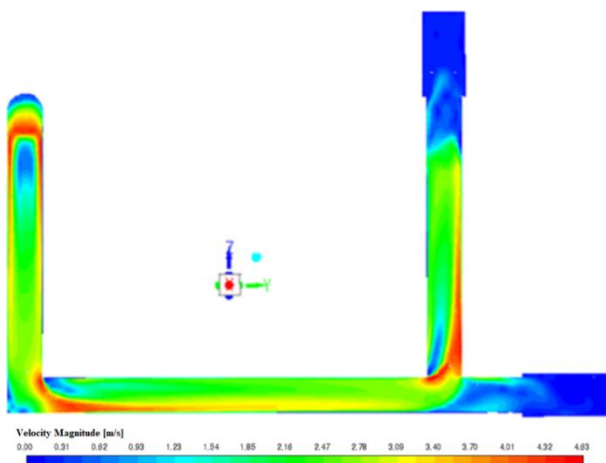


Fig. 17. The contours of velocity in the selected channel section with modified elbows geometry (contractions eliminated) and 1.7 mm thick sediment layer

The elbows with contraction in the above discussed cases are the source of nearly entire observed pressure drop. Therefore, the modification of reduced cross-section area was proposed and the contraction was replaced by a typical 90° elbow. The contours of pressure drop after this modification are shown in Fig. 16. Although there is 1.7 mm layer of sediments, the total pressure drop

is much lower than for the case with contraction (see Fig. 14 for comparison). The corresponding contours of velocity are shown in Fig. 17. Now the maximum observed velocity is below 5 m/s. After the modification, the values of velocity are still above the recommended range but compared to Fig. 15, there is a substantial improvement. The velocity patterns in both elbows are also similar.

## 6. PRESSURE LOSS ALONG THE CHANNEL

To evaluate more precisely the pressure drop on both types of elbows, several transverse planes were created in the CFD model where the average static and dynamic pressures were probed. Location of some of these planes is shown in Fig. 18.

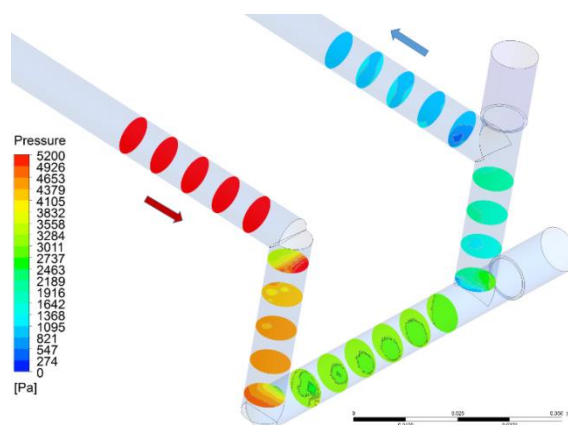


Fig. 18. Cross-sectional planes in the CFD model in which average pressure was calculated

Based on the values of average pressure in each plane, the pressure profiles were constructed as depicted in Fig. 19–22. The dynamic and total pressure predicted from CFD can be compared with the total pressure calculated from the hydraulic model. The results for the original channel geometry without sediment layer are presented in Fig. 19. The total pressure drop according to CFD calculations is lower than the value of the hydraulic model but in general the results show good consistency. Total pressure from CFD decreases on each obstacle, while the dynamic pressure increases inside the narrowings due to the higher values of velocity.

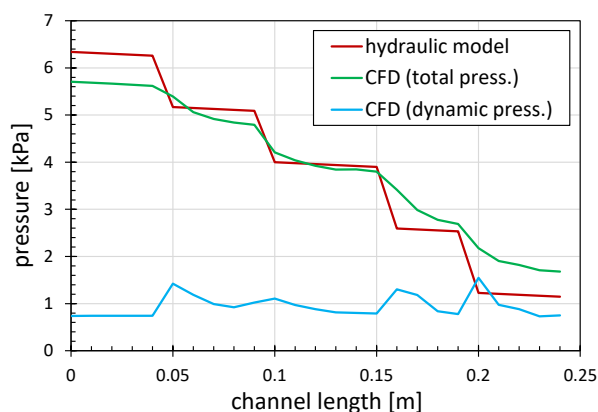


Fig. 19. Pressure profile along the channel of original geometry and without sediments



In Figures 20 – 22, the results for three values of sediment layer thickness (1.3 mm, 1.7 mm and 2.0 mm) are presented. Total pressure drop increases rapidly with the growth of the sediment layer. The results of hydraulic model are in very good agreement with numerical simulation. Therefore, the hydraulic model can be successfully used instead of the much more time consuming CFD calculations. Pressure drop for the channel with 1.3 mm thick sediment layer is presented in Fig. 20. The total pressure drop evaluated from the numerical simulations and hydraulic model is slightly below 40 kPa and the results are consistent for local losses across all obstacles analyzed. For this case the pressure loss on the elbows with contraction is over 2 times higher than for the elbows with recess. The dynamic pressure increases most in the elbow with contraction, where the highest flow velocity was also observed.

In the Fig. 21, there are shown results of pressure drop for the case with 1.7 mm thick sediment layer. The total pressure drop is about 120 kPa but compared with the previous case of 1.3 mm sediment, the pressure loss due to contraction becomes much larger. More than 90% of the total pressure drop in the channel is generated at these obstacles. For the case with 2 mm sediment layer (Fig. 22) the calculated pressure drop is very high, which means that it is almost impossible to maintain the desired flow rate on an actual mold. In this case, the contraction blocks almost entire flow of the coolant.

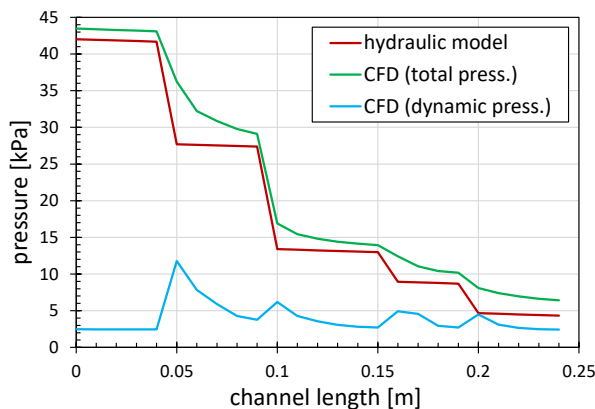


Fig. 20. Pressure profile along the channel of original geometry with sediment thickness of 1.3 mm

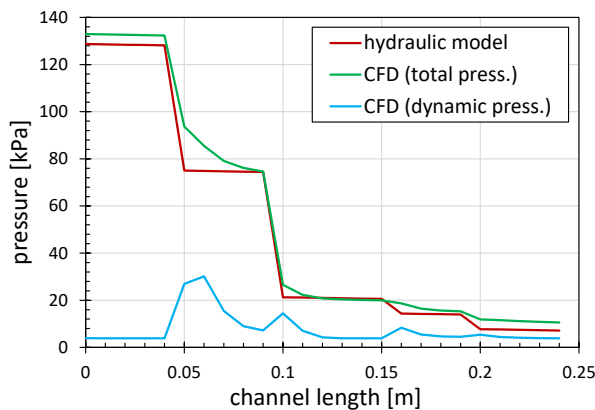


Fig. 21. Pressure profile along the channel of original geometry with sediment thickness of 1.7 mm

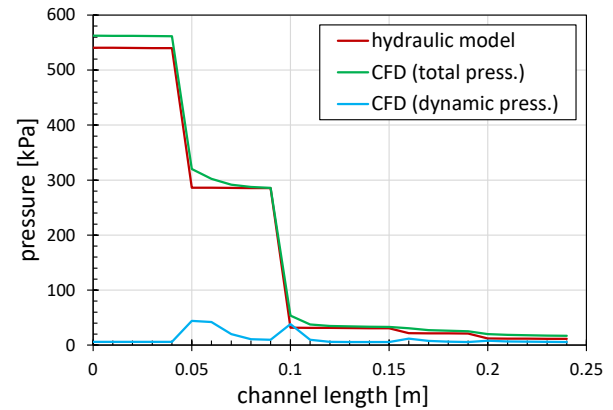


Fig. 22. Pressure profile along the channel of original geometry with sediment thickness of 2 mm

## 7. COMPARISON WITH EXPERIMENT

The cooling channel, which is analyzed theoretically above, was also investigated on the experimental test stand. The pressure losses were measured when the injection mold had been used on the production line for several months. The volume flow of water through the tested cooling channel was set to 6 l/min, the same value as in the presented calculations and simulations. The pressure drop measured along the entire channel was 225 kPa. Total pressure drop over the entire channel calculated from the hydraulic model and from CFD simulations is shown in Fig. 23 for several values of sediment layer thickness. Both methods lead to similar results. Comparing the measured value with the results of hydraulic model and CFD simulations, it can be concluded that such a pressure loss should be observed for the sediment layer thickness around 1.7 mm, as is shown in Fig. 23 by the green marker. The plot in this Figure also shows that the pressure drop increases asymptotically to infinity and becomes unacceptably high as the sediment thickness approaches 2 mm.

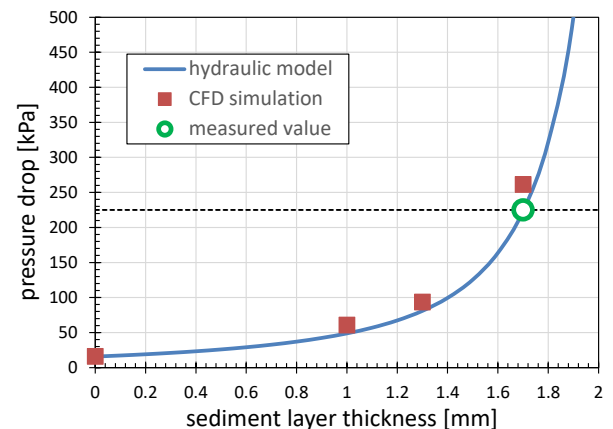


Fig. 23. Total pressure drop along the cooling channel. Comparison of hydraulic model results with experiment and CFD simulation

## 8. SUMMARY AND CONCLUSIONS

The paper presents the analysis of pressure drop in a single cooling channel of an injection mold. The selected channel is representative one to estimate the effect of contractions in the

flow cross-section area, which become increasingly narrower during the mold operation. Specifically, sediment layer growth on the channel wall and its effect on the coolant flow have been analyzed. The hydraulic model for evaluation of the pressure losses has been proposed and used to calculate, among others, the pressure loss in elbows with contraction of a shape that has not been studied in the literature so far. The 1D hydraulic model results were compared with 3D CFD simulations. Based on the work carried out, the following conclusions can be drawn:

- Both approaches (1D and 3D) show good compatibility and lead to similar results, which means that the simplified 1D hydraulic model can be successfully used to quickly determine the pressure drop in an injection mold cooling channels and to identify potential problems at particular flow passages. The proposed hydraulic model is simple to implement and can replace time-consuming CFD simulations, thus eliminating the need to employ a highly qualified IT team and the use a powerful computer.
- Comparison of experimental data with hydraulic model results showed that the sediment layer thickness can be as high as 1.7 mm in the tested channel of the real injection mold. That result shows that the flow in the channel could be totally blocked by the sediments in quite a short time. It can be expected that with a sediment thickness close to 2 mm, the pressure losses would be so high that in the actual mold the flow would be blocked.
- The growth of the sediments layer increases the mold temperature and, in consequence, the quality of plastic products could decline to an unacceptable level because insufficient cooling of the product can cause its deformation.
- A local increase in coolant velocity has a positive effect on the self-cleaning of the channels, but on the other hand it causes a significant increase in flow resistance, resulting in the need to raise the pressure in the cooling channel and thus increase the power of the feed pump.

The hydraulic model presented in this work was validated for the selected cooling channel containing two types of 90° elbows. In the future, the hydraulic model could be extended and validated for cooling channels with other types of elbows to verify its effectiveness in predicting pressure loss, determining sediment layer growth and coolant flow in more complex geometries of the cooling channels found in injection molds.

## REFERENCES

1. Muszyński P, Mrozek K, Poszwa P. Selected methods of injection molds cooling. *Mechanik*. 2016 Sep;(8-9):996–1000. <https://doi.org/10.17814/mechanik.2016.8-9.332>
2. White JL. *Principles of Polymer Engineering Rheology*. John Wiley & Sons. January 1991. ISBN 978-0471853626.
3. Poszwa P, Szostak M. Influence of scale deposition on maintenance of injection molds. *Eksploracja i Niezawodność - Maintenance and Reliability*. 2018; 20(1):39–45. <http://dx.doi.org/10.17531/ein.2018.1.6>
4. Søgaard E. *Injection Molded Self-Cleaning Surfaces*. DTU Nanotech. Denmark, 2014. PhD Thesis.
5. Lalot S. On-Line Detection of Fouling in a Water Circulating Temperature Controller (WCTC) Used in Injection Moulding: Part 1: Principles. *Applied Thermal Engineering*. 2006; 26(11-12): 1087-1094. <https://doi.org/10.1016/j.applthermaleng.2005.11.010>
6. Lalot S. On-Line Detection of Fouling in a Water Circulating Temperature Controller (WCTC) Used in Injection Moulding. Part 2: Application. *Applied Thermal Engineering*. 2006; 26(11-12): 1095-1105. <https://doi.org/10.1016/j.applthermaleng.2005.11.024>
7. Zettler HU, Weiss M, Zhao Q, Müller-Steinhagen H. Influence of Surface Properties and Characteristics on Fouling in Plate Heat Exchangers. *Heat Transfer Engineering*. 2005;26(2):3-17. <https://doi.org/10.1080/01457630590897024>
8. Li J, Liu W, Xia X, Zhou H, Jing L, Peng X, Jiang S. Reducing the Burn Marks on Injection-Molded Parts by External Gas-Assisted Injection Molding. *Polymers*. 2021; 13: 4087. <https://doi.org/10.3390/polym13234087>
9. Vojnová E. The Benefits of a Conformal Cooling Systems the Molds in Injection Molding Process. *Procedia Engineering*. 2016; 149: 535-543. <https://doi.org/10.1016/j.proeng.2016.06.702>
10. Guilong W, Guoqun Z, Huiping L, Yanjin G. Analysis of Thermal Cycling Efficiency Optimal Design of Heating/Cooling Systems for Rapid Heat Cycle Injection Molding Process. *Mater Design*. 2010; 31: 3426-3441. <https://doi.org/10.1016/j.matdes.2010.01.042>
11. Dimla D., Camilotto M., Miani F. Design and Optimisation of Conformal Cooling Channels in Injection Moulding Tools. *Journal of Materials Processing Technology*. 2005;164-165:1294-300. <https://doi.org/10.1016/j.jmatprotec.2005.02.162>
12. Chen SC, Lin YW, Chien RD, Li HM. Variable Mold Temperature to Improve Surface Quality of Microcellular Injection Molded Parts Using Induction Heating Technology. *Advances in Polymer Technology*. 2008; 27(4):224-232. <https://doi.org/10.1002/adv.20133>
13. Kuo CC, Jiang ZF, Lee JH. Effects of Cooling Time of Molded Parts on Rapid Injection Molds with Different Layouts and Surface Roughness of Conformal Cooling Channels. *The International Journal of Advanced Manufacturing Technology*. 2019;103(5-8):2169–82. <https://doi.org/10.1007/s00170-019-03694-2>
14. Kurt M, Kaynak Y, Kamber OS, Mutlu B, Bakir B, Koklu U. Influence of Molding Conditions on The Shrinkage and Roundness of Injection Molded Parts. *The International Journal of Advanced Manufacturing Technology*. 2009 ;46(5-8):571-8. <https://doi.org/10.1007/s00170-009-2149-x>
15. Jafairan AR, Shakeri M. Investigating the Influence of Different Process Parameters on Shrinkage of Injection-Molding Parts. *American Journal of Applied Sciences*. 2005;2(3):688-700. <https://doi.org/10.3844/ajassp.2005.688.700>
16. Choi DS, Im YT. Prediction of Shrinkage and Warpage in Consideration of Residual Stress in Integrated Simulation of Injection Molding. *Composite Structures*. 1999;47(1-4):655–65. [https://doi.org/10.1016/S0263-8223\(00\)00045-3](https://doi.org/10.1016/S0263-8223(00)00045-3)
17. Kovacs JG, Szabo F, Kovacs NK, Suplicz A, Zink B, Tabi T, Hargitai H. Thermal Simulations Measurements for Rapid Tool Inserts in Injection Molding Applications. *Applied Thermal Engineering*. 2015; 85:44-51. <http://dx.doi.org/10.1016/j.applthermaleng.2015.03.075>
18. Shayfull Z, Sharif S, Zain AM, Ghazali MF, Saad RM. Potential of Conformal Cooling Channels in Rapid Heat Cycle Molding: A review. *Advances in Polymer Technology*. 2014; 33(1):21381. <https://doi.org/10.1002/adv.21381>
19. Xu XR, Sachs E, Allen S. The Design of Conformal Cooling Channels in Injection Molding Tooling. *Polymer Engineering & Science*. 2001;41(7):1265–79. <https://doi.org/10.1002/pen.10827>
20. Park HS, Pham NH. Design of Conformal Cooling Channels for an Automotive Part. *Int J Automotive Technology*. 2009;10(1):87-93. <https://doi.org/10.1007/s12239-008-0011-7>
21. Li CG, Li CL. Plastic Injection Mould Cooling System Design by Configuration Space Method. *Computer-Aided Design*. 2008; 40(3):334–49. <https://doi.org/10.1016/j.cad.2007.11.010>
22. Torres-Alba A, Mercado-Colmenero JM, Diaz-Perete D, Martin-Doñate C. A New Conformal Cooling Design Procedure for Injection Moulding Based on Temperature Clusters and Multidimensional Discrete Models. *Polymers*. 2020; 12(1): 154. <https://doi.org/10.3390/polym12010154>
23. Silva HM, Novera JT, Fernandes L, Rodrigues HL, Pontes AJ. Design, Simulation and Optimization of Conformal Cooling Channels in Injection Molds: A review. *The International Journal of Advanced Manufacturing Technology*. 2022; 120(7-8):4291–305. <https://doi.org/10.1007/s00170-022-08693-4>

24. Kanbur BB, Suping S, Duan F. Design and optimization of conformal cooling channels for injection molding: a review. *Int J Adv Manuf Technol.* 2020; 106: 3253-3271. <https://doi.org/10.1007/s00170-019-04697-9>
25. Feng S, Kamat AM, Pei Y. Design Fabrication of Conformal Cooling Channels in Molds: Review Progress Updates. *International Journal of Heat and Mass Transfer.* 2021; 171:121082. <https://doi.org/10.1016/j.ijheatmasstransfer.2021.121082>
26. Yao DG, Chen SC, Kim B. Rapid Thermal Cycling of Injection Molds: An Overview on Technical Approaches and Applications. *Advances in Polymer Technology.* 2008; 27(4):233–55. <https://doi.org/10.1002/adv.20136>
27. Muvunzi R, Dimitrov DM, Matope S, Hams T. A case study on the design of a hot stamping tool with conformal cooling channels. *Int J Adv Manuf Technol.* 2021; 114: 1833-1846. <https://doi.org/10.1007/s00170-021-06973-z>
28. Kanbur BB, Zhou Y, Shen S, Wong KH, Chen C, Shocket A, Duan F. Metal Additive Manufacturing of Plastic Injection Molds with Conformal Cooling Channels. *Polymers.* 2022; 14: 424. <https://doi.org/10.3390/polym14030424>
29. Kuo CC, Xu JY, Zhu YJ, Lee CH. Effects of Different Mold Materials and Coolant Media on the Cooling Performance of Epoxy-Based Injection Molds. *Polymers.* 2022; 14: 280. <https://doi.org/10.3390/polym14020280>
30. Kuo CC, You ZY, Wu JY, Huang JL. Development and application of a conformal cooling channel with easy removal and smooth surfaces. *Int J Adv Manuf Technol.* 2019;102: 2029-2039. <https://doi.org/10.1007/s00170-019-03316-x>
31. Kuo C.C., Chen W.H. Improving Cooling Performance of Injection Molding Tool with Conformal Cooling Channel by Adding Hybrid Fillers. *Polymers.* 2021, 13, 1224. <https://doi.org/10.3390/polym13081224>
32. Wei Z, Wu J, Shi N, Li L. Review of Conformal Cooling System Design Additive Manufacturing for Injection Molds. *Mathematical Biosciences and Engineering.* 2020; 17(5): 5414-5431. <https://doi.org/10.3934/mbe.2020292>
33. Park HS, Dang XP, Nguyen DS, Kumar S. Design of Advanced Injection Mold to Increase Cooling Efficiency. *International Journal of Precision Engineering and Manufacturing-Green Technology.* 2020; 7(2):319–28. <https://doi.org/10.1007/s40684-019-00041-4>
34. Papadakis L, Avraam S, Photiou D, Masurtschak S, Falcón JCP. Use of a Holistic Design and Manufacturing Approach to Implement Optimized Additively Manufactured Mould Inserts for the Production of Injection-Moulded Thermoplastics. *Journal of manufacturing and materials processing.* 2020; 4(4): 100–0. <https://doi.org/10.3390/jmmp4040100>
35. Jahan SA, El-Mounayri H. A Thermomechanical Analysis of Conformal Cooling Channels in 3D Printed Plastic Injection Molds. *Applied Sciences.* 2018 ;8(12):2567. <https://doi.org/10.3390/app8122567>
36. Jahan SA, Wu T, Zhang Y, Zhang J, Tovar A, Elmounayri H. Thermo-mechanical Design Optimization of Conformal Cooling Channels using Design of Experiments Approach. *Procedia Manufacturing.* 2017; 10:898–911. <https://doi.org/10.1016/j.promfg.2017.07.078>
37. Idelchik IE. *Handbook of Hydraulic Resistance.* Jerusalem: Israel Program for Scientific Translations Ltd. 1968.

The work been accomplished under the research Project – grant number POIR.01.01.01-00-0541/19-00, financed by Polish National Centre for Research and Development.

Tomasz Przybyliński:  <https://orcid.org/0000-0001-6045-7430>

Adam Tomaszewski:  <https://orcid.org/0000-0003-2122-8162>

Zbigniew Krzemianowski:  <https://orcid.org/0000-0001-5591-9880>

Roman Kwidziński:  <https://orcid.org/0000-0001-6414-3092>

Paulina Rolka:  <https://orcid.org/0000-0002-3699-9421>

Grzegorz Sapeta:  <https://orcid.org/0000-0003-4080-5973>

Robert P. Socha:  <https://orcid.org/0000-0003-4072-2393>



This work is licensed under the Creative Commons BY-NC-ND 4.0 license.

# APPLICATION OF NUMERICAL INTEGRATION IN ANALYSING THE VOLUME OF REINFORCEMENT PARTICLES IN ALGORITHMS FOR GENERATING REPRESENTATIVE VOLUME ELEMENTS (RVEs)

Grzegorz MIECZKOWSKI\*, Dariusz SZPICA\*, Andrzej BORAWSKI\*

\*Faculty of Mechanical Engineering, Białystok University of Technology, ul. Wiejska 45C, 15-351 Białystok, Poland

[g.mieczkowski@pb.edu.pl](mailto:g.mieczkowski@pb.edu.pl), [d.szpica@pb.edu.pl](mailto:d.szpica@pb.edu.pl), [a.borawski@pb.edu.pl](mailto:a.borawski@pb.edu.pl)

received 13 November 2023, revised 16 May 2024, accepted 20 May 2024

**Abstract:** The paper focuses on spatial modelling of composites with discontinuous reinforcement. The algorithm for creating a representative volume element (RVE) must consider random distribution and size of reinforcing particles (RP), prevention of RP interpenetration, and maintaining the desired volume fraction of the reinforcing phase ( $V_p$ ) in the composite microstructure. Assuming fixed RVE dimensions and randomly determined RP size, the actual  $V_p$  value needs to be continuously determined. If the assumed (desired)  $V_p$  is lower than the current value, additional reinforcement is added to the RVE. As the RP location is random, some particles may extend beyond the RVE limits, affecting  $V_p$  calculation. The research aims to determine the RP volume within the RVE boundaries when RP extends outside. The RVE was discretized with  $N$  points, and the number of  $N_i$  points within the area occupied by RP was determined. The sought value was calculated using the ratio  $N_i / N = V_p / V_{RVE}$ , where  $V_{RVE}$  is the volume of the RVE. Two discretisation methods, systematised (RI) and random (Monte Carlo (MC)), were employed. The study investigated the effects of discretisation type and number  $N$  points on calculation accuracy and microstructure generation time for particle-reinforced composites in sphere, cylinder, and ellipsoid shapes. Systematised discretisation yielded higher accuracy/stability, with number  $N$  dependent on RP dimensions. The MC method reduced generation time but introduced instability and significant errors.

**Key words:** particle-reinforced composites, spatial modelling, representative volume element (RVE), control of volume fraction, numerical integration

## 1. INTRODUCTION

Today, a steady increase in the use of composites can be observed in various sectors of the economy, such as the defence [1], automotive [2–4] and aerospace [5] industries. Composite materials typically have better strength and performance properties compared to homogeneous materials such as ceramics, metals and plastics. This is due to the fact that beneficial properties of both the matrix (e.g. ductility, impact strength) and reinforcements (e.g. high strength, high elastic modulus, wear resistance) are combined in composites [6]. By appropriate selection of the composite components, their proportions and the distribution and geometry of the reinforcement fractions, a material with the desired mechanical, physical and performance properties can be produced [7–10]. Composite design is a complex process that requires the simultaneous use of experimental and numerical studies [11].

Experimental testing plays a key role, enabling direct investigation of the physical [12,13] and mechanical [14,15] properties of composites. A variety of experiments, such as strength tests, fatigue tests, microstructure analysis or thermal and electrical measurements, are carried out and provide important data for the evaluation and validation of numerical models [16,17].

Numerical tests, such as the finite element method (FEM) [18–21] or the boundary element method (BEM) [22,23], allow the virtual simulation of the behaviour of composites. Numerical mod-

els take into account material parameters, geometry and loading conditions to predict and analyse the response of the composite under different operating conditions. They make it possible to optimize the design of the composite, reduce the cost and time associated with experimental testing, and increase the efficiency of the design process.

One of the key steps in FEM/MEB numerical studies is the preparation of a spatial geometrical model of the composite - a composite fragment that is small enough to preserve the characteristic features and properties of the material, while being large enough for numerical analyses and simulations to be performed on it. Furthermore, this fragment should contain the different components of the composite in the right proportions and take into account their distribution and geometry. Such a composite component is called a representative volume element (RVE) [24,25]. It can be assumed that the RVE is a representation of the microstructure of the composite, and by analysing the RVE, the behaviour and macroscopic properties of the whole composite can be predicted.

The algorithm for generating the RVE, which for composites with discontinuous reinforcement usually follows the random sequential adsorption (RSA) scheme [26–28], must take into account a number of key aspects. Among these aspects are the random distribution and size of reinforcing particles (RPs), the elimination of the possibility of RPs interpenetrating each other, and ensuring the desired volume fraction of the reinforcing phase ( $V_p$ ) in the composite microstructure. In the context of this latter

aspect, assuming constant RVE dimensions and randomly determined RP sizes, it is necessary to continuously determine the current Vp value. If the assumed Vp value is less than the current one, another reinforcement particle is added to the RVE. However, it should be noted that the location of the RP is also randomly determined, which means that a certain part of the newly added reinforcement particles may protrude outside the boundaries of the RVE. In this case, only the part of the particle that is within the RVE area should be taken into account when calculating the current Vp value. If the reinforcement particle has a regular shape, such as a sphere, cylinder, ellipsoid or cuboid, and its position is such that the axis of symmetry is perpendicular to any of the boundary walls of the RVE, or in the case of a sphere it protrudes only beyond one wall of the representative element, appropriate mathematical formulas can be used to calculate the volume of the particle contained in the RVE. However, if the reinforcement particle has a more complex shape or its position is such that it is not possible to determine unambiguously which part of the particle is inside the RVE, other techniques may be necessary.

While the first two aspects of the RVE formation algorithm (elimination of reciprocal interpenetration of particles and their random distribution) are well described in the literature reports [29–32], the methodology for controlling the assumed Vp appears to be insufficiently studied. An interesting proposal, to solve this problem, for composites with a sphere-shaped RP, has been proposed in papers [28,33] - when the sphere is partially placed outside the RVE, an additional reinforcement particle is created, crossing the opposite wall of the RVE in such a way that the part of the additional particle remaining in the RVE is identical to that projecting outside the RVE (for the original sphere). Another method to find the volume of the reinforcement particle that remains within the RVE is numerical integration. The purpose of this paper is to define the various integration procedures and to investigate the effect of the adopted RVE discretisation model on the accuracy of the calculations. Chapter 2 describes the procedures used along with the discretisation models used. Chapter 3, on the other hand, presents the results of a study on the influence of the discretisation method and the integration parameters used, on the accuracy of the results obtained.

## 2. APPROACH FOR DETERMINING THE DESIRED VOLUME FRACTION OF REINFORCEMENT PHASE IN RVE

### 2.1. Main principles and block diagram of the RVE generation algorithm for hybrid composites

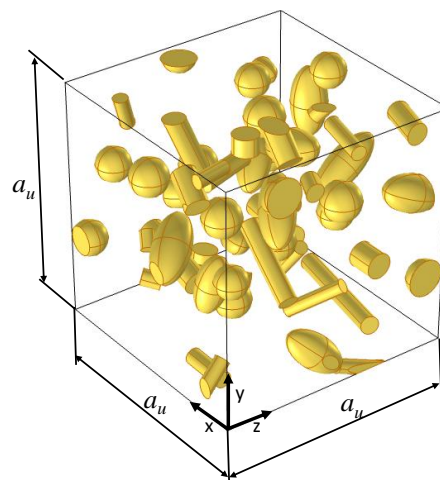
The figure below shows an example of a representative volume element of a hybrid composite (Fig.1a), in which the individual reinforcement particles have the shape of a cylindrical sphere and an ellipsoid. The RVE has the shape of a cube with side  $a_u$ . The magnitude of the RVE (side length  $a_u$ ) is determined by the characteristic dimensions of the RPs and their volume fractions [24,25]. The distribution of the reinforcing particles is random, meaning that the coordinates of the point  $P_i(x_i, y_i, z_i)$  ( $x_i, y_i, z_i \in [0, a_u]$ ) are determined randomly (Fig.1b). For cylindrical or ellipsoidal reinforcement particles, the two Euler angles are also determined in the same way:  $\theta_i, \psi_i$  ( $x_i, y_i, z_i \in [0, a_u]$ ).

Additionally, it is important for the solid objects representing the reinforcement material not to intersect. Therefore, during the generation of subsequent reinforcement elements, the distance

between the axis of the newly formed solid object and the axes of the already existing ones is calculated. The concept of "axis of the solid object" should be understood as follows:

- for a sphere, the axis of the solid object is a line segment of length  $d_i$ , with its centre coinciding with the centre of the sphere;
- for a cylinder, the axis of the solid object is a line segment with its ends located at the centres of the bottom and top circular bases;
- for an ellipsoid, the axis of the solid object is a line segment of length  $l_i$ , with its centre coinciding with the centre of the ellipsoid.

a)



b)

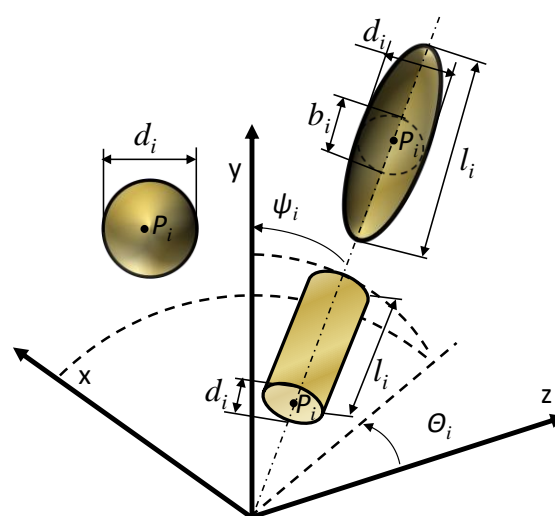


Fig. 1. Representative volume element (a) and single reinforcements in 3D space (b)

This distance must not be less than  $1.05 d_{max}$  [26], where  $d_{max}$  is the maximum transverse dimension ( $d_i, b_i$ , Fig. 1b) of the reinforcement element. The calculation of the distance between RP axes can be carried out as presented in the papers [30,34].

For composites with single reinforcement, algorithms for creating RVEs are discussed in, for example, papers [29,35]. Figure 2 shows a block diagram of the algorithm for creating the RVE of a hybrid composite with the previously described features.

In Figure 2, the operating block, responsible for determining the RP volume remaining within the limits of the RVE when the reinforcement particle extends beyond the representative element, is shown in grey.



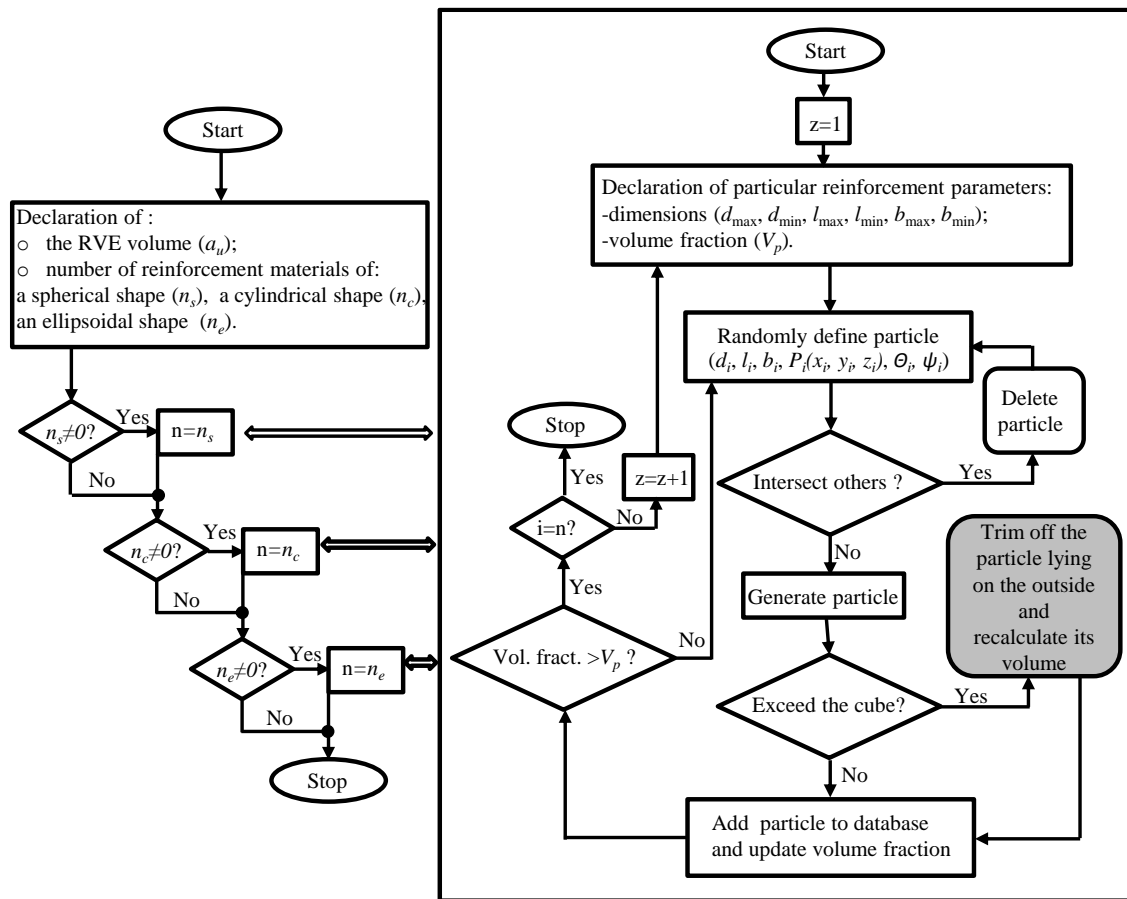


Fig. 2. Block diagram of the algorithm for generating RVE of hybrid composites

The development of operating procedures for this block is the main topic addressed in this paper. The detailed development and description of the processes/procedures involved in its operation are described below.

## 2.2. Numerical integration methods for estimating the volume fraction of the reinforcement phase in RVE: Integration on a regular grid and Monte Carlo method

Numerical integration is a widely used method in the field of scientific materials research and engineering. It is an efficient method for the estimation of various parameters, such as volume, surface area or inertia, which are important for the characterisation and analysis of different structures. In the context of composite materials analysis, an important aspect is the estimation of the volume fraction of the reinforcement phase in a representative volume element. For this purpose, various numerical integration methods are used to calculate the volume of reinforcement particles within the RVE limits. In this chapter, two popular methods of numerical integration are presented, namely the Monte Carlo (MC) method and integration on a regular/systematised grid (RI). Both of these methods are important in the process of generating the RVE when the reinforcing particles, due to a random distribution, project outside the boundaries of the representative element. With these methods, it is possible to estimate the volume of the portion of the newly generated reinforcement particle that is within the boundaries of the RVE. In general, the procedures for determining the volume of the part of the reinforcement particle remain-

ing in the RVE ( $nV_p$ ), by means of the two numerical integration methods used, can be divided into four stages: initialisation, discretisation (point or grid generation), point evaluation and calculation of the  $nV_p$  volume. A detailed description of each stage is provided below.

### 2.2.1. Stages in numerical integration

#### 2.2.1.1. Initialisation

At the beginning of the numerical integration process, it is necessary to establish the parameters needed for the calculation, such as the number of points (MC) or the size of the subdivision grid (RI). Using a larger number of points and a smaller grid size results in increased estimation accuracy while increasing the computational load (increased computation time, increased hardware requirements). In practice, the optimal values for the number of points and grid size will depend on the specific research problem, e.g. the shape and dimensions of the RP. There is no single universal value that is suitable for all cases. It is therefore necessary to experimentally adjust and test different values to find the optimal compromise between estimation accuracy, computational load and execution time.

The Monte Carlo method is based on generating random points inside the study area to estimate various parameters. With this method, it is important to choose the number of points appropriately and to maintain randomness in the generation process.

The number of points is important for the accuracy of the es-

timation. The higher the number of points, the more accurate the results obtained. However, it is important to remember that a larger number of points requires more computational time. Therefore, it is important to find an optimal compromise in order to obtain satisfactory estimation accuracy while taking into account the available computational resources. In the paper presented here, the number of points (MC method) and the grid interval (RI method) depended on the overall dimensions of the RVE and RP and were calculated from equations (1) and (2), respectively.

$$N_{MC} = 5 \cdot 10^4 \cdot n \cdot \frac{\min(d_i, b_i, l_i)}{a_u}, n = 1, 2, 3 \dots \quad (1)$$

$$\Delta = (2.5 \cdot n)^{-1} \frac{\min(d_i, b_i, l_i)^2}{a_u}, n = 1, 2, 3 \dots \quad (2)$$

The formulas (1) and (2) have been adopted based on conducted research in such a way that for  $n=1$ , errors do not exceed 10%.

Knowing the overall dimension of the RVE and the grid interval, the number of grid points can be determined:

$$N_{RI} = \left(\frac{a_u}{\Delta} + 1\right)^3. \quad (3)$$

### 2.2.1.2. Discretisation

With the Monte Carlo method, points are generated within the study area to represent a sample from space. In this method, it is important to preserve randomness in the process of generating these points. For this purpose, a pseudorandom number generator, available in Java, was used, with which values in the interval  $[0,1)$  were generated and multiplied by  $a_u$  to obtain random  $x$ ,  $y$  and  $z$  coordinates. To exclude duplicates, newly generated points were compared with existing points. If a duplicate point was found, the coordinates of the additional point were drawn, as described above.

In the method of integration on a regular grid, the study area is divided into a regular grid of points. When subdividing, the principle applied was to keep the distribution of points homogeneous - the distance between neighbouring points was identical.

### 2.2.1.3. Point evaluation

Once each point has been generated, an evaluation is carried out to determine whether it is within the study area. An example of the RVE discretisation for the RI and MC methods is shown in Figure 3a and 3b respectively.

It was assumed that a point  $M_n$  is considered to be inside the reinforcement particle if the following conditions are met: sphere-shaped RP:

$$|\overrightarrow{P_i M_n}| \leq d_i/2, \quad (4)$$

cylinder-shaped RP:

$$\begin{cases} x'^2_M + y'^2_M \leq \left(\frac{d_i}{2}\right)^2, \\ 0 \leq z'_M \leq l_i \end{cases}, \quad (5)$$

ellipsoid-shaped RP:

$$\frac{x'^2_M}{(d_i/2)^2} + \frac{y'^2_M}{(b_i/2)^2} + \frac{z'^2_M}{(l_i/2)^2} \leq 1, \quad (6)$$

where:  $d_i$ ,  $b_i$ ,  $l_i$  - dimensions of the particles of the reinforcement

fraction (Fig. 1b),  $x'_M, y'_M, z'_M$ -coordinates of the sampling points in the local reference system, the origin of which is located at point  $P_i$  (Fig. 3).

The transformation of the coordinates of the  $M_n$  points from the global system ( $O, x, y, z$ ) to the local system ( $P_i, x', y', z'$ ) was performed based on the following formulae:

$$\begin{bmatrix} x'_M \\ y'_M \\ z'_M \end{bmatrix} = A_1^{3 \times 3} \times A_2^{3 \times 3} \times \begin{bmatrix} x_M - x_P \\ y_M - y_P \\ z_M - z_P \end{bmatrix}, \quad (7)$$

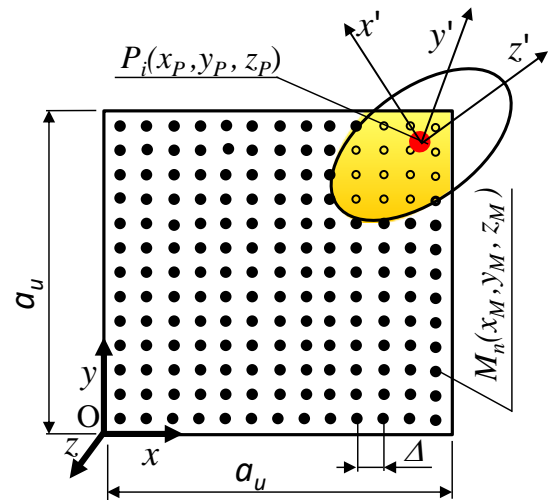
where:  $x_P, y_P, z_P$  - coordinates of point  $P_i$  (base point RP, Fig. 1b) in the global reference system,  $A_1^{3 \times 3}$ ,  $A_2^{3 \times 3}$  -matrices of rotation by given Euler angles (Fig. 1b).

The matrices are defined by the following formulas:

$$A_1^{3 \times 3} = \begin{bmatrix} 1 & 0 & 0 \\ 0 & \cos(\psi) & -\sin(\psi) \\ 0 & \sin(\psi) & \cos(\psi) \end{bmatrix}, \quad (8)$$

$$A_2^{3 \times 3} = \begin{bmatrix} \cos(\theta) & 0 & \sin(\theta) \\ 0 & 1 & 0 \\ -\sin(\theta) & 0 & \cos(\theta) \end{bmatrix}. \quad (9)$$

a)



b)

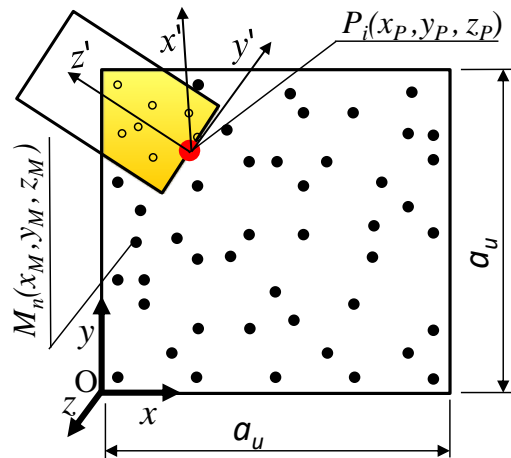


Fig. 3. Sampling in the regular grid integration method (a) and the Monte-Carlo method (b), •-points outside the area of the reinforcement particle, °-points lying inside the reinforcement particle.

The number  $N_i$  of points located in the area of the reinforcement particle is determined by summing the points satisfying the conditions described by formulae (4)÷(6).

#### 2.2.1.4. Calculation of the $nV_p$ volume

On the basis of the number of  $N_i$  points accepted as being inside the study area and the corresponding calculations, it is possible to calculate the estimated volume of the reinforcement phase in a representative volume element (shaded area in Figure 3).

In the RI method, the process involves adding up the volume of all accepted points. A key assumption of this method is that the points are evenly distributed across the study area (Figure 3a). Therefore, the volume of the study area is assumed to be evenly distributed over all grid points. Thus, the volume attributed to one point can be calculated by dividing the total volume of the RVE ( $a_u^3$ ) by the number of points in the grid (3). In practice, if the grid is dense enough, an accurate approximation of the actual volume can be obtained with this approach. However, for sparser grids, the approximation may be less precise and the result may have a significant error.

For the Monte Carlo method, the volume can be calculated from the ratio of the number of points inside the reinforcement area to the total number of points generated and the volume of the study area (1). In other words, the ratio of the number of points accepted as being within the reinforcement area to the total number of points generated in the study area is calculated. This ratio is then multiplied by the volume of the study area ( $a_u^3$ ). To increase the accuracy of the results of this method, it is advisable to carry out multiple simulations for the same RVE case. This process involves repeating the point generation and volume estimation and then averaging the results. The repetition of simulations minimises the influence of random factors and results in more precise results.

The volume of the solid remaining in the RVE was therefore determined using the following formula:

$$nV_p = \frac{N_i}{N} a_u^3, \quad (10)$$

where:  $nV_p$  - the volume of the solid remaining in the RVE,  $N$  - the total number of points used in the sampling ( $N = N_{MC}$  or  $N = N_{MC}$  calculated for the MC and RI methods from equations (1) and (3) respectively),  $N_i$  - the number of points lying inside the reinforcement particle.

### 3. RESULTS AND DISCUSSION

This section of the paper presents the results of the proposed analyses on the use of integration methods (MC and RI) to determine the volume of the reinforcement phase in the RVE. The results obtained are discussed along with their interpretation and analysis. When modelling real composites, the location and dimensions of the reinforcement particles are determined randomly, as this reflects the inherent complexity and heterogeneity of real composite materials. However, in this presented study, it was decided to generate an RVE with a single reinforcing particle whose dimensions and location were identical for all simulations. The main advantage of this approach is that the results can be made comparable. Establishing a single reinforcing particle with the same parameters for all simulations makes it possible to compare results without the influence of randomness on the results. This makes it possible to accurately assess the effect of different analysis methods (Monte Carlo, RI) on the results for the same particle and to investigate the influence of parameters of these methods, such as the number of sampling points or the number of repetitions in the Monte Carlo method. A RVE with cylindrical, spherical and ellipsoidal particles was modelled, using COMSOL Multiphysics software. The dimensions and location were chosen so that the particle protruded outside the RVE (Figure 5). The following characteristic dimensions of the RVE and reinforcing particles were assumed (Figure 1):  $a_u = 50 \mu\text{m}$ ,  $d = 0.2a_u$ ,  $b = 0.25a_u$ ,  $l = a_u$ . For each particle, the reference volume  $V_p$  of the particles remaining in the RVE was determined using COMSOL's built-in measurement tools.

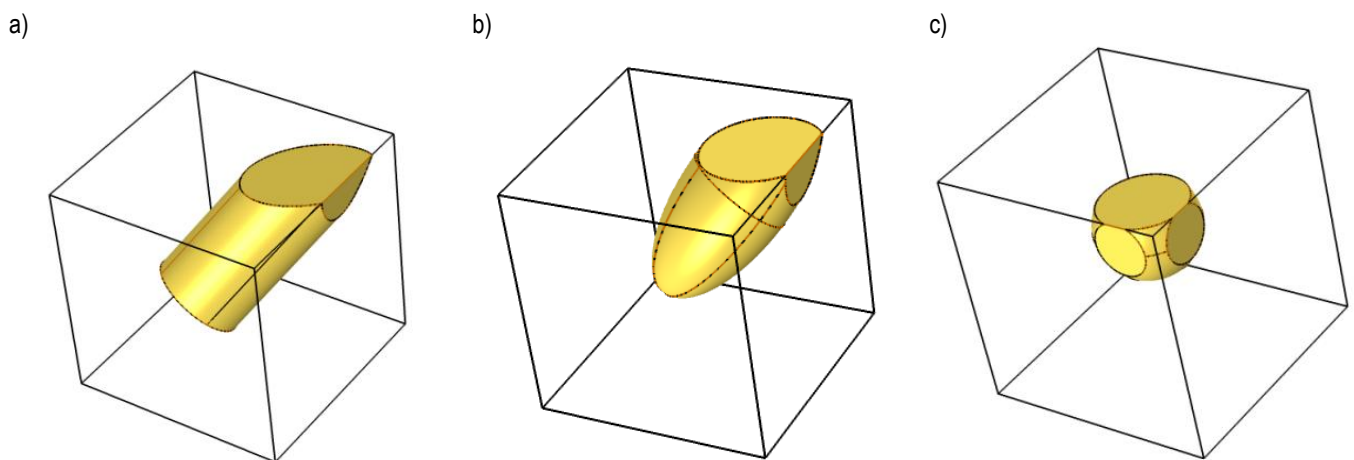


Fig. 4. Modelled RVEs with a reinforcing particle in the shape of a cylinder (a), an ellipsoid (b) and a sphere (c)

The volume  $V_p$  was compared with the results obtained by numerical integration using MC and RI methods and the relative error (11) was determined:

$$\Delta_R = \left| \frac{nV_p - V_p}{V_p} \right| \cdot 100\%, \quad (11)$$

where:  $V_p$  - the reference volume determined using COMSOL's built-in measurement tools,  $nV_p$  - the volume of the reinforcing particle determined using MC and RI (10).

In addition to determining the volume of the particle remaining in the RVE, the calculation time, expressed by the dimensionless parameter  $t_R$ , was also determined:

$$t_R = \frac{nt_p}{t_p}, \quad (12)$$

where:  $nt_p$  - time to generate the RVE microstructure (Fig.4) with the MC and RI integration procedures active,  $t_p$  - time to generate the RVE microstructure (Fig.4) with the MC and RI integration procedures deactivated.

The results of the study of the effect of the method and its parameters on  $\Delta_R$  and  $t_R$  parameters are presented below.

### 3.1. Analysis of the effect of discretisation density and number of simulation repetitions on the accuracy of the determination of the volume of the reinforcement particle remaining in the RVE and the calculation time

#### 3.1.1. RI method

The effect of the discretisation density, expressed by the multiplicative constant  $n$  used in formula (2) to determine the grid interval, on the value of the dimensionless parameters  $\Delta_R$  and  $t_R$  was investigated.

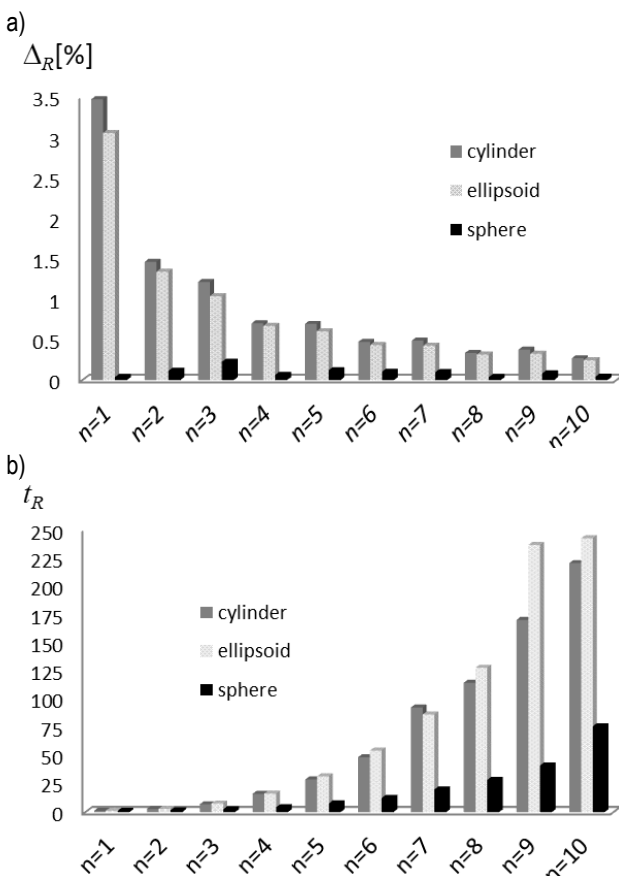


Fig. 5. Effect of discretisation density on calculation time (b) and accuracy (a)

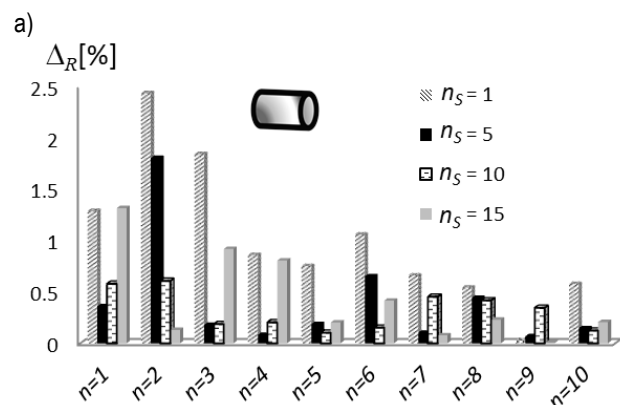
The results obtained are presented in Figure 5. For cylindrical and ellipsoid-shaped reinforcing particles, the calculation accuracy increased with the number of points used for discretisation. For sphere-shaped particles, it was observed that an increase in mesh density could cause a decrease or increase in calculation accuracy. This may be due to the fact that when the grid density is high and the area analysed is relatively small, an edge effect can occur. This is based on the fact that points generated at the edges of spherical particles have a higher probability of being outside the study area. This means that the estimation of the particle volume may be inaccurate, as some points on the edges may be misclassified as outside the area. For cylindrical and ellipsoidal particles, which have a smaller surface-to-volume ratio, the edge effect has less impact on the accuracy of the estimation. The smallest errors were recorded for spherical-shaped particles, while the largest errors were recorded for cylindrical-shaped particles. Differences in calculation accuracy may also be due to the aspect ratio of the solids (ratio of length, width and height) representing the reinforcement. If the solid has a more similar aspect ratio to the interval of the grid of points, the distribution of points will be more uniform, improving the accuracy of the volume estimation. For spherical particles, where the aspect ratio in the three directions is the same, as is the grid interval, the smallest errors were observed.

As for the calculation time, as was to be expected, it always increases with an increase in the number of grid points. The calculation time depended on the shape of the reinforcement particle and was longest for ellipsoid-shaped particles (the condition whose fulfilment causes a point to be considered as being inside the reinforcement particle is the most complex).

Analysing the results shown in Figure 5, it can be seen that there is a compromise between calculation time and accuracy of results, which can be achieved when using, in formula (1), values of  $n$  contained in the range  $5 \leq n \leq 7$ .

#### 3.1.2. MC method

The effect of the number of sampling points, expressed by the multiplicative constant  $n$  used in formula (1), and the number of simulation repetitions  $n_s$  on the value of the dimensionless parameters  $\Delta_R$  (Fig.6) and  $t_R$  (Fig.7) was investigated. In determining the error in  $\Delta_R$ , for  $n_s \neq 1$ , in formula (11)  $nV_p$  is the arithmetic mean of the volume of the particle remaining in the RVE determined in all simulations.



b)

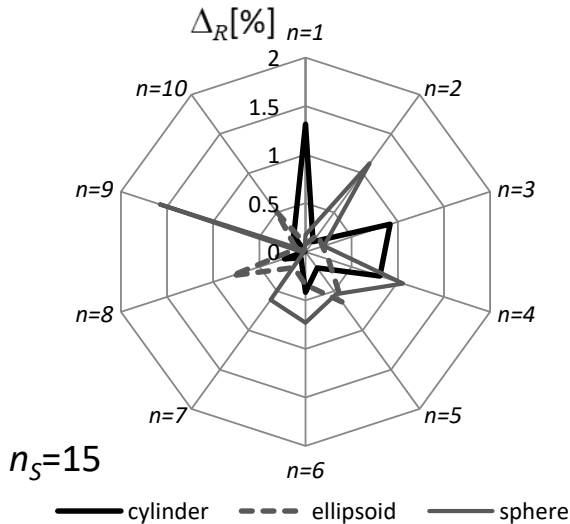
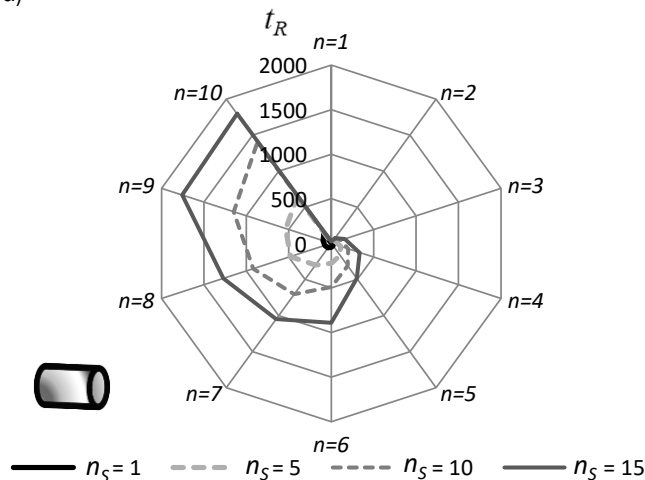


**Fig. 6.** Influence of the number of sampling points used in the MC method on the calculation accuracy: results for a cylinder-shaped particle when using different numbers of simulation repetitions  $n_s$  (a), results obtained for particles of different shapes when using the same number of repetitions  $n_s=15$  (b)

Analysing the results shown in Figure 6, one can conclude that they are characterised by significant randomness, but in most cases a higher number of sampling points and simulation repetitions leads to results with smaller errors. The sensitivity of the method to the shape of the reinforcing particle cannot be clearly determined, as for different numbers of sampling points sometimes more accurate results are obtained for a given particle shape than for others. In most cases, the smallest errors were recorded for sphere-shaped particles. This may be due to their greatest symmetry. Because of this symmetry, the points generated randomly inside a spherical particle are most evenly distributed. This even distribution of sampling points contributes to more accurate analysis results. For particles with other shapes, such as cylinders or ellipsoids, the asymmetry affects a less uniform distribution of sampling points, which can lead to larger errors in the results.

a)



b)

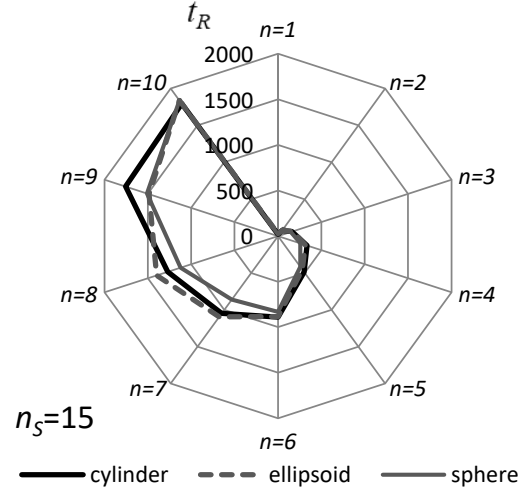
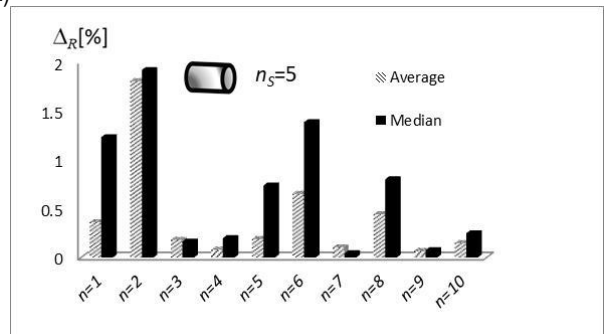


**Fig. 7.** Influence of the number of sampling points used in the MC method on the calculation time: results for a cylinder-shaped particle when using different numbers of simulation repetitions  $n_s$  (a), results obtained for particles of different shapes when using the same number of repetitions  $n_s=15$  (b)

As far as calculation time was concerned, as expected, it increased as the number of sampling points and the number of repetitions increased. The shape of the reinforcing particle also had a slight effect on the calculation time. It was longer for particles for which the condition for verifying that a point belonged to a particle was more complicated - the smallest calculation time occurred for spherical particles and the largest for elliptical particles. The observed deviations from this rule (for example, for  $n=9$  the calculation time for a cylindrical particle was longer than for an elliptical particle) may be due to the fact that when drawing  $n$  points, repeated points are rejected. If such points occur, the calculation time increases.

a)



b)

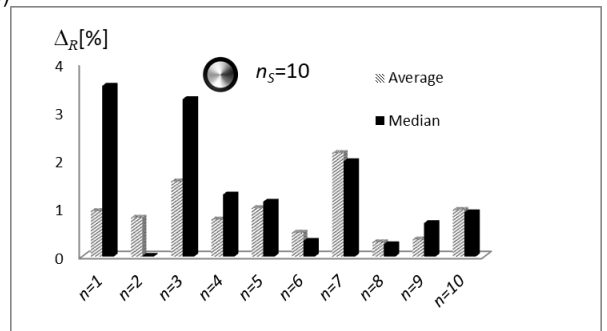


**Fig. 8.** Influence of the chosen method for  $nVp$  determination (arithmetic mean vs median) on the accuracy of the results obtained for cylindrical (a) and spherical (b) shaped particles



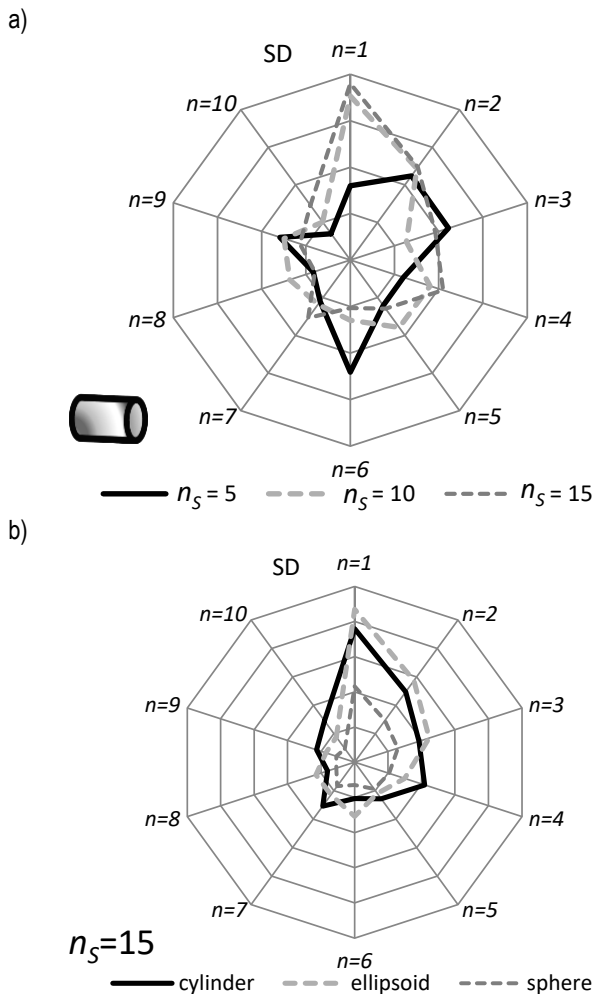


**Fig. 9.** Influence of the number of sampling points and the number of replicates (a) and the shape of reinforcing particles on the distribution of standard deviation (b)

As mentioned earlier, for simulations with  $n_s \neq 1$ ,  $nV_p$  was treated as the arithmetic mean of the volume of particle remaining in the RVE, calculated from all  $n_s$  of the simulation. Alternatively,  $nV_p$  can also be treated as the median of the results obtained over all iterations. A comparison of the effect of the method of determining the  $nV_p$  (arithmetic mean vs. median) on the accuracy of the results is shown in Figure 8. It is noted that, for most of the cases analysed, determining the particle volume using the arithmetic mean led to a higher accuracy of the calculations. There was no significant difference in the computation time of  $nV_p$  when using the arithmetic mean and the median.

The paper also analysed the distribution of the standard deviation (SD) and found it to be random (Fig.9). It was observed that a higher number of sampling and simulation repetitions usually results in a lower standard deviation. This effect is due to the fact that a larger number of samples leads to a more representative sample, which in turn translates into more stable and precise results. Increasing the number of simulation repetitions allows better averaging of the results and reduces errors due to random factors. The smallest scatter is observed for spherical particles, as their symmetry contributes to a more uniform distribution of random sampling points. Other particle shapes may have greater variability in results due to less symmetry.

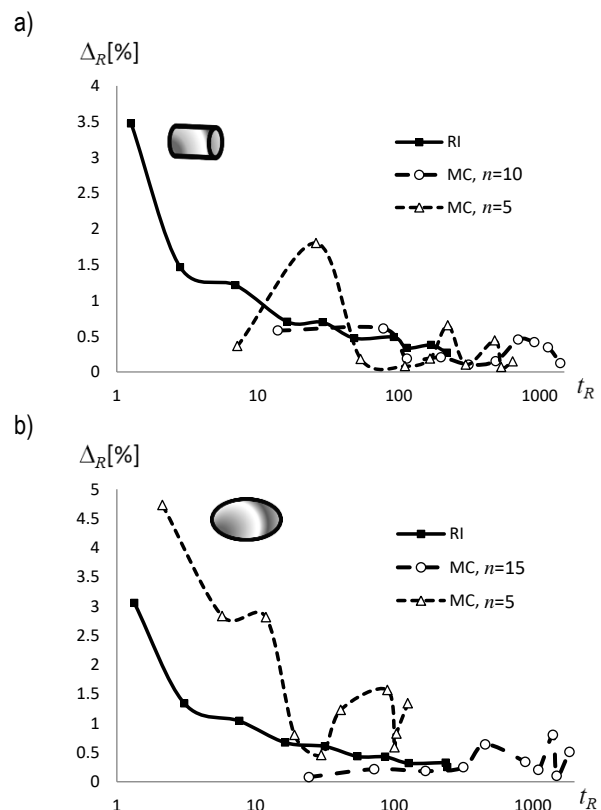
### 3.2. Comparison of accuracy of results and calculation times obtained using different methods of numerical integration

Figure 10 shows the relative calculation error and duration for the RI and MC methods. By analysing the results obtained, it can be seen that the RI method has a higher stability of results compared to the MC method. Both methods allow similar accuracy to be achieved with similar calculation times. However, in the case of the MC method, it was noted that for some cases e.g. (e.g. ellipsoid-shaped particle, Fig. 9.b,  $n=15$ ) it is possible to achieve better accuracy in less time. However, it is worth noting that the results from the MC method are more unstable and subject to greater fluctuations, which often leads to a larger error with longer calculation times. At a desired error rate of, say, 0.5%, it is well-founded to use the RI method, which provides adequate calculation precision. However, when accepting a higher possible inaccuracy, e.g. of the order of 1.5%, it is worth considering the MC method, as in this case the calculation time is shorter, which can be important for certain applications.

It is worth noting that the RI Method performs particularly well for spherical particles, where accurate results are obtained with short calculation times.

When comparing the two methods, it is important to consider both the accuracy of the calculations and the complexity of the implementation. In terms of these issues, the RI method performs slightly better.

The first aspect to consider is the availability of tools and libraries, as well as the ease of integration into existing software. With the Java programming language integrated into the Comsol environment, the RI method is more favourable to implement. The programme code for the RI method is shorter and does not require as many variables to be defined as for the MC method. This means that, in terms of programming resource availability, the RI method can be more efficient and require less effort.



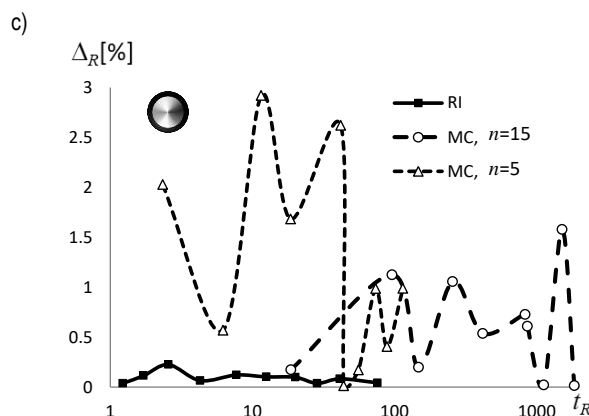


Fig. 10. Relationship between the calculation error and its time for the RI and MC methods for a cylindrical (a), ellipsoid (b) and spherical (c) particle

#### 4. SUMMARY AND CONCLUSIONS

The paper discusses numerical integration procedures employed in analysing the volume of reinforcement particles in algorithms for generating representative volume elements (RVEs) in composites with discontinuous reinforcement, when the reinforcing particles partially extend beyond the RVE. Two methods were compared, where the discretisation was performed in a systematised (RI) or random (MC) manner, focusing on the influence of the integration parameters on the accuracy of calculations and the generation time of the composite microstructure. For the Monte Carlo method, an analysis was conducted on the impact of two parameters: the number of sampling points and the number of simulation repetitions. In the RI method, the focus was solely on the number of sampling points as a parameter. The value of this parameter, for both methods, was related to the size of the reinforcing particles and the dimensional size of the RVE. The study examined how both parameters affect the analysis results and identified their optimal values to achieve precise results with a short microstructure generation time for composites with cylindrical, ellipsoidal, and spherical reinforcing particles.

Both the number of sampling points and the number of simulation repetitions were found to have a significant impact on the accuracy and stability of the results. Increasing the number of sampling points contributed to more precise results, but at the same time increased the RVE generation time. Increasing the number of simulation repetitions in the MC method led to similar effects. In addition, the RI method was observed to have a high stability of results in contrast to the MC method, where significant fluctuation and randomness of the results was noted. Therefore, when an error rate of less than 0.5% is required, the RI method is recommended, as it provides adequate precision in the calculations. On the other hand, when a slightly higher error level, for example 1.5%, is acceptable, the MC method can be considered, which has a shorter calculation time, which can be important in certain applications.

As regards the sensitivity of the tested methods to the shape of the reinforcing particles, in general, the best accuracy of the results was obtained for particles with a spherical shape, which is characterised by the greatest symmetry. Moreover, the calculation time for spherical particles was usually the shortest, while for ellipsoidal particles it was the longest due to the greater complexi-

ty of the condition for checking the belongingness of the sampling point to the particle.

The findings presented here can help designers make decisions regarding the choice of an appropriate discretisation method and number of points when generating models of composites with discontinuous reinforcement. Through optimally selected parameters, designers will be able to achieve accurate analysis results while minimising model generation time, which is of great importance in engineering practice. Further research is planned to focus on developing advanced discretisation algorithms that take into account more complex forms of reinforcement particles.

#### Nomenclature:

- $a_u$  – side length of a representative volume element (RVE)
- $d_i, b_i, l_i$  – characteristic dimensions of the particles of the reinforcement fraction
- $nV_p$  – the estimated volume of the part of the reinforcement particle remaining in the RVE
- $N_{MC}$  – the number of points used in Monte Carlo method (MC)
- $N_{RI}$  – the number of points used in Regular Integration method (RI)
- $\Delta$  – the grid interval used in RI method
- $V_p$  – the reference volume
- $\Delta_R$  – the relative error
- $t_R$  – the relative calculation time
- $n$  – the multiplicative constant
- $n_s$  – numbers of simulation repetitions used in MC method

#### REFERENCES

1. Robinson M. J., Kosmatka J. B. Development of a Short-Span Fiber-Reinforced Composite Bridge for Emergency Response and Military Applications. *Journal of Bridge Engineering* [Internet]. 2008;13(4):388–97. Available from: [https://ascelibrary.org/doi/abs/10.1061/\(ASCE\)1084-0702\(2008\)13:4\(388\)](https://ascelibrary.org/doi/abs/10.1061/(ASCE)1084-0702(2008)13:4(388))
2. Macke A, Schultz B, Rohatgi PK. Metal Matrix Composites Offer the Automotive Industry an Opportunity to Reduce Vehicle Weight, Improve Performance. *Advanced Materials and Processes*. 2012;170:19–23.
3. Mieczkowski G, Szpica D, Borawski A, Diliunas S, Pilkaite T, Leisis V. Application of Smart Materials in the Actuation System of a Gas Injector. *Materials*. Basel Switzerland [Internet]. 2021;14(22). Available from: <https://pubmed.ncbi.nlm.nih.gov/34832384/>
4. Borawski A. Impact of Operating Time on Selected Tribological Properties of the Friction Material in the Brake Pads of Passenger Cars. *Materials* 2021;14(4):884 [Internet]. Available from: <https://www.mdpi.com/1996-1944/14/4/884/html>
5. Beck AJ, Hodzic A, Soutis C, Wilson CW. Influence of Implementation of Composite Materials in Civil Aircraft Industry on reduction of Environmental Pollution and Greenhouse Effect. *IOP Conference Series: Materials Science and Engineering* [Internet]. 2011;26:12015. Available from: <https://doi.org/10.1088%2F1757-899x%2F26%2F1%2F012015>
6. Richerson DW. *Modern Ceramic Engineering: Properties, Processing, and Use in Design*, Third Edition. CRC Press. 2005.
7. Ibrahim IA, Mohamed FA, Lavernia EJ. Particulate reinforced metal matrix composites — a review. *Journal of Materials Science* [Internet]. 1991;26(5):1137–56. Available from: <https://link.springer.com/article/10.1007/BF00544448>
8. Zhao X, Wang J, Chen Q, Jiang H, Chen C, Tu W. Microstructure design and optimization of multilayered piezoelectric composites with wavy architectures. [Internet]. 2023. Available from: <https://www.tandfonline.com/doi/abs/10.1080/15376494.2023.2172234>

9. Mieczkowski G. Static Electromechanical Characteristics of Piezoelectric Converters with various Thickness and Length of Piezoelectric Layers. *Acta Mechanica et Automatica*. 2019;13(1):30–6.
10. Borawski A, Szpica D, Mieczkowski G, Borawska E, Awad MM, Shalaby RM, et al. Theoretical Analysis of the Motorcycle Front Brake Heating Process during High Initial Speed Emergency Braking. *Journal of Applied and Computational Mechanics*. 2020;6(Special Issue):1431–7.
11. Wang C, Ping X, Zhang Y, Xiao Z, Xiao Y. On the three-dimensional singular stress field near the corner front of revolution-shaped inclusions. *Acta Mechanica* [Internet]. 2021;232(12):4867–95. Available from: <https://link.springer.com/article/10.1007/s00707-021-03078-2>
12. Ran Z, Yan Y, Li J, Qi Z, Yang L. Determination of thermal expansion coefficients for unidirectional fiber-reinforced composites. *Chinese Journal of Aeronautics* [Internet]. 2014;27(5):1180–7. Available from: <https://linkinghub.elsevier.com/retrieve/pii/S1000936114000429>
13. Santos JA, Sanches AO, Akasaki JL, Tashima MM, Longo E, Mal-monge JA. Influence of PZT insertion on Portland cement curing process and piezoelectric properties of 0–3 cement-based composites by impedance spectroscopy. *Construction and Building Materials*. 2020;238:117675.
14. Oh KH, Han KS. Short-fiber/particle hybrid reinforcement: Effects on fracture toughness and fatigue crack growth of metal matrix composites. *Composites Science and Technology* [Internet]. 2007;67(7):1719–26. Available from: <http://www.sciencedirect.com/science/article/pii/S026635380600251X>
15. Sijo MT, Jayadevan KR. Analysis of Stir Cast Aluminium Silicon Carbide Metal Matrix Composite: A Comprehensive Review. *Procedia Technology* [Internet]. 2016;24:379–85. Available from: <http://www.sciencedirect.com/science/article/pii/S2212017316301360>
16. Caban J, Drożdż P, Ignaciuk P, Kordos P. The impact of changing the fuel dose on chosen parameters of the diesel engine start-up process. *Transport Problems*. 2019;14(4):51–62.
17. Szpica D. Fuel dosage irregularity of LPG pulse vapor injectors at different stages of wear. *Mechanika*. 2016;22(1):44–50.
18. Duschlbauer D, Böhm HJ, Pettermann HE. Computational Simulation of Composites Reinforced by Planar Random Fibers: Homogenization and Localization by Unit Cell and Mean Field Approaches. [Internet]. 2006;40(24):2217–34. Available from: <https://journals.sagepub.com/doi/10.1177/0021998306062317>
19. Tornabene F, Luo Y. Microstructure-Free Finite Element Modeling for Elasticity Characterization and Design of Fine-Particulate Composites. *Journal of Composites Science* [Internet]. 2022;6(2):35. Available from: <https://www.mdpi.com/2504-477X/6/2/35/htm>
20. Tu ST, Cai WZ, Yin Y, Ling X. Numerical Simulation of Saturation Behavior of Physical Properties in Composites with Randomly Distributed Second-phase. [Internet]. 2005;39(7):617–31. Available from: <https://journals.sagepub.com/doi/10.1177/0021998305047263>
21. Warguła Ł, Wojtkowiak D, Kukla M, Talaśka K. Symmetric Nature of Stress Distribution in the Elastic-Plastic Range of Pinus L. Pine Wood Samples Determined Experimentally and Using the Finite Element Method (FEM). *Symmetry* 2021;13(1):39 [Internet]. Available from: <https://www.mdpi.com/2073-8994/13/1/39/htm>
22. Yao Z, Kong F, Wang H, Wang P. 2D Simulation of composite materials using BEM. *Engineering Analysis with Boundary Elements*. 2004;28(8):927–35.
23. Chen X, Liu Y. Multiple-cell modeling of fiber-reinforced composites with the presence of interphases using the boundary element method. *Computational Materials Science*. 2001;21(1):86–94.
24. Drugan WJ, Willis JR, Drugan WJ, Willis JR. A micromechanics-based nonlocal constitutive equation and estimates of representative volume element size for elastic composites. *JMPSo* [Internet]. 1996;44(4):497–524. Available from: <https://ui.adsabs.harvard.edu/abs/1996JMPSo..44..497D/abstract>
25. Kanit T, Forest S, Galliet I, Mounoury V, Jeulin D. Determination of the size of the representative volume element for random composites: statistical and numerical approach. *International Journal of Solids and Structures*. 2003;40(13–14):3647–79.
26. Widom B. Random Sequential Addition of Hard Spheres to a Volume. *The Journal of Chemical Physics* [Internet]. 1966;44(10):3888–94. Available from: [/aip/jcp/article/44/10/3888/81726/Random-Sequential-Addition-of-Hard-Spheres-to-a](https://aip/jcp/article/44/10/3888/81726/Random-Sequential-Addition-of-Hard-Spheres-to-a)
27. Böhm HJ, Eckschlag A, Han W. Multi-inclusion unit cell models for metal matrix composites with randomly oriented discontinuous reinforcements. *Computational Materials Science*. 2002;25(1–2):42–53.
28. Kari S, Berger H, Gabbert U. Numerical evaluation of effective material properties of randomly distributed short cylindrical fibre composites. *Computational Materials Science*. 2007;39(1):198–204.
29. Lee WJ, Son JH, Park IM, Oak JJ, Kimura H, Park YH. Analysis of 3D random Al18B4O33 whisker reinforced Mg composite using FEM and random sequential adsorption. *Materials Transactions*. 2010;51(6):1089–93.
30. Bailakanavar M, Liu Y, Fish J, Zheng Y. Automated modeling of random inclusion composites. *Engineering with Computers*. 2012;30(4):609–25.
31. Zhou J, Qi L, Gokhale AM. Generation of Three-Dimensional Microstructure Model for Discontinuously Reinforced Composite by Modified Random Sequential Absorption Method. *Journal of Engineering Materials and Technology, Transactions of the ASME* [Internet]. 2016;138(2). Available from: <https://asmedigitalcollection.asme.org/materialstechnology/article/138/2/021001/384156/Generation-of-Three-Dimensional-Microstructure>
32. Jin BC, Pelegri AA. Three-dimensional numerical simulation of random fiber composites with high aspect ratio and high volume fraction. *Journal of Engineering Materials and Technology* [Internet]. 2011;133(4). Available from: <https://asmedigitalcollection.asme.org/materialstechnology/article/133/4/041014/469603/Three-Dimensional-Numerical-Simulation-of-Random>
33. Qing H. Automatic generation of 2D micromechanical finite element model of silicon-carbide/aluminum metal matrix composites: Effects of the boundary conditions. *Materials & Design*. 2013;44:446–53.
34. Eberly D. Robust Computation of Distance Between Line Segments. *Geometric Tools* [Internet]. 2018;1–14. Available from: <https://www.geometrictools.com/>
35. Mieczkowski G. Determination of effective mechanical properties of particle - Reinforced composite material with use of numerical approach. *Engineering for Rural Development*. 2020;19:571–7.

This research was financed by the Ministry of Science and Higher Education of Poland with allocation to the Faculty of Mechanical Engineering Białystok University of Technology for the WZ/WM-IIM/5/2023 academic project in the mechanical engineering discipline.

Grzegorz Mieczkowski:  <https://orcid.org/0000-0002-8090-1671>

Dariusz Szpica:  <https://orcid.org/0000-0002-7813-8291>

Borawski Andrzej:  <https://orcid.org/0000-0001-5817-655X>



This work is licensed under the Creative Commons BY-NC-ND 4.0 license.

# HUMAN VISION AS A MULTI-CIRCUIT MATHEMATICAL MODEL OF THE AUTOMATED CONTROL SYSTEM

Ryszard SZCZEBIOT<sup>\*</sup>, Roman KACZYŃSKI<sup>\*\*</sup>, Leszek GOŁDYN<sup>\*</sup>

<sup>\*</sup>Faculty of Computer Science and Technology University of Łomża,  
ul. Akademicka 14, 18-400 Łomża, Poland

<sup>\*\*</sup>Faculty of Mechanical Engineering, Białystok University of Technology,  
ul. Wiejska 45C, 15-351 Białystok, Poland

[rysard@szczebiot.pl](mailto:rysard@szczebiot.pl), [r.kaczynski@pb.edu.pl](mailto:r.kaczynski@pb.edu.pl), [lgoldyn@al.edu.pl](mailto:lgoldyn@al.edu.pl)

received 9 November 2023, revised 2 April 2024, accepted 12 April 2024

**Abstract:** The paper contains a proposal an original, extended mathematical model of an automatic system of human vision reaction to a forcing light pulse. A comprehensive mathematical model of the vision process was proposed in the form of an equation described in the frequency (dynamics) domain. Mathematical modelling of human senses is very important. It enables better integration of automation systems with a human cooperating with them, also as an automation system. This provides the basis for reasoning based on a mathematical model instead of intuitive reasoning about human reactions to visual stimuli. A block diagram of the proposed system with five human reaction paths is given. The following can be distinguished in the scheme: the main track consisting of: the transport delay of the eye reaction, the transport delay of the afferent nerves, the inertia of the brain with a preemptive action, the transport delay of the centrifugal nerves and the inertial and transport delay of the neuromotor system. In addition, the scheme of the system includes four tracks of negative feedback of motor and force reactions: upper eyelid, lower eyelid, pupil and lens. In the proposed model, the components of each path along with their partial mathematical models are given and discussed. For each reaction path, their overall mathematical models are also given. Taking into account the comprehensive models of all five reaction paths, a complete mathematical model of the automatic system of human reaction to a forcing light impulse is proposed. The proposed mathematical model opens up many possibilities for synchronizing it with mathematical models of many mechatronics and automation systems and their research. Optimizing the parameters of this model and its synchronization with specific models of automation systems is difficult and requires many numerical experiments. This approach enables the design of automation systems that are better synchronized with human reactions to existing stimuli and the selection of optimal parameters of their operation already in the design phase. The proposed model allows, for example, accurate determination of difficulty levels in computer games. Another example of the use of the proposed model is the study of human reactions to various situations generated virtually, for example in flight simulators and other similar ones.

**Key words:** automation system; human vision; mathematical model

## 1. INTRODUCTION

Human has five basic senses, each of which has its own specific characteristics and ways of affecting human, in synchronization with other senses. A lot of different papers have been created on the interaction of human and his senses with machines, robots and automation systems. In this regard, for example, the paper of Zhijun et al. [1] on physical human-robot interaction approaches for the developed robotic exoskeleton using admittance control. The model of human interaction with automation was proposed by Parasuraman et al. [2], but it is a proposal of a very simple model. Daley [3] proposes an algorithm development technique that utilizes modes of the human visual system. The basis of the technique evaluation was the Georgia Tech Vision model. Thomas [4] eight models examined as input-output representations of steady-state vision in humans. Proposed three new models for sensitivity. A nonlinear least squares fitting algorithm produced the optimal parameters for each model. Matsui [5] formulates a nonstationary spatio-temporal human vision model has been formulated based on essential properties of the human vision system. Research reported by Karmakar [6] comprises evaluation of pilot's vision in a jet aircraft in virtual environment to demonstrate how vision

analysis tools of digital human modelling software can be used effectively for such study. From present study, it can be concluded that vision analysis tool of digital human modelling software was found very effective. The paper [7] contains a proposal extend model of the human visual system to predict the effects of age. The complete model, including an empirical neural component, can well explain the differences in sensitivity between old and young observers. In the paper [8] a review of Human Visual System (HVS) based Digital Watermarking schemes are presented with their mathematical model.

So far, there have been no scientific inquiries we have come across which treat the human being as a complex automation system.

However, exceptions can be given, such as in a fairly old book by Antoniewicz [9], in which this issue was briefly considered and a model of treating human and his senses as an automatic system was proposed. The paper of Asadi, et al. [10], is also noteworthy which proposed a mathematical model of the vestibular system to ensure successful human perception modelling and simulation.

Mathematical modelling of human senses is of great importance as it enables better integration of the automation system model with the human model cooperating with them as an automation system. It is then possible to combine the above-

mentioned models and build one coherent multi-circuit mathematical model of an automatic system with signals affecting the human senses.

Most biological processes exhibit marked non-linearity in all its kinds and combinations. Both: sensitivity threshold, saturation range, relay action and hysteresis can be observed. These factors describe the behaviour in steady, static, normalized states.

Analyzing the dynamic time of human behaviour observed in the sphere of reaction to external stimuli, one can notice interactions defined in automation as overshoots or higher-order inertia reactions.

In this approach, a group of human behaviours made up of activities related to excessive reaction to external influences should be taken into account. There is usually some redundancy, a quick, violent reaction to stimuli, which expires over time, e.g. complete closure (covering) of the eye, which is then automatically uncovered. In automation, this is a classic differentiation operation. When analyzing human reactions to external stimuli, behaviour control can be assumed using a natural controller analogous to the PID controller. Such processes take place in many aspects of human behaviour. This applies not only to the sense of sight, but also to maintaining balance, controlling pain, effort, resistance to higher temperatures, etc.

Figure 1 presents a diagram of the structural model of human reaction to the received signals developed by the brain after obtaining information from various human senses, proposed by Antoniewicz [9]. The diagram does not show the sensory blocks that acquire information. The causal signal (input to the scheme) is an impulse developed by the cerebral cortex. In the main path there are effectors, i.e. executive organs of the body that perform or change their activity under the influence of a nerve impulse. The main track, as an effector, performs the reaction, after it has been triggered.

The effectors are usually loaded with an external influence. The effectors, in the model view of a human, are his muscles.

The diagram (Fig. 1) illustrates the entire system from the sensor (eye) to the effector (muscles) in functional terms. The system works on the basis of frequency modulation or the number of pulses. The diagram shows the process of responding to a stimulus in terms of impact. It provides both a track for motor reaction and a track for force reaction. It does not indicate in detail

the groups of muscular-defensive tracks related to the structure of the eye system and their protective functions. However, it shows the strengthening track related to the innervations of the muscles, shown in the diagram as a parallel connection. In this way, the innervations of the muscles are depicted. The reinforcing action is shown, generating opportunities related to overcoming the influence of the load, i.e. disturbances for the reaction. Apart from the main track, the scheme has two branches of active control of the regulatory action related to the general concept of force and motor reaction. These tracks represent two functional reaction tracks that are realized in the excitation-human system.

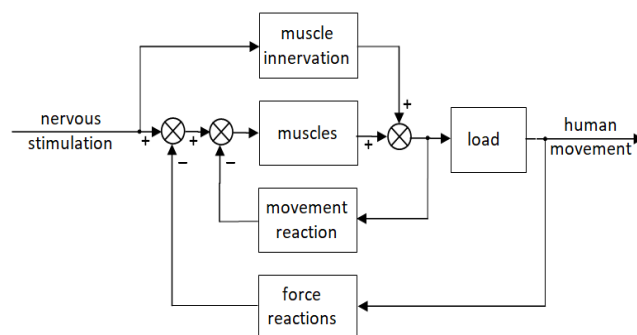


Fig. 1. Block diagram of the excitation pulse system - human reaction [9]

Fig. 2 shows a schematic detailing of the main track without defensive reactions from Fig. 1 of the model structural diagram of the main track of the light signal - human reaction system developed on the basis of Antoniewicz's proposal [9]. The presented system is a series connection, so there are no regulatory actions related to the optimization of the response to the excitation signal. However, it has all the essential terms in the main track with the action command as the output signal. There are no effectors in the diagram, which appear in Fig. 3 in the feedback branches as a reaction to executive and protective actions. To put it simply, it can be assumed that the executive members (effectors) are the last member: the neuromotor system.

In his considerations, Antoniewicz did not propose a mathematical model of the system in Fig. 2.

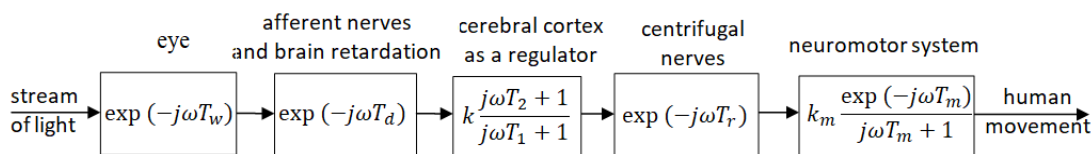


Fig. 2. General equivalent diagram of a human as a controlling operator [9]

## 2. HUMAN VISION AS MATHEMATICAL MODEL OF THE AUTOMATION SYSTEM

The human visual system is an extremely complex sense. The paper contains a proposal developed spectral mathematical structural model of the system describing the process of the influence of the light signal on the organ of vision and the human neuromotor reaction.

Fig. 3 shows a proposed block diagram of human reaction to a stream of light.

A comprehensive mathematical model determined on the basis of the diagram, shown in Fig.3, is a complex model, having several feedbacks associated with specific groups of effectors. The main track is a supplemented and improved reaction track proposed by Antoniewicz [9]. This circuit consists of the transport delay of the eye reaction, the transport delay of the afferent nerves, the inertia of the brain with anticipatory action, the transport delay of the centrifugal nerves, and the inertial and transport delay of the neuromotor system. It also takes into account the power amplification of signals functionally present in this track.



The diagram of the proposed model of the reaction of human movement to a light excitation signal (Fig. 3) consists of four tracks of negative feedbacks:

- negative feedback track of the motor-force reaction of the upper eyelid,
- negative feedback track of the motor-force reaction of the lower eyelid,
- negative feedback track of the pupil's motor-force reaction,
- negative feedback track of the motor-force reaction of the lens.

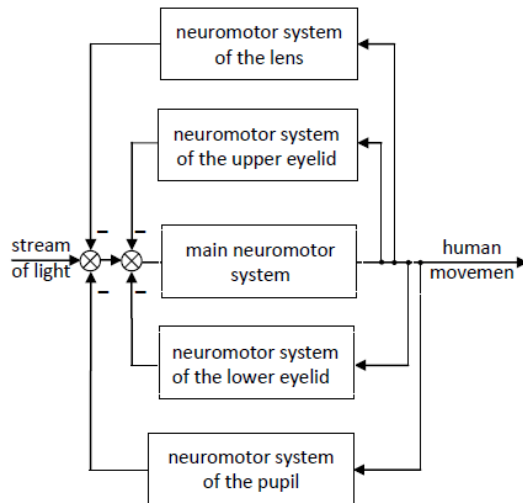


Fig. 3. Block diagram of the light excitation system for human reaction

The diagram shows mathematical models in the frequency domain of the listed components of the main circuit and other circuits.

The block diagram of the light excitation - human reaction system (Fig. 3) is the basis for modelling a complex system. This will enable simulation tests of the model in the time domain as well as in the frequency domain.

Negative feedback track of the motor-force reaction of the upper eyelid is shown in Fig. 4.

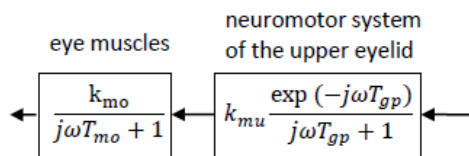


Fig. 4. Negative feedback track block diagram of the motor-force reaction of the upper eyelid

It consists of the neuromotor system of the upper eyelid and the eye muscles. The mathematical model of the negative feedback track of the reaction of the neuromotor system of the upper eyelid and eye muscles has the following form:

$$G_1(s) = k_{mu} \frac{e^{-T_{gp}s}}{T_{gp}s + 1} k_{mo} \frac{1}{T_{mo}s + 1} \quad (1)$$

where:  $k_{mu}$  - amplification factor of the neuromuscular reaction system;  $T_{gp}$  - time constant associated with the transport delay and inertial action of the upper eyelid;  $k_{mo}$  - eye muscle strengthening coefficient;  $T_{mo}$  - time constant of inertia of the eye muscles.

Negative feedback track of the motor-force reaction of the lower eyelid is shown in Fig. 5.

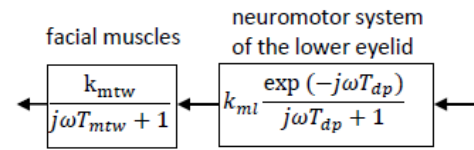


Fig. 5. Negative feedback track block diagram of the motor-force reaction of the lower eyelid

It consists of the neuromotor system of the lower eyelid and facial muscles. The mathematical model of the negative feedback track of the reaction of the neuromotor system of the lower eyelid and facial muscles has the following form:

$$G_2(s) = k_{ml} \frac{e^{-T_{dp}s}}{T_{dp}s + 1} k_{mtw} \frac{1}{T_{mtw}s + 1}, \quad (2)$$

where:  $k_{ml}$  - amplification factor of the neuromuscular reaction system;  $T_{dp}$  - time constant associated with the transport and inertial delay of the neuromotor system of the lower eyelid;  $k_{mtw}$  - coefficient of neuromuscular strengthening of the facial muscles;  $T_{mtw}$  - time constant of inertia of facial muscles action.

Negative feedback track of the pupil's motor-force reaction is shown in Fig. 6.

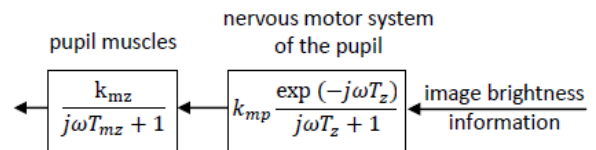


Fig. 6. Negative feedback track block diagram of the pupil's motor-force reaction

It consists of the neuromotor system of the pupil and the muscles of the pupil. The excitation signal is information about the brightness of the image. The excitation signal is information about the sharpness of the image.

The mathematical model of the negative feedback loop of the motor-force reaction of the pupil and the pupillary muscles has the following form:

$$G_3(s) = k_{mp} \frac{e^{-T_z s}}{T_z s + 1} k_{mz} \frac{1}{T_{mz}s + 1}, \quad (3)$$

where:  $k_{mp}$  - amplification factor of the neuromuscular reaction system;  $T_z$  - time constant related to the transport and inertial delay of the eye pupil;  $k_{mz}$  - coefficient of strengthening the pupillary muscles;  $T_{mz}$  - time constant of inertia of the action of the muscles of the pupil.

The negative feedback track of the motor-force reaction of the lens consists of the neuromotor system of the lens and the ciliary muscles is shown in Fig. 7.

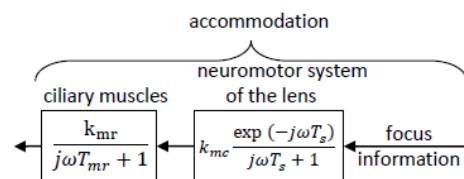


Fig. 7. Negative feedback track block diagram of the motor-force reaction of the lens

The mathematical model of the negative feedback track of the motor-force reaction of the lens and ciliary muscles has the following form:

$$G_4(s) = k_{mc} \frac{e^{-T_s s}}{T_s s + 1} k_{mr} \frac{1}{T_{mr} s + 1} \quad (4)$$

where:  $k_{mc}$  - amplification factor of the neuromuscular reaction system;  $T_s$  - time constant related to the transport and inertial delay of the lens operation when correcting the sharpness of the image;  $k_{mr}$  - ciliary muscle strengthening coefficient;  $T_{mr}$  - time constant of inertia of the action of the ciliary muscles.

In Figure 8, showing the detailed block diagram of the light excitation system for human reaction, the basic track can be distinguished. This is a modification of the track proposed by Antoniewicz in Fig. 2. The equation of the proposed main track in algebraic form is as follows:

$$G_0(s) = \frac{k_w e^{-T_w s} k_d e^{-T_d s} k_c (T_2 s + 1) e^{-T_r s} k_r}{T_1 s + 1}, \quad (5)$$

where:  $k_w$  - eye amplification factor (overall);  $T_w$  - transport delay time (related directly to the eye);  $k_d$  - afferent nerve (optical nerve) gain factor;  $T_d$  - transport delay time related to the transmission of a signal stimulated by the afferent nerve and brain reaction time;  $k_c$  - gain factor of the central part of the nervous system (cerebral cortex);  $T_2$  - lead time related to the self-adjusting regulatory action of the central part of the nervous system;  $T_r$  - transport delay time (signal transmission) of the centrifugal nerve;  $k_r$  - centrifugal (motor) nerve gain factor;  $T_1$  - time constant of inertia associated with the central part of the nervous system.

The generalized holistic model of human reaction to the light flux, in accordance with the diagram in Fig. 8, has the following form:

$$G(s) = \frac{G_0(s)}{(1 + G_0(s)(G_1(s) + G_2(s) + G_3(s) + G_4(s)))} \frac{k_m e^{-T_M s}}{(T_m s + 1)} \quad (6)$$

where:  $k_m$  - amplification factor of the neuromuscular reaction system;  $T_M$  - transport delay time associated with the reaction of the neuromuscular system;  $T_m$  - time constant of inertia of the neuromuscular system.

The relationship shows a complex system of reactions of the eyesight system consisting of four self-regulating tracks in the protective behaviour of the human eye.

Taking into account the detailed mathematical models of all tracks (1, 2, 3, 4, and 5), the generalized overall model of human reaction to the light stream based on equation (6) has the form of the operator transfer function  $G(s)$  generated with the Mathematica program:

$$G(s) = \frac{(e^{-s T_d - s T_M - s T_r - s T_w} k_c k_d k_m k_r k_w (1 + s T_2))}{((1 + s T_1) (1 + s T_m) (1 + (e^{-s T_d - s T_{dp} - s T_{gp} - s T_r - s T_s - s T_w - s T_z} k_c k_d k_{m1} k_{m2} k_{m3} k_{m4} k_{m5} k_{m6} k_{m7} k_{m8} k_{m9} k_{m10} k_{m11} k_{m12} k_{m13} k_{m14} k_{m15} k_{m16} k_{m17} k_{m18} k_{m19} k_{m20} k_{m21} k_{m22} k_{m23} k_{m24} k_{m25} k_{m26} k_{m27} k_{m28} k_{m29} k_{m30} k_{m31} k_{m32} k_{m33} k_{m34} k_{m35} k_{m36} k_{m37} k_{m38} k_{m39} k_{m40} k_{m41} k_{m42} k_{m43} k_{m44} k_{m45} k_{m46} k_{m47} k_{m48} k_{m49} k_{m50} k_{m51} k_{m52} k_{m53} k_{m54} k_{m55} k_{m56} k_{m57} k_{m58} k_{m59} k_{m60} k_{m61} k_{m62} k_{m63} k_{m64} k_{m65} k_{m66} k_{m67} k_{m68} k_{m69} k_{m70} k_{m71} k_{m72} k_{m73} k_{m74} k_{m75} k_{m76} k_{m77} k_{m78} k_{m79} k_{m80} k_{m81} k_{m82} k_{m83} k_{m84} k_{m85} k_{m86} k_{m87} k_{m88} k_{m89} k_{m90} k_{m91} k_{m92} k_{m93} k_{m94} k_{m95} k_{m96} k_{m97} k_{m98} k_{m99} k_{m100} k_{m101} k_{m102} k_{m103} k_{m104} k_{m105} k_{m106} k_{m107} k_{m108} k_{m109} k_{m110} k_{m111} k_{m112} k_{m113} k_{m114} k_{m115} k_{m116} k_{m117} k_{m118} k_{m119} k_{m120} k_{m121} k_{m122} k_{m123} k_{m124} k_{m125} k_{m126} k_{m127} k_{m128} k_{m129} k_{m130} k_{m131} k_{m132} k_{m133} k_{m134} k_{m135} k_{m136} k_{m137} k_{m138} k_{m139} k_{m140} k_{m141} k_{m142} k_{m143} k_{m144} k_{m145} k_{m146} k_{m147} k_{m148} k_{m149} k_{m150} k_{m151} k_{m152} k_{m153} k_{m154} k_{m155} k_{m156} k_{m157} k_{m158} k_{m159} k_{m160} k_{m161} k_{m162} k_{m163} k_{m164} k_{m165} k_{m166} k_{m167} k_{m168} k_{m169} k_{m170} k_{m171} k_{m172} k_{m173} k_{m174} k_{m175} k_{m176} k_{m177} k_{m178} k_{m179} k_{m180} k_{m181} k_{m182} k_{m183} k_{m184} k_{m185} k_{m186} k_{m187} k_{m188} k_{m189} k_{m190} k_{m191} k_{m192} k_{m193} k_{m194} k_{m195} k_{m196} k_{m197} k_{m198} k_{m199} k_{m200} k_{m201} k_{m202} k_{m203} k_{m204} k_{m205} k_{m206} k_{m207} k_{m208} k_{m209} k_{m210} k_{m211} k_{m212} k_{m213} k_{m214} k_{m215} k_{m216} k_{m217} k_{m218} k_{m219} k_{m220} k_{m221} k_{m222} k_{m223} k_{m224} k_{m225} k_{m226} k_{m227} k_{m228} k_{m229} k_{m230} k_{m231} k_{m232} k_{m233} k_{m234} k_{m235} k_{m236} k_{m237} k_{m238} k_{m239} k_{m240} k_{m241} k_{m242} k_{m243} k_{m244} k_{m245} k_{m246} k_{m247} k_{m248} k_{m249} k_{m250} k_{m251} k_{m252} k_{m253} k_{m254} k_{m255} k_{m256} k_{m257} k_{m258} k_{m259} k_{m260} k_{m261} k_{m262} k_{m263} k_{m264} k_{m265} k_{m266} k_{m267} k_{m268} k_{m269} k_{m270} k_{m271} k_{m272} k_{m273} k_{m274} k_{m275} k_{m276} k_{m277} k_{m278} k_{m279} k_{m280} k_{m281} k_{m282} k_{m283} k_{m284} k_{m285} k_{m286} k_{m287} k_{m288} k_{m289} k_{m290} k_{m291} k_{m292} k_{m293} k_{m294} k_{m295} k_{m296} k_{m297} k_{m298} k_{m299} k_{m300} k_{m301} k_{m302} k_{m303} k_{m304} k_{m305} k_{m306} k_{m307} k_{m308} k_{m309} k_{m310} k_{m311} k_{m312} k_{m313} k_{m314} k_{m315} k_{m316} k_{m317} k_{m318} k_{m319} k_{m320} k_{m321} k_{m322} k_{m323} k_{m324} k_{m325} k_{m326} k_{m327} k_{m328} k_{m329} k_{m330} k_{m331} k_{m332} k_{m333} k_{m334} k_{m335} k_{m336} k_{m337} k_{m338} k_{m339} k_{m340} k_{m341} k_{m342} k_{m343} k_{m344} k_{m345} k_{m346} k_{m347} k_{m348} k_{m349} k_{m350} k_{m351} k_{m352} k_{m353} k_{m354} k_{m355} k_{m356} k_{m357} k_{m358} k_{m359} k_{m360} k_{m361} k_{m362} k_{m363} k_{m364} k_{m365} k_{m366} k_{m367} k_{m368} k_{m369} k_{m370} k_{m371} k_{m372} k_{m373} k_{m374} k_{m375} k_{m376} k_{m377} k_{m378} k_{m379} k_{m380} k_{m381} k_{m382} k_{m383} k_{m384} k_{m385} k_{m386} k_{m387} k_{m388} k_{m389} k_{m390} k_{m391} k_{m392} k_{m393} k_{m394} k_{m395} k_{m396} k_{m397} k_{m398} k_{m399} k_{m400} k_{m401} k_{m402} k_{m403} k_{m404} k_{m405} k_{m406} k_{m407} k_{m408} k_{m409} k_{m410} k_{m411} k_{m412} k_{m413} k_{m414} k_{m415} k_{m416} k_{m417} k_{m418} k_{m419} k_{m420} k_{m421} k_{m422} k_{m423} k_{m424} k_{m425} k_{m426} k_{m427} k_{m428} k_{m429} k_{m430} k_{m431} k_{m432} k_{m433} k_{m434} k_{m435} k_{m436} k_{m437} k_{m438} k_{m439} k_{m440} k_{m441} k_{m442} k_{m443} k_{m444} k_{m445} k_{m446} k_{m447} k_{m448} k_{m449} k_{m450} k_{m451} k_{m452} k_{m453} k_{m454} k_{m455} k_{m456} k_{m457} k_{m458} k_{m459} k_{m460} k_{m461} k_{m462} k_{m463} k_{m464} k_{m465} k_{m466} k_{m467} k_{m468} k_{m469} k_{m470} k_{m471} k_{m472} k_{m473} k_{m474} k_{m475} k_{m476} k_{m477} k_{m478} k_{m479} k_{m480} k_{m481} k_{m482} k_{m483} k_{m484} k_{m485} k_{m486} k_{m487} k_{m488} k_{m489} k_{m490} k_{m491} k_{m492} k_{m493} k_{m494} k_{m495} k_{m496} k_{m497} k_{m498} k_{m499} k_{m500} k_{m501} k_{m502} k_{m503} k_{m504} k_{m505} k_{m506} k_{m507} k_{m508} k_{m509} k_{m510} k_{m511} k_{m512} k_{m513} k_{m514} k_{m515} k_{m516} k_{m517} k_{m518} k_{m519} k_{m520} k_{m521} k_{m522} k_{m523} k_{m524} k_{m525} k_{m526} k_{m527} k_{m528} k_{m529} k_{m530} k_{m531} k_{m532} k_{m533} k_{m534} k_{m535} k_{m536} k_{m537} k_{m538} k_{m539} k_{m540} k_{m541} k_{m542} k_{m543} k_{m544} k_{m545} k_{m546} k_{m547} k_{m548} k_{m549} k_{m550} k_{m551} k_{m552} k_{m553} k_{m554} k_{m555} k_{m556} k_{m557} k_{m558} k_{m559} k_{m560} k_{m561} k_{m562} k_{m563} k_{m564} k_{m565} k_{m566} k_{m567} k_{m568} k_{m569} k_{m570} k_{m571} k_{m572} k_{m573} k_{m574} k_{m575} k_{m576} k_{m577} k_{m578} k_{m579} k_{m580} k_{m581} k_{m582} k_{m583} k_{m584} k_{m585} k_{m586} k_{m587} k_{m588} k_{m589} k_{m590} k_{m591} k_{m592} k_{m593} k_{m594} k_{m595} k_{m596} k_{m597} k_{m598} k_{m599} k_{m600} k_{m601} k_{m602} k_{m603} k_{m604} k_{m605} k_{m606} k_{m607} k_{m608} k_{m609} k_{m610} k_{m611} k_{m612} k_{m613} k_{m614} k_{m615} k_{m616} k_{m617} k_{m618} k_{m619} k_{m620} k_{m621} k_{m622} k_{m623} k_{m624} k_{m625} k_{m626} k_{m627} k_{m628} k_{m629} k_{m630} k_{m631} k_{m632} k_{m633} k_{m634} k_{m635} k_{m636} k_{m637} k_{m638} k_{m639} k_{m640} k_{m641} k_{m642} k_{m643} k_{m644} k_{m645} k_{m646} k_{m647} k_{m648} k_{m649} k_{m650} k_{m651} k_{m652} k_{m653} k_{m654} k_{m655} k_{m656} k_{m657} k_{m658} k_{m659} k_{m660} k_{m661} k_{m662} k_{m663} k_{m664} k_{m665} k_{m666} k_{m667} k_{m668} k_{m669} k_{m670} k_{m671} k_{m672} k_{m673} k_{m674} k_{m675} k_{m676} k_{m677} k_{m678} k_{m679} k_{m680} k_{m681} k_{m682} k_{m683} k_{m684} k_{m685} k_{m686} k_{m687} k_{m688} k_{m689} k_{m690} k_{m691} k_{m692} k_{m693} k_{m694} k_{m695} k_{m696} k_{m697} k_{m698} k_{m699} k_{m700} k_{m701} k_{m702} k_{m703} k_{m704} k_{m705} k_{m706} k_{m707} k_{m708} k_{m709} k_{m710} k_{m711} k_{m712} k_{m713} k_{m714} k_{m715} k_{m716} k_{m717} k_{m718} k_{m719} k_{m720} k_{m721} k_{m722} k_{m723} k_{m724} k_{m725} k_{m726} k_{m727} k_{m728} k_{m729} k_{m730} k_{m731} k_{m732} k_{m733} k_{m734} k_{m735} k_{m736} k_{m737} k_{m738} k_{m739} k_{m740} k_{m741} k_{m742} k_{m743} k_{m744} k_{m745} k_{m746} k_{m747} k_{m748} k_{m749} k_{m750} k_{m751} k_{m752} k_{m753} k_{m754} k_{m755} k_{m756} k_{m757} k_{m758} k_{m759} k_{m760} k_{m761} k_{m762} k_{m763} k_{m764} k_{m765} k_{m766} k_{m767} k_{m768} k_{m769} k_{m770} k_{m771} k_{m772} k_{m773} k_{m774} k_{m775} k_{m776} k_{m777} k_{m778} k_{m779} k_{m780} k_{m781} k_{m782} k_{m783} k_{m784} k_{m785} k_{m786} k_{m787} k_{m788} k_{m789} k_{m790} k_{m791} k_{m792} k_{m793} k_{m794} k_{m795} k_{m796} k_{m797} k_{m798} k_{m799} k_{m800} k_{m801} k_{m802} k_{m803} k_{m804} k_{m805} k_{m806} k_{m807} k_{m808} k_{m809} k_{m810} k_{m811} k_{m812} k_{m813} k_{m814} k_{m815} k_{m816} k_{m817} k_{m818} k_{m819} k_{m820} k_{m821} k_{m822} k_{m823} k_{m824} k_{m825} k_{m826} k_{m827} k_{m828} k_{m829} k_{m830} k_{m831} k_{m832} k_{m833} k_{m834} k_{m835} k_{m836} k_{m837} k_{m838} k_{m839} k_{m840} k_{m841} k_{m842} k_{m843} k_{m844} k_{m845} k_{m846} k_{m847} k_{m848} k_{m849} k_{m850} k_{m851} k_{m852} k_{m853} k_{m854} k_{m855} k_{m856} k_{m857} k_{m858} k_{m859} k_{m860} k_{m861} k_{m862} k_{m863} k_{m864} k_{m865} k_{m866} k_{m867} k_{m868} k_{m869} k_{m870} k_{m871} k_{m872} k_{m873} k_{m874} k_{m875} k_{m876} k_{m877} k_{m878} k_{m879} k_{m880} k_{m881} k_{m882} k_{m883} k_{m884} k_{m885} k_{m886} k_{m887} k_{m888} k_{m889} k_{m890} k_{m891} k_{m892} k_{m893} k_{m894} k_{m895} k_{m896} k_{m897} k_{m898} k_{m899} k_{m900} k_{m901} k_{m902} k_{m903} k_{m904} k_{m905} k_{m906} k_{m907} k_{m908} k_{m909} k_{m910} k_{m911} k_{m912} k_{m913} k_{m914} k_{m915} k_{m916} k_{m917} k_{m918} k_{m919} k_{m920} k_{m921} k_{m922} k_{m923} k_{m924} k_{m925} k_{m926} k_{m927} k_{m928} k_{m929} k_{m930} k_{m931} k_{m932} k_{m933} k_{m934} k_{m935} k_{m936} k_{m937} k_{m938} k_{m939} k_{m940} k_{m941} k_{m942} k_{m943} k_{m944} k_{m945} k_{m946} k_{m947} k_{m948} k_{m949} k_{m950} k_{m951} k_{m952} k_{m953} k_{m954} k_{m955} k_{m956} k_{m957} k_{m958} k_{m959} k_{m960} k_{m961} k_{m962} k_{m963} k_{m964} k_{m965} k_{m966} k_{m967} k_{m968} k_{m969} k_{m970} k_{m971} k_{m972} k_{m973} k_{m974} k_{m975} k_{m976} k_{m977} k_{m978} k_{m979} k_{m980} k_{m981} k_{m982} k_{m983} k_{m984} k_{m985} k_{m986} k_{m987} k_{m988} k_{m989} k_{m990} k_{m991} k_{m992} k_{m993} k_{m994} k_{m995} k_{m996} k_{m997} k_{m998} k_{m999} k_{m1000} k_{m1001} k_{m1002} k_{m1003} k_{m1004} k_{m1005} k_{m1006} k_{m1007} k_{m1008} k_{m1009} k_{m1010} k_{m1011} k_{m1012} k_{m1013} k_{m1014} k_{m1015} k_{m1016} k_{m1017} k_{m1018} k_{m1019} k_{m1020} k_{m1021} k_{m1022} k_{m1023} k_{m1024} k_{m1025} k_{m1026} k_{m1027} k_{m1028} k_{m1029} k_{m1030} k_{m1031} k_{m1032} k_{m1033} k_{m1034} k_{m1035} k_{m1036} k_{m1037} k_{m1038} k_{m1039} k_{m1040} k_{m1041} k_{m1042} k_{m1043} k_{m1044} k_{m1045} k_{m1046} k_{m1047} k_{m1048} k_{m1049} k_{m1050} k_{m1051} k_{m1052} k_{m1053} k_{m1054} k_{m1055} k_{m1056} k_{m1057} k_{m1058} k_{m1059} k_{m1060} k_{m1061} k_{m1062} k_{m1063} k_{m1064} k_{m1065} k_{m1066} k_{m1067} k_{m1068} k_{m1069} k_{m1070} k_{m1071} k_{m1072} k_{m1073} k_{m1074} k_{m1075} k_{m1076} k_{m1077} k_{m1078} k_{m1079} k_{m1080} k_{m1081} k_{m1082} k_{m1083} k_{m1084} k_{m1085} k_{m1086} k_{m1087} k_{m1088} k_{m1089} k_{m1090} k_{m1091} k_{m1092} k_{m1093} k_{m1094} k_{m1095} k_{m1096} k_{m1097} k_{m1098} k_{m1099} k_{m1100} k_{m1101} k_{m1102} k_{m1103} k_{m1104} k_{m1105} k_{m1106} k_{m1107} k_{m1108} k_{m1109} k_{m1110} k_{m1111} k_{m1112} k_{m1113} k_{m1114} k_{m1115} k_{m1116} k_{m1117} k_{m1118} k_{m1119} k_{m1120} k_{m1121} k_{m1122} k_{m1123} k_{m1124} k_{m1125} k_{m1126} k_{m1127} k_{m1128} k_{m1129} k_{m1130} k_{m1131} k_{m1132} k_{m1133} k_{m1134} k_{m1135} k_{m1136} k_{m1137} k_{m1138} k_{m1139} k_{m1140} k_{m1141} k_{m1142} k_{m1143} k_{m1144} k_{m1145} k_{m1146} k_{m1147} k_{m1148} k_{m1149} k_{m1150} k_{m1151} k_{m1152} k_{m1153} k_{m1154} k_{m1155} k_{m1156} k_{m1157} k_{m1158} k_{m1159} k_{m1160} k_{m1161} k_{m1162} k_{m1163} k_{m1164} k_{m1165} k_{m1166} k_{m1167} k_{m1168} k_{m1169} k_{m1170} k_{m1171} k_{m1172} k_{m1173} k_{m1174} k_{m1175} k_{m1176} k_{m1177} k_{m1178} k_{m1179} k_{m1180} k_{m1181} k_{m1182} k_{m1183} k_{m1184} k_{m1185} k_{m1186} k_{m1187} k_{m1188} k_{m1189} k_{m1190} k_{m1191} k_{m1192} k_{m1193} k_{m1194} k_{m1195} k_{m1196} k_{m1197} k_{m1198} k_{m1199} k_{m1200} k_{m1201} k_{m1202} k_{m1203} k_{m1204} k_{m1205} k_{m1206} k_{m1207} k_{m1208} k_{m1209} k_{m1210} k_{m1211} k_{m1212} k_{m1213} k_{m1214} k_{m1215} k_{m1216} k_{m1217} k_{m1218} k_{m1219} k_{m1220} k_{m1221} k_{m1222} k_{m1223} k_{m1224} k_{m1225} k_{m1226} k_{m1227} k_{m1228} k_{m1229} k_{m1230} k_{m1231} k_{m1232} k_{m1233} k_{m1234} k_{m1235} k_{m1236} k_{m1237} k_{m1238} k_{m1239} k_{m1240} k_{m1241} k_{m1242} k_{m1243} k_{m1244} k_{m1245} k_{m1246} k_{m1247} k_{m1248} k_{m1249} k_{m1250} k_{m1251} k_{m1252} k_{m1253} k_{m1254} k_{m1255} k_{m1256} k_{m1257} k_{m1258} k_{m1259} k_{m1260} k_{m1261} k_{m1262} k_{m1263} k_{m1264} k_{m1265} k_{m1266} k_{m1267} k_{m1268} k_{m1269} k_{m1270} k_{m1271} k_{m1272} k_{m1273} k_{m1274} k_{m1275} k_{m1276} k_{m1277} k_{m1278} k_{m1279} k_{m1280} k_{m1281} k_{m1282} k_{m1283} k_{m1284} k_{m1285} k_{m1286} k_{m1287} k_{m1288} k_{m1289} k_{m1290} k_{m1291} k_{m1292} k_{m1293} k_{m1294} k_{m1295} k_{m1296} k_{m1297} k_{m1298} k_{m1299} k_{m1300} k_{m1301} k_{m1302} k_{m1303} k_{m1304} k_{m1305} k_{m1306} k_{m1307} k_{m1308} k_{m1309} k_{m1310} k_{m1311} k_{m1312} k_{m1313} k_{m1314} k_{m1315} k_{m1316} k_{m1317} k_{m1318} k_{m1319} k_{m1320} k_{m1321} k_{m1322} k_{m1323} k_{m1324} k_{m1325} k_{m1326} k_{m1327} k_{m1328} k_{m1329} k_{m1330} k_{m1331} k_{m1332} k_{m1333} k_{m1334} k_{m1335} k_{m1336} k_{m1337} k_{m1338} k_{m1339} k_{m1340} k_{m1341} k_{m1342} k_{m1343} k_{m1344} k_{m1345} k_{m1346} k_{m1347} k_{m1348} k_{m1349} k_{m1350} k_{m1351} k_{m1352} k_{m1353} k_{m1354} k_{m1355} k_{m1356} k_{m1357} k_{m1358} k_{m1359} k_{m1360} k_{m1361} k_{m1362} k_{m1363} k_{m1364} k_{m1365} k_{m1366} k_{m1367} k_{m1368} k_{m1369} k_{m1370} k_{m1371} k_{m1372} k_{m1373} k_{m1374} k_{m1375} k_{m1376} k_{m1377} k_{m1378} k_{m1379} k_{m1380} k_{m1381} k_{m1382} k_{m1383} k_{m1384} k_{m1385} k_{m1386} k_{m1387} k_{m1388} k_{m1389} k_{m1390} k_{m1391} k_{m1392} k_{m1393} k_{m1394} k_{m1395} k_{m1396} k_{m1397} k_{m1398} k_{m1399} k_{m1400} k_{m1401} k_{m1402} k_{m1403} k_{m1404} k_{m1405} k_{m1406} k_{m1407} k_{m1408} k_{m1409} k_{m1410} k_{m1411} k_{m1412} k_{m1413} k_{m1414} k_{m1415} k_{m1416} k_{m1417} k_{m1418} k_{m1419} k_{m1420} k_{m1421} k_{m1422} k_{m1423} k_{m1424} k_{m1425} k_{m1426} k_{m1427} k_{m1428} k_{m1429} k_{m1430} k_{m1431} k_{m1432} k_{m1433} k_{m1434} k_{m1435} k_{m1436} k_{m1437} k_{m1438} k_{m1439} k_{m1440} k_{m1441} k_{m1442} k_{m1443} k_{m1444} k_{m1445} k_{m1446} k_{m1447} k_{m1448} k_{m1449} k_{m1450} k_{m1451} k_{m1452} k_{m1453} k_{m1454} k_{m1455} k_{m1456} k_{m1457} k_{m1458} k_{m1459} k_{m1460} k_{m1461} k_{m1462} k_{m1463} k_{m1464} k_{m1465} k_{m1466} k_{m1467} k_{m1468} k_{m1469} k_{m1470} k_{m1471} k_{m1472} k_{m1473} k_{m1474} k_{m1475} k_{m1476} k_{m1477} k_{m1478} k_{m1479} k_{m1480} k_{m1481} k_{m1482} k_{m1483} k_{m1484} k_{m1485} k_{m1486} k_{m1487} k_{m1488} k_{m1489} k_{m1490} k_{m1491} k_{m1492} k_{m1493} k_{m1494} k_{m1495} k_{m1496} k_{m1497} k_{m1498} k_{m1499} k_{m1500} k_{m1501} k_{m1502} k_{m1503} k_{m1504} k_{m1505} k_{m1506} k_{m1507$$

lyzed and described human reactions in a situation of light excitation are self-acting, automatic. Such actions are often referred to as an unconditional reflex.

A block diagram of the proposed system with five human reaction tracks is given. The main track consists of the transport delay of an eye response, the transport delay of the afferent nerves, the inertial action of the brain with anticipation, the transport delay of the centrifugal nerves, and the inertial and transport delay of the neuromotor system. In addition, the system takes into account four tracks of negative feedback of motor and force reactions: upper eyelid, lower eyelid, pupil and lens. In the proposed model, the components of each track along with their partial mathematical models are given and discussed. For each reaction track, their overall mathematical models are also given. Taking into account the models of all five reaction tracks, a complete mathematical model of the automatic system of human reaction to a forcing light impulse is proposed.

Most biological processes exhibit marked non-linearity in all its kinds and combinations. Some of the members, primarily forming the central nervous system and neuromuscular systems, are complex systems with negative feedback and compensation tracks. The system contains many nonlinearities: sensitivity thresholds, ambiguities of positions, overshoots, and the model can be expanded and refined. In practical considerations, it is usually sufficient to assume a more simplified surrogate model for a human.

The proposed mathematical model opens up many possibilities for synchronizing it with mathematical models of many mechatronics and automation systems and their research. Optimizing the parameters of this model and its synchronization with specific models of automation systems is difficult and requires many numerical experiments.

The proposed model is a relatively complicated model. Solving the overall equation of this model and analyzing it is extremely difficult and time-consuming. Simplified partial analyzes of individual branches of the model are possible. This will be continued in the authors' further works. In further research, it is planned to use, among others, genetic algorithms.

The proposed model provides a basis for others to mathematically model issues related to this model. This model and its future solution show a number of aspects of its use. It allows for combining the cooperation of a human and a technical automated system. It will be possible to synchronize the model with the human biological vision system.

Another purpose of the created model is its diagnostic and comparative role.

If the dynamic solution of the human reaction to a light pulse is consistent with the reaction of a representative group of examined people, the presented model can be used as a comparative standard when assessing subsequent people. Another application of the presented model may be related to automatic external support of the quality of vision and support for automatic reflex processes related to the protection of the organs of vision at critical moments of vision.

The mathematical model of the description of the vision process makes it possible to combine it with automation systems in the form of their mathematical models of automation into a unified mathematical model of a complex system. This approach enables the design of automation systems that are better synchronized with human reactions to existing stimuli and the selection of optimal parameters of their operation already in the design phase. The proposed model allows, for example, accurate determination

of difficulty levels in computer games. Another example of the use of the proposed model is the study of human reactions to various situations generated virtually, for example in flight simulators and other similar ones. This approach also makes it possible to adapt models of automation systems to specific, non-standard vision cases. The modeled action therefore includes protective and security processes.

## REFERENCES

1. Zhijun L et al. Physical human-robot interaction of a robotic exoskeleton by admittance control. *IEEE Transactions on Industrial Electronics*. 2018;65(12):9614-9624.
2. Parasuraman R, Sheridan TB, Wickens CD. A model for types and levels of human interaction with automation. *IEEE Transactions on systems man and cybernetics-Part A: Systems and Humans*. 2000; 30(3):286-297.
3. Daley WD et al. Machine vision algorithm generation using human visual models. In: *Precision Agriculture and Biological Quality*. SPIE, 1999; 65-72.
4. Cecil T, Grover CG, Royer FL. Models of contrast sensitivity in human vision. *IEEE transactions on systems, man, and cybernetics*. 1993;23(3):857-864.
5. Toshikazu M. Theoretical reproduction of spatial frequency characteristics for reaction time based on a spatiotemporal human vision model with accommodative dynamics. *Electronics and Communications in Japan (Part III: Fundamental Electronic Science)*. 1999;82(7):39-50.
6. Sougata K et al. Application of digital human modeling and simulation for vision analysis of pilots in a jet aircraft: a case study. *Work*. 2012; 41(1):3412-3418.
7. Mantiuk RK, Ramponi G. Human vision model including age dependencies. In: *2015 23rd European Signal Processing Conference (EUSIPCO)*. IEEE. 2015;1616-1620.
8. Hiraç M et al. Human visual system models in digital watermarking. In: *2015 International Conference and Workshop on Computing and Communication (IEMCON)*. IEEE. 2015; 1-7.
9. Antoniewicz J. *Automation principles*. Wydawnictwa Naukowo-Techniczne. Warszawa 1965.
10. Houshyar A et al. A review on otolith models in human perception. *Behavioural brain research*, 2016;309:67-76.

The authors declares that he has no known competing financial interests or personal relationships that could have appeared to influence the work reported in this paper.

Ryszard Szczebiot:  <https://orcid.org/0000-0002-9084-915X>

Roman Kaczyński:  <https://orcid.org/0000-0001-5736-5367>

Leszek Goldyn:  <https://orcid.org/0000-0002-0689-8590>



This work is licensed under the Creative Commons BY-NC-ND 4.0 license.

## AUTOMATION OF THE OIL EXTRACTION PROCESS PERFORMED BY MEANS OF A SCREW PRESS

Mykhailo LOBUR\*, Vitaliy KORENDIY\*\*, Oleksandr KACHUR\*\*, Volodymyr HAVRAN\*

\*Institute of Computer Science and Information Technologies, Department of Computer-Aided Design,  
Lviv Polytechnic National University, 12 S. Bandera Str., 79013 Lviv, Ukraine

\*\*Institute of Mechanical Engineering and Transport, Department of Technical Mechanics and Engineering Graphics,  
Lviv Polytechnic National University, 12 S. Bandera Str., 79013 Lviv, Ukraine

[mykhaylo.v.lobur@lpnu.ua](mailto:mykhaylo.v.lobur@lpnu.ua), [vitalii.m.korendii@lpnu.ua](mailto:vitalii.m.korendii@lpnu.ua), [oleksandr.y.kachur@lpnu.ua](mailto:oleksandr.y.kachur@lpnu.ua), [volodymyr.b.havran@lpnu.ua](mailto:volodymyr.b.havran@lpnu.ua)

received 26 January 2024, revised 10 May 2024, accepted 20 May 2024

**Abstract:** The continuous development of the oil-manufacturing industries causes the necessity of improving extraction technologies. In this case, the specific interest is focused on the control systems of screw presses. Among a great variety of such machines, the small household presses are in significant demand among consumers. Various seeds and kernels require different technological conditions to be provided in order to maximize the qualitative and quantitative characteristics of the extracted oil. Therefore, the main objective of this research is developing and testing the control system allowing for automation of the oil extraction process. Particularly, the temperature parameters of the pressing chamber, extracted oil, and electric motor are to be monitored and limited. In addition, the consumer should be able to predefine the mass of the oil to be extracted. Considering the small household screw press LiangTai LTP200, the general algorithm (block diagram) of the control system operation is proposed and the corresponding experimental prototype is developed. The latter is based on the Arduino Mega microcontroller and is equipped with three temperature sensors, two coolers (fans), one heater, and one mass sensor. The proposed control system allows for continuous monitoring and limiting of the pressing chamber, oil, and electric motor temperatures, as well as the mass of the extracted oil. The experimental data show that the pressing chamber preheating process lasts for about 3 min (170...190 s) and its maximal temperature does not exceed 44°C. The temperature of the extracted oil does not rise over 61°C. The motor temperature changes within the range of 69...71°C. The oil extraction productivity is as follows: 1.2 kg/h (sunflower seeds), 1.06 kg/h (walnut kernels), 0.9 kg/h (almond kernels), and 0.78 kg/h (peanut kernels). The obtained results can be used in further investigations focused on analyzing the influence of these parameters on the quantitative and qualitative characteristics of the extracted oil.

**Key words:** pressing chamber, experimental prototype, Arduino microcontroller, cooler, heater, asynchronous motor, productivity

### 1. INTRODUCTION

Nowadays we observe the constant growth of interest in the production of oil. Hence, the search for innovative and even more efficient extraction methods becomes quite an important task. There are various technologies available so far. The classic press that extracts oil from vegetable raw materials is becoming the subject of intensive scientific study and technological improvement. The effectiveness of oil extraction depends on a number of factors, such as press design, compression ratio, and a set of optimal conditions for each type of raw material. The high level of mechanization and the possibility of using various types and configurations of presses for different raw materials offer a potential for enhancing the production of oil from vegetable sources. To improve press design and optimize technological parameters, it is important to conduct investigations of the oil extraction process at different press configurations and extraction conditions.

Existing studies allow us to identify ways for the next steps in research and development in the use of the press for oil extraction, as well as to note its advantages in the context of sustainable and efficient production of vegetable oils. Analysis of existing literature provides us with useful information on oil production and

its effect on product quality. Seed oils play a crucial role in both the food and industrial sectors, including biodiesel production. As shown by Choton S, Gupta N et al. in [1], the extrusion technology proves to be cost-effective and efficient, facilitating the production of diverse products while ensuring high quality and the preservation of essential substances. The content of the article [2] written by Nde DB and Anuanwen CF explores optimization techniques, delineating their benefits and examining various modeling methods employed in optimization processes. Enhancing oil recovery is a key aspect of improving product quality and overall yield. In [2], Nde DB and Anuanwen CF emphasize the influence of these methods on the quality of the resulting oil.

Another important aspect described in sources [3] written by Frangipane MT, Cecchini M et al. [4] authored by Guerrini L, Breschi C et al. and [5] by García-González A, Velasco J et al. is the process of oil filtration and its influence on the chemical and sensorial characteristics of the product. The lack of filtration leads to defects and deterioration of quality within a short time, which can reduce the commercial grade of the oil. Filtration during the first few days significantly reduces this risk, ensuring better quality of the oil and preserving it during long-term storage. In [6], the authors Mridula D, Saha D et al. made experiments on optimizing the parameters of oil extraction from cleaned and whole sunflower

seeds at different levels of humidity and temperature of the press head. The box-Behnken method was used with 60-80 g. of cleaned seeds, 20-40 g. of whole seeds, and 6-10% humidity at 50-90°C. As a result, optimum conditions were defined as: 68.64% cleaned seeds, 31.36% whole seeds, and 6% moisture at 71.5°C press head temperature for extracting sunflower oil.

In work [7] written by Gudzenko M, Vasylyv V et al. a twin-screw extruder was investigated to simplify the processing of oilseeds. The influence of the geometric parameters of the screw on oil release was studied. The rational parameters were determined using theoretical calculations and experiments. The dependence of the oil yield on the geometry of the screw was confirmed. The effect of the decline of the free volume of the screw on the efficiency and productivity of the extruder-press was revealed.

The research outlined in reference [8] and authored by Gudzenko M, Vasylyv V et al. delves into the issue of low oil yield in the process of sunflower oil extraction. The essential parameters for enhancing the twin-screw extrusion presses' design to augment oil yield were thoroughly investigated. The study introduces empirical methods and new working components, specifically cylindrical-conical nozzles, leading to a notable increase in oil yield up to 3.1%.

In [9] written by Alabi K, Busari R, Joel O a screw press with a variable width of a cone-shaped shaft was developed to increase the oil production from the palm tree fruits. The machine demonstrated superior performance when operated at 130°C, with a heating duration of 25 min, and with a rotation speed of 60 rpm. Under these conditions, it achieved an oil yield of 83.72%, an extraction efficiency of 97.73%, and an extraction loss of 2.37%.

In the paper [10], the authors Mursalykova M, Kakimov M et al. focused on the simulation of the oil extraction process using a screw press in small enterprises for Safflower production. The article addresses the challenge of extracting the liquid phase from dispersed material. Employing mathematical modeling, the study identifies the optimal parameters for oil extraction, which include a screw rotation speed of 6.2 rad/s. and diaphragm gap of 0.1 mm.

The paper [11] authored by Iskakov B, Kakimov M et al. investigates the improvement of the purification of Safflower oil using biologically based secondary processing products. It has been established that the use of flax fiber for filtering improves the quality of the oil, increasing the content of useful substances and antioxidant components. Optimum centrifugation conditions for increasing the efficiency of Safflower oil processing are proposed. The research [12] written by Zikri A, Aswan A et al. is aimed at maximizing oil yield when obtaining coconut oil from copra using a screw press machine. Factors such as temperature and screw speed are analyzed. Energy intensity and extraction efficiency during the coconut oil production process are also evaluated. The paper [13] authored by Muhammad Afriza Zaini T, Ali S is aimed at analyzing the effect of screw press pressure on palm oil production in the company. It has been found that the correct pressure is important for the quality and quantity of oil obtained.

In the investigation [14] authored by Mansor MN, Salleh SM et al., the focus is on assessing the screw press technology utilized in palm oil production. Its objective is to assess the durability of both twin and single screw designs, aiming to determine which design offers the maximum screw life. The article [15] written by Charan G, Krishna AR et al. concerns the creation, assembly, and testing of press for oil extraction from sesame, coconut, groundnut, and mustard seeds. The press uses a screw mechanism without the use of chemical solvents, ensuring a safe and efficient process. The applied electric motor with a power of 1 hp, the

pressure analysis of the propeller confirms the safety and durability of the device. The study [16] authored by Sarbeni S and Saputra A applies the FMEA method to identify breakdowns and prioritize repairs. Using this method, the authors discovered that the special bearing component required immediate repair.

The research [17] written by Sakdasri W and Silangam P explores in detail the use of screw presses for extracting oil from black cumin seeds. Conditions of oil extraction were optimized by considering parameters such as feed rate, temperature, and humidity. The maximum oil yield (31.67 wt%) was achieved at parameters of 45 g/min, 70°C and 6 wt% moisture. Under optimal conditions (50–54 g/min, 15–18wt%, and 55–60°C), a yield of 22 wt% oil and a thymoquinone content of 10 mg/ml were achieved.

Considering the process of extracting oil in a screw press [18], Bako T, Obetta SE and Umogbai VI developed a theory for the mathematical description of this phenomenon. Using experimental data, a model was determined, which was confirmed using regression analysis. The reliability of the model is emphasized by high indicators of correlation, determination, etc. It is important to note that this model effectively predicts results on commercial presses, which opens up the possibility of collecting press performance data without costly experiments. The analysis presented in [19] and performed by Wang S, Wang J et al. examines the effect of roasting and extraction methods on the quality of rapeseed and linseed oils. The results indicate a great influence of different methods on yield, sensory characteristics, composition of oils, and physicochemical properties. The choice of extraction method is important for the production of oils in large volumes.

The paper [20] written by Bogaert L, Mathieu H et al. studied the mechanical expression of oils in a screw press using a pilot press. It was found that increasing the speed of rotation of the screw improves the productivity of the press, shortens the time of passage, and reduces the extraction of oil. Data fixation made it possible to identify different functional sections of the press. The research outlined in reference [21] authored by Kabutey A., Herák D., and Mizera Ć. evaluated oil yields from different types of seeds, including hemp, sesame, flax, pumpkin, madder, and cumin. Sesame was found to have the highest oil yield (30.60%), while cumin had the lowest (3.46%). The analysis of the quality of the obtained oils revealed certain aspects that require attention, especially in pumpkin oil. Potential for further research includes consideration of temperature impact, efficiency of oil recovery, and other processing aspects. The work [22] written by Kabutey A, Herák D and Mizera Ć determined the optimal conditions for obtaining oil from carded sunflower seeds. The maximum yield of oil (48.869%) was achieved without preheating on the fifth pressing. The quality of the obtained oils meets the standards, and spectral analyses confirm the low content of pigments. Repeated pressing helps extract residual oil from the cake. In the article [23] authored by Wang S, Wang J et al. the development and modeling of an improved screw press for extracting oil from plants are described. The research aims to examine the press design and investigate the stress-deformed state of the screw under difficult conditions. The findings of this study have the potential to enhance the longevity, durability, and reliability of screw presses.

The use of the latest smart technologies in industry allows improving and optimizing production processes. A great example of this is using an Arduino Mega controller to control the oil extraction process. The importance of correct management and control of parameters such as speed and temperature becomes critical to achieve needed results. Arduino Mega controller as an integrated control system is defined as a main element in the smart oil ex-



traction process, ensuring precision and stability in the regulation of several parameters. In particular, the extraction speed can be dynamically adjusted to adapt to different production conditions, ensuring high efficiency of oil extraction. Temperature control is another important function, where the controller monitors the temperature of the shaft and the motor. This avoids overheating, which can affect oil quality and increase energy consumption. Using the Arduino Mega it becomes possible to implement automated functions, such as a cooling system that starts when a certain temperature level is reached, or automatic heating control to maintain a constant temperature during the extraction process. The ability to monitor various parameters such as shaft speed, motor, and shaft temperature makes this system not only a control tool but also a data collection and analysis tool. This contributes to the optimization of the entire process of oil extraction, ensuring high product quality and rational use of resources.

The project [24] developed by Badigannavar R, Kavadamatti A and Kulkarni G deals with the automation of fan speed control depending on the ambient temperature using Arduino. The system obtains temperature information from the sensor and modifies the speed based on the temperature settings specified by the operator. Information about temperature and speed is displayed on the LCD display. If the ambient temperature is higher than the set temperature, the fan will turn on, and vice versa.

The paper [25] authored by Li Y, Jin Z tackles the challenges associated with the traditional screw extruder control system, characterized by low-quality stability, increased manual workload, and a limited level of mechanical automation due to manual feed rate control. The article proposes the implementation of an intelligent screw extruder control system employing a fuzzy control algorithm. Utilizing pressure and temperature data from the oil press for detection, the fuzzy control algorithm mimics expert experience to autonomously regulate the speed of the motor. This mechanism is centralized around a PLC that is used as the main controller, while MATLAB is employed for simulation and testing. Based on the simulation and testing outcomes, the smart screw extruder exhibits enhanced control effectiveness and overall stability using the fuzzy control algorithm. The study [26] carried out by Muliak N, Zdobyskyi A et al. focuses on resolving design problems and enhancing algorithm accuracy in various complex systems. Multiple algorithms were compared based on analytical data and the optimal one was suggested for the design of MEMS.

## 2. MATERIALS AND METHODS

This section considers the following issues: initial design and operational peculiarities of the screw press for extracting oil from different oil-containing plants; main types of seeds and kernels that can be processed and basic technical characteristics of the press; major tasks set for developing the control system intended for automation of the oil extraction process; general algorithm of the control system operation; experimental implementation of the developed control system and modernized screw press.

### 2.1. Initial prototype of the screw press for oil extraction

The general design of the small household screw press LiangTai LTP200 is presented in Fig. 1 [27]. It is intended for cold and hot pressing of different seeds and extracting oil at the

productivity range of 2...5 kg/h depending on the working regimes and type of the oil-containing material. The overall dimensions of the press are 410×160×305 mm and the mass is about 9 kg. The nominal power consumption does not exceed 650 W at the supplied alternating voltage of 220 V of the 50 Hz frequency.

The hopper 1 is filled with the seeds to be processed. The lower discharging cylindrical hole (port) of the hopper is mounted in the conveying chamber 6. The latter is connected with the pressing chamber 7, in which the oil extraction and cake formation processes are conducted. The pipe 8 is used for discharging the cake from the pressing chamber 7 and supplying it to some boxes, bags or packages. The extracted oil is fed to the tank (bowl) 9 and is preliminary filtered with the help of the sieve 10.

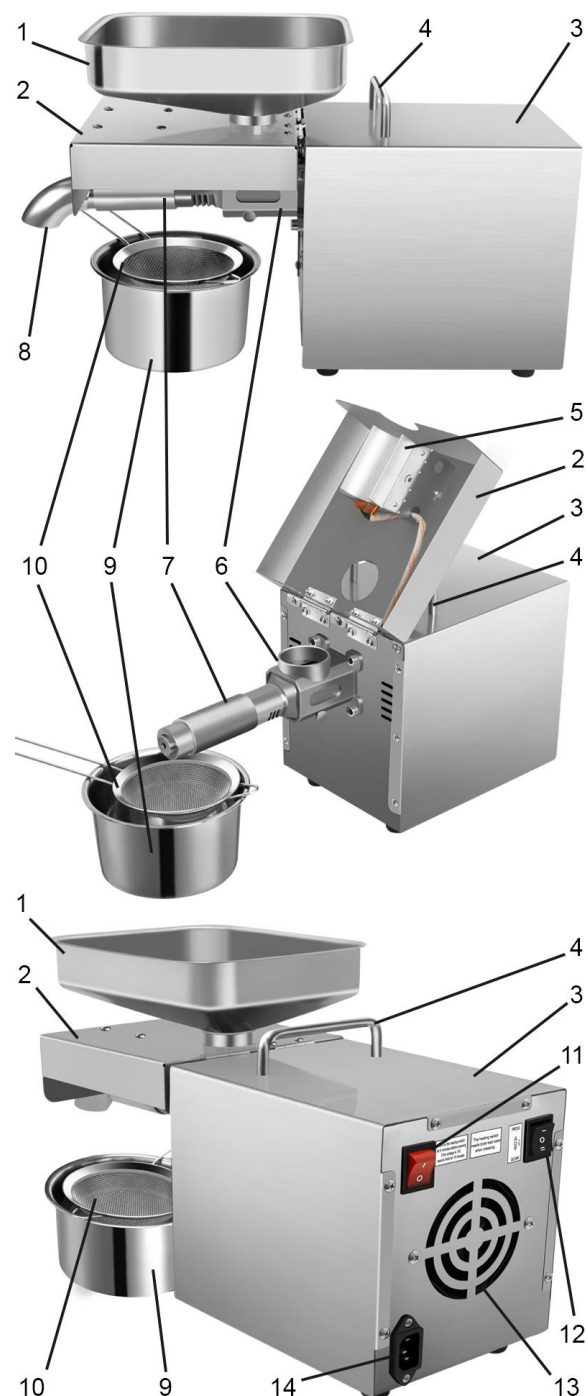


Fig. 1. Initial prototype of the screw press [27]

The flat (hinged) frame 2 is joined with the press body 3. The electric heating element (heater) 5 is fixed on the frame 5, which squeezes it up against the cylindrical surface of the pressing chamber 7. The latter is to be preheated before the working regime starts in order to increase the efficiency of the oil extraction process. The corresponding preheating temperature depends on the type of the seeds to be pressed. The press body 3 is equipped with the additional handle 4 that allows for easy carrying (transportation) of the machine. The general power supply of the screw press is provided from the 220 V (50 Hz) electric network through the connector 14. The two-position switch 11 energizes the heater 5 before the start of the oil extraction process during the technologically prescribed time period. After this, the operator chooses the first position (position "I") on the switch 12 to start the pressing process. If there is a need to stop the machine, the position "0" should be chosen on the switch 12. In the case when the screw cleaning operation should be performed, the operator must change the switch 12 position to "II" providing the reversive rotation of the driving motor shaft. The ventilation openings (holes) 13 are used for the forced supply of the cooling air inside the press body 3, in which the machine drive and control system is installed.

Considering the existent design of the press, the present paper is aimed at developing the control system allowing for automation of the oil extraction process for different seeds and kernels.

2.2. The main types of seeds and kernels that can be processed

The considered household screw press LiangTai LTP200 is intended for extracting oil from the following seeds and kernels: peanut, sesame, rapeseed, sunflower, almond, flaxseed, mustard, walnut, perilla, soybean, hemp, etc. (see Fig. 2 [27]). According to the manufacturer's documentation [27], the approximate oil extraction rate and material processing productivity of the screw press for some types of seeds are presented in Tab. 1.



Fig. 2. Main types of seeds to be pressed [27]

All the mentioned seeds and kernels require different technological conditions to be provided in order to maximize the qualita-

tive and quantitative parameters of the extracted oil. Therefore, there is a need to adjust the working regimes of the press, particularly, the rotational frequency of the screw and the temperature of the pressing chamber. In addition, the customer may need to set the required mass of the oil to be extracted. All these tasks are to be solved by the control system, which will be developed in the following sections of this research.

Tab. 1. Performance characteristics of the press LiangTai LTP200 [27]

Seed (kernel) type	Oil extraction rate [%]	Material processing productivity [kg/h]
Peanut	39...45	2.27...3.63
Rapeseed	30...39	3.63...4.54
Sunflower	41...52	3.18...4.54
White sesame	39...52	3.63...4.54
Black sesame	44...53	3.63...4.54
Walnut	58...68	2.27...3.18
Almond	48...57	2.27...3.18
Flaxseed	31...39	3.63...4.54
Perilla	30...42	3.63...4.54

2.3. Major tasks set for developing the control system

Considering the necessity of extracting oil from different types of seeds mentioned above, different technological parameters are to be provided by the control system. The following parameters are monitored during the press operation: rotational frequency of the screw; temperatures of the pressing chamber, extracted oil, and driving electric motor; mass of the oil; consumption current and voltage of the motor. Based on the technological requirements and recommendations, the nominal temperature of the pressing chamber and the screw rotational frequency should depend on the type of the seeds to be pressed. The optimal operational parameters of the screw press allow for providing the best qualitative and quantitative parameters of the oil extracted.

Taking into account the conclusions drawn above, the enhanced control system of the considered screw press should provide the possibility of regulating the screw rotational frequency and the temperature of the pressing chamber. In addition, the electric motor temperature and consumption current must be limited in order to prevent drive damage (breakdown). The latter can occur in the case when the screw is jammed (wedged). Depending on the oil mass required by the consumer, the control system must stop the pressing process when the necessary mass is reached. The mentioned temperatures can be limited by means of applying additional electric coolers with adjustable rotational frequencies depending on the temperature value.

2.4. General algorithm of the control system operation

The general algorithm of the control system operation can be described by the block diagram (flow chart) shown in Fig. 3. After supplying the electric power to the control system, the corresponding sensors register the temperature  $t_{pr.ch.}$  of the pressing chamber, the mass  $m_{oil}$  of the oil tank (bowl), the temperature  $t_{oil}$  of oil (or air) inside the tank, the temperature  $t_{mot.}$  of the electric motor, and the voltage and current consumed by the enhanced control system and electric drive.



Fig. 3. Simplified block diagram (flow chart) describing the general algorithm of the control system operation

At the beginning, the mass sensor should be calibrated and reset to zero. Then, the consumer must choose the required mass  $m_{oil\ max}$  of the oil to be extracted. By default, the system is programmed to press 100 g of oil. After this, the operator pushes the „START” button and the heater begins to preheat the pressing

chamber to the temperature  $t_{pr.ch.min}$  prescribed by the technological requirements and depending on the type of seeds to be processed. This temperature is registered by the corresponding sensor. At the moment when the temperature reaches the required value, the control system switches the heater off and starts

the electric motor at its nominal (maximal) parameters. In this case, the rotational frequencies of the motor shaft and pressing screw take their maximal values, and the oil extraction process is conducted. When the motor temperature reaches the critical value  $t_{mot. cr.}$  prescribed by the manufacturer, the corresponding cooler is to be switched on to limit the temperature growth. The additional sensor is used for registering the temperature  $t_{oil}$  of the oil being extracted. When this temperature grows over a technologically prescribed value  $t_{oil cr.}$ , the corresponding cooler starts working at the specified frequency (cooling intensity). If the oil temperature continues growing, the cooling intensity is to be increased and the screw rotational frequency is to be reduced. This allows for restricting the oil overheating, which negatively influences its qualitative characteristics. When the temperatures of the oil or motor reach the maximal allowable values  $t_{oil max}$  or  $t_{mot. max}$ , respectively, the control system stops the pressing process. The same algorithms are performed in the case when the mass sensor registers the oil mass  $m_{oil max}$  prescribed by the consumer or when the oil mass is not changing during the specified time period. The latter means that there are no seeds to be pressed or that the pressing chamber is chocked (stuffed) up with the cake. The stopping process is accompanied by the audible alarm and the error description shown on the display. After each stop, the control system provides the reverse motion of the screw in order to clean the pressing chamber. Additionally, the screw reverse rotation can be ensured by means of pushing the „REVERSE” button. At any time moment, particularly, when an emergency situation occurs, the corresponding „STOP” button

should be pressed by the operator (consumer). The starting and stopping processes are continuously (smoothly) conducted according to the programmed algorithm due to the use of the frequency converter (changer). The latter additionally provides the possibility of limiting the maximal consumption current of the electric motor, as well as controlling the rotational frequencies of the motor shaft at different operational conditions (direct and reverse rotation, oil mass  $m_{oil}$  and temperature  $t_{oil}$ , motor temperature  $t_{mot.}$ , pressing chamber temperature  $t_{pr.ch.}$  etc.).

## 2.5. Development of the schematic diagram of the enhanced control system implemented in the press drive

The principle of operation and connection of the control and diagnostic elements in the press control circuit (see Fig. 4) are based on the Arduino Mega microprocessor (U1). The proposed principal scheme involves the use of both digital and analog ports, as well as PWM ports. The status of the temperature sensors (DS18B20 sensors (U4-U6)) and weight module (HX711 (U8)) is displayed on the LCD screen 2004 (U3), which is connected via the I2C bus. The DS18B20 sensors are connected to the analog outputs via pull-up resistors. The possible connection errors or sensor malfunctions are displayed on the LCD. The HX711 weight module is connected to the digital pin. To measure the motor speed, there is used the YS-27 Hall sensor (U5), which is connected to a digital pin that operates in an interrupted mode.

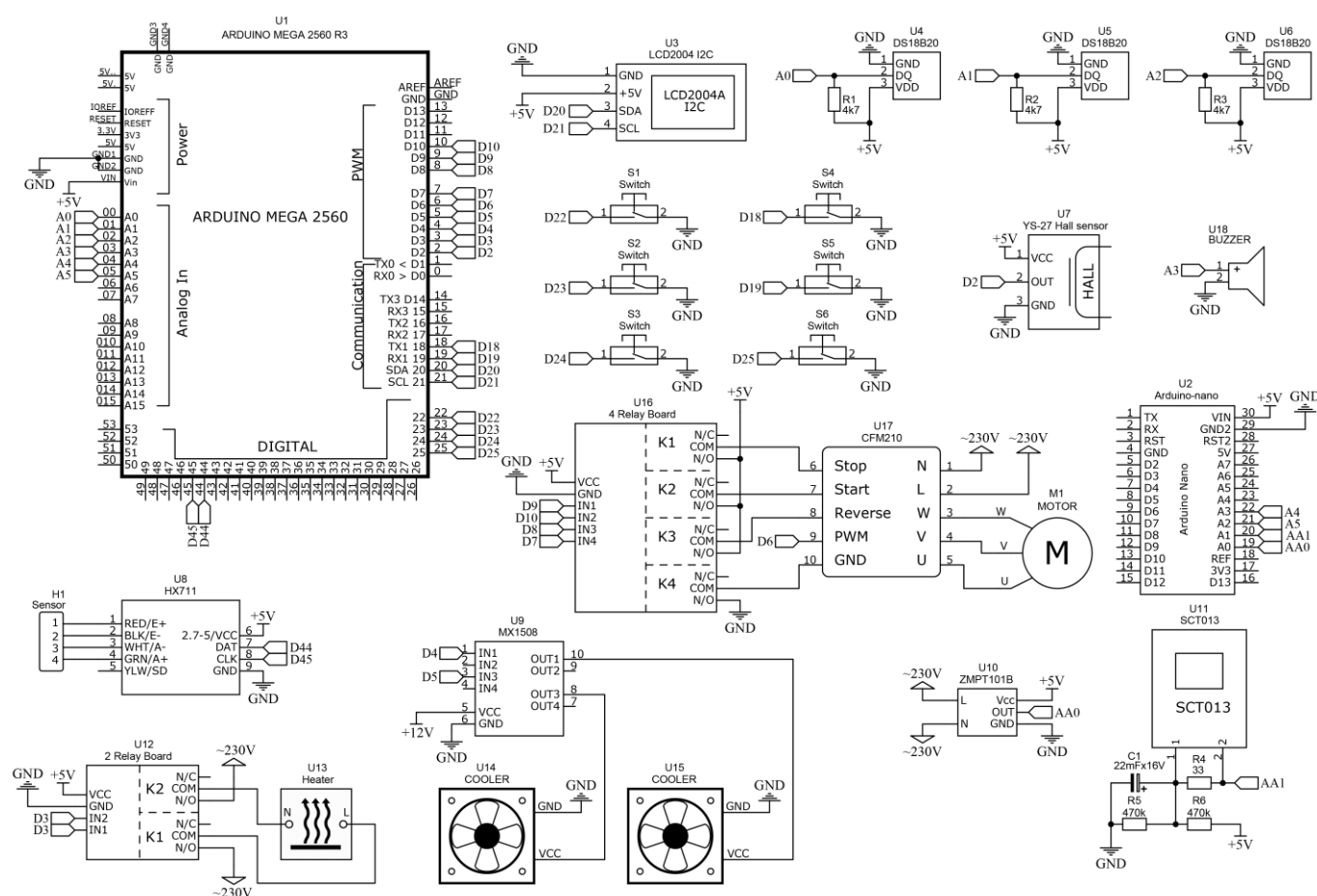


Fig. 4. Schematic diagram of the enhanced control system implemented in the press drive



To display the current and voltage parameters, there are used the ZMPT101B (U10) and SCT013 (U11) sensors, which are connected to the Arduino Nano board (U2). The use of the Arduino Nano microcontroller is due to the fact that the processing of voltage and current sensors takes a significant amount of time, so for the main algorithm to work steadily with interruptions, there is a need to use another microcontroller that will be responsible only for polling these sensors. The fans (coolers) (U14 and U15) are controlled by the MX1508 two-channel motor driver module (U9). The speed of the fans is controlled by a PWM signal.

The pressing chamber is heated by the heater U13. The heater is controlled by the relay module U12, which receives control signals from the Arduino Mega. The motor speed is controlled by the PWM signal, which is supplied directly to the CFM210 frequency converter (U17), and all other functions are controlled through the relay module (U16). The use of the relay module is due to the fact that there is simulated manual control of the converter, which provides the flexibility to choose frequency, rather than prescribe a different algorithm for each one. The asynchronous motor is connected directly to the frequency converter, which allows for adjusting its speed without significant power loss. A buzzer (U18) is provided to signal an emergency or the end of the press operation. The start, stop, and reverse of the motor are controlled by buttons with normally open contacts S1-S3, and the weight parameters are controlled by buttons S4-S6.

## 2.6. Experimental implementation of the control system

The experimental prototype of the modernized screw press equipped with the developed control system is presented in Fig. 5. The seeds are to be charged into the hopper 1, which is installed in the conveying chamber 2. During the machine operation, the seeds are conveyed by the screw 3 to the pressing chamber 4, where they are destructed and the oil is extracted. The oil flows out of the pressing chamber 4 through the holes at its bottom part to the tank (bowl) 5. The cake being formed during the pressing process is discharged through the pipe 6 to the tank (bowl) 7. The rotation of the screw 3 is generated by the two-stage cylindrical gearbox 8 driven by the asynchronous electric motor 9.

Considering the proposed control system, the latter allows for preheating the pressing chamber before the machine operation starts. This allows for improving the qualitative and quantitative parameters of the oil extracted. The corresponding heater 10 is mounted on the sprung arm (bracket) 11, which can change its angular position relative to the press body due to its hinged installation. On the other hand, when the temperature of the extracted oil is larger than the technologically specified value, the additional cooler (fan) 12 is to be activated in order to restrict the oil overheating. The latter can cause the reduction of the oil's qualitative parameters. The temperatures of the extracted oil, pressing chamber 4, and electric motor 9 are monitored by the corresponding sensors 13, 14, and 15. If at least one sensor shows a temperature that is larger than the permissible value, the control system stops the pressing process. If the temperature of the oil or electric motor reaches the specified critical value, the corresponding coolers (fans) 12 and 16 are activated to restrict further growth of the temperature. The mass sensor 17 is applied to monitor the mass of the oil being extracted. The sensor is mounted on the press body by one end, while the other end holds (supports) the plate 18, on which the oil tank (bowl) 5 is placed. Before starting the pressing process, the operator (consumer) prescribes the

required mass of oil to be extracted. When the mass sensor 17 registers the prescribed value, the control system stops the screw rotation. In the case when the oil mass is not changing during the specified time period, the control system stops the pressing process, because there can be no seeds to be pressed or the pressing chamber 4 can be choked (stuffed) up with the cake. Each stopping process is accompanied by the reverse rotation of the screw 3 aimed at cleaning the pressing chamber 4 and by the audible alarm and error description shown on the display 19.

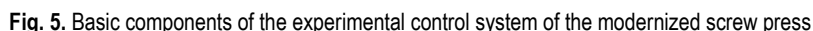
The control system additionally contains the frequency converter 20 intended for regulating the rotational frequency of the electric motor shaft and for providing the programmed algorithms for continuous starting and stopping of the press drive. One of the main components of the control system is the Arduino Mega microcontroller 21 energized by the power supply unit 22. On the top plate of the press body, there are installed the control buttons and display 19. The green button 23 is the „START“ one, which switches on the pressing process. The blue button 24 is used to provide the reverse rotation of the screw 3. The red button 25 is the „STOP“ one, which switches off the power supply to the drive. The other three buttons 26, 27, 28 are used for calibrating (resetting to zero) of the oil mass sensor and for manual increasing and decreasing of the required mass of oil to be extracted.

The display 19 continuously shows the instantaneous oil temperature („Oil:“), temperature of the electric motor („M:“), mass of the oil located in the bowl („IMV:“), and manually prescribed oil mass („Mass:“). The corresponding errors show that the mass of the oil located in the bowl is larger than the prescribed mass („MASS ERR“); the oil temperature is larger than the technologically permissible value („OIL ERR“); the mass of the extracted oil is not changing for a specified time period („EMPTY ERR“); the temperature of the electric motor is larger than the one prescribed by the manufacturer („MOTOR ERR“).

Additionally, the control system allows for registering the instantaneous values of the motor shaft rotational frequency using the Hall-effect sensor 29, and the consumption current and voltage of the whole control system and electric drive with the help of the amperemeter 30 and voltmeter 31. The frequency controller allows for limiting the maximal current supplied to the electric motor in order to provide its reliable and durable operation. Further improvements can be focused on applying additional sound and visual sensors for analyzing specific operational conditions.

The sensors DS18B20 used for measuring the temperature of the pressing chamber, electric motor, and extracted oil are pre-calibrated using the pull-up resistors and are connected to the analog outputs of the Arduino Mega microcontroller. According to the manufacturer's documentation, the sensors are characterized by the working temperatures of  $-55...+125^{\circ}\text{C}$  and the accuracy of  $\pm 0.5^{\circ}\text{C}$  (within the temperature range of  $-10...+85^{\circ}\text{C}$ ). Considering the nominal temperatures of the screw press operation ( $15...85^{\circ}\text{C}$ ), the error of the experimental measurements does not exceed 3.5%. The mass sensor in the form of the strain gauge is used for converting the strain value of the aluminum beam into the electric signal. Then the signal is processed by the HX711 weight module connected to the digital pin of the Arduino Mega microcontroller. According to the manufacturer's documentation, the strain gauge and the weight module can detect the mass within the range of 0...1 kg at the total accuracy of 0.2%. Therefore, the maximal mass error of the extracted oil does not exceed 2 g. The duration of the pressing process is measured using the Arduino built-in functions that return the number of milliseconds since the board started running (the heater started heating the chamber).





This section is devoted to experimental investigations of the developed control system and modernized machine operation during the pressing process of the sunflower, peanut, almond seeds, and walnut kernels. The following parameters are considered: temperature of the pressing chamber; temperature and mass of the oil being extracted; temperature of the electric motor. The minimal temperature of the working chamber for the drive to be powered is set to  $t_{pr.ch.min} = 42^{\circ}\text{C}$ . The critical temperature of the oil for the corresponding cooler (fan) to be activated is the following  $t_{oil\ cr.} = 45^{\circ}\text{C}$ . The maximal permissible temperature of the oil for the press to be stopped is equal to  $t_{oil\ max} = 65^{\circ}\text{C}$ . The critical temperature of the motor for the corresponding cooler (fan) to be activated is the following  $t_{mot.\ cr.} = 70^{\circ}\text{C}$ . The maximal permissible temperature of the motor for the press to be stopped is equal to  $t_{mot.\ max} = 75^{\circ}\text{C}$ . The initial temperature of

### 3.1. Analyzing the changes in the temperature of the pressing chamber

The temperature of the pressing chamber significantly influences the productivity of the oil extraction process and the qualitative parameters of the oil [6, 9, 17]. This fact causes the necessity of regulating the corresponding temperature during the whole pressing process. After supplying power to the control system, the latter starts scanning the sensors and processing the obtained data. Then, the operator (consumer) sets the necessary mass of the oil to be extracted and pushes the "START" button. If the chamber temperature is less than the technologically prescribed value, the electric motor is not powered and the pressing process does not start. According to the time dependence of the tempera-

ture of the pressing chamber (Fig. 6), its initial value is almost equal to the temperature inside the laboratory room (20°C). Therefore, the heater is switched on and the temperature rises to about 42°C for approximately three minutes (170...190 s).

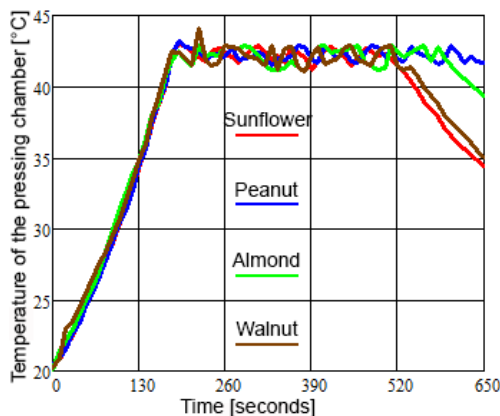


Fig. 6. Dependence of changes in the temperature of the pressing chamber during the pressing of different seeds

After the chamber temperature reaches the minimal value, the electric motor is switched on and the oil extraction process starts. During the seeds (kernels) pressing, the temperature inside the chamber rises. When the temperature of the extracted oil reaches the value of 45°C, the corresponding cooler is switched on. The cooler allows for limiting the temperature of the pressing chamber within the range of 42...44°C during the whole oil extraction process. The reduction of the chamber temperature after 500 s means that the process has been finished and the required mass of the extracted oil has been obtained. After approximately 11 min (650 s), when the latest peanut pressing process ends, the lowest temperature of the chamber of approximately 34°C is observed for the case of the sunflower pressing.

### 3.2. Studying the oil temperature changes

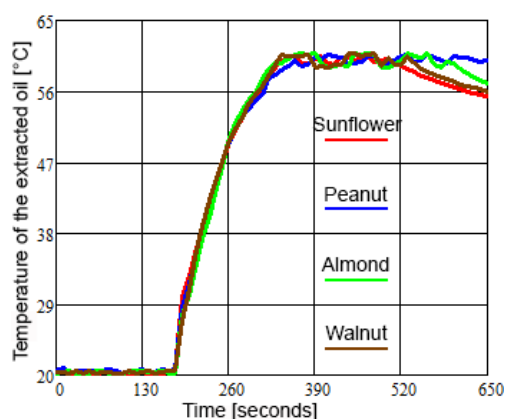


Fig. 7. Dependence of changes in the temperature of the extracted oil during the pressing of different seeds

The temperature of the extracted oil significantly affects its qualitative and taste characteristics. Considering the changes in the temperature of the extracted oil (Fig. 7), it remains unchanged for approximately three minutes (170...190 s), when the pressing chamber preheating process is performed. After this time, the pressing process starts and the oil temperature sensor registers

the corresponding changes. It takes about 2.5...3 min for the oil to reach the nominal temperature of approximately 60°C, which remains almost unchanged during the whole pressing process. When the required mass of the oil is extracted, the pressing process stops and the oil starts cooling down. After approximately 11 min (650 s), when the latest peanut pressing process ends, the lowest temperature of the extracted oil of approximately 55°C is observed for the case of the sunflower pressing.

### 3.3. Monitoring the motor temperature

The electric motor temperature should be restricted due to the manufacturer's recommendations. During the pressing process, when the frequency converter is continuously changing the rotational speed of the pressing screw in accordance with the programmed algorithm, the temperature of the electric motor significantly increases. In order to restrict the motor overheating, the corresponding cooler is switched on, when the motor temperature rises over 70°C. As can be seen in Fig. 8, during approximately 3 min (170...190 s), the motor temperature is almost equal to the temperature inside the laboratory room (20°C). Then the temperature rises to about 70°C and changes within the range of 69...71°C till the end of the pressing process. After approximately 11 min (650 s), when the latest peanut pressing process ends, the lowest temperature of the electric motor of approximately 60°C is observed for the case of the sunflower pressing.

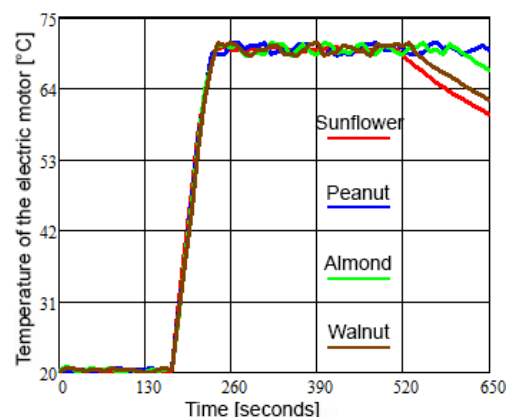


Fig. 8. Dependence of changes in the temperature of the electric motor during the pressing of different seeds

### 3.4. Monitoring the change in the oil mass

As has been already mentioned, after switching on the power supply, the operator calibrates the corresponding sensor (resets it to zero) and chooses the required mass of oil to be extracted. By default, the corresponding mass is programmed to be equal to 100 g. Considering the experimental data presented in Fig. 9, the extracted oil mass takes zero values during the pressing chamber preheating process (about 3 min). Then, the oil extraction process starts and the mass sensor monitors the corresponding changes.

While pressing the sunflower seeds, the nominal mass of the extracted oil was obtained within approximately 490 s from the moment of switching on the power supply. The corresponding durations of the pressing processes for the peanut, almond, and walnut kernels are the following: 650 s, 590 s, and 530 s. Here-with, it should be noted that the separate pressing process lasts

for about 300 s (sunflower seeds), 340 s (walnut kernels), 400 s (almond kernels), and 460 s (peanut kernels).

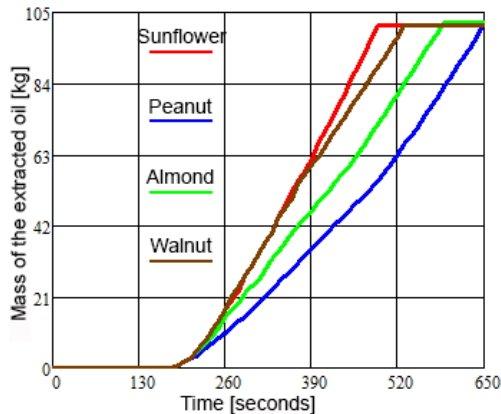


**Fig. 9.** Dependence of changes in the mass of the extracted oil obtained during the pressing of different seeds

### 3.5. Discussion

Based on a thorough analysis of various investigations on the processes of oil extraction from different seeds and kernels of oil-containing plants, particularly [1–3], the present research is focused on developing and experimental testing of the control system allowing for regulating various operational parameters of the pressing process. While performing further investigations on the considered subject, a comprehensive analysis of the influence of these parameters on the quantitative and qualitative characteristics of the extracted oil is to be conducted.

Considering the results shown in Figs. 6–9, the control system is programmed in such a way that the oil extraction process does not start until the temperature of the pressing chamber reaches the prescribed temperature. This regulation has been implemented on the basis of numerous research results, particularly [5, 6, 19, 20, 22], which substantiate the fact that the temperature of the pressing chamber significantly influences the productivity of the oil extraction process and the qualitative parameters of the oil. On the other hand, the temperature of the extracted oil also affects its qualitative and taste characteristics [6, 19, 22]. Therefore, while implementing the corresponding control algorithms of the cooler (fan) operation, the general ideas presented in [24] have been considered.

**Tab. 2.** Experimental data defining productivity of the pressing process

Seed type	Oil mass [g]	Pressing duration [s]	Oil extraction productivity [kg/h]
Peanut	100	460	0.78
Sunflower	100	300	1.2
Walnut	100	340	1.06
Almond	100	400	0.9

Obviously, the maximal working temperature of any electric motor should be limited. The nominal temperature is usually prescribed by the manufacturer. In order to restrict the drive damage (breakdown) due to motor overheating, the additional cooler (fan) is used. The latter allows for maintaining the almost constant temperature of the electric motor during the pressing process.

Some ideas for implementing the corresponding control algorithms have been chosen from [25, 26].

The last parameter that has been monitored during the crew press operation is the mass of the extracted oil, which was initially set by the operator (consumer). This parameter allows for approximately determining the productivity of the pressing process for different seeds and kernels. In the current research, the main attention has been focused on four products: sunflower seeds; peanut, almond, and walnut kernels. The nominal oil mass of 100 g has been chosen for conducting the experiments. The pressing processes, which do not take into account the preheating duration, last for about 300 s (sunflower seeds), 340 s (walnut kernels), 400 s (almond kernels), and 460 s (peanut kernels). These data allow for determining the productivity of the considered screw press for the mentioned seeds and kernels. Considering the experimentally obtained results shown in Tab. 2, the conclusions about their satisfactory agreement with the manufacturer's technical documentation presented in [27] can be drawn.

### 4. CONCLUSIONS

The paper considers the possibilities of automation of the oil extraction process performed by means of the small household screw press LiangTai LTP200. The latter is intended for extracting oil from the following seeds and kernels: peanut, sesame, rapeseed, sunflower, almond, flaxseed, mustard, walnut, perilla, soybean, hemp, etc. Considering the basic design parameters of the press and the main technological requirements set to the oil extraction process, the corresponding control algorithm is developed (see Fig. 3). The proposed control system provides the possibility of regulating the screw rotational frequency and the temperature of the pressing chamber. In addition, the electric motor temperature and consumption current are limited in order to prevent drive damage (breakdown). Depending on the oil mass required by the consumer, the control system stops the pressing process when the necessary mass is reached. The mentioned temperatures are limited by means of applying additional electric coolers with adjustable rotational frequencies depending on the temperature value.

Based on the developed algorithm, the corresponding control system is implemented and experimentally tested. The obtained results show that the pressing chamber preheating process lasts for about 3 min (170...190 s). The maximal temperature of the chamber does not exceed 44°C due to the application additional cooler (fan). Herewith, the temperature of the extracted oil does not rise over 61°C. In order to restrict the electric motor overheating, the corresponding cooler is switched on, when the motor temperature rises over 70°C. Therefore, this temperature changes within the range of 69...71°C during the whole pressing process. The nominal oil mass of 100 g has been chosen for conducting the experiments. The pressing processes, which do not take into account the preheating duration, last for about 300 s (sunflower seeds), 340 s (walnut kernels), 400 s (almond kernels), and 460 s (peanut kernels). Therefore, the corresponding oil extraction productivity of the considered press is the following: 1.2 kg/h, 1.06 kg/h, 0.9 kg/h, and 0.78 kg/h.

While performing further investigations on the considered subject, a comprehensive analysis of the influence of the controllable temperature parameters on the quantitative and qualitative characteristics of the extracted oil is to be conducted.



## REFERENCES

- Choton S, Gupta N, Bandral JD, Anjum N, Choudary A. Extrusion technology and its application in food processing: A review. *Pharma Innov.* 2020;9(2):162-168. <https://doi.org/10.22271/tpi.2020.v9.i2d.4367>
- Nde DB, Anuanwen CF. Optimization methods for the extraction of vegetable oils: A review. *Processes.* 2020;8. <https://doi.org/10.3390/pr8020209>
- Frangipane MT, Cecchini M, Monarca D, Massantini R. Effects of Filtration Processes on the Quality of Extra-Virgin Olive Oil-Literature Update. *Foods.* 2023;12. <https://doi.org/10.3390/foods12152918>
- Guerrini L, Breschi C, Zanoni B, Calamai L, Angeloni G, Masella P, et al. Filtration Scheduling: Quality Changes in Freshly Produced Virgin Olive Oil. *Foods.* 2020;9(8). <https://doi.org/10.3390/foods9081067>
- García-González A, Velasco J, Velasco L, Ruiz-Méndez MV. Attempts of physical refining of sterol-rich sunflower press oil to obtain minimally processed edible oil. *Foods.* 2021;10(8). <https://doi.org/10.3390/foods10081901>
- Mridula D, Saha D, Gupta R, Bhadwal S, Arora S, Kumar P, et al. Oil expelling from whole and dehulled sunflower seeds: Optimization of screw pressing parameters and physico-chemical quality. *International Journal of Chemical Studies.* 2020;8(4):4002-9. <https://doi.org/10.22271/chemi.2020.v8.i4ay.10274>
- Gudzenko M, Vasylyv V, Mushtruk M, Zheplinska M, Palamarchuk I, Burova Z. Influence of geometric parameters of screw nozzles of twin-screw extruder-press on oil yield. *Animal Science and Food Technology.* 2021;12(3):5-17. <https://doi.org/10.31548/animal2021.03.001>
- Gudzenko M, Vasylyv V, Mushtruk M, Zheplinska M, Burova Z. Research on the effectiveness of means for intensifying oil compression in twin-screw extrusion presses. *Animal Science and Food Technology.* 2022;13(4). [https://doi.org/10.31548/animal.13\(4\).2022.7-18](https://doi.org/10.31548/animal.13(4).2022.7-18)
- Alabi K, Busari R, Joel O. Development and Performance Evaluation of a Variable-Pitch Tapered-Shaft Screw Press for Palm Oil Extraction. *Gazi University Journal of Science Part A: Engineering and Innovation.* 2022;9(2):49-61. <https://doi.org/10.54287/gujisa.1069996>
- Mursalykova M, Kakimov M, Kassenov A, Iskakov B, Sergibayeva Z, Kaspakov E. Mathematical modeling of screw press configuration for processing Safflower Oil. *Applied Sciences.* 2023;13(5):3057. <https://doi.org/10.3390/app13053057>
- Iskakov B, Kakimov M, Kudelski R, Mursalykova M, Kassenov A, Satayeva Z, et al. Improving the Technology of Primary Purification of the Safflower Oil Using Secondary Products of Processing on a Biological Basis. *Foods.* 2023;12(17). <https://doi.org/10.3390/foods12173275>
- Zikri A, Aswan A, Erlinawati E, Fatria F, Pratama Y, Anggraini T. Uji Kinerja Screw Oil Press Machine Ditinjau dari Rendemen dan Kualitas Minyak Kelapa yang Dihasilkan. *FLUIDA.* 2020;13(2):46-53. <https://doi.org/10.35313/fluida.v13i2.2305>
- Muhammad Afriza Zaini T, Ali S, Saputra M, Jamaluddin. Pressure Analysis of Oil Mill Screw Press Machine in PT. Ujong Neubok Dalam. *Jurnal Inotera.* 2022;7(2):83-87. <https://doi.org/10.31572/inotera.vol7.iss2.2022.id176>
- Mansor MN, Salleh SM, Fauzi MR, Yahya MN, Juahir A, Hassan H, et al. Total Lifespan Analysis of Screw Press Using Static and Dynamic Simulation. In: *AIP Conference Proceedings.* 2023. <https://doi.org/10.1063/5.0121098>
- Charan G, Krishna AR, Swarup KT, Ali SkS, Mohiddin Sk. Design and fabrication of a high-yield edible oil expeller screw shaft. *International journal of scientific research in engineering and management.* 2023;07(03). <https://doi.org/10.55041/ijsem18000>
- Sarbeni S, Saputra A. Identification of Screw Press Machine Damage Using Failure Mode And Effect Analysis Method in PT. Socinfo Seunagan. *Jurnal Inotera.* 2023;8(1):123-127. <https://doi.org/10.31572/inotera.vol8.iss1.2023.id225>
- Sakdasri W, Silangam P, Chummengyen S, Sukruay A, Ngamprasertsith S, Supang W, et al. Optimization of yield and thymoquinone content of screw press-extracted black cumin seed oil using response surface methodology. *Ind Crops Prod.* 2023;191. <https://doi.org/10.1016/j.indcrop.2022.115901>
- Bako T, Obetta SE, Umogbai VI. Mathematical modeling of mechanical horizontal screw oil extractor. *Agricultural Engineering International: CIGR Journal [Internet].* 2020; 22(2):244-254. Available from: <https://cigrjournal.org/index.php/Ejournal/article/view/5521>
- Wang S, Wang J, Dong G, Chen X, Feng L, Su X, et al. Effect of Different Extraction Methods on Quality Characteristics of Rapeseed and Flaxseed Oils. *Journal of Food Quality.* 2022. <https://doi.org/10.1155/2022/8296212>
- Bogaert L, Mathieu H, Mhemdi H, Vorobiev E. Characterization of oilseeds mechanical expression in an instrumented pilot screw press. *Industrial Crops and Products.* 2018 ;121:106-113. <https://doi.org/10.1016/j.indcrop.2018.04.039>
- Kabutey A, Herák D, Mizera Č. Assessment of Quality and Efficiency of Cold-Pressed Oil from Selected Oilseeds. *Foods.* 2023;12(19):3636. <https://doi.org/10.3390/foods12193636>
- Kabutey A, Herák D, Mizera Č. Determination of Maximum Oil Yield, Quality Indicators and Absorbance Spectra of Hulled Sunflower Seeds Oil Extraction under Axial Loading. 2022;11(18):2866. <https://doi.org/10.3390/foods11182866>
- Kachur O, Korendiy V, Havran V. Designing and simulation of an enhanced screw-type press for vegetable oil production. *Computer Design Systems. Theory and Practice.* 2023;5(1):128-136. <https://doi.org/10.23939/cds2023.01.128>
- Badigannavar R, Kavadamatti A, Kulkarni G. Temperature Based Fan Speed Controller Using Arduino. *International journal of scientific research in engineering and management.* 2022;06(10). <https://doi.org/10.55041/ijsem16609>
- Li Y, Jin Z, Li Q, He L, Zhang Y, Song S. The Design of an Intelligent Screw Extruder Control System Based on Fuzzy Control. *Lecture notes in electrical engineering.* 2019;259-267. [https://doi.org/10.1007/978-981-32-9698-5\\_30](https://doi.org/10.1007/978-981-32-9698-5_30)
- Muliak N, Zdobyttskyi A, Lobur M, Kaczynski R. Optimization of Electromechanical Systems by Intelligent Design Methods. 2022 IEEE XVIII International Conference on the Perspective Technologies and Methods in MEMS Design (MEMSTECH). Polyna (Zakarpattia). Ukraine. 2022; 65-69. <https://doi.org/10.1109/MEMSTECH55132.2022.10002914>
- Household All Stainless Steel Oil Press Ltp200 Electric Small Household Commercial Cold And Hot Pressing Fully Automatic - Specialty Tools - AliExpress [Internet]. <https://www.aliexpress.com/item/1005004330106945.html#navspecification>

Mykhailo Lobur:  <https://orcid.org/0000-0001-7516-1093>

Vitaliy Korendiy:  <https://orcid.org/0000-0002-6025-3013>

Oleksandr Kachur:  <https://orcid.org/0000-0003-2263-6360>

Volodymyr Havran:  <https://orcid.org/0000-0002-6046-6094>



This work is licensed under the Creative Commons BY-NC-ND 4.0 license.

# MULTIPHYSICS SIMULATION AND CONCEPT OF AN ELECTROMAGNETICALLY CONTROL VOLUMETRIC PIXEL AS A STEP TOWARDS A SHAPE MORPHING COMPOSITE

Piotr BARTKOWSKI<sup>\*</sup>, Łukasz PAWLISZAK<sup>\*</sup>, Siddhi G. CHEVALE<sup>\*</sup>,  
Jonathan RUIZ LU<sup>\*</sup>, J. David BRIGIDO<sup>\*\*</sup>

<sup>\*</sup> Faculty of Automation and Constructive Machinery Engineering, Warsaw University of Technology,  
ul. Narbutta 84, 02-524 Warsaw, Poland

<sup>\*\*</sup> University of Bristol, Queen's Building-University Walk, Bristol BS8 1TR, United Kingdom

[piotr.bartkowski@pw.edu.pl](mailto:piotr.bartkowski@pw.edu.pl), [lukasz.pawliszak@pw.edu.pl](mailto:lukasz.pawliszak@pw.edu.pl), [siddhichevale@gmail.com](mailto:siddhichevale@gmail.com),  
[jonathan\\_alfonso.ruiz\\_lu.stud@pw.edu.pl](mailto:jonathan_alfonso.ruiz_lu.stud@pw.edu.pl), [david.brigido.gonzalez@gmail.com](mailto:david.brigido.gonzalez@gmail.com)

*received 29 January 2024, revised 15 May 2024, accepted 18 June 2024*

**Abstract:** Constant development of robotics forces scientists and engineers to work on robots that are more visually and rigidly compatible with the environment around us. To make this possible, new flexible structures are necessary that enable programmatic shape change. To meet this need, in this work we present the concept and modelling methodology of a new structure enabling shape change using electromagnetic forces produced in liquid metal conductor and its stiffening using a granular jamming mechanism. This work presents the structure concept, the description of modelling methodology and empirical validation including the magnetic field, scanned by magnetic field camera, and displacement distribution.

**Key words:** Soft robotics, Soft actuator, Shape morphing composite, Programmable structures, Multiphysics simulation

## 1. INTRODUCTION

As robotics becomes more and more popular, to a certain degree, it forced robot to become more compatible with the current environment. To meet these challenges an entire branch of science called soft robotics was created and is being developed. Main areas of research in the field of soft robotics relates to the development of new structures dedicated for specific tasks, such as swimming [1], flying or walking [2] and moving in the more natural manner. It is also possible to find many different soft robotics applications as a gripper [3] which can hold various objects with different shapes, sizes and weights. Examples of soft robotics being used not only in classical robotics applications but also in other fields of studies. Similar structure we can find in medical devices e.g. touchless human-computer interaction using magnetic skin [4] which has the potential of reducing the infections associated with check-ups and surgeries.

Soft robotics structures usually are built of common materials like silicone rubber compounds and other polymers. In this context, a lack of innovative solutions, which could increase application potential and guarantee better compatibility of a robot with its surroundings is observed. Development of alternative solutions, such as new classes of structures, i.e., new smart material or programmable structures, could accelerate development of the field. Authors from all over the world are trying to work on it. Soft robotics is an emerging field of science and technology with a lot of potential for its advancements.

Various types of actuators and stiffness changing mechanism are used in soft robotics. Previous works have suggested various actuators inputs like temperature [5], light [6], pressure [7, 8] or

magnetic field [9]. Additionally, electroactive polymers (EAP) can be used as an actuator which can predict the whole bending behaviour of the EAP actuator dynamically [10]. Even though the above-mentioned solutions can be considered as good advancement in the field of soft robotics, they bring along some disadvantages, for example, pneumatic actuators have longer reaction time of approximately 0.5s [11]. Additionally, some of them require dangerous high activation voltage ranging between thousands of volts [12] which puts forward threat to humans.

To address the above-mentioned problems, we have proposed a structure that allows for rapid shape change with the low voltage using the Lorentz force generated in liquid metal conductor [13]. Additionally, the structure we have proposed can be stiffened after deformation using a granular jamming mechanism which increases its performance. The above-mentioned structure is an extension of our previous work [8] by adding a double layer of coils filled with liquid metal, which made it possible to increase the structure performance. We also proposed a different shape of the coils, thanks to which we can obtain more complex shapes. Additionally, we proposed the new modelling methods that includes the multiphysics simulations. In this work, we will focus on presenting the concept and characterization of a single volumetric pixel (voxel) structure, which, when combined in multi-voxel composite, can be morph into many different shapes [14, 15, 16, 17].

## 2. GENERAL CONCEPT

The proposed structure, which is shown in Fig. 1 and 2, takes advantage of a combination of two phenomena, development of the



Lorentz force in a liquid metal conductor (like gallium or EGaln) and granular jamming [23]. The structure consists of a granular core, made of coffee grains, and 4 hexagonal coils in pairs. The coils are fabricated by generating the microchannels in silicone rubber ecoflex 0020 (Smooth-On, Inc.) and then filling them with gallium. Since the silicone rubber has the Young Modulus of about 0.055 MPa, and the tension/ bending resistant of liquid metal is almost equal to 0, it allows the structure to be very flexible. In this solution, the coils are in series connection with each other so that the effect of the Lorentz force is doubled. Therefore, when the current carrying sample is placed in a magnetic field, a force is induced which allow the structure to bend. Furthermore, due to the presence of the granular core, filled with ground coffee, it is possible to freeze the shape by vacuum and granular jamming effect [18]. The mentioned phenomenon may also work with other granulates, but due to its very good mechanical properties, we chose coffee [19].

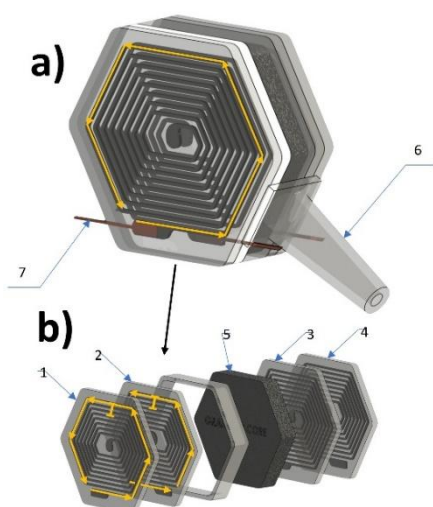


**Fig. 1.** A shape transforming actuator concept. As shown in the figure a and b, the structure consists of four coils, two on each side (1, 2 and 3, 4) connected in series comprising a granular core in between (5). Additionally, the sample is equipped with vacuum (6) and electrical (7) inputs

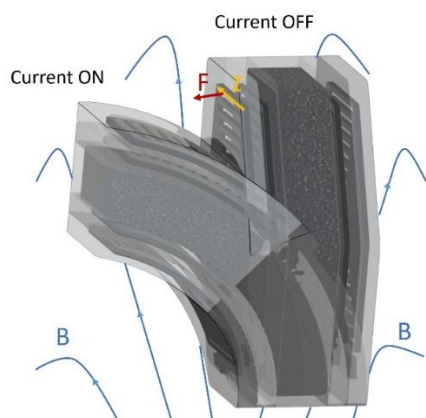


**Fig. 2.** This diagram shows the Lorentz force in action which causes the deformation of the sample. When the sample is placed in the magnetic field from a cylindrical permanent magnet, and current is supplied, the sample undergoes morphing due to the Lorentz force. This morphed shape can be frozen because of the presence of the granular core. B- magnetic field, I- current, F- resulting force

### 3. MULTIPHYSICS SIMULATION

The multiphysics simulations were performed in LS-DYNA environment using the coupling of mechanical and electromagnetic solvers (EM). Model, which is shown in Fig. 3, includes the cylindrical magnets (120 mm x 40 mm) modelled by solid elements that are roughly 5 mm in size and the constant coercive equal to  $900 \frac{kA}{m}$ . The sample, which represents the single voxel, was modelled by solid elements with the size of about 1 mm. The silicone was modelled by linear elastic material model with Young Modulus 0.055 MPa. This is a certain simplification, but research shows that for small deformations, lower than 30%, silicone shows linear behaviour [20]. This approach was also used in the different papers [23]. The granular core was created using user-defined elasto-plastic material model described precisely in the work [21], which is an extension of the von Mises with a different plasticity radius for tension and compression. Model includes the influence of vacuum pressure on the mechanical behaviour. The material's constants for coffee grains were taken from the paper [21]. The boundary conditions are similar to the empirical tests, the lowest surface is constrained, and the current applied to the coils increases linearly from 0 to 5 A. The magnet poles are analogous to test conditions. Using the prepared model, the EM solver calculates the magnetic field distribution based on Maxwell's equations and then by the equation,  $\vec{F} = \vec{j} \times \vec{B}$  (F- Lorentz force, j-current density, B-magnetic field) the Lorentz force in gallium conductor. Since the integration timestep is the same for electromagnetic (EM) and mechanical solver after these calculations, the mechanical solver is able to calculate the sample deformation. We performed calculation and in the next chapters, we have compared the magnetic field distribution and sample displacement with empirical results.

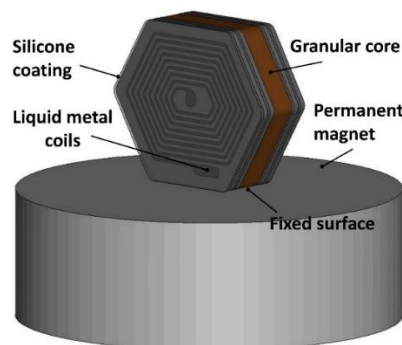


**Fig. 3.** Rendering LS-DYNA numerical model for multiphysics simulations containing general description of major functional parts of the system under study

### 4. SAMPLE FABRICATION

To check the proposed modelling methodology, it was necessary to prepare a test sample. The initial step in manufacturing it was to design in Solidworks CAD various parts which were later fabricated using Reise 3D pro2 plus printer. For the molds fabrication the Polylactic acid (PLA) was used. The next step was to fill the molds with silicone rubber ecoflex 00-20 (smooth-on) [22]. Each of the silicone molds was cured in classical laboratory dryer with  $50^{\circ}C$ , and the curing time was  $\approx 25$  min. Later, the layers were separated from the molds and attached with one electrode per

layer. To complete the circuit, two layers were stuck together such that current carrying coils are in series with each other. Samples from negative molds were glued together thanks to a thin layer created with a spin-coater. The next step was to fill the coils with liquid gallium by injecting a syringe to one end of the coil and pushing the preheated liquid metal through both the layers of voxels. Towards the end of synthesis of the sample, a granular core was incorporated in the assembly which was filled with fine coffee grains. In the final step the housing and pneumatic input were added. The manufacturing process is depicted in Fig. 4.

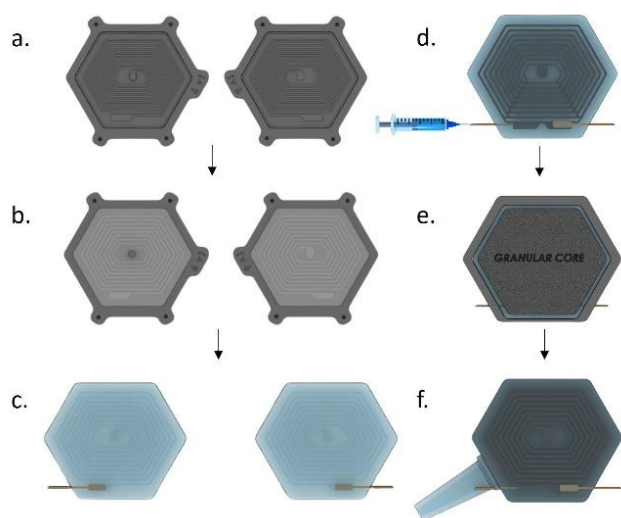


**Fig. 4.** Composite preparation scheme: a) FDM printed coil moulds, b) coil moulds were poured in with silicone rubber, c) silicone rubber mouldings with elastic coils were inserted with electrodes, d) elastic coil moulding comprised of two glued together layers of silicon rubber, injected with liquid gallium, e) integration of the elastic liquid metal coil with granular core pocket, f) complete sample

## 5. EMPIRICAL TESTS AND MODEL VALIDATION

### 5.1. Magnetic field

The distribution of the magnetic field produced by a cylindrical magnet was measured with the MagCam magnetic field scanner equipped with minicube 3D camera. This sensor, thanks to the matrix of more than 16000 hall sensors, allows to measure the magnetic field with the high resolution about 0.1 mm. All individual sensor allows to measure the 3 components of magnetic field ( $B_x$ ,  $B_y$ ,  $B_z$ ) and present a graph which magnetic field distribution of the entire specified range. We scanned the magnetic field in volume 80 mm x 80 mm x 56 mm what is visualized in Fig. 5c, d. The measurement with the Magcam was performed 3 times to get the most accurate data and compatible data. The magnetic field distribution recorded by Magcam scanning and simulation is shown in Fig. 5. Despite the fact that we scanned the entire volume, the results were compared for two surfaces 50.5 and 20.5 mm above the magnet surface which is visualized in Fig. 5a and Fig. 5b respectively. As we can see the general distribution is similar for both test and simulation. The magnetic field is greater at the lower position in the centre of the sample, at point A, and is equal to 0.23 T for both test and simulation. At point B and C the values are 0.19 T. In line with

theoretical predictions, the magnetic field decreases with distance from the source. At the higher position (55.5 mm above the magnet surface) magnetic field is equal 0.113 T, 0.087 T and 0.084 in point A, B and C respectively. In this case the simulation returns slightly different results. In the centre we can see 0.112 T and on the sides 0.085 T. The overall distribution at this position is comparable, and the maximum error does not exceed 3%.

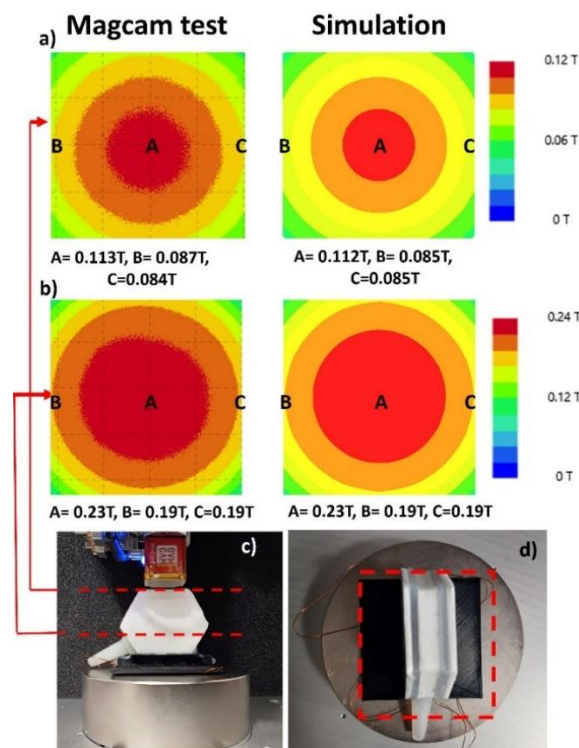


**Fig. 5.** Empirical tests and simulation of magnetic field distribution: a) and b) corresponding the area presented in c) and d) respectively

### 5.2. Deformation distribution

Deformation distribution, which is shown in Fig. 6a, was recorded by a camera with 50MPixels and a laser sensor OMRON ZX 1-LD300A81 which was able to measure the sample displacement. The measurement point was placed in the sample's centre line, 45 mm above the magnet area. The tests were performed for 5 vacuum pressure values (0, 0.02, 0.04, 0.06, 0.08, 0.1MPa). Each test was repeated 3 times. Fig. 6a presents the sample deformations for the different values of current for the atmospheric pressure (upper row) and the vacuum pressure 0.1MPa (lower row). Fig. 6b presents the displacement in function of current for the highest and lowest vacuum pressure for empirical research as well as for simulations. Additionally, Fig. 6c shows the maximum sample deflection in function of vacuum pressure. It can be seen that the maximum deflection for the current 5A is equal to 10.4 mm for the atmospheric pressure. It can be seen that the sample deformation for the maximum vacuum pressure is almost 10 times lower. Generally, we can find the strongly nonlinear characteristic between maximum deflection and vacuum pressure. Fig. 6b shows really good correlation between the simulation and experiments, usually lower than 5% in the whole current range.

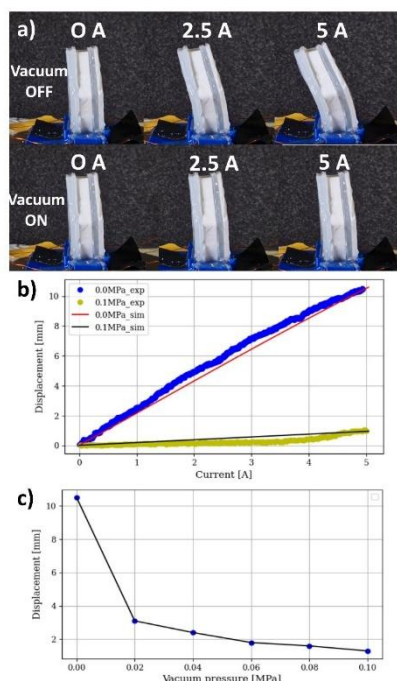


**Fig. 6.** Sample deformation modes a), composite displacement in function of charge current b), maximum displacement in function of vacuum pressure c)

### 5.3. Future morphing composite

Proposed voxel which showed its good properties by being combined into multi-voxel structure could create the deformable composite which could be able to deform in multiple shapes. It is shown as a concept in Fig. 7 where initially flat structure (Fig. 7a) can deform in shape 1 (Fig. 7b) or shape 2 (Fig. 7c). Thanks to granular jamming effect structure could be also frozen after the deformation and therefore would have the ability to bear loads.

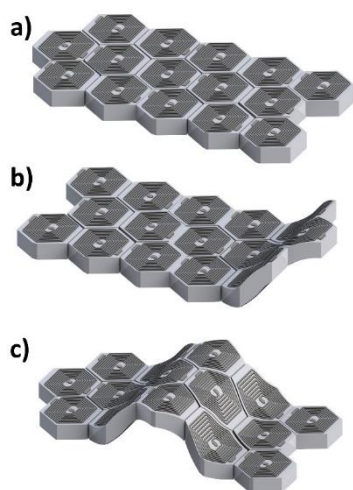


**Fig. 7.** Concept of a morphable composite material comprised of electromagnetically controlled volumetric pixels (voxels). a) a flat plate comprised of voxel with independent control b), c) deformation modes of the composite induced by the Lorentz force arising when charge current is applied selectively to the one most outer rows of voxels and to the center voxels respectively, while the whole structure is placed in the vicinity of external magnetic field

## 6. CONCLUSION

This work shows the concept of the new volumetric pixel (voxel) structure able of changing its shape under Lorentz force generated in liquid metal conductor and retaining it by employing a granular jamming mechanism. This concept is an extension of our previous work presented in paper [23] where we proposed the e-morph actuator. The structure presented in this work consists of double-layered coils, which increase the number of turns and thus the value of the Lorentz force by the factor of two, while ensuring much better compactness of the structure because both electrical current leads are located at the bottom of the structure. This is an undoubted advantage of this structure. Compared to our previous works, here we proposed a hexagonal shape of the coils, not a rectangular one, thanks to which we can obtain more complex deformation shapes. The work showed that the maximum deformation of the structure is 10.4 mm and the stiffness of the structure after applying negative pressure can increase almost tenfold.

In this work we also presented innovative methods for modeling and empirical measurement for the proposed structure. Usually for similar structures, Scientists calculate the Lorentz forces in separate solvers or by analytical methods and then just applied them as a point or linear forces in mechanical solvers. Thanks to our approach and the use of multiphysics simulations, we can obtain a very good correlation with the experiment even in a strongly non-homogeneous magnetic field. The general error in magnetic field distribution in comparison with Magcam measurement was lower than 3%, but the maximum error for deformation was lower than 5%. This proves that our method works correctly, and we can use it to further develop the structure.

The proposed voxel structure can be used in the future e.g., as a building block for a morphable composite material in which its shape can be controlled by selectively generating the Lorentz force locally, for particular set of pixels, as shown in Fig. 7, enabling different modes of the structure. Such a structure would require an extensive development process, but we see huge potential for it.

## REFERENCES

1. Jan F, Noh Y, Macias M, Wurdemann H, Althoefer K. Bio-Inspired Octopus Robot Based on Novel Soft Fluidic Actuator. IEEE International Conference on Robotics and Automation (ICRA). 2018; 1583-1588.
2. Chen Y, Doshi N, Wood R. Inverted and Inclined Climbing Using Capillary Adhesion in a Quadrupedal Insect-Scale Robot. IEEE Robotics and Automation Letters. 2020; 5(3): 4820-4827.
3. He Z, Lian B, Song Y. Rigid-Soft Coupled Robotic Gripper for Adaptable Grasping. Journal of Bionic Engineering. 2023; 20.
4. Zhang J, Chen G, Chen J. Magnetic Skin for Touchless Human-Computer Interaction to Prevent Healthcare-Associated Infections. Advanced Sensor Research published by Wiley-VCH GmbH. 2022;1: 2200008.
5. Wu S, Baker G, Yin J, Zhu Y. Fast Thermal Actuators for Soft Robotics. Mary Ann Liebert. 2021;9.
6. Cunha MP da, Debije MG, Schenning APHJ. Bioinspired light-driven soft robots based on liquid crystal polymers. Chemical Society Reviews. 2020;49(18): 6568-78.
7. Ruiqian W, Chuang Z, Yiwei Z, Wenjun T, Chen W, Lianqing L. Soft underwater swimming robots based on artificial muscle, Advanced Materials Technologies. October 2022; 8(4): 2200962.
8. Kalita B, Leonessa A, Dwivedy SK. A Review on the Development of Pneumatic Artificial Muscle Actuators: Force Model and Application. Actuators. 2022; 11(10): 288.




9. Chung HJ, Parsons AM, Zheng L. Magnetically Controlled Soft Robotics Utilizing Elastomers and Gels in Actuation: A Review. *Advanced Intelligent Systems*. 2021; 3(3): 2000186.
10. Mutlu R, Alici G, Xiang X, Li W. Electro-mechanical modelling and identification of electroactive polymer actuators as smart robotic manipulators. *Mechatronics*. 2014; 24 (3): 241-251.
11. Polygerinos P, Wang Z, Galloway KC, Wood RJ, Walsh CJ. Soft robotic glove for combined assistance and at-home rehabilitation. *Robot. Auton. Syst.* 2015;73: 135-143.
12. Keith F, Shengqiang C, Adrian K, Siegfried B, Zhigang S. Model of dissipative dielectric elastomers. *J. Appl. Phys.* 2012;111(3).
13. Bartkowski P, Suwała G, Zalewski R. Temperature and strain rate effects of jammed granular systems: experiments and modelling. *Granular Matter*. 2021;23.
14. Ni X, Luan H, Kim J-T et al. Soft shape-programmable surfaces by fast electromagnetic actuation of liquid metal networks. *Nat Commun* 2022;13(5576):1234567890.
15. Siefert E, Reyssat E, Bico J, Roman B. Bio-inspired pneumatic shape-morphing elastomers. *Nat Mater* 2019;18:24–28.
16. Franić K, Franzke L. Shape Changing Surfaces and Structures: Design Tools and Methods for Electroactive Polymers. In: *Proceedings of the 2019 CHI Conference on Human Factors in Computing Systems* [Internet]. New York, NY, USA: Association for Computing Machinery. 2019; 1–12.
17. Han MW, Kim MS, Ahn SH. Shape memory textile composites with multi-mode actuations for soft morphing skins. *Compos Part B Eng.* 2020;198:108170.
18. Bartkowski P, Bukowiecki H, Gawiński F, Zalewski R. Adaptive crash energy absorber based on a granular jamming mechanism. *Bull Pol Acad Sci Tech Sci* . 2022; 70(1).
19. Hudson, Shaymus W. Mechanical characterization of jammable granular systems, Massachusetts Institute of Technology. Cambridge. 2012; 36-37
20. Liao Z, Hossain M, Yao X, Navaratne R, Chagnon G. A comprehensive thermo-viscoelastic experimental investigation of Ecoflex polymer. *Polymer Testing*. 2020; 86(1).
21. Brigido JD, Burrow SG, Woods BKS, Bartkowski P, Zalewski R. Flexural Models for Vacuum-Packed Particles as a Variable-Stiffness Mechanism in Smart Structures. *Physical Review Applied*. Bristol-Warsaw Collaboration. 2022; 17(4):044018.
22. Zhenhua W, Qi W, Jianyu H, Yamei Y, Dezhi C, Yusheng S, Bin S. The soft ndfeb/ecoflex composites for soft robot with a considerable magnetostimulated shrinkability, *Composites Science and Technology*. 2021; 109129.
23. Piotr B, Franciszek G, Lukasz P. E-morph as a new adaptive actuator for soft robotics, *IEEE Robotics and Automation Letters*. 2022; (7,4); 8831–8836.


The research was carried out on devices co-funded by the Warsaw University of Technology within the Excellence Initiative: Research University (IDUB) programme.

Piotr Bartkowski:  <https://orcid.org/0000-0002-1460-8389>

Łukasz Pawliszak:  <https://orcid.org/0000-0002-1499-5702>

Siddhi G. Chevale:  <https://orcid.org/0009-0009-5116-0913>

Jonathan Ruiz Lu:  <https://orcid.org/0009-0001-3108-7247>

J. David Brigido:  <https://orcid.org/0000-0003-3559-3718>



This work is licensed under the Creative Commons BY-NC-ND 4.0 license.

## MECHANICAL PROPERTIES OF 3D PRINTED PLA SCAFFOLDS FOR BONE REGENERATION

Paula KUNDRECKAITĖ<sup>\*</sup>, ANDŽELA ŠEŠOK<sup>\*</sup>, Rimantas STONKUS<sup>\*\*</sup>  
 Gediminas GAIDULIS<sup>\*</sup>, Eliza ROMAŃCZUK-RUSZUK<sup>\*\*\*</sup>, Jolanta PAUK<sup>\*\*\*</sup>

<sup>\*</sup>Faculty of Mechanics, Department of Biomechanical Engineering,  
 Vilnius Gediminas Technical University, Plytinės str. 25, Vilnius, Lithuania  
<sup>\*\*</sup>Faculty of Mechanics, Department of Mechatronics, Robotics and Digital Manufacturing,  
 Vilnius Gediminas Technical University, Plytinės str. 25, Vilnius, Lithuania  
<sup>\*\*\*</sup> Institute of Biomedical Engineering, Białystok University of Technology,  
 Wiejska 45A, Białystok, Poland

[paula.kundreckaite@gmail.com](mailto:paula.kundreckaite@gmail.com), [andzela.sesok@vilniustech.lt](mailto:andzela.sesok@vilniustech.lt), [rimantas.stonkus@vilniustech.lt](mailto:rimantas.stonkus@vilniustech.lt)  
[gediminas.gaidulis@gmail.com](mailto:gediminas.gaidulis@gmail.com), [e.romanczuk@pb.edu.pl](mailto:e.romanczuk@pb.edu.pl), [j.pauk@pb.edu.pl](mailto:j.pauk@pb.edu.pl)

received 7 July 2023, revised 2 February 2024, accepted 23 February 2024

**Abstract:** The growing interest in biodegradable scaffolds for bone regeneration created a need to investigate new materials suitable for scaffold formation. Poly(lactic acid) (PLA) is a polymer commonly used in biomedical engineering, e.g. in tissue engineering as a biodegradable material. However, the mechanical behavior of PLA along its degradation time is still not explored well. For this reason, the mechanical properties of PLA scaffolds affected by incubation in physiological medium needs to be investigated to show the potential of PLA to be used as a material for biodegradable scaffold formation. The purpose of this research is to determine the mechanical properties of PLA scaffolds before and after incubation, and to apply constitutive material models for further behavior prediction. Two sets of PLA scaffolds were printed by the 3D printer "Prusa i3 MK3S" and sterilized by ultraviolet light and ethanol solution. The first set of specimens was incubated in DMEM (Dulbecco's Modified Eagle Medium) for 60, 120, and 180 days maintaining 36.5 °C temperature. The mechanical properties of the scaffolds were determined after performing the compression test in the "Mecmesin MultiTest 2.5-i" testing stand with a force applied at two different speed modes. The obtained data was curve fitted with the hyperelastic material models for a model suitability study. The second set of specimens was incubated in PBS (Phosphate Buffered Saline) for 20 weeks and used in a polymer degradation study. The obtained results show that the mechanical properties of PLA scaffolds do not decrease during incubation in physiological medium for a predicted new bone tissue formation period, though hydrolysis starts at the very beginning and increases with time. PLA as a material seems to be suitable for the use in bone tissue engineering as it allows to form biocompatible and biodegradable scaffolds with high mechanical strength, required for effective tissue formation.

**Key words:** scaffold, bone regeneration, poly(lactic acid) (PLA), biodegradable polymers, mechanical properties, hyperelasticity

### 1. INTRODUCTION

The increasing average age and the growing frequency of bone and joint disorders [1] lead to a greater need for the use of polymeric scaffolds [2], which makes the composition of a scaffold and the production methods of the ideal scaffold particularly important. Scaffolds are used in the treatment of bone fractures, especially in people with bone diseases, e.g. osteoporosis, because the bone has a reduced ability to repair itself, and scaffolds support the growth of bone tissues [3,4].

In order to create a suitable and adapted biodegradable scaffold for effective bone healing, the desired bone regeneration time should be considered, which can vary in duration and depend on many factors: human health, age, bone size, trauma, received load, etc. [5]. However, adjusting the mechanical and degradation properties of the scaffold to the required ones is not an easy task. The composition of the scaffold, its structure, manufacturing method, and the environment in which the scaffold operates are the key factors in determining whether the scaffold will maintain the desired functions over time [6]. It is well known that poly(lactic acid) (PLA) itself possesses certain mechanical properties that

influence the scaffold's behavior. It is a stiff material with relatively low ductility and does not form toxic compounds during hydrolysis, therefore, it has been used in biomedicine for a long time [7]. Moreover, its mechanical properties can be modified by adjusting the printing parameters, blending with other materials, or incorporating additives such as reinforcing fibers or particles. PLA composites and manipulation of their mechanical properties by creating different scaffold compositions are widely discussed in the literature [8,9,10]. However, hydrolysis of these composites may release substances that alter pH or otherwise emerge an immune response [11]. The manufacturing method also determines the change in the properties of the scaffold and should be selected, for example, according to the desired size of the pores or the temperature resistance of the material [12].

Mechanical properties such as compressive strength, tensile strength, and elastic modulus are commonly evaluated to assess the scaffold's mechanical integrity [13]. Moreover, the mechanical strength of the 3D-printed PLA scaffold is a critical factor for successful bone regeneration. It determines the scaffold's ability to provide initial structural support and withstand mechanical forces during healing. This raises a new challenge for this study: not only



to determine whether the polymer is suitable for use in the bone regeneration process and retains its mechanical properties for the required time but also to check the suitability of constitutive models to predict further material behavior [14].

Common printing techniques include fused deposition modeling (FDM), stereolithography (SLA), and selective laser sintering (SLS). Each technique has its advantages and limitations in terms of resolution, accuracy, and mechanical properties. For example, FDM-printed scaffolds tend to have anisotropic mechanical properties due to the layer-by-layer deposition process. Recently, 3D printing is increasingly used in various fields of science and industry, due to the possibility of creating models with complex shapes while maintaining high quality standards and high precision [15,16,17]. The advantage of using 3D printing in the production of scaffolds is the possibility of obtaining individual projects with a resolution in the micrometer scale and production without wasting materials. 3D printing technology allows for greater possibilities of producing scaffolds in relation to the size and distribution of pores [18,19].

Therefore, the purpose of this research is to investigate the mechanical properties of PLA scaffolds for bone regeneration and their changes after incubating the scaffolds in physiological medium as well as to determine the degradation of the scaffolds over time. The study addresses the change in the mechanical properties of PLA and the ability to meet the mechanical sustainability of bone tissue.

## 2. MATERIALS AND METHODS

The research was performed in the laboratories of Vilnius Gediminas Technical University. PLA scaffolds with 90% porosity were printed by the 3D printer "Prusa i3 MK3S" using FDM (Fused Deposition Modeling) technology. A nozzle temperature of 215 °C and a heated bed temperature of 60 °C were set for the 3D printing. This printer has a nozzle diameter of 0.4 mm. In order to ensure the favorable performance of printed products, the layer height should be adjusted to the diameter of the nozzle. This procedure affects the value of interlayer cohesion. A widely accepted mathematical model is used to determine the optimum printed layer height:  $h \leq 0.75 \cdot D$  [20]. CAD model used to print specimens is presented in Fig. 1, and 3D printed PLA scaffolds are shown in Fig. 2. Two sets of PLA scaffolds were printed: the first set was used to determine the mechanical properties of the scaffolds, while the second one was involved in a polymer degradation study. The outer dimensions of the printed sample were checked with a micrometer. Regarding length and width dimensions, PLA revealed the accuracy with a minimum shape error of 0.05%.

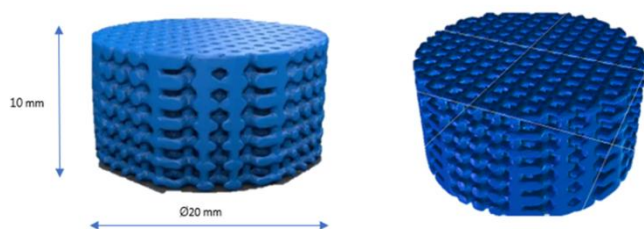


Fig. 1. CAD model, used for 3D printing of scaffold specimens

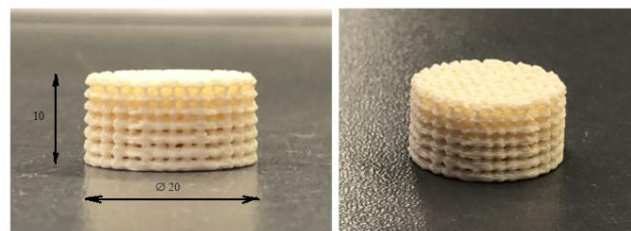


Fig. 2. 3D printed PLA scaffolds

For the more reliable scientific study, specimens must be sterilized to avoid microbial contamination. Contaminated container, specimen, or incubation medium can cause unwanted bacterial growth and formation of enzymes, which might affect PLA hydrolysis. For this reason, the printed scaffolds were sterilized using ultraviolet light and 70% ethanol solution. Such methodology was selected after analyzing method efficiency and possible impact on the mechanical properties of the polymer [21].

In order to determine the mechanical properties of PLA scaffolds, a variety of methods are used providing diverse data on the similarities of scaffold mechanical properties with the ones of natural bone tissue. Such data can be used to develop superior scaffolds for bone regeneration. The method applied in this study is scaffold incubation in physiological medium. DMEM (Dulbecco's Modified Eagle Medium) is a widely used base medium for the growth of many mammalian cells, such as fibroblasts, neurons, glial cells, human umbilical vein endothelial cells (HUVEC), muscle cells, and other cell lines. PLA scaffolds were incubated in a sterile DMEM, maintaining a temperature of 36.5 °C. 20 identical samples were printed from PLA. Specimens were separated into 4 groups and each group was incubated for a different period of time: non-incubation period, 60, 120, and 180 days (Fig. 3).



Fig. 3. Incubation of scaffold specimens in DMEM

The mechanical properties of PLA scaffolds were identified after each incubation period. The compressive force of 800 N was applied to each specimen for 20 cycles at two different loading speed modes: 500 mm/min and 10 mm/min. To study the mechanical properties of PLA scaffolds, the forces acting on the place where the scaffold will be implanted should be taken into account. When a person walks or runs, the force starts to rise from zero when the weight is transferred from the rear leg to the front leg. When walking slowly, a force equal to the weight of a person acts on one leg (suppose a person weighs 80 kg, the force acting on his legs while walking would be equal to a force of 800 N). The maximum loading speed of the testing machine of 500 mm/min was chosen to simulate the mechanical load on the leg

bone during slow walking. 10 mm/min simulates the mechanical load of the arm support. Low-cycle fatigue tests were applied. All experiments were performed in the “Mecmesin MultiTest 2.5-i” force testing stand (Fig. 4). The MultiTest-i is a versatile tensile and compression tester controlled by Emperor software running on a PC. The measurement accuracy is  $\pm 0.1\%$  or  $\pm 0.25\%$  of the capacity of the load cell. The loadcells measure from zero and cover the range from 2 N right up to 2.5 kN.

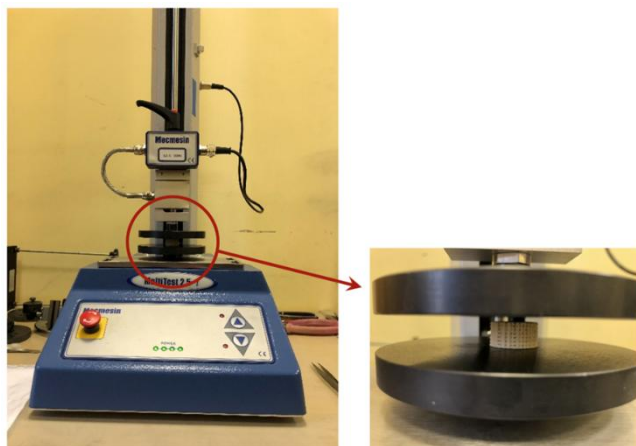


Fig. 4. Compression test performed in the “Mecmesin MultiTest 2.5-i” force testing stand

In addition, a degradation study was performed to determine PLA hydrolysis in time. For this purpose, PLA scaffolds were incubated in PBS (Phosphate Buffered Saline) solution for 20 weeks, maintaining 36.5 °C temperature. Every week specimens were taken out of a buffer, dried, and weighed by analytical scales. Additionally, the pH level was measured using a calibrated pH meter. After that, all specimens were placed in a fresh PBS buffer for further incubation. Transferring samples to fresh PBS buffer after pH measurement and drying helps to maintain a constant environment for further incubation. This ensures that any changes in the specimens are due to the experimental conditions rather than potential variations from the previous buffer. It provides a stable baseline for accurate and reliable results in medical research. Observation of the surface of the samples was carried out on a confocal microscope (Olympus Olympus Lext OLS 4000) after various incubation times in PBS solution.

### 3. RESULTS

#### 3.1. Mechanical properties study

The mechanical properties study of PLA scaffolds consists of two parts: A and B, each corresponding to different compressive loading speed mode of 500 mm/min and 10 mm/min, respectively.

Study A suggests that maximum strain values in the scaffolds with respect to compressive loading increase over the incubation period. During 6 months of incubation, these values changed on average by 0.0073, and, as shown in Fig. 5A, linear and polynomial regressions of data can help to predict the increase of maximum strains during incubation over a longer period of time. The trend of the results in study B is the same: the maximum strain values of PLA samples increase over time. During 6 months of

incubation, the maximum strains in PLA scaffolds changed on average by 0.0015, and regression models (Fig. 5B) suggest that these values will slightly increase along degradation time.

Stress and strain curves of study A (Fig. 6) show that the curve shifts more to the right along the x-axis with increasing incubation time but there are no other features that could be compared. Meanwhile, stress and strain curves of study B (Fig. 7) show no significant changes between incubations. Comparison of studies A and B showed no clear differences that could be distinguished (test data in Fig. 6 and 7 are marked in red).

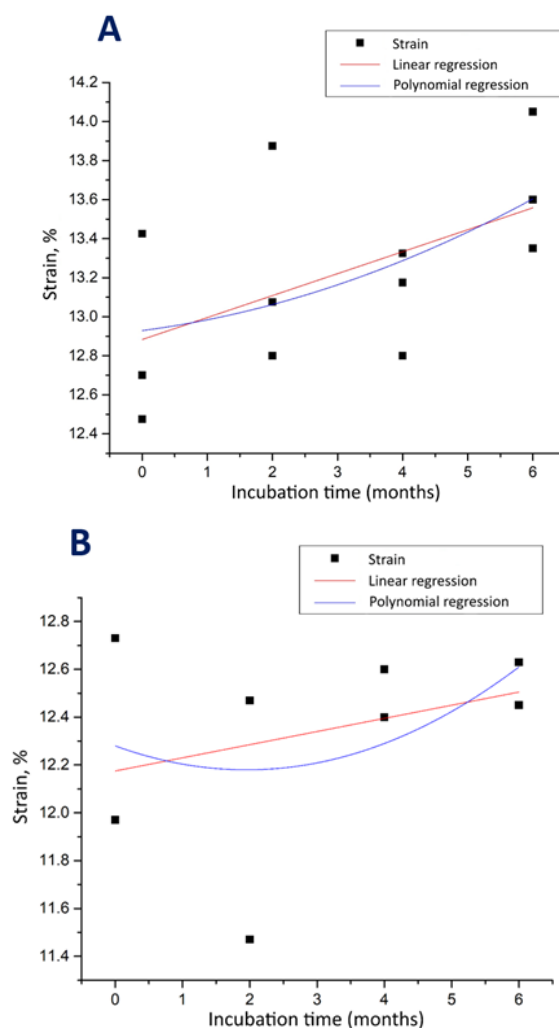


Fig. 5.

Maximum strain values in the scaffolds with respect to compressive loading at two different loading speed modes: 500 mm/min (A) and 10 mm/min (B)

In addition, constitutive material models were curve fitted to the test data for further analysis and the possibility to predict the mechanical behavior of PLA scaffolds with respect to incubation time. Various constitutive models suitable for the prediction of material behavior are described in the literature [22]. Due to the nonlinear stress and strain feature, the classical linear elastic model is not suitable for large deformations. Thus, taking into account the nature of this biodegradable polymer, common hyperelastic material models were used: the 2nd order reduced polynomial model and the Mooney-Rivlin model. The development of such models makes it possible to predict the mechanical behavior of a biodegradable scaffold during its life cycle. The stress

and strain diagrams for both studies are presented in Fig. 6 and 7, showing the fitted Mooney-Rivlin (blue line) and reduced polynomial (green line) curves.

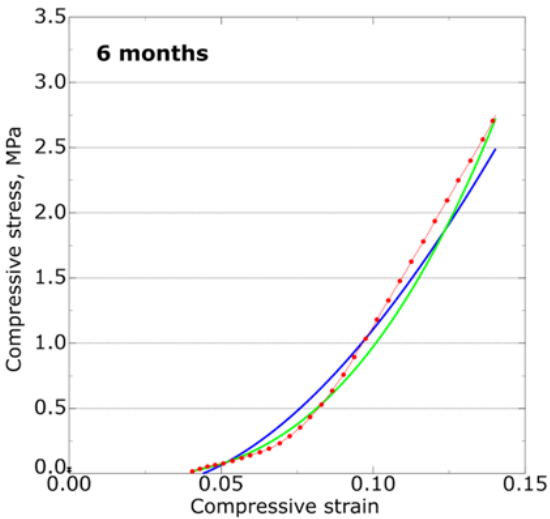
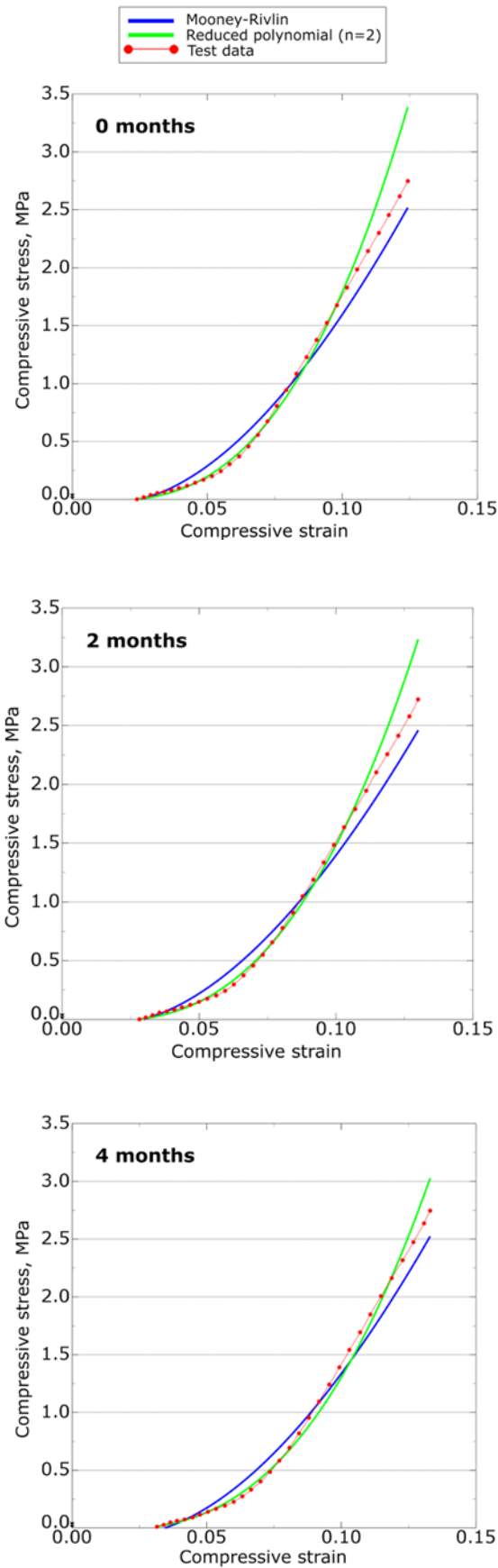
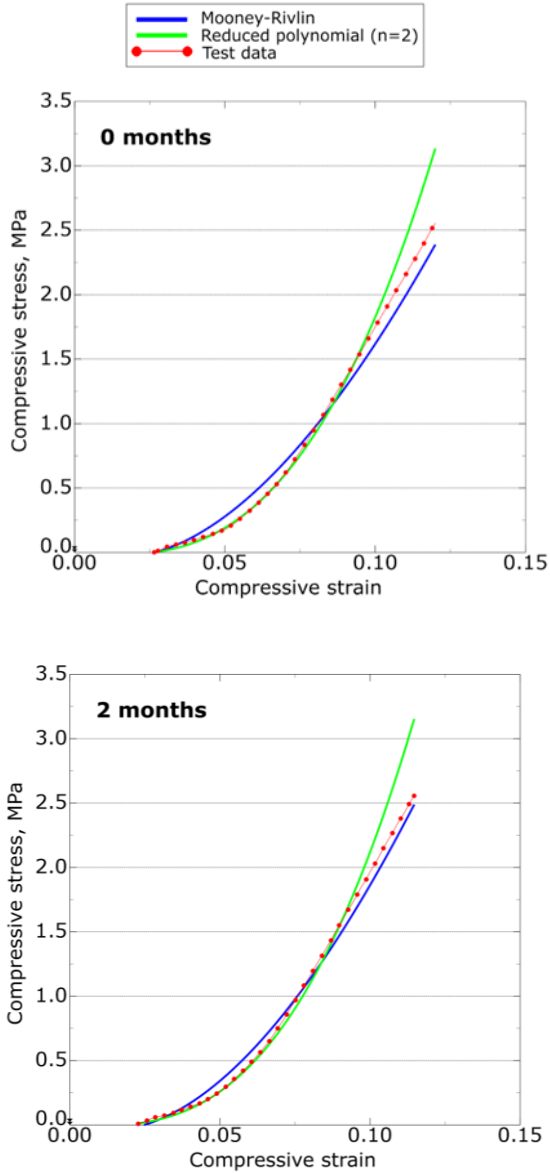
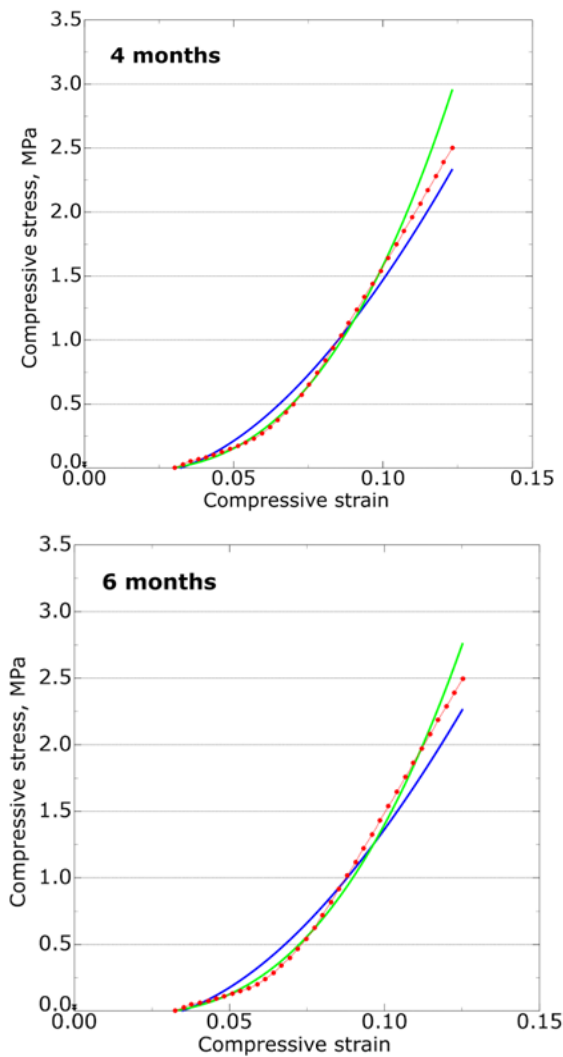


Fig. 6. Study A: stress and strain test data curve fitted with the hyperelastic material models (loading speed is 500 mm/min): 0 months – unincubated samples; 2, 4 and 6 months – incubation period





**Fig. 7.** Study B: stress and strain test data curve fitted with the hyperelastic material models (loading speed is 10 mm/min): 0 months – unincubated samples; 2, 4 and 6 months – incubation period

The Mooney-Rivlin hyperelastic model is commonly used when modeling the nonlinear behavior of high-strain uncompressed materials [23]. It is important to understand that this model does not provide any specific insight into the behavior of the material. It is only a curve of various polynomial data that allows to predict further behavior of the polymer. Fig. 6 and 7 show that the reduced polynomial model is less accurate than the Mooney-Rivlin model. The material parameters C10 and C01 of the Mooney-Rivlin model as well as C10 and C20 of the reduced polynomial model were examined for each specimen (Tables 1 and 2).

**Tab. 1.** Study A: material parameters of the Mooney-Rivlin and reduced polynomial models

Incubation time, months	Mooney-Rivlin		2nd order reduced polynomial	
	C10	C01	C10	C20
0	-26.8901	26.1858	-0.1948	59.5980
2	-26.0619	25.2424	-0.2288	50.9024
4	-26.8167	26.0130	-0.2104	49.6285
6	-25.3135	24.3870	-0.2692	36.4299

**Tab. 2.** Study B: material parameters of the Mooney-Rivlin and reduced polynomial models

Incubation time, months	Mooney-Rivlin		2nd order reduced polynomial	
	C10	C01	C10	C20
0	-28.8934	28.0161	-0.2577	63.2575
2	-30.3108	29.5503	-0.2734	55.4032
4	-27.7097	26.8852	-0.2747	53.5780
6	-27.5727	26.7106	-0.3015	50.5683

The regression of the Mooney-Rivlin material parameter C10 for studies A and B are shown in Fig. 8. The coefficients obtained during this curve fitting reveal that the material is unstable for all strains because the sum of the coefficients is below zero. However, with these coefficients, it is still possible to model a longer-term incubation stress and strain curves and predict further mechanical behavior of the scaffolds.

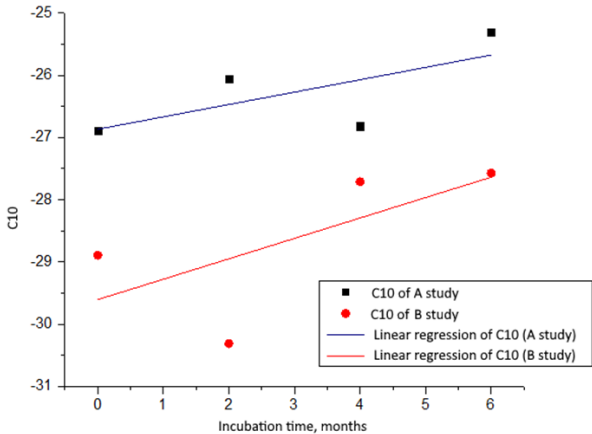


**Fig. 8.** Evolution of Mooney-Rivlin material parameter C10 in time

### 3.2. PLA degradation study

The results of the PLA degradation study show that on average the scaffolds lost about 10% of their weight during the incubation time of 20 weeks. The scatter of the results and their regression is shown in Fig. 9. By modelling further PLA degradation, it can be estimated that PLA would lose up to 20% of its weight over the next 14 weeks of incubation.

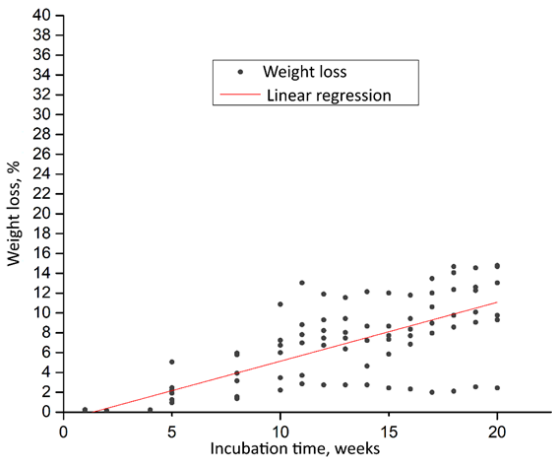


**Fig. 9.** PLA weight loss over time



The observed degradation is quite high, which possibly occurs due to the erosion of the scaffolds. However, the present study confirms that while PLA scaffolds degrade, no toxic compounds that would cause an adverse reaction in the human body or during cell growth *in vitro* are produced. In addition, the pH level measured throughout the study did not change much and remained in the range of 7.0 to 7.4. No precipitation or color change was observed as well.

Figure 10 shows the surface of printed scaffolds conditioned at different times. Fig. 10a shows a PLA sample before incubation in solution. Printed paths have an even surface. There are no widenings in the print paths overlapping subsequent layers, which is visible in samples after incubation in the solution. The surface area of the samples after 5 and 10 weeks was similar (Fig. 10b and c). The 3D printing paths are of equal size and the scaffold walls have the regular shape of the FDM filament extruder. The first changes in the shape of the scaffold walls are visible after 15 weeks. The walls of the scaffolds have narrowing, especially in the spaces where the filament does not lean against the wall from the lower layer (Fig. 10e). In addition, there are pits on the surface, which additionally indicate the degradation process (Fig. 10f). Extending the incubation time of the printed scaffolds resulted in further degradation (Fig. 10d). The walls of the scaffolds were irregular, with large narrowings, and the last layer separated.

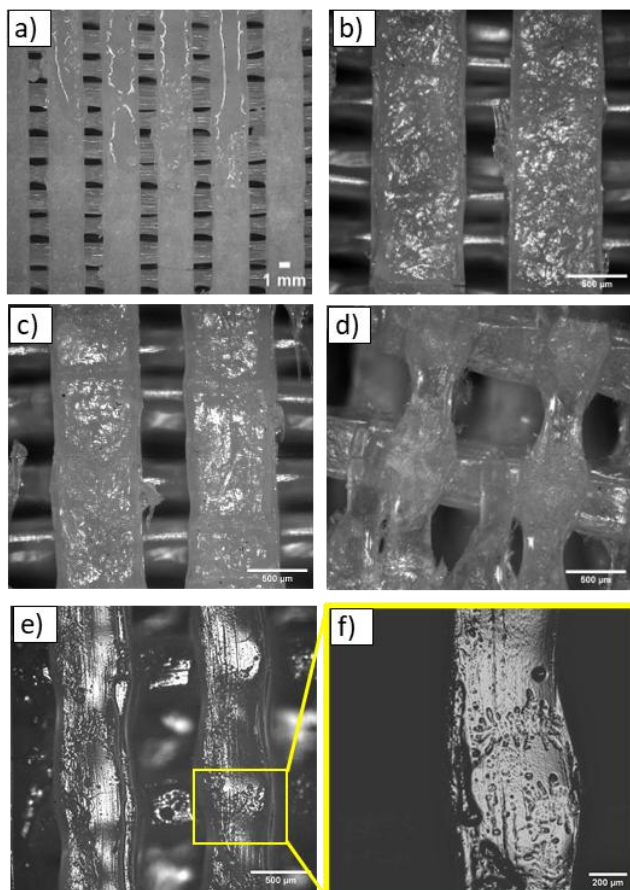


**Fig. 10.** Surface of printed scaffolds after different incubation time in PBS solution: a) 0 weeks, b) 5 weeks, c) 10 weeks, d) 20 weeks, e, f) 15 weeks

#### 4. DISCUSSION

PLA polymer and other copolymers of this material have been widely studied for many years and have a wide range of applications [24]. Although the polymer is being studied at a fundamental level, further research is needed for a more complete understanding of its material properties. This paper presents a way to study the mechanical properties of PLA by manipulating environmental conditions such as temperature, incubation medium, or incubation time. The study confirms that PLA scaffolds are very strong and can withstand extremely high loads.

The results obtained during the present study suggest that the PLA scaffolds did not lose their mechanical strength over incubation time unlike the PLA-PCL copolymer, which was studied by Vieira et al. [9]. In their study, the authors found that under incubation conditions similar to ours the Mooney-Rivlin model parameters of PLA-PCL change much faster, and the material parameters of scaffolds incubated for 16 weeks are twice as big as the ones of non-incubated specimens. Also, comparing the results published by Tew and Bhatia [25] with the ones in the Vieira's study [9], the most suitable mathematical model for describing the behavior of polymers was identified to be the Mooney-Rivlin. Some experiments that determined the accuracy of this model and its possible further applications for the prediction of the material behavior can also be found in the literature [9,23,25,32].

The experimentally determined nonlinear behavior of the material in the present study increases the importance of computational modeling, which can help to understand how the scaffold will behave in a given environment, and to optimize the application of the scaffold for the use in the medical field. A number of developed mechanical behavior models are used to predict the behavior of a material under different loads and environments [22]. These models, if used correctly, can provide insights into the response and subsequent behavior of the required material. Due to the strong interest in this field from both science and industry, the computational modeling of material behavior is and will become more important in the future.

Despite all the advantages of process optimization and microstructural characterization, there is still a lack of an understanding of the mechanical behavior of porous scaffolds while in the human body [6]. One of the unique properties of biodegradable polymers is their ability to degrade under biologically favorable conditions [26]. Degradation, which is a major reason for the successful use of PLA for medical applications, depends on the molecular weight and microstructure of the material, the degree of crystallinity, and the applied chemical and mechanical loading.

While comparing the results obtained during the present study with the ones published in [9] where PLA-PCL composite scaffolds lost 20% of their weight in 28 weeks and a greater change in mechanical properties was observed, it can be concluded that PLA scaffolds degrade at a similar rate but do not lose their mechanical strength. Also, a comparison with the study published by Guo et al. [27] can be made, in which PLA weight loss of 83% after 240 days of incubation in physiological medium was observed. Compared to the results obtained in the present study, the degradation of PLA differs significantly, and by following our estimated degradation model, we can expect up to 20% of PLA degradation over the next 100 days of incubation. However, with the prolonged incubation, the degradation described by linear regression can progress to become exponential thus increasing to significantly higher numbers.

The surface of printed scaffolds can undergo changes over time when incubated in a phosphate-buffered saline (PBS) solution. The specific changes observed depend on several factors, including the material composition of the scaffold, the printing technique used, and the environmental conditions during incubation. Initially, the degradation process was slow, which is confirmed by the literature. Weight loss of conditioned samples was small after 10 weeks, and there were no significant differences on the surface, similar behavior of scaffolds is in the work [27,29]. In the work [29], it was noticed that the parallel arrangement of beams in a layer of the printed scaffold, and the arrangement of successive layers at an angle of 90°, may contribute to faster degradation. In paper [30], a PLA scaffold was studied and compared to a PLA composite with 316L powder. Degradation was tested after 1 week and 1 month. Already after a week, the first defects between the printed layers were noticed, which increased with the extension of the incubation time. In the work of Zhu et al. [31], in which pure PLA was compared with PLA with PEG addition, the biodegradation process in PBS solution after 4, 8 and 24 hours was studied. It was noted that the biodegradation of PLA is a slow process, as no changes were observed after 24 hours. This work also noted a longer biodegradation time as mentioned in Section 3.2. the first changes in the samples were noticed after 15 weeks.

## 5. CONCLUSION

A study of the mechanical properties of PLA scaffolds for bone regeneration revealed that maximum strain values in the scaffolds with respect to compressive loading of 800 N increases over the incubation period. During study A (loading speed of 500 mm/min), it was found that the deformation of scaffolds changed from 12.87% to 13.67% after 6 months of incubation. In study B (loading speed of 10 mm/min), the deformation of scaffolds changed from 12.35% to 12.54%. Such differences are indeed small. The stress-strain curves look similar and do not differ much over all incubation times, though a slight shift along the x-axis of the curve in study A was observed. This suggests that PLA scaffolds did not change their mechanical properties during incubation much. Such results and the coefficients obtained from the curve fitted Mooney-Rivlin model allow to state that the change in the mechanical properties of the material is insignificant and would not affect the effective bone formation.

The degradation study confirms that PLA degrades and loses an average of 10% of its weight during 20 weeks of incubation and that the hydrolysis does not release any toxic compounds. As the pH did not change much and remained neutral (in the range of 7.0 to 7.4), no precipitants or changes of solution color were observed throughout the study.

To summarize, it can be concluded that the mechanical properties of PLA scaffolds do not change much during incubation in physiological medium and such scaffolds could support an effective formation of bone tissue, which lasts for about 6 months. PLA would degrade in the human body over a longer period of time than the required one for the bone formation, and would not impair cell development as it does not form any toxic compounds.

## REFERENCES

1. Amini AR, Laurencin CT, Nukavarapu SP. Bone tissue engineering: recent advances and challenges. *Crit Rev Biomed Eng.* 2012;40(5): 363-408. Available from: <https://doi.org/10.1615/critrevbiomedeng.v40.i5.10>
2. Oguri KS, Jafari T, Ivirico JLE, Laurencin CT. Polymeric biomaterials for scaffold-based bone regenerative engineering. *Regen Eng Transl Med.* 2019;5:128-154. Available from: <https://doi.org/10.1007/s40883-018-0072-0>
3. Belaid H, Nagarajan S, Teyssier C, Barou C, Barés J, Balme S, Garay H, Huon V, Cornu D, Cavallès V, Bechelany M. Development of new biocompatible 3D printed graphene oxide-based scaffolds. *Materials science & engineering. C. Materials for biological applications.* 2020;110:110595. Available from: <https://doi.org/10.1016/j.msec.2019.110595>
4. Tang D., Tare RS., Yang L.Y., Williams DF., Ou K.L. & Oreffo RO. Biofabrication of bone tissue: approaches, challenges and translation for bone regeneration. *Biomaterials.* 2016; 83: 363-382.
5. Ho-Shui-Ling A, Bolander J, Rustom LE, Johnson AW, Luyten FP, Picart C. Bone regeneration strategies: engineered scaffolds, bioactive molecules and stem cells current stage and future perspectives. *Biomaterials.* 2018;180:143-162. Available from: <https://doi.org/10.1016/j.biomaterials.2018.07.017>
6. Eltom A, Zhong G, Muhammad A. Scaffold techniques and designs in tissue engineering functions and purposes: a review. *Adv Mater Sci Eng.* 2019;4:3429527. Available from: <https://doi.org/10.1155/2019/3429527>
7. Hamad K, Kaseem M, Yang HW, Deri F, Ko YG. Properties and medical applications of polylactic acid: a review. *EXPRESS Polym Lett.* 2015;9(5):435-455. Available from: <https://doi.org/10.3144/expresspolymlett.2015.42>
8. Grémare A, Guduric V, Bareille R, et al. Characterization of printed PLA scaffolds for bone tissue engineering. *J Biomed Mater Res A.* 2018;106(4):887-894. Available from: <https://doi.org/10.1002/jbm.a.36289>
9. Vieira AC, Vieira JC, Ferra JM, Magalhães FD, Guedes RM, Marques AT. Mechanical study of PLA-PCL fibers during in vitro degradation. *J Mech Behav Biomed Mater.* 2011;4(3):451-460. Available from: <https://doi.org/10.1016/j.jmbbm.2010.12.006>
10. Al-Itry R, Lamnawar K, Maazouz A. Improvement of thermal stability, rheological and mechanical properties of PLA, PBAT and their blends by reactive extrusion with functionalized epoxy. *Polym Degrad Stabil.* 2012;97(10):1898-1914. Available from: <https://doi.org/10.1016/j.polymdegradstab.2012.06.028>
11. Lyu S, Untereker D. Degradability of polymers for implantable biomedical devices. *Int J Mol Sci.* 2009;10(9):4033-4065. Available from: <https://doi.org/10.3390/ijms10094033>
12. Shick TM, Kadir AZA, Ngadiman NHA, Ma'aram A. A review of biomaterials scaffold fabrication in additive manufacturing for tissue engineering. *J Bioact Compat Polym.* 2019; 34(6): 415-435. Available from: <https://doi.org/10.1177/0883911519877426>
13. Chocholata P, Kulda V, Babuska V. Fabrication of scaffolds for bone-tissue regeneration. *Materials (Basel).* 2019;12(4):568. Available from: <https://doi.org/10.3390/ma12040568>
14. Caballero DE, Montini-Ballarin F, Gimenez JM, & Urquiza SA. Multiscale constitutive model with progressive recruitment for nanofibrous scaffolds. *Journal of the Mechanical Behavior of Biomedical Materials.* 2019;98:225-234.
15. Farto-Vaamonde X, Auriemma G, Aquino RP, Concheiro A, & Alvarez-Lorenzo C. Post-manufacture loading of filaments and 3D printed PLA scaffolds with prednisolone and dexamethasone for tissue regeneration applications. *European journal of pharmaceuticals and biopharmaceutics: official journal of Arbeitsgemeinschaft für Pharmazeutische Verfahrenstechnik e.V.* 2019;141:100-110. Available from: <https://doi.org/10.1016/j.ejpb.2019.05.018>

16. Bracaglia LG, Smith BT, Watson E, Arumugasaamy N, Mikos AG, Fisher JP. 3D printing for the design and fabrication of polymer-based gradient scaffolds *Acta Biomater.* 2017;56:3–13.
17. Martinez-Marquez D, Mirnajafizadeh A, Carty CP, Stewart RA. Application of quality by design for 3D printed bone prostheses and scaffolds *PLoS ONE.* 2018;13. Available from: <https://doi.org/10.1371/journal.pone.0195291>
18. Petcu EB, Midha R, McColl E, Popa-Wagner A, Chirila TV & Dalton PD. 3D printing strategies for peripheral nerve re-generation. *Biofabrication.* 2018;10(3):032001. Available from: <https://doi.org/10.1088/1758-5090/aaaf50>
19. Ghosh U, Ning S, Wang Y, & Kong YL. Addressing un-met clinical needs with 3D printing technologies. *Advanced healthcare materials,* 2018;7(17):1800417.
20. Czyzewski P, Marciniak D, Nowinka B, Borowiak M, Bielinski M. Influence of Extruder's Nozzle Diameter on the Improvement of Functional Properties of 3D-Printed PLA Products. *Polymers: MDPI.* 2022;14:356. Available from: <https://doi.org/10.3390/polym14020356>
21. Dai Z, Ronholm J, Tian Y, Stehi B, Cao X. Sterilization techniques for biodegradable scaffolds in tissue engineering applications. *J Tissue Eng.* 2016;7:2041731416648810. Available from: <https://doi.org/10.1177/2041731416648810>
22. Han QF, Wang ZW, Tang CY, Chen L, Tsui CP, Law WC. Hyperelastic modeling and mechanical behavior investigation of porous poly-D-L-lactide/nano-hydroxyapatite scaffold material. *J Mech Behav Biomed Mater.* 2017;71:262-270. Available from: <https://doi.org/10.1016/j.jmbbm.2017.03.032>
23. Vieira AC, Guedes RM, Marques AT, Tita V. Material model proposal for the design of biodegradable plastic structures. In: *Proceedings of the 10th World Congress on Computational Mechanics.* Blucher: São Paulo. 2014; 2512-2529. Available from: <https://doi.org/10.5151/meceng-wccm2012-18893>
24. Casalini T, Rossi F, Castrovinci A, Perale G. A perspective on polylactic acid-based polymers use for nanoparticles synthesis and applications. *Front Bioeng Biotechnol.* 2019;7:259. Available from: <https://doi.org/10.3389/fbioe.2019.00259>
25. Tew GN, Bhatia SR. PLA-PEO-PLA hydrogels and their mechanical properties. In: Bhatia SK (ed.). *Engineering Biomaterials for Regenerative Medicine.* Springer: New York. 2012; 127-140. Available from: [https://doi.org/10.1007/978-1-4614-1080-5\\_5](https://doi.org/10.1007/978-1-4614-1080-5_5)
26. Da Silva D, Kaduri M, Poley M, et al. Biocompatibility, biodegradation and excretion of polylactic acid (PLA) in medical implants and theranostic systems. *Chem Eng J.* 2018; 340: 9-14. Available from: <https://doi.org/10.1016/j.cej.2018.01.010>
27. Guo Z, Yang C, Zhou Z, Chen S, Li F. Characterization of biodegradable poly (lactic acid) porous scaffolds prepared using selective enzymatic degradation for tissue engineering. *RSC Adv.* 2017; 7(54): 34063-34070. Available from: <https://doi.org/10.1039/C7RA03574H>
28. Rodrigues N, Benning M, Ferreira AM, Dixon L, Dalgarno K, Manu-facture and Characterisation of Porous PLA Scaffolds. *Procedia CIRP.* 2016;46:33-38. Available from: <https://doi.org/10.1016/j.procir.2015.07.025>
29. Karimipour-Fard P, Pop-Iliev R, Jones-Taggart H, Rizvi G. Design of 3D scaffold geometries for optimal biodegradation of poly(lactic acid)-based bone tissue. *AIP Conference Proceedings* 10 January 2020; 2205(1):020062. Available from: <https://doi.org/10.1063/1.5142977>
30. Jiang D, Ning F. Fused filament fabrication of biodegradable PLA/316L composite scaffolds: Effects of metal particle content. *Procedia Manufacturing.* 2020;48:755-762.
31. Zhu X, Zhong T, Huang R, Wan A. Preparation of hydrophilic poly(lactic acid) tissue engineering scaffold via (PLA)-(PLA-b-PEG)-(PEG) solution casting and thermal-induced surface structural transformation. *Journal of biomaterials science. Polymer edition,* 2015;26(17):1286-1296. Available from: <https://doi.org/10.1080/09205063.2015.1088125>
32. Zohoor S, Abolfathi N, Solati-Hashjin M. Accelerated degradation mechanism and mechanical behavior of 3D-printed PLA scaffolds for bone regeneration. *Iranian Polymer Journal,* 2023, 32:1209–1227. Available from: <https://doi.org/10.1007/s13726-023-01191-8>

Paula Kundreckaitė:  <https://orcid.org/0009-0008-6483-0325>

Andžela Šešok:  <https://orcid.org/0000-0001-8194-1539>

Rimantas Stonkus:  <https://orcid.org/0000-0002-1228-9433>

Gediminas Gaidulis:  <https://orcid.org/0000-0002-9317-8160>

Eliza Romanczuk-Ruszk:  <https://orcid.org/0000-0001-5228-4920>

Jolanta Pauk:  <https://orcid.org/0000-0001-8607-7129>



This work is licensed under the Creative Commons BY-NC-ND 4.0 license.

# THE EFFECT OF THE MOLECULAR WEIGHT OF HYALURONIC ACID ON THE RHEOLOGICAL AND TRIBOLOGICAL PROPERTIES OF THE BASE FOR ARTIFICIAL SYNOVIAL FLUID PREPARATIONS

Monika Izabela KARPOWICZ\*, Marcin KLEKOTKA\*, Jan Ryszard DĄBROWSKI\*

\*Faculty of Mechanical Engineering, Białystok University of Technology, Wiejska 45C, 15-351 Białystok, Poland

[monika.grykin@sd.pb.edu.pl](mailto:monika.grykin@sd.pb.edu.pl), [m.klekotka@pb.edu.pl](mailto:m.klekotka@pb.edu.pl), [j.dabrowski@pb.edu.pl](mailto:j.dabrowski@pb.edu.pl)

received 26 September 2023, revised 12 March 2024, accepted 20 March 2024

**Abstract:** The synovial fluid is responsible for adequately lubricating, moisturizing, and nutritional human joints. This liquid should have appropriate viscoelastic properties and ensure a low coefficient of friction in biotribological systems. Many artificial synovial fluid preparations used in viscosupplementation treatments are based on hyaluronic acid. This work aimed to evaluate the influence of molecular weight on the functional properties of solutions based on hyaluronic acid. 1% solutions based on hyaluronic acid with five different molecular weights from 50,000 Da to 2 MDa were made. Rheological (viscosity, viscoelasticity), tribological (coefficient of friction, wear assessment), and wettability tests were carried out. Significant differences were observed in the rheological tests, where the viscosity strictly depends on the molecular weight of the hyaluronic acid. It has been shown that the molecular weight of HA has little effect on the coefficient of friction. On the other hand, the differences in the tribological wear are much more significant. The molecular weight of biopolymers is one of the essential parameters in developing new artificial synovial fluids. Using a higher molecular weight of hyaluronic acid increases viscosity and wettability, resulting in less tribological wear.

**Keywords:** artificial synovial fluid, hyaluronic acid, viscosity, friction, wear

## 1. INTRODUCTION

A lubricant called synovial fluid is an essential component in the lubrication system of synovial joints. It is responsible for the proper functioning of joints and supports all movements performed by this biotribological system (1,2). Synovial fluid is a composition of blood plasma dialysate and particles secreted by cells in the synovial space. These particles include hyaluronic acid and proteoglycan 4 (lubricin and surface zone protein). (3,4). Albumin and globulin also play an important role in the composition of the synovial fluid.  $\gamma$  globulin particles combine with hyaluronic acid molecules. These ingredients are characterized by a high degree of interaction with each other. This combination exhibits strong adsorption with the substrate, creating a lubricating boundary layer. Albumin is mainly responsible for filling the lubricating layer by self-accumulation, while exhibiting low shear. Albumin has the ability to bind to the boundary layer, which is formed by globulin with HA molecules (5,6). The synovial fluid fills the entire joint cavity and mainly performs metabolic functions, i.e., it is responsible for the nutrition of the joint cartilage (3,4,7). It is a clear, viscous liquid with a slightly yellow color. Cellular and molecular components of synovial fluid describe unique properties in maintaining proper joint homeostasis (7,8). The volume of synovial fluid may depend on many aspects. This amount can be different for each person. This is mainly determined by the quality of a person's life, e.g. whether he or she practices sports or has a sedentary lifestyle. It also depends on genetic and physiological conditions. Lifestyle, diet and body posture also have a significant impact. Synovial fluid volume is reported in a wide range in the literature. Hui A.Y. (7) and Blewis M.E. (4) suggest that in the

human knee joints, synovial fluid volume oscillates between 0.5 – 2 ml. Kraus V. (9) and Brannan S. (10) present that the volume of synovial fluid is around 4 ml. However, Gait A., et.al. (11) claim that in a healthy knee joint, the synovial fluid reaches a volume of up to 9.6 ml. Synovial joints are characterized by very complicated mechanics. Their very low motion resistance ( $\mu = 0.001-0.01$ ) makes it difficult to define the type of lubrication clearly. In joints, there is mixed lubrication, which consists of hydrostatic and boundary lubrication (12). Hydrostatic lubrication takes advantage of the unevenness on the joint surfaces and the viscosity of the lubricant provided by hyaluronic acid. It consists of squeezing the intercellular fluid out of the cartilage and creating a layer that separates the surfaces exposed to high friction (1,12). Boundary lubrication occurs mainly during periods of very high load at low speeds, i.e., when the lubricant film is the same as or less than the roughness of the joint surfaces (1,13). Boundary lubrication occurs at the boundaries of the articular surfaces, protecting the rubbing surfaces before cartilage decompression takes place, where fluid desaturation occurs, cartilage can increase in volume by up to 10% (1,12).

The synovial fluid is the main factor contributing to the synovial joints' longevity. The articular surfaces are characterized by very good lubrication and high wear resistance and usually show no signs of wear for most or even the whole life. Despite these advantages, in the case of any injury, the healing of the joint is complicated and time-consuming. The joints in the human body are subject to many debilitating diseases. Any health problems related to the incorrect chemical composition of the lubricant or its incorrect secretion can lead to biological damage to the synovial joints caused by excessive friction (1,2,13–19).

Due to its high biocompatibility, hyaluronic acid is widely used



in medicine and bioengineering (20). Hyaluronic acid is a negatively charged biopolymer. It consists of alternating units of D-glucuronic acid and N-acetylglucosamine. In a healthy synovial joint, its concentration is about 1-4 mg/ml (3,12,21). Hyaluronic acid is mainly responsible for rheological and tribological properties. Molecular weight plays an important role in the organization and arrangement of hyaluronic acid molecules and ensures the ability of synovial fluid to dissipate energy (8,22–24). In addition, many nanotribological studies suggest that the chemical bonding of hyaluronic acid particles with the joint surface is necessary to reduce friction in the biotribological system. As a result, it also reduces the wear of the articular surfaces (1,3). Natural synovial fluid has a molecular weight of 6 000 – 7 000 kDa, while synovial fluid with rheumatoid disease has a lower mass of 3 000 – 5 000 kDa. When any chemical or physical disorder occurs in the synovial joints, the quality of hyaluronic acid deteriorates. This is related to reduced lubricating capacity and reduced rheological properties. (25,26). The properties of hyaluronic acid depend on the molecular weight. With a molecular weight of 0.4 - 4 kDa, hyaluronic acid has non-apoptotic properties and is an inducer of heat shock proteins. At higher molecular weights, such as 20 - 200 kDa, biological processes, such as wound healing or embryonic development and ovulation, are already involved. With a molecular weight above 500 kDa, hyaluronic acid can be used as a space filler (20,27–29). Hyaluronic acid also shows the ability to improve surface wettability, which is a crucial aspect during lubrication. Wettability is related to surface friction; higher wettability, lower wear (30).

In the event of a disease or injury to the synovial joint, there is immediate inflammation and a very large reduction in the viscosity of the synovial fluid. As a result, the lubrication system deteriorates, which can lead to the destruction of the articular surfaces (8). Viscosupplementation is the most commonly used method for treating joint pain caused by the disease. It is a procedure in which preparation is injected into the joint cavity to replace the natural synovial fluid (8,31–37). The literature confirms the appropriateness of administering hyaluronic acid during viscosupplementation. It is effective, especially during degenerative synovitis. Hyaluronic acid improves the fluidity of the synovial fluid, inhibits the degradation of HA in the remains of the natural synovial fluid, increases the viscosity of the synovial fluid, and additionally helps to fight inflammation and relieve pain in the joint (7,8,12,13,21,38).

Although there has been a lot of research into the development of artificial synovial fluid, there are still many aspects that would be good to expand upon. Many of the substitutes used in viscosupplementation today provide relief to patients, but the results are very short-lived or inadequate. For this reason, research has been conducted on the potential basis of artificial synovial fluid. This manuscript focuses on the molecular weight of hyaluronic acid and its influence on the rheological and tribological properties of tested solutions.

Hyaluronic acid with a mass of 750kDa - 1MDa is within the molecular weight range of one of the currently used commercial preparations, which is Hyalgan (39). To demonstrate the differences in lubricity, the molecular weights of the hyaluronic acids were examined over a fairly wide range from 30 kDa to 2 MDa. After dissolving HA in water, the solutions were mixed on a magnetic stirrer until a homogeneous mixture was obtained. All preparations were stored in closed glass containers in a laboratory incubator at 37oC for 24 hours before the test. Each solution was tested three times for statistical purposes.

2. MATERIALS AND METHODS

To evaluate the influence of the molecular weight of hyaluronic acid on the rheological and tribological properties, the solutions shown in Tab. 1 were prepared.

Tab. 1. Chemical composition of hyaluronic acid solutions

Concentration (wt %)	Molecular Weight Hyaluronic acid	Solvent
1 %	30 000 – 50 000 Da (Chemat, CM61910C)	deionized water
	50 000 – 100 000 Da (Chemat, CM00050C)	
	200 – 400 kDa (Chemat, CM01180C)	
	750 kDa – 1 MDa (Chemat, CM77330C)	
	1 – 1,5 MDa (Chemat, CM45820C)	
	2 MDa (Chemat CM39020C)	

Rheological tests were performed on a Rheostress 6000 (Thermo Fisher Scientific, Waltham, MA, USA). Measurements of viscosity and viscoelasticity were conducted in the titanium plate-plate system at 37oC (Fig. 1).

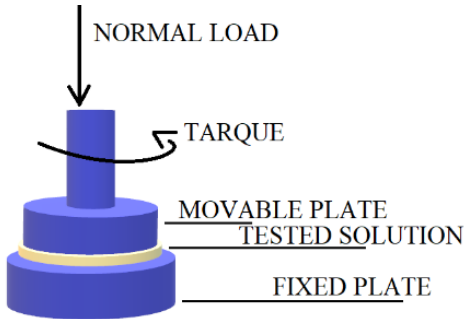


Fig. 1. Scheme of rheological measurement system

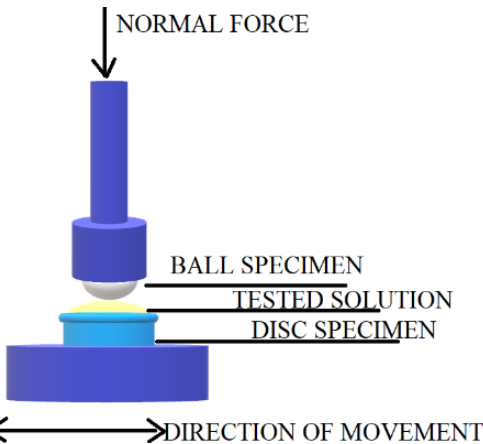


Fig. 2 Ball-on disc tribological system

A moving plate with a diameter of 35 mm was used during the viscosity and viscoelastic tests. The gap between the movable and fixed plates was 1 mm. 1 ml of the solution was used for each test. Viscosity was tested in the range of 0.01 - 100 1/s. In the viscoelastic tests, the loss and storage modulus were determined at a constant strain value of  $\gamma = 0.01$ , in the frequency range of 0.1 – 10 Hz. All measurements were repeated three times to confirm the reliability of the study, and the results were presented as the average value of all samples.

Tribological tests were performed on a UMT TriboLab (Bruker, Billerica, MA, USA) with a ball-on-disc system (Fig. 2).

A metal-ceramic rubbing pair was used in the friction node. The sample was CoCrMo discs (Tab. 2) with a height of 5 mm and a diameter of 8 mm, while the counter-sample was an aluminum oxide (99,5% Al<sub>2</sub>O<sub>3</sub>) ball with a diameter of 6 mm.

**Table 2.** Chemical composition of the CoCrMo sample

Co	Cr	Mo	Mn	Si
rest	27,72	5,78	0,65	0,37
	C	Al	Zr	Ti
	0,036	<0,02	<0,01	<0,01

Before the tribological test, the metal samples were thoroughly ground and polished to a mirror effect. Sandpaper with gradations of 2 500, 3 000, and 5 000 was used for grinding, while Al<sub>2</sub>O<sub>3</sub> suspension was used for polishing. Before the measurement, each sample was washed in an ultrasonic bath in ethanol and deionized water. In tribological tests, a special holder connected to a thermostat was used to maintain the temperature of 37oC. Measurements were made in reciprocating motion at a constant frequency of 2 Hz for 30 minutes. The normal force was 5N. All measurements were repeated three times to confirm the reliability of the study, and the results were presented as the average value of all samples.

Analysis of wear marks was performed using a LEXT OLS4000 confocal microscope (CLSM, Olympus, Tokyo, Japan). The laser in a microscope scans horizontally, but it does it layer by layer. The scanning step pitch was 0.05 μm. The size of the scanned surface, including the friction point, was 1400x480 μm. The images were taken without any filters. The measurements were carried out using special computer software cooperating with a microscope that allows it to work in 3D space and evaluate the volume of wear tracks.

Contact angles were determined using an Ossilla goniometer. A drop of 5 μl of the tested solution was applied to each CoCrMo metal sample using a micropipette (Fig. 3).

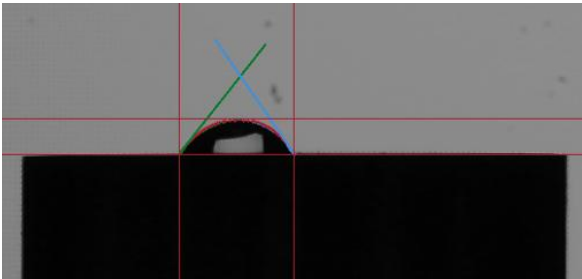


**Fig. 3.** The image of the sample droplet application and the designated angles

Then, the contact angles were determined using specialized goniometer software cooperating with a computer. The red lines at the bottom of the camera image (Fig. 3) indicate the area of the drop. These are lines corresponding to the border points of the preparation drop, which can be set with a slider. The green and blue lines indicate the tilt angle, which allows the left and right angles to be determined. The average of these angles gives the contact angle.

### 3. RESULTS AND DISCUSSION

The effect of molecular weight on the viscosity of tested solutions is shown in Fig. 4.

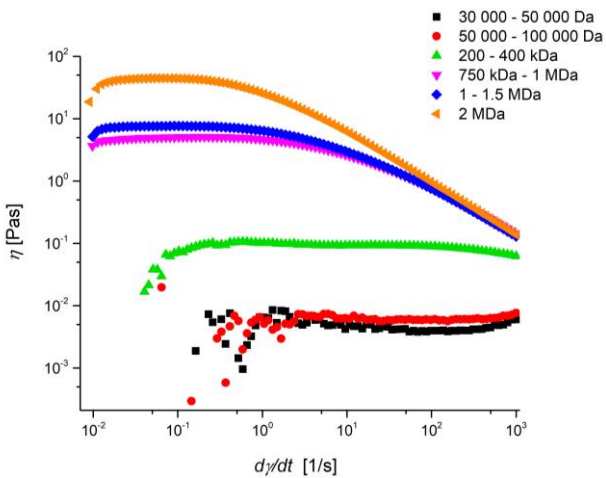


**Fig. 4.** Viscosity of hyaluronic acid based solutions

The viscosity of tested solutions increases with increasing molecular weight, which was confirmed by Snetkov et al. (20). High molecular weight hyaluronic acid exhibits interesting rheological properties by forming a tangled network of flexible polysaccharide molecules. Viscosity is a measure of the flow resistance of a given solution. This means that the molecular weight affects the flow. The lower the molecular weight, the lower the effect on flow, and therefore the lower the viscosity (40). It can be seen that preparations with a higher molecular weight in the range of 750 kDa to 2 MDa are in the viscosity range of natural synovial fluid (1 - 175 Pas) (31). According to the literature, solutions with a viscosity below 1 Pas are considered almost watery, while above this value, solutions are considered viscous (40). Three solutions with the highest molecular weights show a downward trend in viscosity with increasing shear rate. This indicates that these solutions are non-Newtonian fluids, consistent with the behavior of naturally occurring hyaluronic acid in the synovial fluid. The literature shows that the synovial fluid is non-Newtonian because the dynamic interactions between individual hyaluronic acid polymers depend mainly on the shear rate (21,40). Dynamic viscosity is constant at lower shear rates. As the shear rate is increased, it is observed that the solutions are characterized by fluid dilution adequate to the increase in shear rate. Shear-thinning effect occurs. This is characteristic of pseudoplastic fluid (21,41,42). At low shear rates, strong intermolecular interactions occur, creating strong network entanglement, which results in high flow resistance, i.e. high viscosity. However, at high shear rates, intermolecular interactions weaken, which is associated with the disentangling of molecular

networks. This causes the resistance to decrease and the particles to align in the direction of flow, assuming a much lower viscosity (43). Shear rate is a measure of flow. Fluid shear occurs whenever it is forced to move. The highest shear rate tested corresponds to the shear rate of the fluid passing through the syringe. Therefore, the viscosity drops significantly and is independent of the molecular weight. This is due to the arrangement of the particles in the flow current lines. This is a desirable effect in viscosupplementation (20,40,44,45). In contrast, the viscosity at low shear rates is considered zero shear viscosity. It is strongly related to the molecular weight value (20,40,46).

In Fig. 5 is shown the behavior of the storage modulus  $G'$  and the loss modulus  $G''$  as a function of frequency, with a constant strain of 0.01.

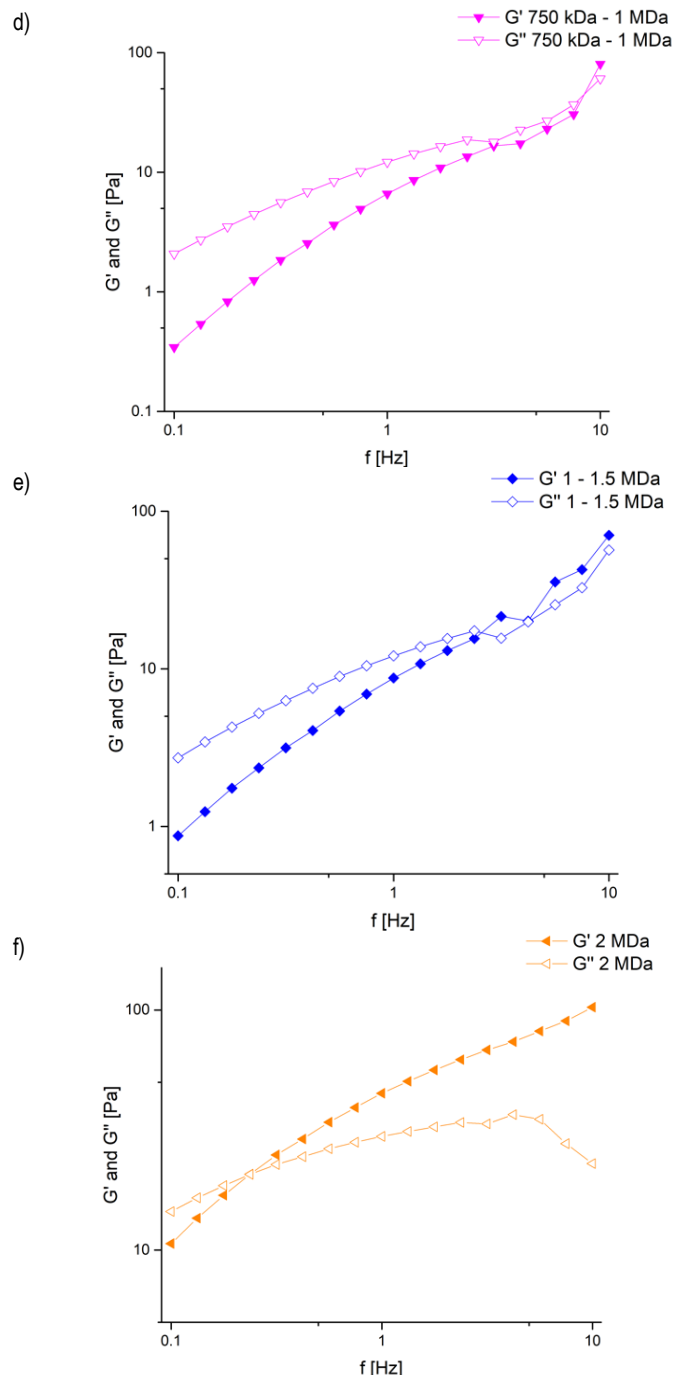
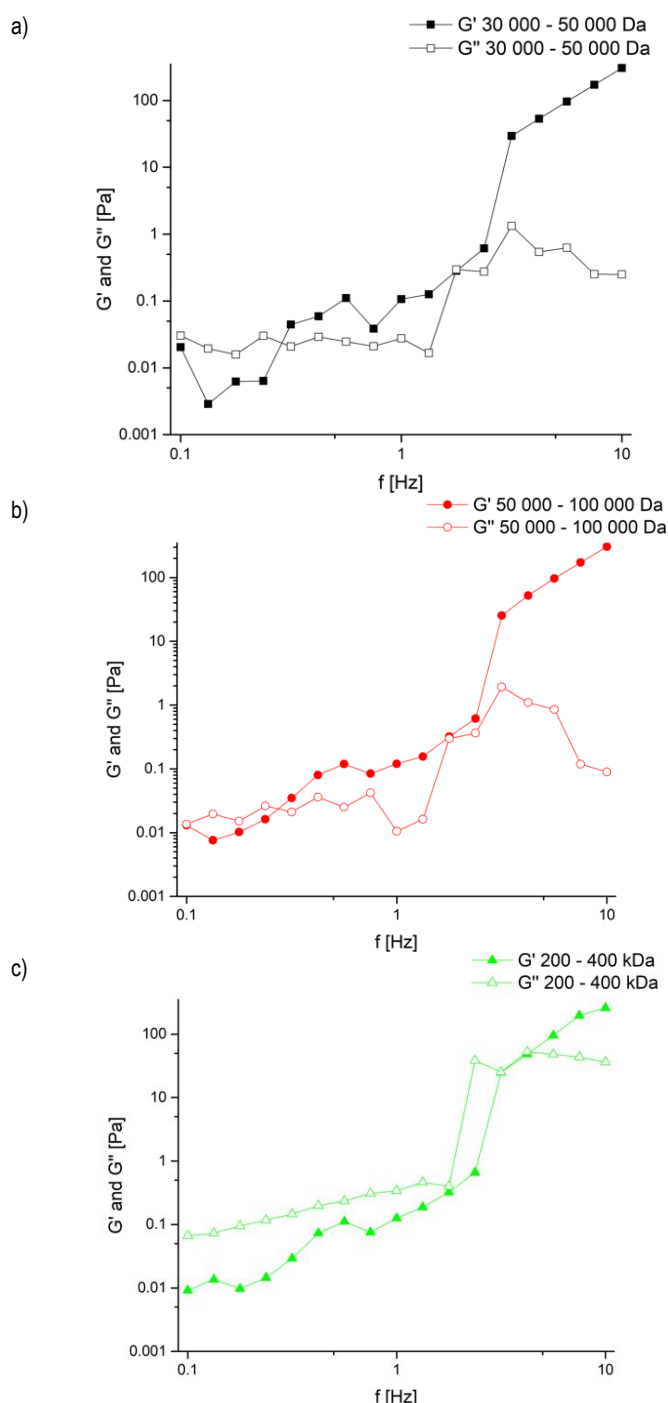


**Fig. 5.** Storage modules  $G'$  and loss modulus  $G''$  as a function of the oscillating frequency  $f$  for solutions based on hyaluronic acid of different molecular weight: a) 30 000 – 50 000 Da, b) 750 kDa – 1 MDa, c) 200 – 400 kDa, d) 750 kDa – 1 MDa, e) 1 – 1.5 MDa, f) 2 MDa

Obtained data can be divided into two groups, according to the previously described viscous and aqueous preparations dependencies. In the upper row, there are preparations based on low molecular weight hyaluronic acid, while in the lower row, there are preparations with high molecular weight hyaluronic acid. For more aqueous formulations, these characteristics are less clear, and the results are more unstable, while in the case of more viscous formulations, the characteristics match literature assumptions. The loss modulus  $G''$  (viscosity) is a measure of the energy dissipated into the material in which the deformation has been imposed. The storage modulus  $G'$  (elasticity) is a measure of the

energy that has been stored in the material in which the deformation has been imposed and is adequate to elastic deformations. The solutions retain a viscous liquid nature at low frequencies ( $G'' > G'$ ) and become more flexible at higher frequencies ( $G' > G''$ ) (7). This parameter is significant in artificial synovial fluids due to the preservation of viscous and elastic properties. Such a fluid can absorb mechanical energy and protect the cartilage from damage or increased wear (20). It should be noted that the higher the molecular weight, the higher the loss modulus  $G''$  and the storage modulus  $G'$ . It can also be seen that the higher the molecular weight, the intersection of  $G'$  and  $G''$  occurs at lower frequencies, this is visible for viscous solutions (7,8,20,47).

Tribological tests were carried out for a broader analysis of the influence of the molecular weight of hyaluronic acid on the functional properties of artificial synovial fluid solutions. The behavior of lubricating solutions during tribological tests is shown in Fig. 6.

All of the tested preparations have similar coefficients of friction, ranging from 0.18 to 0.25. In the results presented, the differences can be considered minor. Also, almost all measurements are within the margin of error. Based on the literature and the results obtained, it can be concluded that different molecular weights of hyaluronic acid do not clearly influence the resistance to movement (48,49).

Although the molecular weight has very little effect on the coefficient of friction, more significant wear trends can be observed. The average volume of the wear tracks is shown in Fig. 7.

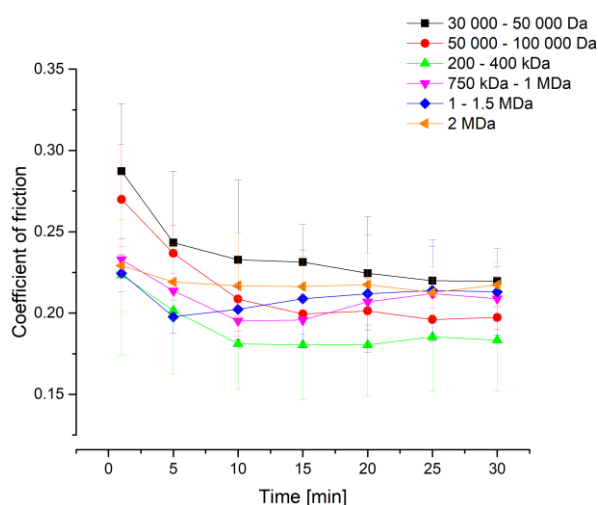


**Fig. 6.** Coefficient of friction as a function of time for solutions based on hyaluronic acid

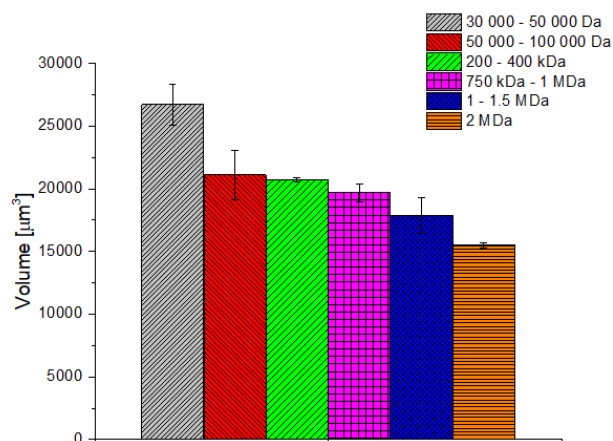


**Fig. 7.** Volume of wear tracks

Solutions based on hyaluronic acid with a molecular weight of 2 MDa showed the lowest wear ( $15\,483 \pm 209 \mu\text{m}^3$ ). However, the highest decrement of metal disc ( $26\,702 \pm 1607 \mu\text{m}^3$ ) has been achieved for the lowest molecular weight solution. The results obtained confirm that wear does not always correlate with friction coefficient. An example is a preparation based on hyaluronic acid with a high molecular weight of 2MDa, which provides the best protection against wear among the tested solutions, while exhibiting one of the highest coefficients of friction. Moreover, there are significant wear protection benefits due to the higher molecular weight. It is likely that the high molecular weight provides better wear protection due to its better ability to capture and immobilize other molecules that initiate loss in the sample material. This is also related to the viscoelasticity, which is higher depending on the higher molecular weight of hyaluronic acid. Higher viscoelastic values provide better adhesion to surfaces while increasing elasticity between surfaces. Protecting surfaces from excessive wear may be more related to the adhesive and elastic properties of the fluid than to the coefficient of friction itself. (49–52).

In this study, contact angle measurements were also performed to evaluate how changes in the molecular weight of hyaluronic acid affect wettability. The results of the contact angle measurements are shown in Fig. 8.

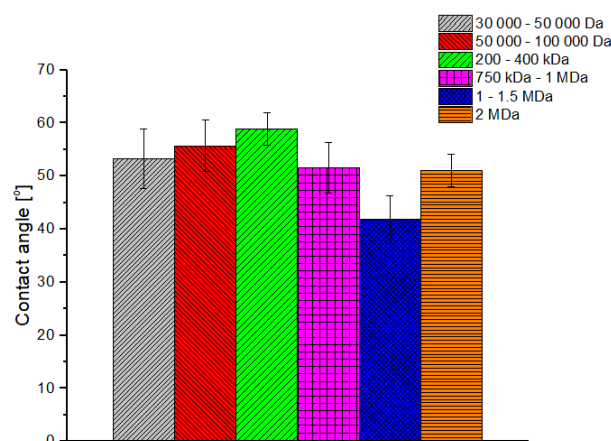


**Fig. 8.** Contact angle for solutions based on hyaluronic acid

Contact angle measurements indicate that molecular weight has no significant effect on wettability. All solutions have contact angles below 90°, which means that they all have a hydrophilic nature and good wettability. There is a slight tendency for higher molecular weight solutions, where the solution is viscous, to have slightly higher contact angles than low molecular weight hyaluronic acid based solutions. Literature reports confirm that the contact angle is not strictly related to the molecular weight of solutions (20,46,53).

Low molecular weight acid is often used for skin regeneration. This is due to its ease of penetration through the skin, one of the benefits of which is to accelerate the wound healing process. In addition, low molecular weight acid has unstable rheological properties, which was confirmed in tests (Fig. 4), and is subject to rapid degradation (54–59). High molecular weight hyaluronic acid is suitable for injection and can act as a space filler, which provides better cushioning. Such an effect is highly desirable because viscosupplementation is used for damaged joints that need support. Furthermore, the literature has confirmed better analge-



sic and anti-inflammatory effects for high-molecular-weight hyaluronic acid. It is definitely longer lasting than using low molecular weight acid (20,27,29,60–62). However, not all commercial artificial synovial fluid preparations are based on a high molecular weight acid, and this work confirms the legitimacy of its use.

#### 4. CONCLUSIONS

The correlation between wear and viscosity is responsible for the proper functional properties of lubricants. The viscosity of the solution depends on the molecular weight. It has a significant effect on whether the solution will be aqueous or viscous. The viscosity of the tested compositions increases with increasing molecular weight. The coefficient of friction is not directly correlated to the wear rating. More relevant information can be deduced from the wear volume - the higher the molecular weight, the lower wear. Good protection of the surface against wear is ensured by high viscoelasticity, which provides a protective layer and ensures better adhesion, eliminating excessive abrasion. The molecular weight of hyaluronic acid solutions does not significantly affect wettability. Higher molecular weight hyaluronic acid solutions show more favorable viscoelasticity, viscosity, and wear results. It should be noted that the results of this study may be helpful in selecting an appropriate base for artificial synovial fluid preparation and are only a starting point for further investigation.

#### REFERENCES

- Jay GD, Waller KA. The biology of Lubricin: Near frictionless joint motion. *Matrix Biol* [Internet]. 2014;39:17–24. Available from: <http://dx.doi.org/10.1016/j.matbio.2014.08.008>
- Schmidt TA, Sah RL. Effect of synovial fluid on boundary lubrication of articular cartilage. *Osteoarthr Cartil*. 2007;15(1):35–47.
- Chang DP, Abu-Lail NI, Coles JM, Guilak F, Jay GD, Zauscher S. Friction Force Microscopy of Lubricin and Hyaluronic Acid between Hydrophobic and Hydrophilic Surfaces. *Soft Matter*. 2009;5(18):3438–45.
- Blewis ME, Nugent-Derfus GE, Schmidt TA, Schumacher BL, Sah RL. A model of synovial fluid lubricant composition in normal and injured joints. *Eur Cells Mater*. 2007;13(858):26–38.
- Nečas D, Vrbka M, Marian M, Rothhammer B, Tremmel S, Wartzack S, et al. Towards the understanding of lubrication mechanisms in total knee replacements – Part I: Experimental investigations. *Tribol Int*. 2021;156(January).
- Yarimitsu S, Nakashima K, Sawae Y, Murakami T. Influences of lubricant composition on forming boundary film composed of synovia constituents. *Tribol Int* [Internet]. 2009;42(11–12):1615–23. Available from: <http://dx.doi.org/10.1016/j.triboint.2008.11.005>
- Hui AY, McCarty WJ, Masuda K, Firestein GS, Sah RL. A systems biology approach to synovial joint lubrication in health, injury, and disease. *Wiley Interdiscip Rev Syst Biol Med*. 2012;4(1):15–37.
- Prekasan D, Saju KK. Tribological effectiveness of viscosupplements for osteoarthritis in knee joint. *SN Appl Sci* [Internet]. 2019;1(9):1–6. Available from: <https://doi.org/10.1007/s42452-019-1030-2>
- Kraus VB, Stabler T V., Kong SY, Varju G, McDaniel G. Measurement of synovial fluid volume using urea. *Osteoarthr Cartil*. 2007;15(10):1217–20.
- Brannan SR, Jerrard DA. Synovial fluid analysis. *J Emerg Med*. 2006;30(3):331–9.
- Gait AD, Hodgson R, Parkes MJ, Hutchinson CE, O'Neill TW, Maricar N, et al. Synovial volume vs synovial measurements from dynamic contrast enhanced MRI as measures of response in osteoarthritis. *Osteoarthr Cartil* [Internet]. 2016;24(8):1392–8. Available from: <http://dx.doi.org/10.1016/j.joca.2016.03.015>
- Moskalewski S, Jankowska-Steifer E. Hydrostatic and Boundary Lubrication of Joints – Nature of Boundary Lubricant. *Ortop Traumatol Rehabil*. 2012;14(1):13–21.
- Waller KA, Zhang LX, Elsaid KA, Fleming BC, Warman ML, Jay GD. Role of lubricin and boundary lubrication in the prevention of chondrocyte apoptosis. *Proc Natl Acad Sci U S A*. 2013;110(15):5852–7.
- Zappone B, Ruths M, Greene GW, Jay GD, Israelachvili JN. Adsorption, lubrication, and wear of lubricin on model surfaces: Polymer brush-like behavior of a glycoprotein. *Biophys J*. 2007;92(5):1693–708.
- Morrell KC, Hodge WA, Krebs DE, Mann RW. Corroboration of in vivo cartilage pressures with implications for synovial joint tribology and osteoarthritis causation. *Proc Natl Acad Sci U S A*. 2005;102(41):14819–24.
- Skou ST, Koes BW, Grønne DT, Young J, Roos EM. Comparison of three sets of clinical classification criteria for knee osteoarthritis: a cross-sectional study of 13,459 patients treated in primary care. *Osteoarthr Cartil* [Internet]. 2020;28(2):167–72. Available from: <https://doi.org/10.1016/j.joca.2019.09.003>
- Lotz MK. New developments in osteoarthritis. Posttraumatic osteoarthritis: Pathogenesis and pharmacological treatment options. *Arthritis Res Ther*. 2010;12(3).
- Anderson DD, Chubinskaya S, Guilak F, Martin JA, Oegema TR, Olson SA, et al. Post-traumatic osteoarthritis: Improved understanding and opportunities for early intervention. *J Orthop Res*. 2011;29(6):802–9.
- Elsaid KA, Fleming BC, Oksendahl HL, Machan JT, Fadale PD, Hulstyn MJ, et al. Decreased lubricin concentrations and markers of joint inflammation in the synovial fluid of patients with anterior cruciate ligament injury. *Arthritis Rheum*. 2008;58(6):1707–15.
- Snetkov P, Zakharova K, Morozkina S, Olekhovich R, Uspenskaya M. Hyaluronic acid: The influence of molecular weight on structural, physical, physico-chemical, and degradable properties of biopolymer. *Polymers (Basel)*. 2020;12(8).
- Jay GD, Torres JR, Warman ML, Laderer MC, Breuer KS. The role of lubricin in the mechanical behavior of synovial fluid. *Proc Natl Acad Sci U S A*. 2007;104(15):6194–9.
- Freemont AJ. Role of cytological analysis of synovial fluid in diagnosis and research. *Ann Rheum Dis*. 1991;50(2):120–3.
- Prekasan D, Saju KK. Review of the Tribological Characteristics of Synovial Fluid. *Procedia Technol* [Internet]. 2016;25(Raerest):1170–4. Available from: <http://dx.doi.org/10.1016/j.protcy.2016.08.235>
- Rwei SP, Chen SW, Mao CF, Fang HW. Viscoelasticity and wearability of hyaluronate solutions. *Biochem Eng J*. 2008;40(2):211–7.
- More S, Kotiya A, Kotia A, Ghosh SK, Spyrou LA, Sarris IE. Rheological properties of synovial fluid due to viscosupplements: A review for osteoarthritis remedy. *Comput Methods Programs Biomed* [Internet]. 2020;196:105644. Available from: <https://doi.org/10.1016/j.cmpb.2020.105644>
- Rothhammer B, Marian M, Rummel F, Schroeder S, Uhler M, Kretzer JP, et al. Rheological behavior of an artificial synovial fluid – influence of temperature, shear rate and pressure. *J Mech Behav Biomed Mater* [Internet]. 2021;115(March 2020):104278. Available from: <https://doi.org/10.1016/j.jmbbm.2020.104278>
- Boeriu CG, Springer J, Kooy FK, van den Broek LAM, Eggink G. Production Methods for Hyaluronan. *Int J Carbohydr Chem*. 2013;2013:1–14.
- Fraser JRE, Laurent TC, Laurent UBG. Hyaluronan: Its nature, distribution, functions and turnover. *J Intern Med*. 1997;242(1):27–33.
- Gupta RC, Lall R, Srivastava A, Sinha A. Hyaluronic acid: Molecular mechanisms and therapeutic trajectory. *Front Vet Sci*. 2019;6(JUN):1–24.
- Yamasaki K, Drolle E, Nakagawa H, Hisamura R, Ngo W, Jones L. Impact of a low molecular weight hyaluronic acid derivative on contact lens wettability. *Contact Lens Anterior Eye* [Internet]. 2021;44(3):101334. Available from: <https://doi.org/10.1016/j.clae.2020.05.003>

31. Mathieu P, Conrozier T, Vignon E, Rozand Y, Rinaudo M. Rheologic behavior of osteoarthritic synovial fluid after addition of hyaluronic acid: A pilot study. *Clin Orthop Relat Res*. 2009;467(11):3002–9.
32. Vincent HK, Percival SS, Conrad BP, Seay AN, Montero C, Vincent KR. Hyaluronic Acid (HA) Viscosupplementation on Synovial Fluid Inflammation in Knee Osteoarthritis: A Pilot Study. *Open Orthop J*. 2013;7(1):378–84.
33. Quilliot J, Couderc M, Giraud C, Soubrier M, Mathieu S. VISCO-SUPPLEMENTATION. *Semin Arthritis Rheum* [Internet]. 2019;49(1):e10–1. Available from: <https://doi.org/10.1016/j.semarthrit.2019.02.001>
34. van der Weegen W, Wullems JA, Bos E, Noten H, van Drumpt RAM. No Difference Between Intra-Articular Injection of Hyaluronic Acid and Placebo for Mild to Moderate Knee Osteoarthritis: A Randomized, Controlled, Double-Blind Trial. *J Arthroplasty* [Internet]. 2015; 30(5):754–7. Available from: <http://dx.doi.org/10.1016/j.arth.2014.12.012>
35. Bell CJ, Ingham E, Fisher J. Influence of hyaluronic acid on the time-dependent friction response of articular cartilage under different conditions. *Proc Inst Mech Eng Part H J Eng Med*. 2006;220(1):23–31.
36. Zhang J-H. Encyclopedia of Tribology. *Encyclopedia of Tribology*. 2013. 110–113 p.
37. Goldberg VM, Buckwalter JA. Hyaluronans in the treatment of osteoarthritis of the knee: Evidence for disease-modifying activity. *Osteoarthr Cartil*. 2005;13(3):216–24.
38. Ogston AG, Stanier JE. The physiological function of hyaluronic acid in synovial fluid; viscous, elastic and lubricant properties. *J Physiol*. 1953;119(2–3):244–52.
39. Nicholls M, Manjoo A, Shaw P, Niazi F, Rosen J. A Comparison Between Rheological Properties of Intra-articular Hyaluronic Acid Preparations and Reported Human Synovial Fluid. *Adv Ther* [Internet]. 2018;35(4):523–30. Available from: <https://doi.org/10.1007/s12325-018-0688-y>
40. Bothner H, Wik O. Rheology of hyaluronate. *Acta Otolaryngol*. 1987;104(S442):25–30.
41. Smith AM, Fleming L, Wudebwe U, Bowen J, Grover LM. Development of a synovial fluid analogue with bio-relevant rheology for wear testing of orthopaedic implants. *J Mech Behav Biomed Mater* [Internet]. 2014;32:177–84. Available from: <http://dx.doi.org/10.1016/j.jmbbm.2013.12.009>
42. Fallacara A, Baldini E, Manfredini S, Vertuani S. Hyaluronic acid in the third millennium. *Polymers* (Basel). 2018;10(7).
43. Simou K, Jones SW, Davis ET, Preece J, Zhang ZJ. Rheological and interface adhesive properties of osteoarthritic synovial fluids. *Biotribology* [Internet]. 2022;32:100227. Available from: <https://doi.org/10.1016/j.biotri.2022.100227>
44. Necas J, Bartosikova L, Brauner P, Kolar J. Hyaluronic acid (hyaluronan): A review. *Vet Med (Praha)* [Internet]. 2008;53(8):397–411. Available from: <https://doi.org/10.17221/1930-VETMED>
45. Fakhari A, Berkland C. Applications and emerging trends of hyaluronic acid in tissue engineering, as a dermal filler and in osteoarthritis treatment. *Acta Biomater* [Internet]. 2013;9(7):7081–92. Available from: <http://dx.doi.org/10.1016/j.actbio.2013.03.005>
46. Falcone SJ, Palmeri DM, Berg RA. Rheological and cohesive properties of hyaluronic acid. *J Biomed Mater Res - Part A*. 2006; 76(4):721–8.
47. Bhuanantanondh P, Grecov D, Kwok E. Rheological study of viscosupplements and synovial fluid in patients with osteoarthritis. *J Med Biol Eng*. 2012;32(1):12–6.
48. Rebenda D, Vrbka M, Čípek P, Toropitsyn E, Nečas D, Pravda M, et al. On the dependence of rheology of hyaluronic acid solutions and frictional behavior of articular cartilage. *Materials* (Basel). 2020;13(11).
49. Lee DW, Banquy X, Das S, Cadivov N, Jay G, Israelachvili J. Effects of molecular weight of grafted hyaluronic acid on wear initiation. *Acta Biomater* [Internet]. 2014;10(5):1817–23. Available from: <http://dx.doi.org/10.1016/j.actbio.2014.01.013>
50. Das S, Banquy X, Zappone B, Greene GW, Jay GD, Israelachvili JN. Synergistic interactions between grafted hyaluronic acid and lubricin provide enhanced wear protection and lubrication. *Biomacromolecules*. 2013;14(5):1669–77.
51. Yu J, Banquy X, Greene GW, Lowrey DD, Israelachvili JN. The boundary lubrication of chemically grafted and cross-linked hyaluronic acid in phosphate buffered saline and lipid solutions measured by the surface forces apparatus. *Langmuir*. 2012;28(4):2244–50.
52. Raviv U, Giasson S, Kampf N, Gohy JF, Jérôme R, Klein J. Lubrication by charged polymers. *Nature*. 2003;425(6954):163–5.
53. Yin C, Qi X, Wu J, Guo C, Wu X. Therapeutic contact lenses fabricated by hyaluronic acid and silver incorporated bovine serum albumin porous films for the treatment of alkali-burned corneal wound. *Int J Biol Macromol* [Internet]. 2021;184(June):713–20. Available from: <https://doi.org/10.1016/j.ijbiomac.2021.06.155>
54. Rayahin JE, Buhman JS, Zhang Y, Koh TJ, Gemeinhart RA. High and Low Molecular Weight Hyaluronic Acid Differentially Influence Macrophage Activation. *ACS Biomater Sci Eng*. 2015;1(7):481–93.
55. Drozdova M, Vodyakova M, Tolstova T, Chernogortseva M, Sazhnev N, Demina T, et al. Composite Hydrogels Based on Cross-Linked Chitosan and Low Molecular Weight Hyaluronic Acid for Tissue Engineering. *Polymers* (Basel). 2023;15(10).
56. Yasin A, Ren Y, Li J, Sheng Y, Cao C, Zhang K. Advances in Hyaluronic Acid for Biomedical Applications. *Front Bioeng Biotechnol*. 2022;10(July):1–12.
57. Cui L, Li J, Guan S, Zhang K, Zhang K, Li J. Injectable multifunctional CMC/HA-DA hydrogel for repairing skin injury. *Mater Today Bio* [Internet]. 2022;14(April):100257. Available from: <https://doi.org/10.1016/j.mtbio.2022.100257>
58. Park HY, Kweon DK, Kim JK. Molecular weight-dependent hyaluronic acid permeability and tight junction modulation in human buccal TR146 cell monolayers. *Int J Biol Macromol* [Internet]. 2023;227:182–92. Available from: <https://doi.org/10.1016/j.ijbiomac.2022.12.106>
59. Vu TT, Gulfam M, Jo SH, Rizwan A, Joo S Bin, Lee B, et al. The effect of molecular weight and chemical structure of cross-linkers on the properties of redox-responsive hyaluronic acid hydrogels. *Int J Biol Macromol* [Internet]. 2023;238(March):124285. Available from: <https://doi.org/10.1016/j.ijbiomac.2023.124285>
60. Chavda S, Rabbani SA, Wadhwa T. Role and Effectiveness of Intra-articular Injection of Hyaluronic Acid in the Treatment of Knee Osteoarthritis: A Systematic Review. *Cureus*. 2022;14(4).
61. Sunte J, Waghmare V. An Electrohydrodynamic Lubrication of Synovial Lubricant on Human Body. 2022;25–35.
62. Farah H, Wijesinghe SN, Nicholson T, Alnajjar F, Certo M, Alghamdi A et al. Differential Metabotypes in Synovial Fibroblasts and Synovial Fluid in Hip Osteoarthritis Patients Support Inflammatory Responses. *Int J Mol Sci*. 2022;23(6):1–13.

This scientific work was realized within the context of works No. WZ/WM-IIB/2/2020 and WI/WM-IIB/3/2023 and financed by research funds of the Ministry of Education and Science, Poland.

Monika Izabela Karpowicz: <https://orcid.org/0000-0002-2808-1274>

Marcin Klekotka: <https://orcid.org/0000-0002-9751-2939>

Jan Ryszard Dąbrowski: <https://orcid.org/0000-0002-0175-0669>



This work is licensed under the Creative Commons BY-NC-ND 4.0 license.

## AUTOMATIC METHOD OF MACULAR DISEASES DETECTION USING DEEP CNN-GRU NETWORK IN OCT IMAGES

Paweł POWROZNIK<sup>\*</sup>, Maria SKUBLEWSKA-PASZKOWSKA<sup>\*</sup>, Robert REJDAK<sup>\*\*</sup>, Katarzyna NOWOMIEJSKA<sup>\*\*</sup>

<sup>\*</sup>Faculty of Electrical Engineering and Computer Science, Department of Computer Science, Lublin University of Technology,  
Nadbystrzycka 38D, 20-618 Lublin, Poland

<sup>\*\*</sup>Faculty of Medicine, Chair and Department of General and Pediatric Ophthalmology, Medical University of Lublin,  
Chmielna 1, 20-079, Lublin, Poland

[p.powroznik@pollub.pl](mailto:p.powroznik@pollub.pl), [maria.paszowska@pollub.pl](mailto:maria.paszowska@pollub.pl), [robertrejdak@yahoo.com](mailto:robertrejdak@yahoo.com), [katarzyna.nowomiejska@umlub.pl](mailto:katarzyna.nowomiejska@umlub.pl)

*received 24 July 2023, revised 2 April 2024, accepted 7 April 2024*

**Abstract:** The increasing development of Deep Learning mechanism allowed ones to create semi-fully or fully automated diagnosis software solutions for medical imaging diagnosis. The convolutional neural networks are widely applied for central retinal diseases classification based on OCT images. The main aim of this study is to propose a new network, Deep CNN-GRU for classification of early-stage and end-stages macular diseases as age-related macular degeneration and diabetic macular edema (DME). Three types of disorders have been taken into consideration: drusen, choroidal neovascularization (CNV), DME, alongside with normal cases. The created automatic tool was verified on the well-known Labelled Optical Coherence Tomography (OCT) dataset. For the classifier evaluation the following measures were calculated: accuracy, precision, recall, and F1 score. Based on these values, it can be stated that the use of a GRU layer directly connected to a convolutional network plays a pivotal role in improving previously achieved results. Additionally, the proposed tool was compared with the state-of-the-art of deep learning studies performed on the Labelled OCT dataset. The Deep CNN-GRU network achieved high performance, reaching up to 98.90% accuracy. The obtained results of classification performance place the tool as one of the top solutions for diagnosing retinal diseases, both early and late stage.

**Key words:** Drusen, Deep CNN-GRU, AMD classification, OCT, deep learning

### 1. INTRODUCTION

Age-related macular degeneration (AMD) is a major cause of visual impairment in elderly population of well-developed countries [26]. AMD involves dysfunction of choriocapillaris and retinal pigment epithelium (RPE) [13]. Drusen are hallmarks of early and intermediate AMD thus they are key to the diagnosis of AMD [7]. Advanced (late) stages of AMD may lead to severe vision loss due to choroidal neovascularization (CNV) – abnormal growth of vessels from the choroidal vasculature to the neurosensory retina through the Bruch's membrane. The abundance of drusen is the largest and best documented intraocular risk factor for AMD progression [29]. Drusen are extracellular deposits between the RPE basal lamina and the inner collagenous layer of Bruch's membrane are dome-shaped, lipid-rich, and often continuous with a thin layer of the same material (basal linear deposit) [6, 37]. Diabetic macular edema (DME) is defined as retinal thickening caused by the accumulation of intraretinal fluid, primarily in the inner and outer plexiform layers of the retina and may be present at any stage of diabetic retinopathy. DME remains the most common cause of vision loss among diabetic patients [39].

In clinical practice, the detection of macular disease, both AMD and DME, is typically performed by optical coherence tomography (OCT), providing cross-sectional images of the retina. OCT is a non-invasive, imaging technology used to visualize the cross-sectional retinal structure [45].

Recent advances in multimodal imaging, as OCT, have al-

lowed one to improve our ability to characterize the AMD phenotype. To help improve our understanding of drusen and their associations, large datasets are essential. Spectral-domain optical coherence tomography (SD-OCT) has been shown to have a much higher sensitivity and specificity detecting subretinal drusenoid deposits (reticular pseudodrusen) compared with the blue channel of color fundus photographs (CFPs), infrared reflectance, fundus autofluorescence, near-infrared fundus autofluorescence, confocal blue reflectance, and indocyanine green angiography [48]. Developing new methods for detection of drusen may inspire new approaches for the clinical practice.

The increasing development of Deep Learning (DL) mechanism allowed ones to create semi-fully or fully automated diagnosis software solutions for medical imaging diagnosis. Machine learning (ML) algorithms have been shown to be powerful tools in the automatic quantification of retinal biomarkers identified in OCT [24] making them ideal for the detection of drusen. Automated algorithms for drusen volume quantification are available including a software for the high definition - OCT Cirrus.

The motivation for this study lies in its potential to revolutionize ophthalmic care. Early and accurate diagnosis is the cornerstone of effective treatment, yet rare eye diseases often present diagnostic challenges due to their low prevalence and the complexity of their symptoms. This can lead to misdiagnosis, delayed treatment or irreversible damage to vision. By developing robust algorithms capable of discerning subtle patterns and anomalies in diagnostic images, clinicians may be equipped with powerful tools

to recognize these conditions early and accurately.

Moreover, the integration of artificial intelligence in ophthalmology can assure access to expert-level screening, particularly in under-resourced regions where specialist knowledge is scarce. With the ability to process vast datasets and learn from each new case, these systems can continuously improve, becoming more precise and reliable over time.

Undertaking this study also offers a unique opportunity to contribute to the broader field of medical AI. Rare diseases, with their unique manifestations, provide a rich and challenging dataset for developing advanced machine learning techniques. Success in this area not only benefits patients with rare eye conditions but also enhances the AI methodologies that can be applied to a myriad of other medical applications.

The main aim of this study is to propose a new network, Deep CNN-GRU for classification of early-stage and end-stages AMD diseases. Three types of disorders have been taken into consideration: drusen, CNV, DME, alongside with normal cases. The created automatic tool was verified on the well-known Labelled Optical Coherence Tomography dataset.

The rest of the paper is organised as follows: Section 2 describes the related works about deep learning approaches for retinal disorders classifications, Section 3 presents the method of conducting experiments, Section 4 shows the obtained results for classification, and finally Section 5 concludes the study and gives future research directions.

## 2. RELATED WORKS

In recent years, an increasing trend of investigating new automatic methods involving artificial intelligence (AI) may be observed [11]. This kind of automatic software may fasten the diagnosis as well as indicate the type of the classified disease. Moreover, the progression may be indicated [2]. These methods extensively applied for OCT analysis may be classified into: single-tasks involving classification or segmentation [2, 44] and multiple-tasks that combine above-mentioned issues [11].

Drusen is stated to be a very important factor of early AMD pathology. That is why various segmentation as well as classification methods applying AI have been developed. In [2] the segmentation method was applied for indicating the outer boundary of the retinal pigment epithelium (OBRPE) and the Bruch's membrane (BM) based on OCT images (166 and 200 volumes). A multitask segmentation network was proposed to capture the area between OBRPE and BM which benefited indicating the characterisation of the drusen as well as non-pathological regions where OBRPE and BM were overlapped. In [4] another segmentation method for OCT images was proposed using a new approach, called Multi-scale Transformer Global Attention Network (MsTGANet). This method utilized encoder-decoder architecture together with multi-semantic global channel and spatial joint attention module (MsGCS) to learn the model multi-semantic global contextual information as well as multi-scale transformer non-local module (MsTNL) for capturing multi-scale non-local features. The studies were performed on 8616 retinal OCT B-scans, collected from the UCSD dataset. In [2] for the drusen segmentation a U-Net architecture with Pyramid Layer was proposed, which was applied on the feature maps before passing it between encoder and decoder part of U-Net. All tests were conducted on OCT data gathered from 38 participants. For training and testing purposes

B-scan images were applied. A Generalized Dice Coefficient as loss function were used.

There are many studies concerning classification of the retinal diseases with new or modified models of CNN. In [44] Opti-Net deep learning method was applied for indicating the AMD areas in spectral-domain SD-OCT images with great success. Two datasets were used consisting 267 AMD, 115 controls and 337 AMD and 46 control cases, respectively. In [25] the new deep neural approach, called Perturbed Composite Attention Model (PCAM), was proposed for classification of macular diseases such as AMD, DME, and CNV based on OCT images. Two attention mechanism were specified. The multilevel perturbed spatial attention (MPSA) and multidimension attention (MDA) were applied for indicating the relevant contextual information in the spatial and channel domains, respectively.

In [36] a multi-scale convolutional tool using VGG16 and feature pyramid network was developed for AMD related pathologies with great success. The study was performed on two datasets: the Noor Eye Hospital (NEH) and the University of Californian San Diego (UCSD) containing OCT B-scans. In order to enlarge the datasets the augmentation methods, including rotation, shearing, brightness change, zoom change, and horizontal flipping were applied. For the NEH dataset the drusen, CNV and normal cases were classified, while for the UCSD drusen, AMD, DME and normal ones.

In [42] healthy cases, CNV and ones with drusen were classified utilizing VGG19 deep network based on 1396 OCT images. The network was pre-trained on non-medical ImageNet dataset to medical domain using an adapted densely connected classifier. The data were collected at the Ophthalmology Department of Intercommunal Hospital Center of Créteil, France.

In [46] both early-stage (drusen) and end-stages (neovascular and geographic atrophy – GA) of AMD forms were classified alongside with normal cases. The pre-trained VGG19 model on ImageNet was proposed. In the model three dense layers were added. The experiments were performed based on OCT images collected from Northwestern Memorial Hospital.

In [30] six retinal diseases: AMD, Central Serous Retinopathy (CSR), Diabetic Retinopathy (DR), CNV, DME, and drusen as well as the normal cases were detected using the proposed an enhanced deep ensemble convolutional neural network based on OCT images. The network was created using EfficientNetV2-B0 and Xception models as well as a capsule network. The verification of the proposed solution was performed on two datasets, containing 108,312 and 572 OCT images, respectively.

In [16] a tool, Label Smoothing Generative Adversarial Network (LSGAN), was proposed for classification drusen, CNV, DME alongside with normal cases. This solution consisted of three parts. Firstly, the generator, created synthetic images imitating OCT. Secondly, the discriminator, was used to differentiate the real OCT image with the generated one. Finally, the classifier, gave the recommendation about the retinal diseases. The classification part involved various types of models, like InceptionV3, ResNet50 and DenseNet121. The evaluation of the tool was performed on two datasets: UCSD and HUCM, consisting of 84,484 and 8,904 OVT B-scan images, respectively.

The objective [33] was to employ OCT images and deep learning techniques for the classification of dry and wet AMD. This goal was achieved by utilizing two deep convolutional neural network architectures, namely AlexNet and ResNet, pretrained by ImageNet dataset. A transfer learning for fine-tune the VGG-16 network was presented in [23] for AMD classification. In the first



step for learning purposes, the ImageNet dataset was used. Subsequently, model tuning was performed using the OCT dataset.

A great number of studies were performed based on the Labelled Optical Coherence Tomography dataset containing 84,495 OCT images [18]. In [31] classification of the retinal diseases, like: CNV, DME and drusen, alongside with normal cases was presented. The CNN with 12 layers, ReLU activation function was proposed.

In [28] a hybrid system for classification retinal diseases provided high accuracy as well as needed small amount of computing load was proposed. The image features were extracted using image preprocessing as well as pre-trained VGG16 and DenseNet121. The Firefly algorithm was applied for selecting the best features. For the classification purposes SVM, Logistic Regression (LR) and Random Forest (RF) were utilized. The experiments were performed on two datasets: Labelled Optical Coherence Tomography and Srinivasan [38], containing 723 images. Various classifications were performed: between normal cases and ones with AMD, between AMD and DME, and between CNV and drusen. The pre-trained VGG16 network was also applied in [23] for the same type of classification.

Detection of CNV, DME, drusen, and normal conditions was performed utilizing CNN model with batch normalization for creating a web application [14]. The CNN model was pre-trained based on ImageNet dataset. It consisted of the following networks: ResNet, Inception, and ResNeXt.

In [5] two CNN networks were proposed for classification of retinal diseases, such as DME, AMD, drusen, and CNV as well as normal cases. The study involved pre-trained networks: Inception V3, VGG16 and modified VGG16 by adding two convolutional layers.

In [47] the same retinal diseases with normal cases were classified utilizing a Multi-branch hybrid attention network (MHA-Net). This deep learning approach involved parallel channel attention and spatial attention mechanisms for identifying the relevant characteristic features. The results showed that the proposed attention mechanism improved the performance of classification of the retinal diseases.

In [41] a hybrid artificial intelligence system, OCTNet, was proposed for AMD classification focusing on CNV, DME, and Drusen, and normal cases. The following networks were used to build the system: Support Vector Machine with Linear kernel (LSVM), Support Vector Machine with Radial Basis Function kernel (RBF SVM), Artificial Neural Network (ANN), k-Nearest Neighbor (kNN), Random Forest (RF), Linear Discriminant Analysis (LDA), Quadratic Discriminant Analysis (QDA), and Naïve Bayes (NB).

In [12] a new approach of deep learning, called Iterative fusion CNN (IFCNN), was proposed that combine features from current and previous convolutional layers to gain high accuracy.

Deep Multi-scale Fusion Convolutional Neural Network (DMF-CNN) was proposed for encoding the retina disease characteristics that were then combined for reliable and high classification [10].

Two deep learning approaches were presented for CNV, DME, drusen and normal cases classification [19]. The first one was developed based on CNN and the second combined the following models: VGG16, VGG19, ResNet50, ResNet151, DenseNet121, as well as Inception V3.

A deep residual network, ResNet50, was applied for DME, CNV, drusen and normal cases classification [3]. A fully connected block was added to the network that both improved the accu-

racy and eliminated the overfitting issues.

In [43] the classification of CNV, DME, drusen and healthy OCT images was presented utilizing various architectures of CNN approach. The solution with the highest accuracy, the seven-layer CNN, was recommended for retinal disease classification.

There are several studies about classification using multi-tasks for retinal diseases purposes. In [11] a new approach was proposed for drusen, CNV and normal retina classification. This dual guidance network involved classification using convolutional neural network (CM-CNN) and segmentation done based on U-Net network (CAM-UNet). The OCT images were analysed. The experiments were performed using two datasets: the UCSD and the other created for the purpose of the studies. The latter one consisted of macular edema and healthy cases.

In [27] non-AMD, early AMD, and intermediate AMD classes were classified utilizing Residual-Attention-UNET model with attention mechanism for segmentation drusen and end-to-end CNNs for final classification. The 2D network was created with three AI solutions: VGG16, EfficientNetB3, and DenseNets. Dataset consisting 366 eyes of 120 subjects divided into: no-AMD (40), early AMD (40) and intermediate AMD (40). OCT scans  $512 \times 128$  were used. In order to increase the images an augmentation was applied based on image dilation and erosion.

Reticular pseudodrusen (RPD) and drusen were classified utilizing a deep learning framework with 3D Inception-V [32]. It consisted of three methods: Ungradable Classification Model and Outlier Model Development for detection ungradable scans and Drusen/RPD Classification Model for drusen, RPD and healthy cases classification. The experiments were performed on the UK Biobank dataset containing 1284 participants. The OCT images were indicated as with drusen, RPD, both drusen and RPD and the control group.

The use of Fully Connected Convolutional Neural Networks for AMD segmentation and classification is discussed in detail in [40]. This solution allows to map the characteristic features into a vector, which gives the possibility of classification. The proposed tool allowed for the segmentation of the retinal region, and then the classification of age-related disorders. The used network was trained on two datasets, the THOCT dataset and the Duke dataset, containing a total of over 3000 OCT images.

The collected results of scientific research on the classification of retinal diseases using deep learning approaches clearly show that the proposed structure of the Deep CNN-GRU network in this paper has not been studied before.

### 3. MATERIAL AND METHODS

#### 3.1. OCT Retina Dataset

The Labelled Optical Coherence Tomography dataset is a widely used collection in the field of medical image analysis. It was firstly introduced in 2018 in [18]. This dataset consists of 84,495 images of a diverse collection of OCT images acquired from different clinical settings and devices. The dataset is organized into three main subsets: a training, validation and testing. Each of them consists of images grouped into four categories:

- NORMAL: This subset includes OCT images of healthy retinas. These images serve as the baseline for comparison with diseased retinas. They showcase the normal anatomical structures and characteristics of the retina, allowing research-

- ers to differentiate between healthy and pathological conditions.
- CNV (Choroidal Neovascularization): This subset contains OCT images of retinas affected by Choroidal Neovascularization. CNV is a condition characterised by the abnormal growth of new blood vessels beneath the retina. The OCT images in this subset highlight the presence of these abnormal blood vessels and associated retinal changes.
  - DME (Diabetic Macular Edema): This subset comprises OCT images of retinas affected by DME. This disease is a complication of diabetic retinopathy and involves the accumulation of fluid in the macula, the central part of the retina. The task of this area is to ensure adequate visual acuity. The OCT images in this subset reveal the presence of macular thickening, fluid accumulation, and other characteristic features of DME.
  - DRUSEN: This subset includes OCT images of retinas with Drusen deposits. Drusen are yellowish-white deposits that accumulate under the retina, commonly associated AMD. The OCT images in this subset demonstrate the presence, size, and distribution of Drusen, aiding in the diagnosis and monitoring of AMD.
- Images collected in the dataset came from adult patients from 5 research centers: the Shiley Eye Institute of the University of California San Diego, the California Retinal Research Foundation, Medical Center Ophthalmology Associates, the Shanghai First People's Hospital, and Beijing Tongren Eye Center. Details regarding demographics are presented in Tab. 1.

Tab. 1. Characteristic of patients from OCT Retina dataset [18]

Diagnosis	DME	CNV	Drusen	Normal
Mean age	57(20-90)	83(58-97)	82(40-95)	60(21-86)
Male	38.3%	54.2%	44.4%	59.2%
Female	61.7%	45.8%	55.6%	40.8%
Caucasian	42.6%	83.3%	85.2%	59.9%
Asian	23.4%	6.3%	8.6%	21.1%
Hispanic	23.4%	8.3%	4.9%	10.2%
African American	4.3%	2.1%	1.2%	1.4%
Mixed or other	10.6%	0%	0%	7.5%

- The example images of the above-mentioned dataset group are depicted in Fig. 1.
- OCT images were preprocessed to enhance quality and normalize them for analysis, it involves a series of following steps:
- Noise reduction techniques, such as filtering algorithms, were applied to remove unwanted noise and improve image clarity.
  - Contrast enhancement can help improve the visibility of important features and structures within the images. Techniques like histogram equalization or contrast stretching were used to enhance the visual quality of the images.
  - Normalization involves standardizing the intensity values of the pixels in the images to a consistent scale. This step ensures that the images are comparable and have a consistent brightness level, which is important for accurate analysis and comparison.

3.2. Deep CNN-GRU

In order to ensure high quality classification of changes in OCT images, the Deep CNN-GRU classifier has been proposed. It consisted of five consecutive blocks. Each of them contained two convolution and one max-pooling layers. The data from the last block was processed by Gated Recurrent Units (GRU) elements, then flattened, processed by a fully-connected layer and subjected to classification process using the Softmax function. The structure of proposed model was presented in Fig. 2 and Tab. 2.

3.2.1. Convolutional Network

Convolutional networks have been extensively studied and have demonstrated remarkable performance in numerous domains. The pioneering work of [22] introduced the concept of CNNs and their application to handwritten digit recognition, known as the LeNet-5 architecture [22]. Since then, numerous advancements have been made, including the popularisation of deeper architectures such as AlexNet [20], VGGNet [35], and ResNet [15].

CNNs are specifically designed for processing structured grid-like data, such as images or audio. Moreover, CNNs have been highly successful in various computer vision tasks, including image classification, object detection, and segmentation.

Structurally, CNNs are composed of several layers that are designed to effectively handle grid-based information, such as images. The main layers in a typical CNN architecture include convolutional layers, activation functions, pooling and fully connected layers.

3.2.2. Convolutional Layer

The first layer is typically a convolutional layer, which is responsible for learning and extracting local spatial patterns from the input data. Each convolutional layer consists of a set of learnable filters. Feature maps are generated by sliding filters across the input data and executing element-wise multiplications and summations. The filters capture different features, such as edges, textures, or shapes, by convolving with the input data. The quantity and dimensions of filters within each layer can be adjusted based on the task's complexity or the preferred network structure [34].

3.2.3. Kernel Layer

The kernel, a small matrix comprised of real values, plays a pivotal role in image processing. It operates on an input matrix, typically an image, in a patch-wise manner, with dimensions equal to that of the kernel. By performing a dot product between the patch and kernel values, a single entry in the feature map is generated. The patch selection process moves systematically across the input image, either horizontally or vertically, based on the chosen stride. This process continues until the entire image has been processed. During training, the kernel values are adjusted iteratively, undergoing changes after each iteration. This dynamic adaptation helps the model strive for optimal accuracy and minimize optimization loss. Ultimately, this operation allows to learn

diverse features such as edges or color-related characteristics, contributing to its ability to analyse and understand images effectively.

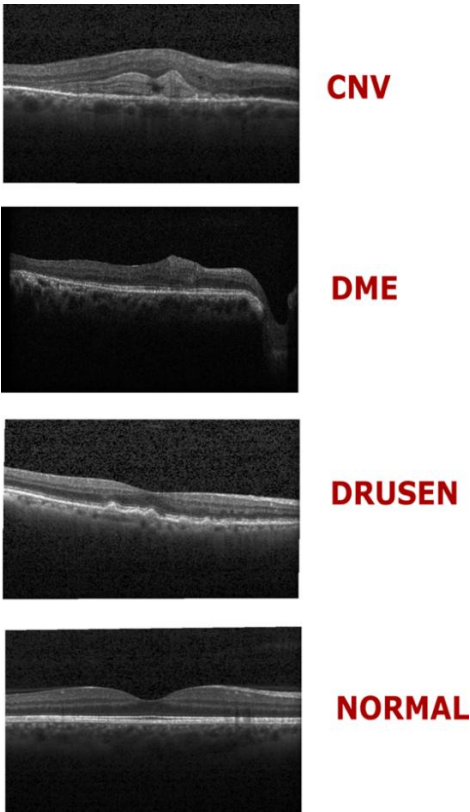


Fig. 1. Example images from OCT Retina dataset

### 3.2.4. Activation function

This dynamic adaptation following the convolution operation, usually, a non-linear transformation is performed on each element by applying an activation function. The Rectified Linear Unit (ReLU) is the prevailing choice for activation functions in CNNs. ReLU effectively replaces negative values with zeros while preserving positive values unaltered, thereby introducing non-linearities into the network. ReLU helps the network learn complex relationships between the input data and the desired output by introducing non-linear transformations. It was also applied in this study. Mathematically ReLU can be expressed as follow:

$$ReLU(x) = \max(0, x) \quad (1)$$

### 3.2.5. Pooling

Pooling operations are used to down sample the spatial dimensions of the feature maps while retaining the most important information. Commonly for pooling, within each region, are used such operators like: max pooling or average pooling, which can divide the feature maps into non-overlapping regions and select the maximum or average value, respectively. Pooling helps reduce the computational complexity and the number of parameters in the network while enhancing translation invariance and providing some degree of spatial invariance. In case of this study the max pooling actions were performed.

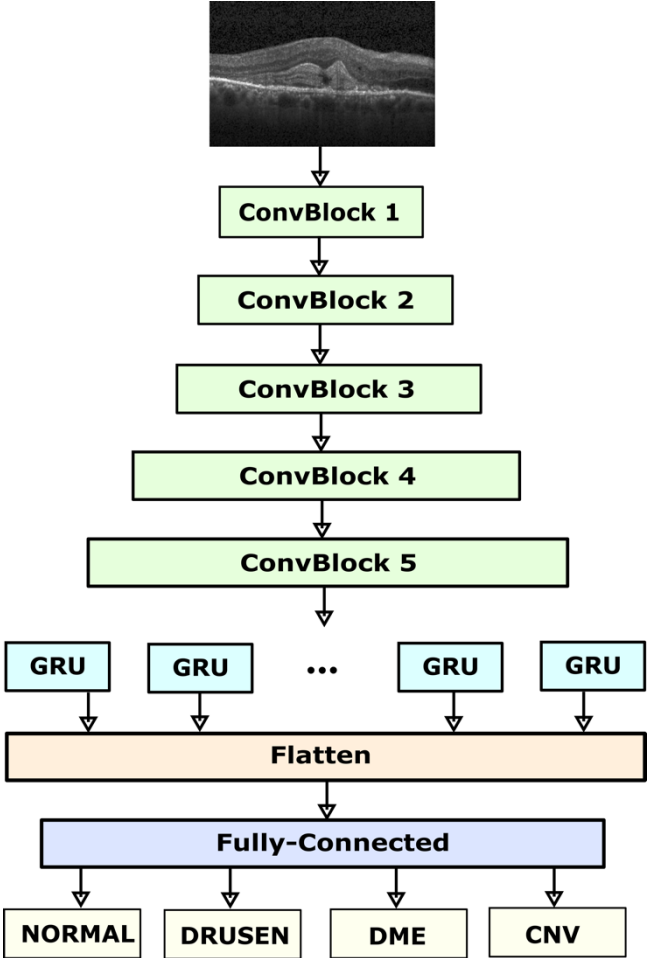


Fig. 2. Deep CNN-GRU architecture

Tab. 2. The summary of Deep CNN-GRU network

Layer	Conv Block No	Type	Kernel size	Features No	Input size
1.	1	Conv2D	3x3	64	3x224x224
2.		Conv2D	3x3	64	64x224x224
3.		Pooling	2x2	-	64x112x112
4.	2	Conv2D	3x3	128	128x112x112
5.		Conv2D	3x3	128	128x112x112
6.		Pooling	2x2	-	128x56x56
7.	3	Conv2D	3x3	256	256x56x56
8.		Conv2D	3x3	256	256x56x56
9.		Pooling	2x2	-	256x28x28
10.	4	Conv2D	3x3	512	512x28x28
11.		Conv2D	3x3	512	512x28x28
12.		Pooling	2x2	-	512x14x14
13.	5	Conv2D	3x3	512	512x14x14
14.		Conv2D	3x3	512	512x14x14
15.		Pooling	2x2	-	512x7x7
16.	-	GRU	-	-	512x49
17.	-	FC	-	64	25088
18.	-	Output	-	4	64

### 3.2.6. Fully-connected Layer

After several convolutional and pooling operations, the high-level features are usually flattened into a vector and passed through fully-connected layers (one or more). The idea of this layer is to connect each neuron with neurons in previous and subsequent layers. In this way the network is able to learn complex relationships between the extracted features and the target output. These layers are often used in the final stages of the network and can have varying sizes depending on the specific task e.g., Softmax for classification.

### 3.2.7. Regularisation

Deep neural networks that possess elevated learning parameters and are trained on lower-quality or noisy data may encounter challenges related to overfitting. This denotes a situation in which the model demonstrates superior performance on the training data, yet struggles to accurately classify new test instances from the same problem domain. To mitigate this problem, a dropout strategy is employed. During the training process, dropout randomly deactivates neurons in fully-connected layers with a probability. The application of dropout can be represented by the following equation [17]:

$$y_k = \sum_{K \in K^*} \text{Probability}(x) y_k^K \quad (2)$$

where:

$y_k$  denotes predicted unit  $k$ ,  $K^*$  is the set of all narrowed networks,  $y^K$  represents the output from unit  $K$ .

### 3.2.8. Loss function

The loss function quantifies the discrepancy between the predicted outputs of the network and the true labels associated with the input data. It measures an error or a distance between the predicted output and the ground truth, providing a single scalar value that indicates how well the network is performing. The objective of the CNN during the training process is to minimize this loss value.

The choice of a specific loss function depends on the nature of the problem being solved. Some commonly used loss functions in the fully-connected layer of a CNN include: mean squared error (MSE), categorical, binary or sparse categorical cross-entropy [17, 34].

During the training process, the loss function is used to calculate the gradient of the loss with respect to the model's parameters. This gradient is then utilized in the optimization algorithm (e.g., stochastic gradient descent) to update the weights and biases of the fully-connected layer, enabling the network to iteratively improve its predictions and minimize the loss. In this study categorical cross-entropy as the loss function was used.

### 3.2.9. Gated Recurrent Unit

The GRU model is a variant of recurrent neural network (RNN). That architecture is widely used in machine learning and natural language processing tasks. It was firstly introduced in [21] as a modification of the traditional RNN and has gained popularity

due to its effectiveness and computational efficiency.

The GRU addresses some of the limitations of the traditional RNN and the Long Short-Term Memory (LSTM) architecture. It is designed to capture and model long-term dependencies in sequential data. One of its main advantages over traditional RNNs is the mitigation of the vanishing gradient problem [9, 21].

GRU also incorporates gating mechanisms to control the flow of information within the network. However, it uses a simplified architecture with two gates: the update and the reset. Its role is to decide about the extent of information preservation from prior time steps and how much new information is to incorporate from the current time step.

The update gate in the GRU controls the information flow from the previous to current hidden state. It decides whether to update the hidden state based on two information: previous value of hidden state and current input value. By selectively updating the hidden state, the GRU can remember or forget information from previous time steps, allowing it to capture long-term dependencies [8].

The reset gate determines the amount of previous information that will be forgotten and how much will go into the current calculation. It acts as a filter, allowing the GRU to adaptively choose which past information is relevant [8].

The GRU's ability to selectively update and reset information makes it effective in wide ranges of tasks strictly connected with medical image processing.

### 3.2.10. Feature extraction

The feature extraction includes the processing of input data through successive layers of convolution, pooling, processing by the GRU, finally flattening and classification. To begin, each OCT image undergoes a series of convolutional layers, which transform it into multiple dimensions, represented by feature maps. The initial convolutional block takes input images of size  $224 \times 224$  with three red, green, and blue channels. This block generates 64 feature maps with dimensions of  $122 \times 122$ , subsequently reduced by a max-pooling layer to  $112 \times 112 \times 64$ .

Likewise, the second convolutional block receives  $122 \times 122$  input with a dimension of 64, producing feature maps with dimensions of  $11 \times 112 \times 128$ . These feature maps are further reduced through a second max-pooling layer to  $56 \times 56 \times 128$ . Following the same pattern, the feature maps pass through the 3rd, 4th, and 5th convolutional blocks. Eventually, the final feature maps are obtained with dimensions of  $7 \times 7 \times 512$ . These feature maps are subsequently fed into a GRU for the purpose of classification.

## 4. RESULTS

### 4.1. Classifier evaluation

The evaluation of the proposed model incorporated the following metrics [4]: Accuracy (eq. 3), Precision (eq. 4), Recall (eq. 5), and F1 score (eq. 6). To ensure robustness, a set of experiments were conducted, involving a random data split into training, validation, and testing sets, with proportions of 60%, 20%, and 20%, respectively. To enhance result consistency, the experiments were independently repeated for 10 iterations.



$$Accuracy = (TP + TN)/(TP + TN + FP + FN) \tag{3}$$

$$Precision = TP/(TP + FP) \tag{4}$$

$$Recall = TP/(TP + FN) \tag{5}$$

$$F1 = 2 \cdot (Precision \cdot Recall)/(Precision + Recall) \tag{6}$$

In case of DRUSEN class, TP refers to accurately predicted DRUSEN cases, FP refers to cases misclassified as DRUSEN (while they are actually NORMAL or DME or CNV by the proposed system), TN represents correctly classified NORMAL or DME or CNV cases, and FN denotes DRUSEN cases misclassified as NORMAL or DME or CNV cases. The same strategy was performed for all analyzed classes.

Tab. 3. shows the accuracy results of the proposed Deep CNN-GRU model for classifying eye diseases based on OCT images. This metric reflects the model's ability to differentiate between healthy cases and those with diseases. The results obtained affirm that utilizing deep learning for eye disease recognition is highly effective. With a mean accuracy surpassing 95%, the classification approach has demonstrated remarkable success. For more detailed insights, Tab. 4. provides accuracy results for the four specified classes: healthy eyes, DME, CNV, and DRUSEN cases found in OCT images. The model achieved a minimum accuracy greater than 92% and nearly reached 99% at its peak performance.

Tab. 3. Accuracy results for Deep CNN-GRU

Class	Mean	Max	Min	±SD
all	95.43%	98.90%	92.20%	3.86%

Tab. 4. Accuracy results for individual classes

Class	Mean	Max	Min	±SD
NORMAL	95.56%	98.90%	92.24%	2.18%
CNV	94.05%	98.85%	94.00%	2.48%
DME	95.77%	98.89%	92.20%	2.89%
DRUSEN	95.45%	98.14%	92.23%	2.73%

Tab. 5. displays the Precision results for the developed tool. The average precision for each class surpasses 96%, ranging between 92% and 98%. Such high values indicate that the network performs numerous correct classifications and only a few misclassifications (Fig. 3.).

Tab. 5. Precision results for individual classes

Class	Mean	Max	Min	±SD
NORMAL	96.28%	98.31%	93.63%	2.51%
CNV	96.29%	98.31%	93.28%	2.52%
DME	96.51%	98.37%	94.09%	2.14%
DRUSEN	96.33%	98.48%	92.46%	2.56%

The Recall metric evaluates the model's ability to accurately classify positive instances. The results, showcased in Tab. 6., demonstrate exceptional performance for the developed tool. The average Recall surpassed 97%, with individual values falling within the range of 92.06% to 99.82%.

Tab. 6. Recall results for individual classes

Class	Mean	Max	Min	±SD
NORMAL	99.31%	99.82%	97.37%	1.07%
CNV	95.79%	98.08%	92.82%	2.69%
DME	95.10%	97.75%	91.57%	3.01%
DRUSEN	95.35%	97.85%	92.06%	2.91%

The F1 score, calculated based on Precision and Recall, yielded high results with a mean value exceeding 94%. The proposed tool demonstrated its highest accuracy in recognizing NORMAL cases. It performed slightly worse for cases with DRUSEN, CNV and DME. However, the differences in mean performance were minimal, up to 0.79%. Notably, all measures (Tab. 3-7) exhibited very low standard deviation, indicating that the observations were closely clustered around the mean, making the results highly repeatable.

Tab. 7. F1 score results for individual classes

Class	Mean	Max	Min	±SD
NORMAL	99.78%	99.06%	95.59%	1.95%
CNV	96.04%	98.19%	93.22%	2.60%
DME	95.41%	98.06%	92.81%	2.71%
DRUSEN	95.83%	98.17%	92.42%	2.75%

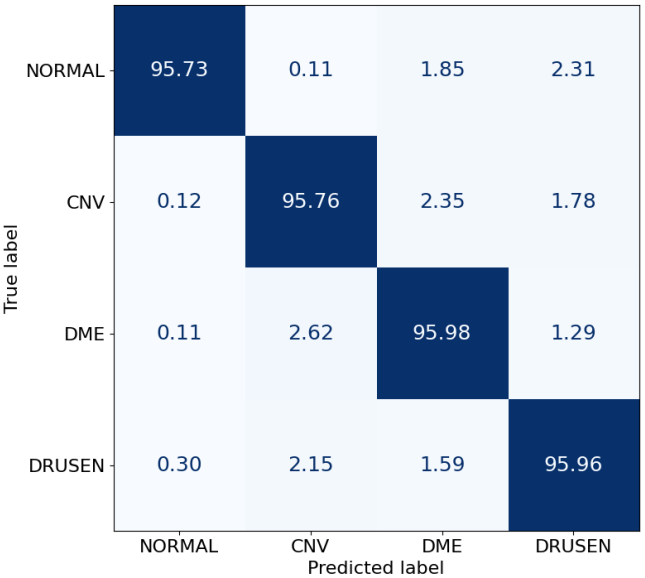


Fig. 3. Confusion matrix

Additionally, in Fig. 4. and 5., the performance evaluation of the Deep CNN-GRU classifier, presented in graphical form, can be observed. These figures depict accuracy and cross-entropy (loss) during both the training and validation phases. Reaching epoch 150, the accuracy achieved in training is 98.7%, while in validation, it is 96.4%. Similarly, the corresponding training and validation loss values for this architecture are 0.54 and 0.76, respectively.

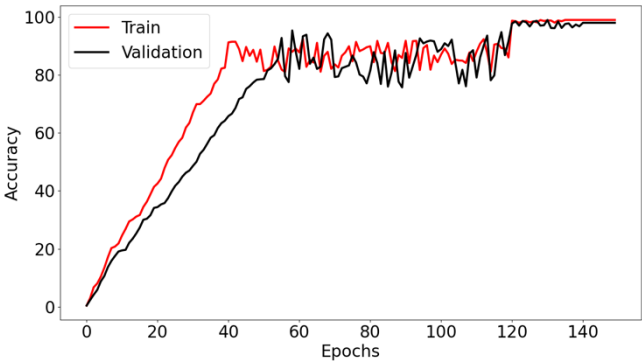


Fig. 4. Accuracy model for Deep CNN-GRU

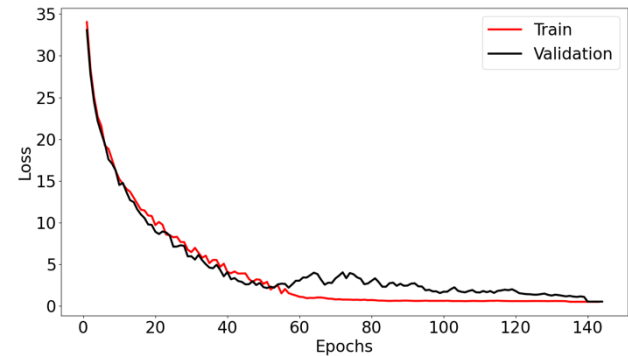


Fig. 5. Loss model for the Deep CNN-GRU

In order to guarantee the precision of the developed model Leave-One-Out Cross-Validation (LOOCV) was conducted. Despite its computational intensity, this method yields dependable and impartial insights into the model's performance. Utilizing LOOCV allowed us to calculate the root mean squared error (RMSE) – Tab. 8.

Tab. 8. Leave-One-Out Cross-Validation result

RMSE	±SD
6.27%	4.18%

#### 4.2. Comparison with the state-of-the-art

The state-of-the-art of deep learning studies performed on the Labelled Optical Coherence Tomography dataset are gathered in Tab. 9. To a large extent they concern well known convolutional approaches that were adjusted to the classification of retinal disorders with great success. The obtained accuracy is in range 85.15% and 99.69%. The proposed tool in this study obtained maximal accuracy equal to 98.90%, which is higher than for classifiers presented in [5, 10, 12, 19, 23, 31, 47]. The proposed Deep CNN-GRU achieved slightly worse results in comparison to studies described in [1] and [3]. The obtained performance for the dataset allows us to draw conclusion that the proposed tool is the proper choice for the DRUSEN, CNV, DME and NORMAL cases classification. It is worth mentioning that the Deep CNN-GRU was trained using one dataset. This approach does not need additional training on other dataset, like ImageNet, and then adjusting it to retinal diseases.

Tab. 9. State-of-the-art classification retinal diseases based on OCT Retina Dataset

Classifiers/method	Accuracy	Study
VGG16	92.19%	[47]
RepVGG	94.45%	
ResNet50	95.31%	
Res2Net50	95.47%	
SENet	95.24%	
SKNet	95.40%	
MHA-Net	96.51%	
CNN	94.35%	[31]
OCCNet	99.69%	[1]
IFCNN	85.15%	[12]
DMF-CNN	96.03%	[10]
VGG16, VGG19, Inception V3	98.30%	[19]
VGG16	98.60%	[23]
ResNet50	99.40%	[3]
CNN	96.50%	[43]
CNN	98.65%	[5]
Deep CNN-GRU	98.90%	Own

#### 5. CONCLUSIONS AND FUTURE WORKS

Nowadays, the DL models have been applied for classification of various retina disorders with great success. These fully- or semi-automated tools are key elements for eye specialists for detection, accelerate treatment diagnosis as well as delay the progress of the diseases.

The proposed classifier, the Deep CNN-GRU, for recognizing rare eye diseases such as drusen, CNV, DME and detecting healthy people obtained very good results. The gained accuracy result of over 98% ensures that the developed tool is suitable for diagnosing retinal eye diseases based on OCT images. The effectiveness of the created solution using deep learning methods turned out to be more appropriate tool for classifying retinal diseases than the methods widely applied in scientific studies (Tab. 9).

Despite achieving high efficiency in detecting retinal diseases, the described method involving the use of a Deep CNN-GRU for the classification of OCT images carries several inherent limitations.

One of it can be the complexity and computation cost. The described architecture is complex with multiple convolutional layers followed by GRU units. This complexity can lead to high computational costs, which can be a limiting factor, especially when deploying in real-time clinical environments or in settings with limited computational resources.

The second restriction might be connected with dataset limitations. The performance of the CNN-GRU model is highly dependent on the quality and diversity of the dataset. If the OCT Retina Dataset lacks variability in terms of devices, patient demographics, or is not representative of the global population, the model may not generalize well to external datasets. Moreover, the quality of the labels in the training dataset is critical. Any mistakes in the annotations of the OCT images can lead to incorrect learning and thus affect the performance of the classifier.

The third limitation might be connected with interpretability and explainability. Deep learning models, including CNNs and GRUs, are often criticized for their lack of interpretability. Medical practitioners may be hesitant to trust and rely on the model's predictions without understanding the rationale behind its decisions.

The last limitation handles of sequential data. While GRUs are designed to deal with sequential data, OCT images are not inherently sequential. If the temporal dynamics of disease progression are not considered or relevant, the benefits of GRUs may not be fully realised.

AI has ability to make new insights into the vast amount of medical digital data. Ethical considerations regarding the practical use of the presented tool should cover many aspects. Firstly, those related to the risk of unauthorised access to medical data. Automated diagnosis tools require access to vast amounts of patient data, which raises concerns about the security of this information and the risk of data breaches.

Moreover, there is a need to ensure that patient information remains confidential and is not shared without consent is a critical ethical obligation. Another aspect which has to be taken under consideration is anonymization. When using patient data to train diagnostic algorithms, it's crucial to anonymize the data to protect patient identities.

Future studies can take three directions. First, it would be interesting to apply our tool to other medical images. Second, the further works may be performed on improving the performance of the proposed classifier. Third, a tool can be extended to the automatic system supporting ophthalmologists.

## REFERENCES

- Alqudah A, Alqudah A. M. Artificial intelligence hybrid system for enhancing retinal diseases classification using automated deep features extracted from OCT images. *International Journal of Intelligent Systems and Applications in Engineering*. 2021; 9(3): 91-100.
- Asgari R, Orlando J I, Waldstein S, Schlanitz F, Baratsits M, Schmidt-Erfurth U, Bogunović H. Multiclass segmentation as multi-task learning for drusen segmentation in retinal optical coherence tomography. *Medical Image Computing and Computer Assisted Intervention*. 2019; 11764: 192-200.
- Asif S, Amjad K. Deep residual network for diagnosis of retinal diseases using optical coherence tomography images. *Interdisciplinary Sciences: Computational Life Sciences*. 2022; 14(4): 906-916.
- Baratloo A, Hosseini M, Negida A, El Ashal, G. Part 1: simple definition and calculation of accuracy, sensitivity and specificity. *Emergency*. 2015; 3(2): 48-49.
- Berrimi M, Moussaoui A. Deep learning for identifying and classifying retinal diseases. In 2020 2nd International Conference on computer and information sciences (ICCIS). 1-6.
- Chen L, Messinger JD, Sloan KR, et al. Abundance and multimodal visibility of soft drusen in early age-related macular degeneration: a clinicopathologic correlation. *Retina*. 2020; 40: 1644-1648.
- Coleman HR, Chan CC, Ferris FL, Chew EY. Age-related macular degeneration. 2008; 372: 11.
- Chollet F. *Deep Learning with Python*. Manning Publications. 2017.
- Chung J, Gulcehre C, Cho K, Bengio Y. Empirical evaluation of gated recurrent neural networks on sequence modeling. 2014; arXiv preprint arXiv:1412.3555.
- Das V, Dandapat S, Bora P. K. Automated Classification of Retinal OCT Images Using a Deep Multi-Scale Fusion CNN. *IEEE Sensors Journal* 2021; 21:23256-23265.
- Diao S, Su J, Yang C, Zhu W, Xiang D, Chen X, Peng Q, Shi F. Classification and segmentation of OCT images for age-related macular degeneration based on dual guidance networks. *Biomedical Signal Processing and Control*. 2023; 84: 104810.
- Fang L, Jin Y, Huang L, Guo S, Zhao G, Chen X. Iterative fusion convolutional neural networks for classification of optical coherence tomography images. *Journal of Visual Communication and Image Representation*. 2019; 59: 327-333.
- Flaxman SR, Bourne RRA, Resnikoff S, et al. Global causes of blindness and distance vision impairment 1990-2020: a systematic review and meta-analysis. *Lancet Glob Health*. 2017; 5: e1221-e1234.
- Haq A, Fariza A, Ramadijanti N. Automatic Detection of Retinal Diseases in Optical Coherence Tomography Images using Convolutional Neural Network. In 2021 International Electronics Symposium (IES), 343-348.
- He K, Zhang X, Ren S, Sun J. Deep residual learning for image recognition. In *Proceedings of the IEEE conference on computer vision and pattern recognition (CVPR)*. 2016; 770-778.
- He X, Fang L, Rabbani H, Chen X, Liu Z. Retinal optical coherence tomography image classification with label smoothing generative adversarial network. *Neurocomputing*. 2020; 405: 37-47.
- Islam M Z, Islam M M, Asraf A. A combined deep CNN-LSTM network for the detection of novel coronavirus (COVID-19) using X-ray images. *Informatics in medicine unlocked*. 2020; 20: 100412.
- Kermany D S, Goldbaum M, Cai W, Valentim C CS, Liang H, Baxter S L, et al. Identifying medical diagnoses and treatable diseases by image-based deep learning. *Cell*. 2019; 172(5):1122-1131. <https://doi.org/10.1016/j.cell.2018.02.010>.
- Kim J, Tran L. Retinal Disease Classification from OCT Images Using Deep Learning Algorithms. In *Proceedings of the 2021 IEEE Conference on Computational Intelligence in Bioinformatics and Computational Biology (CIBCB)*. Melbourne Australia. 2021.
- Krizhevsky A, Sutskever I, Hinton G. E. ImageNet classification with deep convolutional neural networks. *Advances in neural information processing systems*. 2012; 25: 1097-1105.
- Kyunghyun C, et al. Learning Phrase Representations using RNN Encoder-Decoder for Statistical Machine Translation. 2014; arXiv preprint arXiv:1406.1078.
- LeCun Y, Bottou L, Bengio Y, Haffner P. Gradient-based learning applied to document recognition. *Proceedings of the IEEE*. 1998; 86(11): 2278-2324.
- Li F, Chen H, Liu Z, Zhang X, Wu Z. Fully automated detection of retinal disorders by image-based deep learning. *Graefes's Archive for Clinical and Experimental Ophthalmology*. 2019; 257: 495-505.
- Liefers B, Taylor P, Alsaedi A, et al. Quantification of key retinal features in early and late age-related macular degeneration using deep learning. *American Journal of Ophthalmology*. 2021; 226: 1-12.
- Mishra S. S, Mandal B, Puan N B. Perturbed composite attention model for macular optical coherence tomography image classification. *IEEE Transactions on Artificial Intelligence*. 2021; 3(4): 625-635.
- Mitchell P, Liew G, Gopinath B, Wong TY. Age-related macular degeneration. *The Lancet*. 2018; 392: 1147-1159.
- Moradi M, Chen Y, Du X, Seddon J M. Deep ensemble learning for automated non-advanced AMD classification using optimized retinal layer segmentation and SD-OCT scans. *Computers in Biology and Medicine*. 2023; 154: 106512.
- Özdaş M B, Uysal F, Hardalaç F. Classification of Retinal Diseases in Optical Coherence Tomography Images Using Artificial Intelligence and Firefly Algorithm. *Diagnostics*. 2023; 13(3): 433.
- Pollreis A, Reiter GS, Bogunovic H, Baumann L, Jakob A, Schlanitz FG, Sacu S, Owsley C, Sloan KR, Curcio CA, Schmidt-Erfurth U. Topographic Distribution and Progression of Soft Drusen Volume in Age-Related Macular Degeneration Implicate Neurobiology of Fovea. *Investigative Ophthalmology & Visual Science*. 2021; 62(2): 26-26.

30. Rahimzadeh M, Mohammadi M R. ROCT-Net: A new ensemble deep convolutional model with improved spatial resolution learning for detecting common diseases from retinal OCT images. In 2021 11th International Conference on Computer Engineering and Knowledge (ICCKE). 85-91.
31. Saraiva A A, Santos D B S, Pimentel P M C, Sousa J V M, Ferreira N M, Batista Neto J D E S, Soares S, Valente A. Classification of optical coherence tomography using convolutional neural networks. In Proceedings. 2020.
32. Schwartz R, Khalid H, Liakopoulos S, Ouyang Y, de Vente C, González-Gonzalo C, Lee A Y, Guymier R, Chew E Y, Egan C, Wu Z, Kumar H, Farrington J, Müller P L, Sánchez C I, Tufail, A. A Deep Learning Framework for the Detection and Quantification of Reticular Pseudodrusen and Drusen on Optical Coherence Tomography. *Translational Vision Science & Technology*. 2022; 11(12): 3-3.
33. Serener A, Serte S. Dry and wet age-related macular degeneration classification using oct images and deep learning. In 2019 Scientific meeting on electrical-electronics & biomedical engineering and computer science (EBBT). 2019; 1-4.
34. Shah P M, Ullah F, Shah D, Gani A, Maple C, Wang Y, Shahid Abrar M, Islam S. U. Deep GRU-CNN model for COVID-19 detection from chest X-rays data. *IEEE Access*. 2021; 10: 35094-35105.
35. Simonyan K, Zisserman A. Very deep convolutional networks for large-scale image recognition. *arXiv* 2014; preprint arXiv:1409.1556.
36. Sotoudeh-Paima S, Jodeiri A, Hajizadeh F, Soltanian-Zadeh H. (Multi-scale convolutional neural network for automated AMD classification using retinal OCT images. *Computers in biology and medicine*. 2022; 144: 105368.
37. Spaide RF, Curcio CA. Drusen characterization with multimodal imaging. *Retina*. 2010; 30: 1441-1454
38. Srinivasan P P, Kim L A, Mettu P S, Cousins S W, Comer G M, Izatt J A, Farsiu S. Fully automated detection of diabetic macular edema and dry age-related macular degeneration from optical coherence tomography images. *Biomedical optics express*. 2014; 5(10): 3568-3577.
39. Sun J K, Lin M M, Lammer J, Prager S, Sarangi R, Silva P S, Aiello L P. Disorganization of the retinal inner layers as a predictor of visual acuity in eyes with center-involved diabetic macular edema. *JAMA Ophthalmology*. 2014; 132: 1309-1316.
40. Sun Z, Sun Y. Automatic detection of retinal regions using fully convolutional networks for diagnosis of abnormal maculae in optical coherence tomography images. *Journal of biomedical optics*. 2019; 24(5): 056003-056003.
41. Sunija A P, Kar S, Gayathri S, Gopi V P, Palanisamy P. Octnet: A lightweight CNN for retinal disease classification from optical coherence tomography images. *Computer methods and programs in biomedicine*. 2021; 200: 105877.
42. Taibouni K, Miere A, Samake A, Souied E, Petit E, Chenoune Y. Choroidal neovascularization screening on OCT-angiography Choriocapillaris images by convolutional neural networks. *Applied Sciences*. 2021; 11(19): 9313.
43. Tayal A, Gupta J, Solanki A, Bisht K, Nayyar A, Masud M. DL-CNN-based approach with image processing techniques for diagnosis of retinal diseases. *Multimedia Systems*. 2022; 28:1417-1438.
44. Tvenning A O, Hanssen S R, Austeng D, Morken T S. Deep learning identify retinal nerve fibre and choroid layers as markers of age-related macular degeneration in the classification of macular spectral-domain optical coherence tomography volumes. *Acta Ophthalmologica*. 2022; 100(8): 937-945.
45. Wang M, Zhu W, Shi F, Su J, Chen H., Yu K, Zhou Y, Peng Y, Chen Z, Chen, X. MsTGANet: Automatic drusen segmentation from retinal OCT images. *IEEE Transactions on Medical Imaging*. 2021; 41(2): 394-406.
46. Wang Y, Lucas M, Furst J, Fawzi A A, Raicu D. Explainable deep learning for biomarker classification of oct images. In 2020 IEEE 20th International Conference on Bioinformatics and Bioengineering (BIBE) 2020; 204-210.
47. Xu L, Wang L, Cheng S, Li Y. MHANet: A hybrid attention mechanism for retinal diseases classification. *Plos one*. 2021; 16(12): e0261285.
48. Zweifel SA, Imamura Y, Spaide TC, Fujiwara T, Spaide RF. Prevalence and significance of subretinal drusenoid deposits (reticular pseudodrusen) in age-related macular degeneration. *Ophthalmology*. 2010;117(9):1775-1781.

This project has been done within the “Staž za miedzą” restricted grant funded by the Medical University in Lublin, Poland (Chair and Department of General and Pediatric Ophthalmology, Medical University of Lublin, Poland and Faculty of Electrical Engineering and Computer Science, Department of Computer Science, Lublin University of Technology, Lublin, Poland). The study was carried out as a part of the project “Lubelska Unia Cyfrowa – Wykorzystanie rozwiązań cyfrowych i sztucznej inteligencji w medycynie – projekt badawczy”, no. MEiN/2023/DPI/2194.

Paweł Powroźnik:  <https://orcid.org/0000-0002-5705-4785>

Maria Skublewska-Paszkowska:  <https://orcid.org/0000-0002-0760-7126>

Robert Rejdak:  <https://orcid.org/0000-0003-3321-2723>

Katarzyna Nowomiejska:  <https://orcid.org/0000-0002-5805-8761>



This work is licensed under the Creative Commons BY-NC-ND 4.0 license.



## NOVEL PLA COMPOSITES MODIFIED WITH STEEL FIBRES AND (3-THIOPROPYL) POLYSILSESQUOXANE DERIVATIVES

Daria PAKUŁA<sup>\*,\*\*</sup>, Bogna SZTORCH<sup>\*</sup>, Eliza ROMAŃCZUK-RUSZUK<sup>\*\*\*</sup>  
 Bogdan MARCINIEC<sup>\*,\*\*</sup>, Robert E.PRZEKOP<sup>\*</sup>

<sup>\*</sup>Adam Mickiewicz University in Poznań, Faculty of Chemistry, Uniwersytet Poznański 8, 61-614 Poznań, Poland

<sup>\*\*</sup>Adam Mickiewicz University in Poznań, Centre for Advanced Technologies,  
 Uniwersytet Poznański 10, 61-614 Poznań, Poland

<sup>\*\*\*</sup>Institute of Mechanical Engineering, Białystok University of Technology, Wiejska 45C, 15-351 Białystok, Poland

[darapak@amu.edu.pl](mailto:darapak@amu.edu.pl), [bogna.sztorch@amu.edu.pl](mailto:bogna.sztorch@amu.edu.pl), [e.romanczuk@pb.edu.pl](mailto:e.romanczuk@pb.edu.pl)  
[bogdan.marciniec@amu.edu.pl](mailto:bogdan.marciniec@amu.edu.pl), [rprzekop@amu.edu.pl](mailto:rprzekop@amu.edu.pl)

received 4 February 2024, revised 8 August 2024, accepted 16 August 2024

**Abstract:** In recent years, a significant increase in the development of new composite materials with desirable mechanical, thermal or surface properties has been observed. One of the popular polymers on the market is polylactide. This article explores how to modify the polymer using steel fibres and organosilicon compounds (SSQ-SH, SSQ-SH-OCT, and SSQ-SH-OFP) to enhance its properties. Test samples were obtained by injection molding with varying concentrations of 0.5%, 1%, 1.5%, 2.5%, and 5% of steel fibres. Mechanical tests, including tensile strength, elongation at break, and impact strength, were conducted, along with an analysis of the contact angle. The modified samples showed higher impact strength values, with the PLA /steel fibres /SSQ-SH sample seeing an increase of 12%. The addition of modifiers with fluoroalkyl groups led to a contact angle increase of 8.5% compared to neat PLA. Thermal tests (TGA) were also carried out to determine the influence of fibres and organosilicon compounds on decomposition.

**Key word:** polylactide (PLA): steel fibres; composites; organosilicon compound; octa(3-thiopropyl)silsesquioxanes; injection molding

### 1. INTRODUCTION

For several years, researchers have been exploring new composite materials that exhibit desirable mechanical, thermal, or surface characteristics. A widely studied polymer in this regard is PLA, which belongs to the family of polyester polymers. PLA is considered a highly promising option to replace petroleum-based materials as it is derived from sustainable sources such as corn starch or sugarcane [1]. Not only does PLA possess excellent mechanical and thermal properties, but it is also both degradable and biocompatible, making it a highly appealing alternative [2].

Poly lactide can be produced through polycondensation of lactic acid or ring-opening polymerization of cyclic lactic diester (lactide) [3]. Notably, this process is more cost-effective than petroleum-based polymers, requiring significantly less energy (25–55% less). With advancements in technology, it is projected that this energy reduction could decrease to less than 10% in the future [4]. Furthermore, the production of PLA has a significantly lower carbon footprint, generating far fewer greenhouse gas emissions when compared to traditional plastics.

Poly lactide is a remarkably versatile material that can be utilized in a wide range of manufacturing processes. These include injection molding, extrusion, and 3D printing, making it a highly sought-after choice for various industries such as construction, automotive [5], packaging [6], clothing [7], and electronics [8]. Its extensive applications encompass from bottles [9], tea bags, dishes [10], to packaging for cosmetics [11]. One of the most significant advantages of PLA is its high biocompatibility, which

makes it an ideal material for biomedical purposes. In the medical field, it is commonly used to create bioresorbable sutures, implants, orthopedic devices, vascular scaffolds, and drug delivery systems [12].

Poly lactide is a versatile material whose properties can be influenced by a variety of factors such as the isomer ratio, processing temperature, crystallinity, and molecular weight [13-15]. One of the key advantages of PLA is its favorable processing qualities, high transparency, and good strength. However, it also has certain drawbacks that may limit its suitability for some specialized applications. These drawbacks include in particular high brittleness and a relatively slow degradation rate [16]. Given these limitations, researchers are actively exploring new modifiers that can enhance the desired properties of PLA. These modifiers can take the form of natural or chemical fillers, each with their unique set of benefits and drawbacks e.g. calcium carbonate [17], diatoms [18], wood fiber [19], straws [20], husks [21], TiO<sub>2</sub> [22-23], glass fibres [24], graphene [25], graphite [26]. Currently, many works describe the combination of PLA with metallic particles [27-29]. The addition of steel fibers can improve the mechanical properties [30-31]. Steel fibers are often used as reinforcement in composite materials to provide added strength and toughness. In 3D printing, when incorporated into PLA, they can enhance the overall structural integrity of the printed objects [30,32]. Steel is a material commonly used in medicine, it is used to produce, among others: surgical tools, elements of prostheses and orthoses. Special grades of stainless steel are used in medicine, which are characterized by high corrosion resistance and low biological

reactivity [27]. However, it is worth noting that the metallic particles do not integrate with the matrix material (PLA). Therefore, modifiers are being sought to improve the bonding of the metallic particles to the composite matrix. Ultimately, the choice of modifier will depend on the specific needs of the application at hand. One of the effective approaches to modifying polymers is through the incorporation of organosilicon compounds, including silsesquioxanes, silanes, and polysiloxanes, into the polymer matrix [33-34]. These compounds can have a significant impact on various physical and chemical properties, such as rheological or thermal properties, as well as mechanical properties [34]. Silsesquioxanes are a type of hybrid organosilicon compound with a general formula of  $\text{R}_2\text{SiO}_3/2$ , consisting of a core (Si-O-Si) and attached reactive or inert groups like isobutyl or phenyl groups [35]. Silsesquioxanes typically exhibit high biocompatibility and lack of cytotoxicity. Scientific literature provides data demonstrating the high biocompatibility and absence of cytotoxic effects of silsesquioxanes with various functional groups, including those substituted with amino or thiopropyl groups [36]. A detailed description of fillers for polymer applications can be found in our previous review [37].

This paper discusses the enhancement of polylactide by using steel fibers and organosilicon compounds which were used to modify fibers. To gauge the effectiveness of these modifications, different mechanical tests such as tensile strength and impact strength were conducted. Additionally, tests were carried out to determine the impact of these additives on surface properties, specifically through an analysis of the contact angle. Thermogravimetric analysis was also performed to determine the effect of fibers and compounds on thermal stability. The results showed that by adding a small amount of modifiers, the polymer becomes more flexible and has higher contact angle values. This paper presents an effective and economical method of modifying polymers.

## 2. MATERIALS AND METHODS

**Materials:** Polylactide (PLA) Ingeo 2003D type was purchased from NatureWorks (Minnetonka, MN, USA). Low-alloy steel fibers with the following composition were used in the work: Fe, 0.295 % Si, 0.525 % Mn, 2.08 % Ni, 0.535 % Cr, 1.29 % Mo, 0.52 % V, 0.11 % Cu. The chemicals were purchased from the following sources: 3-Mercaptopropyltrimethoxysilane (99%) from UNISIL; methanol p.a. from P.P.H Stanlab; hydrochloric acid (35-38%), toluene, tetrahydrofuran from Chempur. Azobisisobutyronitrile (AIBN) (98%) was purchased from FLUKA, octene (OCT) (97%) from ABCR and chloroform-d from Merck Group. Allyl 2,2,3,3,4,4,5,5-octafluoropentyl ether (Allyl-OFP) was synthesized according to the method described by Maciejewski et al. in the literature [38]. Toluene was degassed and dried by distilling it from  $\text{P}_2\text{O}_5$  under an argon atmosphere. (3-thiopropyl)polysilsesquioxane was prepared according to the literature [39-40] and our previous article [41] (Fig.1).

**Synthesis of chemical modifiers:** A crystalline and amorphous product was obtained by the hydrolytic condensation reaction of 3-thiopropyltrimethoxysilane. The amorphous product (hereinafter referred to as SSQ-SH), which is a viscous, thick oil, consists of closed cages (T8) and incompletely condensed silanols. Two derivatives, partially substituted with hydrophobic groups, were obtained by a radical reaction initiated by AIBN. The functionalization was carried out according to literature data [41] with octene

(hereinafter SSQ-SH-OCT) and allyl 2,2,3,3,4,4,5,5-octafluoropentyl ether (hereinafter SSQ-SH-OFP). Modifiers containing both reactive thiol and hydrophobic groups (octyl, fluoroalkyl) were obtained.

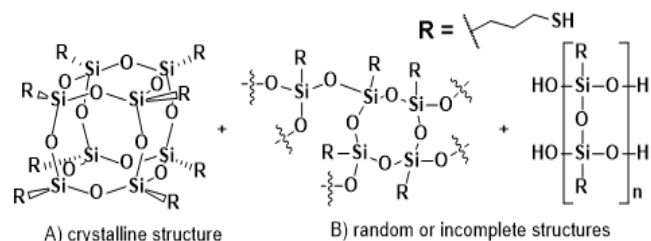


**Fig.1.** Products of the hydrolytic condensation reaction of 3-thiopropyltrimethoxysilane

**Preparation of samples:** Stage 1: The first stage covered the modification of steel fibers with organosilicon compounds. For this purpose, 2 g of a modifier (SSQ-SH or SSQ-SH-OCT or SSQ-SH-OFP) and 100 ml of THF were added to 100 g of fibers, and then mixed on a laboratory evaporator for 2 h at room temperature. The solvent was allowed to evaporate slowly and then the modified fibres were dried at 50°C for 1 hour. Stage 2: The second step involved obtaining a concentrate. The polymer and modified steel fibres were homogenized using a laboratory two-roll mill ZAMAK MERCATOR WG 150/280. A portion of 900 g of PLA Ingeo™ 2003 D was mixed with 100 g steel fibres until the final concentration of the additive of 10% w/w. The mixing was performed at the rolls temperature of 215°C for 15 min., getting to full homogeneity of the concentrates. Masterbatch was granulated by a grinding mill WANNER C17.26 sv.

The prepared masterbatches were diluted 1:1 with PLA directly in the Engel e-victory 170/80 injection molding machine. Standardized specimens for mechanical tests were obtained according to PN-EN ISO 20753:2019-01. Final system concentrations of steel fibres were 0.5% w/w, 1% w/w, 1.5% w/w, 2.5% w/w, 5% w/w.

**Methods:** Water contact angle (WCA) measurements were performed using the sessile drop technique (5  $\mu\text{L}$ ) at room temperature and atmospheric pressure with a Krüss DSA100goniometer (Krüss Optronic GmbH, Hamburg, Germany).

Tensile tests of the obtained specimens were performed on a universal testing machine INSTRON 5969 with a maximum load force of 50 kN. The traverse speed for the tensile strength measurements was set at 2 mm/min.

The Charpy impact strength test (unnotched samples) was performed according to ISO 179-1 on an Instron Ceast 9050 impact pendulum tester.

Thermogravimetry (TG) was performed using a NETZSCH 209 F1 Libra gravimetric analyser (Selb, Germany). Samples of  $4 \pm 0.2$  mg were placed in  $\text{Al}_2\text{O}_3$  crucibles. Measurements were conducted under nitrogen (flow of 20 ml/min) in the range of 30–1000°C and a 10°C/min heating rate.

Images of steel fibres and composites were taken with the digital light microscope Keyence VHX-7000 (Keyence International NV/SA, Osaka, Japan) with a VH-Z100R wide angle zoom lens (Keyence International NV/SA, Osaka, Japan) at 100× magnification. The images were taken using the function of depth composition and 3D image creation.

### 3. RESULTS AND DISCUSSION

From the microscopic analysis, it can be seen that the steel fibers are characterized by different sizes. The length range determined by the optical microscope was from about 40  $\mu\text{m}$  to 2000  $\mu\text{m}$  (Fig.2). Based on the literature review, it has been determined that no research has been conducted to date on the incorporation of modified steel fibers with organosilicon compounds into a polylactide matrix.

The article describes the process of producing polylactide composites reinforced with steel fibers and steel fibers modified with organosilicon compounds having reactive thiol groups and/or hydrophobic groups, respectively. An analysis of tensile strength and impact strength was carried out, as well as surface tests were performed, which allowed to characterize the degree of hydrophobicity of the materials.

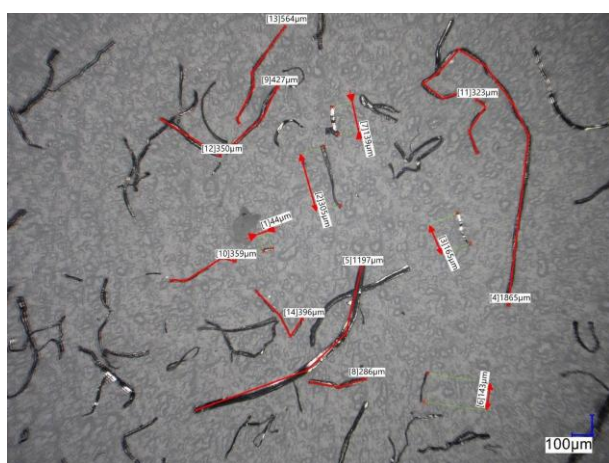


Fig. 2. Optical microscopic images of steel fibres

Fig. 3 presents optical microscope images of the surfaces (left) and fracture surfaces (right) of composites at the highest fiber concentrations (5% wt). Based on these images, the effect of different silsesquioxane (SSQ) additives (SSQ-SH, SSQ-SH-OCT, SSQ-SH-OFP) on the material structure can be observed. The surface of neat PLA is relatively homogeneous, and the fracture surface is smooth. Figure 3B-B' clearly shows steel fibers on the PLA surface, with sharp and distinct boundaries between the fibers and the matrix in the fractures. The fracture surface is rough, indicating poor adhesion between the fibers and PLA. The addition of SSQ-SH improves the adhesion of steel fibers to the PLA matrix, resulting in a more integrated structure and reduced visibility of fibers in the fractures (Fig. 3C-C'). Similarly, SSQ-SH-OCT leads to better dispersion and homogeneity of the material (Fig. 3D-D'). In contrast, the addition of SSQ-SH-OFP shows the presence of fiber agglomerates mainly on the surface (Fig. 3E-E'), which may indicate uneven dispersion and potentially inferior mechanical properties of the material. This is related to the high hydrophobicity of fluoroalkyl groups, leading to poorer miscibility between the system components. The surface of the fractures with additives is less rough, indicating better embedding of the fibers in the matrix.

Fig. 4 shows the impact strength results for neat PLA, steel fiber reinforced PLA, and modified filler/PLA. The measurement method used is characterized by large standard deviations, which is visible on the graph in the form of errors bars. Neat PLA's im-

pact strength is 17.1 kJ/m<sup>2</sup> (black straight line in the graph - reference). The addition of steel fibers did not significantly affect the impact resistance, and the changes in values are within  $\pm 1.0$  kJ/m<sup>2</sup>.

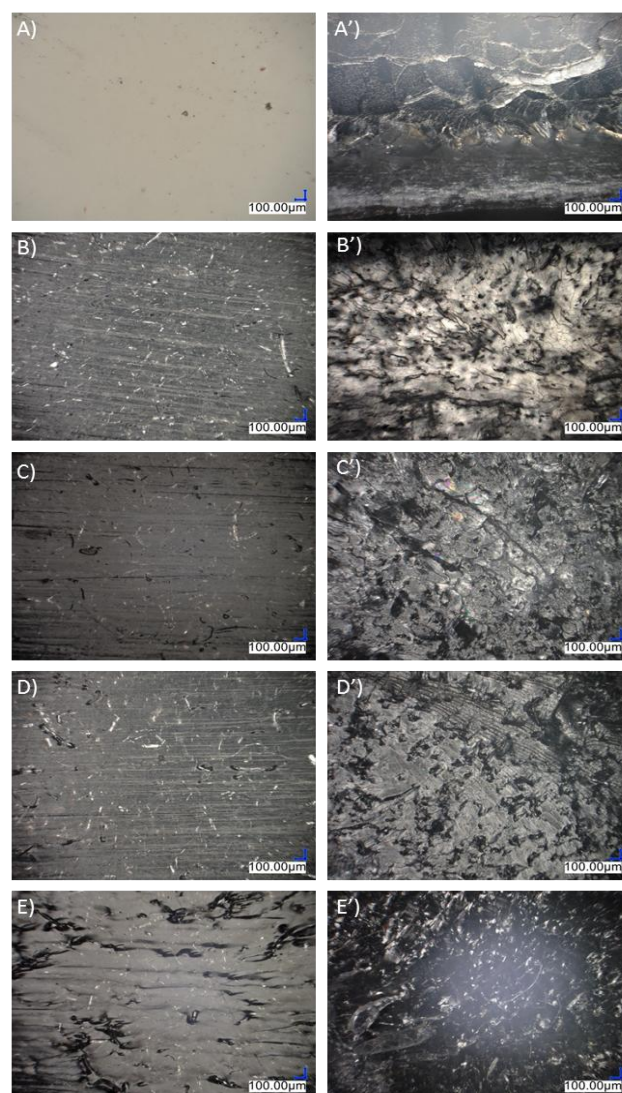


Fig. 3. Microscopic images of composites: A) neat PLA, B) PLA + 5% steel fibres, C) PLA + (5% steel fibres/SSQ-SH), D) PLA + (5% steel fibres/SSQ-SH-OCT), E) PLA + (5% steel fibres/SSQ-SH-OFP)

Composites with the addition of organosilicon modifiers are characterized by higher impact strength values. This may be due to three factors: 1) improved dispersion of the modified fibers in the polymer matrix; 2) plasticizing effect of organosilicon compounds; 3) the influence of thiol groups which may interact with the polylactide matrix. Thiol groups present in modifiers act as proton donors, facilitating the formation of hydrogen bonds between the -SH groups and the carbonyl groups in polylactic acid (PLA) chains. These hydrogen bonds can influence the degree of crystallinity in PLA, which in turn affects its mechanical properties. In our previous work, we presented the impact of (3-thiopropyl) polysilsesquioxane on the mechanical properties of polylactide, including potential interactions between the modifier and the matrix [42]. Modifiers can act as a plasticizer, reducing the brittleness of the polymer, thanks to which the resulting composite is



able to absorb more energy during impact. The highest values were obtained for the PLA/steel fibres/SSQ-SH composite, which may indicate a significant impact of thiol groups on the improvement of the mechanical properties of the polymer. The tests carried out show that the addition of a small amount of organosilicon compounds by weight in relation to the entire composite affects the change in the properties of the materials, which gives an effective method of modification and is also important in the economic aspect.

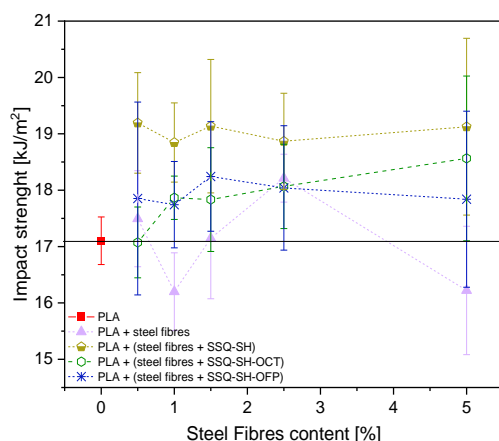


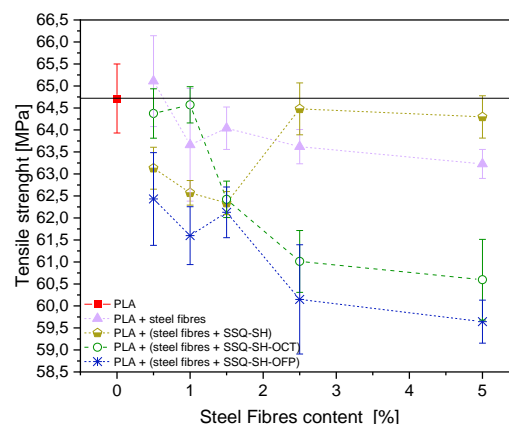
Fig. 4. Impact strength of composites

Tensile strength tests were also carried out (Fig.5A), examples of force-elongation curves for selected materials are shown (Fig. 5B), and elongation at break was determined (Fig.6). Neat PLA has similar characteristics to PLA+(steel fibres+SSQ-SH), but the displacement of the sample with the modifier was higher. Displacement is slightly higher for the samples with modifiers, compared to neat PLA, but the maximum force values are comparable for all tested materials. However, the differences shown for the example samples are not statistically significant (Fig. 5B). The slight differences may be due to the different lengths and uneven arrangement of the steel fibres. The addition of steel fibers did not affect the reinforcement of the composite matrix, and changes in strength values are  $\pm 1$  MPa. The addition of organosilicon compounds (SSQ-SH-OCT, SSQ-SH-OFP) reduced the tensile strength value. Composites with the addition of the SSQ-SH-OFP modifier have the lowest strength. This decrease can be attributed to the highly hydrophobic characteristics of the fluoroalkyl groups within the SSQ-SH-OFP modifier. These hydrophobic groups probably result in diminished interactions between the modifier and the polymer matrix, which is also observed in microscopic photos (Fig. 3). For the sample with 5% concentration (steel fibres/SSQ-SH-OFP) the value decreased by 5.1 MPa. The obtained results show that the new materials, which also consist of organosilicon compounds, are characterized by higher flexibility and lower strength. This may be due to the plasticizing effect of modifiers, as well as the presence of discontinuities in the polymer phase introduced with the addition of filler [33].

Literature data confirm that metal powder act as a weak interface thereby lowering strength and toughness [43]. It is possible that the use of fibers may similarly deteriorate mechanical strength. The addition of organosilicon compounds slightly improves the plasticity of composites. Higher elongation at break

values (Fig.6) indicate increased mobility of the polymer phase, attributable to the addition of a plasticizing modifier. This is due in part to the modifier's penetration between the macromolecular chains of the polymer, which reduces the intermolecular forces acting along these chains [44]. Similar results can be seen in impact tests.

a)



b)

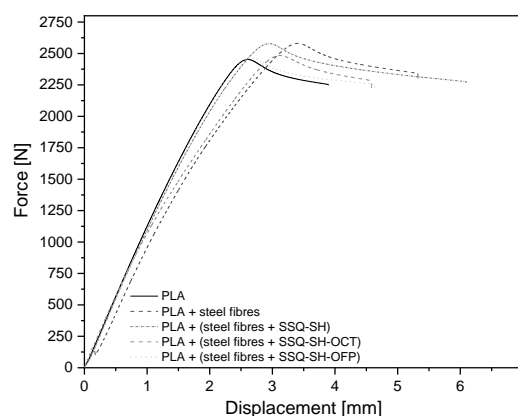


Fig. 5. a) Tensile strength of composites, b) force-elongation curves

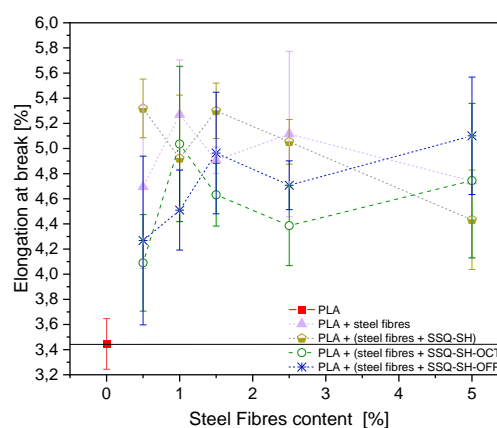


Fig. 6. Elongation at break of composites



In the study, samples with the highest concentration of steel fibers were subjected to thermogravimetric analysis in an inert gas (N<sub>2</sub>) flow (Fig.7). The onset temperature and temperature at the maximum rate of mass loss were determined from the TGA/DTG curves. The results showed a significant decrease in the decomposition start temperatures of the modified composites (Table 1). The introduction of steel fibers was found to lower both the onset temperature and temperature at the maximum rate of mass loss. The analysis of the composites revealed that the thermal stability was not affected by the organosilicon compounds. When 5 wt.% steel fibers or modified steel fibers were added, the onset temperature was lowered from 16.0°C to 18.4°C. Sample fiber/SSQ-SH was characterized by 32.6°C lower temperature at the maximum rate of mass loss compared to neat PLA. One possible explanation for this behavior of the samples is that the steel conducts heat, which results in faster heating of the composite systems and ultimately leads to lower initial temperatures and temperatures at maximum weight loss rates. In the study by Sztorch et al., it was also observed that the addition of metallic powders can lower the onset degradation temperatures of composites. This phenomenon is also evident in the case of adding steel fibers to PLA [45]. Table 2 summarizes the obtained results.

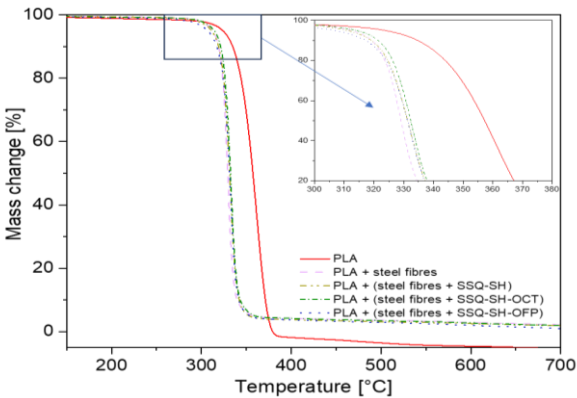


Fig. 7. TGA curves of composites

Tab. 1. Results of TGA analysis

Sample	Onset temperature [°C]	$\Delta T$ [°C]	Temperature at the Maximum Rate of Mass Loss [°C]	$\Delta T$ [°C]
Neat PLA	342.2	-	362.1	-
PLA + steel fibres	323.8	18.4	329.5	32.6
PLA + (steel fibres + SSQ-SH)	324.2	18.0	332.1	30.0
PLA+ (steel fibres + SSQ-SH-OCT)	326.2	16.0	333.1	29.0
PLA+ (steel fibres + SSQ-SH-OFP)	324.5	17.7	332.9	29.2

The neat PLA sample has a hydrophilic surface with a contact angle of 76.5°. The addition of fibres and organosilicon compounds influenced surface changes of the composites (Fig. 8). PLA/steel fibres materials are characterized by a higher water contact angle (for a 1.5% sample, the value is 81.7°). Changes towards higher values may be caused by a change in the microstructure to a rougher one, and thus characterized by higher values of the contact angle. Samples in which SSQ-SH is used are characterized by lower values compared to neat PLA. The thiol groups present in the modifier's structure are moderately polar and hydrophilic because of the difference in the electronegativity of sulfur and hydrogen, which leads to interaction with water, decreasing the contact angle[46]. SSQ-SH-OCT and SSQ-SH-OFP are characterized by the presence of both reactive thiol groups and groups determining the hydrophobic character (octyl, fluoroalkyl). The highest increase in the contact angle value was observed for PLA + composites (steel fibres+SSQ-SH-OFP). With the increase of the organosilicon modifier, the value of the contact angle increases. For the 5% sample, there is a noticeable change of 8.5% compared to neat PLA. Fluorinated materials are characterized by low surface energy and exhibit both oleophobicity and hydrophobicity [47-48]. The addition of the SSQ-SH-OFP derivative led to an increased contact angle. This rise can be explained by the hydrophobic fluoroalkyl groups in SSQ-SH-OFP, which repel water and lower surface energy, thereby enhancing hydrophobicity of materials.

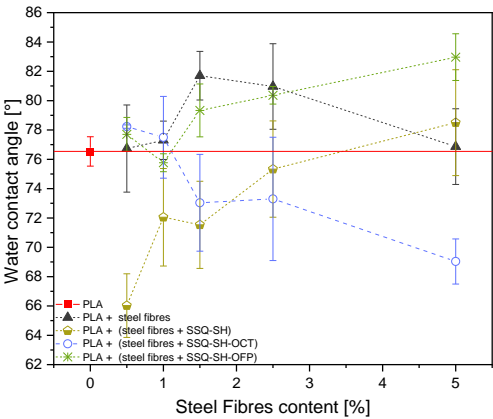


Fig. 8. Water contact angle of composites

#### 4. CONCLUSION

This study presents the first investigation into the modification of steel fibers with organosilicon compounds (SSQ-SH, SSQ-4SH-4OCT, and SSQ-4SH-4OFP), for their incorporation into polylactide matrix. Through a series of mechanical, thermal and surface property tests, it has been demonstrated that these modifications lead to significant changes in the properties of the resulting composites. The incorporation of steel fibres and organosilicon compounds into PLA resulted in changes in their strength properties, including an increase in impact strength and elongation at break values, as well as a change in the contact angle value. The compounds used acted as plasticizers in the polymer matrix, which made the material more flexible. Additionally, the hydrophobic groups in the compounds (primarily fluoroalkyl groups) affected the surface properties (increase of 8.5% compared to neat PLA).

By adding small amounts of organosilicon additives, certain properties were improved, making this an effective, efficient, and economically advantageous method. These findings suggest a promising potential for the use of organosilicon-modified steel fibers in PLA composites. Preliminary tests indicate that this modification strategy can lead to enhanced composite materials with improved performance properties. Future research will focus on further exploring the optimization of these modifications, assessing long-term durability, and evaluating additional applications to fully realize the potential benefits of this innovative approach.

## REFERENCES

- Madhavan Nampoothiri K, Nair NR, John RP. An overview of the recent developments in polylactide (PLA) research. *Bioresource Technology*. 2010; 101(22):8493–501. <https://doi.org/10.1016/j.biortech.2010.05.092>
- Raquez JM, Habibi Y, Murariu M, Dubois P. Polylactide (PLA)-based nanocomposites. *Progress in Polymer Science*. 2013;38(10-11):1504–42. <https://doi.org/10.1016/j.progpolymsci.2013.05.014>
- Anderson K, Schreck K, Hillmyer M. Toughening Polylactide. *Polymer Reviews*. 2008; 48(1):85–108. <https://doi.org/10.1080/15583720701834216>
- Farah S, Anderson DG, Langer R. Physical and mechanical properties of PLA, and their functions in widespread applications — A comprehensive review. *Advanced Drug Delivery Reviews*. 2016;107:367–92. <https://doi.org/10.1016/j.addr.2016.06.012>
- Notta-Cuvier D, Odent J, Delille R, Murariu M, Lauro F, Raquez JM, et al. Tailoring polylactide (PLA) properties for automotive applications: Effect of addition of designed additives on main mechanical properties. *Polymer Testing*. 2014; 36:1–9. <https://doi.org/10.1016/j.polymertesting.2014.03.007>
- Swetha TA, Bora A, Mohanrasu K, Balaji P, Raja R, Ponnuchamy K, et al. A comprehensive review on polylactic acid (PLA) – Synthesis, processing and application in food packaging, *International Journal of Biological Macromolecules*. 2023; 234:123715. <https://doi.org/10.1016/j.ijbiomac.2023.123715>
- Claudio L. Waste Couture: Environmental Impact of the Clothing Industry. *Environmental health perspectives*. 2007;115(9):448–54. <https://doi.org/10.1289/ehp.115-a449>
- Wang J, Yu J, Bai D, Li Z, Liu H, Li Y, et al. Biodegradable, Flexible, and Transparent Conducting Silver Nanowires/Polylactide Film with High Performance for Optoelectronic Devices. *Polymers*. 2020;12(3):604. <https://doi.org/10.3390/polym12030604>
- Kale G, Auras R, Singh S, Narayan R. Biodegradability of polylactide bottles in real and simulated composting conditions *Polymer Testing*. 2007; 26 (8):1049–1061. <https://doi.org/10.1016/j.polymertesting.2007.07.006>
- Abdelrazek Sh, Abou Taleb E, Mahmoud A, Hamouda T. Utilization of Polylactic Acid (PLA) in Textile Food Packaging: A Review". *Egyptian Journal of Chemistry*. 2021;65(3): 725 – 738.
- Sikorska W, Rydz J, Wolna-Stypka K, Musiol M, Adamus G, Kwiecień I, et al. Forensic Engineering of Advanced Polymeric Materials—Part V: Prediction Studies of Aliphatic–Aromatic Copolyester and Polylactide Commercial Blends in View of Potential Applications as Compostable Cosmetic Packages. *Polymers*. 2017;9(12):257. <https://doi.org/10.3390/polym9070257>
- Bergström JS, Hayman D. An Overview of Mechanical Properties and Material Modeling of Polylactide (PLA) for Medical Applications. *Annals of Biomedical Engineering*. 2015;44(2):330–40. <https://doi.org/10.1007/s10439-015-1455-8>
- Ajioka M, Enomoto K, Suzuki K, Yamaguchi A. Basic Properties of Polylactic Acid Produced by the Direct Condensation Polymerization of Lactic Acid. *Bulletin of the Chemical Society of Japan*. 1995;68(8):2125–31. <https://doi.org/10.1246/bcsj.68.2125>
- Julio César Velázquez-Infante, J. Gámez-Pérez, Adrian E, Santana OO, Carrasco F, M. LI. Maspoeh. Effect of the unidirectional drawing on the thermal and mechanical properties of PLA films with different L-isomer content. 2012;127(4):2661–9. <https://doi.org/10.1002/app.37546>
- Bai H, Deng S, Bai D, Zhang Q, Fu Q. Recent Advances in Processing of Stereocomplex-Type Polylactide. *Macromolecular Rapid Communications*. 2017;38(23):1700454. <https://doi.org/doi:10.1002/marc.201700454>
- Su S, Kopitzky R, Tolga S, Kabasci S. Polylactide (PLA) and Its Blends with Poly(butylene succinate) (PBS): A Brief Review. *Polymers*. 2019;11(7):1193. <https://doi.org/10.3390/polym11071193>
- Piekarska K, Piorkowska E, Bójda J. The influence of matrix crystallinity, filler grain size and modification on properties of PLA/calcium carbonate composites. *Polymer Testing*. 2017; 62:203–209. <https://doi.org/10.1016/j.polymertesting.2017.06.025>
- Dobrosielska M, Dobrucka R, Brząkalski D, Frydrych M, Kozera P, Wiecek M, et al. Influence of Diatomaceous Earth Particle Size on Mechanical Properties of PLA/Diatomaceous Earth Composites. *Materials*. 2022;15(10):3607. <https://doi.org/10.3390/ma15103607>
- Pilla S, Gong S, O'Neill E, Yang L, Rowell RM. Polylactide-recycled wood fiber composites. *Journal of Applied Polymer Science*. 2009;111(1):37–47. <https://doi.org/10.1002/app.28860>
- Mihai M, Ton-That MT. Novel bio-nanocomposite hybrids made from polylactide/nanoclay nanocomposites and short flax fibers. *Journal of Thermoplastic Composite Materials*. 2017;32(1):3–28. <https://doi.org/10.1002/pen.23575>
- Sabzoi Nizamuddin, Jadhav A, Sundus Saeed Qureshi, Humair Ahmed Baloch, M. Minhaj Siddiqui, Nabisab Mujawar Mubarak, et al. Synthesis and characterization of polylactide/rice husk hydrochar composite. *Scientific Reports*. 2019;9(1). <https://doi.org/10.1038/s41598-019-41960-1>
- Chanklomp P, Kreetachat T, Chotigawin R, Suwannahong K. Photocatalytic Oxidation of PLA/TiO<sub>2</sub>-Composite Films for Indoor Air Purification. *ACS Omega*. 2021;6(16):10629–36. <https://doi.org/10.1021/acsomega.0c06194>
- Sztorch B, Pakuła D, Kustos M, Romaniczuk-Ruszk E, Gabriel E, Przekop RE. The Influence of Organofunctional Substituents of Spherosilicates on the Functional Properties of PLA/TiO<sub>2</sub> Composites Used in 3D Printing (FDM/FFF). *Polymers*. 2022;14(24):5493. <https://doi.org/10.3390/polym14245493>
- Sun Y, Zheng Z, Wang Y, Yang B, Wang J, Mu W. PLA composites reinforced with rice residues or glass fiber—a review of mechanical properties, thermal properties, and biodegradation properties. *Journal of Polymer Research*. 2022;29(10). <https://doi.org/10.1007/s10965-022-03274-1>
- Browne MP, Pumera M. Impurities in graphene/PLA 3D-printing filaments dramatically influence the electrochemical properties of the devices. *Chemical Communications*. 2019;55(58):8374–7. <https://doi.org/10.1039/c9cc03774h>
- Kjelgård KG, Wisland DT, Lande TS. 3D Printed Wideband Microwave Absorbers using Composite Graphite/PLA Filament. 48th European Microwave Conference (EuMC). Madrid Spain. 2018;859–862. <https://doi.org/10.23919/EuMC.2018.8541699>
- Jiang D, Ning F. Fused Filament Fabrication of Biodegradable PLA/316L Composite Scaffolds: Effects of Metal Particle Content. *Procedia Manufacturing*. 2020; 48, 755–762. <https://doi.org/10.1016/j.promfg.2020.05>
- Sakthivel N, Bramsch J, Young P, Swink I, Averick S, Vora HD. Investigation of 3D printed PLA-Stainless Steel Polymeric Composite through Fused Deposition Modeling based Additive Manufacturing Process for Biomedical Applications. *Medical devices & sensors*. 2020;00:e10080. <https://doi.org/10.1002/mds3.10080>
- Mohammadzadeh M, Lu H, Fidan I, Tantawi K, Gupta A, Hasanov S, Zhang Z, Alifui-Segbaya F, Rennie A. Mechanical and Thermal Analyses of Metal-PLA Components Fabricated by Metal Material Extrusion. *Inventions*. 2020;5(3):44. <https://doi.org/10.3390/inventions5030044>

30. Clarke AJ, Dickson A, Dowling DP. Fabrication and Performance of Continuous 316 Stainless Steel Fibre-Reinforced 3D-Printed PLA Composites. *Polymers* 2024; 16: (63).  
<https://doi.org/10.3390/polym16010063>
31. Clarke A, Dickson A, Dowling DP. Additive manufacturing of reinforced polymer composites with stainless steel fibre. *Proceedings of the 38th International Manufacturing Conference (IMC38) 2022-08-30*. University College Dublin. School of Mechanical and Materials Engineering;
32. Pušnik Črešnar K, Aulova A, Bikiaris DN, Lambropoulou D, Kuzmič K, Fras Zemljč L. Incorporation of Metal-Based Nanoadditives into the PLA Matrix: Effect of Surface Properties on Antibacterial Activity and Mechanical Performance of PLA Nanoadditive Films. *Molecules*. 2021;26(14):4161. <https://doi.org/10.3390/molecules26144161>
33. Raquez J-M, Habibi Y, Murariu M, Dubois P. Polylactide (PLA)-based nanocomposites. *Progress in Polymer Science*. 2013;38(10-11): 1504–1542. <https://doi.org/10.1016/j.progpolymsci.2013.05.014>
34. Xie Y, Hill CAS, Xiao Z, Militz H, Mai C. Silane coupling agents used for natural fiber/polymer composites: A review. *Composites Part A: Applied Science and Manufacturing*. 2010;41(7):806–19.  
<https://doi.org/10.1016/j.compositesa.2010.03.005>
35. Brząkalski D, Sztorch B, Frydrych M, Pakuła D, Dydek K, Kozera R, et al. Limonene Derivative of Spherosilicate as a Polylactide Modifier for Applications in 3D Printing Technology. *Molecules*. 2020;25(24):5882. <https://doi.org/10.3390/molecules25245882>
36. Shen C, Han Y, Wang B, Tang J, Chen H, Lin Q. Ocular biocompatibility evaluation of POSS nanomaterials for biomedical material applications. *RSC Advances*. 2015;5(66):53782–53788.  
<https://doi.org/10.1039/c5ra08668j>
37. Sztorch B, Brząkalski D, Pakuła D, Frydrych M, Špitalský Z, Przekop RE. Natural and Synthetic Polymer Fillers for Applications in 3D Printing—FDM Technology Area. *Solids*. 2022;3(3):508–548.  
<https://doi.org/10.3390/solids3030034>
38. Maciejewski H, Karasiewicz J, Marciniak B. Efektywna synteza fluorofunkcyjnych (poli)siloksanów. *Polimery*. 2012;57,6:449–55.
39. Dumitriu AC, Cazacu M, Bargan A, Balan M, Vornicu N, Varganici CD, et al. Full functionalized silica nanostructure with well-defined size and functionality: Octakis(3-mercaptopropyl)octasilsesquioxane. *Journal of Organometallic Chemistry*. 2015;799-800:195–200.  
<https://doi.org/10.1016/j.jorganchem.2015.09.025>
40. Feher FJ, Wyndham KD, Soulivong D, Nguyen F. Syntheses of highly functionalized cube-octameric polyhedral oligosilsesquioxanes (R<sub>8</sub>Si<sub>8</sub>O<sub>12</sub>). *Journal of the Chemical Society. Dalton Transactions*. 1999;(9):1491–8. <https://doi.org/10.1039/a807302c>
41. Pakuła D, Przekop R, Brząkalski D, Frydrych M, Sztorch B, Marciniak B. Sulfur-Containing Silsesquioxane Derivatives Obtained by the Thiol-ene Reaction: Synthesis and Thermal Degradation. *ChemPlusChem*. 2022;87:e202200099.  
<https://doi.org/10.1002/cplu.202200099>
42. Pakuła D, Sztorch B, Romańczuk-Ruszk E, Marciniak B, Przekop RE. High impact polylactide based on organosilicon nucleation agent. *Chinese Journal of Polymer Science*. 2024;42,787–797.  
<https://doi.org/10.1007/s10118-024-3095-7>
43. Kuentz L, Salem A, Singh M, Halbig MC, Salem JA. Additive Manufacturing and Characterization of Poly(lactic Acid) (PLA) Composites Containing Metal Reinforcements. *National Aeronautics and Space Administration*, <https://ntrs.nasa.gov/citations/20160010284>
44. Safandowska M, Róžański A, Gałęski A. Plasticization of Polylactide after Solidification: An Effectiveness and Utilization for Correct Interpretation of Thermal Properties. *Polymers*. 2020;12(3):561.  
<https://doi.org/10.3390/polym12030561>
45. Sztorch B, Romańczuk-Ruszk E, Gabriel E, Pakuła D, Kozera R, Przekop RE. Metal and metal oxide particles as modifiers for effective layer melting and Z-axis strength in 3D printing. *Polymer*. 2024;294:126684. <https://doi.org/10.1016/j.polymer.2024.126684>
46. Klecker C, Nair LS. Matrix Chemistry Controlling Stem Cell Behavior. *Biology and Engineering of Stem Cell Niches*. 2017;195–213.  
<https://doi.org/10.1016/b978-0-12-802734-9.00013-5>
47. Karasiewicz J, Dutkiewicz A, Maciejewski H. Fluorokarbofunkcyjne silany jako prekursorzy materiałów silnie hydrofobowych. *Chemik*. 2014;68(11): 945–956.
48. Weishuai Di, Wang X, Zhou Y, Mei Y, Wang W, Cao Y. Fluorination Increases Hydrophobicity at the Macroscopic Level but not at the Microscopic Level. *Chinese Phys. Lett*. 2022;39(3):038701.  
<https://doi.org/10.1088/0256-307X/39/3/038701>

Daria Pakuła:  <https://orcid.org/0000-0001-6741-3019>

Bogna Sztorch:  <https://orcid.org/0000-0001-5166-8391>

Eliza Romańczuk-Ruszk:  <https://orcid.org/0000-0001-5228-4920>

Bogdan Marciniak:  <https://orcid.org/0000-0001-5203-1376>

Robert E. Przekop:  <https://orcid.org/0000-0002-7355-5803>



This work is licensed under the Creative Commons  
BY-NC-ND 4.0 license.

## INFLUENCE OF PERFLUORODECALIN CONTENT ON THE PROPERTIES OF BLOOD SUBSTITUTE

Joanna MYSTKOWSKA<sup>\*</sup>, Gabriela PROKOPCZYK<sup>\*</sup>, Dawid ŁYSIK<sup>\*</sup>

<sup>\*</sup> Department of Biomaterials and Medical Devices, Institute of Biomedical Engineering, Białystok University of Technology  
 ul. Wiejska 45c, 15-351 Białystok, Poland

[j.mystkowska@pb.edu.pl](mailto:j.mystkowska@pb.edu.pl), [gabriela.prokopczyk@wp.pl](mailto:gabriela.prokopczyk@wp.pl), [d.lysik@pb.edu.pl](mailto:d.lysik@pb.edu.pl)

received 26 September 2023, revised 18 August 2024, accepted 19 August 2024

**Abstract:** Blood is a vital part of our circulatory system. It is responsible for transporting oxygen and nutrients, regulating body temperature, and fighting infections. However, any imbalances in blood composition or disruptions in the blood production process can affect the body's overall functioning. Anemia is one of the most common blood diseases diagnosed worldwide. It is characterized by a deficiency of red blood cells or hemoglobin, which reduces the body's ability to transport oxygen. To address this issue, researchers are developing blood substitutes with artificial oxygen carriers that can replace or support the natural function of red blood cells in oxygen transport. Perfluorocarbon-based oxygen carriers (PFCs) such as perfluorodecalin (PFD) are promising for treating severe blood disorders because they can deliver O<sub>2</sub> to tissues in various conditions. PFCs have higher storage stability than other oxygen carriers due to their bilayer sphere structure. In this study, we aimed to explore the effects of different concentrations of PFD (1%wt., 2%wt.) and storage time (7, 14, 21, 28 days) on the properties of blood substitutes, including its physicochemical (pH, surface tension, electrolytic conductivity, contact angle, redox potential, oxygen content) and rheological characteristics. The results show that the PFD concentration did not have a statistically significant effect on most of the tested properties, except for the oxygen content, which was higher for the 2%wt. solution after 28 days of incubation. The incubation time significantly impacts the change in surface tension, contact angle, redox potential, and oxygen content. The obtained results are essential due to the use of perfluorodecalin in medicine as an oxygen carrier.

**Key words:** artificial blood, perfluorodecalin, physicochemical properties, blood viscosity

### 1. INTRODUCTION

Blood is a liquid tissue that plays a vital role in the circulatory system, carrying out several essential functions. Blood plays a crucial role in maintaining homeostasis in the human body. Pleiotropic properties of blood provide many functions, such as delivery of necessary substances (such as nutrients and oxygen) to the body's cells, transport of waste products away from cells, immunological functions (circulation of white blood cells, detection of foreign material by antibodies), coagulation (body's self-repair mechanism), information functions (transport of hormones and the signaling of tissue damage) and regulation of body pH and temperature [1].

Blood comprises two primary components: liquid plasma and morphotic elements such as erythrocytes, lymphocytes, and platelets. Plasma, mostly made up of water, proteins, mineral salts, lipids, and glucose, is the primary component of blood and constitutes more than half of its volume [2]. Erythrocytes, also known as red blood cells, are the blood's most numerous morphotic elements, accounting for 44% of its volume. They have a disc-like shape flattened on both sides, which gives them a more favorable surface-to-volume ratio for gas exchange. Erythrocytes are blood cells that contain hemoglobin and non-hemoglobin proteins [3]. Hemoglobin is made up of two components: globin and heme. Globin is composed of four polypeptide chains that are held together by ionic bonds. On the other hand, heme is a pigment consisting of four pyrrole rings with an iron atom at its center. This iron atom binds with oxygen or carbon dioxide to transport them throughout the

body. The production of erythrocytes occurs mainly in the bone marrow and spleen. However, any disruptions to the blood production process can affect the body's functioning.

Anemia is one of the most commonly diagnosed blood diseases affecting people worldwide [4]. It is characterized by a deficiency of red blood cells or hemoglobin, which results in a decreased ability of the body to transport oxygen. The treatment methods for anemia vary depending on the severity and underlying cause of the disease. Oral or intravenous iron supplementation is usually the preferred treatment for iron deficiency anemia. Transfusion therapies or bone marrow transplantation may be necessary for other types of anemia. Despite advances in our understanding of blood diseases and the development of new drugs, treating hematological diseases remains a significant challenge for medical professionals.

Additionally, due to the aging population and other factors, there is a growing need for more blood donors [5]. An alternative to conventional methods of treating blood diseases is artificial blood products. Jägers et al. [6] rightly note that interdisciplinary cooperation is needed. For this reason, numerous works have been done to develop blood substitutes that can support or replace blood in performing its functions [7–9]. Their primary purpose is to ensure oxygen transport by artificial oxygen carriers (AOCs). AOCs are essential in managing blood conditions for patients with serious illnesses. The primary types of AOCs are Hemoglobin-based Oxygen Carriers (HBOCs) [10] and Perfluorocarbon-based Oxygen Carriers (PFCs) [11]. The former refers to the covalent linkage of oxygen and Hb, while the latter involves oxygen dissolution within



a perfluorocarbon (PFC) [12]. HBOCs were first tested in the 1930s using cell-free hemoglobin on a cat with renal toxicity by Amberson et al. [13]. The first modified HBOC, HemAssist, was licensed in 1985, followed by Polyheme, a polymerized Hb clinically developed in 1996 [14]. The concept of PFCs as oxygen carriers started in 1966. A human serum albumin-derived PFC-based AOC, considered a cutting-edge technology [15], was utilized in various in vivo studies and began in 2017 [16]. Since then, work has been underway to obtain a stable albumin-perfluorocarbon emulsion [17].

PFCs dissolve respiratory gases like oxygen, CO, CO<sub>2</sub>, and NO [6]. When both PFC and RBC are present in the circulation, PFC protects Hb-bound oxygen until it reaches hypoxic tissues [18]. PFCs are more resilient than AOCs to pH and temperature changes. They are not affected by pharmacological, environmental, and chemical changes. PFCs are chemically resistant to heat and do not undergo metabolic transformation in vivo, making them safer than HBOCs as AOCs. HBOCs tend to have side effects such as immune reactions, high blood pressure, and a short half-life [19]. The advantages of PFCs are their long shelf-life and ability to penetrate small blood vessels and arterial blockages for oxygen transport [20]. PFCs have higher storage stability than other oxygen carriers due to their bilayer sphere structure, where there is a PFC-nucleus in the center. A shell around this surface is a thin layer of surfactant. The stability of PFC emulsions depends on the sample surface layer elasticity of the surfactant around the particles [19]. A good example of this group is perfluorodecalin (PFD), a type of PFC, a hydrocarbon-based compound in which all hydrogen atoms are replaced by fluorine atoms (Fig. 1).

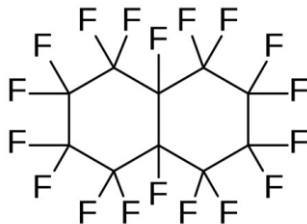


Fig. 1. The structural formula of perfluorodecalin

To the best of our knowledge, no publications have assessed the individual impact of PFDs on synthetic blood preparations' physicochemical and rheological properties. The work aimed to verify the effects of PFD on the properties of artificial blood, including its chemical, physical, and rheological characteristics. The original chemical compositions of the blood solutions were selected experimentally.

## 2. MATERIALS AND METHODS

### 2.1. Perfluorodecalin-based artificial blood solutions

Based on the literature [21], a base solution imitating human plasma was developed (Tab. 1). Organic ingredients (e.g., glucose, albumin, glycerin, cholesterol) and inorganic ingredients (inorganic salts) were dissolved in deionized water. The organic components were used as emulsifiers, cryoprotectants, and consistency modifiers. Their role is to maintain the osmotic pressure, ensure appropriate viscosity, and prevent the formation of clots. Inorganic salts regulate ionic balance, pH, and osmotic pressure.

Then, 1%wt. or 2%wt. perfluorodecalin (PFD) (samples indicated as 1PFD and 2PFD respectively) was added into the plasma solution (control sample indicated as C). Then, the 100  $\mu$ L of each sample was vortexed for 30 s to obtain a homogeneous solution. The prepared samples were stored static in a refrigerator at 2°C.

Tab. 1. Composition of the base solution imitating human plasma

Ingredient	Concentration (g/L)	Function
water	920	solvent
albumin	57	emulsifier, maintaining osmotic pressure
glycerine	8	cryoprotectant, ensuring appropriate viscosity
glucose	1	nutritional properties
cholesterol	4.5	preventing the formation of clots, regulating blood pressure
cholesterol oleate	1.5	emulsifier, viscosity regulator
NaCl	5.2	ionic balance, pH, and osmotic pressure constancy
NaHCO <sub>3</sub>	1.8	ionic balance, pH, and osmotic pressure constancy
MgCl <sub>2</sub>	0.38	ionic balance, pH, and osmotic pressure constancy
CaCl <sub>2</sub>	0.33	ionic balance, pH, and osmotic pressure constancy
KCl	0.30	ionic balance, pH, and osmotic pressure constancy

### 2.2. Physicochemical and rheological tests

The study tested an artificial blood that contained varying concentrations of perfluorodecalin. The physicochemical and rheological properties of the preparations were tested at different intervals after their preparation (0, 7, 14, 21, and 28 days). The measurements were conducted at a laboratory temperature of 23°C using various instruments, including the SevenMulti (Mettler Toledo, Columbus, OH, USA) multifunctional ionconductometer for pH, conductivity, and redox potential measurements. The Oxygen Meter CO-105 electrode (Elmetron, Poland) was used for oxygen concentration testing and the STA1 tensiometer for surface tension analysis. The Contact Angle Goniometer (Ossila, UK) determined the tested preparations' contact angle ( $\theta$ ) in contact with PDMS surface. The viscosity tests were performed using the HAAKE Rheostress 6000 rheometer (Thermo Fisher Scientific, Waltham, MA, USA) with plate-plate (35 mm diameter) system in a shear rate range of 10 to 200 1/s in 37°C. All measurements were conducted five times for each case. The study aimed to determine whether perfluorodecalin and storage time impacted the properties of artificial plasma preparations.

The statistical analysis was performed using Statistica software (TIBCO Statistica® software version 14.0.1, Palo Alto, CA, USA). The average value and standard deviation were calculated based on the results obtained from at least five repeatable test attempts under the same conditions. The results are presented as mean value  $\pm$  SD. One-way ANOVA tests were used to analyze the statistical significance of differences.

### 3. RESULTS

Analysis of pH test results (Fig. 2a) indicates that up to 2% of PFD content in artificial plasma preparations does not significantly affect the pH value. It was observed that the pH of tested samples (7.41-7.43) was within the pH range of natural blood (pH = 7.35-7.43, Tab. 2) for up to 7 days from preparing blood substitutes. Static storage of prepared solutions increases the pH to 7.5-7.6, 7.59-7.65, 7.43-7.67 after 14, 21, and 28 days for tested preparations, respectively. The electrolytic conductivity value of tested PFD-based blood preparations was in the range  $\kappa = 11.7 - 12.7$  mS/cm (Fig. 2b), within the physiological range. We observed significant differences ( $p < 0.05$ ) in freshly prepared solutions between C ( $\kappa = 11.7 \pm 1.1$  mS/cm), 1PFD ( $\kappa = 12.3 \pm 1.1$  mS/cm), and 2PFD ( $\kappa = 12.4 \pm 1.0$  mS/cm). The electrolytic conductivity did not change significantly until 14 days after their preparation. The surface tension results (as shown in Fig. 2c) indicate that this parameter for the tested solutions increased over time. On day 0, the surface tension was approximately  $\sigma = 35$  mN/m, while after 28 days of storage, it increased to approximately  $\sigma = 55$  mN/m. The greatest surface tension increase was observed during the first week of incubation, where it increased to about 50 mN/m, which was statistically significant ( $p < 0.05$ ). In the case of the contact angle values (Fig. 2d), the lowest values were also obtained on day 0. The contact angle for the control sample ( $\theta = 7.7 \pm 0.2^\circ$ ) was statistically lower ( $p < 0.05$ ) in comparison to 1PFD ( $\theta = 28.3 \pm 0.8^\circ$ ) and 2PFD ( $\theta = 29.6 \pm 0.9^\circ$ ). Even 1%wt. addition of PFD statistically influences this parameter. On day 7, the contact angles increased to  $\theta = 48^\circ - 55^\circ$  and were similar to the preparations tested after 14 days. The values were statistically higher ( $p < 0.05$ ) than those obtained after 7 days of storage. Then, the contact angle increased, and the highest angle value ( $\theta \sim 60^\circ$ ) was obtained after 28 days of storage, which was statistically higher than the contact angle measured after 7 days of incubation.

The redox potential data (Fig. 3a) show that all values were positive, meaning that tested solutions have oxidizing properties. The redox potential was in the  $E = 160-169$  mV range on their preparation day. The highest redox potential ( $E = 213 \pm 4$  mV) was obtained for sample 2PFD after 7 days of incubation and was statistically higher ( $p < 0.05$ ) in comparison to the control sample and solution with 1%wt. of PFD addition, which was  $E = 190 \pm 4$  mV. The lowest values ( $E = 90-120$  mV) were obtained on day 14 for the tested samples. The redox potential increased until day 7, then decreased significantly on day 14 and increased again during measurements on day 21. After 28 days, the redox potential for the control sample and PFD-based solutions was in the  $E = 130-140$  mV range. It was statistically lower than solutions tested on their preparation day and after 7 days of storage.

The oxygen concentration results shown in Fig. 3b indicate that the increase in PFD content and the duration of storage of artificial blood solutions are directly proportional to the increase of this parameter for the developed substitutes. On the day of solution preparation, the lowest oxygen content ( $5.67 \pm 0.31$  mg/L) was observed for the control solution (Fig. 3b). For the PFD-based preparations, the oxygen content for 1PFD and 2PFD was  $\sim 7.5$  mg/L and  $\sim 8.1$  mg/L, respectively, and were statistically higher than the solution without PFD addition. After 28 days of storage, the oxygen concentration increased for all tested solutions, and in the case of the sample without PFD and for samples 1PFD and 2PFD, this parameter was  $6.66 \pm 0.31$  mg/L,  $10.12 \pm 0.5$  mg/L, and  $11.66 \pm 0.58$  mg/L, respectively. The oxygen content after 28 days for tested PFD-base

solutions was statistically higher than that of the control sample. The highest oxygen concentration ( $\sim 11.66 \pm 0.58$  mg/L) was obtained for sample 2PFD after 28 days of storage and was statistically higher than that of sample 2PFD tested after 7 days of incubation.

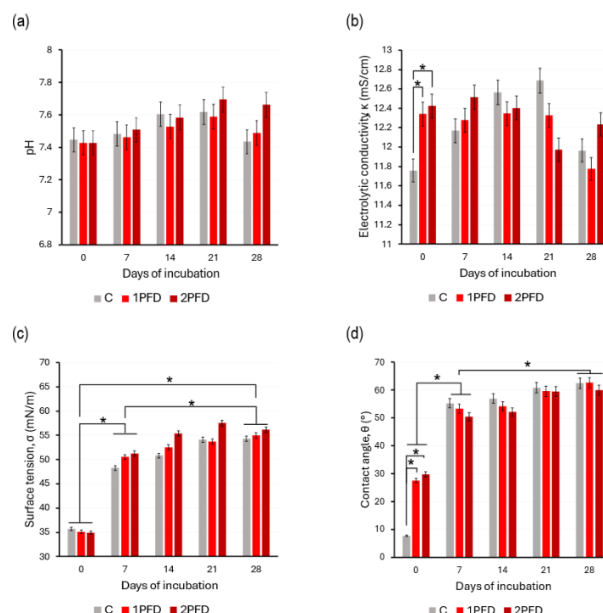


**Fig. 2.** Results of a) pH, b) electrolytic conductivity, c) surface tension, and d) contact angle measurements for perfluorodecalin-based solutions after 7, 14, 21, and 28 days. Mean values with  $\pm$  standard deviation for 5 measurements are presented. The abbreviations C, 1PFD, and 2PFD denote control samples containing no PFD and samples containing 1% and 2% PFD, respectively. (\*) statistically significant differences  $p < 0.05$

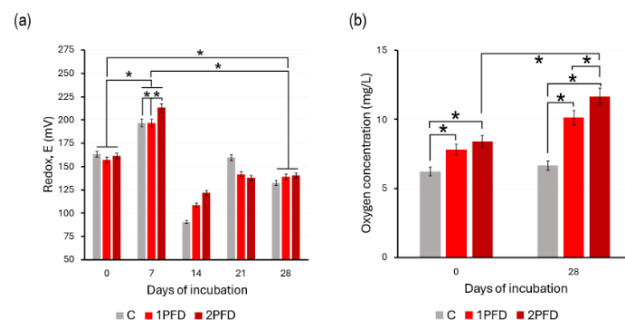


**Fig. 3.** Results of (a) redox potential (after 7, 14, 21, and 28 days); and (b) oxygen content measurements (after 28 days) for perfluorodecalin-based solutions. Mean values with  $\pm$  standard deviation for 5 measurements are presented. The abbreviations C, 1PFD, and 2PFD denote control samples containing no PFD and samples containing 1% and 2% PFD, respectively. (\*) statistically significant differences  $p < 0.05$

Viscosity tests (Fig. 4) showed that the obtained preparations are non-Newtonian, pseudoplastic fluids, just like natural blood. For all solutions tested on the day of preparation (Fig. 4a), the viscosity was in the range of  $\eta = 2.2-2.8$  mPas at the shear rate  $\dot{\gamma} \geq 60$  s<sup>-1</sup>. After 28 days of storage, the viscosity for control samples was about  $\eta \sim 3$  mPas, and for PFD-based solutions was in the range of  $\eta \sim 2-2.2$  mPas at the shear rate  $\dot{\gamma} \geq 60$  s<sup>-1</sup>. The dynamic viscosity values are similar to those of natural blood or plasma ( $\eta \sim 2-$

5 mPas) in the entire range of tested shear rates tested, without incubation and after 28 days of storage. Moreover, PFD had no visible effect on the viscosity of non-incubated samples, but after 28 days of incubation, the PFD reduced the viscosity.

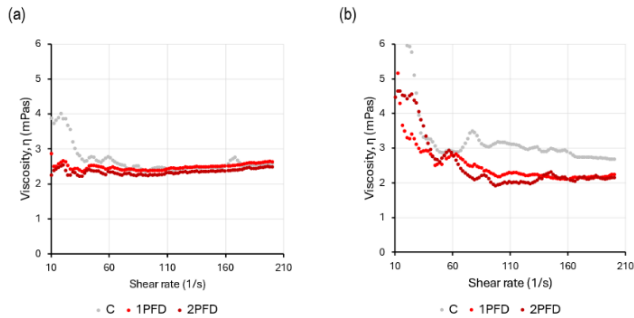


**Fig. 4.** Results of viscosity measurements for perfluorodecalin-based solutions: (a) with no incubation; (b) after 28 days of incubation. Mean values for 5 measurements are presented. The abbreviations C, 1PFD, and 2PFD denote control samples containing no PFD and samples containing 1% and 2% PFD, respectively

#### 4. DISCUSSION

The result of impaired function of the natural blood is a pathogenesis of various disorders. Treatment of blood disorders involves pharmacological therapy or replacement therapy, which is based on the use of artificial substitutes. However, no blood substitutes meet the biological criteria and maintain favorable physicochemical properties and rheological parameters. Directions for improving the biofunctional properties of such preparations should consider their chemical modification. This mainly concerns oxygen carriers, where selecting their type and concentration will enable obtaining a biocompatible preparation. Appropriate selection of artificial blood ingredients makes it possible to influence the kinetics and mechanism of oxygen transport and properties similar to natural blood (Tab. 2). It is also responsible for modifying the biofunctional properties of blood and, concerning the subject of the work, physicochemical and rheological characteristics.

**Tab. 2.** Human blood parameters [22–25]

Parameter	Value
color	red
smell	specific, metallic
taste	sweet and salty
pH	7.35-7.43
osmotic pressure	300 mOsm/L
oxygen capacity	20.1 ml O <sub>2</sub> / 100 ml blood
surface tension	53.45-55.35 mN/m
electrolytic conductivity	10-20 mS/cm
contact angle	40-75°
viscosity	3.5-5.5 mPas

The pH values of tested preparations are 7.41-7.67 during the tested period. The pH of own-prepared blood substitutes increased with time and was higher for higher PFD content. After 28 days of storage, the pH of the tested preparations decreased. The optimal pH value of human blood is in the range of 7.35-7.43 (Table 2),

which is of great biological importance because even slight changes in the acidic or alkaline direction can lead to disturbances in many physiological processes, including the functioning of the nervous system, causing disturbances in consciousness, convulsions, enzyme functioning, and substance transport. Responsible for the stability of hydrogen ions include, among others, carbon dioxide (CO<sub>2</sub>), sodium bicarbonate (NaHCO<sub>3</sub>), sodium salts of phosphoric acid (Na<sub>2</sub>HPO<sub>4</sub>, NaH<sub>2</sub>PO<sub>4</sub>), plasma proteins, and hemoglobin. Lowering the pH value of blood may result in an increased breathing rate to remove excess carbon dioxide, which, together with water, forms acid anhydride, which lowers the pH value. The human blood pH values below 6.8 and above 7.8 can be fatal, as many metabolic processes are disturbed [26]. The obtained results indicate the need to modify the composition of blood products to get a solution with a lower initial pH and better buffering properties.

Natural blood, as a liquid based on water and different electrolytes, has conductivity in the range of  $\kappa = 10 - 20$  mS/cm (Table 2). Electrolytes, especially Na<sup>+</sup>, K<sup>+</sup>, Ca<sup>2+</sup>, Mg<sup>2+</sup>, Cl<sup>-</sup>, and HCO<sub>3</sub><sup>-</sup>, properly conduct electrical impulses in nerves and muscles. Due to electrolytic conductivity, blood can maintain an osmotic balance. Blood's osmotic pressure is related to the concentration of electrolytes in the blood, particularly Na<sup>+</sup> and K<sup>+</sup> ions and plasma proteins [26], and is approximately 300 mOsm/L (Table 2). However, it is characterized by slight fluctuations related to food and drink intake. The values of electrolytic conductivity (11.7-12.7 mS/cm) for tested substitutes determine increased ionic activity. We think this might positively influence ions' transport and diffusion (penetration), which is essential from the point of view of blood functions [27].

The value of blood surface tension depends on the type of food consumed and the amount of fluids. A diet high in fat reduces, while protein-rich increases its value. On average, the surface tension of natural blood is  $\sigma = 53.45-55.35$  mN/m (Table 2) and is slightly higher in women than in men, because of less RBC accumulation and less hematocrit [28]. The measured surface tension values for tested preparations (~55 mN/m) are lower but get closer to this result over time. Surfactants decrease, and inactive agents increase the surface tension of liquids. Surface-active compounds include hydrophilic (e.g., OH) and hydrophobic (e.g., CH<sub>3</sub>) groups. Such substances in the developed preparation include glucose, albumin, glycerin, and cholesterol. Ionic compounds are mainly responsible for increasing their value, i.e., the salts NaCl, NaHCO<sub>3</sub>, MgCl<sub>2</sub>, CaCl<sub>2</sub>, and KCl. The increasing surface tension value may be related to the progressive dissociation of these salts. This property is also fundamental in the breathing process because the appropriate surface tension of blood in the alveoli is essential for proper gas exchange. Due to surface tension properties, the alveoli are kept open, facilitating oxygen absorption into the blood and the release of carbon dioxide. Surface tension also helps maintain the integrity of the blood clot [29–31].

In the literature (Table 2), the value of the blood contact angle is in the range  $\theta = 40-75^\circ$ , depending on the material used for tests [32–34]. This means that blood has good wetting properties so blood cells can adhere well to the vessel walls during clot formation. The wettability angle of blood depends on the type of surface used for tests. The results obtained in this work on day 0 ( $\theta \sim 29^\circ$ ) are lower than those in the literature, while those obtained for 7-28 days ( $\theta \sim 60^\circ$ ) are similar to natural blood. The obtained results of the contact angle measurement indicate that the storage time of the obtained solutions affect the increase of the value of this parameter. The contact angle of the tested solutions increased with time, which may indicate condensation [35]. However, no effect of PFD concentration on the contact angle value was observed. The contact angle

values are similar to the values of natural blood ( $\theta > 40^\circ$ ) observed after 7 days from the moment of preparation and increase to approx.  $\theta \sim 60^\circ$  after 28 days, which is still within the physiological values. Contact angle tests showed values lower than  $\theta = 90^\circ$ , which means that the tested solutions are characterized by good wettability. This property is advantageous because it might reduce the friction between the walls of blood vessels and the flowing fluid.

The tested samples' redox potential ( $E = 75.1\text{--}213.1$  mV) increases until day 7, then decreases on day 14 and increases again. This may indicate that an oxidation reaction has occurred in the tested solutions, as all results are positive. The differences between the solutions are low, meaning that PFD does not affect the redox potential value. This is related to the oxidation and reduction reactions in the tested solutions, resulting from their chemical composition and pH value. These changes may be related to oxidation-reduction reactions between glucose characterized by reducing properties and metal ions, such as  $\text{Mg}^{2+}$  or  $\text{Ca}^{2+}$ , which are electron acceptors. These reactions can affect the redox potential by changing ion concentrations [36, 37].

The oxygen concentration of the solutions increases with increasing PFD content and storage time. The perfluorodecalin (C10F18) is characterized by high oxygen-carrying capacity, dissolving 49 ml of oxygen per 100 ml of PFD, almost 40% more than water or plasma. Kim et al. [38] stated that PFCs-based blood substitutes can dissolve 40 to 70% of oxygen at room temperature. This binding capacity results from fluorine's low polarizability and the ability of perfluorodecalin (C10F18) to form complexes with oxygen through electrostatic and dipole interactions [39]. The fluorine atoms in perfluorodecalin molecules have a partially negative electrical charge that attracts partially positively charged oxygen molecules. As a result of these interactions, a complex is formed (perfluorodecalin oxide - C10F18O), in which perfluorodecalin molecules surround the oxygen molecule. Fluosol-DA is a PFC-based blood substitute that can carry oxygen. Its emulsion contains 14% perfluorodecalin and 6% perfluorotripropylamine. However, its oxygen-carrying capacity is only 7.2% at  $37^\circ\text{C}$ , which is lower than RBCs [40]. Experimental studies using Flucosol-DA doses of 20–500 mL demonstrated no negative effects (side effects) on the heart, liver, kidneys, and hematological function [41]. However, one of the problems is the poor stability of this product, so it must be modified by other ingredients. In the presented work, we examined the effect of deficient PFD concentrations to assess the impact on individual physicochemical properties, which have been evaluated using various methods over the years. According to our results, achieving oxygen concentration in the blood substitute similar to natural blood requires using much higher PFC concentrations of PFCs. An example of a widely tested blood substitute is the Perforan, which contains PFD and FMCP as the PFCs. However, its composition can be problematic and decrease the stability of the emulsion to approximately one month at  $4\text{--}8^\circ\text{C}$ , which is too short to be used as a blood substitute [42]. Thus, second-generation PFCs were developed to eliminate the problems of first-generation products, taking into account the nature and content of the fluorocarbons, which are 2 to 4 times higher in comparison to first-generation PFCs products. Also, they use natural phospholipids as an emulsifier instead of a water-soluble emulsifier and should be stored without freezing [43].

Blood is a stable suspension composed of plasma and solid substances with anti-adhesive properties. The circulatory system can be compared to the capillary system, and blood is classified as a non-Newtonian fluid with thixotropic and viscoelastic properties [44]. Blood viscosity depends on temperature, degree of hydration,

number of blood cells, and the diameter of the vessel through which it flows. Viscosity is a fundamental property because it influences blood flow through blood vessels, thus the transport of oxygen and nutrients. The increase in viscosity may lead to the formation of clots and place a heavy burden on the heart muscle, causing cardiovascular diseases [45, 46]. The plasma solutions prepared using PFD are non-Newtonian, shear-thinning fluids with a viscosity similar to that of blood. However, these liquids are structurally different, and the rheological behavior of whole blood results from different phenomena. Human blood plasma is a Newtonian fluid with a viscosity of  $1.2$  mPa·s at  $37^\circ\text{C}$ . The presence of a second phase, mainly composed of RBCs, is responsible for the non-Newtonian behavior of whole blood [47]. RBC aggregation causes a significant increase in viscosity at low shear rates. Additionally, fibrinogen and globular proteins present in plasma promote RBC aggregation. Shear stress breaks up the RBC clusters bound by these proteins, resulting in reduced viscosity at higher shear rates. At even higher shear rates, only individual cells remain from the aggregates, which deform at critical shear rates above  $100$  1/s, leading to a further reduction in viscosity [48]. The artificial blood studied in this work is a two-phase composition of molecules without cellular elements. Shear-thinning arises from the agglomeration of molecules at lower shear rates, the breaking of these aggregates, and the formation of shear planes at higher shear rates, resulting in decreased viscosity [49]. Concurrently, short-lived clusters/inhomogeneities form due to the emulsive nature of the PFD-solutions in water, causing temporary increases in viscosity.

PFD, along with other elements in the plasma, are not soluble or only slightly soluble in water, thus necessitating proper emulsification. The decline in solution stability can be seen as a rise in solution viscosity at low shear rates, a change we noted after 28 days of incubation. The increase in viscosity caused by solution stability loss was noted in highly concentrated PFD solutions (34%) [50]. A potential remedy for emulsion instability is creating a nanoemulsion through ultrasonication with surfactants Tween 80 and (1H, 1H, 2H, 2H-perfluorooctyl)phosphocholine [51].

## 5. CONCLUSIONS

A vital impulse for developing artificial blood preparations is the need for an alternative form of patient treatment when traditional transfusion is impossible or involves risk. Moreover, these preparations may be used in rescue situations. The physicochemical and rheological properties of the tested perfluorodecalin-based preparations are similar to those of natural blood and should be safe for humans. The electrolytic conductivity changes over time due to the formation of complexes by ions in the solutions, but it is in the natural blood conductivity range. This means the prepared solutions allow the proper exchange of ions between blood and tissues, and PFD does not affect the values of this property—the surface tension increases with higher PFD content. The contact angle increases over time but is lower than  $\theta = 90^\circ$ , proving good wetting properties. The results demonstrate that perfluorodecalin is a neutral compound that does not significantly affect the tested properties of prepared blood substitutes but only increases the concentration of oxygen dissolved in them. These features are essential due to the use of perfluorodecalin in medicine as an oxygen carrier. The obtained results may encourage further experimental research by using higher concentrations of PFD oxygen carriers and other oxygen carriers to find any synergetic effects, aiming to develop a safe



oxygen-carrying agent that can be used by patients requiring this type of supportive therapy.

## REFERENCES

- Alexy T, Detterich J, Connes P, Toth K, Nader E, Kenyeres P, et al. Physical Properties of Blood and their Relationship to Clinical Conditions. *Front Physiol* [Internet]. 2022; 13. Available from: <https://www.frontiersin.org/articles/10.3389/fphys.2022.906768/full>
- Yuyen T. Composition of Blood. In: *Transfusion Practice in Clinical Neurosciences*. 2022.
- Pretini V, Koenen MH, Kaestner L, Fens MHAM, Schiffelers RM, Bartels M, et al. Red blood cells: Chasing interactions. *Frontiers in Physiology*. 2019.
- Stevens GA, Paciorek CJ, Flores-Urrutia MC, Borghi E, Namaste S, Wirth JP, et al. National, regional, and global estimates of anaemia by severity in women and children for 2000–19: a pooled analysis of population-representative data. *Lancet Glob Health*. 2022;10(5).
- Lattimore S, Wickenden C, Brailsford SR. Blood donors in England and North Wales: Demography and patterns of donation. *Transfusion (Paris)*. 2015; 55(1).
- Jägers J, Wrobeln A, Ferenz KB. Perfluorocarbon-based oxygen carriers: from physics to physiology. *Pflugers Archiv European Journal of Physiology*. 2021.
- Spahn DR, Casutt M. Eliminating blood transfusions: New aspects and perspectives. *Anesthesiology*. 2000.
- Grzegorzewski W, Mil E, Golda K, Czerniecka-Kubicka A, Puchala Ł. Progress in the search for blood substitutes, part 1. Preparations currently used in haemotherapy as an indicator of new drug development. *Farm Pol*. 2022;78(8).
- Jahr JS. Blood substitutes: Basic science, translational studies and clinical trials. *Front Med Technol* [Internet]. 2022; 4. Available from: <https://www.frontiersin.org/articles/10.3389/fmedt.2022.989829/full>
- Charbe NB, Castillo F, Tambuwala MM, Prasher P, Chellappan DK, Carreño A, et al. A new era in oxygen therapeutics? From perfluorocarbon systems to haemoglobin-based oxygen carriers. *Blood Rev* [Internet]. 2022; 54:100927. Available from: <https://linkinghub.elsevier.com/retrieve/pii/S0268960X22000017>
- Krafft MP, Riess JG. Therapeutic oxygen delivery by perfluorocarbon-based colloids. *Adv Colloid Interface Sci* [Internet]. 2021; 294:102407. Available from: <https://linkinghub.elsevier.com/retrieve/pii/S0001868621000488>
- Ferenz KB, Steinbicker AU. Artificial oxygen carriers—past, present, and future—a review of the most innovative and clinically relevant concepts. *Journal of Pharmacology and Experimental Therapeutics*. 2019.
- Amberson WR, Mulder AG, Steggerda FR, Flexner J, Pankratz DS. Mammalian Life Without Red Blood Corpuscles. *Science* (1979) [Internet]. 1933; 78(2014):106–7. Available from: <https://www.science.org/doi/10.1126/science.78.2014.106>
- Gould SA, Moss GS. Clinical Development of Human Polymerized Hemoglobin as a Blood Substitute. *World J Surg* [Internet]. 1996; 20(9):1200–7. Available from: <https://onlinelibrary.wiley.com/doi/10.1007/s002689900183>
- Mohanto N, Park Y-J, Jee J-P. Current perspectives of artificial oxygen carriers as red blood cell substitutes: a review of old to cutting-edge technologies using in vitro and in vivo assessments. *J Pharm Investig* [Internet]. 2023; 53(1):153–90. Available from: <https://link.springer.com/10.1007/s40005-022-00590-y>
- Wrobeln A, Laudien J, Groß-Heitfeld C, Linders J, Mayer C, Wilde B, et al. Albumin-derived perfluorocarbon-based artificial oxygen carriers: A physico-chemical characterization and first in vivo evaluation of biocompatibility. *European Journal of Pharmaceutics and Biopharmaceutics* [Internet]. 2017; 115:52–64. Available from: <https://linkinghub.elsevier.com/retrieve/pii/S0939641116305173>
- Jaegers J, Haferkamp S, Arnolds O, Moog D, Wrobeln A, Nocke F, et al. Deciphering the Emulsification Process to Create an Albumin-Perfluorocarbon-(o/w) Nanoemulsion with High Shelf Life and Bioresistivity. *Langmuir*. 2021.
- Bodewes SB, Leeuwen OB van, Thorne AM, Lascaris B, Ubbink R, Lisman T, et al. Oxygen Transport during Ex Situ Machine Perfusion of Donor Livers Using Red Blood Cells or Artificial Oxygen Carriers. *Int J Mol Sci* [Internet]. 2020; 22(1):235. Available from: <https://www.mdpi.com/1422-0067/22/1/235>
- Lambert E, Gorantla VS, Janjic JM. Pharmaceutical design and development of perfluorocarbon nanocolloids for oxygen delivery in regenerative medicine. *Nanomedicine*. 2019.
- Haldar R, Gupta D, Chitranshi S, Singh MK, Sachan S. Artificial Blood: A Futuristic Dimension of Modern Day Transfusion Sciences. *Cardio-vasc Hematol Agents Med Chem*. 2019;17(1).
- Alayash AI. Hemoglobin-based blood substitutes and the treatment of sickle cell disease: More harm than help? *Biomolecules*. 2017.
- Connes P, Alexy T, Detterich J, Romana M, Hardy-Dessources MD, Ballas SK. The role of blood rheology in sickle cell disease. *Blood Rev*. 2016; 30(2).
- Alexy T, Detterich J, Connes P, Toth K, Nader E, Kenyeres P, et al. Physical Properties of Blood and their Relationship to Clinical Conditions. *Frontiers in Physiology*. 2022.
- Woodcock JP. Physical properties of blood and their influence on blood-flow measurement. *Reports on Progress in Physics*. 1976; 39(1).
- James SH, Kish PE, Sutton TP. Biological and Physical Properties of Human Blood. In: *Principles of Bloodstain Pattern Analysis*. 2021.
- Kawthalkar S. Essentials of Haematology. *Essentials of Haematology*. 2013.
- Chintapalli M, Timachova K, Olson KR, Mecham SJ, Devaux D, DeSimone JM, et al. Relationship between Conductivity, Ion Diffusion, and Transference Number in Perfluoropolyether Electrolytes. *Macromolecules* [Internet]. 2016; 49(9):3508–15. Available from: <https://pubs.acs.org/doi/10.1021/acs.macromol.6b00412>
- Yadav SS, Sikarwar BS, Ranjan P, Janardhanan R, Goyal A. Surface tension measurement of normal human blood samples by pendant drop method. *J Med Eng Technol* [Internet]. 2020; 44(5):227–36. Available from: <https://www.tandfonline.com/doi/full/10.1080/03091902.2020.1770348>
- Gersh KC, Nagaswami C, Weisel JW. Fibrin network structure and clot mechanical properties are altered by incorporation of erythrocytes. *Thromb Haemost*. 2009;102(6).
- He D, Kim DA, Ku DN, Hu Y. Viscoporoelasticity of coagulation blood clots. *Extreme Mech Lett*. 2022; 56.
- Litvinov RI, Weisel JW. Blood clot contraction: Mechanisms, pathophysiology, and disease. *Res Pract Thromb Haemost*. 2023; 7(1).
- Pitts KL, Abu-Mallouh S, Fenech M. Contact angle study of blood dilutions on common microchip materials. *J Mech Behav Biomed Mater*. 2013;17.
- Wang Z, Paul S, Stein LH, Salemi A, Mitra S. Recent Developments in Blood-Compatible Superhydrophobic Surfaces. *Polymers*. 2022.
- Pal A, Gope A, Iannacchione G. Temperature and concentration dependence of human whole blood and protein drying droplets. *Biomolecules*. 2021;11(2).
- Gokhale SJ, Plawsky JL, Wayner PC. Experimental investigation of contact angle, curvature, and contact line motion in dropwise condensation and evaporation. *J Colloid Interface Sci* [Internet]. 2003; 259(2):354–66. Available from: <https://linkinghub.elsevier.com/retrieve/pii/S0021979702002138>
- Podolean I, Fergani MEI, Candu N, Coman SM, Parvulescu VI. Selective oxidation of glucose over transitional metal oxides based magnetic core-shell nanoparticles. *Catal Today* [Internet]. 2023; 423:113886. Available from: <https://linkinghub.elsevier.com/retrieve/pii/S0920586122003327>
- Carter DE. Oxidation-reduction reactions of metal ions. *Environ Health Perspect* [Internet]. 1995; 103(suppl 1):17–9. Available from: <https://ehp.niehs.nih.gov/doi/10.1289/ehp.95103s117>
- Kim J-H, Jung E-A, Kim J-E. Perfluorocarbon-based artificial oxygen carriers for red blood cell substitutes: considerations and direction of technology. *J Pharm Investig* [Internet]. 2024; 54(3):267–82. Available from: <https://link.springer.com/10.1007/s40005-024-00665-y>

39. Li S, Pang K, Zhu S, Pate K, Yin J. Perfluorodecalin-based oxygenated emulsion as a topical treatment for chemical burn to the eye. *Nat Commun* [Internet]. 2022; 13(1):7371. Available from: <https://www.nature.com/articles/s41467-022-35241-1>
40. Moradi S, Jahanian-Najafabadi A, Roudkenar MH. Artificial Blood Substitutes: First Steps on the Long Route to Clinical Utility. *Clin Med Insights Blood Disord* [Internet]. 2016; 9:CMBD.S38461. Available from: <http://journals.sagepub.com/doi/10.4137/CMBD.S38461>
41. Habler OP, Messmer KF. Tissue perfusion and oxygenation with blood substitutes. *Adv Drug Deliv Rev* [Internet]. 2000; 40(3):171–84. Available from: <https://linkinghub.elsevier.com/retrieve/pii/S0169409X99000484>
42. Riess JG. The Design and Development of Improved Fluorocarbon-Based Products for use in Medicine and Biology. *Artificial Cells, Blood Substitutes, and Biotechnology* [Internet]. 1994; 22(2):215–34. <http://www.tandfonline.com/doi/full/10.3109/10731199409117416>.
43. Kuznetsova IN. Perfluorocarbon emulsions: Stability in vitro and in vivo (A review). *Pharmaceutical Chemistry Journal*. 2003.
44. Nader E, Skinner S, Romana M, Fort R, Lemonne N, Guillot N, et al. Blood Rheology: Key Parameters, Impact on Blood Flow, Role in Sickle Cell Disease and Effects of Exercise. *Front Physiol* [Internet]. 2019; 10(OCT). Available from: <https://www.frontiersin.org/article/10.3389/fphys.2019.01329/full>
45. Shaik A, Chen Q, Mar P, Kim H, Mejia P, Pacheco H, et al. Blood hyperviscosity in acute and recent COVID-19 infection. *Clin Hemorheol Microcirc* [Internet]. 2022; 82(2):149–55. Available from: <https://www.medra.org/servlet/aliasResolver?alias=iiospress&doi=10.3233/CH-221429>
46. Pop GAM, Duncker DJ, Gardien M, Vranckx P, Versluis S, Hasan D, et al. The clinical significance of whole blood viscosity in (cardio)vascular medicine. *Neth Heart J*. 2002;10(12).
47. Pal R. Rheology of concentrated suspensions of deformable elastic particles such as human erythrocytes. *J Biomech* [Internet]. 2003; 36(7):981–9. Available from: <https://linkinghub.elsevier.com/retrieve/pii/S0021929003000678>
48. Yilmaz F, Gundogdu MY. A critical review on blood flow in large arteries; relevance to blood rheology, viscosity models, and physiologic conditions. *Korea Australia Rheology Journal*. 2008.
49. Vásquez DM, Ortiz D, Alvarez OA, Briceño JC, Cabrales P. Hemorheological implications of perfluorocarbon based oxygen carrier interaction with colloid plasma expanders and blood. *Biotechnol Prog* [Internet]. 2013; 29(3):796–807. Available from: <https://aiche.onlinelibrary.wiley.com/doi/10.1002/btpr.1724>
50. Mukherji B, Sloviter HA. A stable perfluorochemical blood substitute. *Transfusion (Paris)* [Internet]. 1991; 31(4):324–6. Available from: <https://onlinelibrary.wiley.com/doi/10.1046/j.1537-2995.1991.31491213296.x>
51. Syed UT, Dias AMA, Crespo J, Brazinha C, Sousa HC de. Studies on the formation and stability of perfluorodecalin nanoemulsions by ultrasound emulsification using novel surfactant systems. *Colloids Surf A Physicochem Eng Asp* [Internet]. 2021; 616:126315. Available from: <https://linkinghub.elsevier.com/retrieve/pii/S0927775721001849>

This scientific work was realized in the frame of work, No. WZ/WM-IIB/3/2023, and financed from the research funds of the Ministry of Education and Science, Poland.

Joanna Mystkowska:  <https://orcid.org/0000-0002-3386-146X>

Dawid Łysik:  <https://orcid.org/0000-0002-5370-0030>



This work is licensed under the Creative Commons BY-NC-ND 4.0 license.

# DETERMINATION OF HEAT DEFLECTION TEMPERATURE UNDER A LOAD AND VICAT SOFTENING TEMPERATURE OF POWDER COMPOSITES USED FOR ABLATIVE SHIELDS

Przemysław SAPINSKI<sup>\*</sup>, Robert SZCZEPANIAK<sup>\*</sup>, Daniel PLONKA<sup>\*\*</sup>, Aneta KRZYŻAK<sup>\*\*\*</sup>,  
Ewelina KOSICKA<sup>\*\*\*\*</sup>, Grzegorz WORONIAK<sup>\*\*\*\*\*</sup>

<sup>\*</sup>Faculty of Aviation, Polish Air Force University, Dywizjonu 303 Street No 35, 08-521 Deblin, Poland

<sup>\*\*</sup>Wizz Air Hungary Ltd., Laurus Offices, Kőér Street 2/A, Building B, H-1103, Budapest, Hungary

<sup>\*\*\*</sup>Mechanical and Electrical Engineering Faculty, Polish Naval Academy, ul. Śmidowicza 69, 81-127 Gdynia, Poland

<sup>\*\*\*\*</sup>Faculty of Mechanical Engineering, Lublin University of Technology, Nadbystrzycka Street, No 36, 20-618 Lublin, Poland

<sup>\*\*\*\*\*</sup>HVAC Department, Białystok University of Technology, 15-351 Białystok, Poland

[p.sapinski@law.mil.pl](mailto:p.sapinski@law.mil.pl), [r.szczepaniak@law.mil.pl](mailto:r.szczepaniak@law.mil.pl), [d.plonka4290@wsosp.edu.pl](mailto:d.plonka4290@wsosp.edu.pl), [a.krzyzak@amw.gdynia.pl](mailto:a.krzyzak@amw.gdynia.pl),  
[e.kosicka@pollub.pl](mailto:e.kosicka@pollub.pl), [g.woroniak@pb.edu.pl](mailto:g.woroniak@pb.edu.pl)

received 27 April 2023, revised 13 April 2024, accepted 6 May 2024

**Abstract:** This paper presents the results of a study to determine the heat deflection temperature (HDT) and Vicat softening temperature (VST) of polymer matrix powder composites used for ablative shielding. The issue is of particular importance since, during ablative tests, the composite material is partially burnt (ablative layer). However, its remaining parts are additionally heated to a higher temperature, which is consequently associated with a change in the visco-elastic properties that depend, among other things, on the VST and HDT temperatures. In the conducted research, the authors used different mass percentages of powder modifiers (montmorillonite, halloysite, mullite, carbon nanotubes, silicon carbide) matrix base epoxy resin LH 145 Havel with the hardener H147 in the experiments. Apart from observing thermal properties that may change due to a modification of the composition of the composites, the effect of conditioning of the samples on the test results was also noticed. It is preheating a composite at a temperature as low as 55°C was observed to increase the HDT and VST by approximately 20°C and the composite hardness by approximately 3-7%.

**Key words:** deflection temperature, softening temperature, ablative materials, powder composite

## 1. INTRODUCTION

One of the most common forms of modifying material properties is the manufacture of composites, which are materials composed of at least two phases. Due to their comprehensive use in a wide range of industries, various improvements are constantly being sought after, including enhancements with regard to mechanical [1-5], ablative [6], or tribological properties [7,8]. The enhancements mentioned above are made either through novel technological concepts of manufacturing composites [9-11] or by including modifiers in the composition of composites.

When classifying modifiers by origin, it is possible to distinguish [12-15] the following:

- natural organic fillers (e.g., wood flour, flax fibers),
- non-organic (e.g., chalk, talc, quartz),
- synthetic (e.g., glass fibers, carbon fibers).

Taking into consideration the form in which the fillers appear, the following can be distinguished:

- powder fillers (spherical, flake, or short-cut fiber form),
- fiber fillers (e.g., glass fibers, boron fibers).

Defining the requirements for material properties is possible after analyzing the operating conditions of components made of a given material. Among the observed external factors affecting the reliability of machine or equipment components is, among others, temperature, which, in the case of polymers, can contribute to a

change in the state of aggregation in extreme situations. Therefore, testing newly developed materials for their thermal properties seems appropriate. These, in turn, are determined by the heat distortion temperature under a load (HDT) [16] or Vicat softening temperature (VST) [17] in laboratory conditions.

Numerous attempts have been made in the available literature to improve the properties (especially the mechanical ones) of composite materials by adding modifiers in the form of powders; however, on numerous occasions, they were carried out without determining the influence of the modifier on the thermal characteristics of a composite. The authors have decided to select the best-known powder modifiers used in polymer composites, as well as polymer composites treated as a matrix base, in order to supplement the knowledge base with conclusions formulated on the basis of their own research. The details regarding the selected reinforcement and matrix base are presented in the next section.

## 2. MATERIALS AND METHODS

Based on the analysis of the state of available expertise on the thermal properties of polymer composites and the fundamentals of experimental planning, the authors have prepared a methodology for experimental research and proposed the research equipment.

The research focused on powder composites made at the laboratory. For this purpose, different types of powder fillers were used (montmorillonite, halloysite, mullite, MWCNT, silicon carbide), described in the following sections, at different mass percentages (1%, 5%, 20%), which were selected as matrix - also presented in the following sections - LH 145 (Havel Composites) with the hardener H147 (Havel Composites).

After 3 and 15 hours, the thermal properties were determined for both non-heated and heated samples in two temperature ranges (55°C and 80°C). It is also worth noting that the tests were carried out simultaneously on reference samples without the addition of powder fillers. A thermal test model is shown in Fig 1.

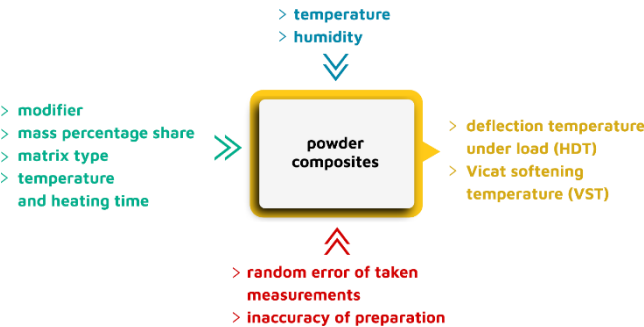


Fig. 1. Scheme of phenomena occurring during sample combustion [6]

The powder modifier, its mass percentage in the composite, the heating temperature, and the heating time were taken as input (independent) factors. The permanent factors included the microclimate in the laboratory rooms, air temperature in the laboratory (22°C), and technical features of the equipment, while the interferences included random error in the measurements and inaccuracy of preparing the powder composites. The thermal properties of the produced composites, as determined by Vicat and HDT test results, were obtained as input data.

### 2.1. Powder reinforcements

Several modifiers described in the available literature and exploited to shape the selected properties of composites (including hybrids) were used to produce powder composites. These modifiers, together with their brief characteristics as well as references to wider descriptions, are presented in Tab. 1.

Tab. 1. Characteristics of used powder modifiers

Modifier's name	Characteristics	Manufacturer
montmorillonite (MMT)	It is one of the most popular representatives of the widely used layered silicates, derived from a group of clay minerals (clays), which are the main component of rocks called bentonites. A small additive of MMT into the polymer matrix base of the composite allows for an improvement in the mechanical and thermal properties of the material and contributes to a reduction in its flammability. Sources: [18–23]	Montmorillonite K 10 in powder form, supplied by the American company Sigma-Aldrich

halloysite (Al <sub>2</sub> Si <sub>2</sub> O <sub>5</sub> (OH) <sub>4</sub> ·2H <sub>2</sub> O)	It is an aluminosilicate consisting of approximately 40% aluminum oxide, approximately 45% silica and water, and traces of metal oxides such as Na <sub>2</sub> O, TiO <sub>2</sub> , FeO, MgO, Al <sub>2</sub> O <sub>3</sub> , K <sub>2</sub> O, TiO <sub>2</sub> , and CaO. Sources: [24–28]	Halloysite Nanoclay in a powder form (nanotubes are 1-3 μm long and 30-70 nm in diameter), supplied by the American company Sigma-Aldrich
mullite (3Al <sub>2</sub> O <sub>3</sub> ·2SiO <sub>2</sub> )	It is characterized by high thermal stability, low thermal expansion, thermal conductivity, high resistance to creep and corrosive substances while maintaining adequate strength and resistance to brittle fracture, the ability to attach various cations and the possibility of forming crystals with various contents of silicon and aluminum oxides. Sources: [29–32]	Aluminum Silicate (Mullite) in the form of powder, supplied by Sigma-Aldrich
carbon nanotubes (MWCNTs)	The biaxial nanotube structure is constructed from rolled graphene planes composed of groupings of hexagonal carbon rings. Apart from a high aspect ratio, the nanotubes are characterized by very low density, high rigidity, and thermal resistance, as well as high bending and tensile strength. Sources: [33–37]	Multi walled MWCNT by Bucky USA (5-10 nm in diameter, 30 μm in length)
silicon carbide (SiC)	It is characterized by high thermal and electrical conductivity, high chemical decomposition temperature, good mechanical strength, and high hardness. High resistance to rapid temperature changes (thermal shocks) and oxidation (occurring only above 1,400°C and accompanied by the formation of a protective layer in the form of silicon oxide SiO <sub>2</sub> ). is also quite relevant. Sources: [38–42]	Carborundum F220 with gradation equal to 53-75 μm

The modifiers were added in specific mass percentages of 1%, 5%, and 20%, respectively. The balance PS2100 R2 Radwag (Radom, Poland) was used to precisely prepare the weighed portions of modifiers.

### 2.2. Section title Resin-based matrix

Due to the wide range of applications of powder modifiers in polymer compositions and the demand of various industries for improved composite properties, it was decided to use polymer resins as a matrix base for the manufactured powder composites. LH 145 resin is a material characterized by relatively low viscosity and high resistance to crystallization at low temperatures.



It shows good resistance to chemical agents. Produced by the Czech company Havel Composites, the resin is made from bi-phenol and epichlorohydrin. Its main application recommended by the manufacturer is the production of boats, tools, and automotive parts. Its low viscosity and chemical neutrality are decisive for a convenient application and good compatibility with fiber reinforcements made of aramid, carbon, or glass. In order to initiate the resin curing process, the authors used the H 147 hardener proposed by the manufacturer in the recommended 100:25 weight ratio. The detailed information on LH 145 is provided in Tab. 2.

Tab. 2. LH 145 resin characteristics [43]

Properties	Values
Density at 25°C	1.15 g/cm3
Flash-point (PMCC)	149°C
Viscosity at 25°C	0.7 Pa·s
Epoxy value	170-179 g
Temperature stability when curing at 25°C (for at least 2 days)	50-60°C
Temperature stability when curing at 50-60°C (for 3 hrs)	80-90°C

2.3. Sample heating

Each sample of prepared samples, differing both in the type of the used reinforcement, its mass percentage, and the matrix, was divided into sets. The first one contained samples that had not undergone heating. Other sets were divided into those heated at 55°C (3 hrs and 15 hrs) and 80°C (15 hrs). The samples were heated in a WKL 64 Weissttechnik climate chamber (Weiss Umwelttechnik GmbH, Heuchelheim, Germany) presented in Fig. 2. By controlling the heating process, the machine maintained a set temperature with an accuracy of ±0.1°C.

A summary Table was prepared, focusing on the distinguishing features of a given sample (see Table 3). It included the following data: sample number, number of samples, type of resin and hardener, name of additive and its mass content, temperature, and curing time, all collected in one place. The specified division and nomenclature will function unchanged throughout the remainder of this work.

Tab. 3. Table showing manufacture parameters of individual series of measurement samples

Sample	Number of samples	Resin	Hardener	Additive	Content of the additive [%]	Heating temperature [°C]	Heating time [hrs]
0/ 0W	3	LH 145	H 147	-	-	-55	-3
1/ 1W				Montmorillonite	5		
2/ 2W				Montmorillonite	20		

3/ 3W				Halloysite	5		
4/ 4W				Halloysite	20		
5/ 5W				Mullite	5		
6/ 6W				Mullite	20		
7/ 7W				MWCNT	1		
8/ 8W				MWCNT	5		
9/ 9W				Silicon carbide	5		
10/ 10W				Silicon carbide	20		

2.4. Determining the deflection temperature (HDT) under load

The prepared samples were subjected to HDT testing on an Instron HV6X HDT test stand (Pianezza, Italy) powered by Instron Bluehill HV software (Bluehill version 1.9, Instron Corporation, Canton, MA, USA). It was used to configure parameters concerning the test method, such as the test type (HDT), the norm under which the test was conducted [44], variant, heating speed, initial temperature, and conditioning time understood as the time of immersion of the samples in oil prior to launching the examination (see Tab. 4).

Tab. 4. HDT test parameters

Instron Bluehill HV programme parameters	Adopted boundary conditions
variant of research	A – 1.8 MPa
rate of oil temperature rise	120°C/h
initial temperature	25°C
time of conditioning	5 min

Time plays an important role in the reliability of the results, as it allows the temperature of the moulding and the oil to level off before the test begins. The next step was to place the samples in the measuring stations, keeping their recommended central position. Special care was taken to ensure that the temperature gauges were positioned at a short distance from the examined profile. The dimensions of each test sample were then entered into the Bluehill programme. This way, the software calculated the load to be applied so as to obtain the bending stress value.

These calculations took into account the pin's weight, which informed the operator which weights to put on a tripod. The dimensions were also used to determine an individual standard deflection value for the subsequent profiles.

At the end of the preparatory procedure, automatic temperature control of the heating bath was started, which was then stabilized at 25°C. After starting the test program from the computer program panel, the heating and cooling systems of the stand were checked for several minutes; the temperature was stabilized, and the specimens were loaded and immersed in the heating liquid. This stage was followed by the main part of the test, during which each station separately recorded deformations occurring in the

sample and the temperature rising at a constant rate around it. The test ended once the last section reached the standard deflection. Next, cooling was activated to reduce the temperature of the liquid to its initial value.

### 2.5. Determination of Vicat softening temperature (VST)

Vicat softening temperature tests were performed on an Instron HV6X stand (Pianezza, Italy). It holds a dedicated indenter and a clip that keeps the sample in position during the test. As in the previous test, the Instron Bluehill HV software (Bluehill version 1.9, Instron Corporation, Canton, MA, USA) was used to configure the test method parameters, such as the test type (VST), standard [45] load variant and heating rate, the initial temperature and the conditioning time, understood as the period for which the sample is immersed in oil prior to the test (see Tab. 5).

Tab. 5. VST test parameters

Instron Bluehill HV programme parameters	Adopted boundary conditions
load variant	A120 - load 10 N
heating speed	120°C/h
initial temperature	25°C
time of conditioning	5 min

The samples were then placed sequentially in the measuring stations, maintaining a recommended position, which ensures a minimum distance of 3 mm between the indenter tip and the edge of the section. Due to the constant load value, the total mass acting on the indenter of each station was the same.

At the end of the preparatory procedure, the automatic temperature control of the heating bath was started, which from now on was stabilized at 25°C. After activating the software, the heating and cooling systems of the station were checked for several minutes; the temperature was stabilized, and the samples were loaded and immersed in the heating liquid. This stage was followed by the main part of the test, during which each station separately recorded the movement of the indenter and the temperature rising at a constant rate around it. The test was terminated once a 1 mm cavity was reached in the last of the profiles or when the test was manually aborted. After this time, cooling was activated to reduce the temperature of the liquid to its initial value.

In accordance with the previously described methodology for determining the Vicat softening temperature, all the measurement series were tested in accordance with method A120. However, it occurred that not all of the tests that were conducted resulted in the penetration of the indenter tip in the material being required to be 1 mm by the norm. The problem mainly affected the profiles subjected to the heating process and made it impossible to determine the sought VST temperature (in accordance with the norm). It was, therefore, decided that for each such series, an agreed softening temperature of the composite material would be determined. The method of "tangents' intersection - increase and stabilization - of the pin's indentation in the material, in the function of temperature" was used in order to determine the temperature of the intersection of two lines tangent to the curve of the experimental course in the function of temperature.

### 2.6. Additional tests and measurements

Apart from the tests aimed at determining the thermal properties of powder composites, the authors additionally decided to

- determine their density values,
- determine their hardness values,
- measure the indentations that occurred during the Vicat test.

In order to provide a more complete presentation of the Vicat study, imaging of the resulting indentation after the study is also presented. The equipment used for this purpose, along with information on the standards underlying the research activities, are presented in Tab. 6.

Tab. 6. Tests and measurements

Type	Device	Standard
determination of values densities	Mettler Toledo XSR 205 analytical balance (Mettler Toledo, Zürich, Switzerland)	ASTM D 792 [46]
determination of values hardness	Digi Test II modular hardness tester (Bareiss, Germany) Shore D/C/DO module	ISO 48 [47]
Measurement of the indentations that occurred during the Vicat test	MicroProf 100 (FRT GmbH, Bergisch Gladbach, Germany)	not applicable

## 3. RESULTS AND DISCUSSION

### 3.1. Density testing

The density of the composite materials was tested using a Mettler Toledo XSR 205 analytical balance with the necessary accessories. The values are listed below in Table 7.

Tab. 6. Mass, density, and volume values of individual resins and additives, the filling levels expressed in mass and volume, as well as the density of the composite

Sample	$m_{res}$ [g]	$\rho_{res}$ [g/cm <sup>3</sup> ]	$V_{res}$ [cm <sup>3</sup> ]	$m_{add}$ [g]	$\rho_{add}$ [g/cm <sup>3</sup> ]	$V_{add}$ [cm <sup>3</sup> ]	$V_{all}$ [cm <sup>3</sup> ]	in masses [%]	by volume [%]	$\rho_{comp}$ [g/cm <sup>3</sup> ]
0	50	1.15	43.48	0	-	-	43.48	0	0	1.15
1	50	1.15	43.48	2.6	2.5	1.04	44.52	5	2	1.178
2	50	1.15	43.48	15	2.5	6	49.48	20	12	1.299
3	50	1.15	43.48	2.6	2.53	1.03	44.51	5	2	1.181
4	50	1.15	43.48	15	2.53	5.93	49.41	20	12	1.308
5	50	1.15	43.48	2.6	3.03	0.86	44.34	5	2	1.185
6	50	1.15	43.48	15	3.03	4.95	48.43	20	10	1.347
7	50	1.15	43.48	0.6	0.08	7.31	50.79	1	14	1.154
8	50	1.15	43.48	2.6	0.08	31.69	75.17	5	42	1.16
9	50	1.15	43.48	2.6	3.15	0.83	44.30	5	2	1.194
10	50	1.15	43.48	15	3.15	4.76	48.24	20	10	1.352

### 3.2. HDT testing

It was decided to present the test results in the form of a clear graphical representation of the deflection as a function of temperature. For scientific purposes, there is only an example of such a measurement (see Fig. 2 and 3. and Tab. 8 and 9). Each of the colored lines reflects successive measuring stations and, thus, successive samples. As the resin without additives is a kind of reference for other composites with fillers, a black line was additionally placed (as a reference line for other materials). Below the graph, there is a table summarizing the most important material parameters and test results for each measurement series. The next part of the graph shows how the heating temperature of the material before the test influenced the change in HDT and how this temperature changed for different resins.

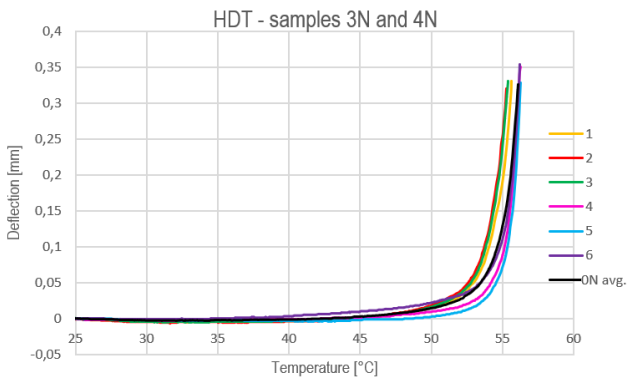


Fig. 2. Examples of HDT temperature measurements in a graphical form combined with tabular values from this graph for composite without heating

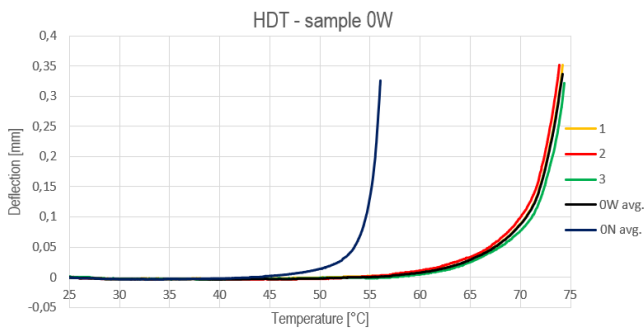


Fig. 3. Examples of HDT temperature measurements in a graphical form combined with tabular values from this graph for heated composite

Tab. 8. Results of HDT experimental tests for exemplary composite samples without heating

Measurement no.	Color	Sample	Load [g]	Deflection std.	Deflection value [mm]	Temp. HDT [°C]
1	Yellow	3 N	315	Achieved	0.33	55.6
2	Red	3 N	335	Achieved	0.32	55.3
3	Green	3 N	329	Achieved	0.33	55.4
4	Pink	4 N	287	Achieved	0.35	56.3

5	Blue	4 N	338	Achieved	0.31	56.2
6	Violet	4 N	291	Achieved	0.34	56.2
0N average						56.0

Tab. 9. Results of HDT experimental tests for exemplary heated composite samples

1	Color	Sample	Load [g]	Deflection std.	Deflection value [mm]	Temp. HDT [°C]
1	Yellow	0 W	289	Achieved	0.35	74.2
2	Red	0 W	287	Achieved	0.35	73.9
3	Green	0 W	334	Achieved	0.31	74.4
0W average	Black	0 W	303	-	0.337	74.2
0N average	Black	0 N	329	-	0.327	56.0

After experimental testing of all the manufactured samples, the average HDT temperature for all the examined composites has been summarized graphically (see Fig. 4).

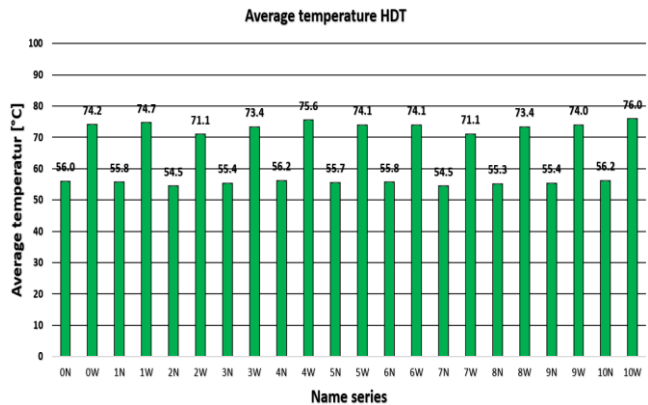
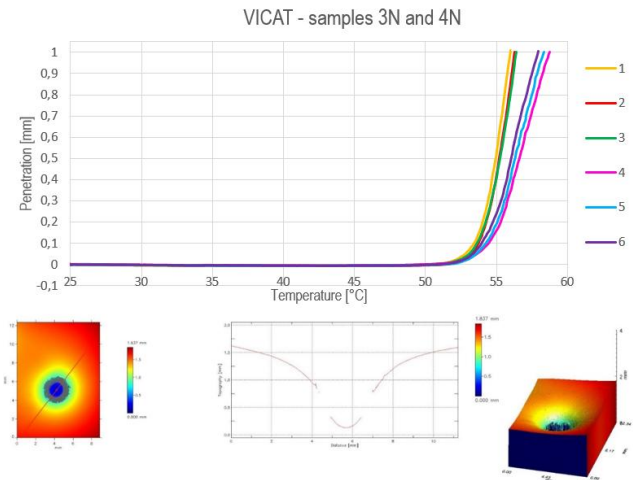


Fig.4. Summary results of average HDT temperature values

### 3.3. Vicat testing and post-test surface profilometry

In accordance with the previously described methodology for determining the Vicat softening temperature, all the measurement samples were tested in accordance with method A120 (Figure 5 and Table 10). However, it turned out that not all of the tests that were conducted resulted in the penetration of the indenter tip in the material, which was required to be 1 mm by the norm. The problem mainly affected the profiles subjected to the heating process and made it impossible to determine the sought VST temperature (in accordance with the norm). It was, therefore, decided that for each such series, an agreed softening temperature of the composite material would be determined. The method of "tangents' intersection - linear increase and stabilization - of the pin's indentation in the material, in the function of temperature" was used in order to determine the temperature of the intersection of two lines tangent to the curve of the experimental course in the function of temperature (Fig. 6 and Tab. 11). The first line described is the tangent to the linear increase in indentation, while

the second is the tangent to the stabilized value of indentation. Thus, the conventional softening temperature of the material was determined, and then it was entered in the column "Temp. VST" in the summary Tables. In order to easily distinguish it from the VST temperature value (in accordance with the standard), a green font was used (see Tab. 11).



**Fig. 5.** Examples of Vicat temperature measurements in a graphic form, combined with tabular values for this graph composite without heating

**Tab. 10.** Results of Vicat experimental tests for exemplary composite samples without heating

Measurement no.	Color	Sample	Penetration (in accordance with the norm)	Depth [mm]	Temp. VST [°C]
1	Yellow	3 N	Achieved	1.000	56
2	Red	3 N	Achieved	1.000	56.3
3	Green	3N	Achieved	1.000	56.4
4	Pink	4N	Achieved	1.000	58.7
5	Blue	4N	Achieved	1.000	58.3
6	Violet	4 N	Achieved	1.000	57.9
Average					56.5

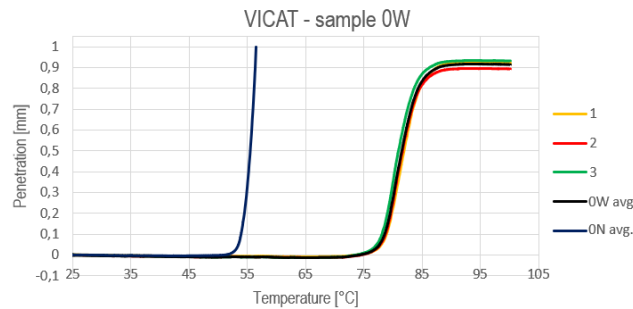


**Fig. 6.** Examples of Vicat temperature measurements in a graphic form, combined with tabular values for this graph: part A - composite without heating; part B - heated composite

**Tab. 11.** Results of Vicat experimental tests for exemplary heated composite samples

Measurement no.	Color	Sample	Penetration (in accordance with the norm)	Depth [mm]	Temp. VST [°C]
1	Yellow	0W	Not achieved	0.928	- ; 84.9
2	Red	0W	Not achieved	0.895	- ; 84.3
3	Green	0W	Not achieved	0.936	- ; 84.0
Average	Black	0 W	-	0.920	- ; 84.4
Average	Black	0 N	-	1.000	56.5

After experimental testing of all the manufactured samples, a summary of the results of the average VST temperature for all the examined composites has been presented graphically (see Fig. 7).

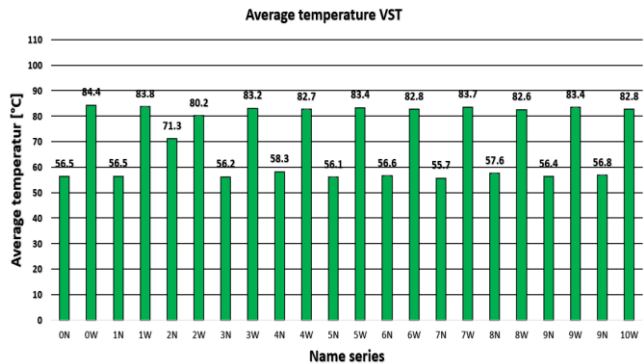


**Fig. 7.** Summary results of average VST temperature values by Vicat

### 3.4. Hardness tests

The tests were carried out 10 times for each profile (one from a given sample), taking care to test at different points away from the edges of the profile. The experimentally obtained hardness values of the tested materials are presented in a graphic form in Figure 8 and Table 12. The authors used colors to distinguish between the heated and non-heated samples. The sets of profiles cured at room temperature are green. The yellow color indicates the samples heated at 55°C. Samples 9 and 10 were measured from both sides in order to control the hardness of the material due to the high density of the powder additive, which resulted in higher sedimentation in the composite; higher hardness was obtained from the bottom side of the sample. Below the graph is a clear summary table with the results of the average hardness and standard deviation of each sample.



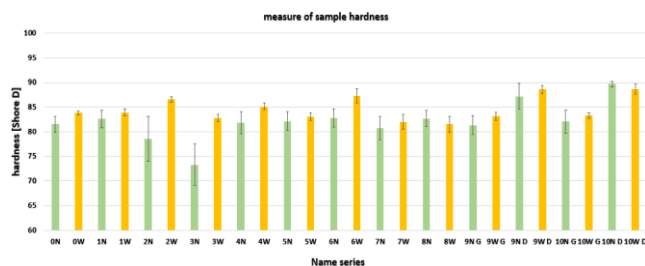


**Fig. 8.** Hardness tests graph showing the average hardness value of each sample (N - not heated. W - heated. G- top. D - down) together with a summary table

**Tab. 12.** Mean values and standard deviation of experimental tests of composite hardness

Sample	0N	0W	1N	1W	2N	2W	3N	3W	4N
$\bar{x}$	81.5	83.8	82.6	83.9	78.6	86.6	73.3	82.8	81.9
$\sigma$	1.58	0.46	1.78	0.71	4.52	0.60	4.20	0.81	2.28
Sample	4W	5N	5W	6N	6W	7N	7W	8N	8W
$\bar{x}$	85.2	82.1	83.0	82.8	87.3	80.8	82.0	82.7	81.5
$\sigma$	0.63	1.89	0.75	1.82	1.42	2.39	1.45	1.61	1.62
Sample	9N G	9W G	9N D	9W D	10N G	10W G	10N D	10W D	
$\bar{x}$	81.4	83.2	87.2	88.6	82.1	83.3	89.7	88.7	
$\sigma$	1.93	0.81	2.55	0.82	2.29	0.54	0.00	1.03	

## 4. CONCLUSIONS

The authors attempted to determine the properties defining the softening and deflection temperatures of powder composites, which are often disregarded in scientific publications. They also placed a great deal of emphasis on examining the selected mechanical properties. Due to the two-track nature of the research, the conclusions have also been split.

### HDT testing

- Non-heated samples - the additives that increased the temperature of deflection under a load are as follows: halloysite (20 wt.%) and silicon carbide (20 wt.%) increased the temperature of deflection by 0.2°C compared to the reference samples. Other powder additives decreased the examined temperature (in the case of montmorillonite by 20% and in the case of MWCNT by 1%, even by 1.5 °C).
- Heated samples - additives that increased the temperature of deflection under a load include montmorillonite (5% of content increased the deflection temperature by 0.5°C compared to the reference samples); halloysite (20 % of content increased the deflection temperature by 1.4°C compared to the reference samples) and silicon carbide (20 % of the content increased the deflection temperature by 1.8°C compared to the

reference samples, with the highest HDT). Other powder additives had a lowering effect on the examined temperature. The lowest values were found in filled profiles: MMT (20 %) of content and MWCNT (1 % of content, by 3.2 °C).

### VST testing

- Non-heated samples - additives that increase the softening temperature include MMT (20 % content of the highest VST, which was equal to 71.3 °C, halloysite (20 % content) an increase up to 58.3 °C; mullite (20 % content) an increase by 0.1 °C, MWCNT (5 % content) an increase up to 57.6 and silicon carbide (20 % of content and two types of filling when tested on the bottom side). Other powder additives had a lowering effect on the examined temperature. The lowest values were found in profiles filled with MWCNT (1 %) of content, with a VST value of 55.7).
- Heated samples - none of the heated profiles with LH 145 resin matrix base reached the standard-defined cavity required for VST temperature determination; however, each of the powder fillers lowered the conventional softening temperature. The composite achieved the value closest to the pure heated resin with an addition of MMT (5% of content). The lowest agreed VST was obtained for a composite with the same additive but with a higher fill level (20%).

## REFERENCES

- Szczepaniak R, Rolecki K, Krzyzak A. The influence of the powder additive upon selected mechanical properties of a composite. IOP Conference Series: Materials Science and Engineering 2019;634(1):01200. 76th Global Conference on Polymer and Composite Materials. PCM 2019. Bangkok. Available from: <https://doi.org/10.1088/1757-899X/634/1/012007>
- Borowiec M, Gawryluk J, Bochenski M. Influence of Mechanical Couplings on the Dynamical Behavior and Energy Harvesting of a Composite Structure. Polymers 2021;13:66. Available from: <https://doi.org/10.3390/polym13010066>
- Ślowski S, Szymiczek M, Kaczmarczyk J, Domin J, Świtoński E. Low Velocity Impact Response and Tensile Strength of Epoxy Composites with Different Reinforcing Materials. Materials 2020;13:3059. Available from: <https://doi.org/10.3390/ma13143059>
- Kosicka E, Borowiec M, Kowalczyk M, Krzyzak A, Szczepaniak R. Influence of the Selected Physical Modifier on the Dynamical Behavior of the Polymer Composites Used in the Aviation Industry. Materials 2020;13:5479. Available from: <https://doi.org/10.3390/ma13235479>
- Komorek A, Komorek Z, Krzyzak A, Przybyłek P, Szczepaniak R. Impact of Frequency of Load Changes in Fatigue Tests on the Temperature of the Modified Polymer. International Journal of Thermophysics 2017;38(8):128. Available from: <https://doi.org/10.1007/s10765-017-2254-2>
- Szczepaniak R, Kozun G, Przybyłek P, Komorek A, Krzyzak A, Woroniak G. The effect of the application of a powder additive of a phase change material on the ablative properties of a hybrid composite. Composite Structures 2021;256:113041. Available from: <https://doi.org/10.1016/j.compstruct.2020.113041>
- Krzyzak A, Kosicka E, Szczepaniak R, Szymczak T. Evaluation of the properties of polymer composites with carbon nanotubes in the aspect of their abrasive wear. Journal of Achievements in Materials and Manufacturing Engineering Open Access 2019;95:5–12. Available from: <http://doi.org/10.5604/01.3001.0013.7619>
- Mrówka M, Woźniak A, Prężyńska S, Ślowski S. The Influence of Zinc Waste Filler on the Tribological and Mechanical Properties of Silicone-Based Composites. Polymers 2021;13:585. Available from: <https://doi.org/10.3390/polym13040585>

9. Yogeshwarana S, Natrayan L, Rajaraman S, Parthasarathi S, Nestro S. Experimental investigation on mechanical properties of Epoxy/graphene/fish scale and fermented spinach hybrid bio composite by hand lay-up technique. *Materials Today: Proceedings* 2021;37(2):1578-1583. Available from: <https://doi.org/10.1016/j.matpr.2020.07.160>
10. Zagorodnuk LKh, Lesovik VS, Elistratkin MY, Sumskey DA, Makhortov DS, Zolotykh SV. New methods for manufacturing composite materials. *Journal of Physics: Conference Series* 2019;1353:012060.
11. Kia HG, Simmer JC. A New Method for Producing Composite Panels with Textured Finish using Open Molding Process: Part I - Technology Development. *Journal of Composite Materials* 2006;40(4):333-344. Available from: <https://doi.org/10.1177/0021998305055191>
12. Petrucci R, Torre L. Filled Polymer Composites. In: *Modification of Polymer Properties*; William Andrew Publishing (Norwich, USA). 2017;23-46.
13. Amgoth C, Phan C, Banavoth M, Rompivalasa S, Tang G. Polymer Properties: Functionalization and Surface Modified Nanoparticles. In: *Role of Novel Drug Delivery Vehicles in Nanobiomedicine*; IntechOpen (London, UK). 2019. Available from: <https://doi.org/10.5772/intechopen.84424>
14. Jasso-Gastine CF, Soltero-Martínez JFA, Mendizábal E. Introduction: Modifiable Characteristics and Applications. In: *Modification of Polymer Properties*; William Andrew Publishing (Norwich, USA). 2017; 1-21.
15. Ambrogi V, Carfagna C, Cerruti P, Marturano V. Additives in Polymers. In *Modification of Polymer Properties*; William Andrew Publishing (Norwich, USA). 2017;87-108.
16. Gooch JW. Heat Deflection Temperature. In: Gooch J.W. (eds) *Encyclopedic Dictionary of Polymers*. Springer. 2011 (New York, USA). Available from: [https://doi.org/10.1007/978-1-4419-6247-8\\_5831](https://doi.org/10.1007/978-1-4419-6247-8_5831)
17. Gooch JW. Vicat Test. In: Gooch J.W. (eds) *Encyclopedic Dictionary of Polymers*. Springer. 2011 (New York, USA). Available from: [https://doi.org/10.1007/978-1-4419-6247-8\\_12522](https://doi.org/10.1007/978-1-4419-6247-8_12522)
18. Bee SL, Abdullah MAA, Bee ST, Sin LT, Rahmat AR. Polymer nanocomposites based on silylated-montmorillonite: A review. *Progress in Polymer Science* 2018;85:57-82. Available from: <https://doi.org/10.1016/j.progpolymsci.2018.07.003>
19. Guo YX, Liu JH, Gates WP. et al. Organo-Modification Of Montmorillonite. *Clays Clay Miner.* 2020;68:601-622. Available from: <https://doi.org/10.1007/s42860-020-00098-2>
20. Mishra S, Shimpi NG, Mali AD. Effect of surface modified montmorillonite on photo-oxidative degradation of silicone rubber composites. *Macromolecular Research* 2013;21(5):466-473.
21. Tokobaro PEA, Larocca NM, Backes EH, Pessan LA. Effects of mineral fillers addition and preparation method on the morphology and electrical conductivity of epoxy/multiwalled carbon nanotube nanocomposites. *Polymer Engineering and Science* 2021;61(2):538-550. Available from: <https://doi.org/10.1002/pen.25598>
22. Ramesh P, Prasad BD, Narayana KL. Influence of Montmorillonite Clay Content on Thermal, Mechanical, Water Absorption and Biodegradability Properties of Treated Kenaf Fiber/ PLA-Hybrid Biocomposites. *Silicon* 2021;13(1):109-118. Available from: <https://doi.org/10.1007/s12633-020-00401-9>
23. Silva LCS, Busto RV, Camani PH, Zanata L, Coelho LHG, Benassi RF, Rosa DS. Influence of Montmorillonite and Clinoptilolite on the Properties of Starch/Minerals Biocomposites and Their Effect on Aquatic Environments. *Journal of Polymers and the Environment* 2021;29(2):382-391. Available from: <https://doi.org/10.1007/s10924-020-01873-x>
24. Szpilka K, Czaja K, Kudła S. Halloysite nanotubes as polyolefin fillers. *Polimery (Polymers)* 2015;6:357-422. Available from: <https://doi.org/10.14314/polimery.2015.359>
25. Muhammad J, Hafiz M, Naveed M. Properties and Modification Methods of Halloysite Nanotubes: A State-Of-The-Art Review. *J. Chil. Chem. Soc.* 2018;63(3):4109-4125. Available from: <http://dx.doi.org/10.4067/s0717-97072018000304109>
26. Bordepong S, Bhongsuwan D, Pungrassami T, Bhongsuwan T. Characterization of halloysite from thung yai district. Nakhon Si Thammarat Province. in Southern Thailand. *Songklanakarin Journal of Science and Technology* 2011;33(5):599-607.
27. Haddar AE, Gharibi E, Azdimousa A, Fagel N, Hassani IE, Ouahabi ME. Characterization of halloysite (North East Rif. Morocco): evaluation of its suitability for the ceramics industry. *Clay Minerals* 2018;53:65-78.
28. Luo Y, Mills DK. The Effect of Halloysite Addition on the Material Properties of Chitosan-Halloysite Hydrogel Composites. *Gels* 2019;5:40. Available from: <https://doi.org/10.3390/gels5030040>
29. Peters PWM, Daniels B, Clemens F, Vogel WD. Mechanical characterisation of mullite-based ceramic matrix composites at test temperatures up to 1200°C. *Journal of the European Ceramic Society* 2000;20(5):531-535. Available from: [https://doi.org/10.1016/S0955-2219\(99\)00250-2](https://doi.org/10.1016/S0955-2219(99)00250-2)
30. Schneider H, Komarneni S. Mullite. *Mullite* 2006;1-487. Available from: <https://doi.org/10.1002/3527607358>
31. Kaya C, Butler EG, Selcuk A, Boccaccini AR, Lewis MH. Mullite (NextelTM 720) fibre-reinforced mullite matrix composites exhibiting favourable thermomechanical properties. *Journal of the European Ceramic Society* 2002;22(13):2333-2342. Available from: [https://doi.org/10.1016/S0955-2219\(01\)00531-3](https://doi.org/10.1016/S0955-2219(01)00531-3)
32. Wang KT, Cao LY, Huang JF, Fei J. A mullite/SiC oxidation protective coating for carbon/carbon composites. *Journal of the European Ceramic Society* 2013;33(1):191-198. Available from: <https://doi.org/10.1016/j.jeurceramsoc.2012.08.009>
33. Mucha M, Krzyzak A, Kosicka E, Coy E, Kościński M, Sterzyński T, Salaciński M. Effect of MWCNTs on Wear Behavior of Epoxy Resin for Aircraft Applications. *Materials* 2020;13:2696. Available from: <https://doi.org/10.3390/ma13122696>
34. Bellucci S, Balasubramanian C, Micciulla F, Rinaldi G. CNT composites for aerospace applications. *J. Exp. Nanosci.* 2007;2:193-206. Available from: <https://doi.org/10.1080/17458080701376348>
35. Setua DK, Mordina B, Srivastava AK, Roy D, Prasad NE. Carbon nanofibers-reinforced polymer nanocomposites as efficient microwave absorber. In *Fiber-Reinforced Nanocomposites: Fundamentals and Applications*; Elsevier Science: Amsterdam. The Netherlands. 2020;395-430. Available from: <https://doi.org/10.1016/B978-0-12-819904-6.00018-9>
36. Singh NP, Gupta V, Singh AP. Graphene and carbon nanotube reinforced epoxy nanocomposites: A review. *Polymer* 2019; 180: 12172-4. Available from: <https://doi.org/10.1016/j.polymer.2019.121724>
37. Shen S, Yang L, Wang C, Wei L. Effect of CNT orientation on the mechanical property and fracture mechanism of vertically aligned carbon nanotube/carbon composites. *Ceram. Int.* 2020;46:4933-4938. Available from: <https://doi.org/10.1016/j.ceramint.2019.10.230>
38. Salazar JM, Barrena MI, Morales G. Compression strength and wear resistance of ceramic foams-polymer composites. *Mater. Lett.* 2006;60:1687-1692. Available from: <https://doi.org/10.1016/j.matlet.2005.11.092>
39. Henager CH, Shin Y, Blum Y, Giannuzzi LA, Kempshall BW, Schwarz S.M. Coatings and joining for SiC and SiC-composites for nuclear energy systems. *J. Nucl. Mater.* 2007;367-370:1139-1143. Available from: <https://doi.org/10.1016/j.jnucmat.2007.03.189>
40. DiCarlo JA, Yun HM, Hurst JB. Fracture Mechanisms for SiC Fibers and SiC/SiC Composites Under Stress-Rupture Conditions at High Temperatures. *Applied Mathematics and Computation* 2004;152: 473-481. Available from: [https://doi.org/10.1016/S0096-3003\(03\)00570-8](https://doi.org/10.1016/S0096-3003(03)00570-8)
41. Suresha B, Chandramohan G, Siddaramaiah B, Sampathkumaran P, Seetharamu S. Mechanical and three-body abrasive wear behaviour of SiC filled glass-epoxy composites. *Polymer Composites* 2008; 29(9):1020-1025. Available from: <https://doi.org/10.1002/pc.20576>
42. Rajesh S, Ramnath BV. Analysis of mechanical behavior of glass fiber/Al2O3-SiC reinforced polymer composites. *Global Cong. Manuf. Manage.* 2014;97:598-606. Available from: <https://doi.org/10.1016/j.proeng.2014.12.288>

43. Product information from Havel Composites Polska Company.  
Available from: [http://www.havel-composites.pl/files/doc/LH\\_145\\_zywica\\_epoksydowa\\_doc.doc](http://www.havel-composites.pl/files/doc/LH_145_zywica_epoksydowa_doc.doc)
44. ISO 75-2:2013 Plastics — Determination of temperature of deflection under load — Part 2: Plastics and ebonite
45. ISO 306:2013 Plastics — Thermoplastic materials — Determination of Vicat softening temperature (VST)
46. ASTM D792 — 20 Standard Test Methods for Density and Specific Gravity (Relative Density) of Plastics by Displacement
47. ISO 48-2:2018 Rubber, vulcanized or thermoplastic — Determination of hardness — Part 2: Hardness between 10 IRHD and 100 IRHD

Przemysław Sapinski:  <https://orcid.org/0000-0002-3974-7676>

Robert Szczepaniak:  <https://orcid.org/0000-0003-3838-548X>

Daniel Plonka:  <https://orcid.org/0000-0001-7109-3599>

Aneta Krzyzak:  <https://orcid.org/0000-0003-1130-3149>

Ewelina Kosicka:  <https://orcid.org/0000-0001-5143-5184>

Grzegorz Woroniak:  <https://orcid.org/0000-0002-2162-7123>



This work is licensed under the Creative Commons BY-NC-ND 4.0 license.

# PLANNING THE COORDINATE MEASUREMENTS OF A FREEFORM SURFACE AFTER MILLING BASED ON A CAD MODEL SIMULATING THE SURFACE AFTER MACHINING

Andrzej WERNER<sup>\*</sup>, Małgorzata PONIATOWSKA<sup>\*</sup>

<sup>\*</sup> Faculty of Mechanical Engineering, Department of Materials Engineering and Production Engineering,  
Białystok University of Technology, ul. Wiejska 45A, 15-351 Białystok, Poland

[a.werner@pb.edu.pl](mailto:a.werner@pb.edu.pl), [m.poniatowska705@gmail.com](mailto:m.poniatowska705@gmail.com)

received 2 April 2024, revised 1 June 2024, accepted 4 June 2024

**Abstract:** This paper proposes the planning of coordinate measurements of freeform surfaces based on a model simulating the surface after machining. This model is created by the determination of a theoretical tool deflection during machining. The determined components of the simulated machining deviations are used in the reconstruction of the nominal CAD model of the surface into a model simulating the geometry of the surface after machining. This model is subdivided into areas corresponding to the assumed machining deviation intervals. This makes it possible to control the number and distribution of measuring points in separate sections of the manufactured surface. Coordinate measurements of the machined surface are made in areas where maximum deviations are expected. Here, the number and distribution of measuring points are controlled over a wide range. Coordinate measurements in other areas are carried out with significantly fewer points or may be omitted altogether. This approach makes it possible to reduce the measurement time without losing important information affecting the evaluation result. The method proposed in this paper has been tested on samples containing freeform surface. The test object was manufactured using a 3-axis milling technique with a spherical end mill.

**Key words:** freeform surface, coordinate measurement, 3-axis milling, CAD surface model

## 1. INTRODUCTION

The manufacturing of objects with freeform surface (e.g. casting moulds, injection mould and dies, etc.) is currently carried out on multi-axis machining centres. Assessment of the accuracy of this class of products is based on the determination of the surface shape deviations after coordinate measurements. At each measuring point, the local deviation from the nominal CAD model is determined. In assessing compliance with the specifications, the shape deviation is determined from the maximum values of the local deviations. Traditionally, coordinate measurement is carried out at points distributed according to a regular grid. A disadvantage of this method is the possibility of missing critical points, which leads to an inaccurate estimate of the shape deviation. This can be eliminated by increasing the number of measuring points. As a result, coordinate measurements of parts of complex geometry can take numerous hours (in extreme cases, the measurement time can be longer than the machining time of the part). For this reason, it has been attempted to develop different methods to reduce measurement time while achieving the same required measurement uncertainty.

Menq et al. in their paper [1] carried out a statistical analysis to determine the number of points on the basis of the profile tolerance and the machining process capability. The proposal is to distribute the points uniformly over the entire surface, abstracting from its geometrical features. Pahk et al. in [2] proposed several sampling strategies for the freeform surface represented by the B-spline surface model: sampling according to a regular grid of points (determining the points at the centre of the grid elements),

curvature-dependent sampling of the mean curvature, and combined sampling. In curvature-dependent sampling, the measurement points were concentrated in the areas with the greatest curvature and completely absent in the areas with less curvature. The authors therefore developed a hybrid method, which is a combination of the first two methods, thus eliminating omission of areas of low curvature. Cho and Kim in [3] proposed to make the distribution of the measuring points dependent on the mean curvature. The measuring points should be concentrated in regions of higher surface curvature because, as it has been showed and illustrated, it is in these regions that the largest machining deviations occur. It has been proposed to divide the CAD surface into a number of regions, determine the average curvature in the regions, and then select the number of measurement points depending on the curvature. Edgeworth and Wilhelm in their paper [4] made the density of measurement points dependent on the values of local geometric deviations. They proposed an algorithm using data on the directions normal to the surface at the measurement points to guide a third-degree B-spline interpolating curve. This curve was then used to determine further measurement points using an iterative procedure. The method ensures the density of measurement points in regions with large deviations and significantly reduces the total number of points compared to the classic method, i.e. evenly distributed points.

The accuracy of the “point-by-point” coordinate measurement increases with the number of measurement points, but the number of points is limited by the measurement time. Therefore, for a limited number of points, it is necessary to precisely determine their location to still accurately describe the shape of the profile. In accordance with this idea, the authors of the paper [5] proposed



algorithms based on the dominant points of the profiles of the nominal CAD model. B-spline curves can be approximated using a certain number of key points, reflecting selected features of the profile such as the curvature. In the works [6] of Rajamohan et al, the dominant points are the ones with the greatest local curvature and points of inflection. Elkott and co-workers proposed in [7] different methods for sampling a NURBS surface composed of multiple patches and an algorithm that automatically selects the most appropriate sampling method depending on the complexity of the surface, curvatures, and patch sizes. This algorithm optimises the distribution of points on the surface by minimising the maximum deviation between the original NURBS surface, which simulates the real surface, and the NURBS surface, matched to the measurement points (a surrogate surface). The same authors presented in [8] new proposals for sampling strategies. They proposed sampling along the isoparametric lines of the CAD model. The iterative sampling process is constrained by assuming a maximum number of lines and a minimum line spacing. The proposed methodology can be applied to a single patch of NURBS surfaces. The paper [9] extends the methodology to surfaces composed of multiple patches.

Obeidat and Raman [10] proposed three algorithms for determining the measurement points on curved surfaces divided into patches. They searched for a strategy which ensures the distribution of points on individual patches would depend on the complexity of their geometry and size in order to best represent the whole surface. Simulations were carried out on models of three surfaces of the same base size but with different degrees of complexity of the nominal geometry. A NURBS surface built on the measurement points and the maximum deviation of the surface resulting from the model simulating the real surface was determined to constitute an accurate representation.

Rajamohan et al. in paper [11] proposed, in addition to two new sampling strategies based on the nominal geometry of the profile, to include the influence of the tip size in the simulation studies. For ease of visualisation, they presented the proposed methods on a 2D profile. The first strategy is based on the lengths of the curve segments, and the second one is based on the dominant points. They compared the proposed new strategies with methods described in the literature and being in common use, and thus they distributed a certain number of points: uniformly in Cartesian space, uniformly in parametric space, and according to the size of the profile segment. In paper [12], the authors extended the method to freeform surface measurements.

A paper by Bowen Y. et al [13] proposes generating sampling points based on a triangular grid generated on a freeform surface to be measured. The length of the side of the triangular element responsible for the distribution of the measurement points depends in this case on the curvature of the surface.

An important aspect of coordinate measurements is proper stylus alignment and collision avoidance when measuring complex 3D objects. The paper [14] presents an algorithm for automatically planning an efficient five-axis inspection path of freeform surfaces. This strategy is based on transforming the inspection path planning problem into a set conversion problem, the solution of which then yields a near-minimum set of inspection paths for surfaces of freeform shape, subject to necessary constraints such as sampling resolution, no collisions, and others. In contrast, the paper [15] proposes a new method for optimising head alignment for contact 5-axis measuring machines. Given the paths of the stylus on a free-form surface, the optimal orientation of the stylus is calculated so that its tilt angle is within a specified range in

relation to the surface normal.

An interesting aspect of measurement strategy planning is the use of both non-contact and contact measurements. The article [16] presents an approach in which the contact measurement strategy is determined based on the results of non-contact measurements (e.g. optical scanning). The critical areas, i.e. where the maximum machining deviations occur, are determined on the basis of the optical scanning. The contact measurements are selected on this basis to ensure higher measurement accuracy. Surface sampling is limited to the critical regions.

The sampling strategy proposals described in the literature require a lot of knowledge and skilled personnel, and most of them are not feasible in an industrial application due to the high density of measurement points and therefore long measurement time. In addition, these strategies require use of a non-standard, expensive software. Methods such as uniform point distribution in Cartesian and parametric space or distribution based on the size of surface patches/segments of the profile do not take into account the influence of machining whatsoever. Methods based on profile length or curvature take it into consideration, nevertheless not assigning it enough significance.

This article proposes planning of the coordinate measurements of freeform surfaces on the basis of a CAD model simulating the surface after machining. This model is determined from the theoretical deflection of the tool (cutter) during 3-axis milling. The proposed method can be implemented using standard CAD/CAM software and measuring equipment used in industrial applications.

## 2. PLANNING COORDINATE MEASUREMENT OF FREEFORM SURFACES

Planning of the coordinate measurements of the freeform surface after milling based on a model simulating the surface after machining contains the following steps:

- determination of deviation values simulated at points on a CAD model of the nominal surface (for the purpose of this article, cutting forces and the resulting deflection of the milling cutter were taken into account),
- creation of a CAD model simulating the surface after machining,
- determination of the location and number of the measurement points,
- carrying out coordinate measurements of surface according to the specified measuring point locations,
- analysis of the measurement results and comparison with the nominal CAD model of the surface in order to assess the accuracy of the machined surface and possible improvement of the milling process in the future.

The application of the steps above ensures effective coordinate measurements of freeform surfaces after three-axis milling.

### 2.1. Determination of the simulated deviation values

The creation of a CAD model simulating the surface after machining starts with determining the values of the simulated machining deviations. In this paper, it is assumed that the dominant influence on machining accuracy is the deflection of the cutter due to the cutting forces. Figure 1 shows the model used to determine the deflection of the milling cutter at a point on the machined surface [19].

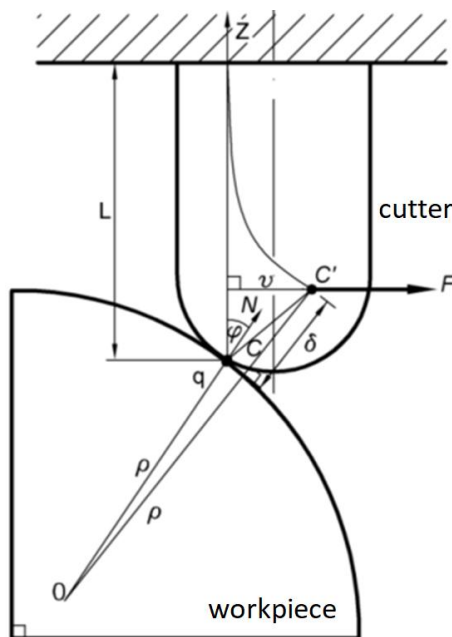


**Fig. 1.** Deflection of the cutter at a point on the machined surface:  $\delta$  – the deviation resulting from the deflection of the cutter,  $F$  – the cutting force perpendicular to the tool spindle axis [N],  $\varphi$  – the angle between the cutter axis ( $Z$ ) and the vector normal to the surface at the  $q$  point,  $q$  – a point on the nominal surface,  $L$  – the distance between the  $q$  point and the tool holder plane along the  $Z$  axis [mm],  $N$  – the vector normal to the surface at the  $q$  point,  $C$  – the point on the cutter blade that cuts the surface at the  $q$  point,  $C'$  – the position of the  $C$  point after applying the  $F$  force,  $v$  – the horizontal deflection of the cutter at the surface machining point  $C$  [19]

The deviation resulting from the deflection of the cutter is determined from the following equation [17]:

$$\delta = \frac{S_u F}{K} = \frac{F \sin \varphi}{K} \quad [\text{mm}] \quad (1)$$

where:  $S_u$  – sensitivity of the deviation to the deflection of the cutter in the horizontal direction, approximately equal to  $\sin \varphi$ ,  $K$  – stiffness of the cutter at the surface machining point [N/m].

To determine the values of the simulated deviations, a nominal CAD model of the machined surface is used. A grid of points is generated on this model, where the values of machining deviations are determined (Fig. 2). Using a typical CAD/CAM system (e.g. MasterCAM), in addition to the coordinates of the determined points, it is possible to obtain information about the direction cosines of the vectors normal to the surface at these points (Tab. 1).

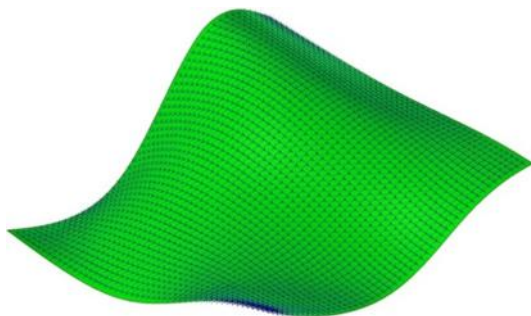


**Fig. 2.** Example grid of points on the nominal CAD model of the machined surface

**Tab.1.** Example coordinates of individual points and directional cosines of individual normal vectors

Xnom [mm]	Ynom [mm]	Znom [mm]	cosa	cosβ	cosγ
-20,7133	-22,9143	-7,3222	-0,035814	-0,309553	0,950208
-20,7064	-21,809	-6,9617	-0,028676	-0,309858	0,95035
-20,7006	-20,7737	-6,6242	-0,022714	-0,309431	0,950651
-20,6954	-19,7199	-6,2816	-0,01726	-0,308519	0,951062
-20,6909	-18,6699	-5,9418	-0,012529	-0,306945	0,951645

Then, using equation (1), the value of the theoretical deviations caused by the deflection of the cutter was determined for each nominal point. The generalized cutting force formulas found in tool manufacturer catalogues can be used to determine the cutting force values. Figure 3 shows a map illustrating an example of the distribution of the simulated deviations.

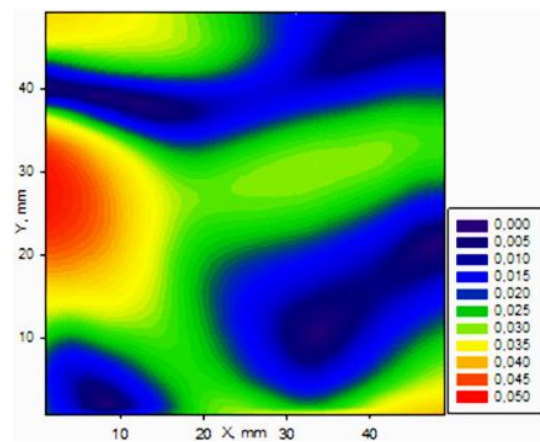


**Fig. 3.** An example map illustrating the distribution of the simulated deviations

## 2.2. Creation of a CAD model to simulate the surface after machining

Starting this step, two sets of data are available: the coordinates of points generated on the nominal CAD model of the machined surface, and the corresponding simulated deviations determined using equation (1). The first step is to carry out a correction of the coordinates of the nominal points by the value of the simulated deviation determined at the point. For this purpose, the equation (2) is used.

$$\begin{aligned} x_{ij}^{cor} &= x_{ij}^{nom} + \delta x_{ij} \\ y_{ij}^{cor} &= y_{ij}^{nom} + \delta y_{ij} \\ z_{ij}^{cor} &= z_{ij}^{nom} + \delta z_{ij} \end{aligned} \quad (2)$$

where:  $x_{ij}^{cor}, y_{ij}^{cor}, z_{ij}^{cor}$  – the corrected coordinates [mm],  $x_{ij}^{nom}, y_{ij}^{nom}, z_{ij}^{nom}$  – the nominal coordinates [mm],  $\delta x_{ij}, \delta y_{ij}, \delta z_{ij}$  – the components of deviations simulated for each axis [mm].

The creation of a CAD model simulating the surface after machining (Figure 4) is performed by techniques used in reverse engineering. First, corrected points are transferred to the CAD system. Then, a series of curves are interpolated on these points, on which the surface patch is then unwrapped. The most suitable

method for describing a surface in this case is the NURBS method.

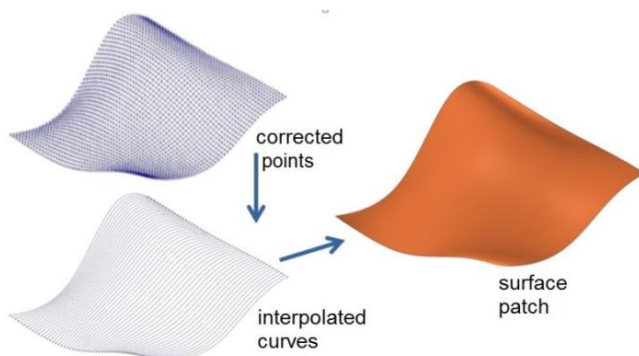


Fig. 4. Creation of a CAD model simulating the surface after machining

### 2.3. Distribution of the measurement points

With a CAD model simulating the surface after machining, it is possible to proceed to planning measurements on the coordinate measuring machine. The main goal is to minimize the measurement time while achieving the required measurement uncertainty. It was assumed that surface sampling would include the critical areas, i.e. the areas where maximum machining deviations are expected to be found.

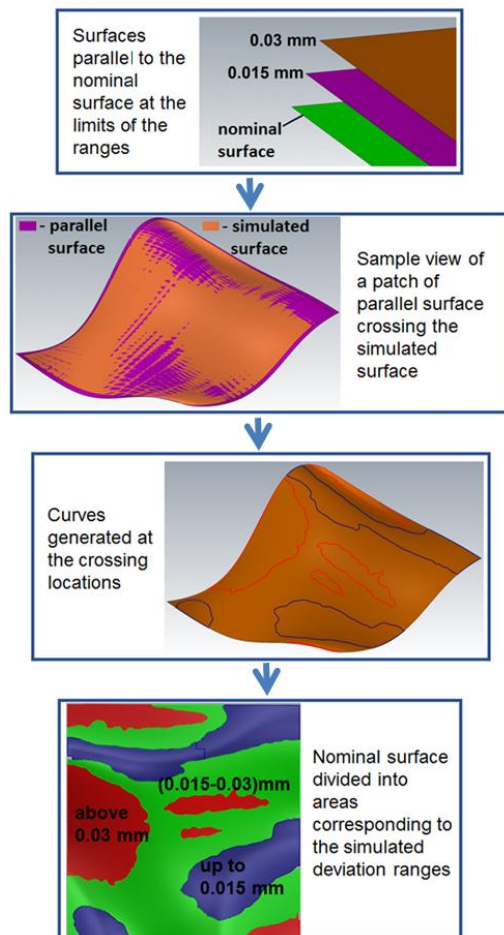


Fig. 5. Dividing the nominal CAD model of the milled surface into areas corresponding to the assumed ranges of the simulated deviations

In order to simplify the adopted measurement strategy, the data should be prepared in the following steps:

- step 1 – division of the nominal CAD surface into areas corresponding to the ranges of the simulated machining deviation values,
- step 2 – transfer of the isolated areas to the software of the coordinate measuring machine (CMM),
- step 3 – generating the measurement points in the selected areas in the CMM software.

The methodology of step 1 is shown in Figure 5.

First, according to the criterion adopted by the user depending on the construction requirements/surface accuracy, the division of the simulated deviation values into the ranges is carried out and the limits of the divisions are determined. Next, surfaces parallel to the nominal surface are created at the limits of the ranges. Each of these surfaces is crossed with a model simulating the surface after machining. Curves are generated at the crossing locations, which are used to divide the nominal surface into areas corresponding to the simulated deviation ranges. The nominal CAD model of the surface prepared this way is transferred to the CMM control software. Using the abilities of the software, the number and location of the measurement points in the measured areas can be managed. The measurements may be limited only to the critical areas, where maximum machining deviations are expected to occur.

### 3. EXPERIMENTAL VERIFICATION OF THE PROPOSED METHOD

Experimental verification of the proposed method has been carried out on the sample shown in Figure 6. It represents a fragment of the closing surface of an injection mould. The specimen was manufactured from steel 1.2344 (X40CrMoV5-1). Three-axis milling (parallel passes) was carried out using a ball-end mill with a diameter of 6 mm. The following machining parameters were used: feed rate 570 mm/min, step size at successive passes 0.05 mm, finishing allowance 0.25 mm.

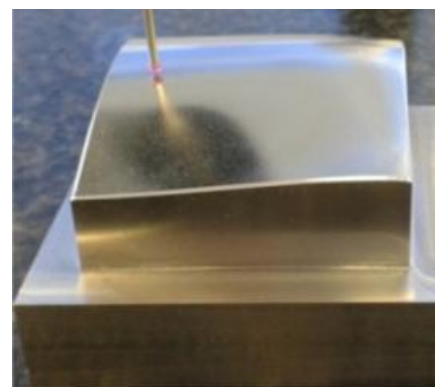
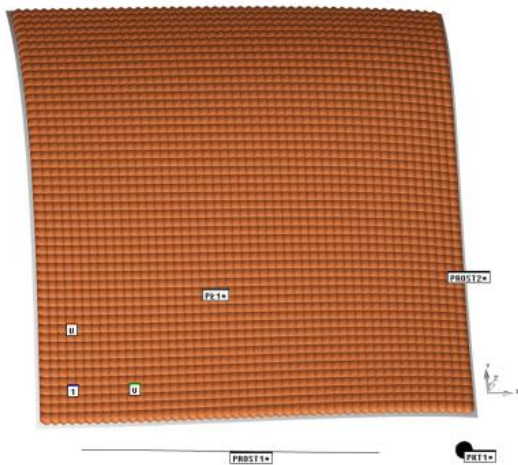


Fig. 6. The manufactured sample

After machining, coordinate measurements were carried out to determine the observed deviations. In this case, a Global Performance measuring machine from Hexagon Metrology was used (PC-DMIS software,  $MPEE = 1.5 + L/333$  [ $\mu\text{m}$ ], Renishaw SP25M measuring head, 20 mm long stylus with a spherical 2 mm diameter tip). Measurements were taken according to a regular



grid of  $1 \times 1$  mm points across the surface (Figure 7). This resulted in 2,500 measuring points.



**Fig. 7.** The distribution of the measurement points over the surface, measurements according to the procedure implemented in the PC DMIS, regular grid, Scan  $u \times v$ ,  $(1 \times 1)$  mm, 2,500 measurement points

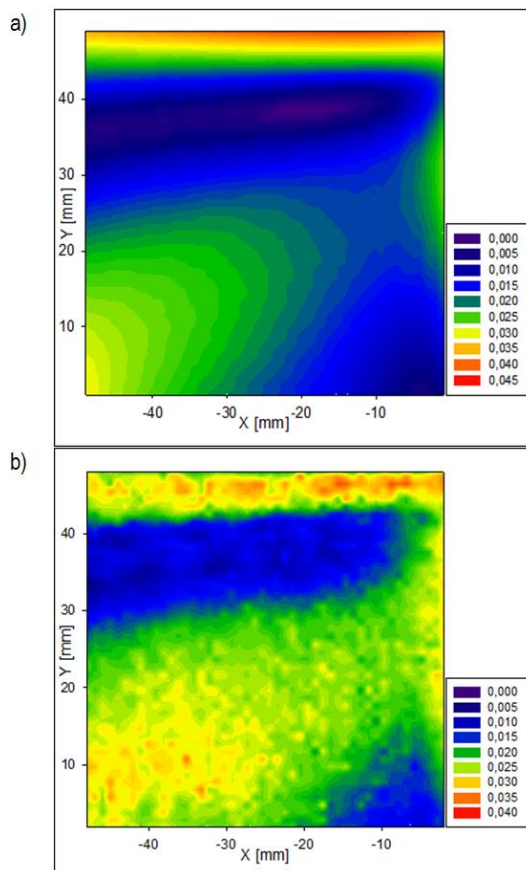


**Fig. 8.** Maps of the machining deviations: a) determined by a simulation, b) determined after machining based on coordinate measurements

After gathering information on the coordinates and the directional cosines from 2,500 measurement points, the corresponding local simulated deviations were determined using equation (1). Fig. 8a shows a map illustrating the distribution of the simulated

deviations. The distribution of the deviations after machining (Fig. 8b) was determined from the coordinate measurements. A high degree of similarity between the numerical simulation and the experimental results can clearly be observed, therefore the experimental verification of the model simulating the machined surface has had a positive result. This allows this model to be adopted to determine the areas representing the ranges of the simulated machining deviations.

The next step was to isolate the areas on the CAD model of the nominal surface corresponding to the assumed ranges of the simulated machining deviation values (the procedure presented in point 1.3). Fig. 9 shows the division of the nominal surface. Different colours represent areas corresponding to four ranges of the simulated deviation values (red - maximum deviation values, green - minimum deviation values).

The nominal CAD model of the surface prepared this way was transferred to the software controlling the coordinate measuring machine (PC-DMIS system). This software allows a wide range of programming 3D surface measurements. The *UVscan* procedure was used in the measurements. Measurements of both the entire surface and selected areas were programmed. The size of the grid of points was also controlled. Figure 10 shows the measurement points generated on the selected areas of the surface.

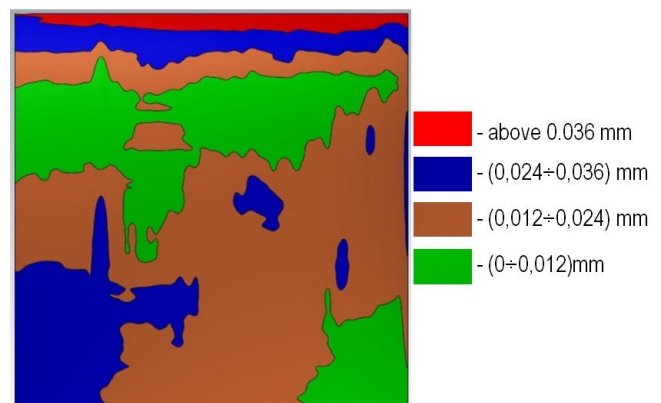


**Fig. 9.** The machined surface divided into 4 areas of the simulated deviation ranges

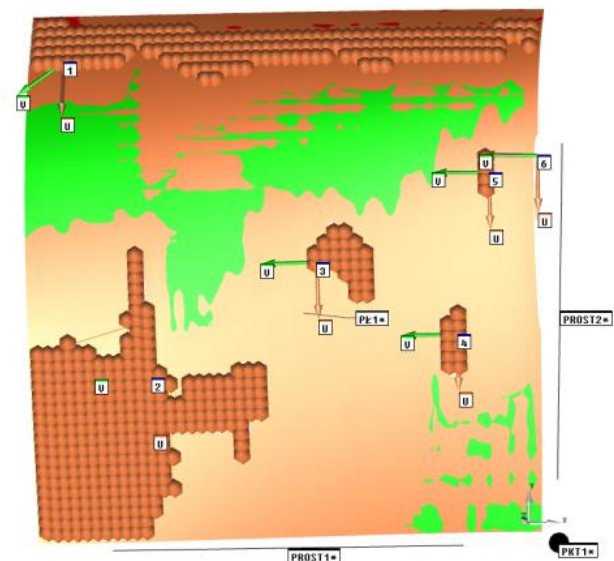


**Fig. 10.** PC DMIS point distribution (UV scan mode) in area corresponding to deviations of  $(0.024-0.036)$  mm



Coordinate measurements were carried out for the entire CAD model of the surface by sampling according to a regular grid of points as shows Fig. 7 (2,500 measurement points) and according to the proposed procedure. Sampling by grid (1 × 1) mm was performed in areas (fig. 9):

- red and blue [red – a critical area for the largest simulated deviation values, blue – corresponding to the range of smaller deviation values (581 points)],
- red (166 points).

Table 2 presents the obtained results of coordinate measurements.

Tab. 2. Coordinate measurement results (d - diameter of spherical stylus tip, s - sampling step)

Measurement parameters		Number of points	Measurement uncertainty [μm]	Max. local deviation [mm]	Standard deviation [mm]
d [mm]	s [mm]				
2	1	2,500	2,6	+0,0479	0,0018
2	1	581	2,6	+0,0491	0,0012
2	1	166	2,6	+0,0501	0,0012

It can be observed (Tab. 2) that there is a high degree of correspondence between the obtained measurement results and different numbers of measurement points. While maintaining the same measurement uncertainty, the number of measurement points was reduced from 2,500 to 581 and 166. The measurement efficiency is numerous times higher in both cases, while the measurement time was significantly reduced from 1 h 40 min (2,500 points) to approx. 7 min (166 points).

4. SUMMARY

This paper presents a procedure in which the freeform surface measurement strategy is determined from a CAD model simulating the surface after machining. Based on the results obtained, it was shown that coordinate measurements do not have to be performed on the entire measured surface. They can be limited only to critical areas where maximum machining deviations are expected to occur, which significantly reduces the number of measuring points and thus the measurement time. The same measurement uncertainty is maintained. The proposed method makes it possible to improve the efficiency of free-form surface measurement - in the presented case, while maintaining optimal measurement uncertainty, the efficiency increased fourteen times. It should be noted that in order to ensure optimum measurement uncertainty, the measurement parameters should be adapted to the tolerances given in the geometrical specification. The measurement results of the new method and the method involving scanning the entire surface may be considered similar.

The advantage of the proposed method is that it does not require special investments. Standard equipment (machine tools, measuring machines) and CAD/CAM software used in engineering practice can be used in this method. The time to prepare the CAD model simulating the machined surface is short, and the time for coordinate measurement is significantly shorter compared to the traditional measurement method in which the whole surface is measured.

REFERENCES

1. Menq CH, Yau HT, Lai GY. Automated Precision Measurement of Surface Profile in CAD-direct Inspection. IEEE Transactions on Robotics and Automation. 1992;8(2):268-278. <https://doi.org/10.1109/70.134279>

2. Pahk HJ, Jung MY, Hwang SW, Kim YH, Hong YS, Kim S.G. Integrated precision inspection system for manufacturing of moulds having CAD defined features. International Journal of Advanced Manufacturing Technology. 1995;10:198-207. <https://doi.org/10.1007/BF01179348>

3. Cho MW, Kim K. New inspection planning strategy for sculptured surfaces using coordinate measuring machine. International Journal of Production Research. 1995;33:427-444. <https://doi.org/10.1080/00207549508930158>

4. Edgeworth R, Wilhelm RG. Adaptive sampling for coordinate metrology. Precision Engineering. 1999;23:144-154. [https://doi.org/10.1016/S0141-6359\(99\)00004-5](https://doi.org/10.1016/S0141-6359(99)00004-5)

5. Park H, Lee JH. B-spline curve fitting based on adaptive curve refinement using dominant points. Computer-Aided Design. 2007; 39(6):439-451. <https://doi.org/10.1016/j.cad.2006.12.006>

6. Rajamohan G, Shunmugam MS, Samuel G.L. Sampling strategies for verification of freeform profiles using coordinate measuring machines. Proceedings of 9th International Symposium on Measurement and Quality Control. Madras India. 2007;135-140.

7. ElKott DF, ElMaraghy HA, ElMaraghy WH. Automatic sampling for CMM inspection planning of free-form surfaces. International Journal of Production Research. 2002;40(11): 2653-2676. <https://doi.org/10.1080/00207540210133435>

8. ElKott DF, Veldhuis SC. Isoparametric line sampling for the inspection planning of sculptured surfaces. Computer-Aided Design. 2005;37:189-200. <https://doi.org/10.1016/j.cad.2004.06.006>

9. ElKott DF, Veldhuis SC. CAD-based sampling for CMM inspection of models with sculptured features. Engineering with Computers. 2007;23:187-206. <https://doi.org/10.1007/s00366-007-0057-y>

10. Obeidat SM, Raman S. An intelligent sampling method for inspecting free-form surfaces. International Journal Advanced Manufacturing Technology. 2009;40:1125-1136. <https://doi.org/10.1007/s00170-008-1427-3>

11. Rajamohan G, Shunmugam MS, Samuel GL. Effect of probe size and measurement strategies on assessment of freeform profile deviations using coordinate measuring machine. Measurement. 2011;44: 832-841. <https://doi.org/10.1016/j.measurement.2011.01.020>

12. Rajamohan G, Shunmugam MS, Samuel GL. Practical measurement strategies for verification of freeform surfaces using coordinate measuring machines. Metrology and Measurement Systems. 2011;18:209-222. <http://dx.doi.org/10.2478/v10178-011-0004-y>

13. Bowen Y, Fan Q, Nuodi H, Xiaosun W, Shijing W, Dirk B. Adaptive sampling point planning for free-form surface inspection under multi-geometric constraints. Precision Engineering. 2021;72:95-101. <https://doi.org/10.1016/j.precisioneng.2021.04.009>

14. Zhaoyu L, Dong H., Xiangyu L, Xiaoke D, Pengcheng H, Jiancheng H, Yue H, Hongyu Y, Kai T. Efficient five-axis scanning-inspection path planning for complex freeform surfaces. Robotics and Computer-Integrated Manufacturing. 2024;86:102687. <https://doi.org/10.1016/j.rcim.2023.102687>

15. Sliusarenko O, Escudero G, González H, Bartoñ A, Ortega N, Lallacalle LNL. Constant probe orientation for fast contact-based inspection of 3D free-form surfaces using (3+2)-axis inspection machines. Precision Engineering. 2023;84:37-44. <https://doi.org/10.1016/j.precisioneng.2023.06.013>

16. Magdziak M. Determining the strategy of contact measurements based on results of noncontact coordinate measurements. Procedia Manufacturing. 2020;51: 337-344. <https://doi.org/10.1016/j.promfg.2020.10.048>

17. Lim EM, Menq CH. The prediction of dimensional error for sculptured surface productions using the ball-end milling process – part 2: surface generation model and experimental verification. International Journal of Machine Tools and Manufacture. 1995;35:1171-1185. [https://doi.org/10.1016/0890-6955\(94\)00045-L](https://doi.org/10.1016/0890-6955(94)00045-L)

This work was prepared within the project "Innovative measurement technologies supported by digital data processing algorithms for improved processes and products", contract number PM/SP/0063/2021/1, financed by the Ministry of Education and Science (Poland) as part of the Polish Metrology Programme.

Andrzej Werner:  <https://orcid.org/0000-0002-3768-5395>

Małgorzata Poniatowska:  <https://orcid.org/0000-0003-2102-7272>



This work is licensed under the Creative Commons BY-NC-ND 4.0 license.

# SLIP BANDS AT THE TIPS OF NARROW SLOT IN BRAZILIAN NOTCHED DISK – PLANE DEFORMATION

Andrzej KAZBERUK\*

\*\* Faculty of Mechanical Engineering, Bialystok University of Technology, ul. Wiejska 45A, 15-351 Bialystok, Poland

[a.kazberuk@b.edu.pl](mailto:a.kazberuk@b.edu.pl)

received 04 November 2024, revised 07 November 2024, accepted 07 November 2024

**Abstract:** Using the method of singular integral equations, the elastic-plastic problem for notched Brazilian disk at plane deformation state was solved. Based on Dugdale model the relationships between load, notch tip opening displacement and the length of the slip bands was established. The results demonstrate the potential of the proposed method for practical applications in engineering, particularly in the assessment of structural integrity under various loading conditions.

**Key words:** cracked Brazilian disk, Dugdale model, slip bands, plastic strips, plane deformation, singular integral equations

## 1. INTRODUCTION

The basic material parameter in fracture mechanics is the critical stress intensity factor, determined experimentally on specimens with initial cracks. In the case of metals, the procedure for determining this parameter is standardized and widely used. The fracture process, in this case, begins with a fatigue-initiated crack. For quasi-brittle materials such as concrete, ceramics, or rocks, it is difficult to obtain an initial crack with strictly defined parameters. Usually, the initial crack is produced during the specimen forming stage. In this way, slots of significant width (2-4 mm) with rounded tips are obtained.

Disk-type specimens are among the most commonly used test samples for determining Mode I and mixed-mode fracture toughness in brittle and quasi-brittle materials like ceramics, concrete, rocks, and rock-like materials. A circular disk specimen subjected to diametric compressive loading is a simple and well-established indirect testing method. These so-called Brazilian tests have been widely used to obtain the tensile strength of brittle materials. An up-to-date review of works concerning various aspects of the Brazilian test can be found in [10,17].

A disk with an internal central crack, as a convenient experimental specimen for testing fracture mechanics parameters, was considered analytically by [18,37-40]. These results concerning stress field distribution and values of the stress intensity factors were confirmed by [2,3,34].

Many recent works have been devoted to the investigation of the fracture process in brittle and quasi-brittle materials using compressed disks with central narrow slots. The papers [1,4,6,31,36] present experimental investigations of the critical value of the stress intensity factor under Mode I and Mode II loading conditions using various fracture criteria. It should be emphasized that the works cited above concern the problem of stress concentration in disk specimens with a strictly defined mathematical crack (i.e., a crack of zero width). The discussion of the influence of the relative crack length and the error of the loading angle on the experimental results for the Brazilian disk was presented by [8].

The semicircular disk with an edge narrow notch was also used as a test specimen [5,6].

Theoretical and experimental investigations have been performed for chevron-notched Brazilian disks [35], or for disks with multiple pre-existing notches [41].

The application of the deformation fracture criterion to the determination of basic fracture mechanics parameters requires knowledge of the relationship between the load level and the opening displacement at the crack tip. This means that, for an arbitrary test element, not only the stress field should be determined, but also the strain field, considering the changes taking place in the fracture process zone. General solutions for cracks or notches in an infinite plane are known ([23], see also [27]), but for particular specimens, these solutions can only be regarded as asymptotic.

In the paper [13], the solution for the elastic-plastic problem for notched Brazilian disks in a plane stress state was presented. Based on the Dugdale model [9,16] (see also [33], where this model is precisely described), and assuming that only one plasticity band emanates from the tip of the narrow slot placed at the center of the Brazilian disk, the relationships between load, notch tip opening displacement, and the length of the slip bands were established.

The aim of this work is similar to that of [13], i.e., to determine the relationship between the load level and the opening displacement at the tip of the narrow slot in a cylindrical specimen under diagonal compression, but in the plane strain state.

It is assumed that in the case of a plane strain state in a body with a sharp V-notch [15,30] or crack [14,19,21-23], the stress concentrator emits two slip bands that form a certain angle with respect to one another. We shall use this approach to solve the elastic-plastic problem for the notched Brazilian disk. We assume that the fracture process zone, characterized by plastic deformations near the vertices of the narrow slot in a perfectly elastic-plastic material under plane strain, localizes in two slip bands. Under symmetrical loading, these bands are simulated with cuts of unknown lengths, with the constant tangential stress equal to the shear yield limit in accordance with the Tresca-Saint Venant plasticity condition given at the cut edges. We suppose that normal displacements are

continuous at the contour cuts, while the tangential displacements exhibit a nonzero discontinuity at these contours.

## 2. PROBLEM FORMULATION

Consider a circular disk weakened by a narrow opening with vertices rounded by circular arcs of the radius  $\rho$  (see Fig. 1a). The slot described by contour  $L_1$  is placed at the disk center (contour

$L_0$ ). Assume that the radius  $R$  of circle  $L_0$  is the unit length parameter. The projection of the slot onto the  $Ox$  axis measures  $2l_1 = 2\gamma_1 R$ . This indicates the total width of the slot. The contour of the slot consists of two parallel straight sections and two semicircles. The semicircles with radii  $\rho$  form the vertices of the narrow slot [12,26,27]. The parameter  $\varepsilon = \rho/l_1 = \rho/(\gamma_1 R)$  is the relative rounding radius of the slot vertices.

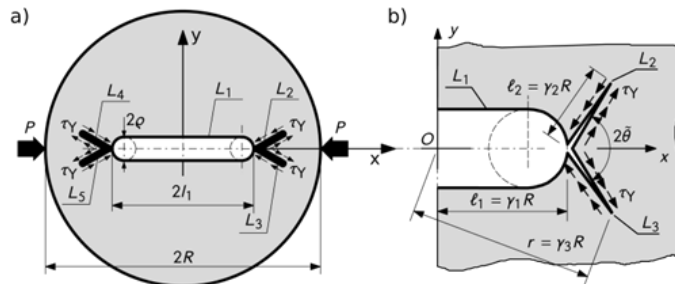


Fig. 1. a) Notched Brazilian disk with slip bands, b) detailed view on slot tip with emanating cracks

We assume that the fracture process zone is characterized by plastic deformations near the vertices of the narrow slot. In a perfectly elastic-plastic material subjected to plane strain, these deformations localize in two plastic bands, referred to as slip bands [21]. Under symmetrical loading, simulate these bands with cuts  $L_2$ ,  $L_3$  and  $L_4$ ,  $L_5$  of unknown lengths  $l_2 = \dots = l_5 = l_Y$  with the constant tangential stress  $\tau_Y$  ( $\tau_Y$  is shear yield limit in accordance with Tresca-Saint Venant plasticity condition  $\tau_Y = \sigma_Y/2$ ) given at the cut edges. Suppose that normal displacements are continuous at contours  $L_2$  and  $L_3$  ( $L_4$ ,  $L_5$  respectively) while tangential displacements reveal a nonzero discontinuity at these contours.

These cuts with the contours  $L_2$  to  $L_5$ ) are symmetrically placed with respect to both axes of the  $Oxy$  system and inclined to the  $Ox$  axis at an angle  $\theta$  (see Fig. 1b). The unknown relative extent of each linear defect that weakens the disk specimen is defined as  $l_2 = \dots = l_5 = l_Y$ .

For the convenience of data composition in numerical calculations, an additional dimensionless geometric parameter  $\gamma_3 = r/R$  is introduced. It defines the total distance of the slip band tip  $r$  from the disk center.

The set of dimensionless geometric parameters ( $\varepsilon$ ,  $\gamma_1$ ,  $\gamma_3$ ) fully describes the domain under consideration. Assuming radius  $R$  as basic unit length, we obtain relationships

$$\begin{aligned} l_1 &= \gamma_1 R, & l_2 = \dots = l_5 &= l_Y = \gamma_2 R, \\ r &= \gamma_3 R, & \rho &= \varepsilon l_1. \end{aligned} \quad (1)$$

The value of the  $\gamma_2$  parameter depends on the values of  $\gamma_1$  and  $\gamma_3$ :

$$\gamma_2 = \sqrt{\gamma_3^2 - \gamma_1^2 \sin^2 \theta} - \gamma_1 \cos \theta. \quad (2)$$

Suppose that hole edge (the smooth contour  $L_1$ ) is free of applied loads. The disk is loaded by two concentrated forces  $P$ , which compress the specimen along the  $Ox$  axis (Fig. 1a). Such type of loading cause concentration of tensile stresses in vertices ( $\pm l_1$ ) of the hole.

The problem will be solved using singular integral equation method [25] (see also [27]). Complex stress potentials are written

in the form [25]

$$\begin{aligned} \Phi_*(z) &= \Phi_0(z) + \Phi(z), \\ \Psi_*(z) &= \Psi_0(z) + \Psi(z), \end{aligned} \quad (3)$$

where functions [20]:

$$\Phi_0(z) = \sigma_p \frac{z^2 + R^2}{2(z^2 - R^2)}, \quad \Psi_0(z) = \frac{2R^4}{(z^2 - R^2)^2}. \quad (4)$$

Nominal stress  $\sigma_p = P/(\pi R)$  is equal to normal stress  $\sigma_y$  alongside  $Ox$  axis,  $z = x + iy$ .

Functions  $\Phi_0(z)$  and  $\Psi_0(z)$  describe the stress state in a solid disk, which is a disk without any holes, loaded by concentrated forces. In contrast, the potentials  $\Phi(z)$  and  $\Psi(z)$  characterize the disturbed stress state caused by the opening ( $L_1$ ) and the cuts ( $L_2$  and  $L_3$ ). These potentials are written in the following form [25]:

$$\begin{aligned} \Phi(z) &= \frac{1}{2\pi} \int_L \left\{ \left[ \frac{1}{t-z} + \frac{\bar{t}}{z\bar{t}-R^2} \right] g'(t) dt + \right. \\ &\quad \left. + \frac{z(t\bar{t}-R^2)(z\bar{t}-2R^2)}{R^2(z\bar{t}-R^2)^2} \overline{g'(t)} d\bar{t} \right\}, \\ \Psi(z) &= \frac{1}{2\pi} \int_L \left\{ \left[ \frac{\bar{t}^3}{(z\bar{t}-R^2)^2} - \frac{\bar{t}}{(t-z)^2} \right] g'(t) dt + \right. \\ &\quad \left. + \left[ \frac{1}{t-z} + \frac{\bar{t}}{z\bar{t}-R^2} + \frac{\bar{t}(z\bar{t}-3R^2)(t\bar{t}-R^2)}{(z\bar{t}-R^2)^3} \right] \overline{g'(t)} d\bar{t} \right\}. \end{aligned} \quad (5)$$

Here  $g'(t)$  ( $t \in L_k$ ,  $k=1, \dots, 5$ ) is an unknown function of the derivative of displacement discontinuity vector across the cut contour.

The boundary condition at the contour  $L$  is expressed as follows:

$$N(t) + iT(t) = p(t) \quad t \in L, \quad L = \bigcup_{k=1}^5 L_k, \quad (6)$$

where  $N$  and  $T$  are normal and tangential components of the stress vector. The right side of the equation (6) is equal [25]

$$\begin{aligned} p(t) &= \sigma_k - \left\{ \Phi_0(t) + \overline{\Phi_0(t)} + \frac{d\bar{t}}{dt} \left[ t\overline{\Phi_0'(t)} + \overline{\Psi_0(t)} \right] \right\}, \\ t &\in L, \end{aligned} \quad (7)$$

It was assumed that constant tangential stress is equal  $\tau_Y = \sigma_Y/2$ . Where  $\sigma_Y$  is equal to the material strength of the specimen



determined in the Brazilian test (compressed disk without slot):

$$\sigma_k = \begin{cases} 0, & k = 1, \\ i\tau_Y, & k = 2, \dots, 5 \end{cases} \quad (8)$$

Fulfilling boundary condition 6) using potentials (5) we obtain the system of singular integral equations with unknown functions  $g'_m(t)$  ( $m=1, \dots, 5$ )

$$\frac{1}{\pi} \sum_{k=1}^3 \int_{L_k} [K_{km}(t, t') g'_m(t) dt + L_{km}(t, t') \overline{g'_m(t)} d\bar{t}] = p_m(t), \quad t' \in L_m, \quad m = 1, \dots, 5, \quad (9)$$

where kernels are as follows:

$$K(t, t') = f_1(t, t') + \overline{f_2(t, t')} + \frac{dt'}{dt} [t' \overline{g'_2(t, t')} + \overline{h_2(t, t')}], \quad (10)$$

$$L(t, t') = f_2(t, t') + \overline{f_1(t, t')} + \frac{dt'}{dt} [t' \overline{g'_1(t, t')} + \overline{h_1(t, t')}], \quad (11)$$

where

$$f_1(t, t') = \frac{1}{2} \left[ \frac{1}{t-t'} + \frac{\bar{t}}{t'\bar{t}-R^2} \right], \quad (12)$$

$$f_2(t, t') = \frac{t'(t\bar{t}-R^2)(t'\bar{t}-R^2)}{2R^2(t'\bar{t}-R^2)^2}, \quad (13)$$

$$g_1(t, t') = \frac{1}{2} \left[ \frac{1}{(t-t')^2} - \frac{\bar{t}^2}{(t'\bar{t}-R^2)^2} \right], \quad (14)$$

$$g_2(t, t') = \frac{R^2(t\bar{t}-R^2)}{(t'\bar{t}-R^2)^3}, \quad (15)$$

$$h_1(t, t') = \frac{1}{2} \left[ -\frac{\bar{t}}{(t-t')^2} + \frac{\bar{t}^3}{(t'\bar{t}-R^2)^2} \right], \quad (16)$$

$$h_2(t, t') = \frac{1}{2} \left\{ \frac{1}{t-t'} + \frac{\bar{t} [4R^4 - 3R^2 \bar{t}(t'+t) + t'\bar{t}^2(t'+t)]}{(t'\bar{t}-R^2)^3} \right\}. \quad (17)$$

### 3. NUMERICAL SOLUTION OF SINGULAR INTEGRAL EQUATIONS

Assume clockwise direction of tracing the contour  $L_1$  so the elastic region stays on the left during tracing. Taking into consideration symmetry of the contour with respect to both coordinate axes, we can write its parametric equation in the form [27]:

$$t = R\omega_1(\xi) = R \begin{cases} \omega_q(\xi), & 0 \leq \xi < \pi/2, \\ -\omega_q(\pi - \xi), & \pi/2 \leq \xi < \pi, \\ -\omega_q(\xi - \pi), & \pi \leq \xi < 3\pi/2, \\ \omega_q(2\pi - \xi), & 3\pi/2 \leq \xi < 2\pi. \end{cases} \quad (18)$$

the function  $\omega_q(\xi)$  describes the segment of contour  $L_1$  laying in the fourth quarter of the coordinate system:

$$\omega_q(\xi) = \begin{cases} 1 - \varepsilon + \varepsilon(\cos c\xi - i \sin c\xi), & 0 \leq \xi < \pi/(2c), \\ \varepsilon c(\pi/2 - \xi) - i\varepsilon, & \pi/(2c) \leq \xi < \pi/2, \end{cases} \quad (19)$$

where parameter  $c=1+2(1/\varepsilon-1)/\pi$ . Total contour  $L_1$  length equals to  $2\pi\varepsilon_1 R c$ .

Parametric equation describing cut  $L_2$  is written in the form

$$t = R\omega_2(\xi) = R \left[ \gamma_1 + \frac{1}{2} \gamma_2 (1 + \xi) e^{i\theta} \right], \quad -1 \leq \xi \leq 1 \quad (20)$$

Contour  $L_3$  is symmetrical to  $L_2$  with respect to the Ox axis so

$$t = R\omega_3(\xi) = \overline{R\omega_2(\xi)}, \quad -1 \leq \xi \leq 1. \quad (21)$$

Contours  $L_4$  and  $L_5$  are symmetrical to  $L_2$  and  $L_3$  with respect to the Oy axis so

$$t = R\omega_4(\xi) = -\overline{R\omega_2(\xi)}, \quad t = R\omega_5(\xi) = -R\omega_2(\xi), \quad -1 \leq \xi \leq 1 \quad (22)$$

Introducing substitutions

$$\begin{aligned} t &= R\omega_1(\xi), \quad t' = R\omega_1(\eta), \quad t, t' \in L_1, \quad 0 \leq \xi, \eta \leq 2\pi, \\ t &= R\omega_k(\xi), \quad t' = R\omega_k(\eta), \quad t, t' \in L_k, \\ k &= 2, \dots, 5, \quad -1 \leq \xi, \eta \leq 1, \end{aligned} \quad (23)$$

one can reduce the system of integral equations (9) to the canonical form

$$\begin{aligned} &\frac{1}{\pi} \int_0^{2\pi} [M_{1m}(\xi, \eta) g'_1(\xi) + N_{1m}(\xi, \eta) \overline{g'_1(\xi)}] d\xi + \\ &+ \frac{1}{\pi} \sum_{k=2}^5 \int_{-1}^1 [M_{km}(\xi, \eta) g'_k(\xi) + N_{km}(\xi, \eta) \overline{g'_k(\xi)}] d\xi = \\ &p_m(\eta), \quad m = 1, 2, 3, \end{aligned} \quad (24)$$

where

$$M_{km}(\xi, \eta) = RK_{km}(R\omega_k(\xi), R\omega_m(\eta)), \quad (25)$$

$$N_{km}(\xi, \eta) = RL_{km}(R\omega_k(\xi), R\omega_m(\eta)), \quad (26)$$

$$g'_k(\xi) = g'(R\omega_k(\xi)) \omega'_k(\xi), \quad (27)$$

$$p_m(\eta) = p(R\omega_m(\eta)). \quad (28)$$

A solution of the system of integral equations (24) consists of five complex functions  $g'_k(\xi)$  assigned to the contours  $L_k$ . Function  $g_1(\xi)$  ( $0 \leq \xi \leq 2\pi$ ) is  $2\pi$ -periodic continuous function. However, in order to obtain a sufficiently accurate numerical solution we have to densify quadrature nodes and collocation points in the vicinity of narrow slot tips. We use here nonlinear variant of sigmoid transformation [11,32] adapted to periodic case [32]:

$$\xi = G(\tau) = \tau - \frac{1}{2} \sin 2\tau, \quad 0 \leq \tau \leq 2\pi. \quad (29)$$

Consequently, the function we are looking for is as follows

$$u_1(\tau) = g'_1(G(\tau)), \quad 0 \leq \tau \leq 2\pi. \quad (30)$$

A solution of the system of integral equations (24) for contours  $L_2$  to  $L_5$  is sought in the class of functions, which have an integrable singularity at the ends of integration interval

$$g'_k(\xi) = \frac{u_k(\xi)}{\sqrt{1-\xi^2}}, \quad -1 \leq \xi \leq 1, \quad (31)$$

where  $u_k(\xi)$  ( $k=2, \dots, 5$ ) are continuous functions. Finally, modified system of singular integral equation (24) takes the form

$$\begin{aligned} &\frac{1}{\pi} \int_0^{2\pi} [M_{1m}(\xi, \eta) u_1(\tau) + N_{1m}(\xi, \eta) \overline{u_1(\tau)}] G(\tau) d\tau + \\ &+ \frac{1}{\pi} \sum_{k=2}^5 \int_{-1}^1 [M_{km}(\xi, \eta) u_k(\xi) + N_{km}(\xi, \eta) \overline{u_k(\xi)}] d\xi = \\ &p_m(\eta), \quad m = 1, 2, 3 \end{aligned} \quad (32)$$

In points  $t = \pm l_1$  where contours  $L_2$  to  $L_5$  intersect contour  $L_1$  the values of  $g'_k(-1)$  ( $k=2, 5$ ) must be finite, thus we should provide four additional equations

$$u_k(-1) = 0, \quad k=2, 5. \quad (33)$$

For numerical integration of singular integral equation (32) two different methods must be used. For closed-loop contour  $L_1$ , we apply midpoint rule [7] and Gauss-Chebyshev quadrature [25] for  $L_2$  to  $L_5$  contours. Finally, we get a system of complex linear algebraic equations which is the discrete analogue of the respective system of integral equations (24)

$$\begin{aligned} & \frac{2}{n_1} \sum_{i=1}^{n_1} [M_{1m}(\xi_i, \eta_j) u_1(\tau_i) + N_{1m}(\xi_i, \eta_j) \overline{u_1(\tau_i)}] G(\tau_i) + \\ & \sum_{k=2}^5 \left\{ \frac{1}{n_k} \sum_{i=1}^{n_k} [M_{km}(\xi_i, \eta_j) u_k(\xi_i) + N_{km}(\xi_i, \eta_j) \overline{u_k(\xi_i)}] \right\} = \\ & p_m(\eta_j), \end{aligned} \quad (34)$$

$$m = 1, \quad j = 1, \dots, n_k, \quad m = 2, \dots, 5, \quad j = 1, \dots, (n_k - 1)$$

where quadrature nodes and collocation points are determined by the formulas:

$$\xi_i = G(\tau_i), \tau_i = \frac{\pi(2i-1)}{n_1}, i=1, \dots, n_1, \quad (35)$$

$$\eta_j = G(\theta_j), \theta_j = \frac{2\pi(j-1)}{n_1}, j=1, \dots, n_1, \quad (36)$$

$$3\xi_i = \cos \frac{\pi(2i-1)}{2n_k}, i=1, \dots, n_k, k=2, \dots, 5, \quad (37)$$

$$\eta_j = \cos \frac{\pi j}{n_k}, j=1, \dots, (n_k - 1), k=2, \dots, 5. \quad (38)$$

Assuming  $n_2 = n_3 = \dots = n_5$  the system (34) consists of  $n_1 + 4(n_2 - 1)$  complex equations. Using Lagrange interpolation on Chebyshev nodes [25] to conditions (33), we obtain four missing equations

$$\begin{aligned} & \frac{1}{n_k} \sum_{i=1}^{n_k} (-1)^{i+n_k} \tan \frac{\pi(2i-1)}{4n_k} u_k(\xi_i) = 0, \\ & k = 2, \dots, 5. \end{aligned} \quad (39)$$

Right side of the equation (34) can be easily calculated using relationship (7). Introducing the relation  $\gamma_Y = \sigma_p / \tau_Y$  ( $\sigma_p = P / (\pi R)$ ) as relative load level parameter, we can write down  $p_m(\eta_j)$  in compact form:

$$p_m(\eta_j) = \begin{cases} p_1(\eta_j), & m = 1, \\ \left(1 - \frac{i}{\gamma_Y}\right) p_1(\eta_j), & m = 2, \dots, 5, \end{cases} \quad (40)$$

where

$$p_1(\eta_j) = \sigma_p \frac{|\omega_k(\eta_j)|^2 - 1}{\omega_k(\eta_j)^2 - 1} \left[ \frac{2}{\omega_k(\eta_j)^2 - 1} \frac{\overline{\omega'_k(\eta_j)}}{\omega'_k(\eta_j)} - \frac{|\omega_k(\eta_j)|^2 + 1}{\omega_k(\eta_j)^2 - 1} \right], \quad (41)$$

$$k=1, \dots, 5.$$

Solution of the problem is symmetrical with respect to the axis  $Ox \parallel Oy$ . Conditions resulting from symmetry concerning the sought function  $u_k(\xi)$  and necessary kernel modifications are described in details in [29] (see also [27]). Thus, the rank of linear system (34), (39), can be easily reduce by a factor of four.

Having obtained values of sought function  $u(\xi_k)$ , one can determine the stress-strain state in whole elastic region by using an integral representation of complex stress potentials (5).

The slot edge (contour  $L_1$ ) is free of applied load, then the contour stress at the edge can be calculated using a simple formula [27].

$$\sigma_s = -4\sigma_p \Im \frac{u_1(\xi)}{\omega'_1(\xi)} = -4\sigma_p \Im \frac{u_1(\tau)}{\omega'_1(G(\tau))}. \quad (42)$$

Stress intensity factors in crack tips  $K_I$  and  $K_{II}$  can be directly expressed through the sought function  $g'_k(t)$  (31). Let us introduce corresponding dimensionless stress intensity factors  $F_I$  and  $F_{II}$  by means of the following relationship

$$K_I^+ - iK_{II}^+ = (F_I^+ - iF_{II}^+) \sigma_p \sqrt{\pi R}. \quad (43)$$

Here upper indexes (+) indicate crack tip at  $\xi = +1$ . Taking into account relation (31), we get for coefficients  $F_I$  and  $F_{II}$  the formula [25]:

$$F_I^+ - iF_{II}^+ = -\sqrt{|\omega_k(+1)|} \frac{u_k(+1)}{\omega_k(+1)}, \quad k = 2, \dots, 5, \quad (44)$$

where

$$\begin{aligned} u_k(+1) &= -\frac{1}{n} \sum_{i=1}^{n_k} (-1)^i u_k(\xi_i) \cot \frac{\pi(2i-1)}{4n}, \\ k &= 2, \dots, 5. \end{aligned} \quad (45)$$

Cracks  $L_2$  and  $L_3$  (and  $L_4, L_5$  respectively) simulate fracture process zones (slip bands) at the tips of narrow slot  $L_1$ , thus stresses at the crack  $L_k$  end must be finite

$$\begin{aligned} g'_k(t = \pm(l_k)) &= g'_k(R\omega_k(+1)) = 0, \rightarrow \\ u_k(+1) &= 0, k=2, \dots, 5. \end{aligned} \quad (46)$$

This condition allows as to calculate unknown length  $l_2 = \gamma_2 R$  using iteration process.

The length of slip band depends on the value of the angle  $\theta$ . It was assumed that there is an unique  $\theta$  angle for which the band length is maximum.

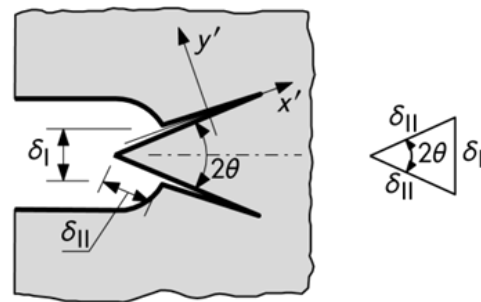


Fig. 2 Slot tip opening displacement

Opening displacement at the notch tip (Fig. 2) can be calculated based on known [25] relationship between function  $g_k(t)$  ( $k=2,3$ ) and displacement discontinuity vector  $(v_k^+ - v_k^-)$  across the contour  $L_k$

$$\begin{aligned} 2G \frac{d}{dx'} (v_k^+ - v_k^-) &= (1 + \kappa) g'_k(x'), \quad x' \in L_k, \\ k &= 2, \dots, 5, \end{aligned} \quad (47)$$

where  $x'$  is a local abscissa at contour  $L_k$ ,  $G$  - shear modulus,  $\kappa$  - Muskhelishvili's constant.

Taking into consideration that in the beginning of cuts  $L_2$  and  $L_3$  only tangential displacements have discontinuity  $\delta_{II}$ , we obtain (see Fig. 2)

$$\delta_I^V = 2\delta_{II} \sin \theta. \quad (48)$$

The relationship  $(1 + \kappa) / (4G) = 2(1 - \nu^2) / E$  is valid in plane strain state, so taking into account (47), one can find the tangential displacement across cut edges  $L_2 =$  in the point  $x' = l_2^-$ , i.e. in the slot tip, as follows

$$\delta_{II} = \Im \delta(l_2^-) = \frac{4(1-\nu^2)}{E} \Im g(l_2^-), \quad (49)$$

where values of function  $g(l_2^-)$  are determined by relationship (45):

$$\tilde{\delta}_I = -\frac{8(1-\nu^2)}{E} \sin \theta \frac{1}{n_2} \sum_{i=1}^{n_2} \Im u_2(\xi_i). \quad (50)$$

In the next section the relationship between the theoretical value of dimensionless notch tip opening displacement  $\tilde{\delta}_I$  and critical load value  $\sigma_c = \sigma_n$  for given geometrical parameters (narrow slot tip radius  $\varepsilon$ , relative slot range  $\gamma_1$ ), and standard material constants (Young's modulus  $E$ , Poisson's ratio  $\nu$ , relative material strength  $\gamma_Y$ ). Knowing the value of the critical load the critical stress

intensity factor  $K_c$  can be calculated with the following formula [23,24]:

$$K_c = \sqrt{\delta_I E \sigma_c} = \sqrt{\tilde{\delta}_I \gamma_Y \sigma_c \sqrt{\pi R}}. \quad (51)$$

#### 4. NUMERICAL RESULTS

The problem as it was stated have two independent geometrical parameters:  $\varepsilon$ ,  $\gamma_1$ , and dimensionless load level  $\gamma_Y$ . The unknown are relative band length  $\gamma_2$  (or extent  $\gamma_3$ ) and the angle  $2\theta$  between bands which emanates from slot tip. In order to reduce the number of independent parameters, it was assumed constant rounding radius of slot tips  $\rho=1/75R$  and the calculations were performed for the relative slot span  $\gamma_1$  chosen from the set  $\gamma_1 = \{0.1, 0.2, 0.3, 0.4, 0.5\}$ , thus relative rounding radius of the slot vertices can be easily calculated as  $\varepsilon=1/(75\gamma_1)$ .

As has been shown in [13,27], plastic deformation near rounded notch tip begins when tangential stresses  $\tau_n$  at lines directed along slip bands reach half of the maximal normal stress  $(\sigma_s)_{\max}$  value. Which lets you calculate corresponding minimal load level  $(\gamma_Y)_{\min}$

$$|\tau_n|_{\max} = \tau_Y = \frac{1}{2} (\sigma_s)_{\max} \rightarrow (\gamma_Y)_{\min} = \frac{2}{R_I} \approx 0.668. \quad (52)$$

The value of the stress rounding factor [26,28] is  $R_I=2.992$ .

The following discrete set of  $\gamma_Y = \sigma_p/\tau_Y$  values was used for calculations:  $\gamma_Y = [0.8, 0.9, 1.0, 1.2, 1.5, 2.0, 5.0]$ . The  $\theta$  values were taken from the  $1^\circ \leq \theta \leq 85^\circ$  range every 5 degrees, decreasing the step in the vicinity of the sought maximum value of  $\gamma_2$ .

Fig. 3 shows the dependence of the  $\gamma_3$  range on the slip band angle  $\theta$  for several loading levels  $\gamma_Y$ . As can be seen, for the minimum  $\gamma_Y=0.8$  value the maximum range of the bands is achieved for an angle of approximately  $\theta=2.3^\circ$  with a corresponding range of  $\gamma_3=0.89$ . For higher values of the load level  $\gamma_Y$  the maxima of the function  $\gamma_3(\theta)$  shift towards  $\theta \rightarrow 0$ .

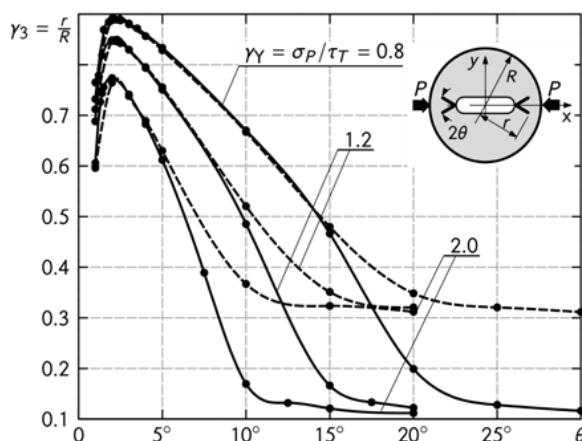


Fig. 3. Dependence of the  $\gamma_3$  range on the slip band angle  $\theta$  for several loading levels  $\gamma_Y$ .

The dependence of the relative length of the slip band  $\gamma_2$  on the narrow slot extent  $\gamma_1$  is shown in Fig. 4. For longer slots the  $\gamma_2(\gamma_Y)$  bandwidth functions become less and less predictable.

Fig. 5 shows the plot of the  $\delta_I$  notch tip opening displacement dependence on the  $\gamma_Y$  load level for several values of the central slot range  $\gamma_1$ .

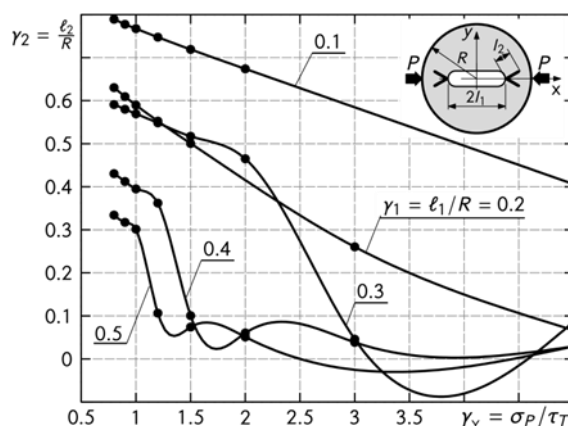


Fig. 4. Dependence of the relative length of the slip band  $\gamma_2$  on the narrow slot extent  $\gamma_1$

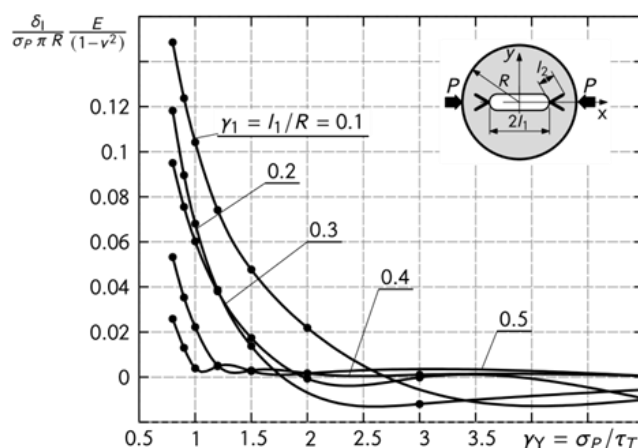


Fig. 5. Notch tip opening displacement  $\delta_I$  dependence on the  $\gamma_Y$  load level for several values of the central slot range  $\gamma_1$

#### 5. CONCLUSIONS

The elastic-plastic problem for Brazilian disk with central narrow slot in plane strain state was solved. The solution was obtained by the method of singular integral equations with complex stress potentials for a system of cracks and openings in two-dimensional circular elastic domain. All necessary analytical background was documented in detail. Based on Dugdale model of fracture process zone, relationships between the load, notch tip opening displacement, and the length of the slip bands were established. Numerical calculations for arbitrary but representative set of geometrical parameters were performed.

The presented solution, despite the obvious simplifications resulting from the adopted assumptions (plane strain state and fracture process zone as a slip band), can be used to estimate the fracture mechanics parameters of quasi-brittle materials determined in the Brazilian test.

#### REFERENCES

1. Atahan HN, Tasdemir MA, Tasemir C, Ozyurt N and Akyuz S. Mode I and mixed mode fracture studies in brittle materials using the Brazilian disc specimen. *Mater. Struct.* 2005; 38:305–12.
2. Atkinson C, Smelser R, and Sanchez J. Combined mode fracture via the cracked Brazilian disk test. *Int. J. Fract.* 1982;18:279–91.
3. Awaji H and Sato S. Combined mode fracture toughness measurement by the disk test. *J.Eng. Mater. Technol.* 1978;100:175–82.

4. Ayatollahi M, Aliha M. Mixed mode fracture in soda lime glass analyzed by using the generalized MTS criterion. *International Journal of Solids and Structures* 2009; 46:311–21.
5. Ayatollahi M and Aliha M. On the use of Brazilian disc specimen for calculating mixed mode I–II fracture toughness of rock materials. *Engineering Fracture Mechanics* 2008;75:4631–41.
6. Ayatollahi M, Aliha M. Wide range data for crack tip parameters in two disc-type specimens under mixed mode loading. *Computational Materials Science* 2007;38:660–70.
7. Belotserkovsky SM and Lifanov IK. *Method of discrete vortices*. CRC Press LLC. Boca Raton. 1993.
8. Dong S. Theoretical analysis of the effects of relative crack length and loading angle on the experimental results for cracked Brazilian disk testing. *Engineering Fracture Mechanics* 2008;75:2575–81.
9. Dugdale D. Yielding of steel sheets containing slits. *J. Mech. Phys. Solids* 1960; 8:100–4.
10. García VJ, Márquez CO, Zúñiga-Suárez AR, Zúñiga-Torres BC, Vilalta-Granda LJ. Brazilian Test of Concrete Specimens Subjected to Different Loading Geometries: Review and New Insights. *International Journal of Concrete Structures and Materials*. 2017;11:343–63.
11. Johnston PR. Application of sigmoidal transformations to weakly singular and near-singular boundary element integrals. *Int. J. Numer. Meth. Eng.* 1999; 45:1333–48.
12. Kazberuk A. Koncentracja naprężeń wokół owalnego otworu. *Acta Mech. Autom.* 2007;1:25–30.
13. Kazberuk A. Application of the Deformation Fracture Criterion to Cracking of Disc Specimens with a Central Narrow Slot. *Acta Mechanica et Automatica*. 2022;16.
14. Kipnis LA, Cherepanov GP. Slip lines at the vertex of a wedge-like cut. *J. Appl. Math. Mech.* 1984; 48:112–4.
15. Kuliev VD. Plastic rupture lines at the tip of a wedge. *Int. Appl. Mech.* 1979; 15:221–7.
16. Leonov MY, Panasyuk VV. Development of a nanocrack in a solid. *Prikl. Mekh.* 1959; 5:391–401.
17. Li D, Wong LNY. The Brazilian disc test for rock mechanics applications: review and new insights. *Rock mechanics and rock engineering* 2013; 46:269–87.
18. Libatskii L, Kovchik S. Fracture of discs containing cracks. *Mater. Sci.* 1967; 3:334–9.
19. Lo KK. Modeling of plastic yielding at a crack tip by inclined slip planes. *Int. J. Fract.* 1979; 15:583–9.
20. Muskhelishvili NI. *Some Basic Problems of the Mathematical Theory of Elasticity. Fundamental Equations Plane Theory of Elasticity Torsion and Bending*. 2nd ed. Noordhoff International Publishing, Leyden. 1977:764.
21. Panasyuk VV, Savruk MP. Model for plasticity bands in elastoplastic failure mechanics. *Mater. Sci.* 1992; 28:41–5.7
22. Panasyuk VV, Savruk MP. Plastic strip model in elastic-plastic problems of fracture mechanics. *Adv. Mech* 1992; 15:123–47.
23. Rice JR. Limitations to the small scale yielding approximation for crack tip plasticity. *J. Mech. Phys. Solids* 1974; 22:17–26.
24. Rice JR. The location of plastic deformation. *Theor. Appl. Mech.* 1976; 1:207–20.
25. Savruk MP. Two-dimensional problems of elasticity for bodies with cracks (in Russian). *Naukova Dumka*. Kiev. 1981.
26. Savruk MP, Kazberuk A. A unified approach to problems of stress concentration near V-shaped notches with sharp and rounded tip. *Int. Appl. Mech.* 2007; 43:182–97.
27. Savruk MP, Kazberuk A. *Stress Concentration at Notches*. Springer International Publishing Switzerland. 2017;498.
28. Savruk MP, Kazberuk A. Two-dimensional fracture mechanics problems for solids with sharp and rounded V-notches. *Int. J. Fract.* 2010; 161:79–95.
29. Savruk MP, Osiv PN, Prokopchuk IV. *Numerical analysis in plane problems of the crack theory (in Russian)*. Naukova Dumka, Kiev. 1989.
30. Savruk MP, Zavodovs'kyi AM, Panasyuk VV. On fracture of bodies with V-notches under plane strain. *Mekhanika i fizyka ruinuvannya budivelnnykh materialiv ta konstruktiv (Mechanics and physics of fracture of building materials and structures)*. Lviv. 2005;10:140–7.
31. Seitl S, Miarka P. Evaluation of mixed mode I/II fracture toughness of C 50/60 from Brazilian disc test. *Frattura ed Integrità Strutturale* 2017; 11:119–27
32. Sidi A. A new variable transformation for numerical integration. H. Brass H. and G. Hämmerlin, editors. *Numerical integration IV*. Ed. by Brass H and Hämmerlin G. 1993;359–73.
33. Sun CT. *Fracture mechanics*. Ed. by Jin ZH. Waltham. Mass. Butterworth-Heinemann/Elsevier. 2012;311 pp.
34. Tang S. Stress intensity factors for a Brazilian disc with a central crack subjected to compression. *International Journal of Rock Mechanics and Mining Sciences* 2017; 93:38–45.
35. Wang Q, Gou X, Fan H. The minimum dimensionless stress intensity factor and its upper bound for CCNBD fracture toughness specimen analyzed with straight through crack assumption. *Engineering Fracture Mechanics* 2012; 82:1–8.
36. Xiankai B, Meng T, Jinchang Z. Study of mixed mode fracture toughness and fracture trajectories in gypsum interlayers in corrosive environment. *Royal Society Open Science*. 2018; 5.
37. Yarema SY, Ivanitskaya G, Maistrenko A, Zboromirskii A. Crack development in a sintered carbide in combined deformation of types I and II. *Strength of Materials* 1984; 16:1121–8.
38. Yarema SY. Stress state of disks with cracks, recommended as specimens for investigating the resistance of materials to crack development. *Mater. Sci.* 1977;12:361–74.
39. Yarema SY and Krestin GS. Determination of the modulus of cohesion of brittle materials by compressive tests on disc specimens containing cracks. *Mater. Sci.* 1967; 2:7–10.
40. Yarema SY, Krestin GS. Limiting equilibrium of a disk with a diametral crack. *Int. Appl. Mech.* 1968; 4:55–8.
41. Zhou S. Fracture Propagation in Brazilian Discs with Multiple Pre-existing Notches by Using a Phase Field Method. *Periodica Polytechnica Civil Engineering* 2018; 62:700–8.

The work has been accomplished under the research project No. WZ/WM-IIM/3/2020.

Andrzej Kazberuk:  <https://orcid.org/0000-0003-4179-0312>



This work is licensed under the Creative Commons BY-NC-ND 4.0 license.



# RECYCLED CARBON FIBERS FROM WIND TURBINE BLADES: ADVANCING THE MECHANICAL PERFORMANCE OF CONCRETE

Julita KRASSOWSKA<sup>\*ID</sup>, Andrzej KAZBERUK<sup>\*\*ID</sup>

<sup>\*</sup>Faculty of Civil and Environmental Engineering, Bialystok University of Technology, ul. Wiejska 45A, 15-351 Bialystok, Poland

<sup>\*\*</sup> Faculty of Mechanical Engineering, Bialystok University of Technology, ul. Wiejska 45A, 15-351 Bialystok, Poland

[j.krassowska@pb.edu.pl](mailto:j.krassowska@pb.edu.pl), [a.kazberuk@pb.edu.pl](mailto:a.kazberuk@pb.edu.pl)

received 26 December 2024, revised 27 December 2024, accepted 27 December 2024

**Abstract:** Recycled carbon fibers from wind turbine blades offer a sustainable approach to enhancing concrete's mechanical properties. This study investigates the preliminary performance of concrete reinforced with fibers recovered via pyrolysis. Experimental results demonstrate improvements in flexural strength (up to 30%) and fracture mechanics parameters (e.g.,  $K_{Ic}$  and  $CTOD_c$ ). Planned research will focus on optimizing mix designs and exploring deformation criteria for quasi-brittle materials, paving the way for environmentally friendly construction solutions.

**Key words:** recycled carbon fibers, fiber-reinforced concrete, fracture properties, sustainable construction

## 1. INTRODUCTION

Wind turbine blades have a service life of approximately 20–25 years, after which they constitute significant waste that is difficult to dispose of in landfills. Due to the large number of turbines installed around the world, the amount of waste generated is constantly increasing. Recycling alleviates environmental pressure by minimizing waste accumulation. Turbine blades are made of high-quality materials, such as carbon fibers, which are energy-intensive in production. Recycling allows these raw materials to be recovered and reused in various industries, which reduces the need for mining new raw materials [1-3]. Recovered materials, such as carbon fibers, can be used in construction, automotive, and aviation, giving them new life and increasing their economic value. The use of fibers in concrete structural elements increases their crack resistance, counteracts the development of shrinkage cracks, and prevents brittle cracking of concrete.

Currently, various types of non-metallic fibers are used in construction: carbon, basalt, glass, plastic as well as organic fibers. Fibers used as concrete additives differ in origin, thickness, length, tensile strength, and modulus of longitudinal elasticity. Thus, they significantly change the mechanical properties of resulting concrete in different ways. Therefore, their effective use requires in-depth analysis that goes beyond simple assessment of compressive and flexural strength. We need to conduct systematic tests of fibrous cement composites and modify existing methods for assessing mechanical properties of fiber-reinforced concrete.

The growing interest in the use of recycled fibers is confirmed by numerous recent publications [4–7]. Recycled tyre cords, feather fibers, steel chips, wood fibers from paper waste and high density polyethylene from PET bottles and woven bags and woven plastic bags are used as additives in concrete [7]. Recycled textile carpet fibers have been shown to increase the tensile and flexural strength of concrete elements [9,10] and the addition of

recycled steel fibers (RSF) to concrete can be a cheaper substitute for steel reinforcement [11,12].

## 2. PRELIMINARY EXPERIMENTAL INVESTIGATION

In our own preliminary research, carbon fibers obtained from recycling wind turbine blades made of carbon composite were used. The fiber recovery process was carried out by Anmet using the pyrolysis method using their own technology. The recovered carbon fibers, characterized by (according to the manufacturer) tensile strength of 1.17 GPa and Young's modulus of 317 GPa. High fiber strength and especially a very high longitudinal elasticity modulus predispose these fibers as good dispersed reinforcement for structural concrete.

A total of 32 series of concrete samples with different types of cement, water to cement ratio ( $w/c = 0.4$  and  $0.5$ ) and fiber content ( $0, 2, 4$  and  $8 \text{ kg/m}^3$ ) were tested. The tests revealed a beneficial impact of the recovered carbon fibers on the compressive strength of concrete. Compared to the reference concrete made of CEM I 42.5R cement, with water to cement ratio ( $w/c$ ) of  $0.5$  and  $0.4$ , a decrease in this strength of about 17% was observed. In the case of concrete with CEM II 42.5 R/B-M (S-V) cement, with a  $w/c$  of  $0.5$  and a fiber content of  $4 \text{ kg/m}^3$ , the compressive strength increased by a maximum of 30%. Young's modulus tests showed that the addition of fibers has a minimal effect on the secant modulus of elasticity of concrete, which confirms general observations in this field. The use of recycled dispersed reinforcement in concrete significantly improved its flexural strength compared to the reference concrete. The largest increase, up to 30%, was observed in the series with CEM I 42.5R cement at  $w/c$  equal to  $0.4$  and fiber content of  $4$  and  $8 \text{ kg/m}^3$ , as well as in the series with CEM II 42.5 R/B-M (S-V) cement at  $w/c$  equal to  $0.4$  and fiber content of  $8 \text{ kg/m}^3$ .

The residual tensile strength of recycled carbon fiber concrete (recC) increased with increasing fiber content from 2 kg/m<sup>3</sup> to 8 kg/m<sup>3</sup>, reaching a maximum increase of 40% for concrete with CEM I 42.5R cement, w/c ratio 0.4 and fiber content 8 kg/m<sup>3</sup>. Concrete containing recC exhibited enhanced fracture mechanics parameters, such as increased stress intensity factor (K<sub>Ic</sub>) and larger critical crack opening displacement (CTOD<sub>c</sub>).

### 3. PLANNED EXPERIMENTAL AND THEORETICAL RESEARCH

The planned own research aims to determine the effect of carbon fibers recovered from the renewable energy sector on the properties of cement concretes. This includes examining both fresh and hardened states of concrete, such as workability, setting time, and early-age strength. Additionally, long-term durability properties like freeze-thaw resistance, chloride ion penetration, and carbonation depth will be investigated to assess the material's suitability for harsh environmental conditions.

The main goal of the first stage of the research will be to develop recipes for concretes with the addition of carbon fibers, taking into account the desired features of the concrete mix and the mechanical properties of the designed concrete, i.e.: compressive strength, tensile strength during shearing, tensile strength during splitting, and Young's modulus. Special attention will be given to optimizing fiber dispersion within the matrix to ensure uniform reinforcement and to minimize potential clustering.

The fracture mechanics parameters of concrete will be tested in accordance with the RILEM TC89 procedure and the general guidelines of the fib Model Code. These tests will include determining stress intensity factors, energy dissipation during cracking, and crack propagation patterns under various loading conditions. An important part of the planned research will be to conduct the necessary theoretical analyses and experimental studies, further developing our own deformation criterion for fracture of quasi-brittle materials. The research will also involve comparative studies to benchmark the performance of recycled carbon fibers against other commonly used reinforcement materials.

### 4. CONCLUSIONS

The incorporation of recycled carbon fibers (recC) into concrete is an innovative approach that significantly improves its mechanical properties, such as compressive strength, flexural strength and fracture toughness. Despite technological challenges, such as uniform fiber distribution or mixture optimization, recC offers significant environmental and economic benefits, supporting sustainable development. Further research in this area is crucial to fully exploit the potential of this material in construction.

### REFERENCES

1. Global Wind Energy Council (GWEC). Decommissioning and Recycling of Wind Turbine Blades. 2021.
2. WindEurope. Accelerating Wind Turbine Blade Circularity. 2020.
3. European Commission European Union. Recycling Wind Turbine Blades to Support Circular Economy Goals. 2021.
4. Merli R, Preziosi M, Acampora A, Lucchetti MC, Petrucci E. Recycled fibers in reinforced concrete: A systematic literature review. *J Clean Prod.* 2020;248:119207. <https://doi.org/10.1016/j.jclepro.2019.119207>.
5. Wang Y, Wu HC, Li VC. Concrete Reinforcement with Recycled Fibers. *J Mater Civ Eng.* 2000;12(4):314–9. [https://doi.org/10.1061/\(ASCE\)0899-1561\(2000\)12:4\(314\)](https://doi.org/10.1061/(ASCE)0899-1561(2000)12:4(314)).
6. Xie J, Kou S, Ma H, Long W-J, Wang Y, Ye T-H. Advances on properties of fiber reinforced recycled aggregate concrete: Experiments and models. *Constr Build Mater.* 2021;277:122345. <https://doi.org/10.1016/j.conbuildmat.2021.122345>.
7. Bui NK, Satomi T, Takahashi H. Recycling woven plastic sack waste and PET bottle waste as fiber in recycled aggregate concrete: An experimental study. *Waste Manag.* 2018;78:79–93. <https://doi.org/10.1016/j.wasman.2018.05.035>.
8. Ahmed HU, Faraj RH, Hilal N, Mohammed AA, Sherwani AFH. Use of recycled fibers in concrete composites: A systematic comprehensive review. *Compos Part B Eng.* 2021;215:108769. <https://doi.org/10.1016/j.compositesb.2021.108769>.
9. Meesala CR. Influence of different types of fiber on the properties of recycled aggregate concrete. *Struct Concr.* 2019;20(6):1656–69. <https://doi.org/10.1002/suco.201900052>.
10. Tran NP, Gunasekara C, Law DW, Houshyar S, Setunge S, Wirzen A. Comprehensive review on sustainable fiber reinforced concrete incorporating recycled textile waste. *J Sustain Cem Based Mater.* 2022;11(1):28–42. <https://doi.org/10.1080/21650373.2021.1875273>.
11. Grzymiski M, Musiał M, Trapko T. Mechanical properties of fibre reinforced concrete with recycled fibres. *Constr Build Mater.* 2019;198:323–31. <https://doi.org/10.1016/j.conbuildmat.2018.11.183>.
12. Savruk MP, Kazberuk A. Stress Concentration at Notches. Springer International Publishing Switzerland; 2017.
13. Kosior-Kazberuk M, Kazberuk A, Bernatowicz A. Estimation of Cement Composites Fracture Parameters Using Deformation Criterion. *Mater.* 2019;12(24).
14. Kazberuk A. Application of the Deformation Fracture Criterion to Cracking of Disc Specimens with a Central Narrow Slot. *Acta Mech Autom.* 2022;16(4).
15. Kazberuk A. Slip bands at the tips of narrow slot in Brazilian notched disk — plane deformation. *Acta Mech Autom.* 2024;18(4):737–742. <https://doi.org/10.2478/ama-2024-0080>

The work has been accomplished under the research projects LIDER14/0206/2023 and WZ/WM-IIM/3/2020.

Julita Krassowska:  <https://orcid.org/0000-0001-9209-1285>

Andrzej Kazberuk:  <https://orcid.org/0000-0003-4179-0312>



This work is licensed under the Creative Commons BY-NC-ND 4.0 license.